UNIVERSITAT JAUME I

Programa de Doctorado en Tecnologías Industriales y Materiales

Escuela de Doctorado de la Universitat Jaume I

Hydrodynamic and biochemical Computational Fluid Dynamic modelling of full-scale anaerobic digesters for wastewater treatment

PhD Thesis

Memoria presentada por María Rosario Arnau Notari para optar al grado de doctora por la Universitat Jaume I

Autora

MARIA ROSARIO\|ARNAU\|NOTARI
Firmado digitalmente por MARIA ROSARIO\|ARNAU\|NOTARI
Fecha: 2022.01.27 09:11:34 +01'00'

María Rosario Arnau Notari

Directores

CHIVA VICENT SERGIO - 52794899D
Firmado digitalmente por CHIVA VICENT SERGIO - 52794899D
Fecha: 2022.01.26 22:19:40 +01'00'

Sergio Chiva Vicent

MARTINEZ CUENCA RAUL - 24385733Y
Firmado digitalmente por MARTINEZ CUENCA RAUL - 24385733Y
Fecha: 2022.01.27 09:06:50 +01'00'

Raúl Martínez Cuenca

Castelló de la Plana, 26 de enero de 2022

This doctoral thesis has been carried out thanks to the financial support provided by:

- Predoctoral scholarship (ACIF/2016/255) from Generalitat Valenciana - Conselleria de Educación, Investigación, Cultura y Deporte.
- Mobility grant (BEFPI/2018/067) from Generalitat Valenciana - Conselleria de Educación, Investigación, Cultura y Deporte.

“Comienza por hacer lo que es necesario; después lo que es possible, y de repente, estaràs haciendo lo imposible.”

San Francisco de Asís

"Start by doing what is necessary; then what is possible, and suddenly you are doing the impossible."

St. Francis of Assisi

AGRADECIMIENTOS

En primer lloc he d'agrair l'acollida del Grup de Fluids Multifàsics de la Universitat Jaume I, equip amb el que he APRÉS des del moment que vaig xafar el despatx de Sergio.

He de dedicar unes paraules als meus directors de tesi per la seua dedicació a aquesta i per descobrir-me el món CFD, m'heu ensenyat una nova professió que de veritat m'ha engantxat. A Sergio Chiva, per vore en mi a una persona a la que poder ensenyar una petita part del seu coneixement. Per les xarrades tècniques sobre la tesi i també per les oportunitats que m'ha brindat al participar a la Càtedra FACSA-UJI o allà on hem anat de visites tècniques. Per el temps que ha pogut traure i per empapar-se de temes que ell desconeixia com la digestió anaeròbia. A Raúl por aportar la versión más física (y no tan física) a esta tesis, por mirar desde una óptica que a otros o a mí se nos escapa, no sólo en sus investigaciones. Por sus aportaciones clave en puntos donde me encontraba perdida y por su dedicación personal en varias ocasiones.

Moltes gràcies a tots els que hem anat passant per tallers aquests anys, Javier, Carlos, Guillem, Jose, Lledó, Pablo, Rubén, Salva i Aina, pel suport tècnic i per les converses als dinars i sobretaules amb les que crec que he estat mentalment sana i que han salvat moltes hores de treball i maldecaps. Gràcies també als nouvinguts, Sergio Iserte, Paloma, Delia i Álvaro amb els que estem treballant colze a colze també actualment. Heu sigut i sou un equip que depara moltes alegries personalment i professionalment.

También quiero acordarme de las personas del grupo de Nanofluidos y la Cátedra, Rosa, Núria, Leo, Alexandra, Laura y José Luis, con los que he compartido laboratorio, reuniones y eventos de la Cátedra. También quiero agradecer a Guillermo Berlanga por hacer hueco al trabajo del grupo de investigación en sus proyectos de IDi y por facilitar junto a Javier la creación de HYDRENS.

I would also like to thank Jules van Lier and Merle de Kreuk for their time during my stay at TU Delft, for the discussions on biogas production and for passing on their process knowledge to me. Also to the colleagues with whom I shared my time there Celma, Noor, Dhruv, Adi, Peng, Antonio and Frederik, and especially to Nuria, Alba and David for taking us away from home and discovering the country together.

Por último, quiero agradecer a mi familia y a Álex su apoyo, paciencia y tiempo de espera siempre y principalmente durante este tiempo.

CONTENT

RESUMEN

La digestión anaerobia es uno de los tratamientos biológicos más utilizados para la estabilización de los lodos de depuradora, el estiércol del ganado o los residuos orgánicos de la agricultura o la industria alimentaria. De hecho, su capacidad para producir biogás o biometano está captando cada vez más la atención del público y de las administraciones debido a la implantación de la economía circular y la creciente crisis climática. De hecho, la mayoría de los esfuerzos realizados en los digestores anaerobios se centran en aumentar la producción de biogás, dejando como objetivo secundario la estabilización de los lodos. En este contexto en el que se da prioridad a la producción de biogás, es aconsejable asegurar una mezcla homogénea de los fangos. Esta mezcla se consigue mediante sistemas de agitación que generan una intensa mezcla en el interior de los digestores anaerobios. Sin embargo, la eficacia de esta mezcla se pone de manifiesto cuando se producen volúmenes muertos o una baja producción de biogás. La técnica de la Dinámica de Fluidos Computacional (CFD) permite analizar la mezcla y la hidrodinámica de estas unidades de proceso, por lo que actualmente es una técnica muy extendida.

En primer lugar, en esta tesis doctoral se ha estudiado la hidrodinámica de un digestor anaerobio a gran escala mediante modelos CFD monofásicos no Newtonianos, evaluando los sistemas de mezcla mediante diferentes escenarios CFD. El modelo CFD se validó de forma exhaustiva y global mediante una curva experimental de 76 días de Distribución del Tiempo de Residencia (DTR), y se evaluaron diferentes parámetros de mezcla en términos de generalidad y utilidad. Los parámetros de mezcla local y global fueron sensibles y ayudaron a definir las diferencias de los escenarios de mezcla, pero los parámetros de diseño fallaron en esta tarea. El escenario B100, con un agitador mecánica instalado en el centro, resultó ser el mejor y más eficiente escenario de mezcla. De hecho, los tiempos de homogeneización se obtuvieron mediante parámetros de mezcla local y fueron inferiores a 30 minutos en el caso de los escenarios de mezcla intensiva e inferiores a 1 hora en el escenario base. Esta información útil se utilizó para definir un régimen de mezcla eficiente con adición de cosubstratos.

A continuación, estos escenarios CFD se utilizaron para evaluar la solidez y la sensibilidad de los criterios de volumen muerto de la literatura. Sin embargo, no cumplieron este objetivo, por lo que se propusieron nuevos criterios de volumen muerto y se calibraron con datos experimentales. Los nuevos criterios consideraron la fuerza de flotación y la dispersión de la turbulencia y son de aplicación general en los modelos CFD de digestores anaerobios a escala real.

En una segunda parte, se desarrolló un nuevo solver en un código CFD de código abierto para acoplar un modelo biológico, es decir, el Modelo de Digestión Anaerobia 1, con la hidrodinámica. El solver incluía el cálculo del pH, la transferencia simplificada del líquido al gas y las ecuaciones del proceso de

digestión anaerobia, denominándose *ADM1Foam*. Se probó a escala de laboratorio y a la escala real estudiada anteriormente: Por un lado, la escala de laboratorio permitió confirmar la correcta implementación del modelo mediante datos experimentales y modelos 0D-CSTR. Por otro lado, se simularon diferentes regímenes de mezcla con este solver en ambas configuraciones, con el fin de obtener algunos conocimientos sobre la relación entre el rendimiento de la digestión anaeróbica y la mezcla. En resumen, el solver reprodujo las simulaciones transitorias y demostró que una mezcla menor sería perjudicial para el proceso de digestión. Este solver es la base para el desarrollo de nuevos modelos avanzados considerando simulaciones CFD bifásicas.

La última parte está dedicada a evaluar el comportamiento hidrodinámico de las burbujas de biogás ascendentes en el interior de una matriz de lodos anaeróbicos mediante modelos bifásicos Euler-Euler de Volumen de Fluido (VOF). Se probaron diferentes tamaños de burbuja y dos tipos de fango anaerobios, de modo que se evaluó la viscosidad aparente, la velocidad terminal y la forma. A partir del análisis del tamaño de las burbujas, las grandes mostraron una gran velocidad terminal, por lo que se fusionarían con las pequeñas en su trayectoria hacia la cámara de biogás. En cuanto a los tipos de lodo, el digestato reveló una menor viscosidad aparente, por lo que se observó una mayor velocidad terminal y formas de burbujas más anchas en contraste con los fangos activos espesados. Además, se probaron diferentes coeficientes de arrastre de bibliografía que pueden utilizarse en modelos CFD de dos fases. No obstante, se propuso una nueva correlación de arrastre de acuerdo con los resultados obtenidos. Al final, las burbujas de biogás mejoran la mezcla local en la matriz de fango anaerobio, por lo que su contribución a la mezcla global debería ser considerada en futuros modelos CFD.

Por tanto, la modelización CFD es una herramienta potente y alternativa para modelizar los digestores anaerobios, reproduciendo su mezcla local y global con modelos monofásicos y bifásicos. Por otro lado, la validación experimental de los modelos CFD tanto de sus propiedades reológicas como de su comportamiento hidráulico es crucial para garantizar modelos precisos y fiables. En un futuro próximo, el CFD podrá reproducir la generación de biogás y la transferencia de masa desde la fase líquida a la fase gaseosa resultante del proceso de digestión anaerobia.

SUMMARY

Anaerobic digestion is one of the most widely used biological treatments for the stabilisation of the sludge from wastewater treatment plants, livestock manure or organic waste from agriculture or the processed food industry. Indeed, its capability to produce biogas or biomethane is gaining more and more attention from the public and administrations due to the implementation of the circular economy and the rising climate crisis. In fact, most of the efforts made on anaerobic digesters are focused on increasing biogas production, leaving sludge stabilisation as a secondary objective. In this context where priority is given to biogas production, it is advisable to ensure homogeneous mixing of the sludge. This mixing is achieved by means of agitation systems that generate an intense mixing inside the anaerobic digesters. However, the efficiency of this mixing becomes evident when dead volumes or low biogas production occur. The Computational Fluid Dynamics (CFD) technique allows the mixing and hydrodynamics of these process units to be analysed, which is why it is now a widespread technique.

Firstly, in this PhD thesis, the hydrodynamics of a full-scale anaerobic digester has been studied by means of non-Newtonian single-phase CFD models, evaluating the mixing systems by means of different CFD scenarios. The CDF model was comprehensively and globally validated using an experimental 76-day RTD curve, and different mixing parameters were evaluated in terms of generality and usability. The local and global mixing parameters were sensitive and helped to define the differences of the mixing scenarios, but the design parameters failed in this task. B100 scenario, with a mechanical propeller installed in the centre proved to be the best and most efficient mixing scenario. Indeed, homogenisation times were obtained by means of local mixing parameters and were less than 30 minutes in the case of intensive mixing scenarios and less than 1 hour in the base scenario. This useful information was used to define an efficient mixing regime with the addition of co-substrates.

These CFD scenarios were then used to assess the robustness and sensitivity of the dead volume criteria from the literature. However, they did not fulfil this goal so new dead volume criteria were proposed and calibrated with experimental dead volume data. The new criteria considered the buoyancy force and low turbulence dispersion and are generally applicable in CFD models of full-scale anaerobic digesters.

In a second part, a new solver was developed in an open-source CFD code to couple a biological model, i.e., the Anaerobic Digestion Model 1, with hydrodynamics. The solver included the pH calculation, simplified liquid-gas transfer and the equations of the anaerobic digestion process and was called

ADM1Foam. It was tested at lab-scale and at the full-scale studied previously: On the one hand, the lab-scale allowed to confirm the correct implementation of the model by means of experimental data and 0D-CSTR models. On the other hand, different mixing regimes were simulated with this solver in both configurations in order to gain some knowledge about the link between anaerobic digestion performance and mixing. In summary, the solver reproduced transient simulations and showed that lower mixing would be detrimental to anaerobic digestion process. This solver is the basis for the development of new advanced models considering two-phase CFD simulations.

The last part is devoted to evaluating the hydrodynamic performance of rising biogas bubbles inside an anaerobic sludge matrix by means of two-phase Euler-Euler Volume of Fluid models. Different bubble sizes and two types of anaerobic sludge were tested, so that apparent viscosity, terminal velocity and shape were evaluated. From the bubble size analysis, the large bubbles showed large terminal velocity, so they would coalesce with the small bubbles on their trajectory to the biogas chamber. As for the sludge types, the anaerobic digestate revealed a lower apparent viscosity, thus a higher terminal velocity and wider bubbles shapes were observed in contrast to waste anaerobic sludge. Moreover, different drag coefficients from literature that can be used on two-phase CFD models were tested. However, a new drag correlation was proposed according to the obtained results. In the end, the biogas bubbles enhanced the local mixing in the anaerobic sludge matrix, so that their contribution to global mixing should be considered in future CFD models.

Accordingly, CFD modelling is a powerful and alternative tool for modelling anaerobic digesters, reproducing their local and global mixing with single-phase and two-phase models. On the other hand, experimental validation of CFD models of both their rheological properties and their hydraulic behaviour is crucial to ensure accurate and reliable models. In the near future, CFD will be able to reproduce the biogas generation and mass transfer from the liquid to the gas phase resulting from the anaerobic digestion process.

1. PROBLEM STATEMENT, OBJECTIVES AND THESIS OVERVIEW

1.1. BACKGROUND AND PROBLEM STATEMENT

In 2015 the United Nations General Assembly adopted the Sustainable Development Goals (SDGs), 17 ambitious goals, each with specific targets to be achieved by 2030 or earlier (United Nations, 2015). Currently, more than 80% of wastewater resulting from human activities is discharged into rivers or the sea without any treatment, causing its pollution (United Nations, 2021). In relation to wastewater and the lack of access to water and sanitation, SDG6 was agreed aiming to "Ensure availability and sustainable management of water and sanitation for all".

On the other hand, the United Nations believes that "urgent action is needed to decrease our dependence on raw materials as well as to increase recycling and circular economy approaches to alleviate pressure and impacts on the environment"(United Nations, 2020). In this sense, Waste Water Treatment Plants (WWTPs) are undergoing a process of change towards circular economy, so that they are Wastewater Resource Recovery Facilities (WRRFs). Thus, WRRFs not only purify and recover water, but also recover nutrients (N and P), organic compounds (biopolymers, PHAs) and energy.

In WRRFs, anaerobic digestion is a key process unit that allows the recovery of digested sludge, which is used as agricultural compost or fuel, and a biogas with a high methane content as a way of recovering the energy contained in the organic matter. In addition, wastewater treatment using anaerobic biological processes may be the answer to advancing wastewater treatment and meeting SDG6.

However, although the microbiological process of the anaerobic process is known in broad terms and the mixing is controlled on a laboratory scale, there is still a great lack of knowledge about the operation on a large scale. In particular, the lack of knowledge in the upscaling of the process lies in the relationship between sludge mixing and biogas production, i.e., the most efficient mixing intensity to maximize the biogas production is under study at lab-scale and remains unknown at upscaling.

In this respect, Computational Fluid Dynamics (CFD) models of anaerobic digesters represent a breakthrough in this respect, as they display the movement of sludge within the digesters (Batstone et al., 2015). Conversely, the challenging observation of the interior of the digesters coupled with the complexity in the control of the biological process, makes the validation of CFD models in anaerobic digesters extremely limited.

Therefore, the challenges focus on creating validated CFD models coupled with biochemical models that explain the physical and biochemical processes that take place within anaerobic digesters. Some phenomena to be taken into account in these CFD models could be mixing, biochemical processes,

sludge settling, biogas formation and movement and mass transfer from the liquid to the gas phase. In short, the motivation of this thesis stems from the need to join mixing and biogas production to expand our knowledge of their bond by means of CFD modelling.

This thesis has been developed in the Department of Mechanical Engineering and Construction of the Universitat Jaume I (UJI), in the Multiphase Flow research group, and economically supported by a predoctoral grant (ACIF/2016/255) from Generalitat Valenciana (Conselleria de Educación, Investigación, Cultura y Deporte).

1.2. OBJECTIVES OF THIS RESEARCH

The general objective of this doctoral dissertation was to bridge our knowledge gap about several anaerobic digestion phenomena, including settlement, mixing, transport of substances, reactions and biogas production, by means of CFD modelling

In order to meet this general objective, the following specific objectives were considered:

- To conduct a literature review and evaluate mixing parameters for the study of anaerobic digestion in full-scale digesters.
- To demonstrate the validation of full-scale anaerobic digestion CFD models with inert tracer experiments.
- To evaluate the dead volume criteria in terms of usability and sensitivity in full-scale digesters and compare them with experimental measurements in full-scale anaerobic digesters.
- To seek energy-efficient mixing regimes that avoid the formation of dead volumes while ensuring homogenous sludge mixing.
- To implement the ADM1 model in a CFD code and validate it against experimental data to reproduce the microbial processes occurring in anaerobic digestion.
- To extend the knowledge on the relationship between mixing and organic material degradation in anaerobic digestion.
- To elucidate the mixing capacity of biogas production in anaerobic digestion using two-phase CFD models.

1.3. THESIS OVERVIEW

The present thesis is divided into 7 chapters and 9 Appendices.

This first chapter is devoted to showing the motivations, the general and specific objectives, and the thesis overview. In Chapter 2, the state of the art of Anaerobic Digestion and Computational Fluid Dynamics (CFD) are presented.

The results obtained throughout the thesis are shown in chapters 3, 4, 5, and 6 as depicted in **Figure 1.1**:

- Chapter 3 provides an extended analysis of several mixing parameters and dead volume criteria by means of a full-scale anaerobic digester CFD modelling with different mixing scenarios. The hydraulic behaviour of this full-scale digester has been checked experimentally by an experimental tracer test to obtain the RTD curve (72 days) so, it serves to validate the CFD model.
- Chapter 4 develops a new solver to include the Anaerobic Digestion Model 1 in a single-phase CFD solver. It is applied to a lab-scale experimental anaerobic digester and compared with a 0D CSTR framework to check its correct implementation.
- Chapter 5 applies the new ADM1-CFD solver to the full-scale setup in chapter 3 to examine anaerobic digestion performance in terms of degradation and methanogenesis in non-ideal hydrodynamic behaviour anaerobic digesters.
- Chapter 6: The rising of single bubbles in the sludge is simulated by using the volume of fluid method. The formulation for the drag coefficient for Non-Newtonian fluids is introduced, a new drag coefficient suitable for anaerobic digestion is proposed, and the effects of bubble induced local mixing are studied.

Finally, Chapter 7 is devoted to the main conclusions obtained in the previous chapters and to future research topics.

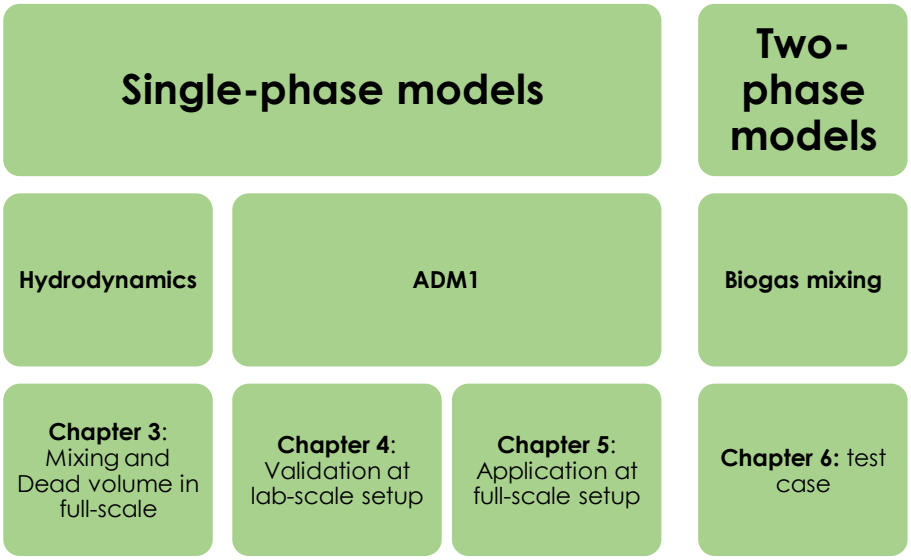

Figure 1.1: Outline of the results of this dissertation.

2. STATE OF THE ART

2.1. ANAEROBIC DIGESTION

At a wastewater treatment plant (WWTP), solids are one of the by-products from main wastewater treatments such as Conventional Activated Sludge (CAS). For this reason, their treatment and disposal in safety conditions has been one of the most costly and difficult problems since the beginning of wastewater engineering (Appels et al., 2008; Tchobanoglous et al., 2004). However, the current framework of the climate crisis and the rising circular economy have changed the outlook of WWTPs to Water Resource Recovery Facilities (WRRFs). Thus, the large amount of sludge produced in WWTPs, and the possible by-products derived from its treatment represent a great opportunity to the new WRRFs.

Different sludge operations prior to the disposal of biosolids exist but the main biological treatment is anaerobic digestion. After a thickening process, anaerobic digestion is used for the stabilisation of the sludge, in which microorganisms break down the biodegradable material in the sludge while oxygen and nitrate are excluded. In this process, the organic matter is transformed into biogas (60-70% methane) so that the resulting sludge has a reduced amount of solids, putrescible organic material and pathogens thus meeting the disposal regulations. (Grady et al., 1999; Tchobanoglous et al., 2004)

The advantages and disadvantages of anaerobic treatment processes explain its general interest for wastewater engineering. Some of the advantages are listed below (Appels et al., 2008; Tchobanoglous et al., 2004; van Haandel and van der Lubbe, 2012):

- High quality of digested sludge: Digested sludge is free of pathogens and has reduced organic material concentration.
- Low energy requirements: the anaerobic treatment requires energy consumption for mixing and increase of temperature. Aerobic processes are high-energy consumers as aeration is essential and requires more energy than an anaerobic process.
- Net energy producer: The biogas can be used as an energy source to meet most of the energy needs of the WWTP so that the process is a net energy producer (Li, 2018; Tchobanoglous et al., 2004).
- Lower biomass production: as already mentioned, the high biomass production of CAS is the major drawback of this process so low biomass production processes are desirable.
- Most organic compounds are degradable with a biological adaptation period: low degradable material is transformed by anaerobic microorganisms after long acclimation periods.
- Higher Volumetric Loading: the organic loading rate (OLR) of an anaerobic process is higher than that of an aerobic process so smaller

tanks and less area are required for the same organic loading rate.

The limitations of anaerobic processes are described below (Tchobanoglous et al., 2004; van Haandel and van der Lubbe, 2012):

- Expensive construction: the system is large and has specific and sophisticated equipment for heating, mixing and biogas control.
- Long start-up periods: the development of complete anaerobic biomass requires months for its complete development while aerobic biomass is ready in a few days.
- Requires pH and alkalinity control: the high toxicity of low pH to the anaerobic microorganisms makes the control of pH and alkalinity compulsory. If the amount of alkalinity provided is not sufficient to preserve an optimum pH, it can be added.
- Nitrogen and phosphorus are not removed: the biological nutrient recovery is only available when anaerobic and aerobic processes are coupled.
- Sensitive to temperature: the biological reaction rates of anaerobic microorganisms are extremely temperature dependent so that maximum reaction rates are achieved at higher temperatures, traditionally above 25ºC.
- Toxics may inhibit microorganisms: the presence of inorganic and organic substances from the influent or by-products from anaerobic activity can inhibit the metabolism of some anaerobic microorganisms reducing their reaction rates.
- Source of odours and corrosive gases: oxidized sulphur compounds from the influent may produce hydrogen sulphide gas (H2S) which is malodorous and corrosive to metals. Additionally, oxidized sulphur compounds can reduce the methane yield due to competition between sulphate-reducing bacteria and methanogenic bacteria.

Despite all these drawbacks, in recent years, anaerobic biological treatment has been widely introduced due to biogas production and low energy cost. In fact, given the opportunity offered by anaerobic processes for green hydrogen production and new European policies (Lambert, 2020), the implementation of anaerobic processes is expected to increase in WRRFs and beyond.

Furthermore, it has been extended to waste water treatment and other waste streams (e.g. agriculture and livestock waste, municipal solid waste,..) with high concentration of biodegradable organic compounds (Grady et al., 1999; Tchobanoglous et al., 2004). In this regard, the addition of co-substrates has become a widespread practice for increasing the anaerobic digester organic load and improving the biogas production rate in medium and large size plants. In fact, the spread of this practice on a small scale also makes anaerobic

digestion technically, environmentally and economically feasible (Arias et al., 2020).

2.1.1. Description of the process

In anaerobic digestion, microorganisms decompose organic material from biosolids to simpler compounds, mainly methane and carbon dioxide, depending on the nature of the organic compounds. These simple compounds escape from the system in the form of gas so thereby reducing the organic load of the biosolids. The biogas produced can be used as an energy source for consumption at the WWTP or for injection into the gas or electricity networks.

The anaerobic digestion process is summed up in 5 stages (Figure 2.1):

- (1 and 2) Disintegration and hydrolysis: In these stages, extracellular processes, which may be biological (hydrolysis) or non-biological (disintegration), break down large organic compounds (dead cells and particulate feed) into simpler soluble constituent parts. Thus, composite particles are broken down into carbohydrates, proteins and lipids and, which are converted into monosaccharides, amino acids and long chain fatty acids (LCFA), respectively. This stage takes place under anaerobic and aerobic conditions and, being first step in the chain of processes, is decisive to methanogenesis, as it regulates the available soluble substrate.
- (3) Acidogenesis: the biological breakdown of amino acids and sugars is continued by acidogenic bacteria where they serve as electron donors and electron acceptors. Organic compounds are degraded by fermentative processes to volatile fatty acids (VFA), acetic acid and hydrogen.
- (4) Acetogenesis: in this stage acetogenic bacteria transforms LCFA and VFA (propionic, butyric and valeric acid) into acetic acid and hydrogen which are direct precursors of methane. This process is considered an oxidation reaction that needs an external electron acceptor, either carbon dioxide or hydrogen ions, which are produced in acidogenesis. Thus, this stage generates hydrogen gas as the main electron transport agent.
- (5) Methanogenesis: the terminal stage includes the processes in which acetic acid and hydrogen are transformed into methane through methanogenic archaea. There are two main groups of methanogenic archaea: acetoclastic archaea, which split acetic acid into methane and carbon dioxide in the acetoclastic methanogenesis; and hydrogenotrophic archaea, which transform hydrogen gas (electron donor) and carbon dioxide (electron acceptor) into methane in a process called hydrogenotrophic methanogenesis. Hydrogenotrophic archaea reduce carbon dioxide by means of hydrogen gas consumption thus helping to maintain balanced hydrogen concentrations for

microorganism survival. In addition, as the energy from the hydrogen has been transferred to methane gas that can escape from the liquid phase, the energy content of the liquid is reduced. Nonetheless, it is thought that approximately two-thirds of the methane gas from anaerobic digestion is produced by acetoclastic mehtanogenesis and one-third from hydrogenotrophic methanogenesis (Grady et al., 1999).

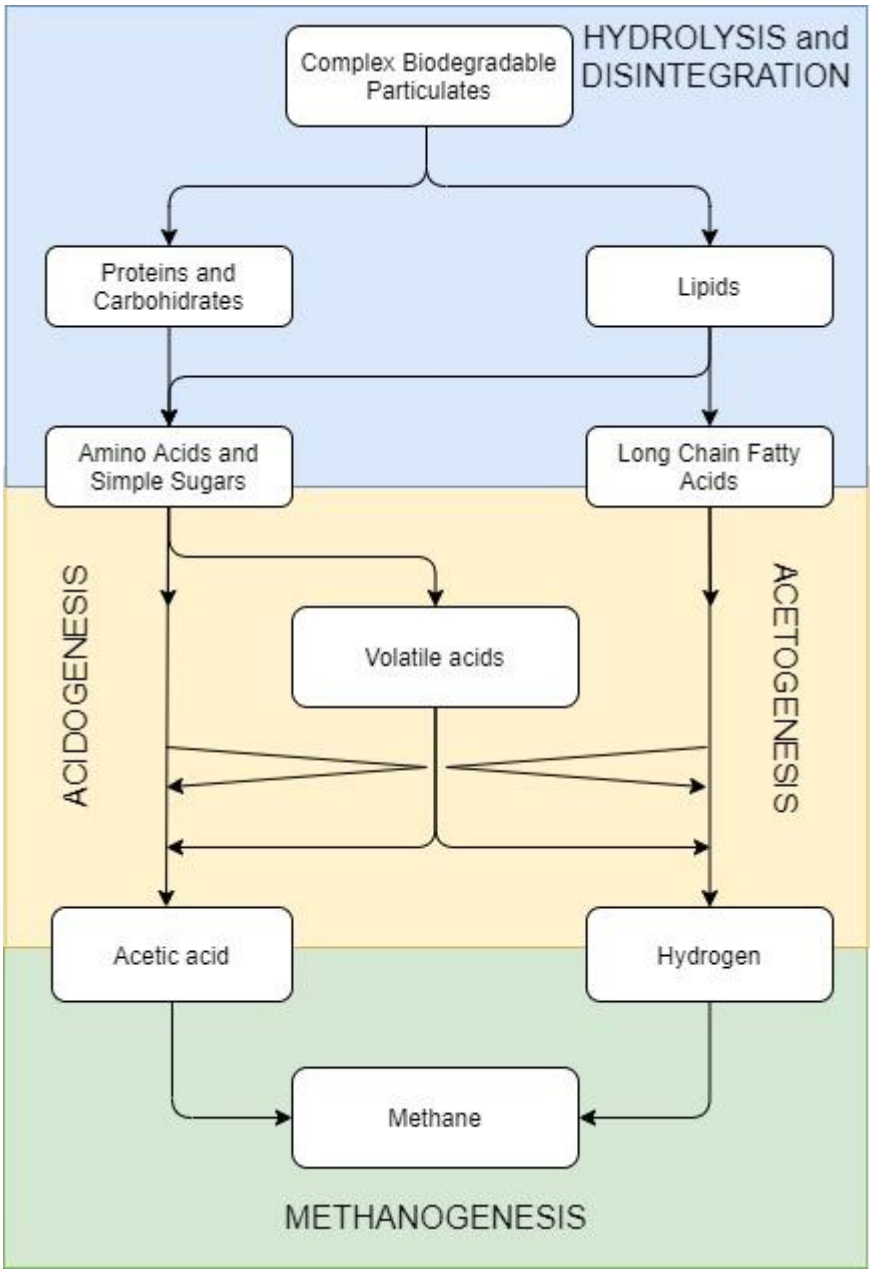

Figure 2.1: Biological transformations at the anaerobic digestion process. Based in Grady et al., (1999)

These different stages occur simultaneously in the digester resulting in a joint growth of all microorganisms involved in the process. Moreover, as most of them depend on the products of the preceding microorganisms, a symbiotic ecosystem is formed inside the anaerobic digester.

Based on the energy balance, some of the electrons from the raw sludge are incorporated into the microorganisms in the new cell material but most of them are removed from the liquid and recovered as methane gas. This reduces the Chemical Oxygen Demand (COD, a measure of the available electrons) of the system, as 16 grams of methane removed means a reduction of 64 grams of COD from the liquid.

The following are the different environmental factors that are important in anaerobic digestion: solids retention time, hydraulic retention time, temperature, pH, alkalinity, inhibitory substances, and organic loading rate.

2.1.2. Solids and Hydraulic Retention Time

Solids Retention Time (SRT) and Hydraulic Retention Time (HRT) are typical operating and design parameters used in wastewater engineering. The SRT represents the average period that solids are retained in the tank, while the HRT defines the average period that its content remains in the tank. Ideally, there is no liquid-solids separation in anaerobic digesters, neither recirculation nor purge of the sludge. Accordingly, HRT and SRT are assumed to have the same value (Grady et al., 1999). In practice slight separation might occur, but there have been no reports noting any difference between these two times. Typical SRTs range from 15 to 20 days which is ten times greater than typical SRTs for activated sludge. Long SRTs are required as methanogens have low growth rates. Additionally, long SRTs also benefit the minimization of inhibitory compounds and influent fluctuations. (Appels et al., 2008; Grady et al., 1999). Due to the great dependency of SRT and temperature, this parameter is discussed extensively in the next section.

2.1.3. Temperature

The anaerobic process is a biological process, so its efficiency is largely dependent on temperature. There are three temperature ranges for anaerobic processes:

- Thermophilic: with temperatures between 50 and 60ºC although the maximum value is always 54ºC.
- Mesophilic: with temperatures between 30 and 40ºC, the most commonly used value being 35ºC.
- Cryophilic: with temperatures below 30ºC.

The higher the temperature, the more the metabolism of the microorganisms accelerates, and greater organic loads and removal efficiencies are achieved. The maximum growth of methanogenic archaea is established in the upper two temperature ranges although growth is possible at lower temperature values. Many authors have found that at lower temperatures, high efficiencies are also possible if solids retention times are increased (Grady et al.,

1999).

The temperature of the digester affects all types of bacteria in the process so many authors have studied this parameter to predict the impact that its annual variation will have on the process. Figure 13.19 from Grady et al., (1999), depicts the relationship between temperature, SRT and effluent quality. The analysis of this figure shows that complete stabilisation of the sludge is achieved at a very different SRT depending on the temperature: at a lower temperature, a greater SRT is required to stabilise the sludge and lower effluent quality is achieved. On the one hand, this phenomenon highlights the need for post-treatment of the effluent at temperatures below 25ºC and establishes 25ºC as the minimum threshold temperature for the correct stabilisation of urban wastewater sludge. On the other hand, it is stated that a SRT of 10 days is feasible but with a very low organic matter removal rate and a very low degree of sludge stabilisation.

In brief, the operation of a thermophilic anaerobic digester results in high energy consumption and greater instability of the process. But it has other benefits: firstly, it increases the efficiency of the process so that a smaller size of digester is required, and secondly, it improves the quality of the digestate, as the lower organic matter and water content reduces the need for post-treatments to degrade organic material and pathogens. However, at full-scale the benefits do not outweigh the high energy consumption and the difficulty of thermophilic temperature operation, so mesophilic ranges are most commonly used.

2.1.4. pH

Control of pH and alkalinity is one of the most important factors in the maintenance of anaerobic processes, because if the pH deviates from a narrow range, the methane yield is reduced, and the process may even be completely inhibited. Hydrolytic and acidogenic bacteria are not affected by pH variations whereas, acetogenic and methanogenic microorganisms are only active in a defined pH range.

The microorganisms most affected by pH variations are the methanogenic archaea. Their activity decreases when the pH is outside the optimum range established between 6.8 and 7.4. A pH between 6.4 and 7.8 is appropriate to maintain the activity of these archaea but higher or lower values are unfeasible for methanogens. This non-viability is due to the high toxicity of the non-ionized forms of volatile acids and ammonia when the pH is less than 6.4 and more than 7.8 respectively (Grady et al., 1999).

Acidogenic bacteria are also affected by pH and, although they do not decrease their activity, they do change their metabolic pathways to other products. For example, when there is a hydrogen build-up, methanogens are not able to degrade it as fast as acetic acid so that hydrogen will accumulate and pH decreases. Accordingly, acidogenic bacteria change their metabolism

towards other metabolic routes forming higher molecular weight VFA, i.e., propionic and butyric.

In conclusion, the narrow pH range of methanogens' activity and different VFAs bulk production are responsible for the anaerobic processes' sensitivity to pH variations. A high OLR will produce more VFAs which may slightly exceed the maximum capacity of the methanogens to use acetic acid and hydrogen. The VFAs will accumulate and lower the pH, so the methanogens will reduce their activity and, as result, a build-up of VFAs and a further pH decrease will occur. Without correction, the methanogens will cease their activity and the anaerobic process will be "sour" or "stuck". (Grady et al., 1999).

To avoid such a phenomenon, the drop in pH must be stopped by altering the operational factors that led to the microbiological imbalance in the process. As an example, the pH can be restored by reducing the OLR so that VFAs are consumed or by adding buffer compounds. Alkalinity therefore plays a very important role as it represents the buffering capacity of the system: the higher the alkalinity, the smaller the variations in pH will be in the reactor.

Sodium bicarbonate is the main buffer reagent used in anaerobic processes, although others such as lime, sodium carbonate and ammonium hydroxide can be used. Buffer capacity is defined as the total alkalinity, which includes the neutralising capacity and part of the VFA and some inorganic bases. Accordingly, the real buffer capacity is only a part of the total alkalinity, and can be calculated as:

$$S_{AlkBic} = S_{AlkTot} - 0.71 \times S_{VFA} \qquad 2.1$$

where S_{AlkBic} is the actual buffer capacity of the reactor as mg/L $CaCO_3$, S_{AlkTot} the total alkalinity and S_{VFA} is the concentration of VFA as acetic acid concentration. A total alkalinity between 2000 and 5000 mg/L $CaCO_3$ is recommended so that a neutral pH can be preserved. (Coyne et al., 2017; Tchobanoglous et al., 2004)

Alkalinity is also consumed by the solubilized carbon dioxide produced in the acidogenesis and methanogenesis stages. Depending on the partial pressure of the carbon dioxide in the biogas, carbon dioxide solubilizes and consumes alkalinity in the form of carbonic acid. Consequently, the carbon dioxide concentration of the biogas indicates the total alkalinity and pH of the digester. Traditionally, when carbon dioxide is between 25 to 45% of the biogas, a neutral pH is also observed.

As VFAs decrease the pH, the stability of the process can also be controlled by the VFAs/alkalinity ratio (Coyne et al., 2017):

- If the VFAs/alkalinity ratio is lower than 0.3, it is possible to maintain the buffer capacity.
- If the ratio is between 0.3 and 0.4, the pH is low and corrective actions must be taken.

- When this ratio is higher than 0.8, methanogenesis will be inhibited.

2.1.5. Inhibitory substances

As explained above, the anaerobic digestion process is inhibited by low pH and the build-up of hydrogen and VFAs but there are also other inhibitory substances such as heavy metals, sulphides and ammonia. Some of the factors that can lead to inhibition are the solubilization of solids with toxic compounds, fast start-ups and antagonism or synergy phenomena.

With regard to toxic substances and their concentration, it is noticeable that microorganisms are able to adapt to high concentrations of toxins when the concentration is progressively increased. In these cases, the process of anaerobic digestion may not be affected.

Some of the inhibitory substances and their inhibitory concentration are listed below (Coyne et al., 2017; Grady et al., 1999):

- Light Metal Cations: some examples of strongly inhibitory substances and their concentrations are calcium at 8000 mg/L, magnesium at 3000 mg/L, potassium at 12000 mg/L and sodium at 8000 mg/L.
- Sulphide: the sulphide ion is a product of sulphate-reducing bacteria, which are responsible for transforming sulphate into sulphur. These bacteria generate a double inhibition in the methanogenic archaea: firstly, the sulphur generated from reduction of the sulphate is toxic for methanogenics and its producers and, secondly, both types of microorganisms compete for the same organic substrate. A sulphide concentration of 200 mg/L is strongly inhibitory.
- Heavy metals: although some of them are micronutrients, some are inhibitory at high concentrations. Examples of inhibitory heavy metals and their concentration are copper at 0.5 mg/L, zinc at 1. mg/L, chrome+6 at 3.0 mg/L and niquel 2.0 mg/L.
- Ammonia: in addition to being an essential nutrient, it is also toxic and inhibitory at certain concentrations. The concentration at which ammonium is toxic depends largely on pH and substrate, so the concentration that inhibits 50% of the methanogenic activity has a wide range. It has also been observed that acetogenic bacteria are more sensitive to ammonia than methanogenic bacteria. Ammonia concentrations of 1500 to 3000 mg/L at pH greater than 7.4 are inhibitory and those above 3000 mg/L are toxic.

2.1.6. Organic Loading Rate

The Organic Loading Rate (OLR) is a measure of the amount of organic substrate fed into the anaerobic digester at a given time. It is referred as (kg of

COD or Volatile Solids)/(m^3·day) and it is considered as the biological conversion capacity of an anaerobic digestion system. Traditionally, the OLRs of anaerobic treatments are higher than those of aerobic treatment and typical high-rate systems are designed from 1.6 to 6.4 kg VS/m^3·d. (Coyne et al., 2017; Tchobanoglous et al., 2004)

This parameter is an important control parameter in continuous systems. Indeed, feeding the system above its sustainable OLR results in the accumulation of inhibiting substances, such as fatty acids or hydrogen, which can lead to low biogas yield (Chen et al., 2008). In such a case, the inflow rate must be rapidly reduced to save the anaerobic process.

2.2. ANAEROBIC DIGESTION CONFIGURATIONS

There are several classifications and configurations of Anaerobic Digestion. The total solids concentration (TS%) is used to make a preliminary categorisation as follows (Mata-Alvarez, 2003):

- Wet: content with 16% or less TS.
- Semi-dry: content between 16% to 22% TS.
- Dry: content between 22% to 40% TS.

The higher the TS%, the smaller the anaerobic digester volume required. In addition, higher concentration of the digestate also leads to different advantages such as lower heat requirements, lower energy requirements for mixing as the digester volume is smaller, less dilution of the biological substrate (higher COD concentration), better control of the process and lower production of supernatant. Consequently, a higher TS% results in cheaper construction and operation of the anaerobic digester, making sludge thickening almost indispensable.

In addition to this classification, the typical configuration of anaerobic digestion is the one that can be made according to the SRT: Low-rate and High-rate anaerobic digestion.

Low-rate or standard-rate digesters (see Figure 2.2a) are neither mixed nor heated, so that a vertical stratification with different layers can be distinguished: scum layer, supernatants, active digesting zone and solids or digested sludge. Consequently, these systems have two functions: the stabilisation of the sludge by anaerobic digestion and the sedimentation of the solids so that supernatant is free of digested solids. In some systems, the settled solids are recirculated which allows operation at high SRTs with low HRTs. This configuration has a low digestion rate as its SRT is no more than15 days. To alleviate this, it is necessary to return the supernatant to the biological reactor or to increase the mixing, so it wouldn't serve as a settling system. Consequently, this configuration is falling into disuse in favour of High-rate digestion. (Appels et al., 2008; Grady et al., 1999; van Haandel and van der Lubbe, 2012)

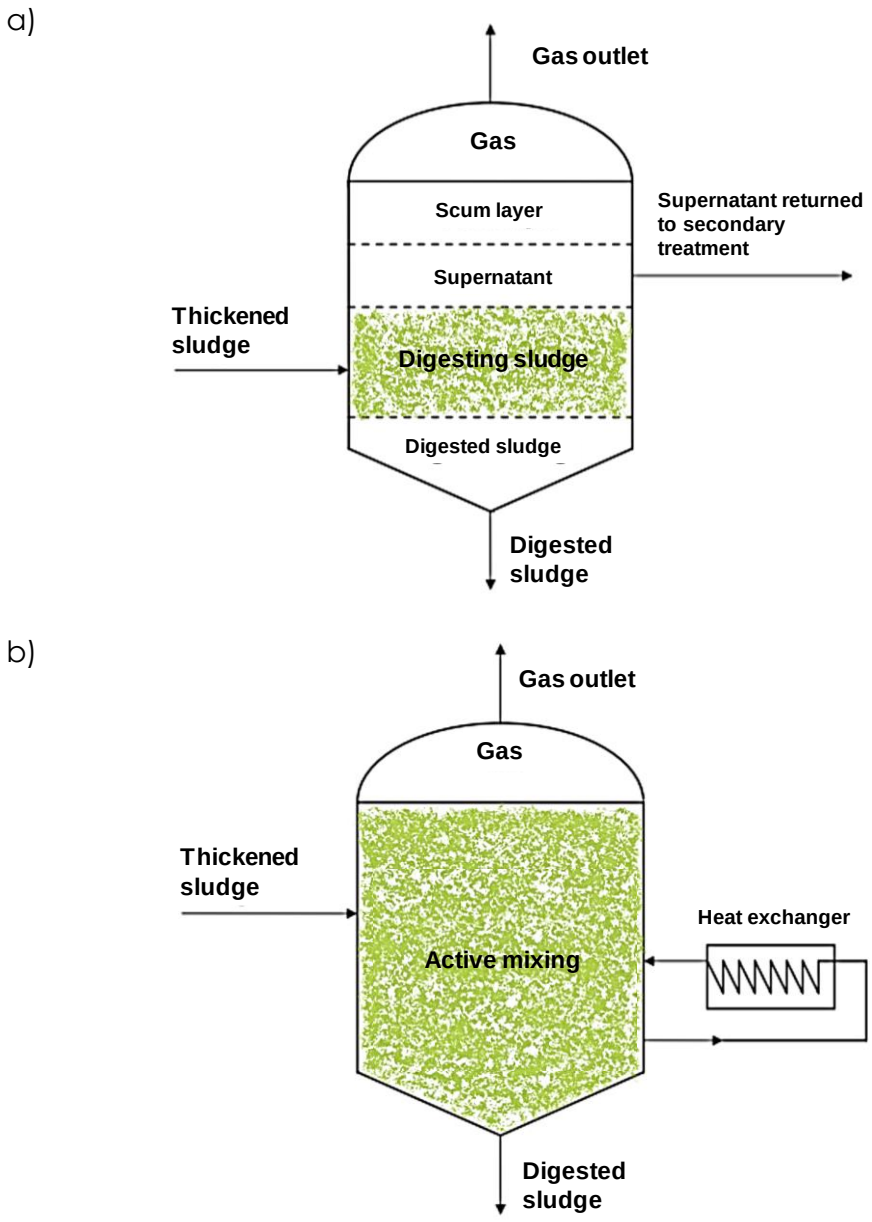

Figure 2.2: Low-rate (a) and high-rate (b) anaerobic digesters. Modified from Appels et al., (2008)

High-rate digesters (see Figure 2.2b) can be one or two units. In a single-stage high-rate digester, temperature and mixing are controlled and constant by means of a heating and a mixing system. This favours the contact of the anaerobic biomass with the substrate, thus achieving higher digestion rates. The heating systems are mainly external heat exchangers, but some of them use internal heat exchangers and steam injection such as the HEATAMIX system. (Appels et al., 2008; Grady et al., 1999; Tchobanoglous et al., 2004; van Haandel and van der Lubbe, 2012)

High-rate digesters with two units are hardly ever used, but they have some advantages over one-unit digesters. The anaerobic digestion process, both

acidogenesis and methanogenesis, occurs mainly in the first digester, which is mixed and heated. In the second digester, settlement takes place, and some anaerobic activity may occur as there is no mixing. This second digester has advantages in terms of maintenance and process flexibility as well as operational stability with optional recycling flows. However, the construction costs of a second digester encourage the construction of sludge lagoons instead of a second digester. (Tchobanoglous et al., 2004; van Haandel and van der Lubbe, 2012)

To ensure the proper performance of a high-rate digester, the following characteristics must be fulfilled (Appels et al., 2008; van Haandel and van der Lubbe, 2012):

- Continuous feeding to guarantee process stability.
- Agitation and mixing to achieve a homogeneous mixture of influent sludge throughout the digester volume.
- Thickening and recycling of the digested sludge at an optimal rate so that viscosity does not affect the process mixture.
- Heating of the sludge to maintain the temperature inside the digester.
- In short, uniform conditions inside the digester are decisive for optimising anaerobic digestion process performance.

2.3. DESIGN OF ANAEROBIC DIGESTERS

Anaerobic digestion has been suggested to stabilize sludge in medium to large WWTPs, i.e., in populations of more than 35,000 equivalent inhabitants. Its function is to stabilize biodegradable organic particulate material, so their efficiency is always defined by Volatile Suspended Solids (VSS) removal (Grady et al., 1999). Traditionally, a digested sludge is required that meets less than 60% of VSS,

The process takes place in enclosed vessels, referred to as anaerobic digesters, so the first step in their design is to select the retention time needed to achieve the desired VSS reduction (Tchobanoglous et al., 2004). As the limiting step in an anaerobic digestion process is generally hydrolysis, its rate will determine the SRT design so the expected VSS removal is achieved. Indeed, VSS removal is dependent on the process temperature, as described in section 2.1.3 (see Figure 13.19 from Grady et al., (1999)). Therefore, SRT and temperature can be considered as the key parameters that control the stabilisation of the sludge's organic content and consequently determine the dimensions of the anaerobic digesters.

Consequently, the design process of the anaerobic digester would follow the steps below:

1. Select a SRT to achieve the desired COD effluent concentration or VSS

removal.

2. Determine the daily sludge production from previous stages of the WWTP, choose a solids concentration and calculate the solids mass in the tank.
3. Based on the daily sludge production and SRT, calculate the volume of the tank since the HRT is equal to the SRT.
4. Calculate the volumetric organic loading.
5. Calculate the gas production.
6. Determine the amount of excess sludge consumed and the nutrient requirements.
7. Determine the alkalinity requirements.

Generally, an anaerobic digester has three elements: a closed vessel, a mixing system, and a heating system. The traditional vessel is a cylindrical concrete tank with diameters between 8 and 35 m and sidewall depths between 5 and 10 m (Grady et al., 1999). Its bottom is cone-shaped, and the cover is made of concrete or steel. Another geometry that improves mixing and reduces grid and scum accumulation is the egg-shaped geometry, due to the steep slope and high height/diameter ratio (Grady et al., 1999; Wu, 2010a).

The tank is always sealed by means of fixed or floating covers. Fixed covers are either dome-shaped or flat and are generally made of concrete, steel, or fibreglass-reinforced polyester. Floating covers are usually made of steel and can either lie on the sludge, without storing biogas, or can leave a space to store gas.

2.3.1. Mixing significance and mixing system

The significance of mixing for the proper performance of an anaerobic digester has been briefly mentioned in section 2.2. Verhoff et al., (1974) studied the physical principles of mixing in anaerobic digesters using fluoride as an inert tracer in gas-mixed digesters. Based on their results, a theoretical analysis of the principles of mixing highlighted the importance of hydrostatic force, natural convection and other fluid forces in mixing inside anaerobic digesters.

Proper mixing avoids hydraulic defects inside tanks and reactors and, in addition, provides the following benefits in anaerobic digestion (Appels et al., 2008; Clair N. Sawyer and Jay S. Grumbling, 1961; Meroney and Colorado, 2009):

- Guarantees uniform chemical, physical and biological conditions inside the digester.
- Allows complete mixing between active sludge and fresh influent sludge.
- Avoids sludge stratification and sand deposition.
- Promotes rapid dispersion of possible inhibiting or toxic compounds.

Uniform conditions inside the tank are decisive for optimizing the

anaerobic digestion process performance. Therefore, a mixing system is always compulsory in this process. Hence, the following mixing systems in anaerobic digesters should be highlighted:

1. Mechanical mixing: This mixing system is carried out by the rotational movement of the impellers. They can be installed directly inside the digester or inside draft-tubes. It is the most efficient mixing system in terms of input power (Lindmark et al., 2014b; Singh et al., 2019) Nonetheless, mechanical mixing has many disadvantages, particularly in terms of maintenance: moving parts inside the tank means a higher risk of breakdown that would lead to shutting down the anaerobic digester. Additionally, equipment replacement costs are considerably higher than for other systems. However, it is the most widely used mixing system in Europe, despite its disadvantages (Lindmark et al., 2014b).
2. Gas mixing: This mixing system consists of a series of pipes that collect the biogas from the cover and inject it back into the bottom part of the anaerobic digester. There are different methods of this system depending on the equipment used to introduce the gas (tubes or diffusers) and the location of the equipment (through the floor or through the roof). Nevertheless, gas mixing encourages scum layer formation (Singh et al., 2019).
3. Slurry recirculation: this mixing system involves a vertical pipe installed inside a central column through which the sludge is sucked from the digester to an external pump. This external pump discharges the evacuated sludge with fresh sludge at different points of the tank. Different commercial systems exist depending on the configuration of the discharge nozzles, e.g., DYNOMIX and ROTAMIX. The discharge points of the sludge must have sufficient vertical and horizontal separation to ensure a locally low speed gradient.
4. Steam injection: is a hybrid configuration used to heat and mix the contents of the digesters. This system entails several tubular units arranged symmetrically outside the digester. Sludge and pressurised biogas are recirculated through the inner sleeve of the tubes, while hot water circulates through the outer sleeve to heat the sludge to the optimum temperature for the digestion process. (Appels et al., 2008).

The design of the mixing system is one of the most important steps in the design of anaerobic digesters, therefore different parameters known as "rules-of-thumb" are described in Section 3.2.1.

2.4. BIOLOGICAL MODELS

The modelling of biological processes is one of the most important parts in the design and operation of WWTPs. The most widely used biological models are the Activated Sludge Model 1 (M. Henze, 1987) and the Anaerobic Digestion

Model 1 (Batstone et al., 2002) created by different task groups of the International Water Association (IWA). They are 0D mass balance models that describe the kinetics of different variables and their relationship. The basic equation for a mass balance in a completely stirred tank reactor (CSTR) system with a single input and output stream, and constant liquid volume ($q_{out} = q_{in}$) is:

$$\frac{dS_i}{dt} = \frac{q_{in}S_{in,i}}{V_{liq}} - \frac{S_i q_{out}}{V_{liq}} + \sum_j \rho_j \nu_{i,j} \qquad 2.2$$

where i are the different variables of the biological model, S_i is the concentration of the i^{th} variable inside the reactor, V_{liq} is the liquid volume of the reactor and $\sum_j \rho_j \nu_{i,j}$ is the source term. The source term is defined in a matrix format following the work of Petersen, (1965). **Table 2.1** shows the simplest example where heterotrophic bacteria grow in an aerobic environment:

***Table 2.1**: Process kinetics and stoichiometry for heterotrophic bacterial growth in an aerobic environment from Henze et al., (2000).*

Component i / Process j	X_B	S_S	S_O	Process Rate ρ_j (M/L³T)
1. Growth	1	$-\frac{1}{Y}$	$-\frac{1-Y}{Y}$	$\frac{\mu S_S}{K_S + S_S} X_B$
2. Decay	-1		-1	bX_B
Observed Conversion Rates (M/L³T)	$r_i = \sum_j r_{ij} = \sum_j \nu_{ij}\rho_j$			Kinetic Parameters: Maximum specific growth rate, μ Half-velocity constant, K_S Specific decay rate, b
Stoichiometric Parameters: True growth yield Y	Biomass (M DQO/L³)	Substrate (M DQO/L³)	Oxygen (M (-DQO)/L³)	

According to this example, two processes are present in the heterotrophic bacterial growth in an aerobic environment: growth and decay of the heterotrophic bacteria. Each process has its own process rate (far right-hand column) and three components are involved in both processes: heterotrophic biomass (X_B), substrate (S_S) and oxygen (S_O). The internal cells of the matrix are stoichiometric coefficients.

Each source or reactive term is the result of summing the stoichiometric coefficients (internal cells) and the process rate expression (right column) for the component i. In this example, the reactive term of the heterotrophic biomass (X_B) is:

$$r_{X_B} = \frac{\mu S_S}{K_S + S_S} X_B - bX_B \qquad 2.3$$

2.4.1. Anaerobic Digestion Model 1

The most widely accepted biological model describing the anaerobic digestion process is the Anaerobic Digestion Model 1 (ADM1) (Batstone et al., 2002). This mathematical model explains the anaerobic biological process, i.e., disintegration, hydrolysis, acidogenesis, acetogenesis and methanogenesis. It was established for the design of full-scale industrial plants, operational analysis and control of anaerobic digestion and the basis for research and further studies. ADM1 calculates time evolution of 24 state variables, divided into soluble, particulate and gas components, considering biological and physicochemical processes, i.e., gas-liquid exchanges of bioproducts and ion association/dissociation.

Figure 2.3 shows an overview of the ADM1 and describes the steps and process rates equations:

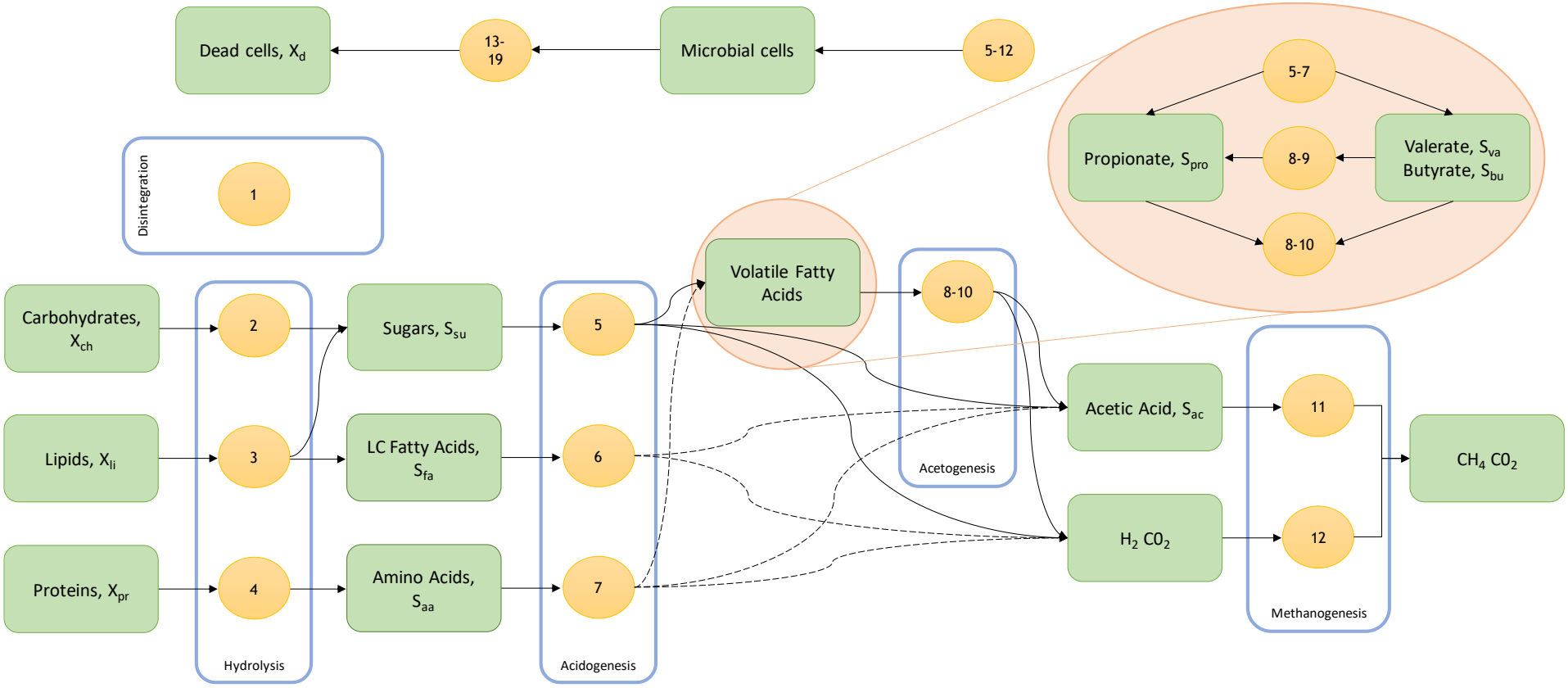

Figure 2.3: *Overview of biological processes of ADM1: The blue squares represent the different steps; the yellow circles signify the ADM1 processes and; the green squares define the ADM1 state variables.*

2.4.1.1. Biochemical processes

This model comprehends the following biochemical processes:

- Disintegration and hydrolysis: As explained above, these steps represent the breakdown of particle substrates into fatty acids, monosaccharides and amino acids. These processes are represented by first-order kinetics proportional to substrate concentration in the process rate equations 1 to 4. Additionally, other empirical first-order time constants describe enzyme and microbial concentration and other factors that affect these processes. The process rates equations are:

  ρ_1: Disintegration

$$\rho_1 = k_{dis} X_c \tag{2.4}$$

  ρ_2: Hydrolysis of carbohydrates

$$\rho_2 = k_{hyd,ch} X_{ch} \tag{2.5}$$

  ρ_3: Hydrolysis of proteins

$$\rho_3 = k_{hyd,pr} X_{pr} \tag{2.6}$$

  ρ_4: Hydrolysis of lipids

$$\rho_4 = k_{hyd,li} X_{li} \tag{2.7}$$

- Acidogenesis and acetogenesis: Both steps are intimately linked so that sugars, amino acids, LCFA and VFA are broken down into acetic acid and ammonia, hydrogen and carbon dioxide are created. Acidogenesis and acetogenesis are considered from processes 5 to 9 and acetogenesis only in process 10. The uptake of substrates and growth of the microbial community are modelled by means of Monod kinetics, whose growth are only limited by the substrate concentration, so that they grow at its maximum rate until saturation. The saturation concentration is considered by the Monod constant K_S, which defines the substrate concentration where the growth rate is 50%.

  ρ_5: Uptake of Sugars

$$\rho_5 = k_{m,su} \times \frac{S_{su}}{K_{Ssu} + S_{su}} \times X_{su} \times I_{IN,lim} \times I_{pH,aa} \tag{2.8}$$

  ρ_6: Uptake of Amino Acids

$$\rho_6 = k_{m,aa} \times \frac{S_{aa}}{K_{Saa} + S_{aa}} \times X_{aa} \times I_{IN,lim} \times I_{pH,aa} \tag{2.9}$$

  ρ_7: Uptake of LCFA

$$\rho_7 = k_{m,fa} \times \frac{S_{fa}}{K_{Sfa} + S_{fa}} \times X_{fa} \times I_{IN,lim} \times I_{pH,aa} \times I_{h2,fa} \tag{2.10}$$

ρ_8: Uptake of Valerate: Competitive uptake inhibition between valerate and butyrate is introduced as the same group of microorganisms consume valerate and butyrate.

$$\rho_8 = k_{m,c4} \times \frac{S_{va}}{K_{Sc4} + S_{va}} \times X_{c4} \times I_{va} \times I_{IN,lim} \times I_{pH,aa} \times I_{h2,c4} \quad 2.11$$

ρ_9: Uptake of Butyrate with competitive uptake inhibition between valerate and butyrate.

$$\rho_9 = k_{m,c4} \times \frac{S_{bu}}{K_{Sc4} + S_{bu}} \times X_{c4} \times I_{bu} \times I_{IN,lim} \times I_{pH,aa} \times I_{h2,c4} \quad 2.12$$

ρ_{10}: Uptake of Propionate

$$\rho_{10} = k_{m,pr} \times \frac{S_{pro}}{K_{Spro} + S_{pro}} \times X_{pro} \times I_{IN,lim} \times I_{pH,aa} \times I_{h2,pro} \quad 2.13$$

- Methanogenesis: Methane is produced by two different types of archaea by means of acetic acid and hydrogen breakdown. Methane, water and carbon dioxide are the products of both processes which are also defined by Monod kinetics.

  ρ_{11}: Uptake of Acetate- acetoclastic methanogenesis.

  $$\rho_{11} = k_{m,ac} \times \frac{S_{ac}}{K_{Sac} + S_{ac}} \times X_{ac} \times I_{IN,lim} \times I_{pH,ac} \times I_{nh3} \quad 2.14$$

  ρ_{12}: Uptake of Hydrogen- hydrogenotrophic methanogenesis

  $$\rho_{10} = k_{m,h2} \times \frac{S_{h2}}{K_{Sh2} + S_{h2}} \times X_{h2} \times I_{IN,lim} \times I_{pH,h2} \quad 2.15$$

- Inhibition: There are four different types of inhibition included in the uptake processes: pH inhibition, competitive inhibition, competitive uptake and secondary substrate limitation. Inhibition factors range from 0 to 1, where 1 means uninhibited and 0 means completely inhibited.

  pH inhibition is defined by different formulations, but the most applied formulation is the following empirical equation:

  $$I_{pH} = e^{-3\left(\frac{pH - pH_{UL}}{pH_{UL} - pH_{LL}}\right)^2} \quad 2.16$$

  where pH_{UL} and pH_{LL} are the upper and lower pH limit for each type of microorganism.

  As for competitive inhibition, hydrogen inhibits acidogenesis and acetogenesis and ammonia inhibits aceticlastic methanogenesis so, the following formula with constant K_I (inhibition concentration where there is a 50% of inhibition) is defined:

  $$I_{h2}\ and\ I_{nh3} = \frac{1}{1 + \frac{S_{S,I}}{K_I}} \quad 2.17$$

As explained above, competitive uptake inhibition is produced in the growth of valerate and butyrate degraders and is introduced as follows:

$$I_{va} = \frac{S_{va}}{S_{bu} + S_{va} + 1e^{-6}} and\ I_{bu} = \frac{S_{bu}}{S_{bu} + S_{va} + 1e^{-6}} \quad 2.18$$

Microorganisms need nitrogen to create biomass, therefore, secondary substrate inhibition is produced when there is a lack of nitrogen, as follows:

$$I_{IN,lim} = \frac{1}{1 + \frac{K_{S,IN}}{S_{IN}}} \quad 2.19$$

- Cell decay: There is always a loss of microorganism biomass in a given time which is described by first order kinetics in process rate equations13 to 19.

ρ_{13}: Decay of sugar degraders

$$\rho_{13} = k_{dec,Xsu} X_{su} \quad 2.20$$

ρ_{14}: Decay of amino acid degraders

$$\rho_{14} = k_{dec,Xaa} X_{aa} \quad 2.21$$

ρ_{15}: Decay of LCFA degraders

$$\rho_{15} = k_{dec,Xfa} X_{fa} \quad 2.22$$

ρ_{16}: Decay of C4-acid degraders

$$\rho_{16} = k_{dec,Xc4} X_{c4} \quad 2.23$$

ρ_{17}: Decay of propionate degraders

$$\rho_{17} = k_{dec,Xpro} X_{pro} \quad 2.24$$

ρ_{18}: Decay of acetate degraders

$$\rho_{18} = k_{dec,Xac} X_{ac} \quad 2.25$$

ρ_{19}: Decay of hydrogen degraders

$$\rho_{19} = k_{dec,Xh2} X_{h2} \quad 2.26$$

2.4.1.2. Physicochemical processes

Different physicochemical processes are included in the ADM1 model: acid-base reactions, liquid-gas transfer, surface evaporation and headspace-collector transport. The most important ones are:

- Acid-base reactions: Some state variables of the ADM1 are made up of acid-base pairs, e.g. $S_{bu,total} = S_{bu-} + S_{hbu}$. Acid-base reactions are decisive in the pH calculation of the ADM1. These reactions can be solved with different approximations such as ODE or algebraic equations and

each framework solves them in a different way. Different suggestions to solve the acid-base reactions are described in Batstone et al., (2002)and Rosen et al., (2006)

- Liquid-gas transfer: VFA, carbon dioxide, ammonia, hydrogen and methane are different volatile substances in ADM1 that can leave the liquid-phase in gas form. Only hydrogen, methane and carbon dioxide have a low solubility so they are the only ones able to leave the reactor's liquid. Their volatilisation is based on the film mode for convective mass transfer and their transfer rate equations contain the global mass transfer coefficient multiplied by the specified area ($k_L a$) and the Henry's constant ($K_{H,i}$):

  ρ_{T8}: Hydrogen transfer

$$\rho_8 = k_L a(S_{h2} - K_{H,h2} p_{gas,h2}) \quad 2.27$$

  ρ_{T9}: Methane transfer

$$\rho_9 = k_L a(S_{ch4} - K_{H,ch4} p_{gas,ch4}) \quad 2.28$$

  ρ_{T10}: Carbon dioxide transfer

$$\rho_{10} = k_L a(S_{co2} - K_{H,co2} p_{gas,co2}) \quad 2.29$$

The matrix describing the stoichiometry of the processes and the biochemical parameters are not presented here, but they have been extensively described in literature (Batstone et al., 2002).

Despite the wide acceptance of the ADM1, it contains several limitations that have prevented it from being understood by WWTP operators. The first limitation that has to be faced is based on on the large number of state variables and parameters needed for the proper performance of the mathematical model (Rodríguez and Patón, 2018). Numerous methods for feed characterisation have been proposed, but they are far from simplicity and anaerobic digestion routine testing (Arnell et al., 2016; Batstone et al., 2015).

The most important physical limitation lies in the different time scales that intrinsically exist in the ADM1 model. On the one hand, biological processes rates lie on the order of days, while, chemical processes, i.e., charge equilibrium and pH calculations, occur instantaneously or in seconds. Therefore, this implies that, while the resolution of biological processes demands a time step of days, the calculation of the pH requires time steps of seconds. This difference creates a major limitation in the calculation as the calculation efforts are focused on the calculation of a single component which is pH. On the other hand, calculations related to hydrogen also require a great calculation effort because of its importance in the anaerobic process: firstly, it is one of the products resulting from all the processes of hydrolysis and consumption of LCFA and VFA; secondly, it is also an inhibitory component for acidogenic bacteria; and it is consumed in

large quantities by hydrogenotrophic archaea. Due to the great contribution of hydrogen in the anaerobic process, its calculation also entails greater complexity than other state variables so that greater calculation efforts are required. Consequently, pH and dissolved hydrogen calculation states problems in the implementation of ADM1 in different calculation frameworks, requiring time steps of seconds and complex calculation methods. (Batstone et al., 2002; Rosen et al., 2006) This fact suggets that the correct adjustment of the model and, therefore, its utility and functionality will rely on the choice of the time scale and its variation.

The application of ADM1 in different frameworks has been addressed by different authors in a way that its limitations have been solved (Batstone et al., 2006). ADM1 has been included in different calculation frameworks: C++, FORTRAN, Matlab (Rodríguez et al., 2009; Rosen et al., 2006). ADM1 has also been implemented with ASM1 in the Benchmark Simulation Model no. 2 (BSM2) (Jeppsson et al., 2007) in different WWTP simulation codes (WEST, SIMBA, STOAT, Aquasim, GPS-X, ...).

2.5. CFD MODELLING

Computational fluid dynamics or CFD is part of the science of fluid mechanics that solves fluid flow, heat transfer and related phenomena by means of numerical methods solved with computer-based simulations. CFD modelling was initially integrated into the aerospace industry in the 1960s. Since then, it has been applied to the combustion and motor vehicle industries, where nowadays is an essential tool in the processes and product design stage. Its use has increased exponentially in the last decade as result of the development of new efficient algorithms to solve the main fluid flow equations. Thus, some of the application areas are industrial and non-industrial, such as hydrology and oceanography, biomedical engineering, meteorology, chemical process engineering, electrical and electronic engineering, power plants or environmental engineering. (Tu et al., 2013; Versteeg and Malalasekera, 2005)

CFD has become a new branch that merges fluid mechanics, mathematics and computer science: On the one hand, fluid mechanics is the science of fluids either at rest or in motion, and CFD is devoted to fluids in motion i.e., fluid dynamics. On the other hand, fluid motion is defined by means of mathematical equations including heat transfer or chemical reactions. Partial differential equations are traditionally used and named CFD governing equations. Finally, aiming to solve the governing equations, computer scientists transform them into high-level computer programs in different software packages.

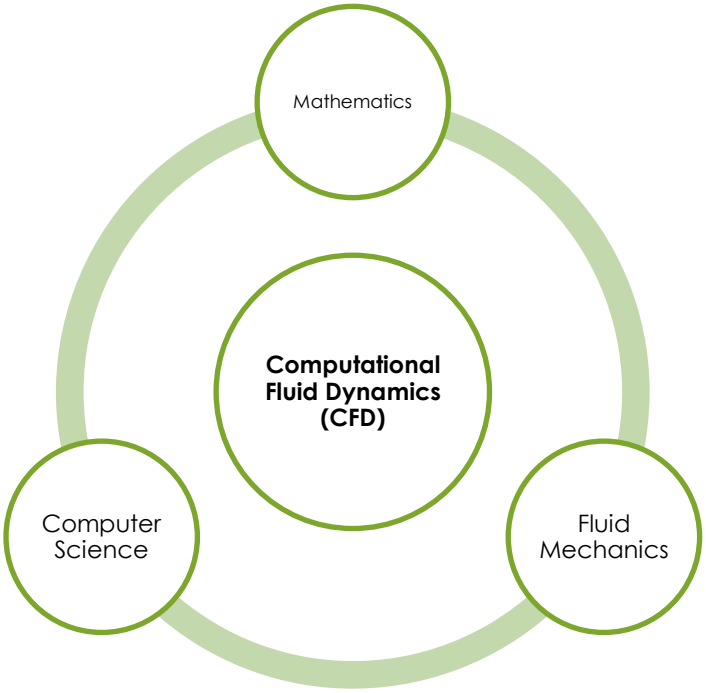

Figure 2.4: *Disciplines integrated in CFD. (adapted from Tu et al., 2013)*

The CFD modelling process can be schematically divided into five different stages:

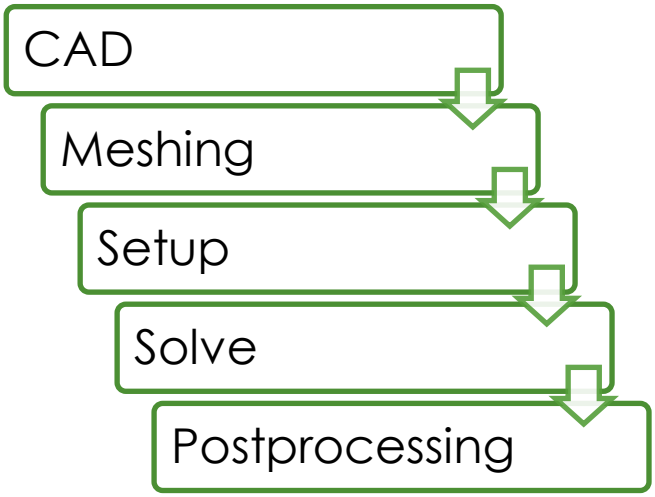

Figure 2.5: *CFD Workflow.*

2.5.1. CAD and Meshing

The CFD modelling process starts with the identification of the physical objective or problem and the purpose of the model. From these, key assumptions will be defined to simplify and guide the CFD modelling, e.g. the 2D or 3D

dimensions, the number of phases or processes considered. Based on this, the physical domain is first constructed as a CAD (computer-aided design) model which is identified as the domain in which the equations are applied.

The second step is the spatial discretisation of the domain or meshing into a finite number of control volumes or cells. This second step is key to achieving reliable results, since an excessively large mesh size or long resolution time steps may provide results that are far from the real behaviour. Therefore, it is necessary to construct a sufficiently fine mesh so that the system can be solved with a short time step and does not increase the computational time excessively. There are two calculations to check whether the size of the nodes is appropriate.

On the one hand, the first of these is the calculation of boundary layer nodes (inflation) or the node structure near the wall. For each turbulence model and flow characteristics there is a requirement for the number of boundary layer nodes, e.g. in the k-epsilon model, a Y+ of 0.2 and 15 boundary layer nodes with wall functions are needed. To perform this check, simulation is necessary, so a first mesh is generated and simulated. Subsequently, the value of the variable Y+ and the number of nodes in the boundary layer are evaluated to estimate what size of nodes is necessary in the boundary layer or inflation. The process is started iteratively until the requirements for Y+ and the number of nodes in the inflation layer are met.

On the other hand, the second calculation is the estimation of the Courant-Friedrichs-Levy number (Courant number). The calculation of the CFD model is carried out by solving the differential equations system by moving forward in time by means of timesteps with a selected size, Δt.

$$Co = \frac{u}{\Delta x}\Delta t \sim 1 \qquad 2.30$$

where Co is the Courant number (dimensionless), u is the velocity flow in direction x and Δx is the distance between two nodes or the cell size (m). The Co should be close to 1 to ensure a good timestep size and cell size. This calculation is only possible after the solution of the CFD model so, as in the estimation of the Y+ number, a first run of the simulation is needed. Nonetheless, the maximum admissible time step, Δt_{max}, is a good guide in terms of mathematical and physical restrictions:

$$\Delta t_{max} < Co \times \frac{\Delta x}{c} \qquad 2.31$$

being c the velocity in the order of the velocity of the sound. The timestep size or the cell size will be changed to fulfil Co close to 1.

These two calculations to check the size of the nodes require the CFD model to be solved. However, there are other parameters to check the quality of the mesh without the need to solve the model; orthogonal quality (ranging from 0 to 1), aspect ratio and the skewness (ranging from 0 to 1) are good examples. A good quality mesh has an orthogonal quality higher than 0.95, an

aspect ratio close to 1 and a skewness lower than 0.25.

Additionally, a grid convergence study assesses the spatial discretisation error of CFD models, in which several CFD solutions with different grids (with decreasing distances between cell centres, Δx) are obtained and compared. As a result of the grid convergence study, the most suitable mesh reproducing the problem is found. The most widely used method for standardized reporting of grid convergence studies is the Grid Convergence Index (GCI) described by Roache (1998):

2.5.1.1. Grid dependence procedure: Grid Convergence Index

Three grids, from coarse to fine cell size, are solved and their CFD results are compared (subscript 1 for the fine mesh and subscript 3 for coarse mesh), i.e. the fluid velocity field is considered the reference variable to compare between them at different critical points, planes or volumes in the domain.

This method was modified by Tanaka (2014) and Tanaka et al. (2016) and it has been used in this thesis. The absolute error (ε_{ij}) between each mesh pair is obtained as follows:

$$\varepsilon_{21} = f_2 - f_1; \qquad \varepsilon_{32} = f_3 - f_2 \tag{2.32}$$

where f_3 is the value in the coarse mesh and f_1 is the value in the fine mesh. Next, the mesh refinement factor (r_{21}, see Eq. 2.33) is calculated and the order of convergence p_j is solved iteratively using equations 2.34 to 2.36 considering $p_j = 2$ as the initial value (Tanaka, 2014; Tanaka et al., 2016):

$$r_{21} = \left(\frac{N_1}{N_2}\right)^{\frac{1}{Dim}}; \; r_{32} = \left(\frac{N_2}{N_3}\right)^{\frac{1}{d}} \tag{2.33}$$

$$\tilde{p}_j = \frac{ln\left[\frac{(\varepsilon_{32})_j}{(\varepsilon_{21})_j} + q(p_j)\right]}{ln(r_{21})} \tag{2.34}$$

$$q(p_j) = ln\left[\frac{\left({r_{21}}^{p_j} - s_j\right)}{\left({r_{32}}^{p_j} - s_j\right)}\right] \tag{2.35}$$

$$s_j = 1 \times sign\left\{\frac{(\varepsilon_{21})_j}{(\varepsilon_{32})_j}\right\} \tag{2.36}$$

where N is the number of nodes of each mesh and Dim is the dimensions of the CFD model. If $\tilde{p}_j$ is less than 1, the order of convergence (p_j) should be at least 1. At this point, the GCI can be solved as (Roache, 1998; Tanaka, 2014; Tanaka et al., 2016):

$$GCI_j = F_s \times \frac{\left|\frac{(\varepsilon_{21})_j}{(f_1)_j}\right|}{({r_{21}}^{p_j} - 1)} \tag{2.37}$$

where the safety factor (F_s) can be 1.25 and 3 according to the following equation:

$$F_s = 1.25\ if\ \{1 < p_j \leq 2\}$$
$$F_s = 3\ if\ \{p_j \leq 1\ or\ 2 < p_j\} \quad 2.38$$

A GCI lower than 0.03 (3%) is considered the threshold value to choose the grid with lower spatial discretization error. The GCI evaluates the CFD solution's numerical error due to discretization but it does not assess the errors that may arise from inaccurate physical models or strong approximations. These errors must be evaluated by comparing CFD results with detailed experimental results (Oberkampf and Trucano, 2002).

2.5.2. Setup

This third stage is devoted to setting the physics, fluid properties and the boundary conditions that mimic the real domain, i.e. fluid flow and boundary properties. At the end of this stage, the CFD model is prepared for the numerical solving process.

Different flow physics can have a strong influence on the overall fluid dynamics within the computational domain, so that the user can initially define which flow considerations and physics the CFD model may include. There are two states of fluid regimes (**Figure 2.6**):

- Laminar flow: in this state, the particles of the fluid follow regular paths in parallel layers. It appears in small pipes or at low flow velocities with low to moderate Reynolds numbers.
- Turbulent flow: in contrast to the laminar state, the fluid particles have an irregular movement so eddies and wakes appear, and the flow is unpredictable. Turbulence is characterized by random flow field fluctuations in time and space and appears in large pipes or at high flow rates from moderate to high Reynolds numbers.

Additionally, both flows can coexist together in a transitional flow. These states can be described by the 3D Navier-Stokes equations.

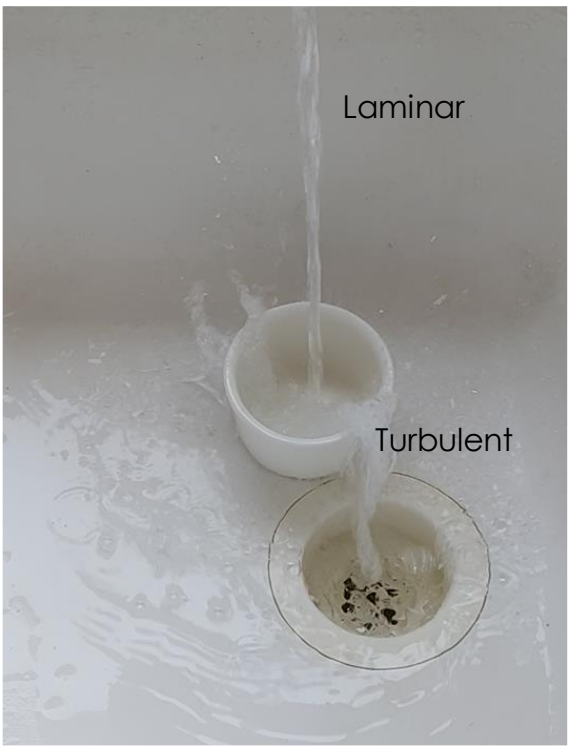

Figure 2.6: Laminar and turbulent flow regimes.

One of the main properties of a fluid is its viscosity. Fluids are classified according to their behaviour when a given shear rate is applied. When the viscosity does not depend on the shear rate conditions and a linear relation between shear rate and shear stress is shown, these are Newtonian fluids. Nonetheless, Non-Newtonian fluids do not behave linearly under shear rate conditions due to their internal structure. Anaerobic sludge is considered a Non-Newtonian fluid (Baudez et al., 2011; Eshtiaghi et al., 2013) (see Section 2.7.1).

In this thesis, the energy transport equation was not solved, but a fixed temperature was set for the evaluation of the fluid properties (e.g. when using an ideal gas or an anaerobic sludge), i.e. isothermal modelling was considered.

CFD models can consider one phase, single-phase flow model, or more than one phase that do not mix due to an interface that separates them, multiphase flow model. In this thesis, the multiphase flows defined are two-phase flow with sludge as the main or primary phase and gas as the secondary phase. Multiphase flow dynamics are strongly dependent on the flow structure, so several two-phase flow regimes can be defined based on the flow rate (Pellacani, 2012) (**Figure 2.7**):

- Bubbly flow: a high liquid flow rate is introduced so the liquid-phase is the primary one and the low gas flow rate appears as dispersed bubbles. This is one of the most common two-phase flow regimes.
- Annular flow: this is the opposite of bubbly flow, whereby a low liquid flow rate appears surrounded by a speedy primary gas phase.
- Slug flow: in this regime, liquid slugs alternate with large gas bubbles, as

both flow rates are high.

- Wavy flow: the gas flow rate is higher than the liquid flow rate, so a wavy gas-liquid interface is formed as the gas flows over the liquid phase.
- Stratified or segregated flow: appears at low liquid and gas flow rates, where a horizontal interface divides the liquid and gas phases.

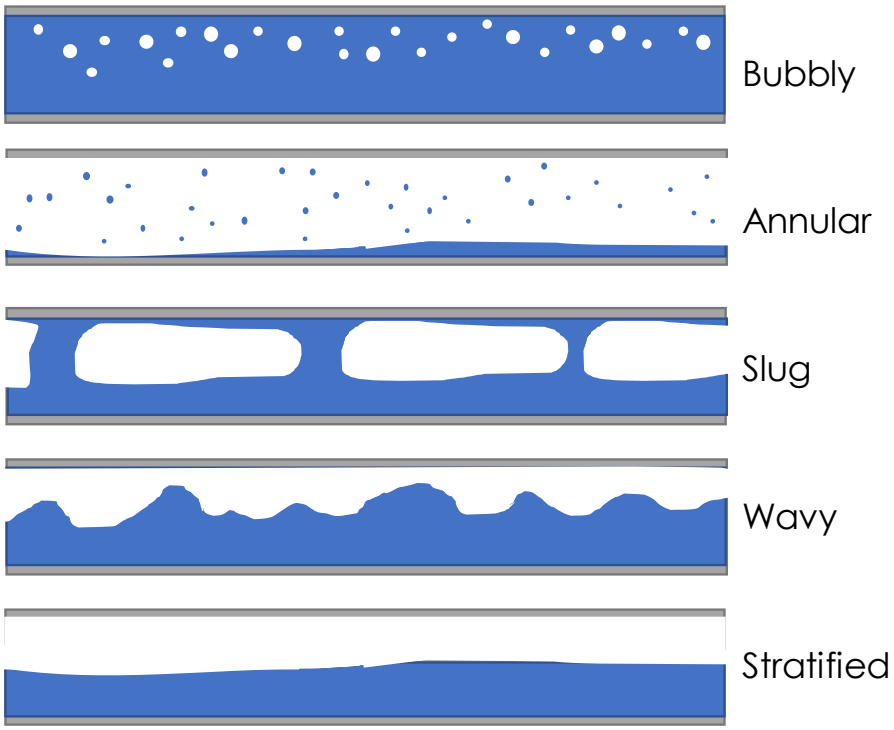

Figure 2.7: Two-Phase flow gas-liquid regimes.

Once fluid regimes and two-phase regimes have been defined, three different categories group the numerical methods to solve turbulence modelling (Versteeg and Malalasekera, 2005):

1. Direct Numerical Simulation (DNS): this type of simulation is the most detailed, as it computes the mean flow and all types of turbulent fluctuations. It resolves the unsteady Navier-Stokes equations in detailed, i.e. it is mathematically well conditioned, as four fields have to be solved (three of velocity and one pressure), and four differential equations are available to relate them (three from Navier-Stokes and one for pressure). Nonetheless, fine mesh and small timesteps are required to solve the unsteady Navier-Stokes equations, so the computational resources required are greater than the others, so it is not used for industrial design.
2. Large Eddy Simulation (LES): this method is an intermediate numerical method that resolves mean flow and large eddies and models small eddies. It resolves unsteady Navier-Stokes equations after space filtering. As a result, the computational time is shorter than in DNS and is used in industrial and research areas.

3. Turbulence models for Reynolds-Averaged Navier-Stokes (RANS) equations: this simulation computes the mean flow and the effects of turbulence on the mean flow. Thus, the Navier-Stokes equations are time averaged and extra terms appear. These extra terms are modelled with different turbulence models, i.e. the $k-\varepsilon$ model and the Reynolds stress model. The computational resources are feasible, so this simulation is the main simulation used in most industrial areas.

Therefore, WWT engineering problems use RANS simulations as it is not necessary to resolve the turbulent flow in detail. This work is focused on the Reynolds-Averaged Navier-Stokes equations for single and two-phase flow approaches.

2.5.2.1. Turbulence models for RANS equations

RANS predict the effects of turbulence with statistical turbulence models that modify the original unsteady Navier-Stokes equations. Thus, additional unknown terms called "Reynolds-stresses" tensors are introduced from the averaging procedure and modelled by additional equations that rely on strong approximations to achieve closure, i.e. there are enough equations to solve all the unknowns. (Wilcox, 1993)

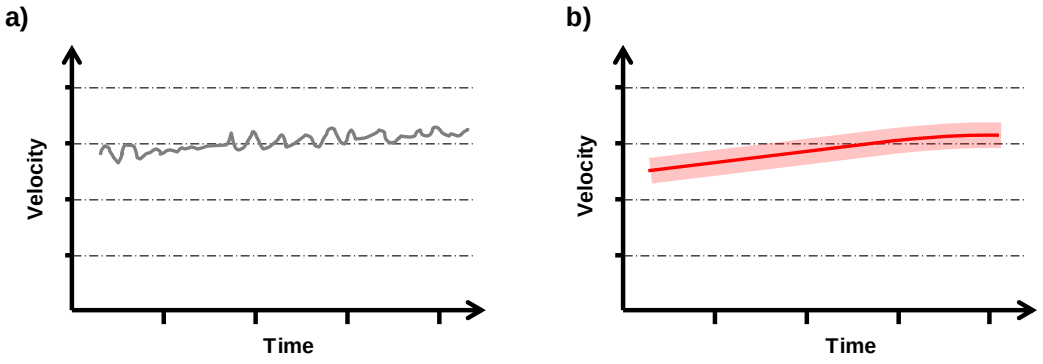

Figure 2.8: Decomposition of turbulence in RANS.

Note that there are three averaging concepts in turbulence model research: time average, spatial average and ensemble average. The most used Reynolds averaging is the time average process. Thus, RANS turbulence models allow the instantaneous velocity to be expressed as the sum of the mean and a fluctuating component (Wilcox, 1993). For example, **Figure 2.8**a illustrates the evolution of velocity at the central point of a pipe with turbulent flow where the maximum velocity is achieved. Although pipe pumping power can be considered as constant, the velocity is not constant over time and presents small temporary fluctuations. The decomposition of Reynolds takes this behaviour as shown in **Figure 2.8**b, i.e. as an average velocity field (solid line) and a field that describes the amplitude of fluctuations (degraded area).

Thus, the instantaneous velocity, $u_i(x,t)$ is the sum of the mean $U_i(x)$ and fluctuating $u'_i(x,t)$ components as:

$$u_i(x,t) = \bar{u}_i(x) + u'_i(x,t) \qquad 2.39$$

The averaged component is given by:

$$\bar{u}_i(t) = \frac{1}{\Delta t}\int_t^{t+\Delta t} u_i(\mathrm{t})\ dt \qquad 2.40$$

where Δt stands for a time scale that is large compared to the turbulent fluctuations, but small compared to the time scale on which the equations are solved.

2.5.2.2. *Single phase*

At a single-phase flow, the original transport equations are transformed substituting the averaged quantities, so that the RANS equations in Cartesian tensor form are as follows. For the sake of simplicity, which term corresponds to each effect in the conservation equation is shown.

Continuity Equation:

Local variation of density Source term

$$\frac{\partial \rho}{\partial t} + \frac{\partial}{\partial x_i}(\rho \bar{u}_i) = S_m \qquad 2.41$$

Net Mass Flux

Momentum Equation:

Local acceleration Pressure gradient Reynolds Stress (Turbulence)

$$\frac{\delta(\rho \bar{u}_i)}{\delta \mathrm{t}} + \frac{\partial}{\partial x_j}(\rho \bar{u}_i \bar{u}_j) = -\frac{\delta \mathrm{p}}{\delta \mathrm{x_i}} + \frac{\partial}{\partial x_j}\left[\mu\left(\frac{\partial \bar{u}_i}{\partial x_j} + \frac{\partial \bar{u}_j}{\partial \mathrm{x_i}} - \frac{2}{3}\delta_{ij}\frac{\partial \bar{u}_i}{\partial \mathrm{x_i}}\right)\right] + \frac{\partial}{\partial x_j}\left(-\rho\overline{u'_i u'_j}\right) + S_m \qquad 2.42$$

Convective Term Diffusive term Source term

The continuity equation has not been modified, but the momentum and scalar transport equations include turbulent flux terms in addition to the molecular diffusive fluxes. These are the Reynolds stresses, $\rho\overline{u'_i u'_j}$, that arise from the nonlinear convective term in the un-averaged equations and introduce convective transport due to turbulent velocity fluctuations. These will enhance mixing over and above that caused by thermal fluctuations at the molecular scale. Thus, at high Reynolds numbers, molecular fluxes are depreciable compared to large turbulent velocity fluctuations.

2.5.2.3. *Two Phase Model: Volume Of Fluid*

The Volume Of Fluid (VOF) model is a surface-tracking technique applied

to a fixed Eulerian mesh, useful when the position of the interface between two or more immiscible fluids is of interest (Hirt and Nichols, 1981). This approach solves a single set of momentum equations and tracks the volume fraction (α) of each phase in the computational domain. The volume fractions represent the space occupied by each phase. In a two-phase VOF model, there is a primary phase (p) and a secondary phase (q) where the volume fraction of the i phase in a cell is α_{pi}. In each control volume, the sum of the volume fraction of all phases is 1 so three different conditions may be possible in each cell (ANSYS FLUENT, 2017) (see **Figure 2.9**):

1. The cell is full of the primary fluid: $\alpha_p = 1$ and $\alpha_q = 0$.
2. The cell is empty of the primary fluid: $\alpha_p = 0$ and $\alpha_q = 1$.
3. The cell contains the interface between the p and q fluids. $0 < \alpha_p < 1$ and $0 < \alpha_q < 1$.

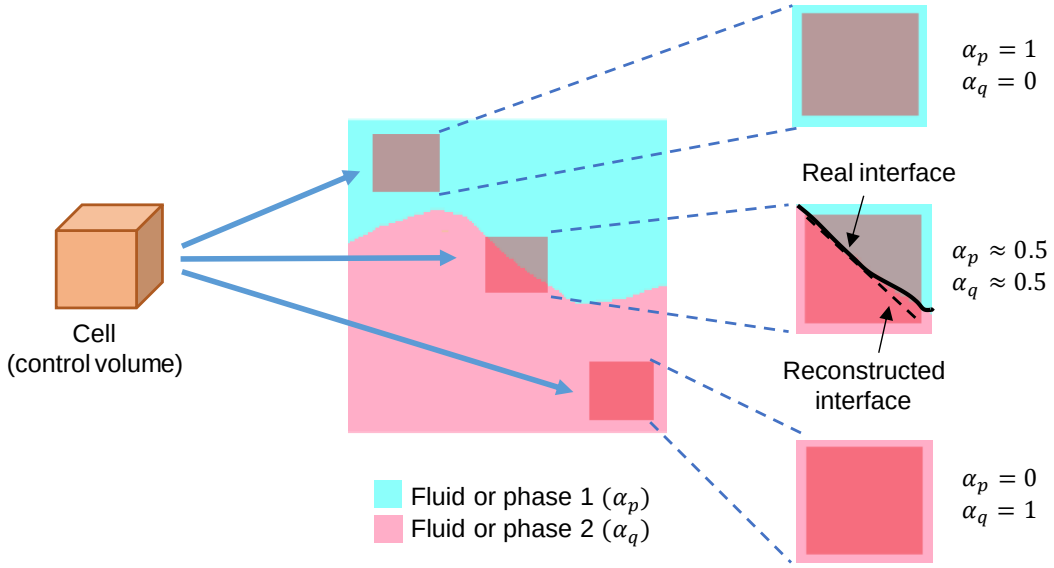

Figure 2.9: *Interface tracking based on the VOF approach (adapted from Prades Martell, (2018)).*

For each additional fluid introduced in the VOF model, a new volume fraction variable of the new fluid must be introduced so that, the volume fraction of each fluid is known at every position. The fields for all variables and properties are shared by the phases so that the variables or properties in a given control volume depend on the volume fraction of each phase in that control volume. Accordingly, this means that the control volume properties and variables within the domain can be entirely representative of one of the fluids (if α_{pi} is 1) or a mixture of the fluids (when α_{pi} is between 0 and 1).

The solution of a continuity equation for the volume fraction of one (or more) of the phases is used to track the interface(s) between the phases. For a secondary phase, the equation is defined using the following expression:

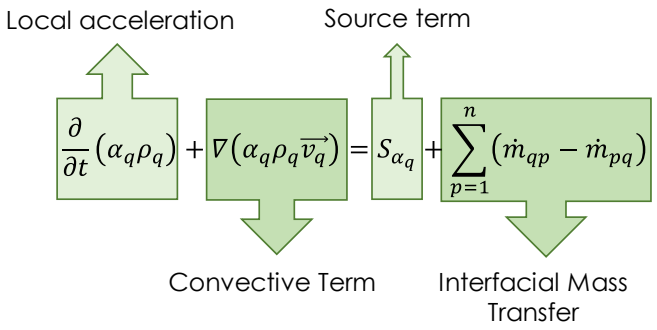

2.43

where $\rho_q is$ the density of the phase q, t is the time, $\vec{v}_q$ is the velocity in the phase q, S_{α_q} is the source term and $\dot{m}_{qp}$ is the mass transfer per unit volume from phase q to p and $\dot{m}_{pq}$ is the mass transfer per unit volume from phase p to phase q.

Nevertheless, the volume fraction equation (Eq. 2.43) will not be computed for the primary phase. Instead, the primary phase volume fraction will be solved based on the following equation:

$$\sum_{q=1}^{n} \alpha_q = 1 \qquad 2.44$$

The volume fraction equation can be solved either through implicit or explicit time discretization, but in this case, it is solved through explicit time formulation. Further details can be found in the ANSYS Fluent Theory Guide (ANSYS FLUENT, 2017).

The properties in the continuity equation are based on the local appearance of the component phases in each cell. For example, in this case, which is a two-phase system with phase p and phase q, the density in a cell with a mixture of both phases is solved as the volume-averaged density as the following expression:

$$\rho = \alpha_q \rho_q + (1 - \alpha_q)\alpha_p \qquad 2.45$$

All other properties are solved in this way. Considering that the local properties in each control volume, i.e. density and viscosity, are dependent on the volume fractions of all phases, the momentum equation is also dependent on them. Thus, the momentum equation is solved throughout the computational domain as the following expression and the resulting velocity field is shared among the phases:

$$\frac{\partial}{\partial t}(\rho\vec{v}) + \nabla(\rho\vec{v}\vec{v}) = -\nabla p + \nabla[\mu(\nabla\vec{v}\nabla + \nabla\vec{v}^T)] + \rho\vec{g} + \overrightarrow{F_{ST}} \qquad 2.46$$

where p is the pressure, g is the acceleration of gravity and F_{ST} is the surface tension force. Surface tension arises at the surface of fluids as result of attractive forces between the fluid's molecules, so that a radially inward inter-molecular force appears. The surface tension model in Fluent is based on the Continuum Surface Force (CSF) model proposed by Brackbill et al.(1992) so that the surface

tension is added in the VOF calculation as a source term in the momentum equation.

2.5.2.4. Two Phase Model: Eulerian-Eulerian

With this model one phase interpenetrates the other one where, as in VOF, phase volume fractions (α_{pi}) are considered. Each phase satisfies the laws of conservation of mass and momentum individually. The continuity and momentum conservation equations for phase q are:

Continuity Equation:

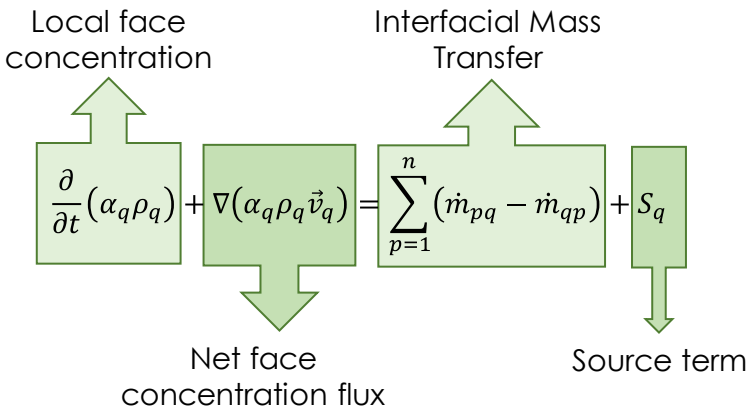

2.47

Momentum Equation:

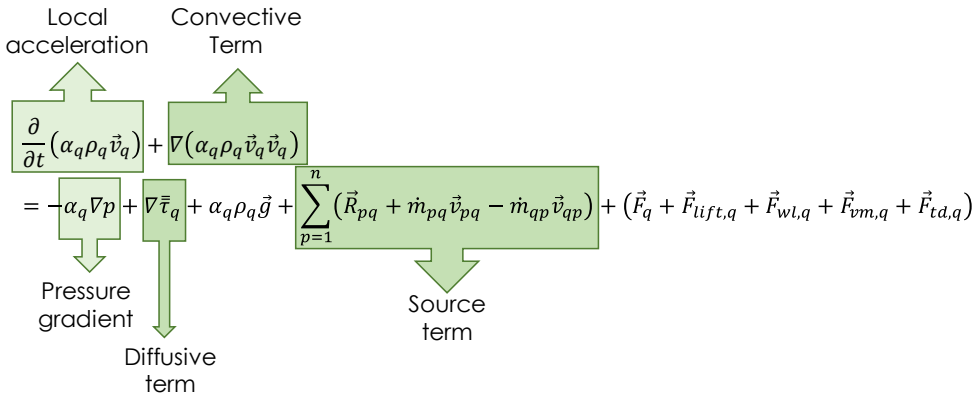

2.48

where $\vec{v}_q$ is the velocity of phase q, $\dot{m}_{pq}$ defines the mass transfer per unit volume from the p to q phase, $\dot{m}_{qp}$ is the mass transfer per unit volume from the q to p phase, $\bar{\bar{\tau}}_q$ is the q phase stress-strain tensor, $\vec{F}_q$ is an external body force, $\vec{F}_{lift,q}, \vec{F}_{wl,q}, \vec{F}_{vm,q}, \vec{F}_{td,q}$ are the interfacial forces and $\vec{R}_{pq}$ is an interaction force between phases.

The interfacial forces have a great influence on the dynamics of two-phase flows. On the one hand, parallel to the flow direction, it is the drag force. On the other hand, the non-drag forces are perpendicular to the flow direction (Pellacani, 2012; Peña-Monferrer, 2017; Yamoah, 2014):

- Drag force: represents the resistance between the dispersed phase and the continuous phase. It stems from the viscous force acting around the surface of the dispersed phase and the pressure differences caused by the shape of the dispersed phase and is opposite to the motion.
- Lift force ($\vec{F}_{lift,q}$): the presence velocity gradients or rotational strain leads to this perpendicular force to the motion direction.
- Wall lubrication force ($\vec{F}_{wl,q}$): appears near the wall region pushing the dispersed phase away in the direction perpendicular to the wall.
- Turbulent dispersion Force ($\vec{F}_{td,q}$): the turbulent energy of the continuous phase drives the dispersed phase to zones with lower concentration, so it flattens the void fraction distribution.
- Virtual mass force ($\vec{F}_{vm,q}$): this is related to the mass of the liquid carried by the dispersed phase and its magnitude is proportional to the bubble acceleration but opposite to its motion.

Extensive research on the importance of the interfacial forces and their closure relations has been carried out, but their accurate modelling still remains a bottleneck in numerical simulations of bubbly flow. However, there is some agreement among researchers that the drag force is the most important interfacial force.

2.5.3. Solvers

In the solving stage, the governing equations are solved and fluid-dynamic results are obtained, making it is the main part of the CFD modelling process. The solving process comprises the following steps (Tu et al., 2013):

- Initialization and solution control: the user can specify some initial conditions to help in the solution convergence and, can set up the proper parameters for solution control (suitable discretization schemes and iterative solvers).
- CFD calculation: An iterative algorithm solves the governing equations to obtain a fluid-dynamic solution.
- Check solution convergence during the CFD modelling calculation: The imbalance of the mass and flow conservation equations are monitored until the convergence criteria are achieved.

There is a lot of software available to solve a CFD model and three different ones were employed here:

- ANSYS-CFX: This is a commercial software from ANSYS Inc, that uses a Vertex-Centered Finite Volume approach. (single phase) CFX has been used in chapter 3 for single-phase and two-phase simulations.
- ANSYS-Fluent: Like CFX, it is also a commercial code from ANSYS Inc.

Nevertheless, Fluent is a Cell-Centered Finite Volume approach capable of handling 2D CFD models. Thus, Fluent was chosen to apply the VOF model in 2D-CFD models in chapter 6.

- OpenFOAM: Unlike the previous ones, it is an open source code developed by OpenCFD Ltd and OpenFOAM Foundation. OpenFOAM (from "Open-source Field Operation And Manipulation") is an open-source C++ toolbox for the solution of continuum mechanics, mainly CFD problems with also a Cell-Centered Finite Volume approach. Its structure and availability to modify the source code enables the user to customize their numerical solvers or build their own. This was the main reason for choosing this code for the development of new solvers in chapters 4 and 5. Additionally, it provides pre- and postprocessing utilities for their solution. More information about it is provided in Section 4.2.

2.5.4. Post-processing

It is the last stage where the CFD model's results are studied. CFD results are usually shown with colourful and vivid images, as post-processing codes incorporate different striking visualization tools, but CFD results can also be presented by means of plots, tables or animations. In this thesis, the following tools have been used for results processing:

- ANSYS CFD-Post: this is a tool available in the ANSYS package with a user-friendly graphical interface. The user can add expressions by means of a simple programming code, create tables, plots and graphs with the available data or new post-processing calculations. It has been used in chapters 3 and 6 for data processing of CFX and Fluent results.
- Paraview: this is an open-source graphical application for data processing and visualization that can read different data formats. ParaView is able to process large datasets using distributed memory computing resources and it can also be run on high performance computers. Like CFD-Post, it has different simple 3D tools to add planes, lines, and so on, with many possibilities. Additionally, the user can add new expressions for data processing based on his/her own python code. This software has been used in chapters 4 and 5 for OpenFOAM results' processing.
- Gnuplot: this is a freely distributed portable command-line graphing tool for different platforms (Linux, OS/2, MS Windows, etc.). With this tool, the user can analyse large datasets and plot them in whatever format they are in. The user can use it with just a few programming notions which are also available online. This tool has been used in chapters 4 and 5 for OpenFOAM results' processing.
- "libIOFunctionObjects.so" OpenFOAM library: this is a library available in OpenFOAM that allows data processing during the solving process. The library has different options to calculate different simple and useful

expressions such as averages, sums, simple operations and integrals of different variables in different locations of the CFD domain (volumes, boundaries or faces). This library has been used extensively in chapters 4 and 5 for OpenFOAM results' processing.

2.6. CFD STUDIES IN ANAEROBIC DIGESTION

At present, CFD modelling in WWT has to be considered as a complement to existing simulation tools: CFD models allow for detailed study of specific problems in the different process units and deeper examination into detailed the mechanisms that drive the treatment processes (Karpinska and Bridgeman, 2016).

It is known that the daily operation of anaerobic digesters presents biological problems as result of hydraulic defects in fluid dynamics (Lindmark et al., 2014b). Through CFD modelling, complex studies on equipment and fluid dynamics can be carried out, even when two-phase (Vesvikar and Al-Dahhan, 2005; Wu, 2014) or three-phase (Yu et al., 2013a) are considered, to compute phenomena such as:

- Hydraulic short-circuiting.
- Dead volumes induced by low flow velocity zones.
- Deficient mixing degree.
- Concentration gradients of contaminants and suspended solids.
- Flow stratification phenomena.
- Fluid-dynamic effect of internal elements such as baffles
- Effect on the flow of mixing systems.

The need to incorporate CFD modelling into anaerobic digestion analysis arises because biological 0D-simulators do not accurately reproduce hydrodynamic behaviour. 0D-models consider ideal CSTR performance so that hydrodynamics and their impact on the process performance are ignored. Accordingly, the biogas production yields calculated from the 0D-model ADM1 implemented in a CSTR often differ from the yields obtained in the real anaerobic digester. However, some of the disadvantages of CFD modelling are its complexity and high computational time. Validation of the models is a great disadvantage that is particularly complex for full-scale anaerobic digesters as they are not very accessible. CFD modelling verification and validation will be described extensively in Section 2.7.

Taking into account the detailed information about hydrodynamics arising from CFD modelling, anaerobic digestion has been extensively studied through CFD models with different mixing types and dimensions (see some references in **Table 2.2**). On the one hand, at lab-scale, mechanical mixing with propellers or impellers and gas mixing has been modelled by different authors (Dapelo et al.,

2015; Latha et al., 2009; Vesvikar and Al-Dahhan, 2005; Zhang et al., 2016). Different types of mixing have also been analysed through models that have been validated using tracers and velocity profiles (see Section 2.7). Different turbulence and kinetic energy models have also been widely studied (Wu, 2010b), which are very relevant in the configuration of CFD modelling. On the other hand, at pilot and full-scale, all mixing systems described above have been studied, such as mechanical mixing with impellers inside the vessel (Bridgeman, 2012; Wu, 2011; Yu et al., 2011), or in a draft tube (Craig et al., 2013; Meroney and Colorado, 2009; Wu, 2010a); slurry recirculation using external pumps (Hurtado et al., 2015; Mendoza et al., 2011; Wu and Chen, 2008); gas mixing with different configurations (Bel Fdhila et al., 2013; Coughtrie et al., 2013; Karim et al., 2007; Wu, 2014) and steam injection (López-Jiménez et al., 2015).

Regarding full-scale anaerobic digesters, the first studies were focused on studying the impact of geometry and mixing systems on the anaerobic digester's hydrodynamics. Different full-scale egg-shaped anaerobic digestion CFD models can be found in the literature (Meister et al., 2018; Wu, 2010a). Meister et al. (2018) studied the influence of external slurry recirculation and an impeller within a draft tube and stated that slurry recirculation was not enough to provide good mixing in an egg-shaped anaerobic digester. Steam injection was also studied in a full-scale anaerobic digester where great hydraulic defects were identified (López-Jiménez et al., 2015). Mechanical mixing has been widely studied using single-phase CFD models. Different ageing of anaerobic sludge and turbulence models were assessed in a digester mixed through a draft tube impeller mixer (Craig et al., 2013). Sludge properties such as total solids concentration and ageing were identified as crucial for development of the internal flow within the vessel, with great differences in the fluid flow nearby the impeller (Craig et al., 2013) and in the global hydrodynamics (Terashima et al., 2009). The assessment of different mechanical mixing configurations in anaerobic digestion by means of CFD modelling confirms the convenience of CFD for the study of mixing inside the vessels (Meroney and Colorado, 2009; Wu, 2011).

Furthermore, CFD modelling has increased the knowledge about different mixing strategies in anaerobic digestion. With slurry recirculation as a mixing system, intermittent mixing was modelled and a slight decrease in active volume was observed (Hurtado et al., 2015). In this study, DYNOMIX system was studied within a single-phase Newtonian CFD model where dead zones were located in the middle and the wall of the bottom part of the digester. A correlation between power input and velocity zones was also studied at lab-scale and pilot-scale and a linear correlation was found between them (Wu and Chen, 2008). Another correlation studied with CFD modelling was experimental biogas yields and mixing velocity (Bridgeman, 2012). In this study at lab-scale, no improvement in biogas yield was found with increasing mixing velocity but it did state that biogas could be produced at velocity gradients lower than the design recommendations. The same finding was reported at a gas mixed full-scale anaerobic digester in Wu, (2014). Regarding mixing intensity, Lindmark *et al.*,

(2014a) pointed out the difficulty of defining a mixing regime statement for optimal biogas production at different scale-ups. Accordingly, some authors agree on the existence of a mixing threshold for each anaerobic digester. In this sense, optimization of intermittent mixing could be the best mixing practice to save energy costs and maintain a good biogas production (Kariyama et al., 2018; Lindmark et al., 2014b; Zhai et al., 2018).

To date, there is some work related to the multiphase CFD modelling of anaerobic digestion, and it is generally limited to an analysis of the liquid and gas phases from a monodisperse Eulerian point of view, i.e. without population balance. Thus, Vesvikar and Al-Dahhan, (2005) published a first work modelling the lab-scale anaerobic digester characterized by Karim et al., (2004). Since mixing was provided by gas injection into a tubular structure, their research focused on the influence of the geometry of this tubular structure on the liquid velocity and dead volume. Buoyancy and drag forces were considered to define the gas phase and the Grace model was used to calculate the drag coefficient. The same set-up was later studied to optimise mixing inside the tank (Wu, 2014, 2010c). In these works, the influence of different mixing systems (mechanical, gas mixing and slurry recirculation) pointed to gas mixing as the best mixing system. A great effort was made to improve the description of the continuous phase: a rheological study helped with the description of the non-Newtonian model and extensive validation of the most common turbulence models was also carried out with the best results using the SST k-ε model with corrections for low Reynolds numbers. Regarding the gas phase, buoyancy and drag were also considered and, a Schiller-Nauman model was used for the drag coefficient.

Dapelo et al., (2015) modelled a pilot-scale anaerobic digester (4 L) using a Lagrangian approach, but not including break-up and coalescence effects. Apart from an adequate rheological study for the continuous phase, a correlation for the drag coefficient developed specifically for non-Newtonian flows was used (Dewsbury et al., 1999), as well as the Tomiyama correlation for Lateral support. The extensive validation, focused on liquid phase velocities, gives high reliability to this CFD model, although its application is limited to small set-ups.

Regarding the inclusion of the solid phase, there are still major difficulties for its CFD modelling in anaerobic digestion. Yu et al., (2013) developed a Eulerian model with the three phases in a 70-L reactor and set the Kinetic Theory of Granular Flow (KTGF) for the simulation of the movement of the solids. The solid and gas phases were considered monodisperse and of constant size; the effect of the injection of different gas flows on the movement of solid particles of different sizes was mainly studied (Yu et al., 2013a). Conversely, other anaerobic bioreactors CFD models with three phases have been considered such as Upflow Anaerobic Sludge Beds (UASBs) (Azargoshasb et al., 2015).

***Table 2.2**: Several scientific works about CFD modelling in anaerobic digestion.*

Note: G=gas mixing; SR= Sludge Recirculation and M=Mechanical. LS= lab-scale; PS=pilot-scale and FS= full-scale.

Reference	Mixing system	Description of Mixing System	Phases	Size	Volume
(Vesvikar and Al-Dahhan, 2005)	G	Draft tube with a gas sparger.	2	LS	(Karim et al., 2004)
(Karim et al., 2007)	G	Draft tube with a gas sparger.	1	LS	(Karim et al., 2004)
(Wu and Chen, 2008)	SR	External agitation	1	PS	1 o 5 m^3
(Meroney and Colorado, 2009)	M	Draft tube impeller mixer	1	FS	111 to 10045 m^3
(Terashima et al., 2009)	M	Draft tube impeller mixer	1	FS	1100 m^3
(Latha et al., 2009)	G	Hydrogen injection.	2	LS	3 L
(Wu, 2010a)	M	Draft tube impeller mixer	1	FS	4888 to 14664 m^3
	SR	External agitation	1	FS	4888 m^3
(Wu, 2010c)	G	Draft tube with a gas sparger.	2	LS	(Karim et al., 2004)
	G	Gas draft tube mixer	2	PS	791,28 m^3
	SR	External agitation	2	PS	791,28 m^3
	M	Propeller	2	PS	791,28 m^3
(Mendoza et al., 2011)	SR	External agitation	1	FS	6504 m^3
(Wu, 2011))	M	Impeller	1	FS	760 m^3
	M	Impeller	1	LS	4,5 L

Reference	Mixing system	Description of Mixing System	Phases	Size	Volume
(Yu et al., 2011)	M	Impeller	1	LS	4,5 L
(Bridgeman, 2012)	M	Impeller	1	LS	6 L
(Craig et al., 2013)	M	Draft tube impeller mixer	1	FS	1250 m^3
(Coughtrie et al., 2013)	G	Draft tube with a gas sparger.	1	LS	(Karim et al., 2004)
	G	Draft tube with a gas sparger.	2	LS	(Karim et al., 2004)
(Yu et al., 2013a)	SR	External agitation	3	LS	70 L
(Wu, 2014)	G	Bottom diffusers	2	FS	791,28 m^3
	G	Gas draft tube mixer	2	FS	791,28 m^3
	G	Lances	2	FS	791,28 m^3
	G	Bubble guns	2	FS	791,28 m^3
(Hurtado et al., 2015)	SR	External agitation	1	FS	3325 m^3
(López-Jiménez et al., 2015)	SR	HEATAMIX	1	FS	2380 m^3
(Dapelo et al., 2015)	G	Bottom diffuser	2	LS	4 L
(Sajjadi et al., 2016)	SR	External agitation	1	LS	5 L
(Zhang et al., 2016)	M	Impeller	1	LS	8 L
(Meister et al., 2018)	M and SR	External agitation and impeller within a draft tube	1	FS	2500 m^3
(Wei et al., 2018a)	G	Gas draft tube mixer	2	LS	(Karim et al., 2004)
(Fernandes del Pozo et al., 2019)	M	Impeller	1	LS	71.6 L
(Tobo et al., 2020)	M	Impellers	1	FS	9000 m^3

2.7. MEASUREMENTS AND MODEL VALIDATION

There are numerous methods in literature for validating CFD models and the most suitable for this would be the measurement of hydrodynamic variables, i.e. velocity or turbulence. On the one hand, the use of flow-following sensors could be a great tool to describe these variables, but the measurement of these variables has always been difficult at full-scale and even more difficult in anaerobic digesters (Bisgaard et al., 2020). On the other hand, positron emission particle tracking (PEPT) and computer-aided radioactive particle tracking (CARPT) have been used at lab-scale in anaerobic digesters (Dapelo et al., 2019; Hoffmann et al., 2008; Karim et al., 2004; Sindall et al., 2017) and even in aerated reactors (Chiti et al., 2011; Khopkar et al., 2005) to obtain the velocity field and turbulence. However, they need a large number of detectors to record the signal and the intensity loss through the walls or the fluid. Thus, their complexity and expensive cost are the biggest drawbacks for the application of these technologies on a large-scale. Despite this, it is important to highlight verification and validation work at lab-scale or pilot-scale with anaerobic sludge or gum solutions (Coughtrie et al., 2013; Fernandes del Pozo, 2020; Karim et al., 2007; Vesvikar and Al-Dahhan, 2005; Wei et al., 2018a; Wu, 2012a, 2012b, 2011, 2010c).

Accordingly, the absence of information inside the digester caused by the difficulty of following hydrodynamic variables, restricts or prevents the direct validation of the CFD models. Even so, it is possible to obtain global information on the process behaviour useful for the validation of CFD models by means of experimental techniques, such as inert tracers or physical-chemical analyses obtained from the sampling points or access to the digester.

The experimental cases analysed and different bibliography CFD models highlight the need for new tools to extensively observe inside anaerobic digesters. Currently, the following analytical measures are considered essential to apply to anaerobic digesters' CFD simulation and their accurate validation:

2.7.1. Fluid properties: Solids content and Non-Newtonian fluid performance

The fluid phase of an anaerobic digester must be correctly characterized in different parameters such as the concentration of solids (TS) or organic material (VSS). However, the study of the rheology of the anaerobic sludge is even more important for the CFD simulation, so the sludge should be sampled, and different tests should be performed with a rheometer to fully characterize the fluid. In the case of full-scale anaerobic digesters, it would be necessary to characterize and take samples of sludge from different locations in order to determine the concentration of solids, organic matter and rheological behaviour of the anaerobic sludge. This yields an exhaustive sampling and analysis campaign with expensive equipment and specific experts (Fernandes del Pozo, 2020), which

may be excessive compared to the ultimate goal of developing the CFD model.

Thus, the analysis of different local samples inside the digester is very different from the current practice in which only one sludge sample is taken and analysed. Furthermore, the knowledge of the total solids content in one sample allows the sludge to be compared with literature data, so that similar properties to those in the literature are established in the CFD model.

As far as the total solids content is concerned, in the anaerobic digestion process the particulate organic matter is solubilised or removed. Therefore, the concentration of total and volatile solids is reduced in anaerobic digestion so, waste activated sludge or primary sludge have a higher solids content than anaerobic digestate.

Regarding the rheology of anaerobic sludge, it has been described as shear-thinning Non Non-Newtonian fluid (Baudez et al., 2011; Eshtiaghi et al., 2013) with a variable density depending on TS content. In Non-Newtonian fluids, the apparent viscosity depends on the shear rate as the following equation:

$$\eta = \frac{\tau}{\gamma} \qquad 2.49$$

where τ is the shear stress (Pa), η is the apparent viscosity of sludge (Pa·s) and γ is the shear rate (s^{-1}). There are different models to describe the behaviour of the Non-Newtonian fluids to shear rate and waste activated sludge and anaerobic digestate are usually described with the Ostwald model (power-law model), the Bingham model or the Herschel-Bulkley model (Eshtiaghi et al., 2013; Ratkovich et al., 2013). The Ostwald model is the simplest rheological model and it is defined as Eq. 2.50. The Herschel-Bulkley model (Eq. 2.51) combines the power law and the Bingham model.

$$\tau = K\gamma^n \qquad 2.50$$

$$\tau = \tau_0 + K\gamma^n \qquad 2.51$$

where K is the fluid consistency index ($Pa \cdot s^n$), n is the power law index (-) and τ_0 is the yield stress (Pa). Experimental measurements of shear rate, shear stress and apparent viscosity are fitted to these models to set them at the CFD model. The calibration of τ_0 is probably the most difficult in these measurements, as low shear rates (lower than 1 s^{-1}) and accurate equipment are needed.

An exhaustive characterization of anaerobic sludge Non-Newtonian models can be found at different works depending on the solids concentration, temperature or digestion stage (i.e. digested or waste activated sludge) (Baudez et al., 2013a, 2013b, 2011; Markis et al., 2014; Mbaye et al., 2014; Monteiro, 1997; Wei et al., 2018b).

2.7.2. Tracer test procedure

A correct prediction of the reactor's hydrodynamic behaviour would require a full representation of the velocity field. This task would be a complex technique and almost impossible in anaerobic digesters. Instead, a Residence Time Distribution (RTD) study is less challenging but feasible and will provide enough information to elaborate the hydrodynamic behaviour of the fluid in the anaerobic digester. This information, although costly, can be determined relatively easily by means of the experimental stimulus-response technique using inert tracers (Gujer, 2007).

The inert tracer technique is based on the introduction of an inert (non-reactive, non-biodegradable and not solvable to solids) compound into the process unit, in order to know the hydraulic behaviour of the unit. Accordingly, the hydraulic behaviour is known through the following procedure: measurement of the tracer concentration, calculation of the RTD curve and its approximation to ideal hydraulic behaviour (CSTR or plug-flow reactor)(Cholette and Cloutier, 1959; Levenspiel, 1999).

Initial works using RTD in the analysis and study of chemical reactors date from the mid-20th century (Danckwerts, 1953; MacMullin and Weber, 1935). RTD is defined as the time that the fluid's molecules remain inside the tank. When constant flowrates are considered in reactors, ideal hydraulic behaviours, such as CSTR or plug-flow reactors, are assumed. However, the real RTD of the fluid may be non-ideal so that not all the molecules that pass through the reactor remain the same length of time. This behaviour is due to the appearance of hydraulic defects: part of the feed passes directly to the output (i.e. short-circuiting), areas where the fluid is practically not renewed, reagents or products form conglomerates and do not mix well with each other or depositions are produced (i.e. dead volumes), etc. Accordingly, there is a non-ideal flow that could be studied by means of inert tracer techniques (Cholette and Cloutier, 1959; Levenspiel, 1999).

One of the most important issues to highlight in the choice of the tracer is that it must have physical properties similar to those of the reaction mixture: it must be completely soluble in the mixture and must not be adsorbed on the surfaces or walls of the anaerobic digester or on any substance contained in the mixture. Regarding the different tracer injection methods, the most used methods are "by pulse" and "by step" (Gujer, 2007; Levenspiel, 1999). Among its use in full-scale anaerobic digesters, the use of the pulse input is recommended as a small amount of tracer is used. The quantification method of the inert tracer concentration in the output or recirculation flow depends on the tracer used, so that absorbance, pH, electrical conductivity, or fluorescence can be used (Levenspiel, 1999). Accordingly, the type of tracer, the quantification method and the equipment determine the cost of the inert tracer experience. In addition to these issues, a 95% recovery of the tracer is highly recommended as a lower amount of tracer recovery would invalidate the tracer test results (Climent

Agustina, 2019; Kadlec and Wallace, 2009).

In the case of full-scale anaerobic digesters, it is important to know the tracer's detection limit and its baseline concentration that will define the tracer mass to be introduced. Additionally, the high HRT of the system entails a large number of samples to be collected and processed, as it is recommended that the total sampling time to obtain the RTD in a vessel is approximately three times the HRT (Rieger et al., 2013). Hence, the total cost of these tracer test is often the main barrier to their application in full-scale anaerobic digesters.

The most commonly used injection method in anaerobic digesters is input by pulse. An amount M (moles or grams) is injected instantaneously into the inflow and the tracer concentration is measured as a function of the elapsed time to obtain the concentration-time curve or $C(t)$ curve. The tracer test will continue until outlet's tracer concentration is zero (or constant in the case of step injection). The RTD or $\mathrm{E}(\theta)$ (dimensionless residence time distribution) can be calculated from the effluent tracer concentration or $C(t)$) curve:

$$E(\theta) = t_m E(t) = \frac{V}{q} E(t) = \frac{V}{M} C(t) \qquad 2.52$$

where θ is the dimensionless time scale ($\theta = \frac{\mathrm{t}}{t_m}$), t_m is the mean residence time(s), $E(t)$ is the temporal residence time distribution (s^{-1}), V is the anaerobic digester volume (m^3), q is the influent flow rate.

After obtaining the experimental RTD curve, its shape can be analysed to determine the hydrodynamic behaviour and detect hydraulic defects (Froment and Bischoff, 1990). Different protocols help in the tracer test's design (Rieger et al., 2013) that recommend intensive sampling time in the initial times of the tracer test in systems closer to the CSTR behaviour, such as most of the anaerobic digesters. These initial times of the tracer test contained most of the information about hydrodynamic defects. Thus, the initial tracer concentration compared to the theoretical concentration $\left(\frac{M}{V}\right)$ and the time of first tracer detection can be used to quantify dead volumes and short-circuiting. For example, a short-circuiting is revealed by an early sharp peak of the curve, dead volumes are shown when the experimental mean residence time is lower the theoretical HRT of the tank and an ideal CSTR would be a smooth exponential decay of $C(t)$. However, it is also important to extend the sampling times in order to quantify the tail of the curve (Levenspiel, 1999). These curves can be characterized analytically to calculate the mean residence time and to produce a real flow model with adjustable parameters, either n-series tanks or degree of axial dispersion (d) in a plug-flow reactor (Froment and Bischoff, 1990; Levenspiel, 1999; Tchobanoglous et al., 2004).

This technique has already been used in anaerobic digesters using radioactive isotopes as tracers in the early days (B. L. Loffell, 1959; White, 1974; Zoltek and Gram, 1975). Nevertheless, a wide variety of chemicals have been used as tracers, such as fluoride (Monteith and Stephenson, 1981; Verhoff et al.,

1974) or lithium (Terashima et al., 2009). This technique helps to report dead volumes and short-circuiting in full-scale anaerobic digesters with different mixing configurations and volumes as in Monteith and Stephenson, (1981), who reported up to 75% dead volume, and Smart, (1978), who detected from 10 to 89% dead volume and from 18 to 72% short-circuiting.

Attending to its usability, the inert tracer technique can be used to validate the CFD model and has already been used by different authors (Alvarado et al., 2012; Le Moullec et al., 2008). The CFD model will be validated, if it can reproduce the same experimental RTD curve. In order to reproduce the inert plotter curve, a transient simulation is performed in which the real experience with inert plotters with different meshes and turbulence models is reproduced. The correct CFD model will be the one whose mesh and turbulence model can reproduce the experimental RTD curve as it confirms that our CFD model behaves hydraulically like the real process unit.

This procedure was used by Meroney and Colorado, (2009); they validated their CFD simulations by reproducing a tracer experience from the bibliography. Additionally, the tracer technique was used in a hydrodynamic study of four different circular anaerobic digesters. Another validation of the CFD model was done in Terashima et al., (2009) through a tracer test in an egg-shaped full-scale anaerobic digester but without reproducing the complete RTD. Kinyua et al., (2015) validated their tubular full-scale anaerobic digester CFD model with a tracer test performed with KCl for 30 days.

Different authors have highlighted the large amount of inert tracers and the difficulty of performing tracer tests in full-scale anaerobic digesters (Terashima et al., 2009). However, the same authors applied Lithium Chloride as inert tracer in an egg-shaped anaerobic digester of 1100 m^3. Their sampling time was only 6 days, but they reproduced their experimental results accurately with CFD modelling (Terashima et al., 2009).

3. EVALUATION OF MIXING AND DEAD VOLUMES IN A FULL-SCALE ANAEROBIC DIGESTER USING CFD AND EXPERIMENTAL VALIDATION

The work developed in this chapter focused on the assessment of literature parameters traditionally applied to anaerobic digesters' mixing evaluation. Thus, design, local mixing and global mixing parameters were tested in several CFD scenarios. Furthermore, an examination of the dead volume literature criteria was made applying these criteria to the CFD models aiming to evaluate their usefulness. The design parameters showed some drawbacks for calculating the mixing power. For their part, the coupling of the local mixing parameters was convenient to define the mixing intensity and type. A new global mixing parameter and dead volume criteria were proposed: On the one hand, the new global mixing parameter stated a great robustness and effectiveness to calculate the homogenisation time. On the other hand, the new dead volume criteria were calibrated with experimental data from tracer test so, they clearly identified the dead volumes.

Abstract: Anaerobic digestion has become an essential process for sludge treatment and its optimum performance is related to the mixing performance. In this study, a full-scale anaerobic digester with an external recirculation mixing system was studied via single-phase 3D-CFD simulations as well as experimentally through inert tracer tests to assess the influence of the recirculation flow and a 3-blades propeller at different configurations and validate the CFD model. Design and mixing parameters were studied to characterize the degree of mixing in different scenarios. Dead volumes under different criteria were also compared with experimental ones. The second-order moment was proposed as a global mixing parameter that describes geometrical and local mixing. In addition, new dead volume criteria were proposed including buoyancy force and low turbulence dispersion phenomena. The different mixing strategies studied, state that intermittent propeller mixing is a superior strategy to reduce energy consumption without causing dead volumes.

Keywords: Full-scale; Homogeneity; Intermittent Mixing; Tracer; Dead Volumes.

A modified version of this chapter was published in Chemical Engineering Science X as:

R. Arnau, J. Climent, R. Martínez-Cuenca, J. Rodríguez, and S. Chiva, 2022. Evaluation of hydraulic mixing performance in a full-scale anaerobic digester with an external liquid recirculation system using CFD and experimental validation

3.1. INTRODUCTION

The microbial community responsible for the anaerobic digestion consists of numerous bacteria and archaea which must work in balanced harmony for the process to remain stable (Kleerebezem, 2014). Inadequate mixing can result in zones of high substrate concentrations leading to fast local accumulation of acid intermediates or other inhibitors with negative repercussions on process effectiveness, and even possible consequences such as process inhibition and destabilisation.

Anaerobic digesters are designed to fulfil a hydraulic retention time (HRT) greater than 10 days to ensure the biological treatment of the influent organic material. Thus, they are expected to provide proper mixing and homogenisation of their content (Tchobanoglous et al., 2004). Several design parameters, known as 'rules-of-thumb' (Meroney and Colorado, 2009), have been proposed to provide the dimensions and operating conditions for optimal mixing and homogenisation. However, their application to real setups sometimes produces poorly mixed tanks, with short-circuits, apparent inhomogeneities, or even dead volume formation. In the worst scenarios, solids settling may be noticeable and a significant reduction of the HRT can be observed (Monteith and Stephenson, 1981). As a result, the performance of faultily-designed anaerobic digesters is far from the ideally mixed tank that is generally assumed (Terashima et al., 2009).

In practice, these faulty designs are difficult to identify and solve. The anaerobic atmosphere forces these systems to be sealed, so, it is not easy to install proper instrumentation for the flow characterization (see Section 2.7). A common practice is the use of tracer methods (Cholette and Cloutier, 1959; Levenspiel, 1999; Monteith and Stephenson, 1981) to evaluate the overall hydrodynamic performance from the RTDs and to detect short-circuiting and dead volumes (Meroney and Colorado, 2009; Monteith and Stephenson, 1981; Terashima et al., 2009) (see Section 2.7.2 for the description of this technique). Nonetheless, they do not provide any useful information that can be used to identify why they take place, so it is not possible to propose solutions based on their results.

Accordingly, the use of CFD has been proposed to get a better insight into the hydraulic behaviour of working setups (Paul et al., 2004). CFD provides detailed 3D descriptions of the velocity field and turbulence inside the tanks. The visualization of CFD results, i.e. fluid velocity vectors, streamlines, and/or particle trajectories, helps to understand the mixing process and to identify the origin of the faulty hydraulic behaviour for each case (Meroney and Colorado, 2009).

Current research has focused on the development of full-scale CFD models to analyse different mixing systems and evaluate hydraulic defects as described in Section 2.6. The global digesters hydraulic behaviour is complex to

analyse and up to now, several parameters have been proposed to characterize the hydraulic and mixing performance of anaerobic digesters, as well as the formation of hydraulic defects. Terashima et al., (2009) proposed the Uniformity Index (UI) to characterize the mixing and degree of homogenisation. The UI was also used to determine the homogenisation time, i.e. the time needed to accomplish complete mixing (Dapelo and Bridgeman, 2018). Concerning the formation of hydraulic defects, Karim et al., (2004) and Vesvikar and Al-Dahhan, (2005) proposed different criteria to predict the extent of dead volumes from CFD simulations. Later works (Bridgeman, 2012; Hurtado et al., 2015; Karim et al., 2007; López-Jiménez et al., 2015; Wu and Chen, 2008) have applied these criteria to different geometries. It is important to note that these works have used different criteria with different values for each parameter, there is currently no clear agreement, and the set of threshold parameters for the same criteria is modified in each work, showing their lack of generality.

The present work aims to analyse the hydraulic performance of a full-scale anaerobic digester with two different configurations, with liquid recirculation and mechanical mixing, using single-phase 3D CFD models. The numerical model was validated using inert tracers, and to the authors' best knowledge, this is the first time that a complete RTD is used to check the global hydraulic performance in a full-scale Anaerobic Digester and validate a CFD model. Different CFD mixing scenarios were considered in order to study the influence of recirculation flow and an internal propeller on the setups' hydrodynamics. An extensive analysis of parameters from literature, such as design parameters (DVTT, UP, and G), local velocity gradient, or UI, is then done and applied to the different CFD scenarios. An assessment of the CFD's dead volume criteria in anaerobic digesters is carried out and compared with experimental dead volume. Finally, to establish mixing parameters and dead volume criteria of general application, a new global mixing parameter and dead volume criteria are proposed.

3.2. CHARACTERIZATION OF THE ANAEROBIC DIGESTER PERFORMANCE

The literature is rich in parameters that describe the performance of mixing in tanks. Here, we briefly introduce the most used ones. For the sake of clarity, these parameters are arranged in four categories, according to their application to design, mixing or defect studies. This section ends with the proposal of new parameters to account for the formation of dead volumes.

3.2.1. Design parameters

Design parameters, usually known as "rules of thumb", aim at providing the proper dimensioning of the mixing tanks and their operating conditions (Meroney and Colorado, 2009; Tchobanoglous et al., 2004).

- The HRT, calculated in days, is expressed as

$$HRT = \frac{V}{q_{inlet}} \quad 3.1$$

where V is the digester's volume (m^3) and q_{inlet} (m^3/day) is the inlet flowrate (not including recirculation). Ideally, the HRT should be similar to the mean residence time obtained from the tracer curves. Strong deviations indicate the apparition of hydraulic defects, such as short-circuits or dead volumes.

- The Digester Volume Turnover Time (DVTT), designed in minutes, is obtained as

$$DVTT = \frac{V}{q_{recirc}} \quad 3.2$$

where q_{recirc}(m^3/min) stands for the recirculation flow.

- The Unit Power (UP) or Mixing Energy Level (MEL), measured in W/ m^3, is defined as

$$UP = \frac{P}{V} \quad 3.3$$

where P is the power input (W), i.e. the pumping power.

- The global RMS Velocity Gradient, $\bar{G}$, measured in s^{-1}, has been used as a mixing criterion to quantify the power input needed in a setup. It can be calculated as

$$\bar{G} = \sqrt{\frac{\mathrm{P}}{\mu \times \mathrm{V}}} \quad 3.4$$

where μ is the dynamic viscosity (Pa·s).

The US UEPA (1979) proposed the recommended design parameter values in **Table 3.1** to achieve efficient mixing:

***Table 3.1**: Recommended design parameters. (US EPA, 1979)*

HRT(day)	DVTT(min)	UP or MEL(W/m^3)	$\bar{G}$(s-1)
15-30	30-45	5-8 3	50-85

A typical route for the design of an anaerobic digester would be to set the volume from Eq 3.1. Then the recirculation flow and Power Input from these values and Eqs. 3.2 to 3.4.

Note that there is an alternate design approach following the work of McLeod et al., (2019), who relate the power input and the total mass of solids, M_S (kg), as

$$\left(\frac{P}{M_S}\right) = 0.01456 \times e^{0.09725 \times TS} \quad 3.5$$

where TS is the inlet solids concentration (kg/ m^3). The volume and recirculation flow are calculated as before, and the power input is calculated from Eq. 3.5.

3.2.2. Local Mixing parameters

To estimate the degree of local mixing in the anaerobic digester from CFD simulations, a local RMS Velocity Gradient (s^{-1}) can be computed as (Changgen Luo, 1997; Sindall et al., 2013),

$$G = \sqrt{\frac{\varepsilon}{\nu}} \quad 3.6$$

where ε is the energy dissipation per unit mass (m^2/s^3) and ν is the kinematic viscosity of the fluid (m^2/s). Then, the spatial average of the local RMS velocity Gradient provides the global RMS Velocity Gradient defined in Eq. 3.4.

Another parameter to describe the mixing degree locally within the anaerobic digester is the Dispersive mixing efficiency (α_{DME})(-). It was described with the following equation (Khapre and Munshi, 2016; Manas-Zloczower, 1994):

$$\alpha_{DME} = \frac{\|\dot{\gamma}\|}{\|\dot{\gamma}\| + \|\omega\|} \quad 3.7$$

where $\dot{\gamma}$ is the rate of strain tensor and ω is the vorticity tensor, both variables available in the numerical simulations. It relates to the type of deformation the fluid undergoes within the tank: On the one hand, the deformation caused by elongation or symmetric deformation is defined by the shear rate. On the other hand, the anti-symmetric deformation caused by irrotational flow is described by the vorticity tensor. The value of this parameter can define the type of flow that is producing the mixing within the vessel as:

- $\alpha_{\mathrm{DME}} = 0$ for pure rotation no effective mixing or rotational flow
- $\alpha_{\mathrm{DME}} = 0.5$ a shear flow
- $\alpha_{\mathrm{DME}} = 1$ a dispersive flow by pure elongation

As the local mixing parameters can be computed in every cell of the

numerical simulation, they give more information about the mixing efficiency and mixing type than other ones.

3.2.3. Global Mixing parameters

One of the major concerns in the study of anaerobic digesters is their ability to homogeneously mix their content, so it is quite convenient to develop a set of performance parameters that allow for the quantification of how well a given ADer is mixing. The global RMS Velocity Gradient is typically used as a design parameter but lacks generality, as the required value depends on the vessel size and the configuration of its internals. The use of CFD simulations provides a better insight into the AD behaviour, allowing the definition of new more relevant mixing parameters. As this set of parameters are calculated from the local characteristics of the flow, their formulation is expected to be generally applicable. The exposed global mixing parameters in this section need an inert tracer experience to be studied. The description of this experience is detailed in Section 3.3.3.4.2.

Terashima et al. (2009) proposed the first mixing parameter based on CFD simulations: the Uniformity Index (UI) (-). Later on, it was modified (Dapelo and Bridgeman, 2018) so that can be calculated as

$$UI = \frac{\sum_{i=1}^{m}\{|C_i - \bar{C}|V_i\}}{2\,V\,\bar{C}} \qquad 3.8$$

where V_i is the cell volume (m^3), C_i is the cell tracer concentration (ppm), and $\bar{C}$ is the average tracer volume concentration (ppm), computed as

$$\bar{C} = \frac{\sum_{i=1}^{m} C_i V_i}{V} \qquad 3.9$$

Note that the UI takes 1 as the maximum value when all the tracer is located in just one cell (completely non-uniformly distributed), and it equals 0 when the tracer is homogeneously distributed within the region (same concentration in each cell). According to Terashima et al., (2009), a homogenisation time, t_{UI} (time), can be defined as the time for which the UI reaches a value of 0.01 (-) (0.99 percentile). The UI only describes how much the digester is mixed globally but not how that degree of mixing has been reached.

Thus, we propose the use of a new set of mixing parameters based on the moments' theory (Papoulis, 1984). Central moments are a valuable mathematical tool to characterize the location, spread, and shape of mathematical distributions, such as the tracer concentration within the setups volume. The first-order moments account for the location of the distribution centroid, so they are expected to change over time as the tracer pulse advances. The first-order central moments account for the location of the distribution centroid. Using cylindrical coordinates (r, θ, z) they can be calculated as:

$$\bar{r}(t) = \frac{1}{V\bar{C}} \int_{CV} r\, C(r,\theta,z,t)\, dV \qquad 3.10$$

$$\bar{\theta}(t) = \frac{1}{V\bar{C}} \int_{CV} \theta\, C(r,\theta,z,t)\, dV \qquad 3.11$$

$$\bar{z}(t) = \frac{1}{V\bar{C}} \int_{CV} z\, C(r,\theta,z,t)\, dV \qquad 3.12$$

The second-order central moments are related to the distribution spread and can be computed as:

$$\sigma_r^2(t) = \frac{1}{V\bar{C}} \int_{CV} (r-\bar{r})^2\, C(r,\theta,z,t)\, dV \qquad 3.13$$

$$\sigma_\theta^2(t) = \frac{1}{V\bar{C}} \int_{CV} (\theta-\bar{\theta})^2 C(r,\theta,z,t)\, dV \qquad 3.14$$

$$\sigma_z^2(t) = \frac{1}{V\bar{C}} \int_{CV} (z-\bar{z})^2\, C(r,\theta,z,t)\, dV \qquad 3.15$$

Note that the second-order moment for the azimuthal component cannot be directly compared with those for radial and axial directions, as they have different units. To make them comparable, we use the following dimensionalized version of the moment:

$$\hat{\sigma}_\theta^2(t) = \bar{r}^2(t)\sigma_\theta^2(t) \qquad 3.16$$

As a result of this dimensionalization, this moment can be interpreted as the width of the distribution across the azimuthal direction, so it can be compared to the radial and axial widths.

Using this set of second-order moments it is easy to check if the mixing is performed isotropically or not. This is the major benefit over the UI, since the second-order moments show the direction that encourages the homogenisation of the anaerobic digester. Furthermore, it is possible to quantify the degree of homogenisation. When the tracer pulse enters the domain, these moments will be nearly zero, as the tracer is localized on the inlet region. As time advances, the tracer will start to spread, and these moments will increase. Eventually, the tracer would be homogeneously distributed having a constant value throughout the domain, i.e. $C(r,\theta,z,t) = \bar{C}$. When the tracer is homogeneously distributed and stationary, these moments become $\sigma_{r,h}^2, \hat{\sigma}_{\theta,h}^2, \sigma_{z,h}^2$, and could be expressed as:

$$\sigma_{r,h}^2 = \frac{1}{V} \int_{CV} (r-\bar{r})^2\, dV \qquad 3.17$$

$$\hat{\sigma}_{\theta,h}^2 = \frac{\sigma_{r,h}^2}{V} \int_{CV} (\theta-\bar{\theta})^2\, dV \qquad 3.18$$

$$\sigma_{z,h}^2 = \frac{1}{V}\int_{CV}(z-\bar{z})^2 \; dV \qquad 3.19$$

This leads to the definition of a set of normalized second-order central moments, with an initial value of 0 and a homogeneous value of 1, as:

$$\tilde{\sigma}_r^2(t) = \frac{\sigma_r^2(t)}{\sigma_{r,h}^2} \qquad 3.20$$

$$\tilde{\sigma}_\theta^2(t) = \frac{\hat{\sigma}_\theta^2(t)}{\hat{\sigma}_{\theta,h}^2} \qquad 3.21$$

$$\tilde{\sigma}_z^2(t) = \frac{\sigma_z^2(t)}{\sigma_{z,h}^2} \qquad 3.22$$

From this definition, a homogenisation time can be estimated as the time when all the normalized second-order moments remain over 0.99.

Table 3.2 shows a summary of the parameters described above: design parameters, local mixing parameters and global mixing parameters.

***Table 3.2**: Summary of parameters.*

Type of parameter	Parameter	Recommended values/ Normal values
Design	HRT	15-30 days
	DVTT	30-45 min
	UP/MEL	5-8 W/m^3
	$\bar{G}$	50-85 s^{-1}
Local Mixing	Local RMS Velocity Gradient	50-85 s^{-1}
	α_{DME}	0-1 [-]
Global Mixing	UI	1-0 [-]
	Second-Order Moments	-

3.2.4. Dead volume

As explained in Section 2.3.1, the development of dead volumes and solids settling is the second major concern in the design of anaerobic digesters. Dead Volumes or Stagnant Zones are isolated regions inside tanks where the flow velocity is low or the fluid does not move at all (Li et al., 2017). They are usually

characterized by large static eddies, and if the flow velocity is small, they might lead to settling. The settling of particles reduces the effective volume of the vessel causing a reduction of the residence time.

At present, there are no mathematical tools to predict their occurrence from global parameters. To this aim, recent research studies have proposed the analysis of CFD results. To date, the most accepted definition of dead zone from CFD simulations is the one proposed by Vesvikar and Al-Dahhan, (2005): all regions with less than 5% of the maximum velocity are inactive zones that will be converted into dead volumes. Therefore, the total dead volume, V_D, can be computed as:

$$V_D = \int_V step(\, v_{lim} - v)\, dV \qquad 3.23$$

where the $step$ function values 1 when its argument is greater than 0, and 0 otherwise. The limiting velocity, in this case, is given by,

$$v_{lim} = 0.05\, v_{max} \qquad 3.24$$

As the $step$ function only provides binary values, 0 or 1, this definition can be stated from a probabilistic viewpoint: every region in the domain is contributing to the formation or washing of the settled volume. Regions where the flow velocity exceeds the limiting value do not contribute to the dead volume (probability 0), whereas regions below it contribute with a probability of 1. The overall dead volume results from the integration of these cell probabilities over the tank volume.

This definition has been used by different authors (Bridgeman, 2012; Hurtado et al., 2015) in their CFD models but with no validation. Wu and Chen, (2008) used a similar criterion, but had to change the limiting velocity to $v_{lim} = 0.001\, m/s$ to obtain a reasonable dead volume value. In other words, they had to change the original limiting value to their specific configuration.

Note that these approaches are based on single-phase flow considerations while the actual fluids in these tanks are multiphase mixtures, in which the suspended solids play a central role. Hence, it is apparent that a reliable criterion must depart from two-phase flow considerations as proposed by Karim et al., (2004). From this outlook, the buoyancy force drives settling, so the particles will settle unless the upward component of the flow velocity, v_v, exceeds the settling velocity, v_t. Therefore, the dead volume can be computed as:

$$V_D = \int_{\forall_{ADer}} step(\, v_t - v_v)\, d\forall \qquad 3.25$$

Additionally, they proposed to use Stoke's law to calculate the terminal velocity as:

$$v_t = \frac{(\rho_f - \rho_l)g}{18\mu} d_p \qquad 3.26$$

In this equation, ρ_l and μ stand for the liquid density (kg/m^3) and dynamic viscosity (Pa.s), respectively; whereas ρ_p and d_p stand for the solids density (kg/m^3) and diameter (m) of the suspended particles. The authors stated that the size and the settling velocity of activated sludge flocs collected from full-scale WWTPs are in the range of 0.06–12 mm, so their terminal velocities were estimated to be in the range of 0.02–2 cm/s. As a result, they proposed the use of an intermediate value of 0.2 cm/s. In a later work, Karim et al., (2007), a slightly higher value (0.32 cm/s) was proposed to provide adequate results for a different configuration. Recently López-Jiménez et al., (2015) proposed a value of 2 cm/s for non-Newtonian fluid simulations. So, in practice, authors following this criterion ended up adjusting the terminal velocity or floc diameter to match reasonable dead volumes at their CFD models.

Table 3.3 shows a summary of dead volume criteria described in literature.

***Table 3.3**: Summary of dead volume criteria from the literature.*

Reference	Number	Criteria
Vesvikar and Al-Dahhan, (2005)	DV1	$0.05\ v_{max}$
Wu and Chen, (2008)	DV2	v < 0.001 m/s
López-Jiménez et al., (2015)	DV3	v_v < 2 cm/s
Karim et al., (2007)	DV4	v_v < 0.32 cm/s
Karim et al., (2004)	DV5	v_v < 0.2 cm/s

In this work, we propose a new set of criteria that considers that the formation of dead volumes is driven by two main causes: buoyancy force and low turbulence dispersion. The first effect can be accounted for as in Eq. 3.25: each cell in the domain contributes to the formation/washing of dead volumes depending on the magnitude of the vertical flow velocity with respect to the terminal velocity. Nevertheless, the $step$ function only assigns values 1 and 0 to every cell, so it establishes the same probability of formation of dead volumes (value of 1) to cells that slightly exceed the terminal velocity and to those that exceed it by orders of magnitude. Physically, it would be more convenient to assign a probability with values ranging from 0 to 1 considering the magnitude of the difference between the two velocities. In this way, the transition between the formation/washing of dead volume would be smoother. For this reason, we propose the following buoyancy probability density function (PDF),

$$0.5 + 0.5 \tanh\left(\frac{(v_t - v_v)}{C_v . v_t}\right) \quad 3.27$$

where the smoothness of the transition between 0 and 1 is controlled by the velocity constant C_v (**Figure 3.1**a). The influence of the velocity constant on the resulting dead volume will be revised later on.

To further improve this first effect contribution, we note that the terminal velocity of the particles depends on their size, which is influenced by the flow characteristics: the floc diameter results from a balance between the shearing forces in the flow that tends to break them, and the aggregation rate that induces their coalescence. This balance was investigated by Bache et al., (1999), who proposed the following expression for the theoretical mean floc diameter:

$$d_f = \frac{\sigma \upsilon^{1/4}}{\rho_f \varepsilon^{3/4}} \quad 3.28$$

where σ is the floc strength estimate 0.00126 N/ m^2 according to the works of (Bache et al., 1999; Biggs and Lant, 2000), υ is the kinematic viscosity of the fluid and ε is the rate of energy dissipation per unit mass of fluid (N m s^{-1} kg^{-1}). As the energy dissipation appears as the denominator, the size of the floc increases in regions with low turbulence. Consequently, the regions with low turbulence develop big flocs that settle at faster velocities.

The second effect is related to the turbulent dispersion of the flocs. High turbulence will homogenise the tank so that the formation of dead volumes is reduced. The contribution of this effect can be formally introduced as a second factor multiplying the buoyancy PDF: the turbulent PDF. On the one hand, this function should take a value of 1 when there is no turbulence and particles create dead volume and, should approach 0 when turbulence increases. The two most common PDFs that meet this requirement are the Exponential Decay and the Gaussian function. On the other hand, the function must include dimensionless parameters that take into account both turbulence level and ADer size. According to Roberts and Webster, (2003), when particles fall in a turbulent flow (see **Figure 3.1**b), they follow different paths due to the turbulent dispersion. As a result, particles that are close together at a given time, are spread within a diffusion cone of diameter, σ_{exp}(m), given by,

$$\sigma_{exp} = \sqrt{\left|\frac{2 \cdot D_T . y}{v_t}\right|} \quad 3.29$$

being y the vertical distance from the calculation point to the lowest point of the tank and D_T the turbulence diffusivity (m^2/s);

$$D_T = \frac{\mu_T}{(\rho_f \times 0.9)} \quad 3.30$$

where μ_t (kg/m s) represents the turbulent eddy viscosity.

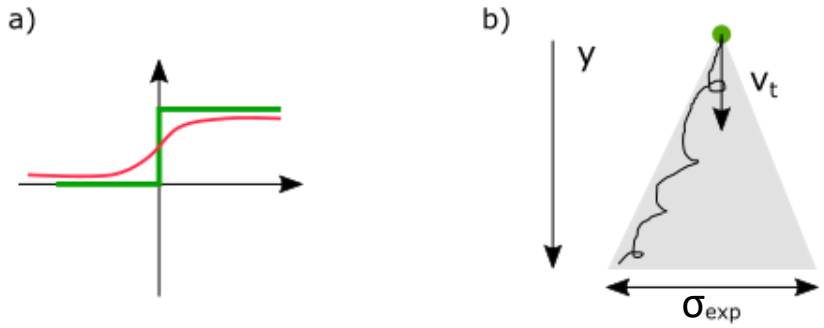

Figure 3.1: *a) step function (green line) vs tanh function (red line). b) Particle movement due to turbulent dispersion.*

By combining both effects, the following PDFs are proposed:

$$\text{Bouyancy PDF: } V_D = \int_{\forall_{ADer}} \left[0.5 + 0.5\tanh\left(\frac{(v_t - v_v)}{C_v \cdot v_t}\right)\right] d\forall \qquad 3.31$$

$$\text{Exponential Decay PDF: } V_D = \int_{\forall_{ADer}} \left(\left[0.5 + 0.5\tanh\left(\frac{(v_t - v_v)}{C_v \cdot v_t}\right)\right] \times exp\left[-\left(\frac{4 \cdot \sigma_{exp}}{C_t \cdot \emptyset_{ADer}}\right)\right]\right) d\forall \qquad 3.32$$

$$\text{Gaussian PDF: } V_D = \int_{\forall_{ADer}} \left(\left[0.5 + 0.5\tanh\left(\frac{(v_t - v_v)}{C_v \cdot v_t}\right)\right] \times exp\left[-\left(\frac{0.5 \cdot {\sigma_{exp}}^2}{(C_t \cdot \emptyset_{ADer})^2}\right)\right]\right) d\forall \qquad 3.33$$

where C_t is a turbulence coefficient and $\emptyset_{ADer}$ is the ADer diameter. In order to find the correct expression that agrees with experimental dead volume, they are computed and compared with experimental dead volume values. In addition, the velocity constant and turbulence coefficient values are calibrated. Therefore, the set of velocity and turbulence constants employed in the calibration process is found in **Table A.1** and **Table A.2**, respectively. As result, an accurate dead volume criterion in agreement with experimental dead volume will be found.

3.3. MATERIALS AND METHODS

An anaerobic digester in different setups was studied through inert tracer experiences and CFD models. The setups have a DYNOMIX system (external recirculation pump) as a mixing device. Additionally, one of them has an internal propeller to enhance bottom mixing. They were modelled under a Non-Newtonian single-phase CFD to evaluate different mixing configurations.

3.3.1. Description of the setups

This study is based on a full-scale anaerobic digester with two different configurations aiming to evaluate several mixing parameters, asses different

dead volume criteria and propose new ones. Thus, **Table 3.4** overviews the CFD model and the experimental dead volume for each configuration.

Table 3.4: *Overview of the anaerobic digesters.*

Setup	CFD Model	Experimental Dead Volume
1	A100 and B100	0% and Intermittent mixing
2	A100	13 %

Both setups are installed at different WWTPs in Spain and are more than 3000 m^3. The setups have the same dimensions and similar TS% so **Figure 3.2** provides a general overview of their geometry and the locations of their internal components. They have a cylindrical-like shape, with their bottom surface slightly inclined forming a conical geometry.

Therefore, one CFD model has been developed to reproduce both setups. **Table 3.5** summarizes the main dimensions as well as the three main flowrates in both setups: the feed flow of waste (activated sludge), the heat exchanger flow, and the recirculation flow. The feeding and heat exchanger flows are introduced together into the tank through the inlet nozzle (**Figure 3.2**a). The recirculation is injected using two nozzles (**Figure 3.2**b). The flow leaves the setup through the Outlet, located at the bottom of the tank, close to its axis. The heat exchanger is fed using a suction pipe (**Figure 3.2**c) located close to the wall, at 4.2 m above the bottom. Another suction pipe, located near the top of the tank, removes the recirculating flow (**Figure 3.2**d). To provide further mixing, a three-blade submersible propeller (WILO EMU MAXI PROP TR 315.33, 1.5 m diameter blades, and 3.5 kW power) is installed close to the bottom (see **Figure 3.2**a). The appendix provides a full description of the dimensions and its internal elements (**Figure B.1** and **Table B.3**). The central column shown was initially designed to remove the recirculation flow but it is not in use.

Table 3.5: *Main dimensions and flows of the anaerobic digester.*

Diameter (m)	23
Height of the liquid free surface (m)	8.25
Volume (m^3)	3432
Feed flow (m^3/h)	8.3
Heat exchanger flow (m^3/h)	35 (4.2 times feed flow)
DYNOMIX recirculation flow (m^3/h)	680 (81.9 times feed flow)

The first setup (hereafter referred to as Digester 1) operates alternating two hydrodynamic regimes. In the first one, the external recirculation pump system is active, and the propeller remains off. The setup operates most of the time (162 hours per week) under this regime and this is defined as the base scenario, A100. In the second regime, the internal propeller is turned on while the DYNOMIX system remains active. This configuration runs only 6 hours per week approximately and is defined as scenario B100.

The second setup is the one described in Climent et al., (2013) with dimensions and nozzles identical to those of Digester 1. However, it does not have an internal propeller, so its external recirculation pump system is always active. Accordingly, the base CFD model (A100) shows the hydrodynamic performance of Digester 2 (see **Table 3.4**).

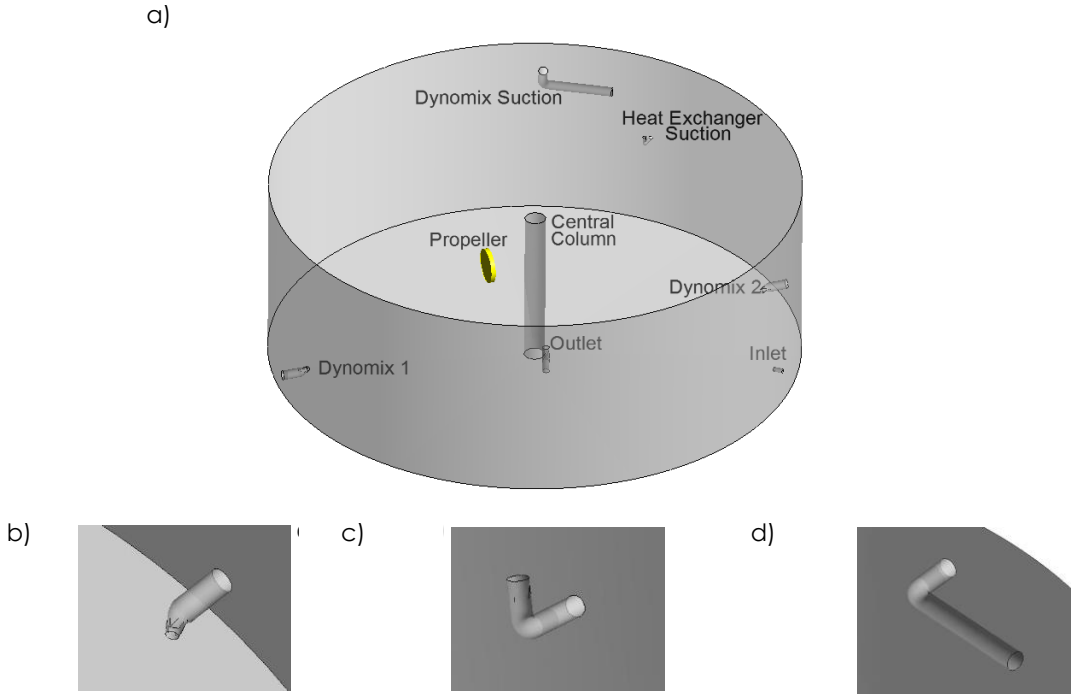

Figure 3.2: *Details of Digester geometry: a) general view of the digester, with the propeller in yellow; b) DYNOMIX nozzle; c) heat exchanger suction pipe; and d) DYNOMIX recirculation's suction tube.*

3.3.2. Experimental measurements

To experimentally determine the global hydraulic behaviour of both full-scale setups, tracer experiments were found in literature (Climent et al., 2019, 2013). In addition, the rheology of the sludge was characterized using a rotational rheometer.

3.3.2.1. Hydraulic behaviour study: Tracer test

Typically, the overall hydraulic characterization of a full-scale anaerobic

digester is limited to tracer studies. In this case, two experimental tracer tests were conducted in Climent et al., (2019) for Digester 1 and in Climent et al., (2013) for Digester 2.

Firstly, a fluorescent tracer was used at Digester 2. Batch experiments were performed to quantify the tracer's absortion to solids and the background concentrations were measured from samples collected from the influent and effluent. In these batch test, the fluorescent tracer did absorb so the complete RTD could not be obtained in this setup. However, the short tracer test was used to calculate the dead volume of Digester 2 by means of the following equations:

$$\%\ \text{Dead Volume} = \frac{(\mathrm{C_{max}} - \mathrm{C_{theoretical}})}{\mathrm{C_{max}}} \times 100 \qquad 3.34$$

where $\mathrm{C_{max}}$ (conc.) is the maximum concentration detected, $\mathrm{C_{theoretical}}$ (conc.) is the expected concentration when the tracer mass is dissolved in the digester's volume, V. Thus, the Digester 2 showed 13% of dead volume according to the initial tracer concentrations (Climent et al., 2013) (see **Table 3.4**).

Lithium chloride (LiCl) was then used to perform the tracer experiment in Digester 1. Batch experiments were also conducted and LiCl was neither degraded nor adsorbed at the batch test so, the complete RTD was obtained from Digester 1. Lithium concentrations in samples were measured and results are presented in Section 3.4.1. The mean residence time was obtained to assess the global mixing performance of the anaerobic digester through (Levenspiel, 1999):

$$t_m = \frac{\int_0^\infty t \cdot C(t)dt}{\int_0^\infty C(t)dt} = \frac{\sum_{i=1}^\infty t_i \cdot C(t_i)\Delta t_i}{\sum_{i=1}^\infty C(t_i)\Delta t_i} \qquad 3.35$$

where t_m is the mean residence time (time units) and C and t are tracer concentration (concentration units) and time (time units), respectively. In an ideally mixed tank (CSTR), $t_m$and HRT are equal but they may differ if hydraulic defects emerge such as short-circuits or dead volumes (Levenspiel, 1999; Li et al., 2017). As previously mentioned, in **Table 3.4**, the LiCl tracer experiment revealed that there was no dead volume in Digester 1.

3.3.2.2. Sludge rheology

The TS of both anaerobic digesters was similar so, the sludge rheology of one of them was measured. The rheological characterization of Digester 1's sludge was conducted using a rotational rheometer (Haake RheoStress 1, Thermo Scientific) with a two-cylinder geometry at 38ºC. An anaerobic sludge sample was introduced in the gap between the two concentric cylinders (34 mm and 36.88 mm). The sample was conditioned prior to the test by causing a slight shear stress at 0.5 Pa for 30 s and then left to stand for the same time before starting the measurement at 38ºC. The resulting experimental data (see **Figure 3.3**) was used to fit an Ostwald-de-Waele submodel (Schramm, 1994):

$$\eta = K\gamma^{n-1} \quad 3.36$$

where η is the apparent viscosity (Pa·s), K is the fluid consistency index (Pa·s^n), γ is the shear rate (s^{-1}), and n is the flow behaviour index (-). The sample had a total solids concentration of 2.67±0.43%. The K and $n-1$ values were fitted as 0.0789 Pa·s$^{0.415}$ and -0.585, respectively.

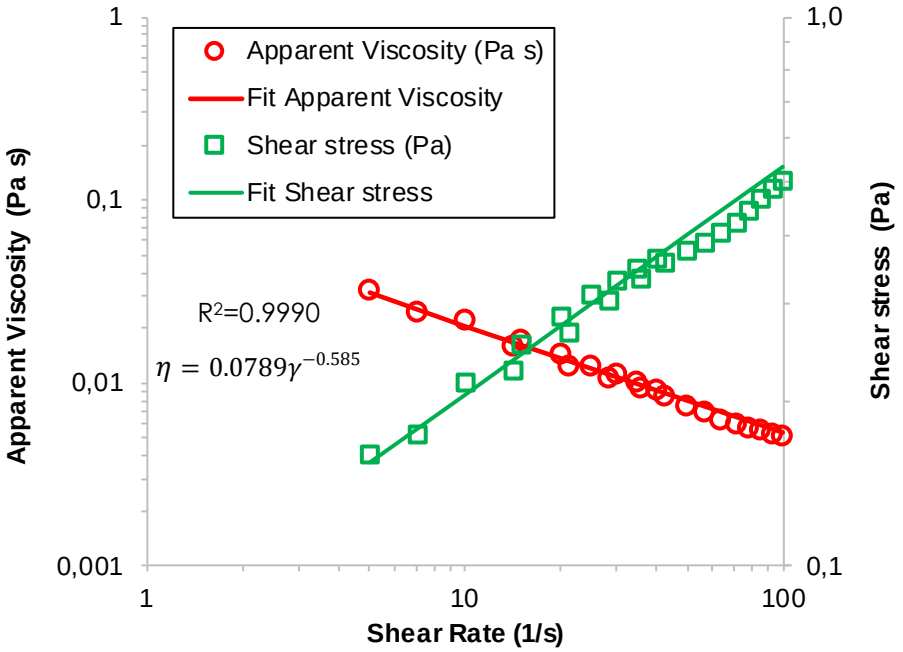

Figure 3.3: *Rheological measurement of the anaerobic sludge at 2.67% of total solids concentration.*

3.3.3. Modelling

The numerical simulations were accomplished using the commercial computational fluid dynamics code ANSYS CFX 17.2. (ANSYS CFX, 2017). All simulations were solved via parallel computing with 8 processes on a computer with an Intel Core i7-3770 processor (3.40GHz) and 32Gb RAM. First, details of the different simulations conducted, and their corresponding operating conditions are presented. Then, a description of the mesh and its quality is done. Finally, the boundary conditions of the steady simulations and transient simulations are defined.

3.3.3.1. Outline of CFD simulations

To provide full insight into the global hydrodynamic behaviour and the influence of the operational parameters on the setups' performance, several CFD simulation scenarios were conducted (see **Figure 3.4**):

Scenario A100: This is the base scenario, and it was run with the DYNOMIX

recirculation flow set at the plant (680 m^3/h) and the propeller switched off. Digester 1 currently operates 162 hours per week under this scenario and Digester 2 always operates under this scenario, so it is of particular interest as it has a strong influence on residence time, settling, mixing, etc. It was used to conduct the grid convergence study (Section 3.3.3.2), the tracer validation (Section 3.4.1), and to study the basic hydrodynamics of the DYNOMIX system (section 3.4.2).

Scenarios A200, A50, and A0: These scenarios were run using recirculation flows higher and lower than the base scenario to study their influence on the digester performance. The variation in the recirculation flow in relation to the base scenario (RF) is specified in **Figure 3.4**.

Scenario B100: The propeller is switched on 6 hours per week in Digester 1 to avoid dead volumes forming. To study its start-up influence, a transient simulation (comprising 1-hour evolution) was performed by taking the base scenario, A100, as the initial condition.

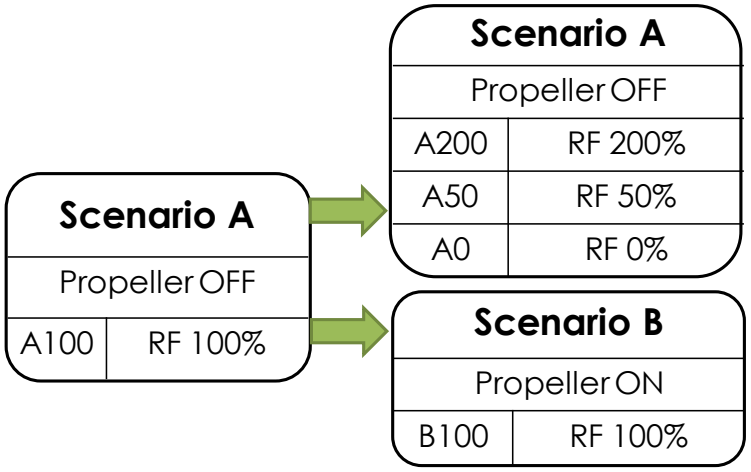

Figure 3.4: *Scheme of the CFD simulations.*

3.3.3.2. Model geometry and Meshing

The 3D geometry was reproduced, and vessel geometry and nozzles were introduced in detail (see **Figure 3.2**). The propeller was modelled as a cylindrical volume in the setup as will be explained in 3.3.3.3. ANSYS Meshing 17.2 was used to mesh the 3D geometry and three grids were developed to assess the grid convergence.

Different mesh properties that can influence mesh quality (such as orthogonality or skewness of the elements) are summarized in **Table 3.6**. The three grids had an average aspect ratio close to 1 and an average skewness lower than 0.25 so they agreed with the guidelines suggested by the software in CFX Best Practices Guide for Numerical Accuracy (ANSYS CFX, 2017).

Additionally, to ensure the mesh independency of the CFD results, a grid

sensitivity study was carried out based on the GCI Roache, (1998) (see the GCI calculation in Section 2.5.1.1).

In short, a given simulation setup is run with three meshes with an increasing number of nodes, N. **Table 3.7** summarizes the results from the GCI test performed. Three meshes with N_1=5195492, N_2=2992010, and N_3=1490787 were used, and the GCI was computed at several locations in the A100 scenario. The results provided by the intermediate grid were considered to be mesh independent as the GCI remained below 3% when calculated between the two finer meshes. A more detailed explanation of the GCI calculation can be found in Appendix C: GCI Calculations.

Table 3.6: *Description of the grids.*

Variable	M3	M2	M1
Number of Nodes	1490787	2992010	5195492
Tetrahedra	1059704	1451663	1344992
Pyramids	18946	41201	46207
Wedges	17673	23138	57997
Hexahedra	994413	2220196	4176523
Max edge length ratio	95.4084	54.9199	50.3683
Element quality Average	0.73±0.26	0.75±0.26	0.76±0.26
Aspect Ratio Average	3.52	3.15	2.99
Skewness Average	0.179	0.131	0.081
Courant Number Average	1.60	2.08	2.55

Table 3.7: *Grid Convergence Index.*

GCI	Max	Ave
GCI_{32} (%)	3.2	1.5
GCI_{21} (%)	2.6	1.1

3.3.3.3. Setup

All CFD simulations assumed a single isothermal (38°C) and incompressible fluid as the primary phase. The single-phase was defined as a non-Newtonian fluid using the Ostwald-de-Waele submodel with K= 0.0789 and $n-1$ =-0.585.

The selected turbulence model was the Shear Stress Transport (SST)

turbulence model developed by Menter, (1994) which is very robust and widely used. The SST model is a two-equation eddy-viscosity turbulence model that combines the k-ε turbulence model (in the free shear flow) and the k-ω turbulence model near the walls. The advantage of the SST model versus the k-ε lies in a better description of shear stress in the wall through k-ω turbulence model wall treatment. Boundary conditions are described in **Table 3.8**.

***Table 3.8**: Boundary Conditions (see flow rates in **Table 3.5**.*

Patch	Boundary Type	Value
Inlet	Inlet: Mass Flow Rate	Inflow + Heat Exchanger Flow
Outlet	Outlet: Mass Flow Rate P= 1 atm	Inflow
Heat Exchanger Suction	Outlet: Mass Flow Rate	Heat Exchanger Flow
Dynomix 1	Inlet: Mass Flow Rate	45% of Dynomix Flow
Dynomix 2	Inlet: Mass Flow Rate	55% of Dynomix Flow
Dynomix Suction	Outlet: Mass Flow Rate	Dynomix Flow
Wall	Wall: Non-Slip Wall	-
Top	Wall: Free Slip Wall	-

A momentum source approach was set for the intermittent propeller operation. A cylindrical subdomain was used to replace the propeller geometry and contained a momentum source to drive fluid movement. The volumetric momentum source, M (kg m^{-2} s^{-2}), can be calculated according to the propeller technical sheet with the following expressions:

$$M = \frac{\rho}{V_S}\left(\frac{q}{D_a}\right)^2 \qquad 3.37$$

where D_a is the actual diameter of the blades (m), ρ is the fluid density (kg m^{-3}) and V_S (m^3) is the volume of the cylindrical subdomain. The flow rate propelled, q (m^3/s), can be obtained as:

$$q = D_a\sqrt{\frac{\omega}{\omega_o}\frac{F_o}{\rho}} \qquad 3.38$$

where F_o is the design thrust force (N), ω_o is the rotational speed (rpm) for the propeller and ω is the actual rotational speed. The propeller was set by a thrust force of 1500 N, a cylinder diameter of 1.5 m, and a cylinder length of 0.2 m. The momentum source resulted in 4244 kg m^{-2} s^{-2}.

3.3.3.4. Solver and convergence

All the scenarios had the same outline: firstly, a steady-state simulation was run to solve the hydrodynamics of a particular scenario. Once the steady-state finished, a transient simulation was run to solve the transport of the tracer inside the setup.

3.3.3.4.1. Steady-state simulations

Steady-state simulation was applied to accurately obtain the hydrodynamics of the mixing configurations studied by focusing on analysing sludge behaviour and detecting slow-velocity zones. The advection and turbulence schemes were high-resolution, which is an accurate and bounded scheme where β is computed locally and kept close to 1 (ANSYS CFX, 2017). To terminate the numerical calculations, different criteria were met in all the steady-state simulations:

- At least, 15000 iterations with a time step of 1s were set.
- A reliable convergence criterion based on the root mean square (RMS) residual of 1x10 $^{-5}$ was adopted. Note that the residuals used by the software are the normalized residual imbalance in the linearized system of discrete equations (see more details in ANSYS CFX, (2017)).
- The velocity at several points located around the geometry, was below 5% of the final value in the last 100 iterations.
- The solution imbalances in the conservation equations (conservation of mass, momentum, energy) were less than 0.001% for all the equations.

3.3.3.4.2. Transient simulations: inert tracer experience

When the tracer tests were conducted, the recirculation flow was constant while the influent flow was variable. Nevertheless, as the influent flow was much lower than the recirculation flow (see **Table 3.5**), the hydrodynamics were steady in the tracer experiments. Therefore, after the steady-state simulation, the calculation of hydrodynamics was frozen, and a transient simulation was run to solve the tracer's transport equation over the steady hydrodynamics. These simulations were performed to study mixing and homogenisation in the different scenarios. The real tracer experience in Digester 1 was reproduced: an additional variable was introduced into the domain and a short pulse with the total mass was introduced through the inlet nozzle. Its transport equation was defined as (ANSYS CFX, 2017):

$$\frac{\partial(\rho\varphi)}{\partial t} + \nabla(\rho U\varphi) = \nabla\left(\left(\rho D_{\phi} + \frac{\mu_t}{Sch_t}\right)\nabla\varphi\right) + S_{\varphi} \qquad 3.39$$

where U is the fluid velocity, ρ is the fluid density, $\boldsymbol{\phi}$ is the concentration, φ is the conserved quantity per unit mass ($\boldsymbol{\phi}$ /ρ), $S_{\boldsymbol{\phi}}$ is the volumetric source term (zero in this case), D_{ϕ} is the kinematic diffusivity for the scalar (m^2/s), μ_t is the turbulent viscosity (kg/m s) and Sch_t is the turbulence Schmidt number (-). LiCl kinematic

diffusivity was established at 2.919x10 $^{-9}$ m^2/s (Holz et al., 2000) and a Schmidt Number of 0.9 was chosen as it is the default value in ANSYS CFX and according to Bujalski et al., (2002). The influence of the turbulence Schmidt Number may have a great influence on the results but this study is out of the scope of this thesis.

A variable time step was implemented with Eq. 3.40 and 3.41 (Climent et al., 2018):

$$t_i = t_0 r^i \qquad 3.40$$

$$T = \sum_{i=1}^{N} t_i = t_0 \frac{1 - r^N}{1 - r} \qquad 3.41$$

where i is the iteration number, t_i is the time step, t_0 is the initial time step, and r is the increasing rate so that Eq. 3.40 gives the size of every time step. The total simulation time (T) is calculated using Eq. 3.41 where N is the total number of iterations. t_0, r, and T were set as 0.1s, 1.002, and 76 days respectively. Previous equations were used to reduce the simulation time and to apply a variable time step (a shorter time step in the first iterations and a longer time step as the simulation progressed).

3.4. RESULTS

This section is devoted to the analysis of digester performance based on the CFD simulations. First, the validity of the model is evaluated by means of a tracer test. Once the model's validity has been established, a detailed study of the so-called base scenario is presented in Section 3.4.2. Its hydrodynamic behaviour is analysed, pointing out the main characteristics of these types of tanks (compartmented structure and high circumferential velocity), as well as its efficiency in providing homogeneous mixing. This base scenario serves to analyse the influence of the two main operational parameters that can be changed in practice: the recirculation rate and the internal propeller activation. Then, a comprehensive assessment of the mixing scenarios performance is performed, including design and mixing parameters described in Section 3.2 as well as a critical study of current criteria to estimate settling and dead volume formation. At the last section, a final discussion on the application of intermittent mixing is made.

3.4.1. Tracer test and global hydraulic validation of the model

The tracer test in Digester 1 yielded a mean residence time of 19.6 days so a short-circuiting of 12% of the total influent flow was detected but no dead volume was observed (Climent et al., 2019).

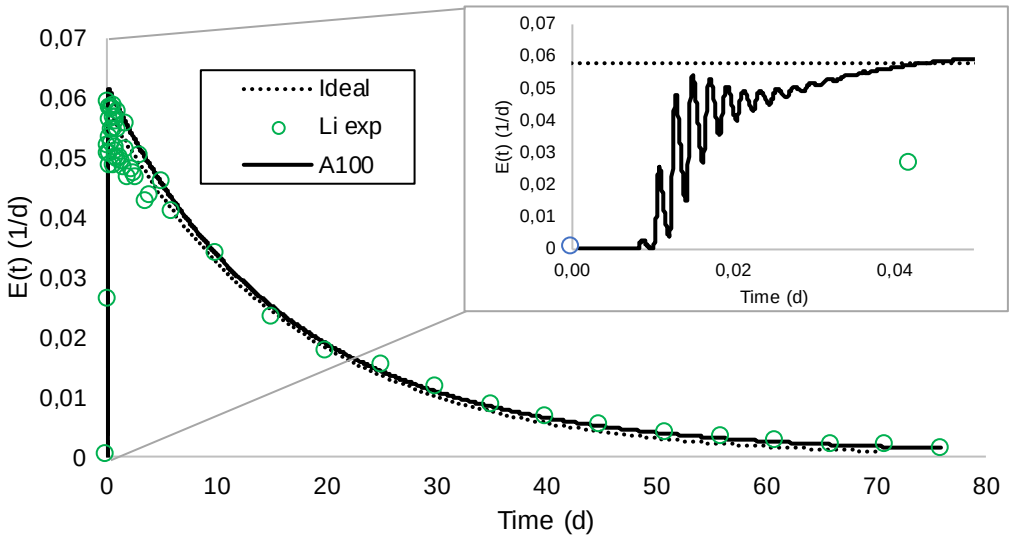

Figure 3.5: *Digester 1's experimental E curve and A100 E curve in the outlet.*

As in Terashima et al., (2009), the tracer test was used to validate the CFD simulation. For this purpose, a tracer pulse was set at the model's inlet in the A100 scenario. A transient simulation spanning several days provided the calculated tracer curve. The plot in **Figure 3.5** compares the resulting E curve (A100) with the experimental one, showing a strong agreement between the two, especially for long times for which an RMS error of about 0.04 ppm has been calculated. This agreement stands for the global validation of the base scenario, which can reproduce Digester 1's hydrodynamics. In addition, a detailed analysis of the A100 curve at the beginning (see detail in **Figure 3.5**) depicted minor internal recirculation or short-circuiting before the first tracer sample was taken. This hydraulic defect in the A100 scenario fitted the experimental short-circuiting detected in the tracer test.

3.4.2. Hydrodynamic behaviour of the base scenario

The base scenario hydrodynamics were especially important because both setups normally work under these conditions. Understanding it from the CFD solutions allowed users to realise how dead volumes and possible inhomogeneous mixing were formed, but also provided more accurate knowledge about the behaviour of the internal flow and its implications during process performance. This work proposed to identify three main regions with very specific hydrodynamic characteristics for each zone, in order to point out possible compartmental modelling. The circumferential velocity was then assessed looking for a turbulent vortex structure. Finally, mixing behaviour was studied by relating it to the local mixing parameters in Section 3.4.2.4 and evaluating the different global mixing parameters in Section 3.4.2.5 with the transient simulation results.

3.4.2.1. Compartmental structure of the ADer

A careful examination of the velocity field in the tank volume suggested that it is divided into three regions: a cylindrical region along the axis of the vessel (labelled 1 in **Figure 3.6**), and two annular regions at different heights, the one labelled 2 close to the ground and the one labelled 3 at the top.

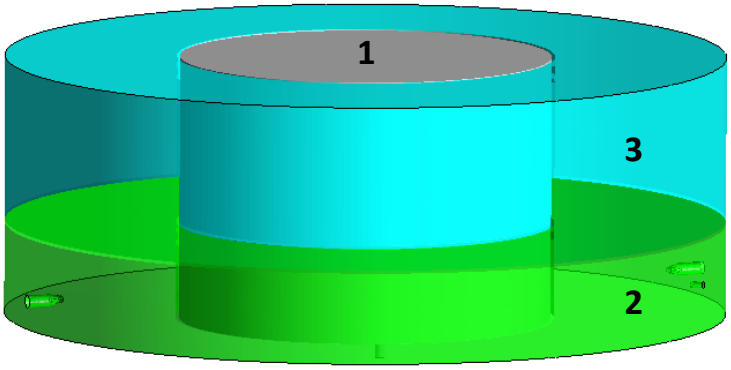

Figure 3.6: *Three regions defined in the vessel according to hydrodynamics: CORE of the vessel (1); DYNOMIX region (2) and Turbulent Flow region (3).*

The first region was referred to as the CORE as it was located in the centre of the vessel. The limits of this region could be noticed clearly from the circumferential velocity contours shown in **Figure 3.7**a, with its boundary being about 6 m away from the anaerobic digester axis. Note that the flow in this region moved at low velocities, slower than 0.2 m/s for all the heights shown. With respect to the axial component, see **Figure 3.7**b, it was positive in the right half of this region, and negative in the left half. As the axial velocity values were one order of magnitude smaller than circumferential ones, the flow was spinning around the centre with smooth upward and downwards excursions. To sum up, the CORE zone was a region with low circumferential velocity and antisymmetric upward and downward flows, dominated by a large and quite uniform circumferential velocity. Hence, since velocity gradient was almost constant, the dynamic viscosity in this region remained at almost uniform values of about 0.079 Pa s.

The second region was located close to the ground and was referred to as the DYNOMIX region as its hydrodynamics were strongly influenced by the DYNOMIX jets. The circumferential velocity contours (**Figure 3.7**a) at various heights helped to establish the upper boundary of this region. The circumferential velocities typically ranged between 0.2 m/s and 0.3 m/s, especially for the heights of 5 and 7 m. Nevertheless, the contour plot at 1 m height showed that the DYNOMIX jets clearly increase the circumferential velocity. The contours at 3 m height indicated little influence of the jets on this velocity component. A similar trend was noticed for the other velocity components, which showed a strong

influence of the jets at the bottom of the digester that could be neglected for heights over 3 m approximately. Accordingly, the upper boundary of the DYNOMIX region could be established at about 3 m height. Referring to the axial component, see **Figure 3.7**b, it was positive near the Core region (upward direction), but is negative near the wall (downward direction), its values being about one order of magnitude below the circumferential component. This implies the development of a secondary flow as the one shown in **Figure 3.8**. Finally, as the DYNOMIX flow entered the tank directed towards the centre of the vessel, the radial component of the velocity was negative (**Figure 3.7**c). As the DYNOMIX flux circulated, it was deviated towards the outer wall so the radial velocity was positive. Also, the axial component was positive, so the jets were pushed upwards in this geometry. This phenomenon became apparent by analysing the streamlines outcoming from the DYNOMIX nozzles. For instance, the streamlines in **Figure 3.9**a) and b) depart from DYNOMIX 1 and were rapidly deviated so that they did not reach the CORE region. Instead, they were pulled towards the wall and after a whole round they were almost completely attached to the wall. The streamlines departing from DYNOMIX 2 showed similar behaviour. The streamlines departing from the inlet attached to the wall even more rapidly (**Figure 3.9** c and d), and when they met the DYNOMIX flow they were rapidly diluted. In summary, the second region was located in the bottom part of the setup surrounding the CORE region, and its hydrodynamics were influenced by the DYNOMIX jets in such a way that the inlet flow was diluted quite fast. Close to these jets the dynamic viscosity was strongly reduced up to 0.010 Pa s, so the Non-Newtonian effects were more noticeable in this region.

The third region was located above the second one and will be referred to as the Turbulent Flow region (TFR), as its circumferential profile resembled that of a fully-developed turbulent flow (see Section 3.4.2.2 for further details). As stated before, the circumferential velocity was almost uniform in this region. Nevertheless, a local influence of the DYNOMIX suction pipe could be found at 7 m height, see **Figure 3.7**a. As the DYNOMIX suction pipe was in the counter-clockwise direction, there was a strong dissipation of the suction energy of this flux, so its influence on the velocity field was limited to a small (compared to the DYNOMIX jets) volume surrounding the pipe. With regards to the axial component, see **Figure 3.7**b, it was positive near the wall and negative near the CORE region. As for the other regions, this component was approximately one order of magnitude lower than the circumferential velocity. As result, a secondary flow developed in this region that rotated in the opposite direction to the secondary flow in the DYNOMIX region, (see **Figure 3.8**). The other two components indicated that the flow enters the suction pipe from the top but almost symmetrically with respect to the lateral sides. Nevertheless, as for the axial velocity, the radial component was one order of magnitude lower than the circumferential component. In conclusion, the TFR was located at the top part of the anaerobic digester and surrounding the CORE region. As the velocity components were quite uniform, the rheology was almost Newtonian with

dynamic viscosity values about 0.0789 Pa s.

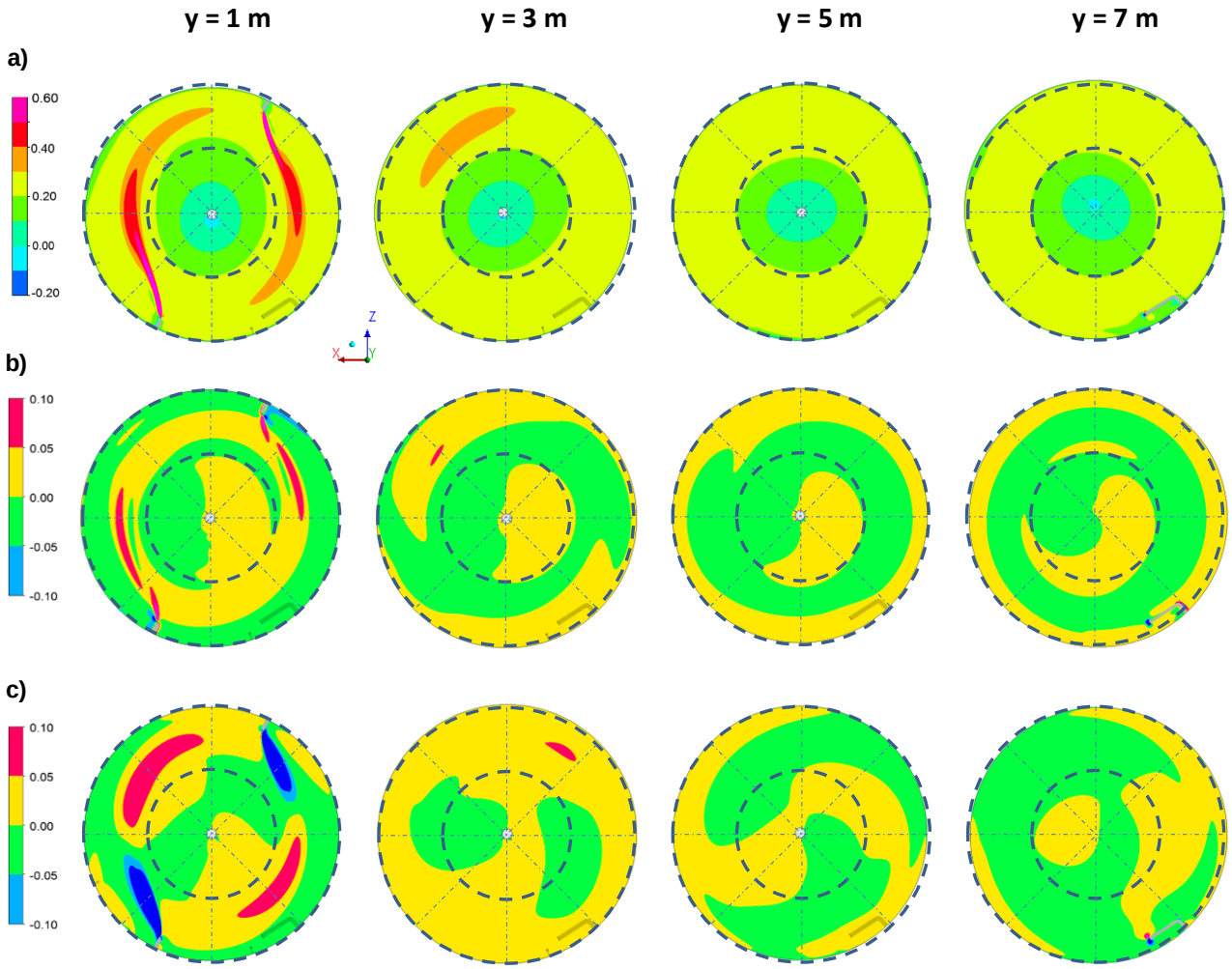

Figure 3.7: *Velocity contours (m/s) in different horizontal planes. The circumferential component is depicted in a), the axial component in b) and the radial velocity in c). Note: a positive circumferential velocity means clockwise movement, while a negative one denotes counter-clockwise movement. Positive axial velocity is upward velocity, while the negative one is downward velocity. Positive radial velocity indicates an outward movement, while a negative one denotes movement towards the centre.*

Figure 3.8*: Upwards and downwards secondary flows in DYNOMIX and Turbulent Flow regions.*

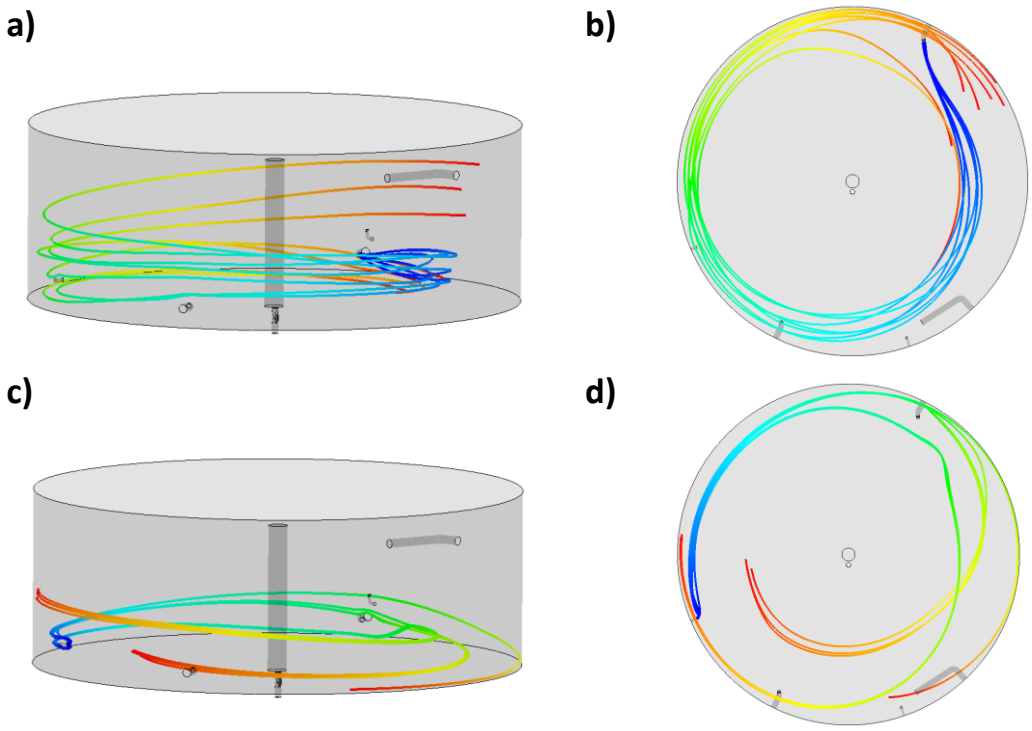

Figure 3.9: *Streamlines at 250s of its output from a and b) DYNOMIX nozzle 1, c and d) DYNOMIX nozzle 2.*

According to the circumferential and axial velocity, the movement of a theoretical particle within the vessel could be drawn. The mean rotational velocity and mean upward velocity within the vessel were 20.64 cm/s in a clockwise direction and 0.27 cm/s in an upward direction. Considering the perimeter of the setups, the theoretical particle at the mean rotational velocity could make a turn around the digester in 5.8 minutes. As the digesters were 8.25 m high, the particle with the mean axial velocity could reach the top part in 51.3 minutes. Since the TRH was 17 days, the particle could achieve 2,097.71 turns and reach the top 238.62 times before exiting the tank. This particle explored on its way most of the points of the setup in one TRH so that, all biological processes of anaerobic digestion could take place in most points of the vessel. This ensured that all stages of the anaerobic digestion would happen within the tank and the completion of the anaerobic digestion would be achieved.

3.4.2.2. Circumferential flow: turbulent vortex structure

From previous discussions, it was apparent that the circumferential velocity was typically one order of magnitude over the other components across the whole digester, so that the flow basically spun around the setups' axis. As in most rotating systems, the development of a vortex-like structure was expected. **Figure 3.10** a and b show the circumferential velocity (v_θ) and angular circumferential

velocity ($\omega = v_\theta/r$) for several profiles located at different heights in a vertical plane (**Figure 3.10**c). The circumferential velocity distribution in the CORE region looked like a vortex, and the almost constant angular velocity supported such behaviour. Several mathematical models have been proposed to describe the distribution of tangential velocities in the core of a free vortex. Tangential velocities increase linearly from the rotation axis up to a maximum value at radius R_C and decrease from this point outwardly and proportionally to the inverse of the radius. A simple laminar vortex model, such as the Burgers' vortex (Burgers, 1948), can represent this behaviour. In **Figure 3.10**a, the dashed black line depicts the simplified version of Burger's model applied to this case. The velocity profiles in the CORE region (radial distance approximately below R_C =8 m) closely matched the laminar vortex structure, for which velocity increased linearly with the radial distance (i.e. at a constant angular velocity, indicating a rigid-like motion). In contrast, the profiles in the DYNOMIX and TF regions strongly deviated from the laminar vortex profile. The profile at 1 m clearly indicated that the DYNOMIX jet broke the laminar vortex structure in the DYNOMIX region. The profiles at 3 m, 5 m and 7 m showed that the circumferential velocity remained almost constant after reaching its maximum value at a radial distance of about 8 m, while the angular velocity decreased linearly. Near the wall, the circumferential velocity indicated the same behaviour as the velocity distribution in the boundary layer of a fully-developed turbulent channel. Hence the velocity profile fitted a power-law expression as in (White, 2011):

$$\mathrm{w(r)} = \mathrm{w_o}\left(1 - \frac{\mathrm{r}}{\mathrm{R_{ADer}}}\right)^{\mathrm{n_\tau}} \qquad 3.42$$

where r stands for the radial coordinate, $w(r)$ is the circumferential velocity component, R_{ADer} is the ADer radius, w_o denotes the circumferential velocity immediately beyond the boundary layer velocity, and n_τ is the turbulent exponent constant, with a value close to 1/7. For our base scenario, this constant was 1/7.6 (see **Figure B.3** for the fitting procedure). In summary, the outer regions, DYNOMIX and Turbulent Flows were seen as a fully-developed turbulent channel, while the inner region (the CORE region) resembled a vortex structure. All the regions had secondary flows that helped to understand the mixing process, but their velocities were one order of magnitude lower.

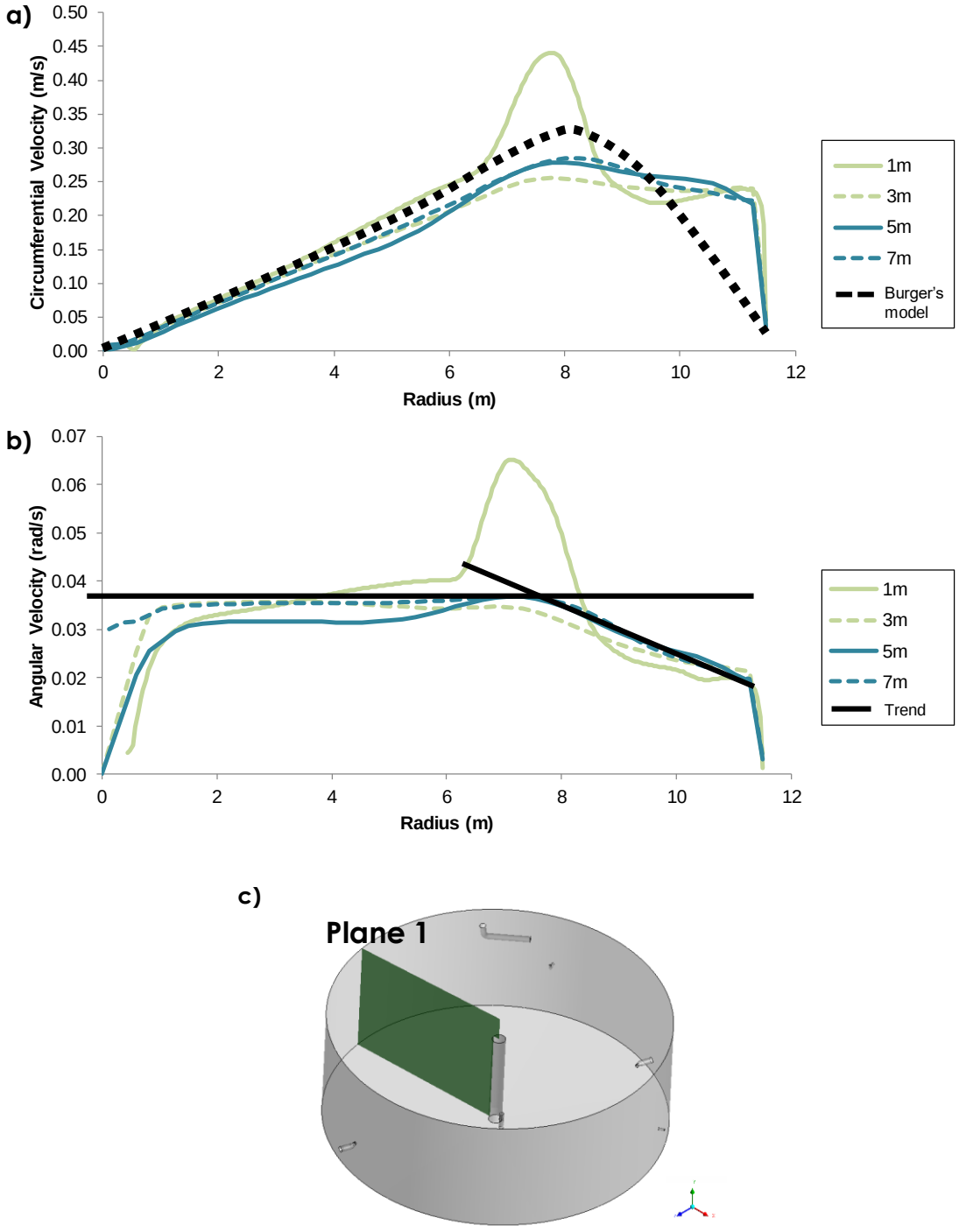

***Figure 3.10**: a) Circumferential velocity profile, b) angular velocity profile at different heights and trending lines and c) location of the plane containing the profiles in the plots.*

3.4.2.3. Design parameters assessment

In this section, the design parameters were analysed (Section 3.2.1) by means of the power consumption of both digesters (see **Table 3.9**) compared to the recommended design parameters (see the values in brackets in **Table 3.9**):

Table 3.9: *Design parameters for Digester 1 and 2 vs US EPA, (1979) in brackets.*

HRT (d)	DVTT (h)	UP (W/m^3)	$\overline{G}$ (s^{-1})
17.0 (15-30)	5.10 (30-40 min)	2.13(5-8.3)	5.15 without propeller// 6.2 with propeller (50-80)

The DYNOMIX system inputs 7.3 kW, i.e. 22 kW with 33% efficiency according to the engine technical sheet, and the impeller uses 3.5 kW, but only 6 hours per week. So, the digesters had a longer DVTT (5.10 h) and a lower UP (2.13 W/m^3) compared to the design values. This meant that bad mixing performance could be expected due to a slow recirculation flow with low pumping power. Nonetheless, the tracer experiment depicted CSTR performance with slight short-circuiting in Digester 1. Therefore, it stood that proper mixing with less power input could be achieved with good local power input distribution. These disagreements between real performance and design parameters could be partially explained by impeller intermittent performance, which avoided dead volumes forming. Additionally, these disagreements suggested that DVTT and UP are design parameters that hardly define the setup's mixing degree. For example, the same recirculation flow applied to two different setups with the same volume have the same DVTT and UP, but different mixing degrees depending on the recirculation flow distribution with nozzles.

The aim of the global RMS velocity gradient was to relate the ideal mixing power to good mixing performance in a global parameter. On the one hand, using Eq. 3.4, the global parameters, i.e. average dynamic viscosity of 0.0789 Pa s and real power input, $\overline{G}$ stood for 5.15 s^{-1} without the propeller and 6.27 s^{-1} with the propeller. These values were one order lower than the proposed design values and, thus, the digesters' mixing performance would be bad according to $\overline{G}$. On the other hand, according to the design standards, the range of power that should be applied in the digester to achieve between 50 s^{-1} and 80 s^{-1} would be between 683 kW and 1976 kW. As this required power input was extremely high compared to that installed in the real systems, it would not be feasible to apply it to a full-scale setup.

This is clearly in line with other authors (Sindall et al., 2013; Wu, 2014), who

have pointed out that the global RMS velocity gradient cannot accurately characterise the local mixing of full-scale anaerobic digesters. Hence, this parameter should not be used for designing the mixing systems of setups.

With the aim of obtaining the needed power input, it was also calculated by means of the McLeod et al., (2019) correlation, Eq. 3.5. Their correlation worked in their lab-scale experiments, but they showed great limitations in full-scale setups. In this case, as the TS concentration is 2.67%, the minimum power input for mixing should be 18.1kW which is almost twice the actual power input (7.26 +3.5 kW). Nevertheless, if the TS concentration were to suddenly increase to 3%, the power input should be around 28 kW. Thus, the power input should be increased by 55%, which would not be feasible in a full-scale setup.

Briefly, the design parameters can be useful for comparing different anaerobic digesters but fail to define the mixing degree because it depends on the mixing systems' efficiency and location. Additionally, DVTT was only applicable with hydraulic mixing anaerobic digesters, and UP and $\overline{G}$ were too global to capture the local mixing phenomena that take place in anaerobic digesters.

3.4.2.4. Local mixing analysis

Large anaerobic digesters usually display heterogeneous hydraulic behaviour, and although global analysis is useful, tools are needed to analyse local behaviour and its effects on mixing. The local mixing produced by a recirculation system can be studied using two local parameters: the local RMS velocity gradient and the α_{DME}. The local RMS velocity gradient, Eq. 3.6, was computed by turbulent kinetic energy dissipation per unit mass and local viscosity, with CFD results. **Figure 3.11**a shows a histogram that depicts the distribution of the local RMS velocity gradients for every region. As expected, the CORE region was the one with the worst mixing because the RMS velocity gradients remained below 0.2 s^{-1}. The TFR had higher velocity gradients and the gradient velocity of most of its volume was between 0.2 and 0.8 s^{-1}. So, the TFR's mixing was more homogeneous than in other regions. Conversely, the gradients in the DYNOMIX region were widely distributed, with more than 2 s^{-1} in 10% of its volume thanks to the action of jets, with a peak value of 20 s^{-1} near the DYNOMIX nozzles. These values in the digester were several orders of magnitude below the design threshold of 50-85 s^{-1} recommended in the design parameters. This shows that lower local RMS velocity gradients can also state proper mixing in full-scale anaerobic digesters as the tracer depicted CSTR performance in Digester 1.

Type of mixing is described by α_{DME} (see Eq. 3.7). **Figure 3.11**b shows the α_{DME}'s distribution for every region. In the CORE region, this value was lower than 0.5, so, the mixing came from the sludge's solid-liquid laminar vortex. α_{DME} increased in the outer regions with values above 0.5, so the mixing in these regions arose from the shear flow in the DYNOMIX region (towards values < 0.5) and the dispersive flow in the TFR (towards values > 0.6).

Overall, the results of both local parameters agreed with the turbulent structure described in Section 3.4.2.1. While the CORE region has a rotational flow with no local mixing due to a laminar vortex, outer regions had better local mixing and comprised a turbulent channel flow produced by the recirculation flow and its interaction with the outer wall. Moreover, the TFR was the digester's most efficient mixing region as its local RMS Velocity gradients were significant and homogeneous, and widely dispersed by the pure elongation flow.

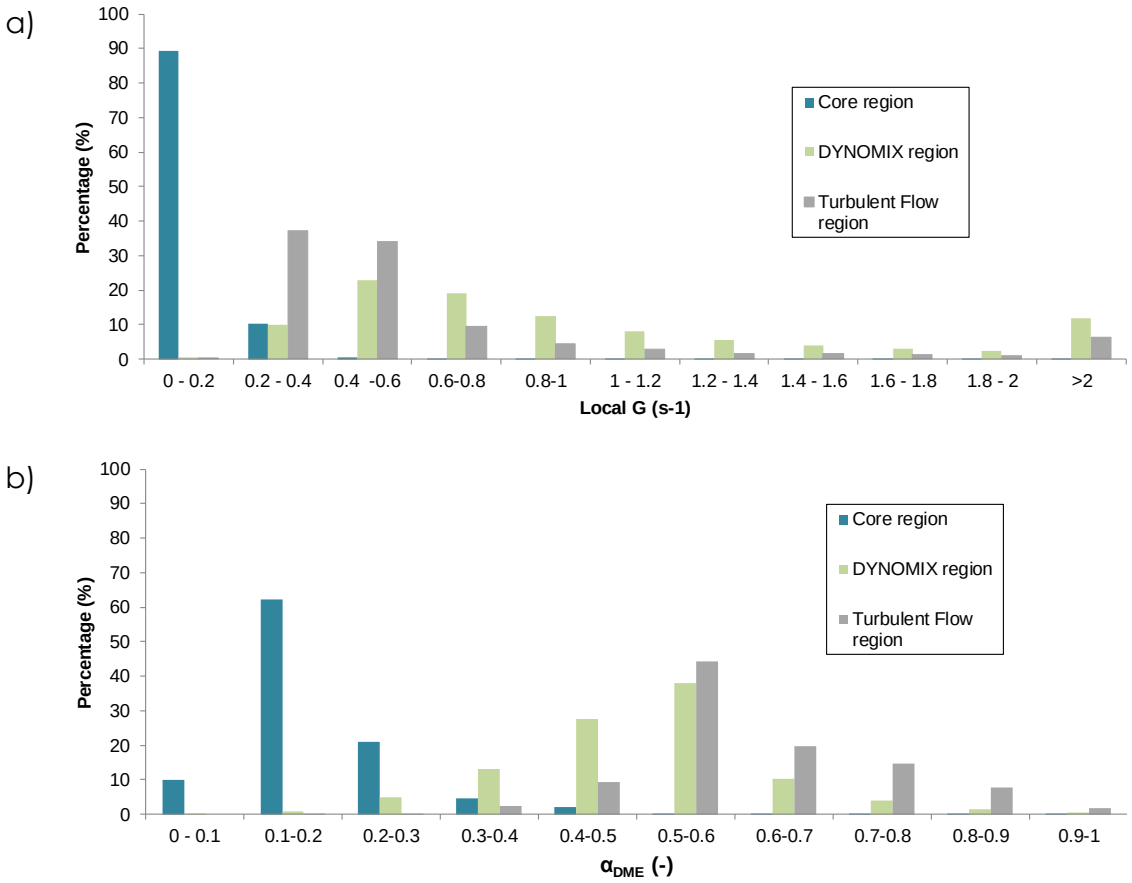

***Figure 3.11**: Histograms for a) the RMS velocity gradient and b) the dispersive mixing efficiency for every region.*

3.4.2.5. Global mixing parameters assessment

Having studied local mixing, the homogeneity of the components inside the setup can be studied by the tracer curve. Hence the tracer experience enables the study of the UI, the mean tracer concentration, and the second-order moment of the tracer distribution in the different regions.

On a semi-logarithmic scale, **Figure 3.12** depicts the tracer concentration average (**Figure 3.12**a) and the UI curves (**Figure 3.12**b) for each region and for the whole setup. As the total tracer mass was introduced into the anaerobic digester at 10 s, both figures had this time as their initial timescale value.

Regarding the average tracer concentration, **Figure 3.12**a also includes the outlet's curve and a dashed line showing the average tracer concentration for the whole setup. Firstly, as flow entered from the inlet located in the DYNOMIX region, the concentration in this region started at the maximum value and remained almost constant for the first minutes. Its value lowered when the tracer started to enter the TFR. To this end, the CORE region was the last to receive the tracer, although it had been previously detected in the outlet, which is located in the lower part of this region. As the CORE region extended over the entire ADer height, the outlet's tracer was occasional and independent of the entire extent of the CORE.

Figure 3.12b shows a similar pattern to **Figure 3.12**a: the lower UI was sequentially noted in the DYNOMIX region, then in the TFR and lastly in the CORE region. At the beginning, the concentration in both the DYNOMIX and TF regions was very low and located in small volumes inside them, and the initial UI was 1 in these regions. Then the tracer occupied the whole setup and its UI lowered. Conversely, the UI in the CORE region was 0, indicating that there was no tracer inside it. After 1 minute, the UI value rose to 1 in the CORE as the tracer entered it and the mean tracer concentration increased. From the curves, the homogenisation time, t_{UI} , can be obtained for each region, with 28.8 min in the DYNOMIX region, 36 min in the TFR and 54 min in the CORE region. As the CORE region was the last to accomplish complete mixing, the setup's t_{UI} was 54 min. According to the homogenisation time, if an improvement in the mixing degree is necessary, efforts should focus on improving the mixing in the CORE region to reduce the tank's homogenisation time.

Although the UI has been widely applied in CFD studies, it only describes the global mixing degree. When considering it independently in the different regions in this case, more information is obtained about the tracer's movement and the mixing degree achieved in each region. Nevertheless, the analysis of the central moments of the tracer concentration provides further information on the tracer path and its dispersion over time. **Figure 3.13**a shows the second-order central moments curves for every spatial direction. According to the plot, the circumferential moment rapidly increased over the axial and radial second-order moments, which implies that the tracer pulse quickly elongated with the very fast DYNOMIX circumferential velocity (see the elongation of the tracer plume in **Figure B.0.2**). Axial and radial spreads were similar in magnitude and were driven by turbulent dispersion. Hence the second-order moment indicated that circumferential flow drove the mixing inside the tank more than the axial and radial components did. Thus, the benefit of the second-order moment over the UI was based on defining the preferential mixing direction. The three curves obtained a constant value, indicating that the tracer distribution was fully homogeneous inside the tank after a given time. From the normalised second-order moments (**Figure 3.13**b), a homogenisation time was defined in a similar way to t_{UI}, i.e. the time at which the three curves reached 99% of the constant

value. In A100, 99% was reached at 19.6 min in the axial direction, at 44.6 min in the circular direction and at 54.6 min in the radial direction. Hence the homogenisation time was 54.6 min, which is similar to t_{UI}.

a)

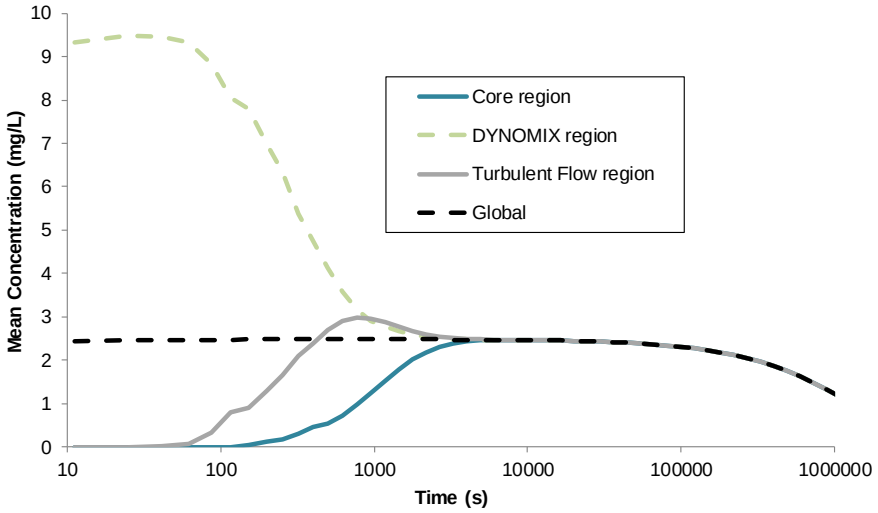

b)

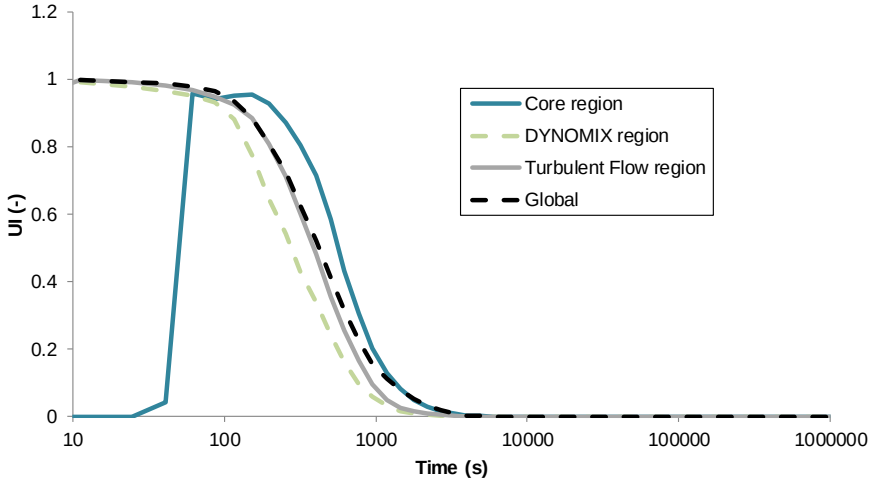

***Figure 3.12**: Time evolution of the a) Mean tracer concentration and b) Uniformity index in CORE, DYNOMIX and TF regions and the global ADer.*

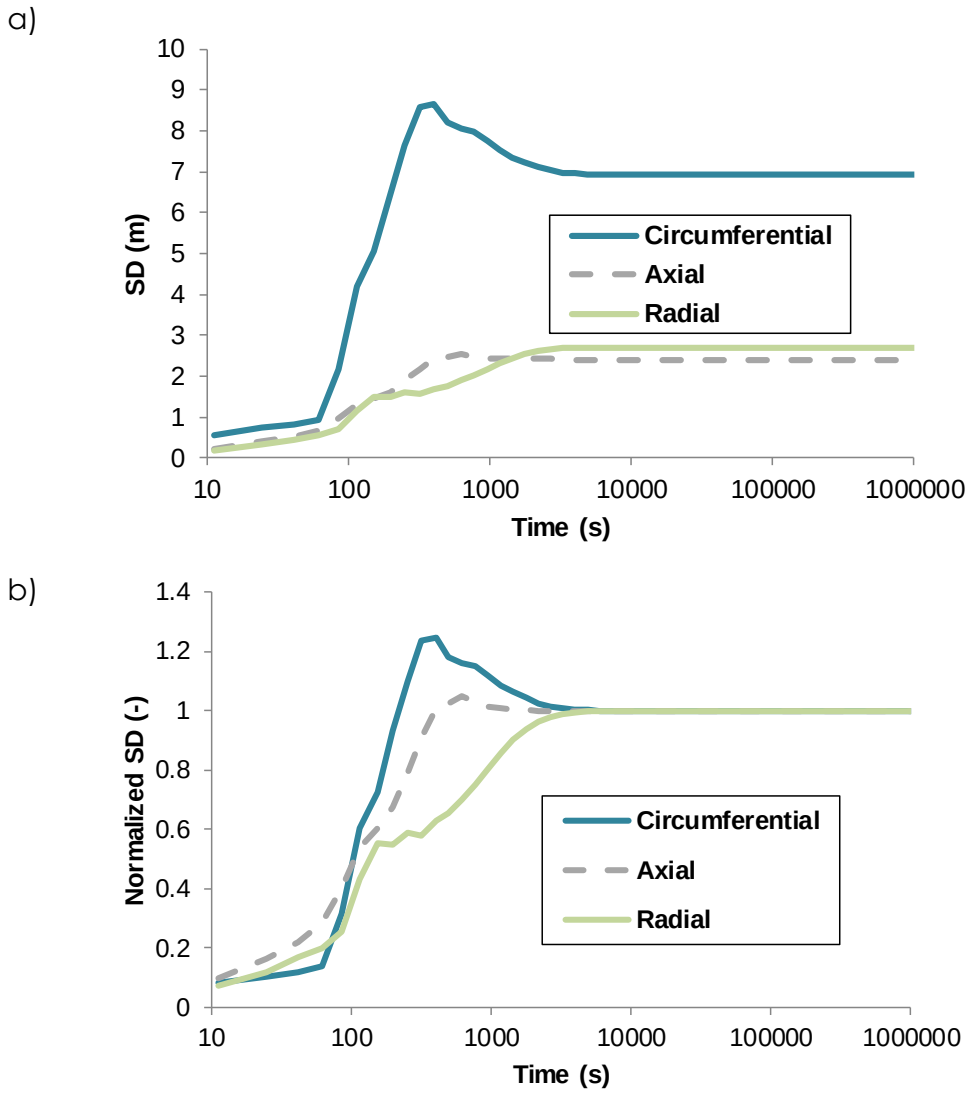

***Figure 3.13**: a) Second-order central moment curves along the three spatial directions. b) Normalized second order central moment curves along the three spatial directions.*

3.4.3. Anaerobic Digester performance assessment

In this section, the scenarios described in Section 3.3.3.1, were evaluated following the same structure as the previous one.

3.4.3.1. Compartmental structure

As described in Section 3.4.2.2, the circumferential velocity was the most important velocity component in the base scenario's compartmental structure. So, this velocity component was used in sketching the compartmental structure of the different CFD scenarios.

Figure B. 4 shows the circumferential, axial and radial velocity contours in the A0 scenario. In this scenario without DYNOMIX recirculation flow, the

compartmental structure described in Section 3.4.2.2 was not present as result of the absence of the recirculation flow. Indeed, it was not possible to find any other pattern associated with the operational conditions of this scenario.

Secondly, the A50's compartmental structure could be studied by means of the velocity contours in **Figure B. 5**. In this scenario, the influence of the DYNOMIX recirculation flow was shown in the circumferential velocity at 1m height so that the DYNOMIX region was clearly present in this operational condition. Once again, the inner part had less circumferential velocity at different heights, thus the CORE region would be defined in the A50 scenario. The TFR was also defined as the circumferential velocity was lower at 5 and 7 m height. Additionally, the secondary flows were manifest as the axial and radial contours (see **Figure B. 5**b and c) showed the same pattern as **Figure 3.6**. To sum up, the same compartmental structure of the base scenario was found in A50.

Thirdly, in **Figure B.6** the circumferential, axial and radial velocity contours of the A200 scenario were shown. As the DYNOMIX recirculation flow was doubled compared to the base scenario, the velocity components had increased their magnitude from the bottom to 3m height so that the DYNOMIX region could be also defined. In addition, the CORE region remained as the section with less circumferential velocity at all heights. The axial and radial velocity in the A100 scenario were also conserved here without changing their magnitude i.e. the contours of the axial and radial components at the CORE region were equal in both A100 and A200 scenarios. As the other regions were defined in this scenario, the TFR was also depicted.

The last scenario was the B100 scenario depicted in **Figure B. 7** where the circumferential velocity at the inner part was like the A200 scenario. Nevertheless, the axial and radial velocities had a different magnitude and different patterns compared to the A100 and A200 scenarios: The impeller effect in scenario B100 brought about considerable internal recirculation inside the CORE region, and the radial and axial velocities increased in the zone directly affected by the impeller.

Briefly, the compartmental structure of the A100 scenario remained in the case of A50 and A200 and was similar in the B100 scenario. Without the recirculating flow, A0 showed a very slow circumferential velocity and, thus, the compartmental structure was not maintained.

3.4.3.2. Circumferential flow: turbulent vortex structure

As in the base scenario, the circumferential velocity was one order of magnitude over the other velocity components in scenarios A50, A100, A200 and B100. However, in scenario A0, all the velocity components had the same magnitude because there was no recirculation flow to induce the spinning movement around the setup's axis (see the circumferential velocity at 5 m height in **Figure 3.14**a). As expected, the circumferential velocity increased

proportionally to the recirculation flow. Although B100 had slower circumferential velocities than A200 from a 6m radius to the wall, it was almost equal for both scenarios in the CORE region. According to this trend, an increase in the DYNOMIX recirculation flow brought about a faster circumferential velocity in the DYNOMIX and TF regions. Low circumferential velocities were always located in the CORE region, this would most likely create areas of settlement and dead volume in reality.

As was done in Section 3.4.2.2, the circumferential velocity was studied to assess which type of vortex was induced by the mixing systems. **Figure 3.14**b depicts the normalised circumferential velocity in the different scenarios and a typical laminar vortex profile (dashed line). As seen in A100, the CORE region in scenarios A50, A100, A200, and B100 agrees with the laminar vortex, and a turbulent vortex profile was encouraged by the circumferential movement of the DYNOMIX jets in the DYNOMIX and TF regions. Nonetheless, the A0 scenario did not follow any vortex profile in the inner region but showed a turbulent profile in the region near the wall as did all the scenarios.

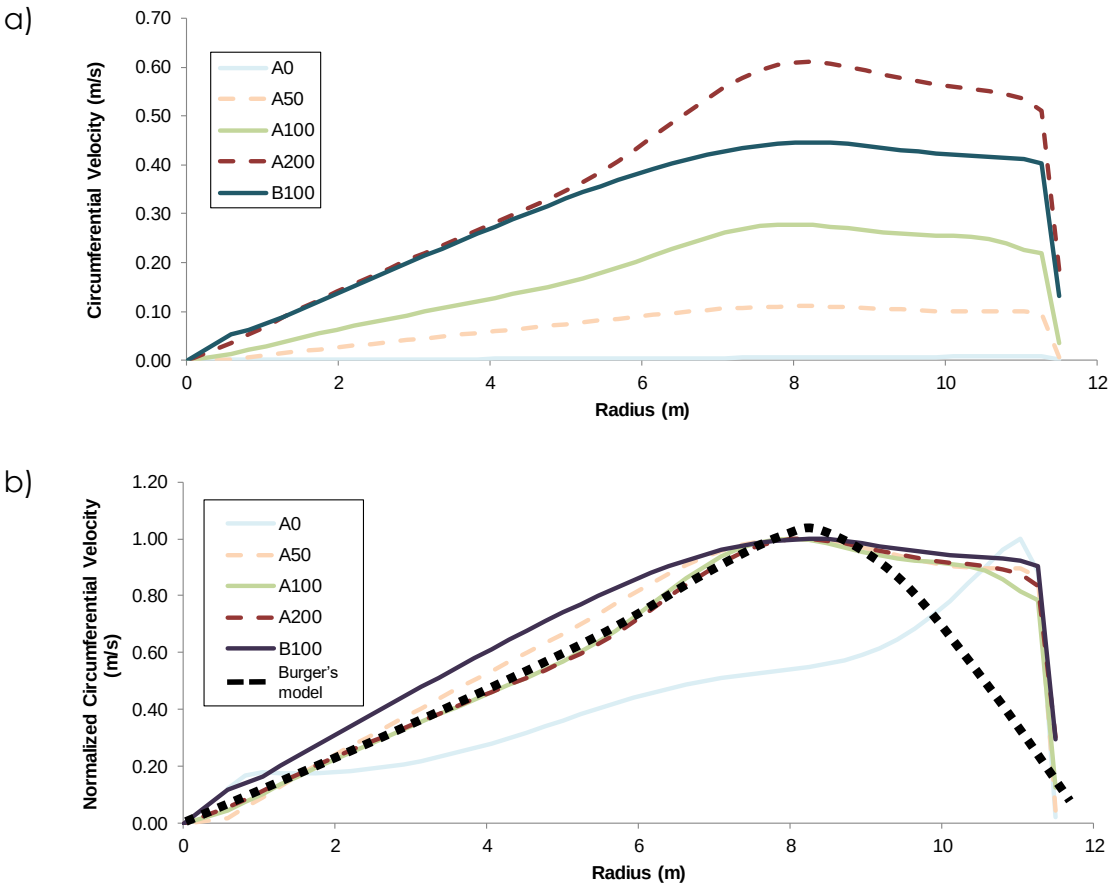

***Figure 3.14**: a) Circumferential velocity and b) normalized circumferential velocity at the 5 m height for the different scenarios.*

3.4.3.3. Local mixing analysis

Given the importance of the local mixing parameters presented in Section 3.2.2, the local RMS Velocity gradient and α_{DME} are assessed in the different scenarios for the various regions (see **Figure 3.15**).

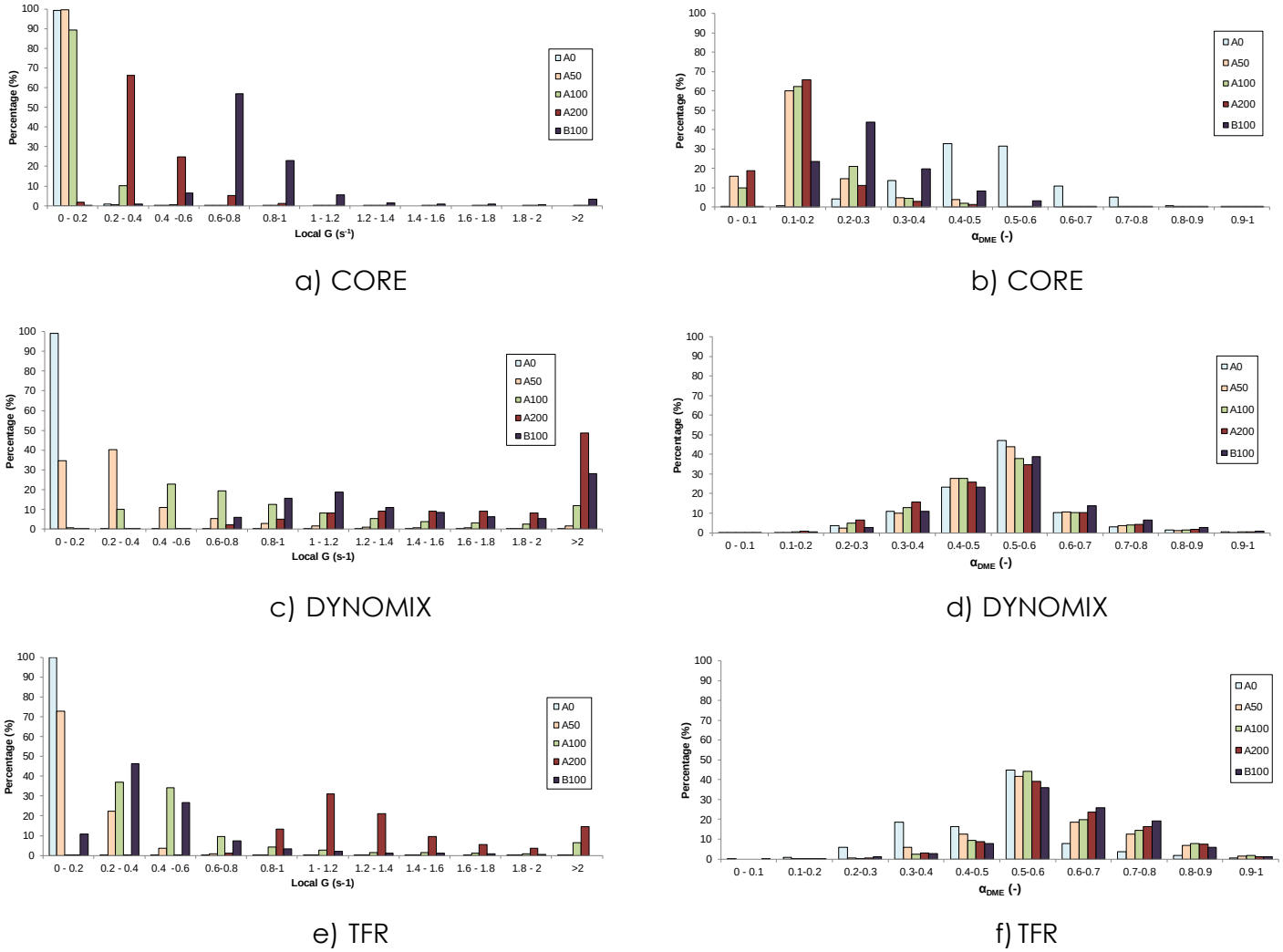

***Figure 3.15**: Histograms for the local RMS velocity gradient (a,c,e) and α_{DME} (b,d,f) for every scenario at different regions.*

Firstly, as marked similarities appeared between the DYNOMIX and TF regions, they were analysed together (see **Figure 3.15** c to f): According to the local RMS velocity gradient, both regions showed higher local RMS velocity gradients than the CORE region in all the scenarios with the DYNOMIX system, i.e. mixing was encouraged by the DYNOMIX jets in A50, A100, A200 and B100. On the contrary, the local gradient in A0 remained at low gradients in every region. Therefore, the better-mixed scenario in these regions was A200, and its mean local gradient was higher than that of the other scenarios, above 2 s^{-1} and between 1 and 1.2 s^{-1} in the DYNOMIX and TF regions, respectively. For the α_{DME} in the DYNOMIX and TRF regions, a similar distribution was found in all the

scenarios, and their mean value was between 0.5 and 0.6. Hence the type of mixing in these regions was mainly shear flow. Nevertheless, the volume distribution showed that mixing moved towards a rotational shear flow in the DYNOMIX region and towards a dispersive flow in the TFR. The rotational movement in the DYNOMIX region agreed with the DYNOMIX system, but the rotational movement in A0 could be neglected due to the local gradients lower than 0.2 s^{-1}.

Secondly, the CORE region was studied in detail as sludge can easily settle there (see **Figure 3.15** a and b). On the one hand, the local RMS velocity gradient in scenarios A0, A50 and A100 had mainly gradients below 0.2 s^{-1}, but A200 had 60% of its volume between 0.2 and 0.4 s^{-1}, and B100 had 50% from 0.6 to 0.8 s^{-1}. Thus, B100 had the highest local RMS velocity gradient as a result of the source of the propeller's momentum. This would make B100 the most efficient scenario for mixing the CORE. Generally, as the lowest values of velocity gradient were located in the CORE, it was the worst mixed region within the tank so, the development of dead volumes or settling of the sludge were feasible in this region. On the other hand, α_{DME} implied that mixing came from the rotational flow, i.e. α_{DME} <0.5, in all scenarios except for A0. In contrast, a shear flow mixed in A0 as α_{DME} exceeded 0.5, although the local RMS velocity gradient remained below 0.2 s^{-1}. Hense, this shear flow was not high enough.

Therefore, the joining of the local RMS velocity gradient and α_{DME} implied excellent parameters for describing mixing performance in anaerobic digesters. Additionally, B100 was established as the best for the mixing of the CORE region, but A200 was the better-mixed scenario because its DYNOMIX recirculation flow considerably improved overall mixing.

3.4.3.4. Global mixing parameters assessment

The global mixing parameters were studied using the tracer test simulations performed in the different scenarios. A complete 76-day RTD was obtained (see **Figure 3.16**) and avoided having to carry out tracer experiments for every scenario which can reduce the study's cost. **Figure 3.16** shows that the RTD was similar and without peaks in A100, A200, and B100. Thus, their global hydraulic performance came close to a CSTR. Conversely, A0 and A50 clearly showed a tracer fluctuation and a sharp peak, respectively, so major hydraulic defects appeared in them (**Figure 3.16** detail): the fluctuation in A0 could be an internal recirculation or a short-circuit, while the sharp peak at A50 could be a short-circuit. These short-circuits should be taken into when adding co-substrates because the influent flow would leave the ADer almost immediately without dilution or treatment. Thus if co-substrates are to be introduced, scenarios A100, A200 and B100 will dilute them.

Then, the global mixing parameters are computed: **Figure 3.17** depicts the UI for all scenarios in the three regions and **Figure 3.18** deploys the normalized second-order moment in each direction. **Table 3.10** shows the time at which the

tracer enters each region (second to forth column) and the homogenisation times according to the UI and 2nd-order moment.

The UI is traditionally applied globally in CFD models but, in this study, it was applied in the different compartments. The tracer's behaviour in the DYNOMIX scenarios (A50, A100, A200 and B100) was very similar: the inlet flow introduced the tracer directly into the DYNOMIX region and the recirculation flow drove it to the DYNOMIX region. The tracer then entered the TFR and lastly the CORE. This pattern could be stated with time when the tracer enters each region in **Table 3.10**. In the CORE, scenario A0 was the first one to reach a UI of 1 as it was the first one where tracers entered this region (see **Figure 3.17**a) but A0 was the one with longest period at higher UI in all regions (up to almost 10,000 s), so the short-circuiting avoided homogenisation of the sludge. In contrast, the DYNOMIX scenarios (A50, A100, A200 and B100) reached the maximum UI in the CORE region later than in A0 but reached homogeneity earlier: the first one to reach homogeneity was B100 followed by the others depending on their DYNOMIX flow, i.e. A200, A100 and A50. In DYNOMIX and TFR, B100 and A200 were quite similar and reached homogeneity around 1,000s. Then, A100 reached homogeneity followed by A50. Thus, B100 was the most effective mixing scenario as the tracer entered all the regions in the shortest time.

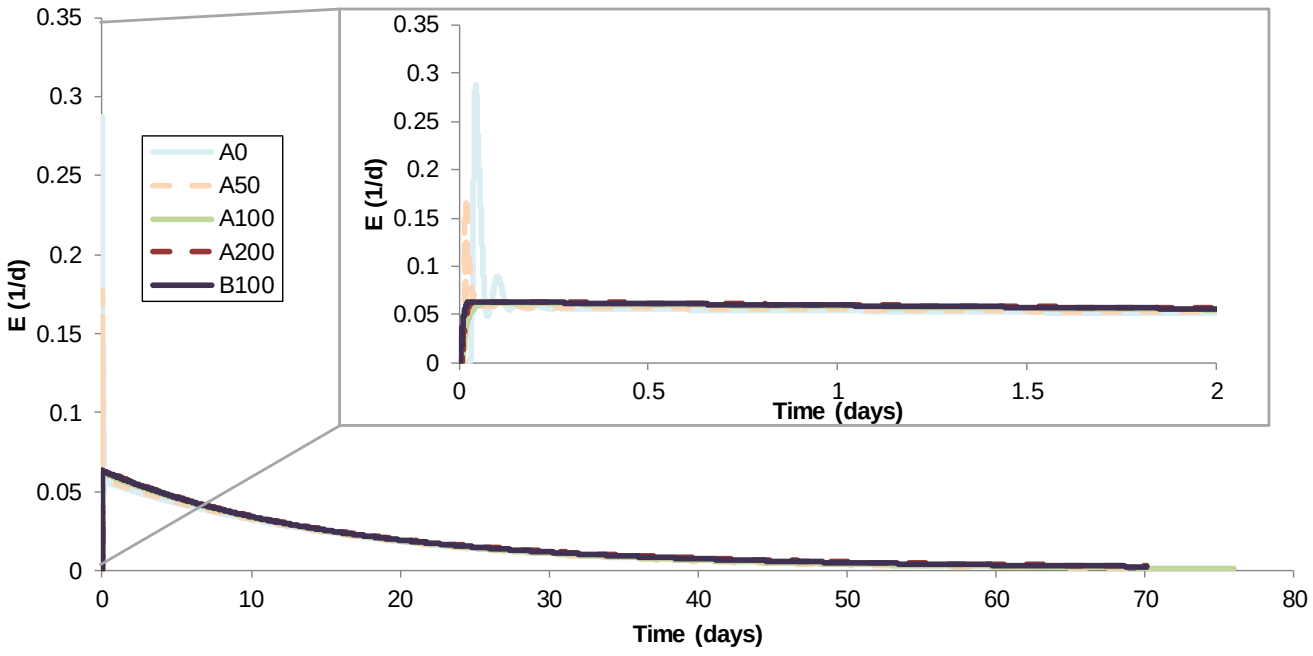

Figure 3.16: *E curve of lithium in the outlet in scenarios A0, A50, A100, A200 and B100, complete and detailed until day 2.*

As in Section 3.4.2.5, the second-order moments' curves for every spatial direction were computed in each scenario (see **Figure 3.18**). In the circumferential direction, complete tracer's mixing was reached before 1000 s in

A200 and B100 and after 1000 s in A100 and A50. As no DYNOMIX flow was present in A0, tracer is not spread in this direction, so its elongation is delayed to 10,000 s. Conversely, vertical tracer's spread was first reached in A200, followed by A100 and B100. Radial mixing is slower, so uniform mixing is fulfilled at 1000 s at A200 and B100, but it is delayed at A100 and A50, which have similar behaviour. A0 is the last scenario to reach complete mixing in all directions so, it is clearly not recommended to homogenise the anaerobic digester. When assessing the homogenisation times in the different directions, the circumferential direction was the preferential one because it had the shortest times, while the radial direction was disadvantageous as it had the longest homogenisation times. This local mixing behaviour could only be drafted from the second-order moments' curves.

Table 3.10: *First time that the tracer entered each region (T_0) and the homogenisation time with the UI and the second-order moment for the whole CFD simulation*

Scenario	T_0 CORE Region	T_0 DYNOMIX Region	T_0 TF Region	UI Homogenisation Time (min)	Second-order Moment Homogenisation Time (min)
A0	24	0	400	366.7	223.3
A50	200	0	90	91.7	91.7
A100	150	0	60	54	54.7
A200	100	0	25	25	30
B100	85	0	40	21.7	24.2

Lastly, the homogenisation time with the UI, t_{UI}, and second order moments are shown in **Table 3.10**. Similar times were obtained with both parameters and a similar pattern was described: the lower the DYNOMIX recirculation flow rate, the longer the homogenisation time; thus, A0 had the highest one. Indeed, the large difference from A0 to A50 emphasised the impact of the recirculation flow on the global mixing, which implies the need to include mixing devices in full-scale setups. Note that B100 was the scenario with the shortest homogenisation time, which makes this scenario the fastest way for the anaerobic digester to mix. Finally, B100 and A200 reduced the homogenisation time by about 50% compared to A100.

Overall, the UI and second-order moments led to similar conclusions and homogenisation times, although the UI findings were established thanks to the compartmental UI study. The agreement between both parameters endorses the robustness and consistency of second-order moments. In short, the UI provides local information about the mixing degree using compartmentalisation. However, second-order moments provide local information with a global parameter without having to resort to compartmentalisation. Additionally,

second-order moments state the direction with less mixing and, thus, show the direction in which mixing should be encouraged in bad mixing scenarios.

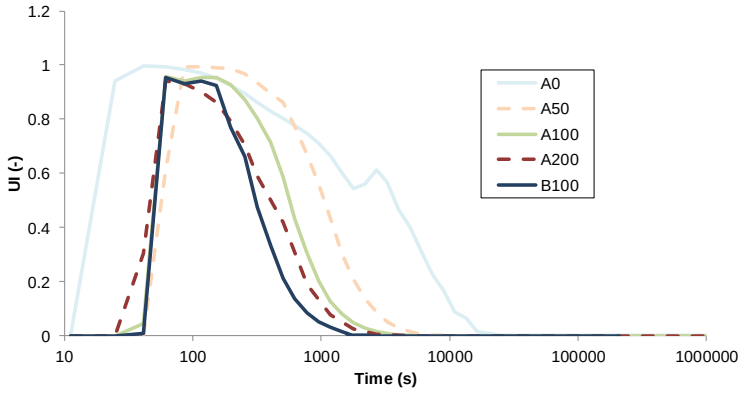

a) CORE

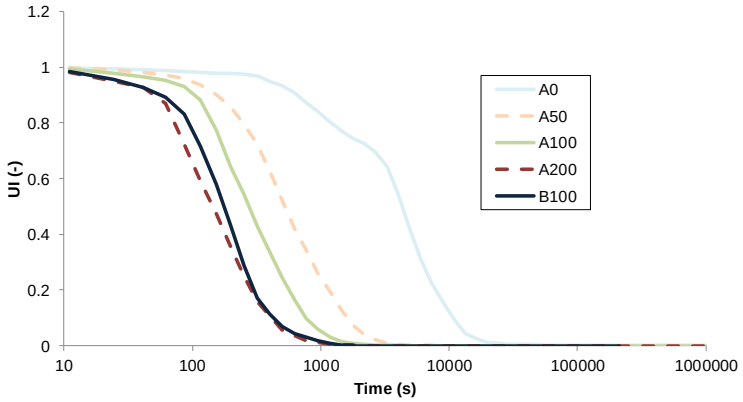

b) DYNOMIX

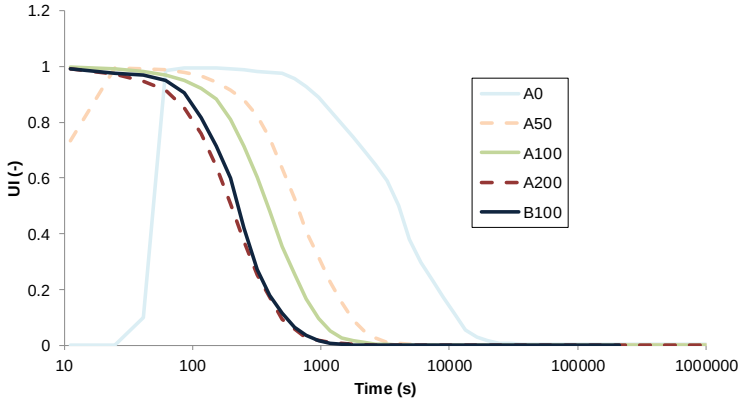

c)TFR

Figure 3.17: *Time evolution of the Uniformity index for all scenarios at different regions.*

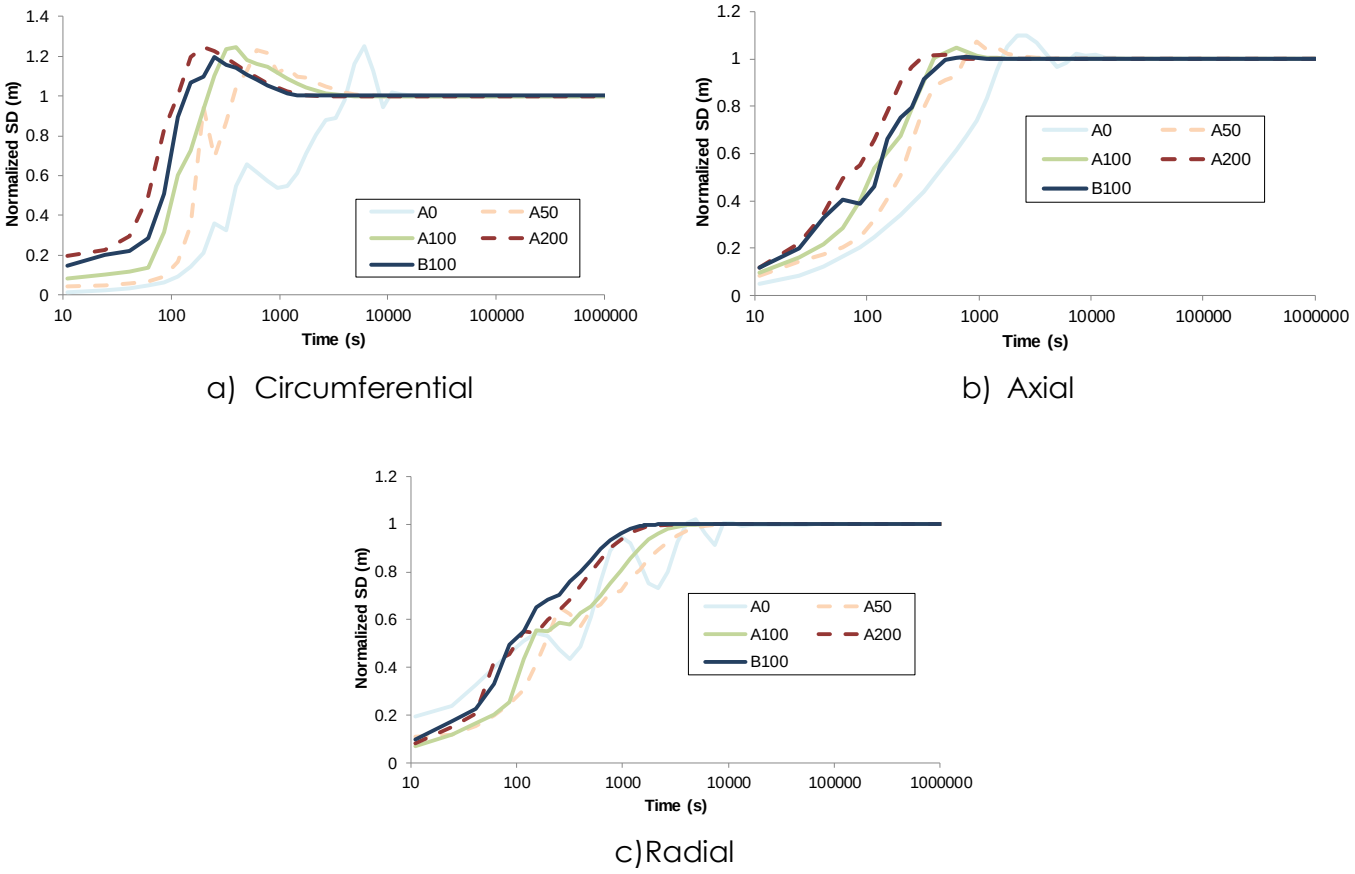

***Figure 3.18**: Normalized second order moment curves for all scenarios*

3.4.4. Dead volumes evaluation

In this section, the numerical results about dead volumes assessment are described. In a first section, the literature dead volume criteria are obtained and compared with real dead volumes. Then, the new dead volume criteria outlined in Section 3.2.4 are calibrated and applied to the different scenarios to state their dead volume.

3.4.4.1. Dead volume criteria assessment

In this section, dead volume criteria found in literature (see Section 3.2.4) were applied in the different scenarios aiming to meet the real dead volumes found experimentally in Digesters 1 and 2. **Table 3.11** shows the dead volumes found in each scenario for the different bibliography criteria.

Literature criteria showed appreciable disagreement between them in the different scenarios (see **Table 3.11**). For example, the second criterion (Wu and Chen, 2008) was the one that stood less stagnant volumes in all simulations and, e.g. only 3.19% low velocity volume was stated in A0 where there was no sludge recirculation. Thus, this criterion was the least sensitive to calculate the

dead volume. In contrast, the other criteria deploy clear differences between different recirculation flow rates, so that the higher recirculation flow rate, the lower zones with lower velocities. Thus, the criterion with a wider range between each scenario was the criterion of Vesvikar and Al-Dahhan, (2005), which is the only one that takes as threshold parameter the maximum velocity reached by the fluid in each scenario. **Figure 3.19** shows the dead volume of this criterion in two different scenarios where it was noticeable that the walls and the central column of the setup were low velocity zones and, accordingly, dead volumes. It could therefore be used in defining the anaerobic digesters' dead volumes as it was the most sensitive criteria. As another example of dead volume criteria, **Figure 3.20** depicts the dead volume (blue) with Karim et al., (2004) criterion and higher velocity zones (yellow) which were located in different zones to those in **Figure 3.19**. Overall, it was noticeable that all literature criteria were based on the velocity field.

When assessing the real dead volumes and the literature criteria, the real dead volume of Digester 1 agreed with that calculated in B100 with Wu and Chen (2008) (DV 2 (Wu and Chen, 2008)). Nevertheless, none of the dead volume criteria met the 13% of dead volume in A100 (Digester 2) so none of them reflected reality: four of the criteria were greater than the real 13% of dead volume while the second criterion (DV 2 (Wu and Chen, 2008)) defined that there was no dead volume when the DYNOMIX system was on. As the literature dead volume criteria did not meet experimental dead volume, new dead volume criteria would be necessary.

Table 3.11: *Calculation of dead volume's percentage for different literature criteria: DV 1 (Vesvikar and Al-Dahhan, 2005), DV 2 (Wu and Chen, 2008), DV 3 (López-Jiménez et al., 2015), DV 4 (Karim et al., 2007) and DV 5 (Karim et al., 2004).*

Simulation	DV 1 (%)	DV 2 (%)	DV 3 (%)	DV 4 (%)	DV 5 (%)
A0	98.8	3.19	100	97.0	92.3
A50	67.7	0	96.6	70.8	65.3
A100	32.1	0	88.06	61.8	58.9
A200	26.04	0	77.1	58.8	56.6
B100	8.6	0	73.2	53.9	52.1

Regarding to the difference between the scenarios, B100 had the smallest dead volumes in any criterion so, it would be the best configuration to avoid the formation of dead volume. Indeed, it had more effect than A200 (doubling the external recirculation flow). Currently, in the actual operation of Digester 1, a change is made between B100 and A100, i.e. the propeller is turned on for 6 hours

per week and turned off, and this hydrodynamic variation seemed to be key to avoid the formation of low velocity zones inside Digester 1, since the experimental RTD curve did not show a dead volume.

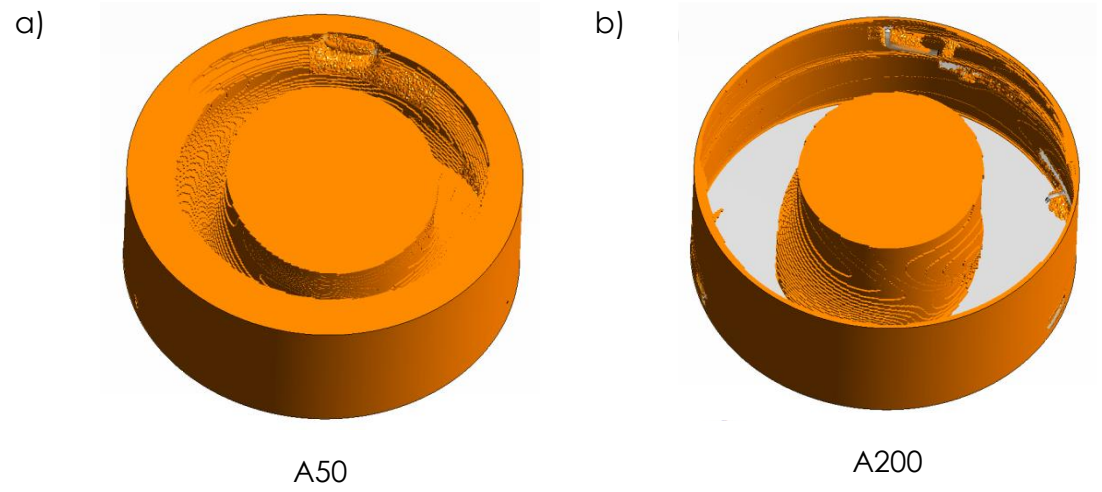

Figure 3.19: *Representation of dead volume for Vesvikar and Al-Dahhan (2005) criterion for different CFD simulations: a) A50, and b) A200.*

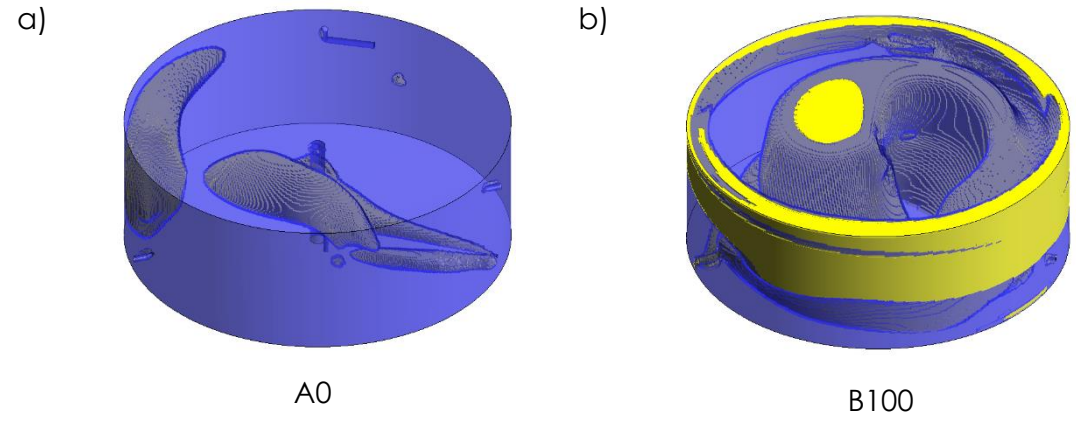

Figure 3.20: *Velocity zones with axial velocity higher than 0.002 m/s (yellow) and lower than 0.002 m/s (blue)in different scenarios: a)A0 and b)B100*

3.4.4.2. New Dead volume criteria calibration

Eqs. 3.31 to 3.33 were applied to A100 and B100 scenarios, which are the real scenarios of Digester 1 and 2, with different velocity and turbulence constants (see Appendix A: Dead Volume Criteria Constants) to find the accurate dead volume criterion and calibrate the velocity and turbulence constants. As these criteria were probability functions ranging between 0 and 1, 0.5 was the threshold between the formation or washing of dead volume, so this value was used to calculate and locate it (see **Figure 3.22**).

Firstly, the dead volume values obtained showed that the Buoyancy PDF

(Eq. 3.31) remained constant at 58% and 52% of dead volume in scenarios A100 and B100, respectively, so, they could not be fitted to experimental values (see black lines in **Figure 3.21**). As the Buoyancy PDF only included the velocity field, this implied that buoyancy or velocity field should not be the only one in the dead volume criteria and, therefore this criterion could be omitted. Conversely, Exponential decay PDF and Gaussian PDF reached the experimental dead volume at certain velocity and turbulence constants so, the Exponential decay and Gaussian PDFs were the best criteria to fit the experimental dead volumes. Note that Exponential decay and Gaussian PDFs (Eqs. 3.32 and 3.33) combine buoyancy and turbulence dispersion effect, so their inclusion was essential in the dead volume criteria.

Secondly, the study of the different velocity and turbulence constants clearly stated that the value of the velocity constant C_v (data not shown) had no impact on the dead volume's value. Thus, the velocity constant was fixed as one. Nevertheless, the turbulence coefficient depicted a great impact on the dead volume's value as deployed in **Figure 3.21**: As result, a turbulence coefficient of 0.3 and 0.22 for the Exponential Decay PDF and Gaussian PDF were stated according to the experimental dead volumes of Digester 1 and 2.

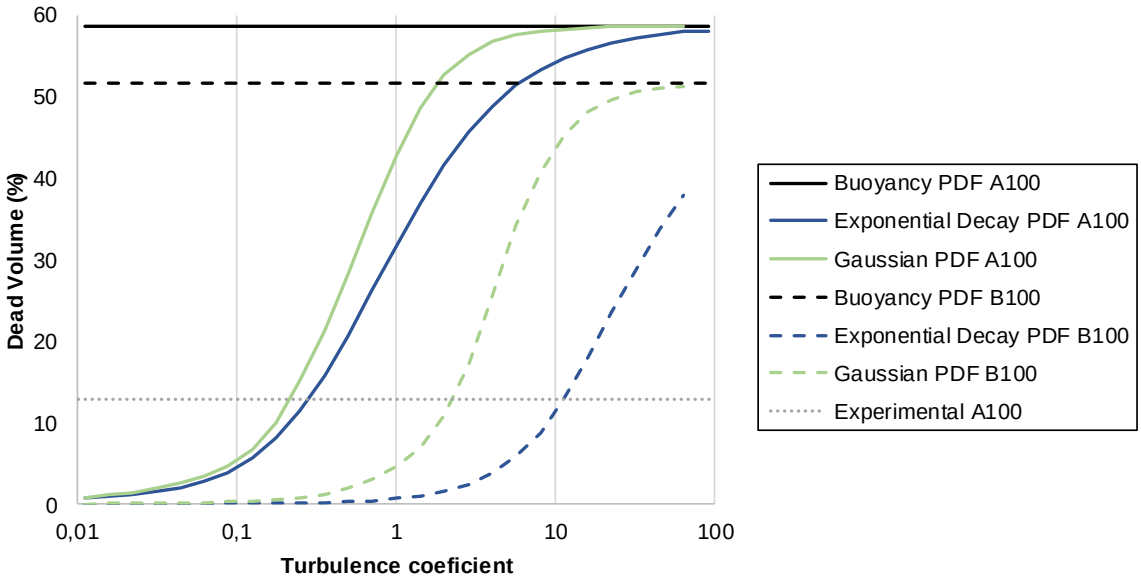

Figure 3.21: *Calculated dead volume with different turbulence coefficients at A100 and B100 scenarios.*

Attending to the great results of the Exponential Decay PDF and Gaussian PDF, they were computed for all scenarios with recirculation flow (see **Table 3.12**). Scenario A0 depicted 87.12% dead volume in the Exponential Decay PDF and 87.7% dead volume in the Gaussian PDF, so this scenario was excluded from the discussion. The theoretical mean floc diameter was linked to the velocity, so low velocities allowed floc growth entailing higher floc size and accordingly dead

volume formation. Therefore, A50 was the scenario with greater dead volume, more than half of the anaerobic digester volume. In Digester 1 with intermittent mixing, flocs could grow in A100 (see **Figure 3.22**a) due to low velocities but, when the propeller was activated 6 hours per week (B100 scenario), big flocs would be broken due to the high shear rate induced by the propeller. Consequently, the flocs were not able to form a dead volume inside Digester 1 (see **Figure 3.22**b). The dead volume found in A200 and B100 were pretty similar but A200 would entail a higher energy consumption (44kW A200 vs 25.5kW B100) so that it would not be feasible to apply on the WWTP. In short, these new criteria were sensitive to the operational conditions and were able to deploy intermittent mixing between the A100 and B100 scenarios.

Table 3.12: *Dead volumes in all scenarios by means of new dead volume criteria.*

Scenario	Exponential Decay PDF (%)	Gaussian PDF (%)
A50	50.337	58.987
A100	13.645	13.051
A200	1.361	1.225
B100	0.873	0.674

a) b)

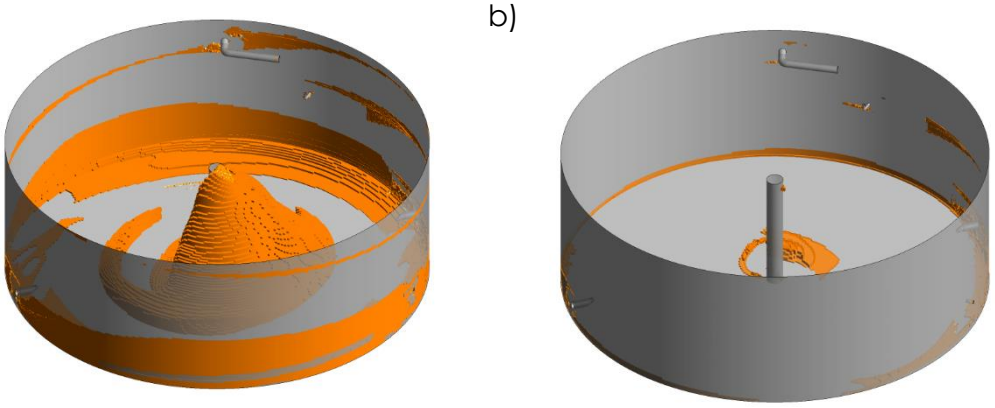

Figure 3.22: *Dead volumes in a) scenario A100 with Exponential Decay PDF and b) scenario B100 with Gaussian PDF.*

3.4.5. Intermittent mixing

Based on these analyses, it is easy to draw some conclusions about the mixing regime of Digester 1 and 2. The global parameters and dead volume criteria have shown that the mixing in A200 and B100 was very similar, however,

the energy consumption in A200 was much higher (44kW) than in B100 (25.5 kW). Therefore, if mixing was to be maximised, it should be done with B100.

Currently, A100-B100 intermittent mixing is performed in Digester 1, but could intermittent mixing be done between A50 and B100? This would be a feasible and simple practice to reduce the ADer energy demand and complete mixing would only be delayed by 2200 seconds (37 minutes) with A50 mixing. Additionally, dead volume analysis showed that almost half of the anaerobic digester would be dead volume if A50 were applied. Hence, if A50-B100 intermittent mixing were performed, the B100 agitation time should be increased from 6 hours per week to at least a couple of hours per day. In this way, the input of co-substrates could be done in the period in B100 to favour their dilution and avoid short-circuiting and dead volumes in A50.

On the other hand, if energy savings were to be maximised, A0-B100 intermittent mixing should be practised, but was it feasible in terms of mixing and homogenisation? Firstly, the number of hours in B100 would be much higher than it is currently. Secondly, the A0's short-circuiting from **Figure 3.16**b was depicted as an early large peak in the CORE region. Attending to the UI (see **Figure 3.17**), A0 was the one with a longer period at higher UI in all regions (up to almost 10 000 s), avoiding homogenisation. Second-order moment curves in A0 agreed with UI so their homogenisation time was fairly increased. Thus, A0 was clearly not recommended for homogenising the ADer so A0-B100 intermittent mixing was dismissed.

3.5. CONCLUSIONS

The hydrodynamics of a full-scale anaerobic digester in two different configurations with an external recirculation pump mixing system was studied through CFD models and tracer test results. Non-Newtonian single-phase CFD simulations were performed to assess the recirculation system (DYNOMIX) and a 3-blades propeller by means of different scenarios: without recirculation flow, A0; with 50%, 100% and 200% recirculation flow, A50, A100, and A200, respectively; and with 100% recirculation flow and a 3-blades propeller, B100. The base model (A100) was thoroughly verified in a transient state to accurately reproduce the actual operating conditions, its global validation being unique through an experimental complete RTD of 76 days.

Firstly, CFD models' hydrodynamics showed a great circumferential velocity driven by liquid recirculation jets, whose pattern clearly drew a compartmental structure with 3 regions at all scenarios except for A0. Low velocities were gathered in a CORE region at the centre of the setup with secondary vertical flows. Furthermore, recirculation jets pushed a spinning movement around the central axis, so a laminar vortex structure was depicted in the CORE region. Nevertheless, the laminar vortex disappears in its surroundings, where instead a fully-developed turbulent channel was shown. These regions

surrounding the CORE are the DYNOMIX region, where DYNOMIX jets offer the highest velocities, and the Turbulent Flow region, with lower velocities than the DYNOMIX region but higher than those of the CORE.

After the assessment of the anaerobic digesters' hydraulics, different mixing parameters from literature were studied in depth. The design parameters, i.e. DVTT, HRT, UP, and G, were evaluated and, attending to the experimental RTD and current energy demands, the authors agreed with literature works that the design parameters thresholds should be reviewed: they failed to define the energy needs and were too global to depict the local mixing.

Concerning the local mixing parameters, local RMS Velocity Gradient and α_{DME}, they define the mixing degree and mixing type, respectively. They were studied in each region of the different scenarios, and they were stated as key to define the mixing performance of the anaerobic digesters. Local RMS Velocity Gradient depicted the CORE as the region with the lowest mixed region and the DYNOMIX region as the one with the highest mixing in all scenarios. With this parameter, B100 was found to be the most efficient scenario in the CORE's mixing due to the propeller's momentum. The α_{DME} depicted the type of phenomena that pushed the mixing, stating a solid-liquid laminar vortex movement in the CORE region, a shear flow in the DYNOMIX region, and a dispersive flow in the TFR. Thus, the outer regions are the better-mixed ones through shear and disperse phenomena.

The UI as a global mixing parameter was then evaluated in the different scenarios and regions. The tracer's trajectory was equal in A50, A100, A200 and B100 scenarios: the tracer enters the digester in the DYNOMIX region and recirculation jets pushed the tracer to the TFR and lastly to the CORE. The tracer enters the CORE more rapidly in B100 so that it was stated as the most effective scenario. Additionally, the second-order moments were proposed as a new global mixing parameter to study the anaerobic digesters' mixing degree in each direction. The new parameter restated the circumferential direction as the preferential one in all scenarios and the great similarities between A200 and B100. On the contrary, the radial direction was found to be less important in the mixing process, so it could be enhanced in the mixing strategies, i.e. in B100. Thus, the second-order moments were able to provide geometrical local mixing information without compartmentalization yielding second order moments as simpler and more valuable than UI.

Finally, the homogenisation times were established with the UI and second-order moments, so the setups were homogenised in less than 1h. A200 and B100 showed similar homogenisation times, 30 min and 24.2 min, respectively, which are about 0.10% of the HRT. Thus, the difference between the two scenarios was likely to have little influence on the overall process and both could be used to dilute inhibiting compounds or co-substrates rapidly. Nonetheless, due to the great energy consumption of A200, B100 was more appreciated.

Regarding intermittent mixing, A100-B100 current operation has been declared without hydraulic defects utilizing the experimental RTD but, if energy consumption needs to be reduced, A50-B100 could be considered. In this case, an influent nozzle modification could avoid the appearance of the short-circuiting in A50. Nonetheless, the chance of dead volume formation needed to be reviewed.

Accordingly, dead volumes were quantified through the different scenarios with literature dead volume criteria. Experimental dead volumes were 13% and 0% in A100 and B100, respectively; but none of the dead volume criteria agreed with the experimental one. Criteria 3 to 5 overpredicted the dead volume and the second criterion underpredicted the dead volume formation. Vesvikar and Al-Dahhan, (2005) criterion was the most sensitive to the definition of dead volume, but it only takes liquid velocity into account.

At this point, new dead volume criteria were proposed taking into account the buoyancy force and low turbulence dispersion. The criteria were calibrated through a coefficient adjustment and experimental dead volume. The Exponential Decay PDF and Gaussian PDF were then established as the best criteria to estimate anaerobic digesters' dead volumes.

The dead volume in A50 was established as 50% and 59% so an A50-B100 intermittent mixing could lead to the appearance of dead volumes. Thus, aiming to avoid the formation of dead volumes, a future study should look at the time required in B100 to work in A50-B100 intermittent mixing avoiding hydraulic defects.

In short, the analysis of the different scenarios showed that the additional mixing provided by propellers was more effective in digesters with this type of liquid recirculation system than an increase of the recirculation flow. It had been shown that propellers reduce the low-velocity areas and, consequently, minimize the appearance of dead volumes inside anaerobic digesters. The foregoing conclusions state that CFD simulations help to understand full-scale digesters' hydrodynamics, which are experimentally difficult to explore due to their anaerobic conditions. Additionally, transient simulations with virtual tracer tests help to carry out exhaustive analyses of mixing patterns within large bioreactors.

4. TOWARDS ADM1 INTO CFD (I): VALIDATION AT LAB-SCALE

This chapter was devoted to creating an anaerobic biological CFD solver able to display the anaerobic digestion process in one-phase CFD models. Thus, *ADM1Foam* solver has been developed in this chapter facing different challenges such as pH calculation or liquid-gas transfer. Due to the large amount of input data needed to achieve this aim, the new solver has been validated by means of experimental data and a 0D-CSTR model from a lab-scale setup. As a result, a new anaerobic biological CFD solver has been developed and validated, so it can be used as a base point for more advanced applications and biological processes.

Abstract: The Anaerobic Digestion Model 1(ADM1) has been implemented in an open-CFD software as a solver called *ADM1Foam*. This solver has been tested in a lab-scale setup from Zaher, (2005) to validate the correct implementation of the pH calculation and the biological processes. *ADM1Foam* results were compared with the experimental data but also with a 0D-Matlab Framework (Patón and Rodríguez, 2019) to test its capabilities in a transient state. As a result, the lab-scale setup proved that CFD can simulate ADM1 in a single-phase model as a 0D simulation framework does, but also considering experimental transient behaviour. Thus, the agreement with experimental and 0D models proved the correct implementation and validity of *ADM1Foam*. An additional scenario with lower mixing stated slight mixing impacts on anaerobic digestion but further research would be needed to link mixing and anaerobic bioprocesses. Additionally, further research is needed to transform *ADM1Foam* single-phase solver to a two-phase one.

Keywords: CFD; ADM1; Anaerobic Digestion; biological model; pH calculation

4.1. INTRODUCTION

One of the problems faced in WRRFs is the control of the biological processes that occur in them. Control of CAS is solved mainly by the introduction of probes and daily sampling. However, these practices are much more difficult to carry out in the anaerobic digestion process, so the control of anaerobic digestion has been simplified in WRRFs. Thus, monitoring of anaerobic digestion has been limited to weekly sampling and online measurement of biogas production. In addition, the development of new anaerobic based wastewater treatment technologies has undergone great growth worldwide (Seghezzo et al., 1998) and there is a need for better control of anaerobic processes.

Mathematical modelling and numerical simulation have been extended as potential tools in the design, operation, optimization and process control of a WWTP, but always with a focus on CAS (Jacek Makinia and Ewa Zaborowska, 2020). Therefore, they can be extended to anaerobic digestion and anaerobic wastewater treatments. Simulators, such as GPS-X, WEST, Simba, BioWin or Sumo, are based on mass balances with biological models implemented (Jeppsson, 1996) and some of them include the ADM1 (Batstone et al., 2002) for anaerobic digestion. ADM1 (described in Section 2.4.1) includes biochemical and physic-chemical processes such as gas-liquid exchanges of bioproducts and ion association/dissociation. Furthermore, the identification and quantification of compounds and biochemical parameters are the major drawback for the application of the ADM1, as well as some weaknesses in its structure (Kleerebezem and van Loosdrecht, 2006). Even so, ADM1 has been used by technologists and different users as the best tool to evaluate the anaerobic digestion process (Batstone et al., 2015, 2006).

The process modelling software uses the approach of tank in-series (Levenspiel, 1999) in which each tank is modelled as a fully stirred tank reactor (CSTR). As previously seen, the CSTR concept is a simplification of the hydrodynamic phenomena taking place within the tanks. On the one hand, defective hydraulic designs typically lead to mixing behaviours far from the ideal CSTR so these models do not match the real performance. On the other hand, good mixing has been proven to be crucial in anaerobic digestion to ensure maximum removal efficiency and to avoid different operational problems, e.g., stratification, sedimentation, and formation of accumulations. In this context, CFD models are the most detailed simulation framework capable of accurately describing sludge behaviour so that they can be used to detect hydraulic problems in 3D, including multiphase flow models coupled to biokinetics. Hence, considering the great importance of hydrodynamics in anaerobic reactors, CFD simulations are expected to be a powerful tool for the analysis and optimization of anaerobic processes. One example can be found in Hoffmann et al., (2008) who reported some correlation between mixing intensities and some anaerobic digestion pointers i.e. methane production and the appearance of some

microbial populations, by means of CFD simulations.

Moreover, CFD coupled to biokinetics has been widespread in the WWT sector and is considered a useful tool for troubleshooting (Climent Agustina, 2019). Therefore, anaerobic digestion kinetics coupling, such as ADM1, has been requested in the literature to understand local transport phenomena of state variables and help in the design of efficient mixing digesters (Batstone et al., 2015; Fernandes del Pozo, 2020; Lindmark et al., 2014b; Yu et al., 2013b) or biohydrogen production (Kariyama et al., 2018). In the light of this, different authors have included part of ADM1 in commercial CFD codes (Tobo et al., 2020; Wu, 2012c) where the complexity of the model has been the greatest obstacle to its complete inclusion. Gaden, (2013) coupled hydrodynamics with the complete ADM1 in an open-source CFD code but it was only verified in a 2D lab-scale anaerobic digester with a fixed parabolic momentum source.

In this work, the ADM1 was coupled with the hydrodynamics in a CFD solver called *ADM1Foam*. To ensure the correct implementation of the ADM1, it was calibrated and validated with a real lab-scale setup. The *ADM1Foam* results were compared with experimental data and a 0 Dimension (0D) Matlab-Excel framework to prove its validity in lab-scale and transient simulations.

4.2. OPENFOAM

OpenFOAM has different multiphysic capabilities thanks to solvers in different areas:

- CFD
- Heat transfer and conjugate transfer
- Combustion and chemical reactions
- Multiphase flows
- Mass transfer
- Fluid-structure interaction
- Particulate Fluids (DEM, DSMC, MD)
- Dynamic meshing, adaptive meshing
- Acoustics, finance, molecular dynamics, electromagnetism, stress analysis of solids, etc.

Nonetheless, the development achieved at the CFD code is outstanding compared with other solvers.

4.2.1. Solver scalarTransportFoam

scalarTransportFoam is a basic solver contained in the OpenFOAM library which solves a passive scalar transport equation, i.e. Eq. 4.1.

$$\frac{\partial \phi}{\partial t} + \nabla(U\phi) - \nabla^2(D_T\phi) = S_\phi \qquad 4.1$$

where ϕ is the transported scalar, U is the fluid velocity, D_T is the molecular diffusion coefficient divided by the fluid density and S_ϕ is the source term of the scalar. Its code is as follows and it would be the base for the development of a new ADM1 solver:

```
    Info<< "\nCalculating scalar transport\n" << endl;

    #include "CourantNo.H"

    while (simple.loop())//Time loop
    {
        Info<< "Time = " << runTime.timeName() << nl << endl;

        while (simple.correctNonOrthogonal())
        {
            fvScalarMatrix TEqn //Create object TEqn
            (
                fvm::ddt(T)
              + fvm::div(phi, T)
              - fvm::laplacian(DT, T)
             ==
                fvOptions(T)
            );//Scalar Transport Equation

            TEqn.relax();//Implicit relaxation is applied to TEqn
            fvOptions.constrain(TEqn);
            TEqn.solve(); //The TEqn is solved
            fvOptions.correct(T);
        }

        runTime.write(); //Write the solution in the runtime folder
    }

    Info<< "End\n" << endl;

    return 0;
```

4.2.2. OpenFOAM simulations structure

OpenFOAM simulations structure is organized by several plain texts located across the following three directories (see **Figure 4.1**):

- 0: this is the initial time directory where initial and boundary conditions are defined. Inside it has the field files compulsory to run each solver.
- constant: this contains the fluid's properties, mesh and boundary data.
  - Polymesh: mesh data is stored in this directory.
  - Other directories and files
- system: the numerical solver, interpolation, numerical methods, discretization methods and time control are controlled by the plain text files in this directory.

- controlDict: this sets the type of solver, the time control and the convergence criteria during the numerical solution.
- fvSchemes: this sets the equation discretization method.
- fvSolution: this sets the solving numerical methods.
- fvOptions (optional)
- Other directories and files

When the solving process starts, new directories are generated:

- Result time directories: they contain field results attending to an iteration count or time.
- postProcessing: this folder is generated by function objects data solution at the user's request, i.e. it is not generated by default but the use of function objects data solution is highly recommended.

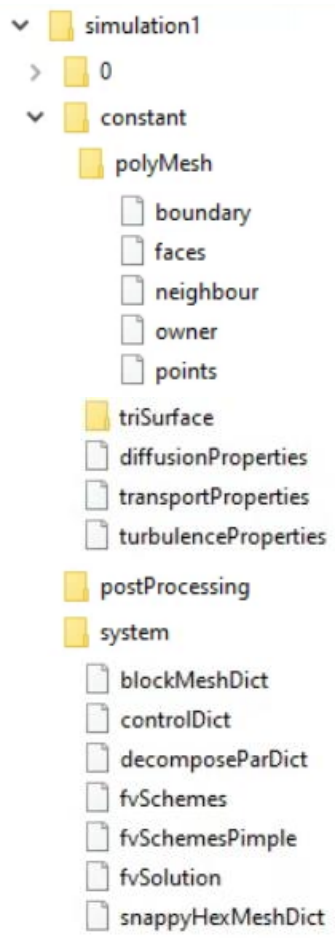

Figure 4.1: *Example of OpenFOAM simulation structure files.*

4.3. MATHEMATICAL FORMULATION: *ADM1FOAM*

A new solver called *ADM1Foam* was developed to introduce ADM1 in a CFD software. In this solver, the *scarlarTransportFoam* solver (Eq. 4.1) was modified to build *ADM1Foam* so that ADM1 variables are introduced as scalars with a turbulent transport equations as,

$$\frac{\partial \phi_k}{\partial t} + \nabla(U\phi_k) - \nabla^2\left[\left(D_T + \frac{\nu_t}{Sch_k}\right)\phi_k\right] = S_k \qquad 4.2$$

solved for k equations where k is the ADM1 state variable. ϕ_k is the transported scalar, i.e. the concentration of the ADM1 state variable; U is the fluid velocity; D_T is the molecular diffusion coefficient divided by the fluid density; ν_t is the kinematic viscosity [m^2/s]; Sch is the turbulent Schmidt Number [-] and S_k is the source term for k transported ADM1 species [1/s]. The molecular diffusivity of the ADM1 state variables was fixed at 2.8x10^{-11} and 1x10^{-10} m^2/s for biomass and substrates, respectively.

It is important to highlight the additional terms added to Eq. 4.2 with respect to Eq. 4.1: the turbulent diffusivity and the source term. Turbulent diffusivity is the most widely applied term to study the scalar's transport in turbulent flows, and the gradient diffusion calculation requires a value for the turbulent Schmidt Number, i.e. the ratio of momentum diffusivity to mass diffusivity (Gualtieri et al., 2017). The turbulent Schmidt Number is related to the turbulent flow characteristics and there is no standard value generally established so it varies from 0.1 to 100 depending on the numerical resolution (Gualtieri et al., 2017). In this case, it was set at 0.7 as it is the default value set by OpenFOAM developers and it is similar to the 0.9 chosen in chapter 3 for ANSYS CFX. The source term is the term $\sum_j \rho_j \nu_{k,j}$ defined for each k ADM1 state variable by the ADM1 matrix (Batstone et al., 2002) where j is the ADM1's process, ρ_j the process rate and $\nu_{k,j}$ the kinetic parameter for k ADM1 state variable and j ADM1's process.

Table 4.1 describes all transported scalars considered by *ADM1Foam,* i.e. 27 variables with their turbulent scalar transport equation. It is noticeable that the particulate and soluble ADM1 state variables have been considered equal and associated to the single liquid phase of the model in a similar way to other literature works (Climent et al., 2018; Tobo et al., 2020).

Table 4.1: *Scalar transport equations of ADM1Foam.*

Variable	Name	Units	Variable	Name	Units
Ssu	Monosaccharides	kmol/m³	Xc	Composites	kmolC/ m³
Saa	Amino acids	kmol/ m³	Xch	Carbohydrates	kmolC/ m³
Sfa	Long chain fatty acids	kmol/ m³	Xpr	Proteins	kmolC/ m³
Sva	Total Valerate	kmol/ m³	Xli	Lipids	kmolC/ m³
Sbu	Total Butyrate	kmol/ m³	Xi	Particulate inerts	kmolC/ m³
Spro	Total Propionate	kmol/ m³	Xd	Particulate dead biomass	kmolC/ m³
Sac	Total Acetate	kmol/ m³	Xsu	Sugar degraders	kmolC/ m³
Sch4	Methane	kmol/ m³	Xaa	Amino acid degraders	kmolC/ m³
Sh2	Hydrogen	kmol/ m³	Xfa	LCFA degraders	kmolC/ m³
Sic	Inorganic Carbon	kmolC/ m³	Xc4	Valerate and butyrate degraders	kmolC/ m³
Sin	Inorganic Nitrogen	kmolN/ m³	Xpro	Propionate degraders	kmolC/ m³
Scat	Cations	kmol/ m³	Xac	Acetate methanogens	kmolC/ m³
San	Anions	kmol/ m³	Xh2	Hydrogen methanogens	kmolC/ m³
Si	Soluble Inerts	kmol/ m³			

Regarding the pH calculation, it is not a transported scalar, so its calculation is done by means of a pH loop built to reduce the stiffness of the ADM1. As described in Volcke et al., (2005), the pH differential equation is approximated to an implicit algebraic equation which is solved iteratively by the Newton-Raphson method. The ion concentration (S_{H^+}) is calculated at each new timestep t as:

$$S_{H^+,t+1} = S_{H^+,t} - \frac{E(S_{H^+,t})}{dE(S_{H^+})/dS_{H^+}|_{S_{H^+,t}}} \qquad 4.3$$

being $S_{H^+,t+1}$and $S_{H^+,t}$ the concentration at actual iteration and previous iteration, respectively; $E(S_{H^+,t})$ the algebraic equation that must be zero at the equilibrium 4.4, and $dE(S_{H^+})/dS_{H^+}|_{S_{H^+,t}}$ the gradient of the algebraic Eq. 4.5.

$$E(S_{H^+,t}) = S_{cat^+,t} + S_{nh4^+,t} + S_{H^+,t} - S_{hco3^-,t} - S_{ac^-,t} - S_{pr^-,t} - S_{bu^-,t} - S_{va^-,t} - \frac{K_W}{S_{H^+,t}} - S_{an^-,t} \qquad 4.4$$

$$dE(S_{H^+})/dS_{H^+}|_{S_{H^+,t}} = 1 + \frac{K_{a,IN} \times S_{IN}}{(K_{a,IN} + S_{H^+,t})^2} + \frac{K_{a,CO_2} \times S_{IC}}{(K_{a,CO_2} + S_{H^+,t})^2} + \frac{K_{a,ac} \times S_{ac}}{(K_{a,ac} + S_{H^+,t})^2} + \frac{K_{a,pro} \times S_{pro}}{(K_{a,pro} + S_{H^+,t})^2} + \frac{K_{a,bu} \times S_{bu}}{(K_{a,bu} + S_{H^+,t})^2} + \frac{K_{a,va} \times S_{va}}{(K_{a,va} + S_{H^+,t})^2} + \frac{K_w}{(S_{H^+,t})^2} \qquad 4.5$$

Eq. 4.3 is solved iteratively until $E(S_{H^+,t})$ achieves the tolerance value of 10^{-12}, which is normally achieved in a maximum of 5 iterations.

A scheme of this solver is shown **Figure 4.2**: Firstly, the timestep loop is initialized and an internal loop for the pH calculation is solved progressively at every single cell of the CFD model. When pH convergence criteria are fulfilled in all cells, the source terms of ADM1 species are also calculated in every single cell. The last step is the solution of the transport equation of all ADM1 state variables.

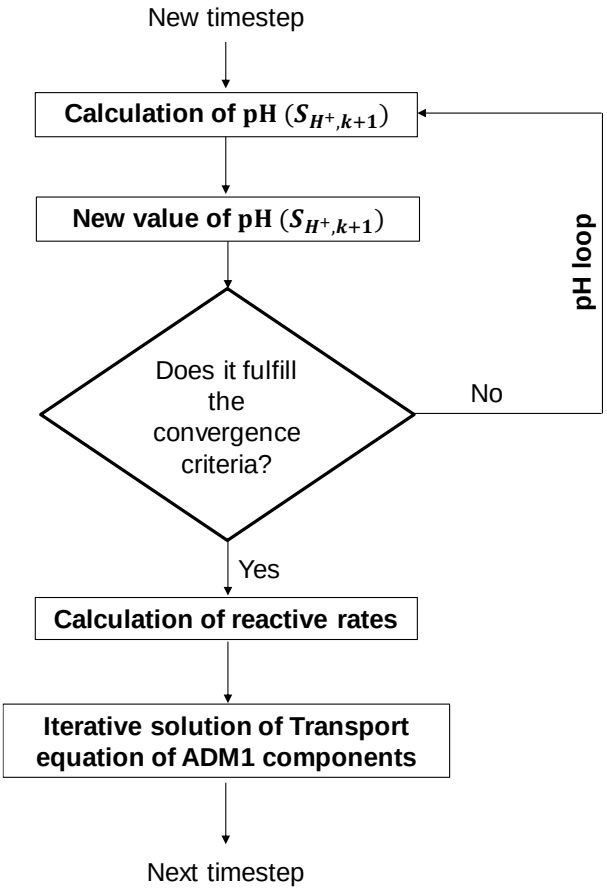

Figure 4.2: *Calculation scheme of ADM1Foam.*

Prior to the application of the *ADM1Foam,* different input data must be calculated and defined. On the one hand, the most important data to run the solver are the hydrodynamics of the CFD model because *ADM1Foam* does not calculate them, as described in **Figure 4.2**. They can be calculated by means of an OpenFOAM single-phase solver, such as *simpleFoam* or *pimpleFoam,* so that velocity (U) and kinematic viscosity (nut) fields are obtained. Then, the *ADM1Foam* is solved using previous hydrodynamic results, i.e. without hydrodynamics calculation. On the other hand, the different ADM1 related parameters and state variables must be defined, i.e. the biological parameters and the ADM1 state variables concentration for the different boundary conditions and initial values of the tank.

It is important to note that this first approximation of the ADM1 in CFD requires an input value of the biogas partial pressures from the gas phase to calculate the degassing rates. The biogas partial pressures are considered equal

for the whole CFD-model and can be modified during the transient simulation. Thus, the biogas partial-pressures are provided as input values and the concentration of hydrogen, methane and carbon dioxide in the liquid phase is calculated by *ADM1Foam*. In this first model, the gas phase is not included in order to test the correct implementation of the ADM1 model in the liquid phase. In addition, the inclusion of the gas phase implies more computational time, which would also imply more computational resources for the resolution of the model.

4.3.1. Structure of *ADM1Foam*

The source code of the *ADM1Foam* is structured as (see **Figure 4.3**):

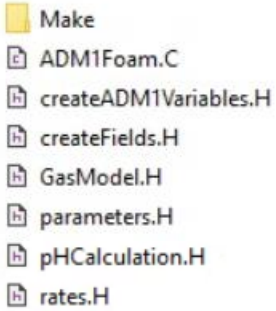

Figure 4.3: *Files of the ADM1Foam solver.*

- ADM1Foam.C: This is the main code that calls different parts of the code and finally solves the transport equation of the ADM1 state variables, i.e. Eq. 4.2. A summary of the core code is shown below:

```
    while (simple.loop())
    {
        Info<< "Time = " << runTime.timeName() << nl << endl;
        while (simple.correctNonOrthogonal())
        {
////////////////////////////////ADM1//////////////////////////
    //Call pH calculation
#  include "pHCalculation.H"

    //Rates
#  include "rates.H"

  //Gas Model Calculation
#  include "GasModel.H"

/////////////Solve ADM1 Variables Transport equations///////////////

 //Same scheme at convective term for all ADM1 Variables
 tmp<fv::convectionScheme<scalar>> mvConvection
(
    fv::convectionScheme<scalar>::New
    (
```

```
        mesh,
        fields,
        phi,
        mesh.divScheme("div(phi,ADM1Var)")
    )
);


  Info<< "Solve ADM1 Variables Transport equations"<< endl;

    fvScalarMatrix SsuEqn
   (
            fvm::ddt(Ssu)
            + mvConvection->fvmDiv(phi,Ssu)
            - fvm::laplacian(DTt,Ssu)
            ==0.166667*r2+0.0118558*r4-r5+f_su_xd*r20
   );

 SsuEqn.solve();

[…]

//////////////////////END OF ADM1////////////////////////////////
        }
        runTime.write();
        runTime.printExecutionTime(Info);
    }
// * * * * * * * * * * * * * * * * * * * * * * * * * * * * * * * * * * //
```

- parameters.H: This file defines the stoichiometric and physico-chemical parameters that are used in the pH calculation, rates and gas rates. An example of this code is as follows:

```
    ///////////Stoichiometric parameters//////////////////////////
    dimensionedScalar stoich10
("stoich10",dimensionSet(0,0,0,0,0),0.9581);
    dimensionedScalar stoich11
("stoich11",dimensionSet(0,0,0,0,0),0.949999959);
    dimensionedScalar stoich12 ("stoich12",dimensionSet(0,0,0,0,0),-
0.265000013);
[…]

  dimensionedScalar Y_su ("Y_su",dimensionSet(0,0,0,0,0),0.599974225);
    dimensionedScalar Y_aa
("Y_aa",dimensionSet(0,0,0,0,0),0.0834617064);
[…]

    dimensionedScalar f_si_xc
("f_si_xc",dimensionSet(0,0,0,0,0),0.107683924);
[…]
// * * * * * * * * * * * * * * * * * * * * * * * * * * * * * * * * * * //
```

- createFields.H: This file has two main functions: on the one hand, to create

the ADM1 state variables (calling the file "createADM1Variables.H") and rates, and on the other hand, to read parameters or fields found in the input files (see Section 4.3.2), including biochemical parameters, the molecular diffusion coefficient, the Schmidt Number and the velocity and viscosity fields of the liquid phase. An extract of this file is as follows:

```
////////ADM1 KineticParameters////////////////////////////////////

Info<< "Reading ADM1KineticParameters\n" << endl;

IOdictionary ADM1KineticParameters
(
    IOobject
    (
        "ADM1KineticParameters",
        runTime.constant(),
        mesh,
        IOobject::MUST_READ_IF_MODIFIED,
        IOobject::NO_WRITE
    )
);

    //Biochemical parameters
Info<< "Reading Biochemical parameters \n" << endl;

dimensionedScalar k_dis
(
    ADM1KineticParameters.lookup("k_dis")
);

[…]
///////////ADM1 Variables////////////////////////////////////
#  include "createADM1Variables.H"

///////////ADM1 rates//////////////////////////////////////////
Info<< "Creating rate fields from ADM1\n" << endl;

volScalarField r1
(
    IOobject
    (
        "r1",
        runTime.timeName(),
        mesh,
        IOobject::READ_IF_PRESENT,
        IOobject::AUTO_WRITE
    ),
    k_dis*Xc
);

[…]
// * * * * * * * * * * * * * * * * * * * * * * * * * * * * * * * * * * * * //
```

The kinetic parameters considered by the solver are described in **Table 4.2**.

Table 4.2: *Biological parameters at ADM1Foam.*

Parameter	**Units *ADM1Foam***
kdis	1/s
k_hyd_ch	1/s
k_hyd_pr	1/s
k_hyd_li	1/s
km_su	kmolSsu/kmolCxfer·s
Ks_su	kmolSsu/ m^3
km_aa	kmolCsaa/kmolCxaa·s
Ks_aa	kmolCsaa/ m^3
km_fa	kmolCsfa/kmolCxfa·s
Ks_fa	kmolCsfa/ m^3
km_va	kmolSva/kmolCxc4·s
Ks_va	kmolSva/ m^3
km_bu	kmolSbu/kmolCxc4·s
Ks_bu	kmolSbu/ m^3
km_pro	kmolSpro/kmolCxpro·s
Ks_pro	kmolSpro/ m^3
km_ac	kmolSac/kmolCxac·s
Ks_ac	kmolSac/ m^3
km_h2	kmolSs2/kmolCxs2·s
Ks_h2	kmolSh2/ m^3
Ks_IN	kmolSin/ m^3
Ki_h2_fa	kmolSh2/ m^3
Ki_h2_c4	kmolSh2/ m^3
Ki_h2_pro	kmolSh2/ m^3
Ki_nh3	kmolSnh3/ m^3
k_dec_Xsu	1/s
k_dec_Xaa	1/s
k_dec_Xfa	1/s
k_dec_Xc4	1/s
k_dec_Xpro	1/s
k_dec_Xac	1/s
k_dec_Xh2	1/s
k_hyd_Xd	1/s
pHll_acet_acid	[]
pHul_acet_acid	[]
pHll_ac	[]
pHul_ac	[]
pHll_H2	[]
pHul_H2	[]
Ks_co2	kmol-Sco2/ m^3

- createADM1Variables.H: This creates all ADM1 state variables and internal fields to solve the pH and gas rates in the same way as the "rates" fields have been created in `"createFields.H"`.
- pHCalculation.H: This calculates the pH of each cell before solving the ADM1 state variables transport equation as described in Volcke et al., (2005) applying Eqs. 4.3 to 4.5. Additionally, the inhibition indexes are also calculated and will be used in the processes rates.
- rates.H: This calculates the processes rates before solving the ADM1 state variables transport equation. An example of the first and fifth process rates is as follows:

```
//Desintegration of Xc
r1=k_dis*Xc;

[…]
//Ssu Consumption
r5=k_m_su*(Ssu/(k_s_su+Ssu))*Xsu*((Sin/(k_s_IN+Sin))*Iph_aa);

[…]
// * * * * * * * * * * * * * * * * * * * * * * * * * * * * * * * * * * * * //
```

- GasModel.H: in this file the transfer rates of hydrogen, methane and carbon dioxide from liquid to gas are solved.

```
//////////////////////Gas Model////////////////////////////////
  Info<< "Solve Gas Model"<< endl;

  //Sh2 gas transfer
  rT8=kLa*(Sh2-K_H_h2*pgas_h2);

  //Sch4 gas transfer
  rT9=kLa*(Sch4-K_H_ch4*pgas_ch4);

  //Sco2 gas transfer
  rT10=kLa2*((Sic-Shco3Neg)-K_H_co2*pgas_co2);
// * * * * * * * * * * * * * * * * * * * * * * * * * * * * * * * * * * * * //
```

4.3.2. Input files

An OpenFOAM CFD model always has a "system" folder, a "constant" folder and an initial time folder.

In the "system" folder, the files and content that are compulsory to solve the *ADM1Foam* are fvSchemes, fvSolution and controlDict. The other files are used in meshing, decomposing and hydrodynamics solution (see **Figure 4.4**a):

- fvSchemes: This sets the numerical schemes for the advection divergence

terms of the ADM1 state variables. An example with some ADM1 state variables is shown below:

```
// * * * * * * * * * * * * * * * * * * * * * * * * * * * * * * * * * * * * * //
ddtSchemes
{
    default          Euler;
}

gradSchemes
{
    default          Gauss linear;
}

divSchemes
{
    default          none;

    div(phi,ADM1Var)  Gauss multivariateSelection
    {
    Ssu       linearUpwind grad(Ssu);
    Saa       linearUpwind grad(Saa);
    Sfa       linearUpwind grad(Sfa);
    Sva       linearUpwind grad(Sva);
    Sbu       linearUpwind grad(Sbu);
    Spro      linearUpwind grad(Spro);
    Sac       linearUpwind grad(Sac);
    Sh2       linearUpwind grad(Sh2);
    Sch4      linearUpwind grad(Sch4);
[…]
    };
}
// * * * * * * * * * * * * * * * * * * * * * * * * * * * * * * * * * * * * * //
```

- fvSolution: The fvSolution dictionary sets the equation solvers, tolerances and algorithms to solve the ADM1 state variables. Below is an example of some ADM1 state variables:

```
solvers
{
    p
    {…}

    pFinal
    {…}

    "(U|k|epsilon)"
    {…}

    "(U|k|epsilon)Final"
    {…}

    Saa
    {
        solver          PBiCGStab;
        preconditioner  DILU;
        tolerance       1e-06;
```

```
        relTol          0;
    }

    Sh2
    {
        solver          PBiCGStab;
        preconditioner  DILU;
        tolerance       1e-09;
        relTol          0;
     }

    Sch4
    {
        solver          PBiCGStab;
        preconditioner  DILU;
        tolerance       1e-08;
        relTol          0;
     }

    Sgas_ch4
    {
        solver          PBiCGStab;
        preconditioner  DILU;
        tolerance       1e-06;
        relTol          0;
     }

    Xpro
    {
        solver          PBiCGStab;
        preconditioner  DILU;
        tolerance       1e-06;
        relTol          0;
     }
[…]

    pH
    {
        solver          PBiCGStab;
        preconditioner  DILU;
        tolerance       1e-06;
        relTol          0;
     }

}
```

The files and content that are compulsory in the "constant" folder to solve the *ADM1Foam* are (see **Figure 4.4**b):

- kineticParameters: the value of all kinetic parameters of the solver is set in this file in the SI units. An example of this file with some kinetic parameters is shown below:

```
// * * * * * * * * * * * * * * * * * * * * * * * * * * * * * * * * * * * * * //
k_dis           k_dis [0 0 -1 0 0 0 0]5.787e-6;
k_hyd_ch        k_hyd_ch [0 0 -1 0 0 0 0]0.000115741;
k_hyd_pr        k_hyd_pr [0 0 -1 0 0 0 0]0.000115741;
k_hyd_li        k_hyd_li [0 0 -1 0 0 0 0]0.000115741;
// * * * * * * * * * * * * * * * * * * * * * * * * * * * * * * * * * * * * * //
```

- diffusionProperties: in this short file the constants to calculate the diffusion term are set. The following code is a complete example:

```
// * * * * * * * * * * * * * * * * * * * * * * * * * * * * * * * * * * * * * //

DT              DT [0 2 -1 0 0 0 0] 1e-9;// Molecular diffusion
coefficient divided by the fluid density

Sct             Sct [0 0 0 0 0 0 0] 0.7;//Schmidt Number

// * * * * * * * * * * * * * * * * * * * * * * * * * * * * * * * * * * * * * //
```

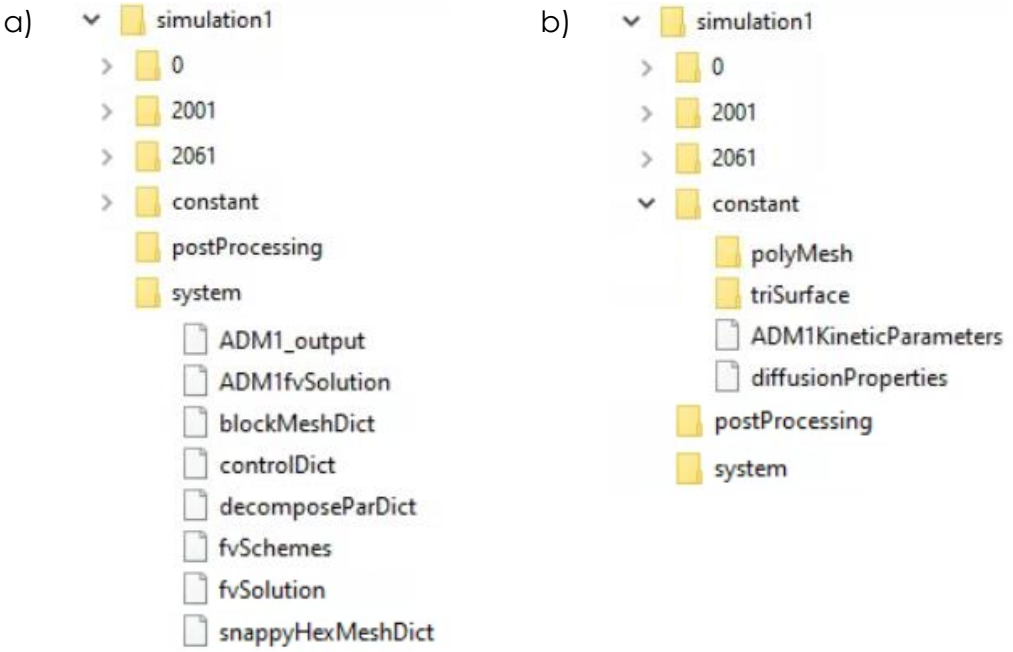

Figure 4.4: *Structure of folders "system" and "constant" to start the simulation with ADM1Foam.*

As the *ADM1Foam* does not solve hydrodynamics (U and nut), it is necessary to solve them before launching the solver. Thus, the first timestep of the solver is the one with hydrodynamic fields, in this case at time of 2001 seconds as depicted in **Figure 4.5**. Thus, the input folders and files at the first timestep folder are (see **Figure 4.5**):

Folders:

- Polymesh: contains the mesh data.
- Uniform: folder created when the solution of the ADM1Foam is done and contains timestep information and, if requested, function object data.

Files:

- nut, U: other variables, such as Co, nu, p, k and epsilon, may appear but U and nut are the input hydrodynamic variables needed to solve the transport equation of the ADM1 variables.

- 27 ADM1 variables: these files are needed to introduce the boundary conditions of each variable at the defined boundary patch and to define the initial domain values
- 5 Dummy variables: These variables are needed to solve the *ADM1Foam* so their file sets the initial conditions to solve the pH and inhibition. These dummy variables are listed in **Table 4.3**.

Table 4.3: *Dummy variables of ADM1Foam for different calculations needed initially.*

Variable	Name	Units
Shco3Neg	Bicarbonate	kmol C/ m^3
Iph_aa	Inhibition terms	-
Iph_ac		-
Iph_h2		-
Shlon	H+ ions	kmol/ m^3

Figure 4.5: *Folder structure to start the simulation with ADM1Foam.*

When the *ADM1Foam* is solved, a saved timestep looks like **Figure 4.6** so additional files are added when compared with the first timestep folder:

- The rates of all processes in *ADM1Foam* (r1-r20, rT8-rT10): a file for each process rate contains the results obtained in the solution of the solver.
- DTt: the value of the diffusion term (molecular + turbulent diffusion) is saved in this file.
- 10 intern pH files (E_Shion, SacNeg, SbuNeg, Shco3Neg, Shco3NegInt, ShIonNew, ShionOld, Snh4Pos, SproNeg, SvaNeg): These files are obtained during the pH loop solution and are internal variables that can be checked any time.
- 27 ADM1 variables
- 5 Dummy variables

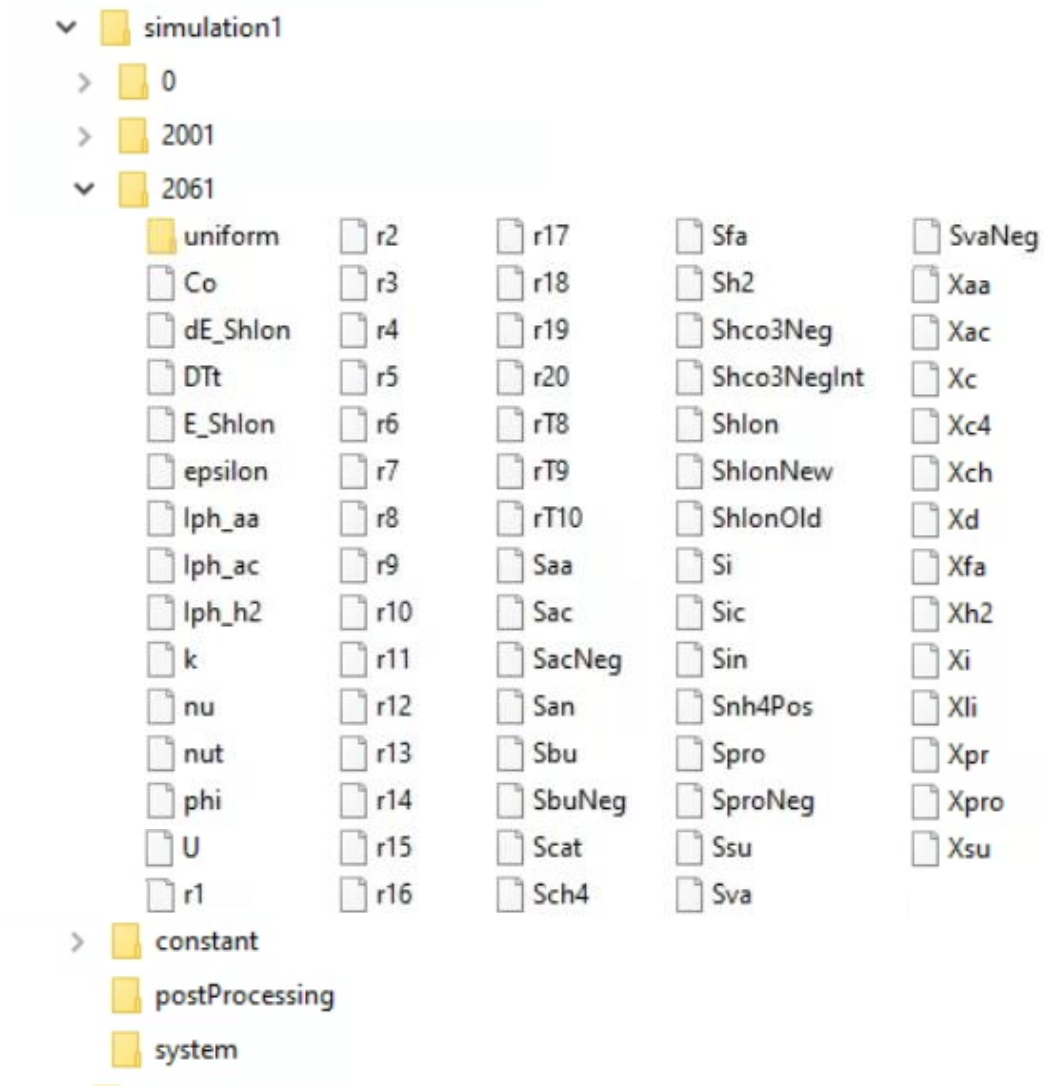

Figure 4.6: *Folder structure of a solved timestep.*

To sum up, **Figure 4.7** depicts a scheme of the solution process of *ADM1Foam;* the files that are read from the simulation case folder, the files of the solver that calculate it and the files that are generated in the simulation case folder.

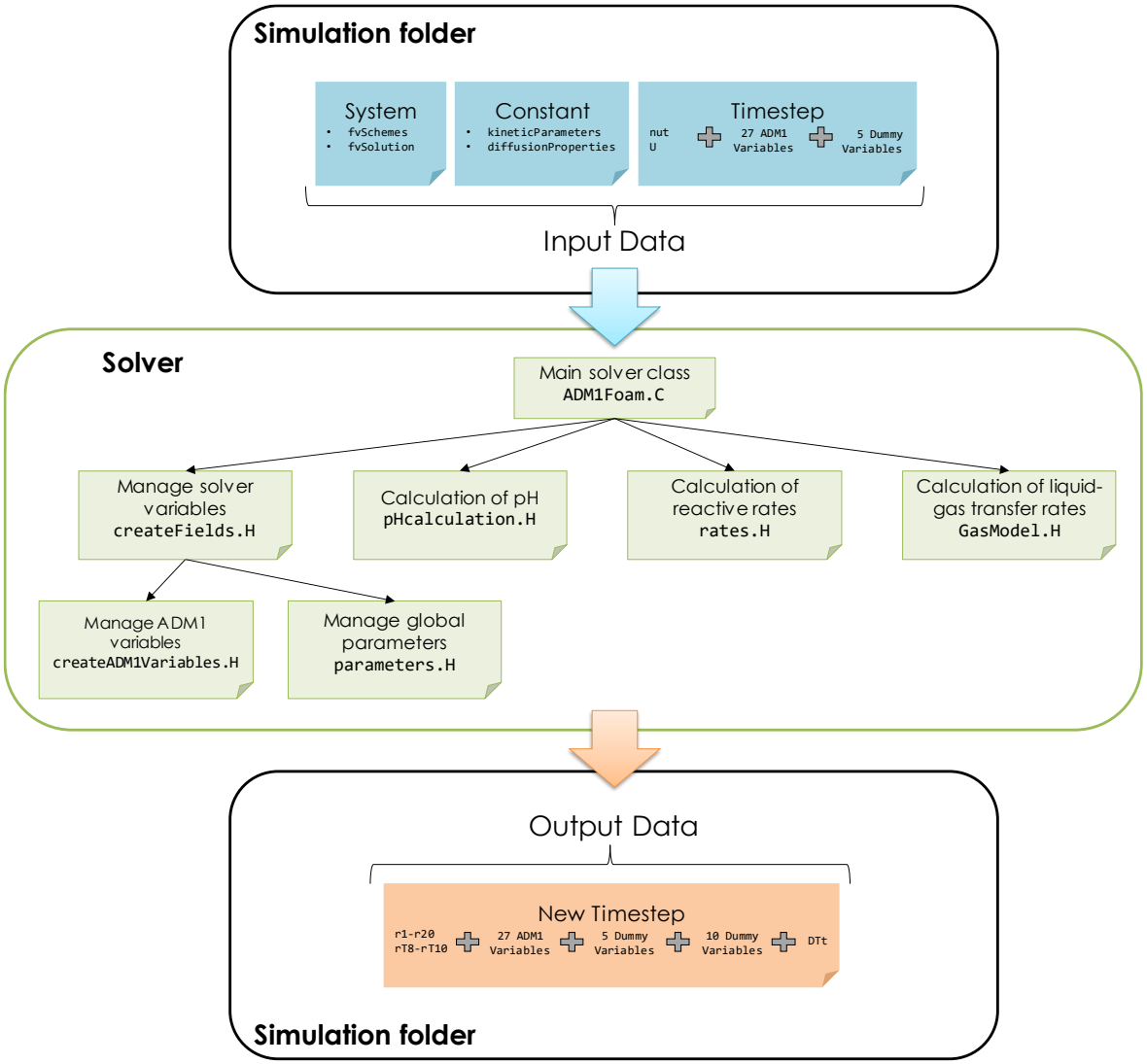

Figure 4.7: *Overview of ADM1Foam solution.*

4.4. MATERIALS AND METHODS

In order to calibrate and validate the implementation of the ADM1 model at the *ADM1Foam*, experimental values and 0D model results from a lab-scale setup were used. The experimental lab-scale setup is described in Section 4.4.1 and further details of the CFD modelling carried out to model this setup are defined in Section 4.4.2.

4.4.1. Lab scale setup description

Aiming to validate the new CFD-ADM1 solver, the experimental setup described in Zaher, (2005) was chosen. This lab-scale setup was also used in Patón and Rodríguez, (2019) to test a standard ADM1 model and two biokinetic models by means of a 0D framework. Thus, the availability of experimental data and a 0D model validated with it, was the reason for choosing this lab-scale setup.

The experimental setup was a lab-scale 2L liquid volume reactor to treat alcohol distillery wastewater (see **Figure 4.8**a). The setup had a thermostatic jacket to fix the temperature at 37°C and a Rushton turbine working at 200 rpm. The initial concentration of the setup was 6 g VSS/L and the total solids concentration of the concentrated wastewater was 1.7 g/L. The influent flow, pH and temperature were monitored online.

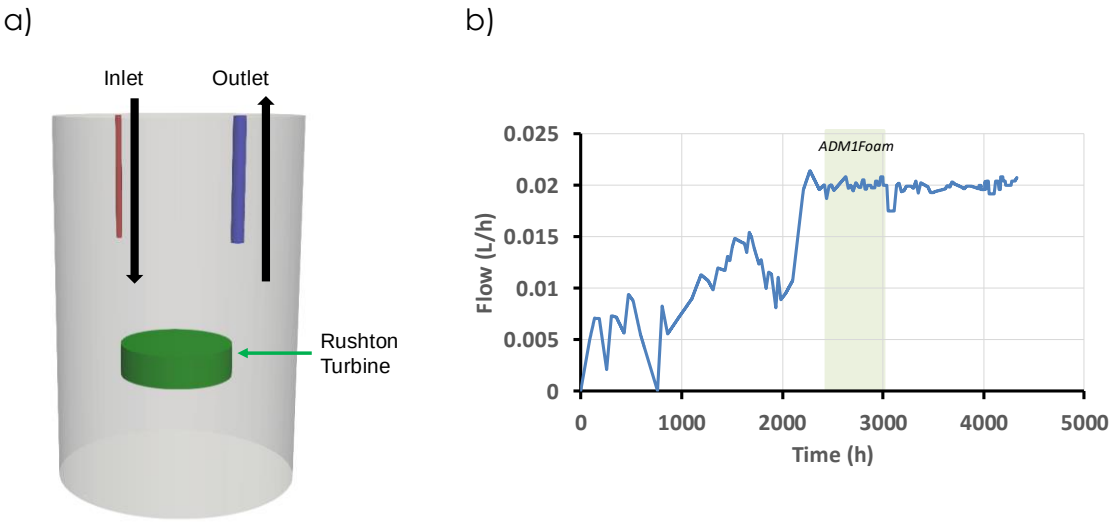

Figure 4.8: *a) 3D model of the lab-scale setup, b) influent flow at the lab-scale setup.*

4.4.2. 0D-ADM1 modelling

The lab-scale setup was further modelled in Patón and Rodríguez, (2019) by means of a 0D Matlab-Excel (Simulink) framework described in Rodríguez et al., (2009). As explained before, three different 0D models were modelled in Patón and Rodríguez, (2019) one of them being a standard ADM1. The 0D model assumes CSTR behaviour and applies a complete ADM1 with pH calculation (hereafter referred to as 0D-model or 0D simulation). Furthermore, this model was validated with experimental values from Zaher, (2005) lab-scale setup. Accordingly, this validated 0D standard ADM1 model was used in this study to validate *ADM1Foam* performance, which is extensively detailed in the following section.

4.4.3. CFD Modelling

The CFD simulations carried out had two parts: the calculation of the Hydrodynamics and the *ADM1Foam* solution. Furthermore, the lab-scale setup was modelled under two different mixing intensities so that two different scenarios were obtained (see a scheme of the different simulations in **Figure 4.9**):

- LS-200: the lab-scale setup was simulated at 200 rpm, which is the original mixing intensity to validate *ADM1Foam*.
- LS-20: this was a theoretical scenario at 20 rpm to test the capabilities of the new solver with different mixing intensities.

The numerical simulations were solved via parallel computing in two different pieces of equipment. One the one hand, the hydrodynamic simulations were solved using one node of a cluster with AMD Opteron ™ Processor 6274 (maximum 32 cores at 2.2 GHz) and 98.2Gb RAM. On the other hand, the *ADM1Foam* modelling was performed using 4 nodes of Tirant 3 supercomputer at the Universitat de València (UV). Each node in this facility is equipped with 2 Intel Xeon SandyBridge E5-2670 (8 cores at 2,6 GHz each) for a total of 16 cores and 32 GB RAM DDR3.

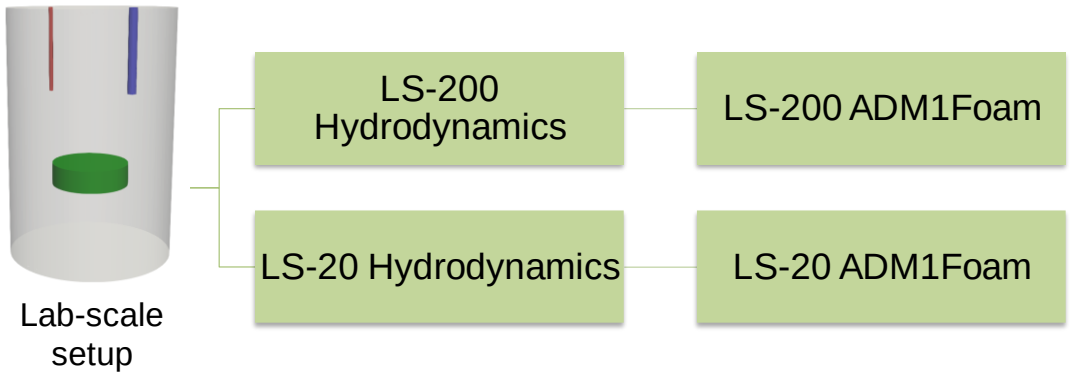

Figure 4.9: *Overview of the CFD simulations.*

4.4.3.1. Geometry and Meshing

A 3D geometry of the setup was reproduced in detail by means of a commercial geometry code. Then, the *snappyHexMesh* tool in OpenFOAM was used for meshing three grids to assess the grid convergence.

The grid convergence study proposed in Tanaka, (2014) and Tanaka et al., (2016) was used (see Section 2.5.1.1 for the description of the methodology) so that three meshes were developed and their hydrodynamics were solved. The grid convergence studies are always calculated by means of area-weighted average velocities in different planes located in the CFD model, but since this model has small dimensions, volume-weighted average velocities were used instead. On this basis, **Figure 4.10** shows the volumes for calculating the weighted average velocities.

Table 4.4 shows the cell size, total cells and the volume weighted average velocities of each mesh used on the grid convergence study. The GCI_{21} was lower than 1% in 3 out of 5 of the selected volumes (see **Table 4.5**) so mesh 2 was chosen for *ADM1Foam* calculations.

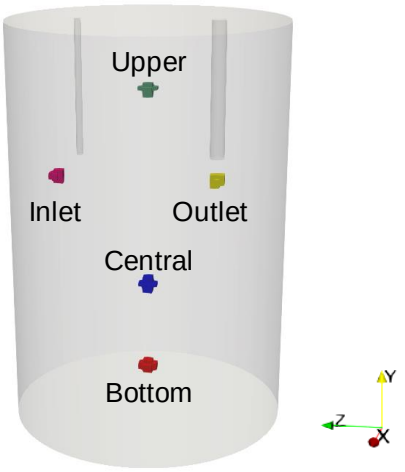

Figure 4.10: *Position of the volumes used in the grid convergence study.*

Table 4.4: *Volume-weighted average velocities at the volumes shown in* ***Figure 4.10****.*

	Cell size (mm)	Number of nodes	Central Sphere	Bottom Sphere	Upper Sphere	Inlet Sphere	Outlet Sphere
M3	2	371450	0.0071	0.0078	0.012	0.033	0.032
M2	1	686104	0.007	0.00702	0.0117	0.031	0.029
M1	0.8	1277346	0.0069	0.007	0.0116	0.030	0.028

Table 4.5: *GCI parameters and results.*

	Central	Bottom	Upper	Inlet	Outlet
ε_{32}	0.00013	0.00082	0.00058	0.00186	0.00256
ε_{21}	0.00004	0.00001	0.00011	0.00089	0.00102
p_j	5.48	21.72	8.23	3.63	4.54
Fs	3	3	3	3	3
GCI_{32} (%)	2.68	0.44	3.44	16.64	17.45
GCI_{21} (%)	0.86	0.005	0.63	8.06	7.04

4.4.3.2. Setup

The inlet and outlet surfaces were set as inflow and outflow patches, respectively, and remaining surfaces were set as wall (see **Table 4.6**). The liquid phase was set as a Newtonian fluid with water viscosity (0.000001 m^2/s) since the average total solids concentration of the setup was less than 2% total solids (Sadino-Riquelme et al., 2018).

Table 4.6: *Boundary conditions.*

Patch	Inlet	Outlet	Wall
U	flowRateInletVelocity 5.52e-09 (0.02 L/h)	flowRateInletVelocity -5.52e-09 (0.02 L/h)	noSlip
p	zeroGradient	fixedValue uniform 0	zeroGradient
k	fixedValue uniform 2.29e-11	zeroGradient	kqRWallFunction uniform 1e-09
epsilon	fixedValue uniform 1e-14	zeroGradient	epsilonWallFunction Cmu 0.09 kappa 0.41 E 9.8 value 0 lowReCorrection 0
nut	calculated uniform 0	calculated uniform 0	nutkWallFunction Cmu 0.09 kappa 0.41 E 9.8 uniform 0
nuTilda	fixedValue uniform 0	fixedValue uniform 0	zeroGradient

The momentum source of the Rushton turbine, $\underline{F_{rotor}}$ (N), was introduced as a cylindrical volume with the following equation:

$$\underline{F_{rotor}} = \int_0^{2\pi} \int_0^{L} \int_0^{R} N_{blades} \frac{1}{4\pi} \eta \, f \, \rho \, C_D \, \omega^2 \, r^2 \, dr \, dz \, d\theta \qquad 4.6$$

where L, is the turbine length; R, is the rotor blade radius; N_{blades}, is the number of blades; η, is the turbine efficiency; f, is the filling factor of the blades ($f \sim 0.4$); ρ, is the fluid density; C_D, is the drag coefficient of a long flat plate at high Reynolds numbers ($C_D \sim 1$); ω, is the angular speed (rad s^{-1}); r, is the turbine radius.

4.4.3.3. Solver and convergence

The hydrodynamics of both scenarios were solved by means of the *pimpleFoam* solver, which is a single-phase transient solver with variable timestep size and a Courant Number lower than 50. The solver was run until different criteria were met:

1. At least 600 seconds of simulation time were modelled.
2. The solution imbalances in the conservation equations (conservation of

mass, momentum, energy) were less than 0.001% for all the equations

3. The velocity magnitude at several points located in the model were under 5% of the final value in the last 50 iterations.

As previously explained in chapter 2, tracer studies are a simple way to verify the hydrodynamic performance of a CFD model. Traditionally, the tracer study is done experimentally and compared with ideal hydraulic behaviours such as CSTR or tanks-in-series. Nevertheless, the tracer test can be performed "virtually" in the CFD modelling to find out hydrodynamic defects and adjust to ideal hydraulic behaviours. In this case, the tracer test was not done experimentally so its tracer test was done virtually introducing a total mass tracer of 0.0552 g in 10 seconds by means of the *scalarTransportFoam* solver with turbulent dispersion and a Schmidt Number of 0.7.

The numerical schemes used in hydrodynamic and virtual tracer test modelling are described in **Table 4.7**.

4.4.3.4. ADM1Foam Modelling

Both lab-scale scenarios were simulated by means of *ADM1Foam* from the 2345th hour of experimental time up to one month. This time period was selected because of the stability of the influent flow rate at approximately 0.02 L/h, as this allowed a constant influent flow of 0.02 L/h to be maintained in the CFD model (see **Figure 4.8**b). Therefore, the hydrodynamics were fixed, i.e. steady-state, and the biochemical evolution between the 0D and 3D model could be compared. The numerical schemes used in these simulations are described in **Table 4.7**.

The 0D-simulation data was used as input data for the *ADM1Foam* due to limited experimental data. The influent data and effluent composition were used to define the influent boundary conditions and initial reactor composition of the *ADM1Foam*, (see G.i Lab-scale setup). Moreover, the biogas partial pressures obtained with the 0D-model were used to define the biogas fraction of the degassing terms. The biokinetic parameters used at the 0D simulation and at the *ADM1Foam* 3D-CFD model are depicted in Appendix G.i Lab-scale setup.

Table 4.7: *Numerical schemes for the CFD modelling.*

Simulation	Variable	Numerical scheme
Hydrodynamics	div(phi,U)	bounded Gauss linearUpwind grad(U)
	div(phi,k)	bounded Gauss upwind
	div(phi,epsilon)	bounded Gauss upwind;
	div(phi,R)	bounded Gauss upwind
	div(R)	Gauss linear
	div(phi,nuTilda)	bounded Gauss upwind
Tracer tests	ddt	Euler
	div((nuEff*dev2(T(grad(U)))))	Gauss linear
	div(phi,T)	Gauss upwind
ADM1Foam	ddt	Euler
	div(phi,ADM1 Variables)	Gauss linearUpwind grad(ADM1 Variable)

4.5. RESULTS

This section is devoted to showing the CFD modelling results of the lab-scale. First, a virtual tracer test was conducted in the CFD model to test its CSTR behaviour (Section 4.5.1). Then, the hydrodynamic behaviour of the lab-scale setup is introduced in Section 4.5.2. Once the hydrodynamic results have been presented, the assessment of the *ADM1Foam* performance begins, and its performance on the lab-scale setup serves to validate it and test its capabilities in the last section.

4.5.1. Virtual tracer test

The virtual tracer test was computed, and outlet tracer concentration over time was obtained. **Figure 4.11** depicts the tracer test results in the LS-200 model and compares it with an ideal CSTR model. These results showed a small and rapid short-circuiting at the beginning of the tracer curve, that accounted for 18.6% of the influent flow. The theoretical HRT of the lab-scale setup was 4.2 hours, but the virtual mean residence time was 6.2 hours, which stated the short-circuiting previously noticed.

Nevertheless, the LS-200 tracer curve agreed perfectly with the CSTR model, so the LS-200 could be approximated to CSTR hydraulic behaviour. Thus, *ADM1Foam* results could be compared with the results obtained in the 0D-model from Patón and Rodríguez, (2019) since the 0D-model considered CSTR performance.

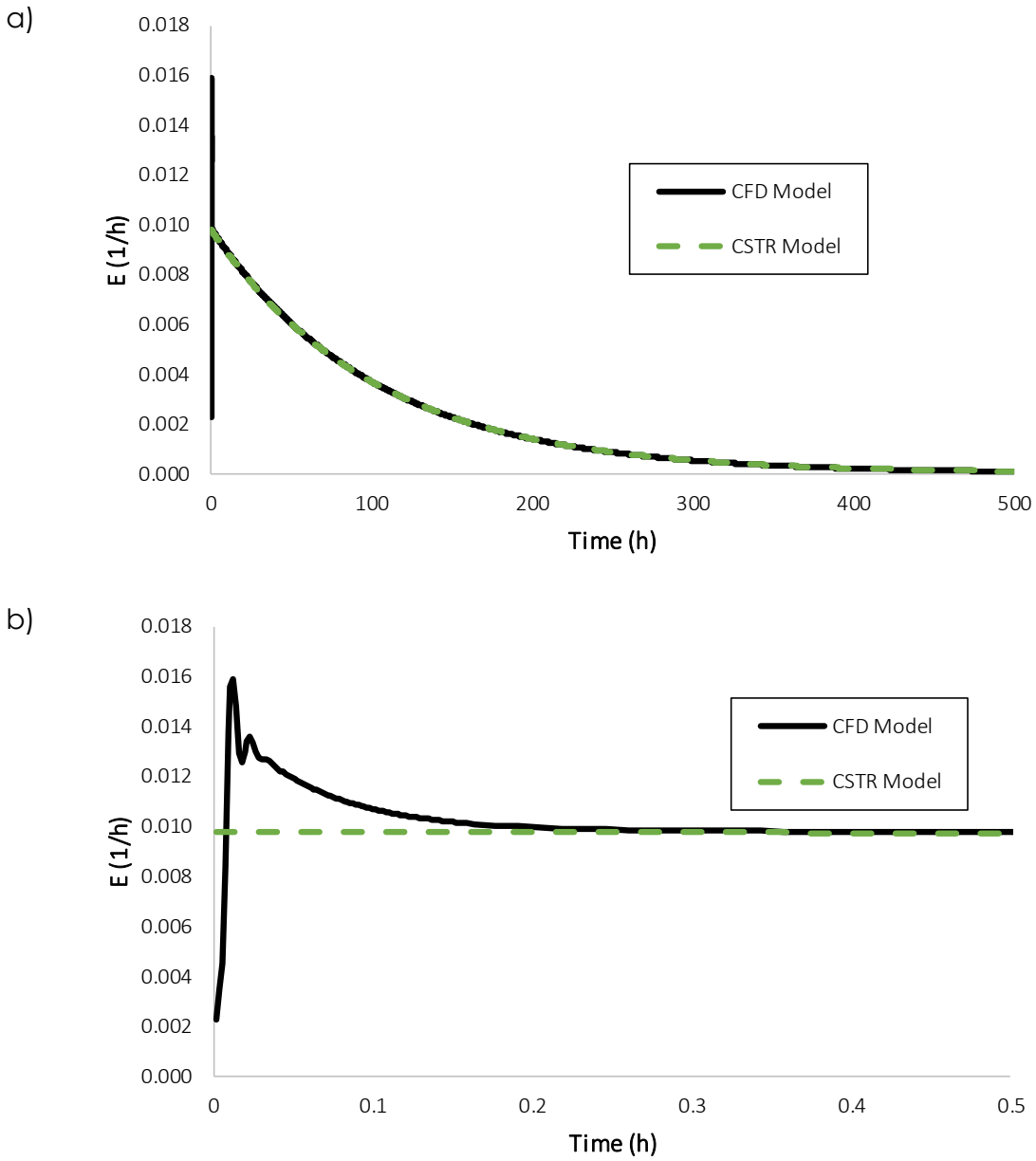

Figure 4.11: *Comparison of ideal-CSTR model and CFD model tracer test curves: a) long tracer test curve and b) detail of tracer test curve.*

4.5.2. Hydrodynamics analysis

CFD models are one of the best tools for a better knowledge of the mixing process inside bioreactors. Accordingly, the hydrodynamics of both scenarios (200 rpm and 20 rpm, LS-200 and LS-20 respectively) were studied and compared: **Table 4.8** described different velocity statistics in both scenarios, **Figure 4.12** depicts the velocity magnitude distribution in the radius of the setup at several heights, **Figure 4.13** the horizontal and vertical velocities and **Figure 4.14** the flow vectors from both scenarios.

Table 4.8: *Velocity statistics in the lab-scale setup.*

Case	Velocity Magnitude-Maximum (cm/s)	Velocity Magnitude-Minimum (cm/s)	Velocity X-Maximum (cm/s)	Velocity Y-Maximum (cm/s)	Velocity Z-Maximum (cm/s)
LS-200	5.4	0.017	5.1	1.1	2.3
LS-20	0.7	0.00002	0.5	0.3	0.4

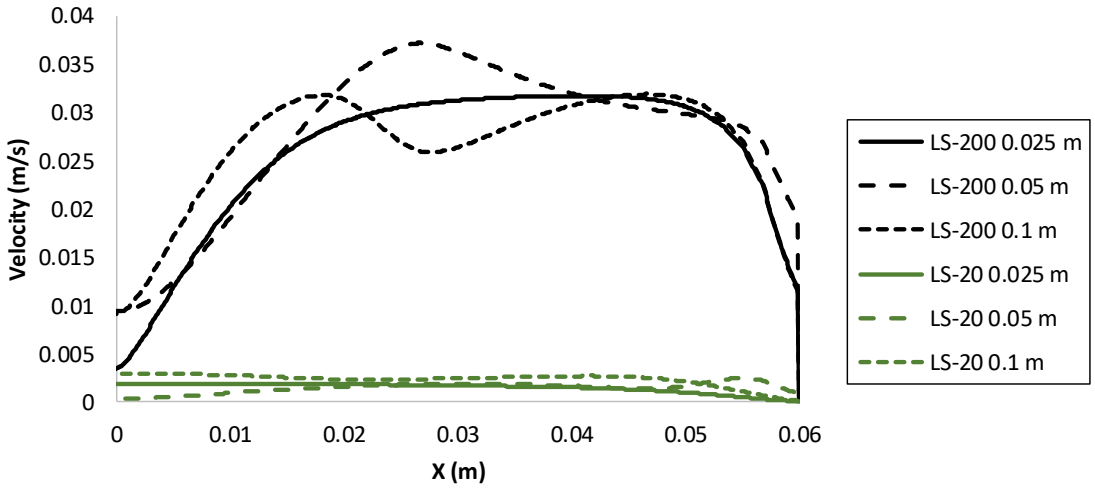

Figure 4.12: *Distribution of the velocity magnitude radially (from the centre of the reactor to the wall at different heights for both mixing regimes).*

The lab-scale setup had a Rushton turbine as the mixing device so the hydrodynamics were controlled by its momentum source. On the one hand, the intensity of the Rushton turbine momentum source was clearly shown in **Figure 4.12** and **Table 4.8**, where a clear difference was shown in the velocity field of both setups with different turbine intensity. The velocity magnitude was symmetrically distributed along the setup's diameter and in LS-20 was 10% of the one in LS-200 (see **Figure 4.12**).

On the other hand, the turbine provided a general clockwise movement (see **Figure 4.13**a and b and **Figure 4.14** a and b) so that the vertical speed (Y) was always lower than the velocity in X and Z (see the maximum velocities in **Table 4.8**). Secondly, there were two secondary vertical flows as a secondary outcome of the turbine's momentum source, depicted in **Figure 4.14**c. One of these flows was located under the turbine so that it went upwards in the centre and downwards in the walls of the tank. The second one was created in the upper part of the turbine and went upwards in the walls and downwards in the centre (see **Figure 4.13** c and d). The impact of these hydrodynamics on the anaerobic digestion performance will be assessed in the comparison of both

scenarios by means of the *ADM1Foam* results.

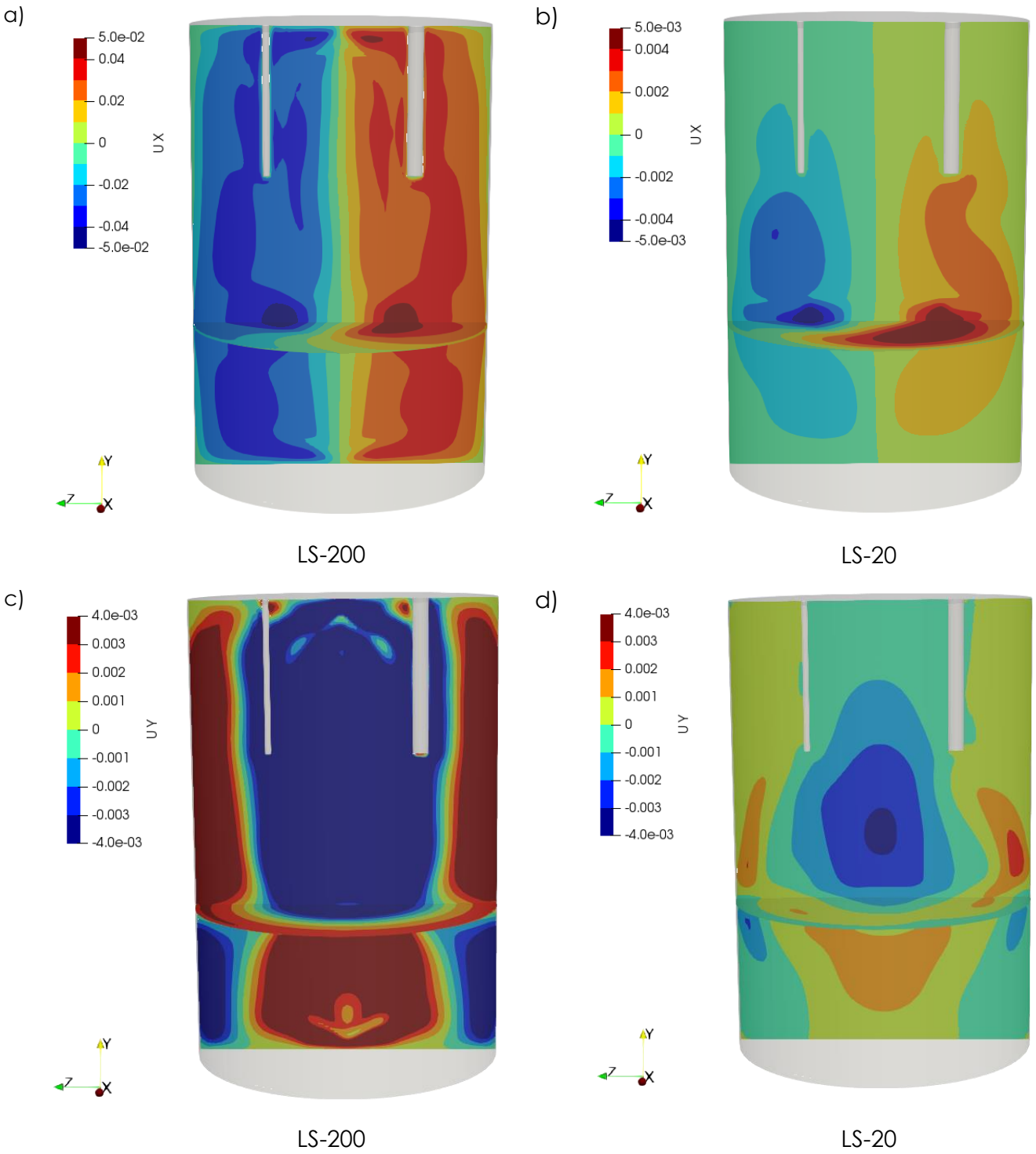

Figure 4.13: *Velocity contours at the lab scale a) and b) X Velocity; c) and d); Y Velocity. a) and c) LS-200 and b) and d) LS-20.*

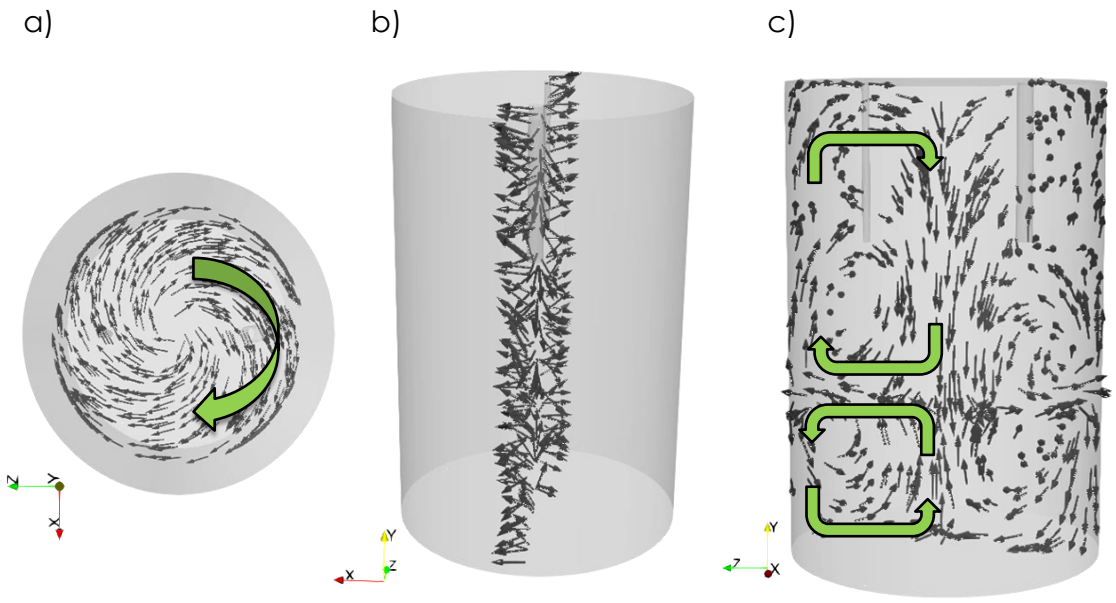

Figure 4.14: *a and b) Main clockwise flow and c) secondary convective cells) in the LS setup.*

4.5.3. ADM1 results

Aiming to validate *ADM1Foam*, the 3D-CFD model results were compared with those of the 0D-model results. The output of the 0D-model was a single value for each ADM1 state variable, representing the average concentration of this variable in a CSTR digester. However, the 3D-CFD model calculated a value for each single cell.

Looking at the 3D-CFD model concentrations, it was noticeable that their concentrations experienced slight variations of concentration between cells (see **Figure 4.15**), the biggest source of discrepancy being the cells near the inlet. These constant values of the ADM1 state variables stemmed from the global mixing produced by the Rushton turbine, i.e. the state variables were diluted by hydrodynamic phenomena and could be compared with a CSTR framework model. This issue will be addressed in depth in Section 4.5.4. Indeed, due to great homogeneity of the ADM1's state variables concentration, the volume average concentration was used for comparison with the 0D-model and the experimental values.

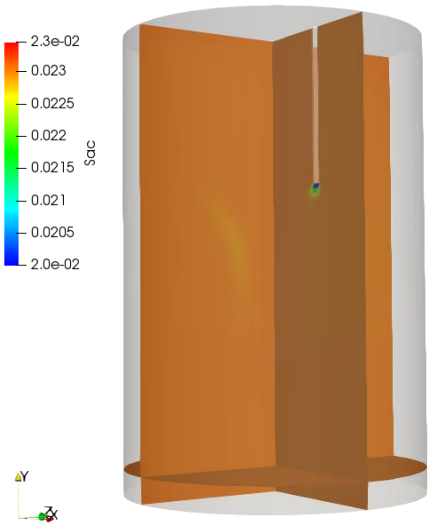

Figure 4.15: *Acetate concentration (kmol/ m³) in the LS-200 setup.*

Figure 4.16 and **Figure 4.17** depict the experimental results from Zaher, (2005), 0D-model from Patón and Rodríguez, (2019), and the average volume concentration from the 3D-CFD model for different ADM1 state variables. **Figure 4.16** represents the time evolution of the main products of the acidogenesis and acetogenesis processes: Firstly, butyric and valerate are shown in **Figure 4.16**a: both models mostly agreed on the prediction of the concentration of both variables with minor disagreement from the peak concentration at the 3000th hour. Secondly, propionate is depicted in **Figure 4.16**b, where both models widely met and showed the experimental trends of the acid concentration. Then, the acetate concentration is depicted in **Figure 4.16**c. As with propionate, the experimental trends were capture by both models but, in this state variable, both models anticipate an increase in the concentration of acetate at the 2800th hour. The 3D-model anticipated the acetate increase around the 2550th hour, which was earlier than the 0D-model (2600th hour) and the experimental (2800th hour).

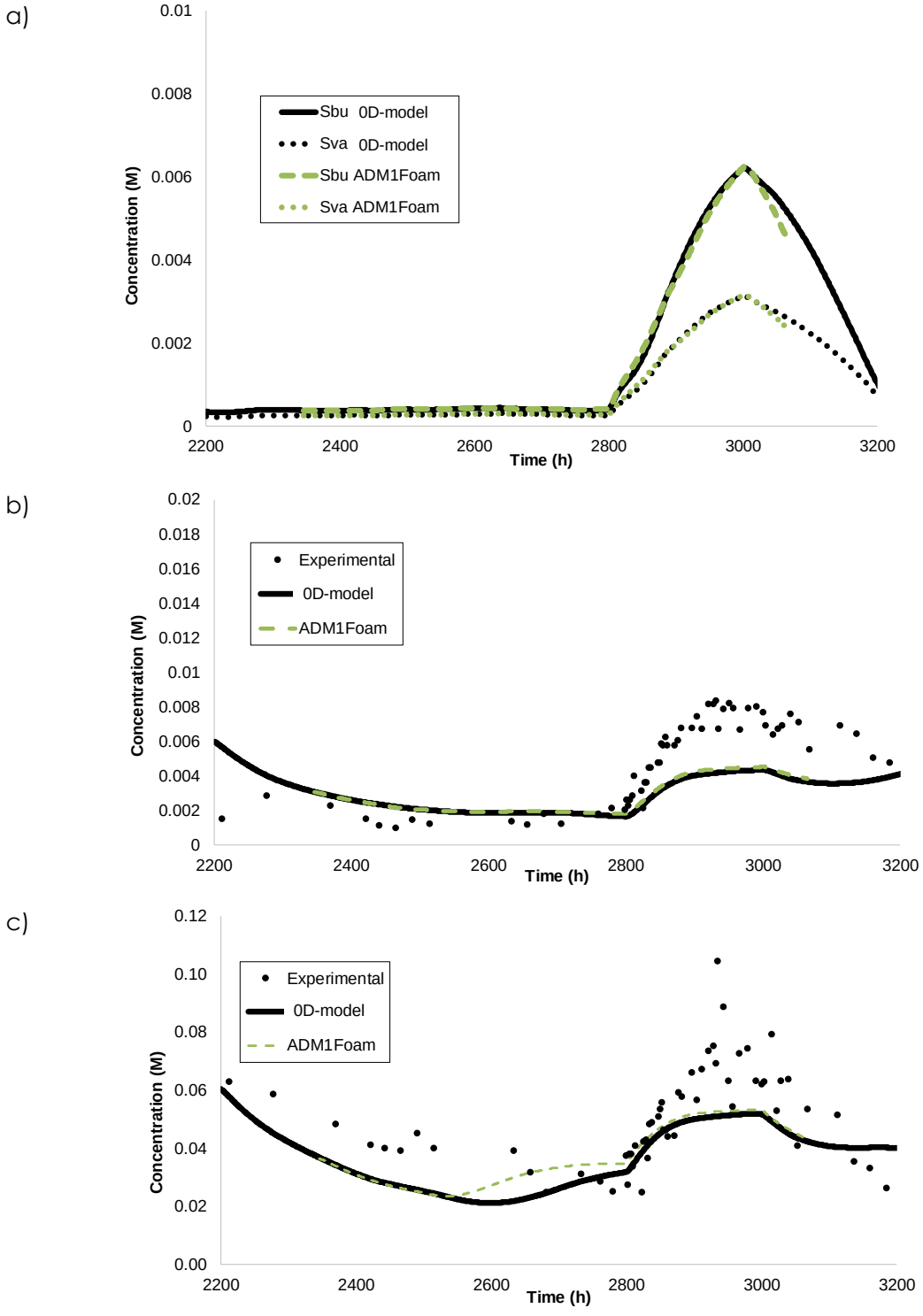

Figure 4.16: *Volume average concentration at LS-200 setup of a) butyrate (Sbu) and valerate (Sva), b) propionate (Spro) and c) acetate (Sac). Units: kmol/m^3.*

As explained above, *ADM1Foam* needed the partial pressure values of the biogas. With this, the concentration in the liquid phase of hydrogen, methane and carbon dioxide was calculated by the *ADM1Foam* in the entire CFD model.

Figure 4.17 shows the time evolution of hydrogen and methane concentration in the liquid phase in both models. Both models substantially agreed on the concentration of both state variables which was particularly noteworthy in the case of hydrogen due to the stiffness of its calculation.

To sum up, the 3D-CFD model results agreed better with those of 0D-models than with the experimental data. Nonetheless, this fact ensured that *ADM1Foam* was correctly implemented and thereby validated. These stated that the *ADM1Foam* was able to reproduce CSTR 0D-models and can be used as an additional tool for the anaerobic digestion control and simulation.

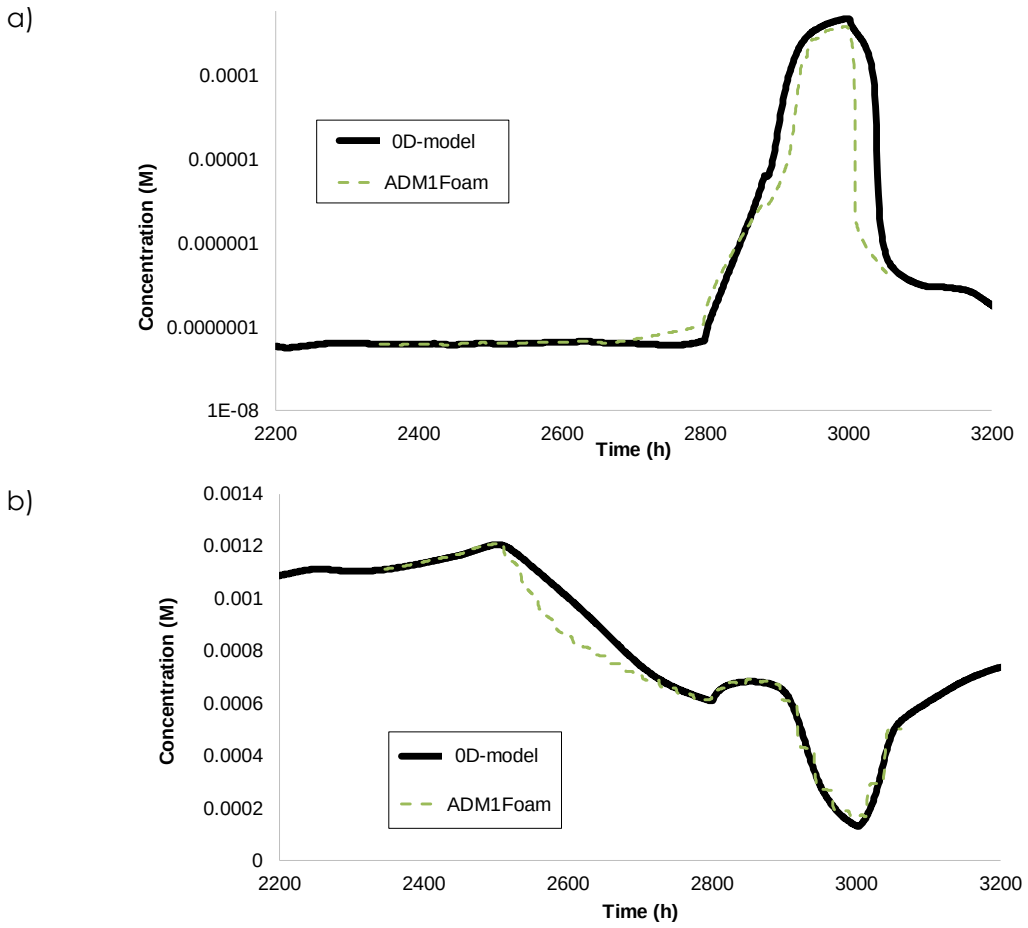

Figure 4.17: *Volume average concentration at the LS-200 setup of a) hydrogen and b) methane.*

4.5.4. Mixing impact on anaerobic digestion performance

Another theoretical lab-scale scenario was the LS-20, in which the Rushton Turbine had 20 rpm velocity. *ADM1Foam* was applied in this case as in the LS-200 and their results were compared (see Appendix H ADM1 state variables). **Figure 4.18** and **Figure 4.19** depict some contours of ADM1 state variables and processes rate in both mixing scenarios and **Figure 4.20** depicts the relative difference between both scenarios for different acids.

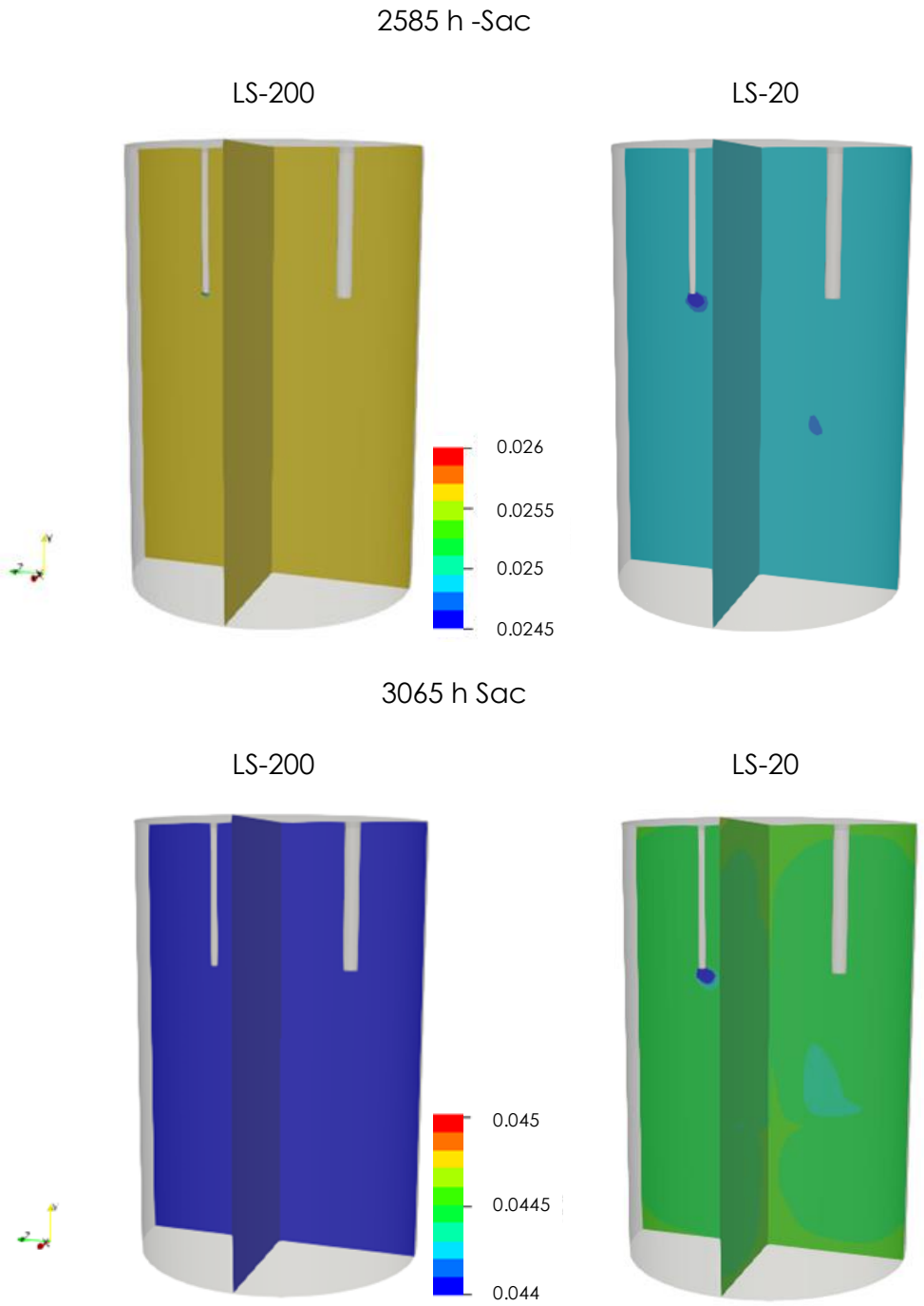

Figure 4.18: *Contours of Sac at different times in LS-200 and LS-20.*

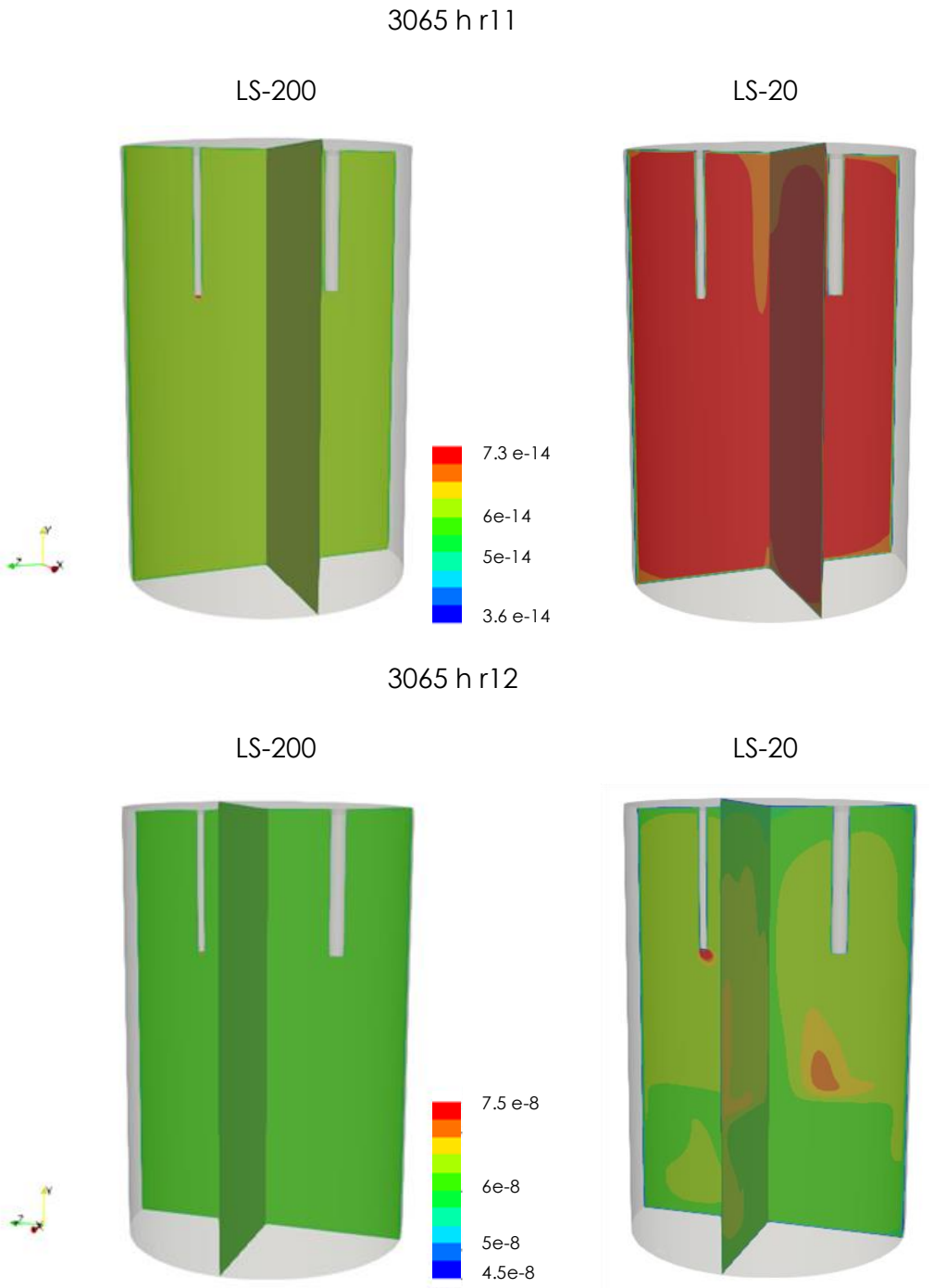

Figure 4.19: *Contours of different processes rate in LS-200 and LS-20.*

On the one hand, similarly to what was observed in the LS-200 scenario in **Figure 4.15**, no local variations in ADM1 concentrations were observed in the LS-20 scenario in **Figure 4.18** either. On the contrary, the concentration evolved temporally with an overall concentration in the whole CFD model in both scenarios (see **Figure 4.18**) and only slightly local concentration gradients were observed in LS-20. The reason for this homogeneity could stem from the hydrodynamics or the source terms. Nevertheless, as shown in **Figure 4.19**, the

magnitude and gradient of these rates were several orders lower than the concentration and very homogeneous in the case of the LS-200 scenario. Therefore, homogeneity could not be due to the source terms, but was due to hydrodynamic mixing phenomena that diluted the influent with the entire contents of the setup.

On the other hand, the impact of the Rushton turbine speed on the performance of the anaerobic digestion process can be evaluated with data from **Figure 4.20**. Based on the results, it was stated that a mixing reduction from LS-200 to LS-20 may generally lead to a decrease of the acids concentration. The maximum reduction was produced in propionate whose concentration would be reduced by about 10% around the 2800th hour. Butyrate and valerate experienced the same behaviour as they were degraded by the same bacteria group, i.e. X_{C4}, valerate and butyrate degraders. Accordingly, they had almost the same concentration reduction at the beginning and a slight disagreement around the 2850th hour. The acetate concentration experienced a reduction of less than 3% around the 2600th hour, then recovered the same concentration as in the LS-200 setup and finished with a slightly greater concentration.

The differences in performance between the two scenarios were not very noticeable, so further experimental and modelling research would be necessary to be able to relate mixing intensity to anaerobic digestion performance. Some aspects to be studied would be the variability of biokinetic parameters and biogas production with different mixing degrees. However, it is widely known that less mixing could avoid a good homogenisation of the tank and thus the primary products could not contact their degraders so the production of the remaining secondary products would be generally hampered.

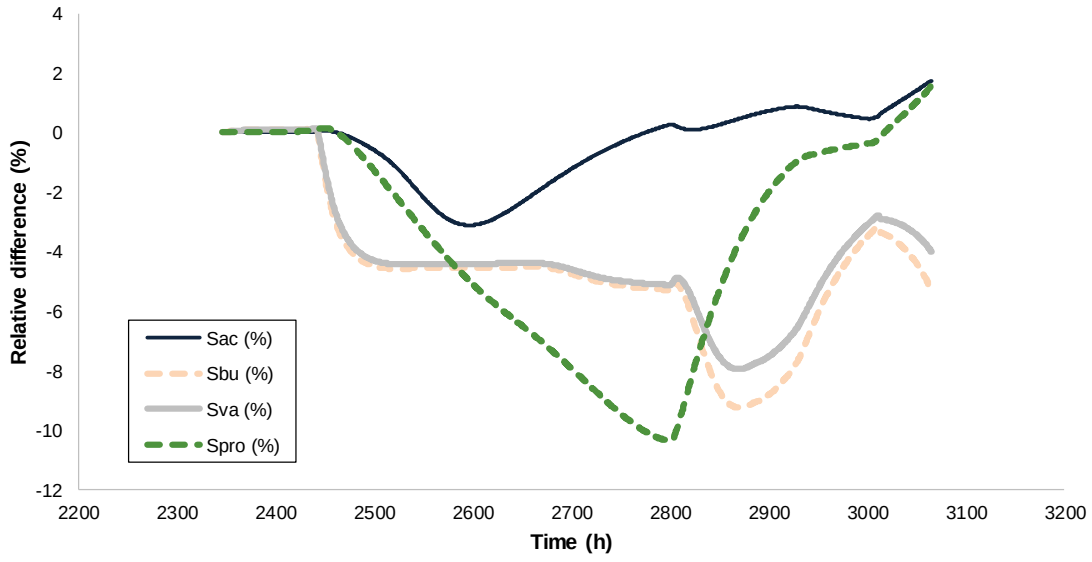

Figure 4.20: *Relative difference between 200 rpm and 20 rpm.*

4.6. CONCLUSIONS

A new CFD single-phase solver with ADM1, *ADM1Foam,* has been developed with the inclusion of the pH calculation and simplified liquid-gas transfer equations. All ADM1 state variables and process rates have been included in the solver considering algebraic algorithms to solve the pH calculation.

ADM1Foam has been successfully tested in a real 2L lab-scale setup found in literature (Zaher, 2005) and one month of simulation was conducted successfully. To check that the ADM model was well implemented in the *ADM1Foam*, the biochemical evolution was compared with the 0D-CSTR model of Patón and Rodríguez, (2019). The results of the *ADM1Foam* agreed with the lab-scale experimental data and 0D-model results, so that the implementation of all equations and pH calculations was confirmed. This fact enabled the validation of the *ADM1Foam* solver to accurately reproduce real setups in transient simulations.

Then, another mixing scenario of the lab-scale setup was also modelled to see the impact of less mixing intensity in anaerobic digestion performance. In conclusion, lower acid production was observed with lower mixing, but further experimental research would be needed to confirm this conclusion firmly. Nonetheless, the modelling methodology followed in this study proved to be correct for the study of performance in different mixing scenarios in transient conditions.

The *ADM1Foam* solver has made it possible to observe small local variations in concentrations and processes rates that are imperceptible to 0D models, so the resolution of the 3D-CFD model is good and sensitive to mixing changes. In fact, as process rates or source terms were slower than hydrodynamic phenomena, the application of this solver would make more sense than 0D-models in full-scale setups where hydrodynamics are key to homogenise their content.

To sum up, *ADM1Foam* can provide some insights into how mixing can affect anaerobic treatment in different scenarios. The inclusion of ADM1 in a CFD code can be a powerful tool in different applications in anaerobic conditions e.g. anaerobic digestion, codigestion and anaerobic wastewater treatment. Indeed, it could be used as a base model for the development of other models including pH calculations such as water chlorination, the SHARON process and the production of alcoholic beverages. In fact, the *ADM1Foam* solver can be used as a base for a two-phase CFD solver that takes into account liquid-gas transfer.

5. TOWARDS ADM1 INTO CFD (II): FULL-SCALE APPLICATION AND MIXING OUTLOOK

In this chapter, the *ADM1Foam* solver developed in the previous chapter has been applied in the full-scale setup in three different mixing scenarios. The motivation of this work was to test that the solver can reproduce the anaerobic digestion process in full-scale setups where local mixing plays an important role in the homogeneity. Thus, the removal efficiency and process rates have been assessed to find the most efficient mixing scenario from a biological process perspective. Indeed, the study aims to expand the knowledge about the link between mixing and the anaerobic digestion process: whether mixing or homogeneity favours anaerobic digestion, what is the transport or biological phenomenon causing this mixing and how much.

Abstract: The *ADM1Foam* solver has been applied in a full-scale setup at three different scenarios with different mixing intensities (100%, 50% and 0% recirculation flow) aiming to test the validity of the solver in full-scale setups. *ADM1Foam* results have been compared with a 0D-Matlab-Excel framework (Patón and Rodríguez, 2019) in transient state. The large amount of data produced was assessed by means of different parameters, including the removal efficiency and processes' rates in the different scenarios. The different mixing regimes led to differences in the local mixing that formed some inhomogeneous concentration patterns. This local mixing stemmed different anaerobic digestion performance between the different mixing regimes, so FS-A0 was found to be less productive. The characteristic time of several phenomena has been calculated to depict which phenomenon drove the homogenisation of the anaerobic digester. Thus, the hydrodynamic phenomena were found as responsible for the global and local mixing. Overall, the solver deployed the FS-A50 scenario as the most efficient scenario in the full-scale setup, although intermittent mixing with high intensity mixing scenarios should be applied to avoid the appearance of dead volume.

Keywords: CFD; ADM1; Anaerobic Digestion; biological model; local mixing; homogeneity.

5.1. INTRODUCTION

As outlined in the previous chapter, mathematical modelling and numerical simulation is being extended to anaerobic processes where mixing plays a key role. In this context, CFD modelling, coupled with biokinetics can be a troubleshooting tool to study the link between mixing intensity or mixing regimes and anaerobic performance.

Regarding mixing intensity, high mixing intensities and large shear stress has been pointed out to be detrimental to biogas production due to the possibility of floc breakage (Kaparaju et al., 2008; Kim et al., 2017; Lindmark et al., 2014a; Singh et al., 2019). Additionally, it has been argued that intensive mixing is unfavourable in the start-up period of lab-scale anaerobic digesters and, accordingly, a waste of energy in this period (Hoffmann et al., 2008). For example, Sindall et al., (2013) proposed a velocity gradient threshold between 7.2 and 9.7 s^{-1} to avoid the breakage of microbial flocs.

On the other hand, the ideal CSTR configuration has been criticised so that intermittent mixing has been noted as a clear opportunity to reduce energy demands, as one of the main functions of anaerobic digestion is to return energy in the form of biogas to the WRRF. It has been shown that intermittent mixing is able to maintain biogas production when compared to CSTR, without compromising biogas production (Kariyama et al., 2018; Lindmark et al., 2014b; Singh et al., 2019; Zhai et al., 2018) or generating even higher biogas production (Lindmark et al., 2014b). In addition, this type of mixing benefits the tasks related to equipment maintenance and reduces its running hours.

Experimental data have mostly been carried out on a laboratory scale, where several mixing regimes have been investigated comparatively. Thus, low mixing intensity or discontinuous mixing can be beneficial during the initial phase to allow methanogenic biomass growth and ease process instability problems (Lindmark et al., 2014b). Nonetheless, there is a full-scale reference, in which the absence of mixing for 2h before feeding benefited the stability of the process and the start-up of the thermophilic process (55ºC) (Leite et al., 2017). Table 1 in Lindmark et al., (2014b) shows that intermittent mixing can provide process improvements (number 1 refers to improvement while 0 refers to a result worse than the baseline).

The most current research is aimed at relating mixing modes with the different stages of the anaerobic digestion process; since the mixing intensity and intermittent cycles could specifically favour some microorganisms and thus may facilitate several stages of the process. Hence, it is possible to promote and roughly identify areas in which, depending on the mixing degree, the different stages mentioned above are promoted or not (Wang et al., 2020). This supports previous hypotheses showing that excessive mixing in highly OLR systems can acidify the medium (Vavilin and Angelidaki, 2005) due to different spatial

phenomena in microscale mixing, related to local substrate-microbe interaction (Stroot et al., 2001). Conversely, minimal mixing can favour areas with a higher percentage of methanogens that can help prevent inhibition by excessive VFA production. This is of particular interest both for anaerobic digestion processes in a single tank, (with a wide range of mixing modes, intensities and co-substrate feed), and for those that are carried out in two-stages.

In summary, experimental research to date has shown that intensity of mixing and mixing duration have direct effects on biogas production (Lindmark et al., 2014b). Nevertheless, there is no common agreement on the intensity and periods of intermittent mixing in experimental results but, it is thought that an optimum intensity and mixing period exists for every single anaerobic digester (Kariyama et al., 2018; Lindmark et al., 2014a).

ADM1Foam solver was developed in the previous chapter coupling hydrodynamics and biokinetics of anaerobic digestion to address whether mixing really favours the anaerobic digestion process or not. In this chapter, this solver has been applied to the full-scale anaerobic digester described in chapter 3 to test its usability at this scale. In addition, three different mixing scenarios have been modelled in the full-scale digester with the biochemical solver: the base scenario (A100), the base scenario with 50% mixing (A50) and the base scenario without mixing (A0). Scenarios with less agitation have been simulated to compare their degradation and methanogenesis capacity. In this way, the scenario that produces the maximum biogas production with the lowest mixing was obtained and some insights on the impact of mixing on the performance of anaerobic digestion could be gained.

5.2. MATERIALS AND METHODS

The *ADM1Foam* solver has been applied to the full-scale setup studied in chapter 3 aiming to test if the solver is able to work in full-scale anaerobic digesters. It was simulated with three different mixing configurations: with fully internal recirculation flow (FS-A100), with 50% internal recirculation flow (FS-A50) and without internal recirculation flow (FS-A0). These different mixing scenarios will show how mixing affects the anaerobic digestion performance.

An outline of the models and mixing scenarios calculated in this work is given in **Figure 5.1**. Firstly, as was done in chapter 4, the biochemical evolution of the anaerobic digester was calculated by means of the 0D-CSTR model described in Patón and Rodríguez, (2019) to compare with an ideal CSTR performance. After that, the hydrodynamics of each mixing scenario were solved and then the *ADM1Foam* solver was applied. Accordingly, this section is devoted to the description of the full-scale modelling.

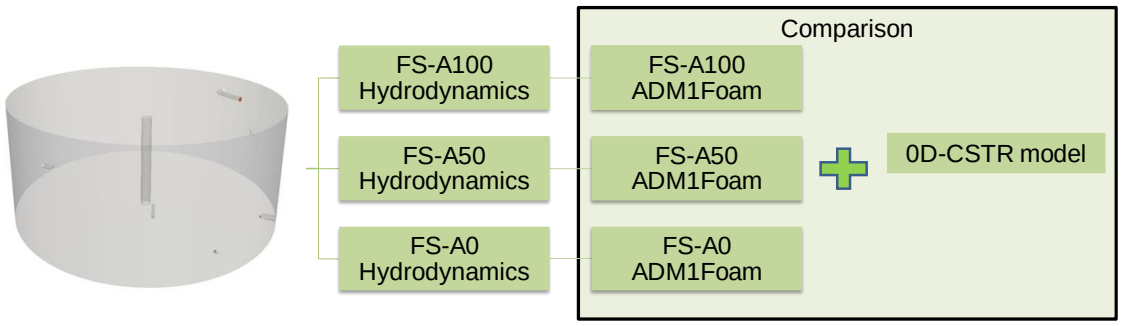

Figure 5.1: *Outline of CFD and 0D models.*

5.2.1. Full-scale anaerobic digester and ADM1modelling

The full-scale setup was described extensively in Section 3.3.1: it is a full-scale anaerobic digester of up to 3000 m^3 volume located at a WWTP in Spain. Its main mixing system is an external recirculation pump system (DYNOMIX).

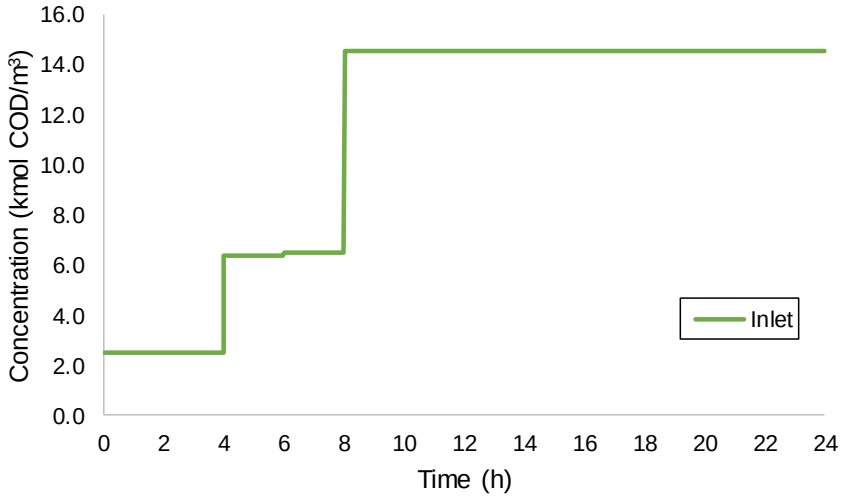

Figure 5.2: *Influent COD concentration.*

Note: the biomass COD is not included.

Regarding the ADM1 modelling by means of the *ADM1Foam* and the 0D-model (Matlab-Excel framework), the influent boundary conditions, initial reactor concentration and kinetic parameters were approximated to the BSM2 framework (Rosen et al., 2006). The initial conditions and parameters are presented in Appendix G.ii Full-scale setup. In this anaerobic digester, the influent and recirculation flows were constant to ensure a hydrodynamic steady-state. As far as biochemical components are concerned, an increasing influent COD concentration was introduced in two-hour periods to assess the impact of variable influent on the rates and anaerobic digestion stages (see **Figure 5.2**). After 8 hours, the influent COD concentration was kept constant until 24 hours of simulation were completed. Biogas partial pressures from the 0D-model were

used in the *ADM1Foam* 3D-CFD model.

5.2.2. CFD Modelling

As in the previous chapter, the CFD simulations had two parts, the hydrodynamics and the *ADM1Foam* modelling, which were solved via parallel computing on two different devices. The hydrodynamic simulations were solved using one node of a cluster with an AMD Opteron ™ Processor 6274 (maximum 32 cores at 2.2 GHz) and 98.2Gb RAM. The *ADM1Foam* modelling was performed using 4 nodes of a Tirant 3 supercomputer at the Universitat de València (UV). Each node in this facility is equipped with 2 Intel Xeon SandyBridge E5-2670 (8 cores at 2,6 GHz each) for a total of 16 cores and 32 GB RAM DDR3.

5.2.2.1. Geometry and meshing

The previously developed 3D geometry from chapter 3 was used reconfigured in OpenFOAM (see the new geometry in **Figure 5.3**). A new mesh was then generated by means of the *snappyHexMesh* tool with 0.1x0.0975 m maximum cell size. The statistics of the mesh in **Table 5.1** complied with standard values of good practice (see Section 2.5.1) so it was not considered a GCI study.

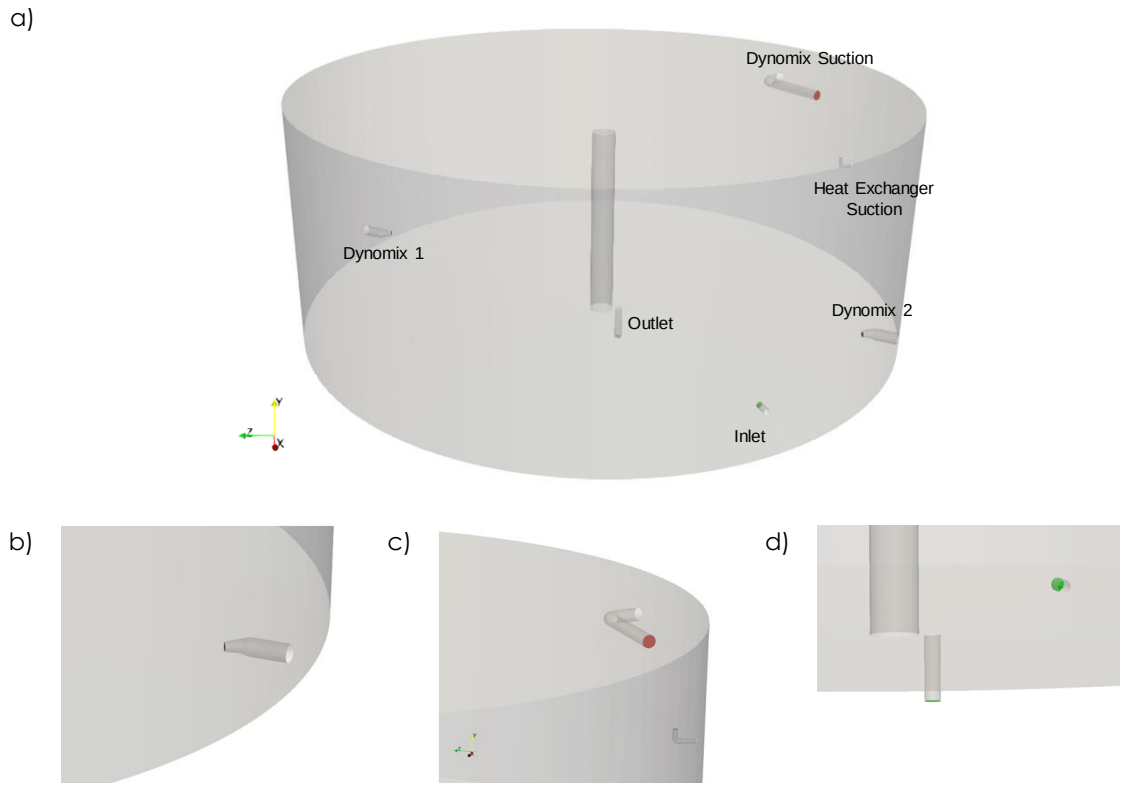

Figure 5.3: *Details of the full-scale setup: a) general view of the model; b) DYNOMIX nozzle; c) heat exchanger suction pipe and DYNOMIX recirculation's suction tube, and d) outlet and inlet nozzles.*

Table 5.1: *Mesh statistics.*

Number of Cells	4,141,347
Hexahedra	3,951,400
Prisms	94,315
Polyhedra	95,426
Tet wedges	206
Minimum cell volume (m^3)	7.3×10^{-6}
Maximum cell volume (m^3)	0.0013
Maximum aspect ratio	6
Maximum skewness	2.7
Maximum non-orthogonality	55.4
Average non-orthogonality	4.7

5.2.2.2. Setup

According to previous numerical calculations, the same boundary conditions described in **Table 3.8** and the sludge properties from Section 3.3.2.2 were set as described in **Table 5.2**.

Table 5.2: *Boundary conditions.*

Patch	Inlet	Dynomix 1	Dynomix 2	Outlet	Heat Exchanger	Suction Dynomix	Wall
U	flowRateInletVelocity 0.01208	flowRateInletVelocity 0.084915	flowRateInletVelocity 0.103785	flowRateInletVelocity -0.00236	flowRateInletVelocity -0.00972	zeroGradient	noSlip
p	zeroGradient	zeroGradient	zeroGradient	zeroGradient	zeroGradient	fixedValue uniform 0	zeroGradient
k	fixedValue uniform 0.0002274	fixedValue uniform 0.00690586	fixedValue uniform 0.00981139	zeroGradient	zeroGradient	zeroGradient	kqRWallFunction uniform 1e-05
epsilon	fixedValue uniform 3.3e-06	fixedValue uniform 0.0005	fixedValue uniform 0.00093	zeroGradient	zeroGradient	zeroGradient	epsilonWallFunction uniform 1e-05
nut	calculated uniform 0	calculated uniform 0	calculated uniform 0	calculated uniform 0	calculated uniform 0	calculated uniform 0	nutkWallFunction uniform 0
nuTilda	fixedValue uniform 0	fixedValue uniform 0	fixedValue uniform 0	fixedValue uniform 0	fixedValue uniform 0	fixedValue uniform 0	zeroGradient

5.2.2.3. Solver and convergence

The hydrodynamics of the mixing scenarios were solved by means of the *pimpleFoam* solver with a 0.005 s timestep size. The solver was run until the same criteria described in Section 4.4.3.3 were met, although the minimum simulation time was increased to 2000 seconds.

The experimental tracer test in this full-scale anaerobic digester was performed experimentally (see Section 3.3.2.1) and showed that the FS-A100 scenario behaves like an ideal CSTR with a small short circuit. Accordingly, the experimental tracer test was reproduced again with OpenFOAM by means of the *scalarTransportFoam* solver with turbulent dispersion and a Schmidt Number of 0.7.

The numerical schemes used in hydrodynamic and virtual tracer test modelling are described in **Table 5.3**.

Table 5.3: *Numerical schemes for the CFD modelling.*

Simulation	Variable	Numerical scheme
Hydrodynamics	div(phi,U)	Gauss linearUpwind grad(U)
	div(phi,k)	Gauss upwind
	div(phi,epsilon)	Gauss upwind
	div(phi,R)	Gauss upwind
	div(R)	Gauss linear
	div(phi,nuTilda)	Gauss upwind
Tracer tests	ddt	Euler
	div((nuEff*dev2(T(grad(U)))))	Gauss linear
	div(phi,T)	Gauss upwind
ADM1Foam	ddt	Euler
	div(phi,ADM1 Variables)	linearUpwind grad(ADM1 Variable)

5.2.2.4. ADM1Foam Modelling

All scenarios were simulated by means of *ADM1Foam* for 24 hours with fixed hydrodynamics and constant influent flow (see **Table 5.2**). The numerical schemes used in these simulations are described in **Table 5.3**.

The initial conditions, influent concentration and biokinetic parameters used in the 0D model and in the *ADM1Foam* 3D-CFD model, are depicted in Appendix G.ii Full-scale setup. Moreover, the biogas partial pressures obtained with the 0D-model were used to define the biogas fraction of the degassing

terms.

5.3. RESULTS

This section is focused on the validation of the CFD model and the analysis of the full-scale *ADM1Foam* results. First, the CFD model developed in this chapter needs to be validated against experimental and numerical results. Then, the analysis of the *ADM1Foam* results starts with the ADM1 state variables distribution in Section 5.3.2 and the removal efficiency and process rates in Section 5.3.3 to define which is the most efficient full-scale scenario. After that, the dilution and homogenisation phenomena are evaluated from two different mixing perspectives so that the most important mixing phenomenon is found and somehow quantified (see Section 5.3.4). Finally, in the last section some future needs and perspectives about the *ADM1Foam* solver are described.

5.3.1. Validation of the CFD model

In order to validate this new OpenFOAM model of the full-scale digester described in chapter 3, two different tests have been carried out. On the one hand, a virtual tracer test was done to simulate the experimental tracer test and compare its results with the experimental values. On the other hand, the circumferential velocity of this OpenFOAM model has been compared with the CFX model from chapter 3 (A100 or base model).

The virtual tracer test was computed in FS-A100 and the outlet tracer concentration over time was obtained. The experimental tracer test was discussed in Section 3.3.2.1 and showed that the full-scale setup behaves like an ideal CSTR with around 12% short-circuiting. **Figure 5.4** compares the experimental and virtual tracer curves where the virtual tracer coincided with the overall trend of the experimental values, so that the FS-A100 model was validated and can reproduce the setup hydrodynamics. Additionally, short-circuiting was noticeable at the beginning of the virtual test, which was not shown in the experimental curve as it was previous to the first tracer sample, i.e. before the 1-hour sample. Thus, the virtual tracer test could capture different hydraulic defects that were not visible in an experimental tracer test. Additionally, FS-A100 could be approximated to an ideal CSTR so, the *ADM1Foam* results can be compared with the 0D-model results obtained with the Matlab-Excel (Simulink) framework.

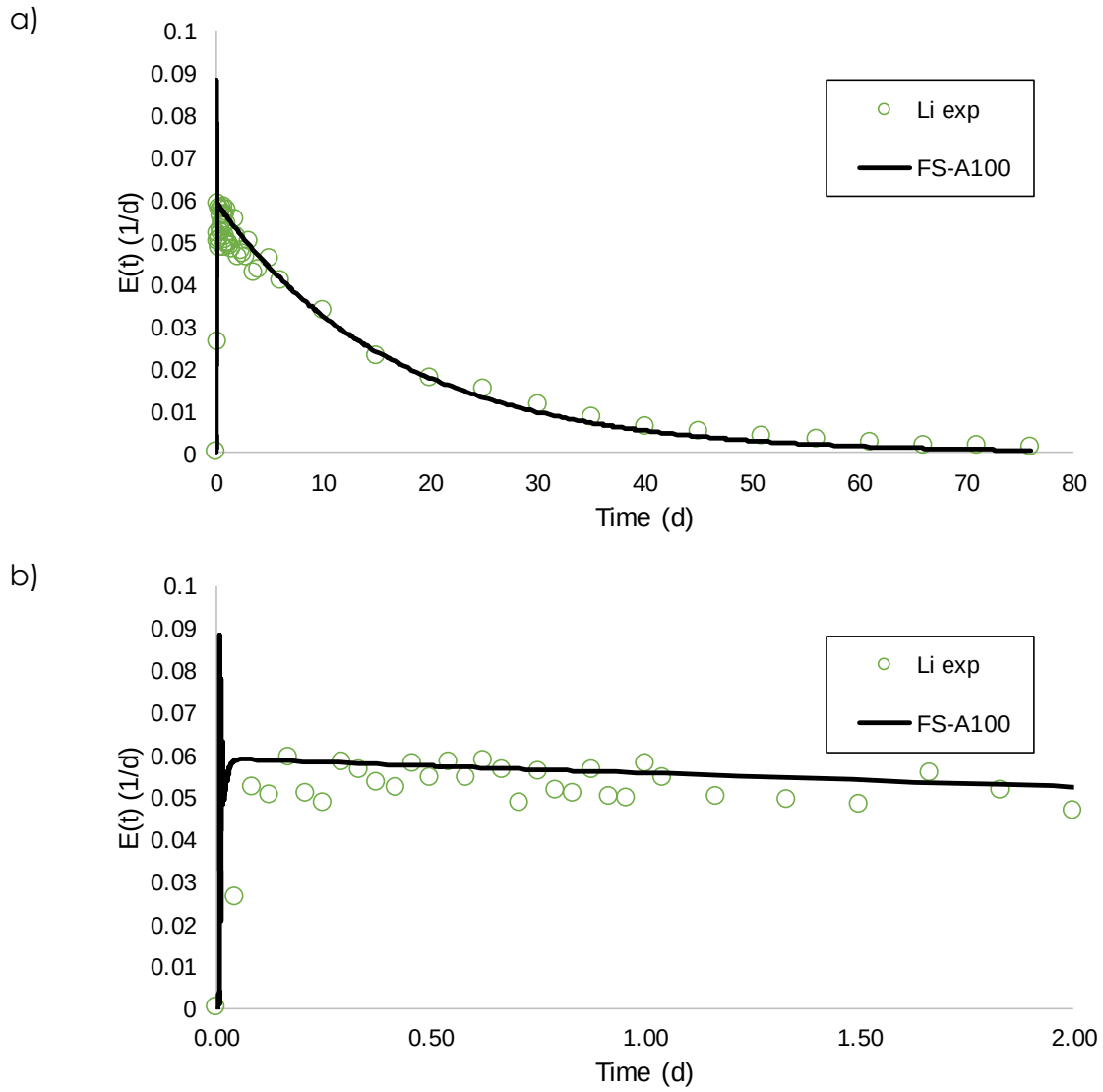

Figure 5.4: *Comparison of experimental and CFD model tracer test curves: a) long tracer test curve and b) detail of tracer test curve.*

On the other hand, it was considered important to compare both CFD code results from the same anaerobic digester setup. **Figure 5.5** depicts the circumferential velocity at different heights obtained with the CFX model from chapter 3, i.e. A100, and the OpenFOAM model developed in this chapter, i.e. FS-100. It is important to highlight that the grids were different from one code to another but, both codes mostly agreed in the circumferential velocities. In both models, the sludge recirculation jets were noticed at 1 meter height between 6 to 8 m radius and the shapes of the curves at 3, 5 and 7 m were correctly mirrored. Hence, both models were comparable and the *ADM1Foam* has been applied to the OpenFOAM model.

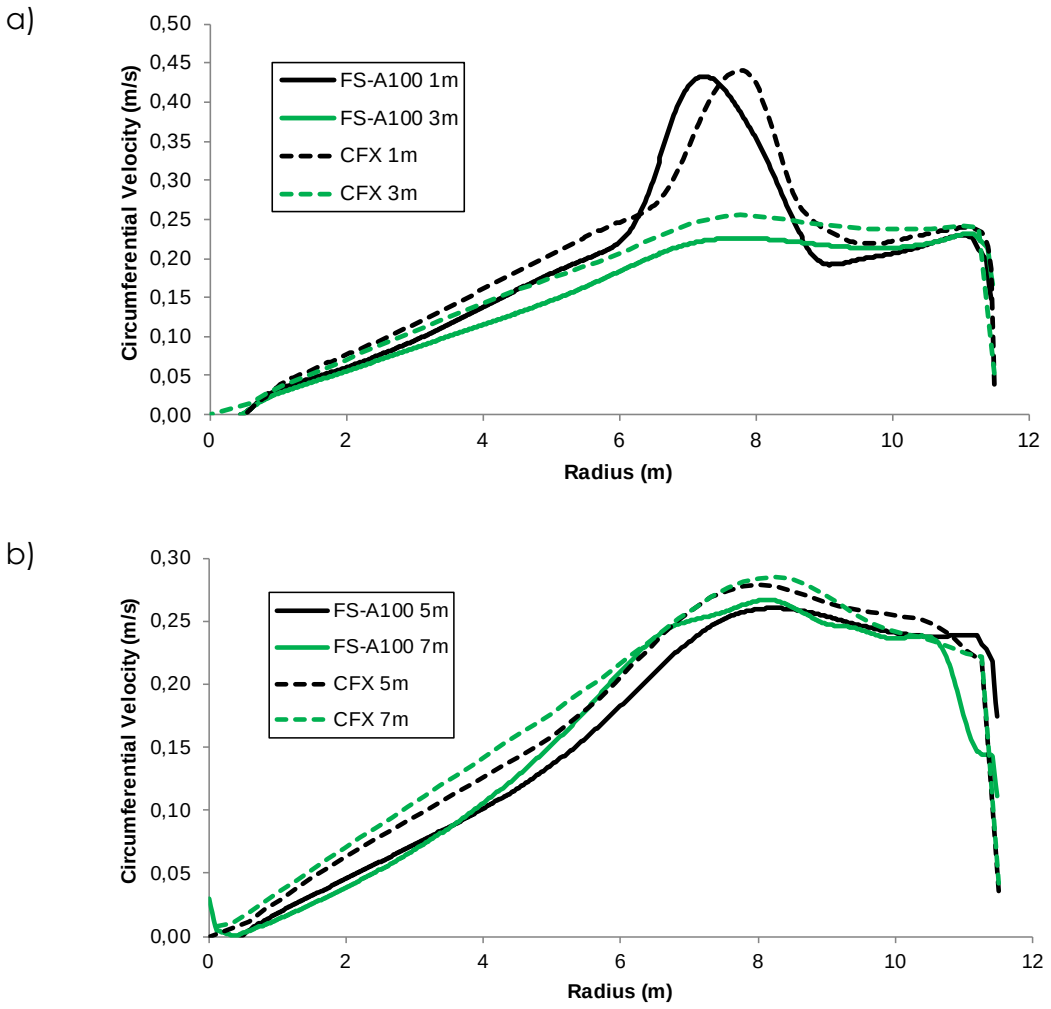

Figure 5.5: *Comparison of circumferential velocity at different heights for both CFD models (FS-A100 from this chapter modelled in OpenFOAM and CFX from chapter 3 modelled in ANSYS CFX): a) 1 and 3 meters and b) 5 and 7 meters.*

5.3.2. ADM1 Results at full-scale setup

The *ADM1Foam* was used in the full-scale setup in the A0, A50 and A100 scenarios modelling 24 hours of simulation. On the one hand, their results were compared with 0D simulation results as FS-A100 was fitted to a CSTR performance. Accordingly, Appendix I.i ADM1 state variables and I.ii ADM1 state variables-relative difference, depicts a comparison of ADM1 results from the 0D simulation and the 3D-CFD model, considering the volume integrate value in the domain as the value in the 3D-CFD model.

Generally, a global agreement between both models was found at the beginning of the simulation. Therefore, it was stated that *ADM1Foam* was also useful in full-scale setups with different mixing regimes. As the simulation progressed, the 3D-CFD model results started a decoupling from 0D simulation, so different 3D-CFD's hydrodynamics entailed different anaerobic digestion

results. Regarding the pH, a slight disagreement was encountered. The reason for this disagreement between the two frameworks could be found in the pH methodology, since 0D simulation has applied the ionic strength method and *ADM1Foam* has deployed the ionic balance method.

On the other hand, sugar and acetic acid concentration distribution in the full-scale setup 3D-CFD model are shown in **Figure 5.6** and **Figure 5.7** in the different full-scale scenarios at some simulation times.

Regarding the sugar state variable (Ssu), its initial concentration was $6.7x10^{-5}$ kmol/m^3 and one hour later (**Figure 5.6**a) Ssu had increased to over $1x10^{-4}$ kmol/m^3 in all scenarios. At 4 and 24 hours (**Figure 5.6** b and c), in scenarios FS-A0 and FS-A50, Ssu showed great gradients inside the digester. In FS-A0, the area in front of the inlet had the greatest concentration (at 4 and 24 hours Ssu wass almost $1.5x10^{-4}$ and $1x10^{-3}$ kmol/m^3, respectively) whereas the area near the inlet had the lowest concentration reaching values lower than the initial concentration in **Figure 5.6**b. Conversely, Ssu FS-A50 results were more homogeneous than those of FS-A0, but some gradients were shown near the inlet. In FS-A100, Ssu did not have local Ssu gradients inside the digester and remained mainly uniform from the first (**Figure 5.6**a) to the fourth hour (**Figure 5.6**b).

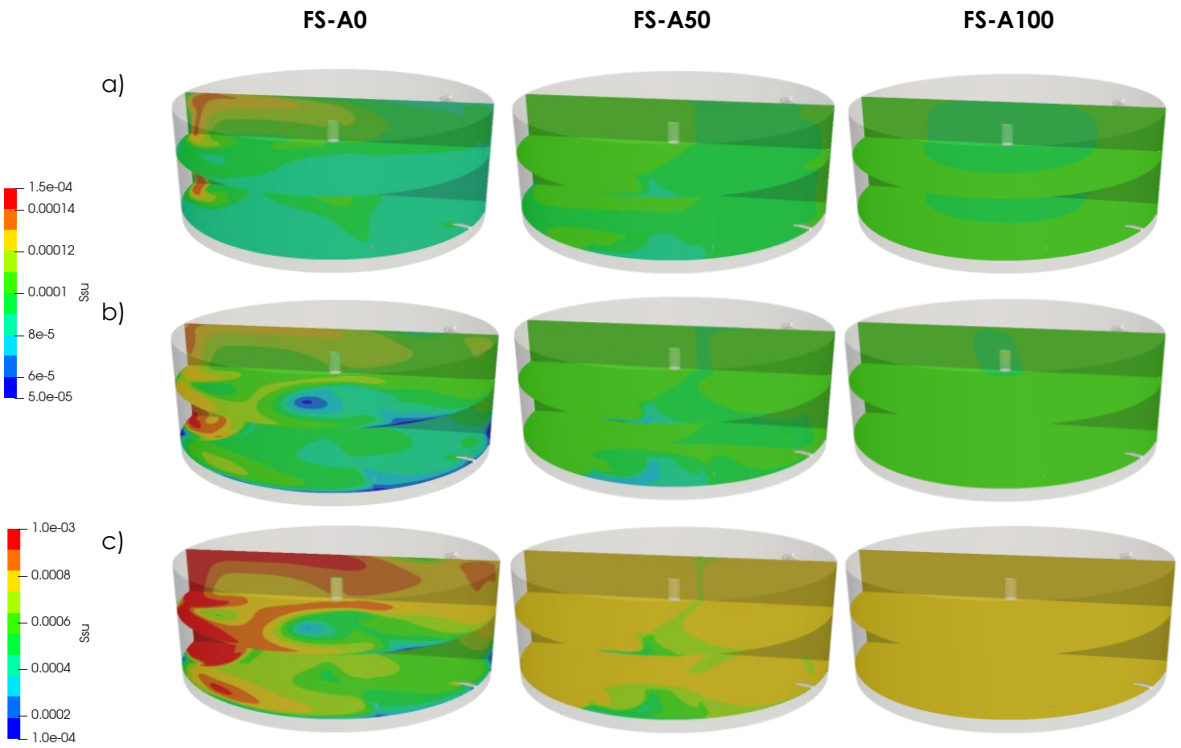

Figure 5.6: *Sugar concentration (kmol/ m^3) distribution: a) 1 hour, b) 4 hours and c) 24 hours simulation for different scenarios.*

With regards to the acetic acid state variable (Sac), its initial concentration was $3.4x10^{-3}$ kmol/ m^3 and its concentration kept rising over time

(**Figure 5.7**). As observed with the Ssu, different inhomogeneities and local gradients were shown, in front of the inlet in FS-A0 and near the inlet in FS-A50.

In chapter 3, the analysis of different hydraulic and mixing parameters showed that an increase of the recirculation flow rate meant a reduction of the mixing time. This could be seen with the distribution of these two ADM1 state variables in these figures: FS-A100 scenario basically had a uniform concentration in the entire volume as its mixing time was lower than In FS-A50 and FS-A0. The scenarios with lower recirculation flow rates (FS-A50 and FS-A0) did not have a homogeneous concentration in the system so that different peaks could be seen in the area in front of the influent nozzle. The impact of these inhomogeneities will be assessed in the following section.

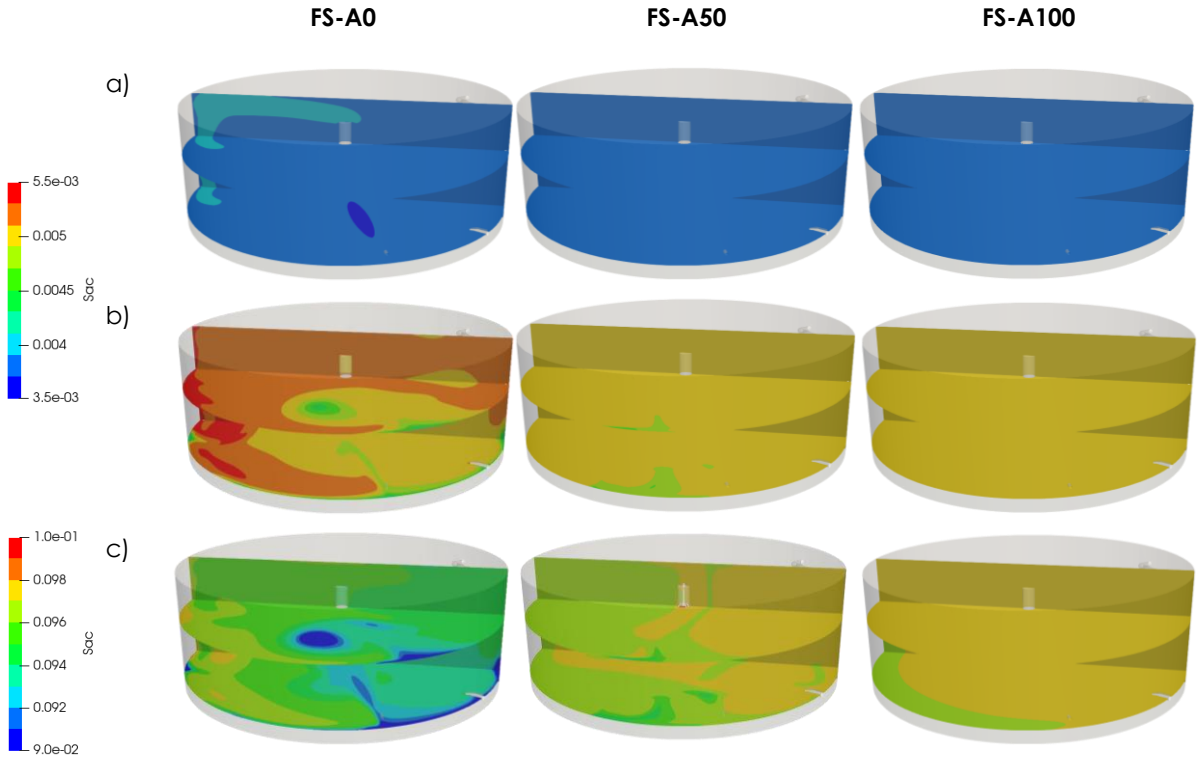

Figure 5.7: *Acetic acid concentration (kmol/ m^3) distribution: a)1 hour, b)4 hour and c)24hours simulation for different scenarios.*

5.3.3. Mixing perspective

In general, it has been stated that mixing in anaerobic digestion is compulsory to homogenise the digester content (see Section 2.3.1 for more details). Thus, Ssu and Sac distribution (**Figure 5.6** and **Figure 5.7**) exposed partial homogeneity in FS-A50 and complete homogeneity in FS-A100, as the mixing system was active in these scenarios. But what is the impact of these inhomogeneities? Additionally, mixing is proposed to increase the proficiency of the biological activity but, does mixing or homogeneity really favour the

anaerobic digestion process? Is it possible to verify this with *ADM1Foam*? *ADM1Foam* made it possible to evaluate the ADM1 state variables and the processes rates in the system. Thus, full scale scenarios could be compared in different ways to test if any scenario or mixing regime benefited anaerobic digestion.

One of the main objectives of anaerobic digestion is the removal of organic material to form a digestate with low organic material concentration. Thus, the removal efficiency was assessed according to inlet and outlet concentrations. **Figure 5.8** and **Figure 5.9** show the removal efficiency of some ADM1 variables, both particulate and soluble, respectively. Firstly, note that different steps with a saw-tooth shape were depicted in all variables fitting with the influent steps and the products' accumulation from the beginning of the step to its end.

First, the particulate variables in **Figure 5.8** showed removal efficiencies above 99% over the entire simulated period. In addition, a lower efficiency was observed in the FS-A0 scenario, which may result from poor sludge mixing. As explained in the ADM1 (see Section 2.4.1), these particulate compounds triggered the anaerobic digestion process and were degraded by the biomass into other soluble compounds. Therefore, it was necessary to evaluate the soluble compounds into which they were transformed.

Then, hydrolysis of carbohydrates, lipids and proteins produced sugars (Ssu), long chain fatty acids (Sfa) and amino acids (Saa). The removal of Ssu is depicted in **Figure 5.9**a where 90% removal was achieved during the whole simulation period, with a slight decrease in removal efficiency at FS-A0. Sfa's removal efficiency was not shown as its concentration in the outlet or in the digested sludge has been always higher than the inlet concentration, so its removal efficiency was 0 and no differences were found between the scenarios. Saa's removal efficiency is also found in **Figure 5.9**a which showed removal efficiencies lower than 80%. In this variable, FS-A50 and FS-A100 showed the same behaviour but FS-A0 exhibited four times less removal efficiency. Accordingly, poor mixing in FS-A0 led to a global increase of Saa, so that its removal efficiency has always been lower than 40%.

Regarding propionate (Spro) in **Figure 5.9**b, its removal efficiency increased according to the inlet step-concentration: the inlet concentration increased from the 4th hour onwards, so its removal efficiency improved showing a peak when the inlet concentration increased at 4, 6 and 8 hours. Nonetheless, the efficiency decayed before these peaks as Spro built up in the anaerobic digester. Spro accumulated in the anaerobic digester due to influent intake and production in the uptake of sugars and amino acids, but it was also consumed by the biomass. As a result, a saw-tooth shape was found with values below 80% removal efficiency. Note that FS-A0 revealed a slightly higher removal efficiency than FS-A50 and FS-A100. Thus, as the mass of Spro introduced was the same in all scenarios, it suggested that less Spro was produced or more Spro was

consumed in FS-A0 compared to the others.

Valerate (Sva) and butyrate (Sbu) removal efficiency is deployed in **Figure 5.9**c where the same pattern described in Spro was found: the removal efficiencies were lower than 80% and showed a saw-tooth pattern. As well as Spro, Sva and Sbu were also produced on the uptake of sugars and amino acids and were consumed by the biomass. In this case, FS-A0 had higher removal efficiencies than FS-A50 and FS-A100, so that the same behaviour established in Spro could be withdrawn: Sva and Sbu were produced in less quantity or were more consumed in the FS-A0 than in FS-A50 and FS-A100.

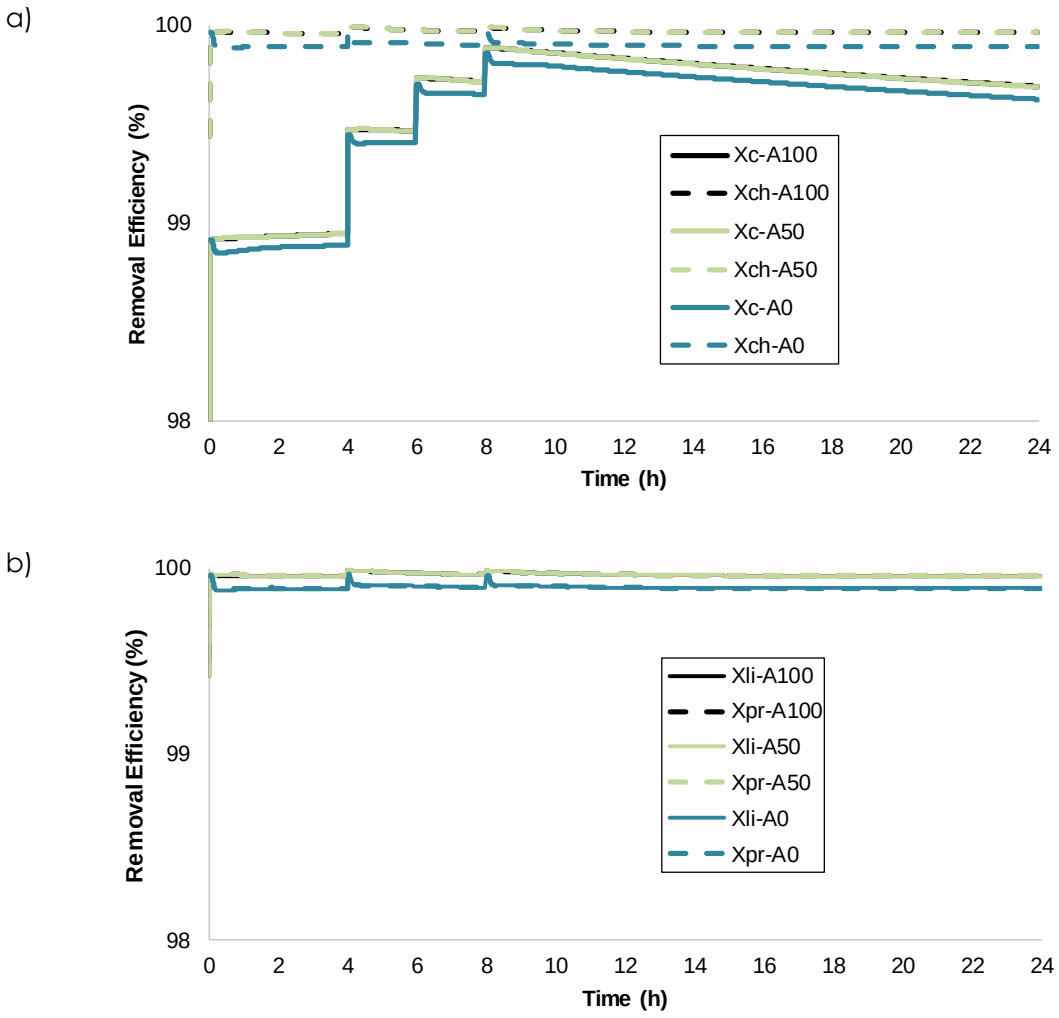

Figure 5.8: *Removal efficiency of some particulate ADM1 variables a) Xc and Xch and b) Xli and Xpr.*

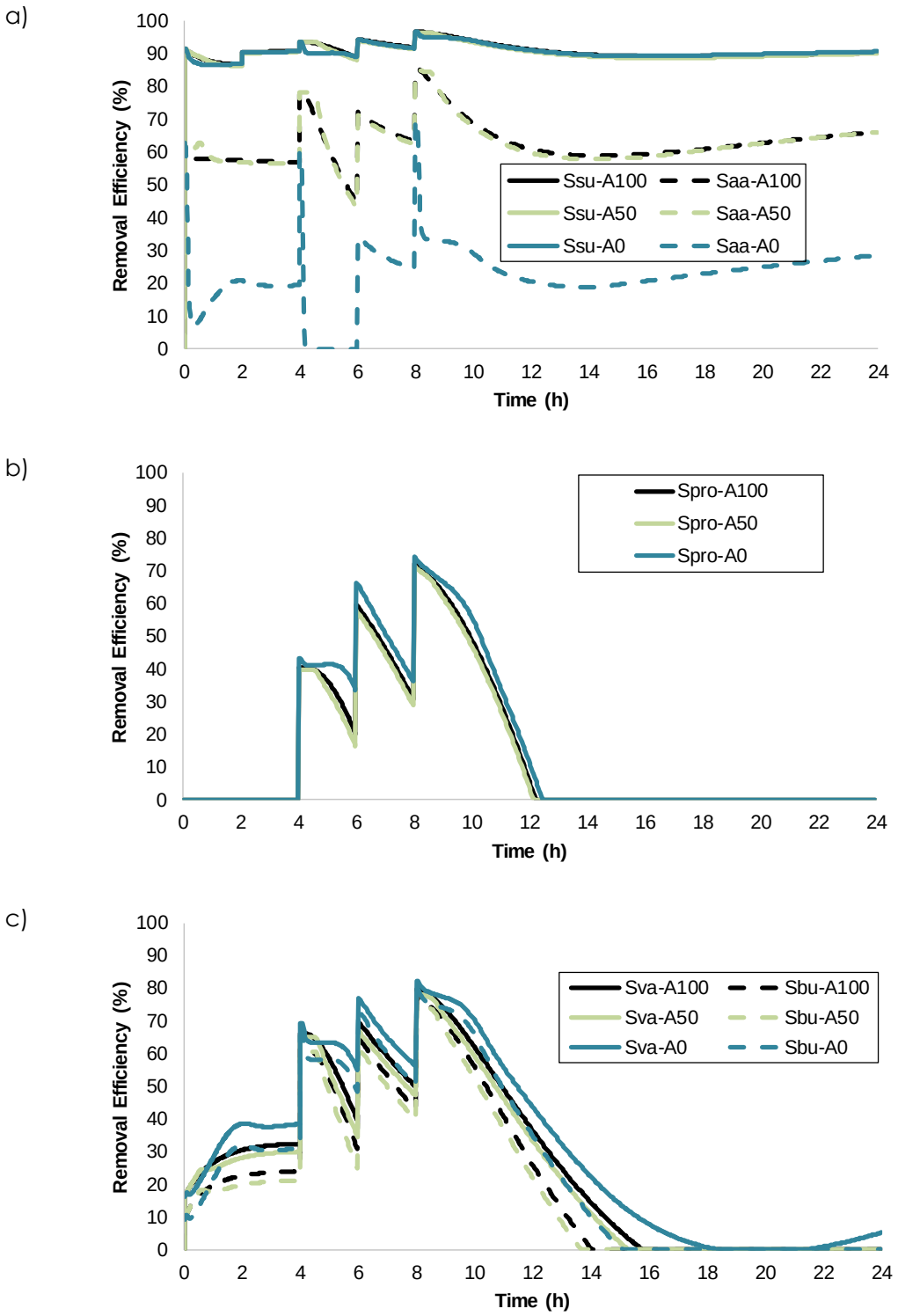

Figure 5.9: *Removal efficiency of some soluble ADM1 variables a) Ssu and Saa, b) Spro and c) Sva and Sbu.*

These analyses of the different variables did not clearly establish which was the most favourable mixing scenario so a more general parameter was

calculated. Accordingly, the COD concentration in the outlet was obtained and shown in **Figure 5.10** where the variables considered are Saa, Sac, Sbu, Sch4, Sfa, Sh2, Si, Spro, Ssu, Sva, Xc, Xch, Xd, Xi, Xli and Xpr. Attending to this figure, it was clear that FS-A0 concentration was the highest and that FS-A50 and FS-A100 reached the same concentration. This clearly indicated that FS-A50 and FS-A100 accomplished further degradation than FS-A0, meaning that both mixing regimes were feasible and preferred.

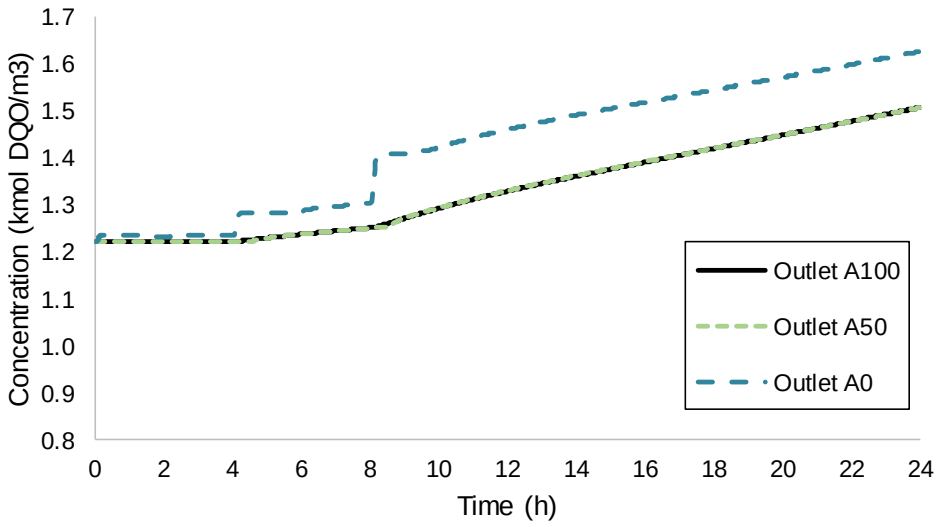

Figure 5.10: *COD concentration at the outlet.*

One of the advantages of the *ADM1Foam* stemmed from the storage of different data, such as the value of the process rate equations. The process rate fields could be used to evaluate the performance of each of the anaerobic digestion stages: first stage, disintegration and hydrolysis as the sum of the process rates from ρ_1 to ρ_4; second stage, acidogenesis and acetogenesis as the sum of the process rates from ρ_5 to ρ_{10} and; third stage, methanogenesis as the sum of ρ_{11} and ρ_{12}. Thus, the volume integrate of the anaerobic digestion stages was compared with 0D simulation results in the different scenarios as a relative difference in **Figure 5.11**.

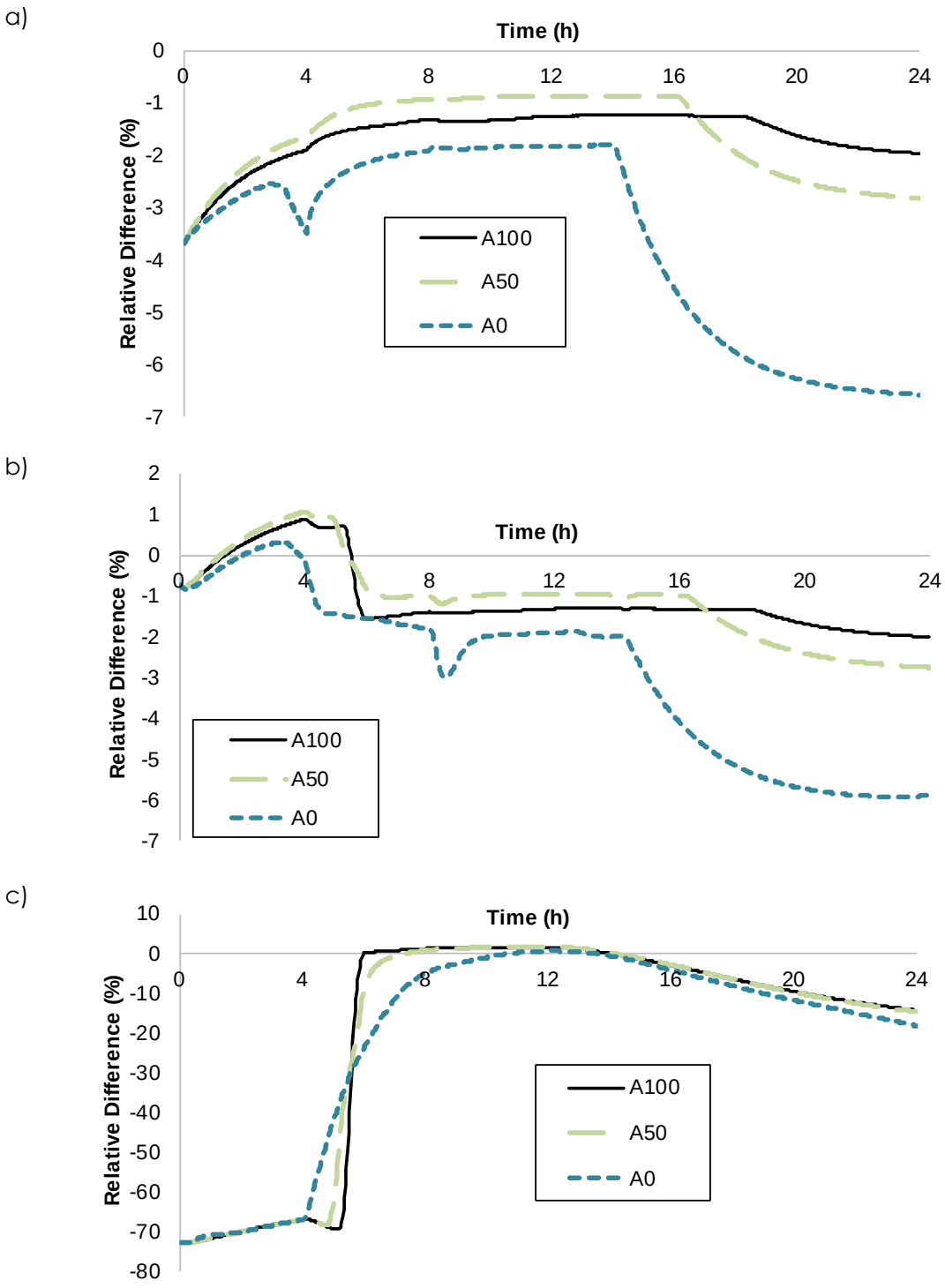

Figure 5.11: *Relative difference between 0D and 3D-CFD of the sum of the process rates' volume integrate at FS: a) disintegration and hydrolysis, b) acidogenesis and acetogenesis and c) methanogenesis.*

Overall, it was observed that globally all scenarios showed lower rates than 0D-simulation, with the relative difference being less than 7% in the first and second stage and up to 70% less in methanogenesis. These results state that a 0D-

model (an ideal CSTR configuration) favoured all stages of the digestion process so that: on the one hand, these scenarios could not be approximated to a CSTR performance and, on the other hand, the 3D-CFD model would be on the safe side by showing lower processes rates. As demonstrated by these simulations, it was difficult to achieve a CSTR ideal configuration by means of full-scale 3D-CFD models. Hence, 3D-CFD models with *ADM1Foam* would be a new generation of anaerobic digestion models that expose the influence of mixing on the anaerobic digestion process in non-ideal performance setups.

Figure 5.11 a and b depict a very similar time evolution: On the one hand, FS-A0 was always lower than the rates obtained in the FS-A50 and FS-A100 scenarios. This demonstrated that the local concentration gradients or inhomogeneities that occurred in the FS-A0 scenario were counterproductive for these two stages, so this mixing scenario was discouraged. On the other hand, the FS-A50 scenario showed slightly higher rates than FS-A100, so that an intermediate mixing may produce a better overall performance than a more intense mixing. Finally, it was noteworthy that the rates started to decrease in a generalised and gradual way in all three scenarios: rates decreased from hours 14, 16 and 18 in FS-A0, FS-A50 and FS-A100, respectively. Attending to the figures in Appendix I.i ADM1 state variables, these decreasing patterns found in the first and second stages should stem from the differences in the variables Xc, Xli, Xpr, Saa and Ssu at the 14th hour in FS-A0, the 16th hour in FS-A50 and the 18th hour in FS-A100.

As far as methanogenesis is concerned (see **Figure 5.11**c), the scenarios showed a similar time evolution. At the beginning, the initial adjustment of Sh2 (see figure in Appendix I.i ADM1 state variables) entailed initial rates 70% lower in all scenarios. Nonetheless, from the 4th hour onwards the rates increased and became equal to the 0D simulation: the FS-A100 scenario was the one with a later but faster increase, reaching rates globally equal to the 0D case from the 6th to the 14th hour. FS-A50 achieved globally the same rates as 0D before the 8th hour and up to the 14th hour and the FS-A0 scenario only achieved 0D production for 2 hours (from the 12th to the 14th hour). From the 14th hour onwards, the methanogenesis stage was reduced in all three scenarios and was slightly lower in the FS-A0 case.

At the beginning of this chapter, the question was raised as to whether or not complete homogenisation was necessary to carry out the digestion process and whether it really increased the performance of the digestion process. According to these results, excessive mixing was not mandatory, nor was complete homogenisation of the system, as the FS-A50 and FS-A100 scenarios have shown very similar removal efficiencies and production rates in all three stages of anaerobic digestion.

Based on the homogeneity patterns, removal efficiency and rates of each step, different mixing strategies could be studied and applied depending on the goals of the facility manager. For example, in this full-scale anaerobic digester

there was intermittent mixing between FS-A100 and FS-B100 (FS-A100 with an internal propeller). Thus, a FS-A50-FS-B100 intermittent mixing could be feasible to reduce the energy consumption of the DYNOMIX recirculation pumps as FS-A100 and FS-A50 showed similar process results. Nonetheless, FS-B100 should be activated a few hours a day to avoid dead volumes.

5.3.4. Dilution phenomena and Characteristic Time

As expected, the results shown in the hydrodynamic analysis (chapter 3) and these observed patterns in the ADM1 variables support that hydrodynamics greatly favoured dilution in scenarios with a mixing system, FS-A50 and FS-A100. Regarding the inhomogeneity pattern in FS-A0, i.e. with higher concentration in front of the inlet and dilution near the inlet; it was depicted in all ADM1 state variables. This pattern could be drawn from the inlet flow that drove the sludge to the inlet's opposite wall (see **Figure 5.12**). Nonetheless, it is reasonable that dilution was also produce by other phenomena included in the transport equation, such as the biological processes, and not only produced by hydrodynamics.

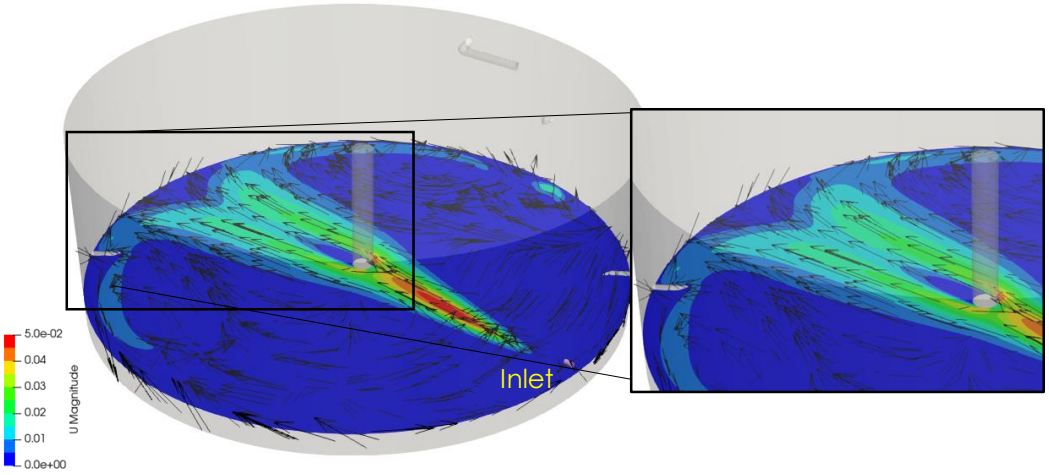

Figure 5.12: *Fluid vectors and velocity contours in FS-A0 at a plane at 1m height.*

The homogenisation effect of each phenomenon in the transport equation is unknown but it could be drawn from the order of magnitude of the time constants. Therefore, as calculated in Picioreanu et al., (1999), the order of magnitude of time constants or the characteristic time (CT) for different phenomena could be computed by assuming a distinctive distance and area. The CT showed which phenomenon drove and defined the dilution of each transported state variable, so that the lower the CT, the greater the contribution of the phenomena to the homogeneity and the more homogeneity appeared. These phenomena included hydrodynamics, such as convective transport and molecular and turbulent diffusion, and ADM1 kinetics, such as hydrolysis, growth and death. The parameters considered in the calculation of CT are described in **Table 5.4**. The quartiles 0.25 and 0.75 were considered in the velocity magnitude

and the viscous turbulent diffusion constants due to the great variability of these fields. Nevertheless, the minimum and maximum constants were considered in the biological processes, as their range was shorter than the hydrodynamic ones.

Table 5.4: *Parameters to calculate the characteristic time.*

Parameter	Units	Low value	Max value
Velocity in FS-A100	m/s	0.141	0.243
Velocity in FS-A50	m/s	4.10E-03	2.74E-02
Velocity in FS-A0	m/s	1.27E-03	4.01E-03
Molecular diffusion coefficients	m2/s	1.00E-10	2.80E-11
Viscous Turbulent diffusion constants in FS-A100	m2/s	3.24E-04	8.30E-03
Viscous Turbulent diffusion constants in FS-A50	m2/s	8.16E-05	1.16E-03
Viscous Turbulent diffusion constants in FS-A0	m2/s	1.27E-05	4.82E-04
Hydrolysis Constant	h-1	0.0208	0.4167
Growth Constant	h-1	0.128	2.06
Decay Constant	d-1	0.02	1

Note: Viscous Turbulent Diffusion constants are: $\frac{\nu_t}{Sch_k}$

Two different perspectives were studied for the analysis attending to assumed distance and area. On the one hand, from a global perspective or macro-scale, the radius of the full-scale set-up was considered as the distinctive distance and area. On the other hand, the mean floc diameter from chapter 3, i.e. 1344µm, was considered for the CT analysis from a micro-scale perspective.

Figure 5.13 depicts the CT from a global and a micro-scale perspective with a vertical line showing the HRT. The CT from a global perspective stands for the time that is needed to homogenise the digester by each process. Looking at **Figure 5.13**a, molecular diffusion was the lowest process, as its CT was 6 orders of magnitude greater than the HRT. Accordingly, it could not produce the homogenisation of the full-scale setup by itself before the accomplishment of THE HRT. Viscous turbulent dissipation in FS-A50 and FS-A0 and biomass decay homogenisation may not be completed before the accomplishment of the HRT. Conversely, convective processes required a shorter CT to be observed, so they homogenised the setup faster than others and less time was needed to see their effects. Additionally, scenarios with lower mixing had greater CT so the convective process in low mixing scenarios was not decisive: the contribution to homogeneity of convective processes in FS-A100 was almost two orders of magnitude lower than biological processes but, in FS-A0, it was equal to biomass growth, so convective processes and biomass growth phenomena drove homogeneity equally.

From a micro-scale perspective, the phenomenon that has driven the micro-mixing or homogeneity is deployed in **Figure 5.13**b. Note that convection

and turbulent dissipation processes were decoupled from biological processes and required up to 3 orders of CT lower than biological processes in all scenarios, so hydrodynamic processes, i.e. turbulent flows and eddies, drove micro-scale mixing. Nevertheless, biological processes and molecular diffusion had between 1800 s to 50 days (4.32 million of seconds) CTs, so their influence on micro-homogeneity was not noticed in comparison to other hydrodynamic processes. In short, all micro-scale mixing phenomena took place before the HRT was accomplished except for biomass death which exceeded HRT.

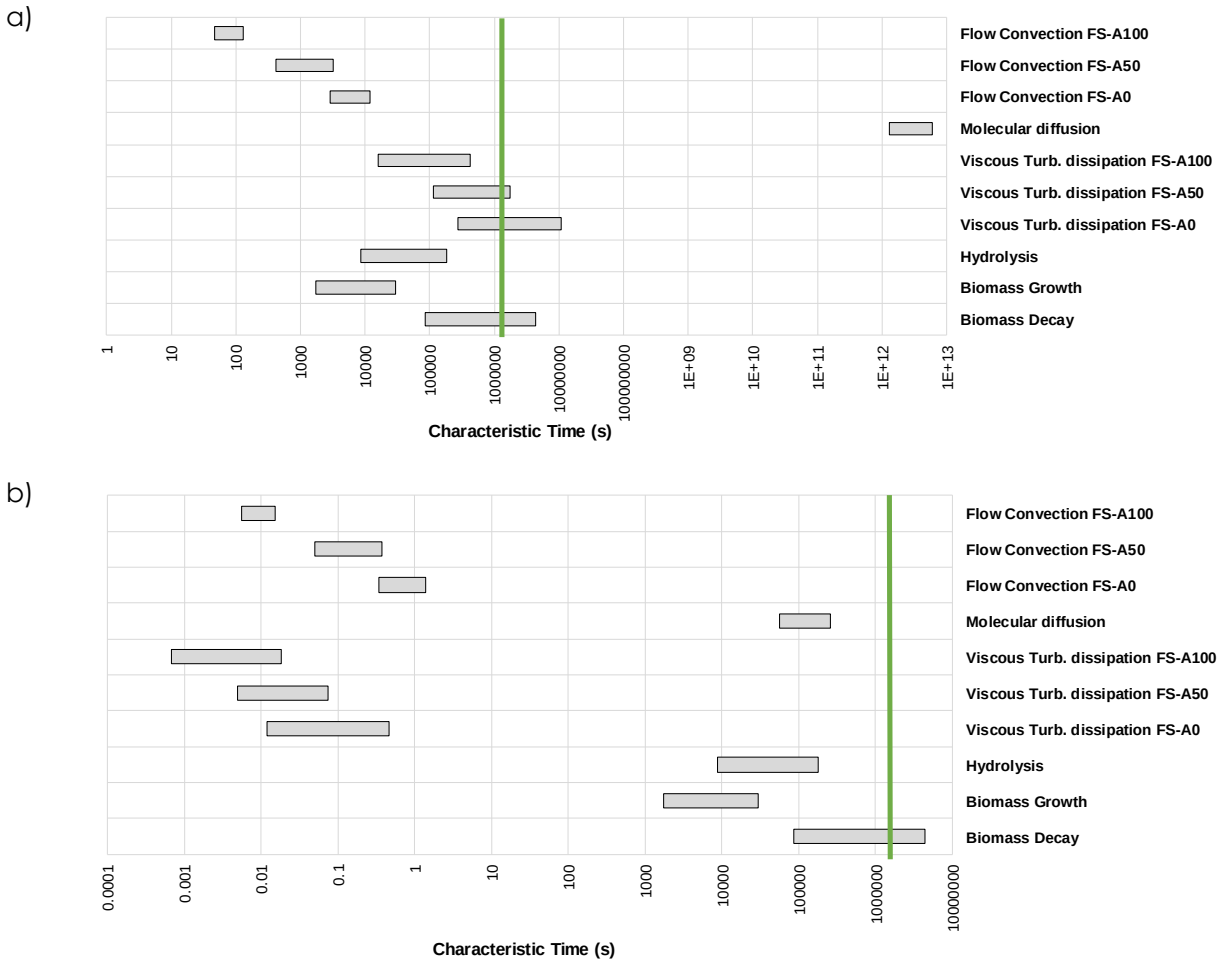

Figure 5.13: *Characteristic time from a) global and b) a micro-scale perspective. The green line shows the HRT of the full-scale setup.*

Overall, hydrodynamic phenomena were faster than biological processes so their influence on mixing was key for the anaerobic digestion process. Additionally, FS-A100 was the scenario with higher mixing and homogenisation as its CT's addition was globally the lowest in comparison to FS-A50 and FS-A0.

5.3.5. Future needs

One of the big drawbacks of CFD models is their high computational time.

The coupling of the ADM1 model in the CFD models also required large computational times. As an example of this, the computational time for the calculation of a 1s of simulation time in the lab-scale setup from chapter 4 and the full-scale setup are presented in **Table 5.5**. In the lab-scale setup, the computational time was less than the real time, since the timestep was greater than the wall time per 1 s of simulation. Nevertheless, in the full-scale setup, the wall time/1s of the simulation was greater than 1s, so the computational time exceeded the time simulated by the *ADM1Foam*.

Several factors affected the *ADM1Foam*'s computational time: On the one hand, CFD models with a higher number of cells and less structured meshes generally require more computational time than CFD models with a lower number of cells and simple meshes. On the other hand, the *ADM1Foam* was calculated from the previously calculated hydrodynamics, so the convective and diffusive terms of the ADM1 variables transport equation required more computational time in CFD models with more turbulence and velocity, e.g. LS-200 and FS-A100. In order to reduce the computational time of *ADM1Foam*, simpler biological models or hydrogen algebraic calculations would be needed.

From the hydrodynamics computational time, the *ADM1Foam* calculation could be compared with the *pimpleFoam* calculation for solving hydrodynamics in FS-A100, which is the most turbulent scenario (last row in **Table 5.5**): in this case, the number of processors was low but the wall time/1s was 2 orders greater than the *ADM1Foam* computational time, so, the hydrodynamics calculation would increase the computational time exponentially if the *ADM1Foam* had been implemented at *pimpleFoam.*

Table 5.5: *Time consumption of simulations.*

Case	Solver	N processors	Timestep (s)	Wall time/1s (s)
LS-200	*ADM1Foam*	64	1	0.38
LS-20	*ADM1Foam*	64	1	0.21
FS-A100	*ADM1Foam*	64	0.1	20
FS-A100	*pimpleFoam*	18	0.015	1459
FS-A50	*ADM1Foam*	64	0.1	20
FS-A0	*ADM1Foam*	64	0.1	15

The anaerobic digestion process actually takes place in two phases, the liquid phase (sludge) and the gas phase (biogas), but the *ADM1Foam* was a single liquid phase solver. Therefore, it would be necessary to develop a second solver with two phases. This two-phase solver would allow to calculate the local and differential methane, hydrogen and carbon dioxide transfer rates and to simulate the hydrodynamic effect of the biogas production (see chapter 6). In

addition, this solver would allow to locate the critical points of high and low biogas production to, for example, encourage mixing at low production points. However, the exponential increase in computational time revealed in **Table 5.5** has to be taken into account when considering a two-phase CFD model coupled with the ADM1 model.

Nevertheless, this solver and its results combined with 0D-CSTR modelling could be used as input data for training a CFD Neural Network (Kim et al., 2019; Wiewel et al., 2018). Neural networks are able to reduce computational time so, the computational time in full-scale CFD simulations would make *ADM1Foam* modelling feasible.

5.4. CONCLUSIONS

ADM1Foam, which was developed in chapter 4, was successfully applied to a full-scale setup where it has been successfully solved in three different mixing scenarios. The dynamic influent demonstrated the usefulness of the *ADM1Foam* solver in full-scale anaerobic digesters with variable influent content.

Regarding the comparison of the mixing scenarios, it is important to note several conclusions. On the one hand, the *ADM1Foam* revealed several inhomogeneities in FS-A50 and FS-A0 that had not been noticed with 0D-modelling. On the other hand, its application in these scenarios has established that the FS-A50 scenario allows the same process performance as the FS-A100 scenario. Therefore, it has been proposed to change the mixing regime to A50-B100 intermittent mixing with the aim of reducing the mixing energy costs without the appearance of dead volumes.

The CT calculation has shown that homogeneity was mainly mediated by hydrodynamic phenomena. Thus, the convective phenomena became 2 orders of magnitude more important than biological processes at the global mixing scale and even 5 orders of magnitude at the micro-scale.

To sum up, *ADM1Foam* would help the knowledge of local species distributions and local anaerobic process evolution. Secondly, it would be the base model for the next generation ADM1-CFD models where mixing influence is appreciated. Thirdly, this methodology with 0D-models and *ADM1Foam* solver would be used to test new anaerobic digesters designs where only 24 hours of ADM modelling is sufficient to observe inhomogeneities and its efficiency.

6. LOCAL MIXING AND TERMINAL VELOCITY CREATED BY RISING BIOGAS BUBBLES

The main motivation of this chapter was to gain knowledge about the local mixing produced during the biogas production by using Volume Of Fluid models. In this research, some knowledge has been found about the influence of apparent viscosity on the terminal velocity of biogas bubbles. Moreover, this chapter has also focused on analysing different drag models in order to fit the estimated terminal velocity of the biogas bubbles. Additionally, the local velocity gradient was employed as an indicator of the local mixing (chapter 3) produced by biogas bubbles. Thus, this research stated that the decompression of biogas bubbles inside an anaerobic sludge matrix produces significant mixing of the sludge which cannot be neglected on the design of anaerobic digesters' mixing systems.

Abstract: The actual flow within anaerobic digesters is of multiphase nature. For low biogas bubbles concentrations, the flow dynamics of the main phase will remain unchanged. As the bubbles concentration increases, their effect on the main flow dynamics will become more apparent. In any case, the bubbles motion will be strongly influenced by the drag force as it determines their vertical speed thus influencing other forces (lift, wall lubrication). Also, the turbulent dispersion depends on the drag coefficient, and the fact that bubbles of different sizes rise at different velocities determines the rate of buoyancy coalescence. Given the difficulties in the experimentation with bubbles in these anaerobic digesters, this chapter addresses the determination of the drag coefficient from CFD simulation. Different biogas bubble sizes were tested to evaluate the terminal velocities of the biogas bubbles and the viscosity fields around them. Waste activated sludge (WAS) and anaerobic digestate (AD) samples were tested using different bubble sizes. Numerical simulations showed that biogas bubbles smaller than 10 mm will be entrapped by the surrounding viscous sludge. Increasing the shear rate and decreasing the apparent viscosity have an important effect on the increase of terminal velocity of the biogas bubbles. The terminal velocity of the biogas bubbles was fitted with different drag coefficients, but no single model matched all bubble sizes at different anaerobic sludge matrix. Thus, a new drag coefficient equation was fitted to the CFD results. The mixing of biogas bubbles inside the anaerobic sludge matrix was deployed as a RMS Velocity Gradient. It was measured between 5 to 20 $s^{-1,}$, so biogas production significantly upgrades anaerobic digester mixing.

Keywords: CFD; Non-Newtonian fluid; Biogas Production; Local Mixing; Drag Coefficient

A modified version of this chapter was presented at the 16th Anaerobic Digestion Conference (2019) as:
R. Arnau, P. Wei, R. Martínez-Cuenca, M. de Kreuk, J. B. van Lier, and S. Chiva, 2019. Assessment of local mixing and terminal velocity created by rising biogas bubbles in an anaerobic sludge matrix.

6.1. INTRODUCTION

Traditionally, optimizing mixing systems in anaerobic digesters has been the focus of CFD modelling of these tanks. The different mixing processes that have been studied are mechanical mixing, gas mixing and hydraulic mixing applying external pumps. Some studies also perform two-phase simulations studying gas mixing (Dapelo et al., 2015; Wei et al., 2018a; Wu, 2010c).

Despite these studies, the production of biogas and its effects on anaerobic digester hydrodynamics are neglected in CFD models or experiments studying mixing behaviour. Indeed, studies comprising gas phenomena include correlations based on experiments performed in Newtonian fluids although anaerobic sludge is a Non-Newtonian fluid. The difficulties in the measurement of the gas phase production inside the thick dark anaerobic sludge, combined with a non-oxygen atmosphere, complicates obtaining reliable data that can be used for the development of more specific correlations for biogas inside anaerobic sludge. Similar difficulties for the experimental visualization of air inside Non-Newtonian fluids are reported in different works (Margaritis et al., 1999; Premlata et al., 2017).

With the aim of studying the local hydrodynamic effect of biogas production, CFD modelling would help with drawing some guidelines to assess mixing (Zhang et al., 2010). The effects of sludge's shear-thinning behaviour and its effect on bubble rising velocity, could impact local mixing inside anaerobic digesters, e.g. by reducing dead volumes, short-circuiting, and could thus increase the degree of mixing within the entire anaerobic digester. In order to study these effects, the liquid phase should be set with real sludge properties.

Wastewater sludge has been described as a Non-Newtonian fluid and its behaviour has been defined with different rheological models. Due to the high solids concentration (higher than 1% Total Suspended Solids), waste activated sludge (WAS) and anaerobic digestate (AD) behaviour are commonly defined by the Ostwald model (power-law model) or the Herschel-Bulkley model.

On the one hand, the Ostwald model has been used in previous studies describing activated sludge (Seyssiecq et al., 2008), membrane biological reactor sludge (Pollice et al., 2007), primary, secondary and anaerobic digested sludge (Lotito et al., 1997; Moeller and Torres, 1997; Wei et al., 2018b), and digested waste from different sources (Mbaye et al., 2014). Different CFD studies that address anaerobic digestion set this model to describe the rheological properties of the sludge. Thus, Wu and Chen, (2008) employed bibliography data to describe liquid manure at different total solids concentration. The liquid manure was described with the Ostwald model and the same model was applied by the same author (Wu, 2011, 2010a, 2010b, 2010c) and other studies (Bridgeman, 2012; López-Jiménez et al., 2015). Another example of the employment of the Ostwald model is Climent et al., (2013) where they employed

their own experimental rheological measurements.

On the other hand, the Herschel-Bulkley model has also been found as the best model to described biofilms (Prades Martell, 2018), primary and secondary sludge (Markis et al., 2014; Ramin et al., 2014; Wei et al., 2018b) and digested waste (Mbaye et al., 2014). Anaerobic sludge has been described by Herschel-Bulkley and Bingham models and extensively studied depending on temperature (Baudez et al., 2013b), shear stress (Baudez et al., 2011) and aging process (Baudez et al., 2013a; Monteiro, 1997). Accordingly, some CFD studies focused on anaerobic digestion have been using the Herschel-Bulkley model to describe their liquid phase (Craig et al., 2013; Dapelo and Bridgeman, 2020; Tobo et al., 2020).

In reference to the coexistence of Non-Newtonian fluids, such as anaerobic sludge, and biogas bubbles in anaerobic digesters, their hydrodynamics and interaction should be properly established. Moreover, the different behaviour of bubbles between Newtonian and Non-Newtonian fluids is decisive in heat and mass-transfer between gas-liquid phases (Margaritis et al., 1999; Premlata et al., 2017). In anaerobic digestion, the behaviour of the biogas bubbles inside the sludge could determine the methane and carbon dioxide diffusion from sludge to the biogas phase depending on the residence time, movement, shape and velocity of the biogas bubble inside the vessel. Accordingly, a deeper study is necessary of the interaction of these phases experimentally.

The motion of the gas phase inside a liquid matrix is governed by different interaction forces i.e. gravity, buoyancy, viscosity, interfacial tension, drag and the memory force. Nevertheless, the easiest way to correlate the liquid and gas properties and the rising velocity of a bubble, is by obtaining a relation between the drag coefficient and the Reynolds number (Kulkarni and Joshi, 2005). Accordingly, this study is focused on obtaining a drag coefficient for biogas bubbles rising in an anaerobic sludge matrix.

As there is no experimental data on biogas production e.g. bubble size, tracking of their movement and size evolution and biogas composition; this chapter with numerical simulations was designed as the starting point to study the influence of biogas bubbles on the hydrodynamics of the anaerobic sludge. The case under study will be limited to the simplest case: a single bubble rising in a quiescent fluid. Different two-dimensional two-phase simulations were set up, applying the Volume Of Fluid (VOF) method with different bubble sizes. The terminal velocity of the bubbles was computed and compared with different drag models in the bibliography. Additionally, the local mixing of the rising bubbles was calculated attending to mixing parameters.

6.2. MODELLING AND SETUP

In this case, the numerical simulations emulate the bubbles produced

throughout the anaerobic digestion process, as there is no experimental information on biogas production. Accordingly, the focus of the study would be the interface between bubbles and sludge, so the VOF model was chosen as the best option for this study. A finite-volume commercial software, FLUENT, was used to model a biogas bubble rising in an anaerobic sludge matrix (ANSYS FLUENT, 2017) and its theoretical equations are explained in detail in Section 2.5.2.3.

The numerical domain and the setup of the numerical simulations are described in this section. Thus, the numerical domain and mesh of the simulations are described first. Then, the main assumptions, parameters and numerical schemes are established. Lastly, an extensive description of the anaerobic sludge matrix as continuous phase is given.

6.2.1. Description of the Domain and Mesh

The benchmark geometry for two-dimensional rising bubbles in liquid columns proposed by Hysing et al., (2009) was used as the computational domain for this study (**Figure 6.1**). In this geometry, the following initial state is set: a circumferential area at the bottom centre of the domain for the gas phase (coloured in orange in **Figure 6.1**) is surrounded by the liquid phase (coloured in blue in **Figure 6.1**). The liquid phase is a rectangular area dependent on bubble's diameter with dimensions $2d_b \times 4d_b$ where d_b is the bubble diameter. At this geometry, the gas phase ranges from 0.5 mm to 40 mm and its centre is located at $1d_b$ of distance from the bottom and both sides (see **Figure 6.1**).

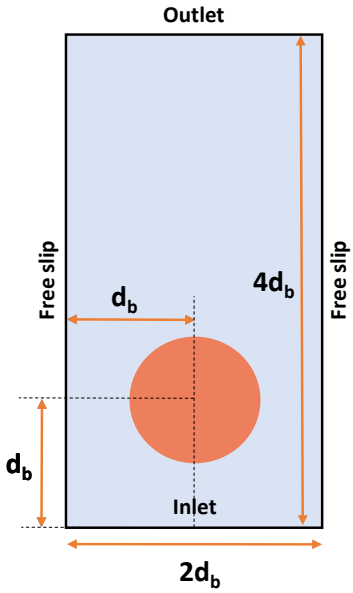

Figure 6.1: *Dimensions and boundary conditions of the simulation domain.*

Regarding the boundary conditions, the inlet was considered in the bottom part where the velocity and pressure of the mixture were set as 0. The top of the domain was considered as the outlet and both sides of the symmetry were set as free slip wall (see **Figure 6.1**).

As the interface of the bubble is tracked, the interface length scale must be smaller than the grid scale (ANSYS FLUENT, 2017). This implies that VOF models necessarily have a fine mesh or a reduced timestep (less than 0.0001 s). Therefore, a structured grid composed of 320×640 cells was developed for all bubble sizes, and the time step was set to 1μs.

6.2.2. Assumptions and parameters of the model

The motion of a single biogas bubble rising driven by buoyancy in an anaerobic sludge matrix is considered with the following assumptions:

1. The anaerobic sludge matrix and the biogas bubble are defined as two separate phases connected by an interface.
2. The fluids in both phases are compressible.
3. The two-phase flow is isothermal.
4. The two-phase flow is initialized with the velocity field set to 0. As the biogas bubble tries to rise, the velocity field is modified from its initial state and becomes laminar.
5. The liquid phase is the anaerobic sludge matrix, and the gas phase is the biogas bubble.
6. The anaerobic sludge matrix is assumed to be a Non-Newtonian fluid (see Section 6.2.4) and the biogas is a Newtonian fluid.

Several simulations were performed to explore the effects of the apparent viscosity of the anaerobic sludge and the bubble size. The disperse phase was defined as a gas mixture with 60% methane and 40% carbon dioxide with 1.213 kg/m^3 density (determined using the volume weighted mixing law) and $1.236 \cdot 10^{-5}$ Pa s viscosity (Herning and Zipperer, 1936).

In the initialization step, the position of the biogas bubble needs to be set by defining the volume fraction of the bubble at its location. The volume fraction of the biogas phase was initialized inside the computational domain by patching the region defined in orange (**Figure 6.1**) and setting the biogas volume fraction equal to 1 in that region.

An important parameter that may be set in VOF models is the surface tension (F_{ST}) between the continuous and disperse phase (ANSYS CFX, 2017). The measurement of the surface tension has encountered different problems in the past, such as the rapid sedimentation of solid particles while measuring. In this case, surface tension was set to 60 mN/m according to literature (Boe et al., 2012; Elmitwalli et al., 2001).

6.2.3. Numerical simulations

The governing equations were discretized using the second-order upwind scheme. The interpolation of the pressure values at the cell faces, by means of the momentum equation, was carried out using the PRESTO (PREssure STaggering Option) scheme and the SIMPLE algorithm was used to obtain the pressure-velocity coupling. The choice of the previous schemes and a segregated solver helped to save computational time and also improved convergence and computation stability. In the implemented VOF method, the momentum equations were solved throughout the domain, and the resulting velocity field was shared among the phases. To track the free surface deformation, the geo-reconstructed scheme was also applied. The transient simulations were run with the first order implicit formulation.

6.2.4. Continuous phase

One of the objectives of the study was to consider the two sludge ages; WAS and AD. Accordingly, WAS and AD with 3.6% TS content were defined as continuous phase, based on the availability of experimental measurements. For the description of the WAS, a three-segment rheological curve was applied with a user-defined function into the CFD code; Herschel-Bulkley (segments 1 and 2) and Ostwald (segment 3) models were applied and fitting parameters described in Wei et al., (2018b) were set for a better description of the sludge (see **Table 6.1**). Nevertheless, AD from the anaerobic digestion of the WAS was sampled and its rheological properties were measured (see **Figure 6.2**). The Herschel-Bulkley model was suitable to fit the experimental results (rheological fitting parameters in **Table 6.1**).

Table 6.1: *Fitting parameters of the rheological model for the waste activated sludge and anaerobic digestate.*

Type of sludge	Use	Rheological Model	Shear rate range	K	n	τ_0
WAS	CFD modelling	Herschel-Bulkley	Segment 1 (0.01 - 0.29 s^{-1})	0,06	-0,83	5,52
		Herschel-Bulkley	Segment 2 (0.29 - 9.6 s^{-1})	1,72	0,74	4,94
		Ostwald	Segment 3 (9.6 - 1000 s^{-1})	7,1	0,32	-
WAS	Section 6.4.5	Herschel-Bulkley	Whole range	4,08	0,39	4,24
AD	CFD modelling and Section 6.4.5	Herschel-Bulkley	Whole range	0.3939	0.5676	0.967

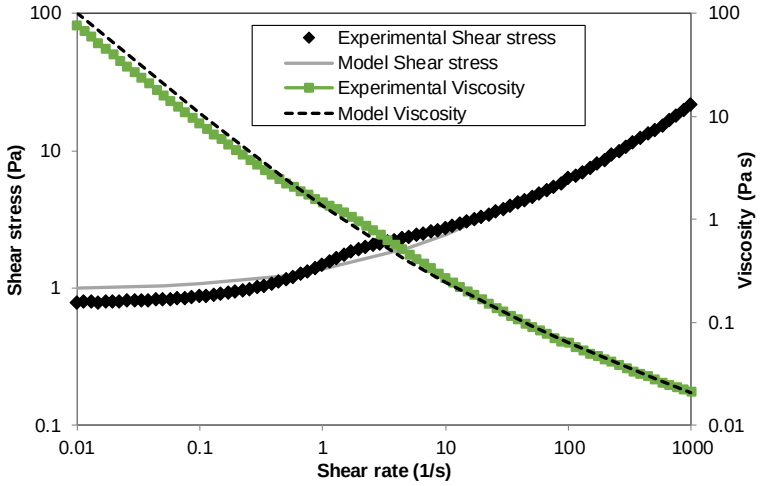

Figure 6.2: *Rheological measurements and Herschel-Bulkley model of the anaerobic digestate.*

To introduce the rheological properties of the continuous phase, user-defined functions (UDFs) are implemented as C functions in ANSYS Fluent solver. UDFs are used to implement 'tailored' user-defined specifications such as material properties and source terms in transport equations. ANSYS Fluent provides DEFINE macros to construct the UDFs and access Fluent solver data. For more details on the implementation of UDFs in ANSYS Fluent, see ANSYS FLUENT, (2017).

A UDF with a DEFINE_PROPERTY macro provided by Fluent was used to describe the three-segment rheological model of the WAS so that, the UDF was set as viscosity in the sludge phase. In this UDF, the shear rate in each cell is accessed with C_STRAIN_RATE_MAG(c, t) function so that the rheological model is switched from one segment to another depending on the shear rate of each cell.

6.3. DRAG COEFFICIENT FOR NON-NEWTONIAN FLUIDS

There are different drag coefficients in literature to calculate the terminal velocity of a bubble. Tomiyama's drag coefficient (Tomiyama et al., 1998) is one of the most famous drag coefficients for single bubbles rising in quiescent fluids. On the one hand, at small bubble sizes, it gives higher terminal velocities than the experimental ones observed by Clift et al., (1978). On the other hand, it is correct for bubble sizes larger than 1mm, so it has been the most widely used drag coefficient for Newtonian fluids.

Nevertheless, Tomiyama's drag coefficient could not be used for Non-Newtonian fluids such as WAS or AD. Accordingly, another correlation is needed for the inclusion of the drag force into numerical simulations in Eulerian-Eulerian or Eulerian-Lagrangian models with shear-thinning Non-Newtonian fluids as is our continuous phase.

Chhabra (1988) conducted an extensive review of drag force studies in

Non-Newtonian fluids. He proposed the following equation:

$$C_D = \frac{24}{Re}\frac{2+3X_E}{3+3X_E}X \qquad 6.1$$

where Re is the Reynolds number, $X_E = \frac{\mu_g}{\mu_l}$ and X is the drag factor. The drag factor has different formulas as listed by Chhabra (Table 6.2 in Chhabra, 2006) for different fluid models.

Similar to Chhabra's studies, different authors have studied the movement of rising bubbles inside power-law Non-Newtonian fluids. These authors agreed on the assumption that the average shear rate over the entire bubble surface is equal to $\frac{U_t}{d_b}$ (Chhabra, 1986; Lali et al., 1989). This statement helps in the calculation of the Reynolds number in Non-Newtonian fluids, which depends on fluid viscosity and terminal velocity. In power-law fluids, this assumption is introduced in the apparent viscosity as:

$$\mu_l = K\left(\frac{U_t}{d_b}\right)^{n-1} \qquad 6.2$$

where K is the fluid consistency index (Pa·s^n) and n is the power law index. Therefore, Reynolds number is expressed as:

$$Re = \frac{\rho_l {d_b}^n {U_t}^{2-n}}{K} \qquad 6.3$$

The terminal velocity of rising bubbles inside 21 different Non-Newtonian polysaccharide solutions was studied in Margaritis et al., (1999). A new drag curve was developed by means of the experimental results: the drag coefficient can be calculated using the modified Hadamard–Rybczynski model by Miyahara and Yamanaka, (1993) for Reynolds numbers below 60 as:

$$C_D = \frac{16}{Re}(1+0.173Re^{0.657}) + \frac{0.413}{1+16300Re^{-1.09}} \qquad 6.4$$

while at Re >60 the drag coefficient was 0.95. The Hadamard-Rybczynski model was also used in Rodrigue et al., (1998). They studied polyacrylamine solutions (power law Non-Newtonian fluids) and proposed to include the physical properties of the non-Newtonian continuous phase, not only in the Reynolds numbers, but also in the drag equation. Thus, their drag coefficient is:

$$C_D = \frac{16}{Re}Y_{(n)} = \frac{16}{Re}\left[2^{n-1}3^{(n-1)/2}\frac{1+7n-5n^2}{n(n+2)}\right] \qquad 6.5$$

n stands for the power-law index and $Y_{(n)}$ stands for a correction function dependent on the power-law index.

For the case of rising bubbles in contaminated Newtonian fluids, the drag coefficient for solid particles developed by Turton and Levenspiel (1986) was adjusted by Karamanev, (1996) as:

$$C_D = \frac{24}{Re}(1 + 0.173Re^{0.657}) + \frac{0.413}{1 + 16300Re^{-1.09}} \quad 6.6$$

while Re<135, and

$$C_D = 0.95 \quad 6.7$$

while Re<135. Then, Mei et al., (1994) studied small clean bubbles and low Reynolds numbers and proposed an empirical drag coefficient to calculate the history force of a spherical bubble:

$$C_D = \frac{24}{Re}\left\{\frac{2}{3} + \left[\frac{12}{Re} + 0.75\left(1 + \frac{3.315}{Re^{\frac{1}{2}}}\right)\right]^{-1}\right\} \quad 6.8$$

Hassan et al., (2008) studied the movement of rising bubbles at a higher Reynolds number in water (Re>1000) and xanthan gum solutions (Re>10) and compared their results with drag coefficients from literature. Their results agreed with previous studies about drag coefficient in water and power-law Non-Newtonian fluids. In this case, the Reynolds number is lower than 10, as the velocity fields of the continuous phase and the disperse phase were set to 0.

Previous articles studied power-law Non-Newtonian fluids but, in this case, biogas bubbles rise inside Herschel-Bulkley Non-Newtonian fluids. Accordingly, the same assumption of Eq. 6.2 is introduced into the apparent viscosity of Herschel-Bulkley fluids as:

$$\mu_a = \frac{\tau_0 + K\left(\frac{U_t}{d_b}\right)^n}{\left(\frac{U_t}{d_b}\right)} = \tau_0\left(\frac{U_t}{d_b}\right)^{-1} + K\left(\frac{U_t}{d_b}\right)^{n-1} \quad 6.9$$

Hence, Reynolds number is expressed as:

$$Re = \frac{\rho_l {U_t}^2}{\tau_0 + K\left(\frac{U_t}{d_b}\right)^n} \quad 6.10$$

According to Chhabra, (1988), a drag coefficient for rising bubbles inside Helschel-Bulkley fluids has not been published so, Ostwald's drag coefficients are applied to Helschel-Bulkley fluids according to Eq. 6.10.

6.4. RESULTS

In this section, the main outcomes of the numerical VOF simulations are reported. Firstly, the problems related to the appearance of spurious currents are outlined. Nevertheless, the model is validated by means of experimental data from literature with Newtonian and Non-Newtonian fluids in Section 6.4.2. Next, the effect of viscosity on shear rate, the shape of the bubble and terminal velocity are analysed. Regarding the terminal velocity of the biogas bubbles, it is obtained and some guidelines about the biogas bubbles behaviour are drawn.

Additionally, terminal velocity with different drag coefficients from literature is compared with the CFD results and the drag coefficients from CFD simulations are obtained in 6.4.5. At the end, the local mixing promoted by the biogas bubbles in the anaerobic sludge matrix is addressed.

6.4.1. Spurious or parasitic currents

The resolution of the VOF method sometimes entails the formation of numerical disturbances due to the treatment of the surface tension force. These numerical errors are known as spurious or parasitic currents, and they are deployed as vortices in the velocity field in the interface region. Spurious currents have been traditionally reported in static bubble modelling with the VOF method (Albadawi et al., 2013; Nichita et al., 2010) and they were also reported at the interface of some bubble sizes in this study (see **Figure 6.3**). The spurious currents induced numerical errors in the velocity field resolution as virtual vortices, so that the terminal velocity obtained disagreed with the general trend of other bubble sizes. The only way to solve spurious currents is to reduce the timestep or the cell size. Accordingly, the computational requirements would greatly increase, so this phenomenon constrained the bubble diameters in this study to 5, 8, 10, 20 and 40 mm in WAS and 1, 2, 3, 5, 8, 10, 20 and 40 mm in AD.

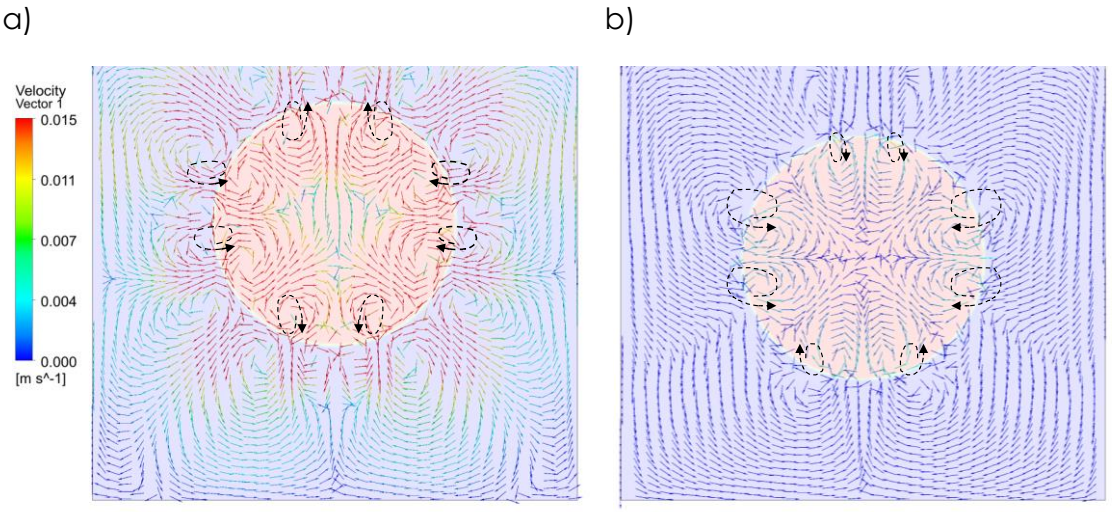

Figure 6.3: *Spurious or parasitic currents at 0.5mm biogas bubble in a) water and b) WAS.*

6.4.2. Validation

As there are no experimental results to validate the results of biogas bubbles and the anaerobic sludge matrix, the CFD results were compared with experimental data found in the literature with Newtonian and Non-Newtonian fluids as a continuous phase. The CFD results were compared with experimental results from Margaritis et al., (1999) and Clift for CMC solutions and water, respectively. For validation of the results, different solutions of CMC (1.48% and

0.374% concentration) and water were used as continuous phase and air bubbles were set as discrete phase. Additionally, different bubble sizes (and, as consequence, different dimensions of the geometry) were modelled with CMC 1.48% as continuous phase. The mesh was 320×640 cells, as in the anaerobic sludge matrix CFD model.

To validate the CFD model, the terminal velocity for different bubble volumes was calculated through CFD results and compared with experimental results. **Figure 6.4** shows the experimental and CFD terminal velocity in the different solutions of CMC and water. On the one hand, the terminal velocity in the CFD model was slightly lower than the experimental results with CMC 1.48% as continuous phase in the different bubble sizes. Conversely, the CFD terminal velocity greatly agreed with the experimental one with water and CMC 0.374% as primary phases. On the other hand, no spurious currents were found in either water or CMC, as the apparent viscosity of these continuous phase was lower than that of the anaerobic sludge matrix. In conclusion, the CFD results mostly agreed with the experimental results for different bubble sizes, so that this geometry and mesh could be used with the anaerobic sludge matrix as the primary phase.

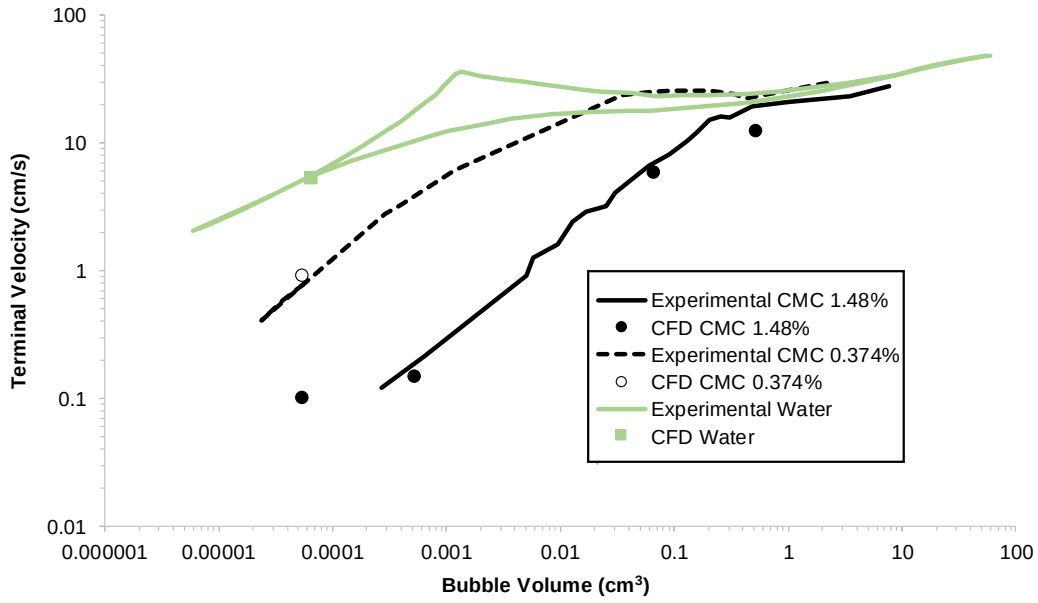

Figure 6.4: *Terminal velocity comparison for different bubble sizes between experimental and CFD results in water and in different CMC solutions.*

6.4.3. Effects of viscosity on biogas bubbles

As anaerobic sludge is a Non-Newtonian fluid, the comprehension of the shear rate and apparent viscosity is outstanding. Firstly, **Figure 6.5** depicts the apparent viscosity and shear stress as a function of the shear rate in both

anaerobic sludges studied (**Figure 6.2** only depicted the AD). Note that the apparent viscosity and shear stress in WAS were always higher than in AD, which is in agreement with the outcomes of Monteiro, (1997).

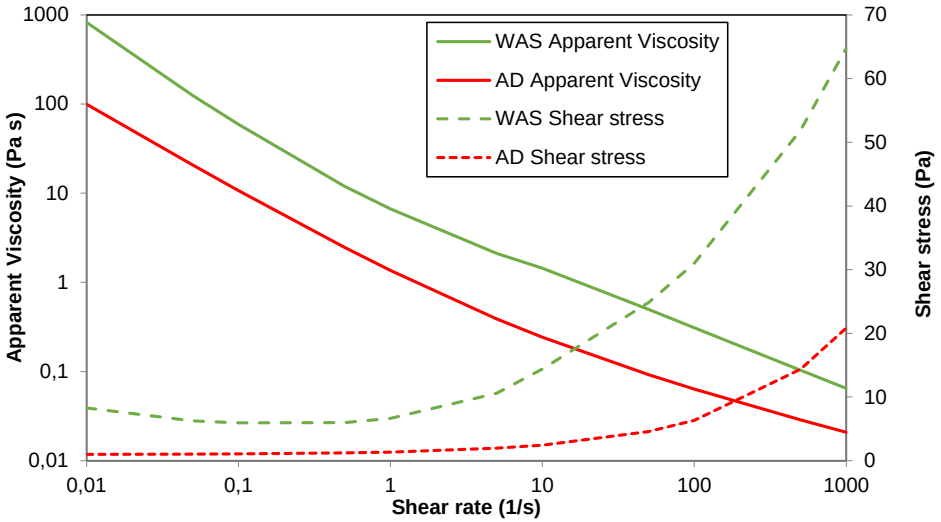

Figure 6.5: *Apparent viscosity and shear stress as function of shear rate in WAS and AD.*

Shear rate and apparent viscosity are shown for the numerical simulations at 0.1 s in **Figure 6.6** for WAS and in **Figure 6.7** for AD.

On the one hand, it is remarkable that for the same bubble size the shear rate was higher in AD (see **Figure 6.7**) than in WAS (see **Figure 6.6**) and, on the contrary, the apparent viscosity was higher in WAS than in AD. This trend stemmed from the rheological models of each type of sludge as pointed out in **Figure 6.5**. Regarding the time evolution of these fields from zero to 0.1s, the same pattern was observed in all simulations: the bubble interface increased the shear rate in the matrix around it, as the biogas bubble started moving upwards, so subsequently, the apparent viscosity around the bubble interface decreased. Furthermore, the bubble size affected the hydrodynamics of the bubble: the bigger the bubble, the higher the flotation force, and, accordingly, the greater the shear rate increase and the greater apparent viscosity decrease. In summary, this hydrodynamic behaviour in the full-scale anaerobic digester would entail that, anaerobic digesters with higher SRTs (AD) would experience higher shear stress and lower apparent viscosity.

On the other hand, the bubble shape of the rising biogas bubbles was studied. Different literature works have clearly stated experimentally that an air bubble cannot maintain its spherical shape during its ascendant movement in water (Clift et al., 1978). Accordingly, the numerical simulations performed in this study shown that the biogas bubbles face the same phenomena (see **Figure 6.6** and **Figure 6.7**): In both anaerobic sludge matrices, the spherical shape was maintained at small diameters, but this shape changed from spherical to other shapes at 20 mm and 5 mm bubble diameter in WAS and AD, respectively.

Moreover, the bubble shape changed to a cap shape in WAS, whereas in AD the shape of the bubble could be ellipsoidal (5 mm and 8 mm diameter), ellipsoidal-cap (10 mm diameter) and skirted (20 mm and 40 mm diameter).

As for the case of bubbles with free rise velocity, common correlations for bubble shapes inside Newtonian fluids have been obtained, such as Clift et al., (1978), but new correlations might be needed for Non-Newtonian fluids experimentally. Additionally, many more bubble shapes have been described in Non-Newtonian fluids than in Newtonian fluids (Chhabra, 2006). In practice, it has been shown that the spherical shape is maintained in Non-Newtonian fluids at low Reynolds numbers owing to surface tension forces (Chhabra, 1988). At higher Reynolds numbers, the spherical shape can change to different shapes such as prolate-tear, oblate and cusped. Hence, further research is needed to study experimentally the evolution of bubble shape inside anaerobic sludge.

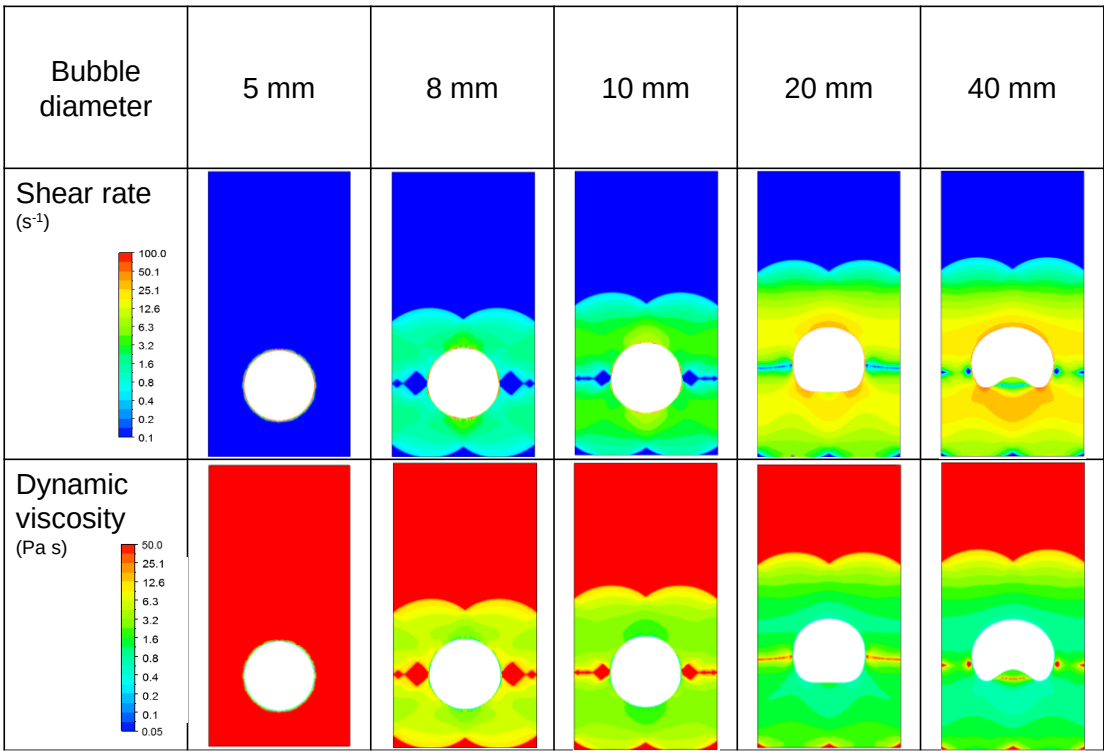

Figure 6.6: *Shear rate and Dynamic viscosity for different bubble sizes at 0.1s in WAS.*

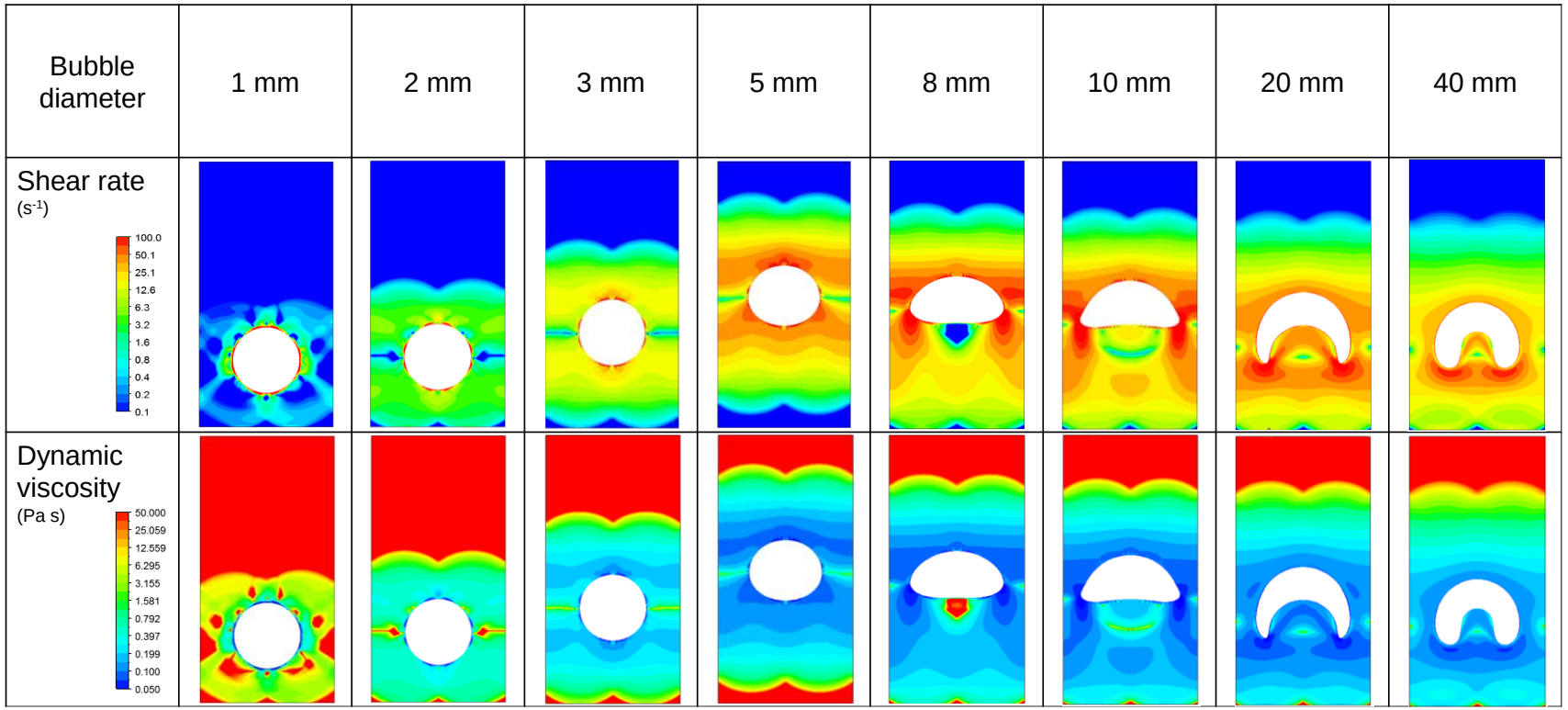

Figure 6.7: *Shear rate and Dynamic viscosity for different bubble sizes at 0.1s in AD.*

6.4.4. Terminal velocity of biogas bubbles

The CFD results enabled the calculation of terminal velocities for different biogas bubble sizes at WAS and AD. In this sense, **Figure 6.8** compares the obtained results with Tomiyama's terminal velocity curve, which is a characteristic terminal velocity correlation in water, as a representative Newtonian fluid (Tomiyama et al., 1998). The behaviour was significantly different between sludge and water as the terminal velocity of bubbles in water was higher than the bubbles' velocity in sludge. As shown in **Figure 6.8**, the type of sludge type was also important on the terminal velocity's magnitude as it is two orders of magnitude lower in WAS compared to water. This trend stood for the necessity of specific CFD drag models with anaerobic sludge and biogas.

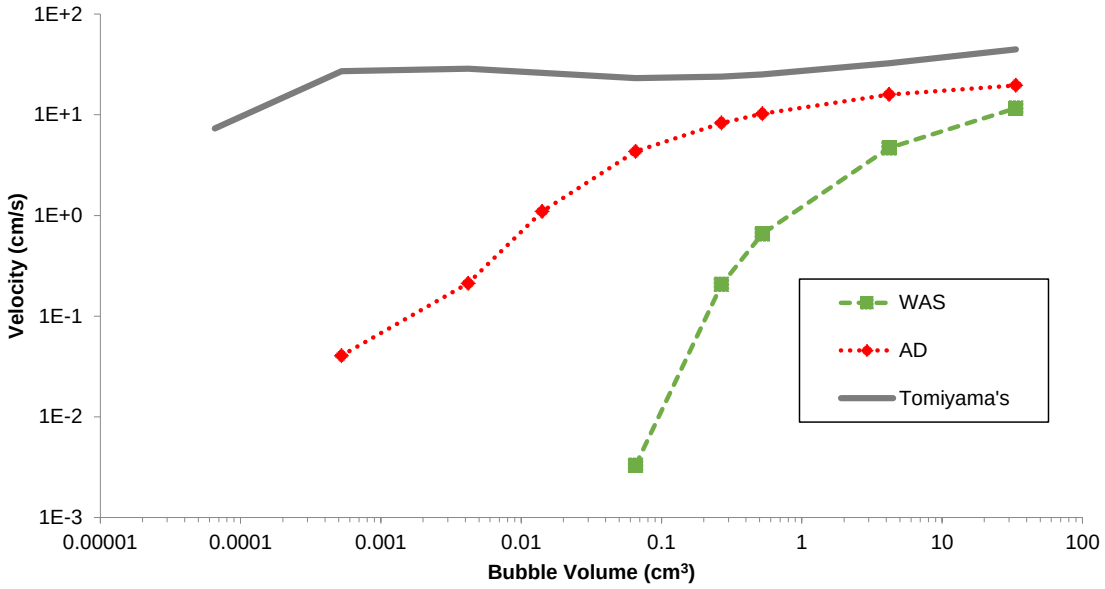

Figure 6.8: *Terminal velocity of single biogas bubble as function of bubble volume in WAS and AD and water with Tomiyama's drag coefficient.*

Attending to terminal velocity in anaerobic sludge, different trends were noticeable for each type of anaerobic sludge. On the one hand, there was a critical bubble volume in WAS located at 0.27 cm^3 (<8 mm biogas bubble diameter) in which the terminal velocity decreased rapidly to values below 0.01 cm/s. In contrast, bubbles above the critical bubble volume suffered from an increase in their terminal velocity and they moved faster at velocities higher than 0.2 cm/s. On the other hand, the critical bubble volume could be neglected in AD, as the terminal velocity increase was not as sharp as in WAS.

The critical bubble volume has been observed in experimental studies as a step in the terminal velocity, so it has been called bubble volume-terminal velocity curve discontinuity. It has been reported in Non-Newtonian fluids by

different authors (Acharya et al., 1977; Astarita and Apuzzo, 1965; Rodrigue et al., 1998), while others have found no discontinuity (Margaritis et al., 1999; Miyahara and Yamanaka, 1993). Generally, the conditions under which the discontinuity in the free rise velocity is produced have not been clarified, but bubble diameter and the physical properties of the continuous phase were the main factors controlling it. Thus, it has been thought that the discontinuity arises from the shift in the bubble behaviour from solid-like to the shear-free condition (Chhabra, 1988; Kulkarni and Joshi, 2005).

In short, the numerical simulation results agreed with experimental works with Non-Newtonian fluids in literature. In AD, bubbles with less than 0.0042 cm^3 of biogas bubble volume (<2 mm bubble diameter) had a terminal velocity smaller than 0.1 cm/s. Higher terminal velocity in AD could derive from its smaller apparent viscosity in comparison to the apparent viscosity of WAS. Attending to these results, small bubbles would remain almost stagnant inside the sludge mixture (with less than 1 cm/s upward velocity), i.e. they would remain trapped. Subsequently, if the big bubbles tended to move upwards rapidly, they would coalesce with the smaller bubbles that remained entrapped or had a low terminal velocity. This bubble behaviour would mean that the small bubbles trapped in the sludge or with small velocities could be the sink for methane, carbon dioxide and hydrogen produced during the anaerobic digestion process. Accordingly, these compounds would be transferred from the liquid phase to the small bubbles, which would increase in volume and terminal velocity until they were detached and released from the liquid phase.

Besides that, the apparent viscosity was also responsible for the time evolution of the terminal velocity. Thus, CFD modelling revealed that larger biogas bubbles faced a progressively increasing terminal velocity over time (see some examples in **Figure 6.9**): in the case of WAS, the gradually increasing velocity was shown from 8 mm biogas bubbles, while in AD the gradual increase was faced even in 2 mm biogas bubbles. This difference between the two sludge types was another consequence of the higher viscosity of WAS at low shear rates compared with AD.

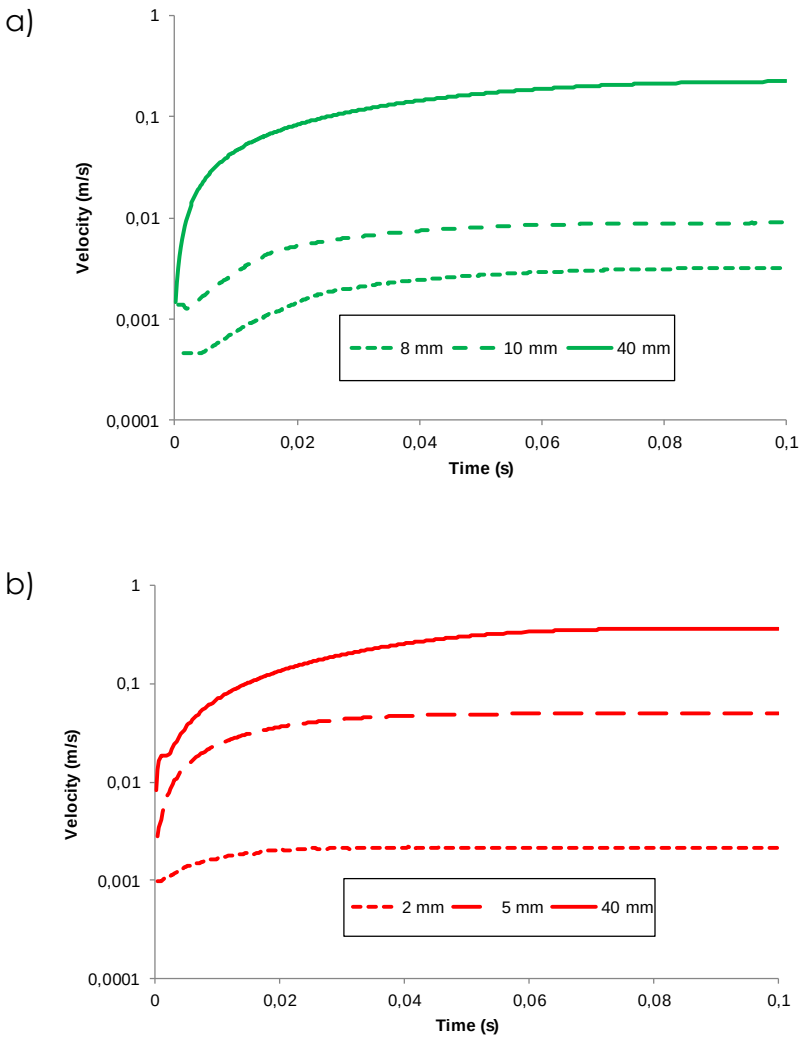

Figure 6.9: *Evolution of bubble velocity in a) WAS and b) AD for different bubble sizes.*

Accordingly, the time evolution of the terminal velocity could be described by the following steps. Firstly, the initial velocity of the bubble increased the shear rate of the anaerobic sludge matrix. The rheology of the anaerobic sludge determined that a higher shear rate led to a decrease in the apparent viscosity. Thus, the decrease in apparent viscosity enhanced the terminal velocity of the biogas bubble. And the loop was started again with greater terminal velocity than the initial one which increased the shear rate of the anaerobic sludge matrix. This effect in Non-Newtonian fluids was in agreement with experimental and numerical results reported in literature (Premlata et al., 2017; Zhang et al., 2010). In an anaerobic digester, this phenomenon would mean that biogas bubbles in the upper part of digesters would experience higher terminal velocities than the bubbles at the bottom. Hence, higher turbulence and lower apparent viscosity would also be shown in the upper part.

6.4.5. Calculation of drag coefficient for anaerobic sludge

Terminal velocity of rising biogas bubbles is intimately related to the drag force, so terminal velocity could be used to find a drag coefficient that fitted the behaviour of biogas bubbles inside an anaerobic sludge matrix. Hence, the theoretical terminal velocity with the drag coefficients presented in Section 6.3 was calculated iteratively by means of Eqs. 6.4-to 6.8 (hereafter, these correlations will be referred as literature models). To do so, the Reynolds Number for Herschel-Bulkley Non-Newtonian fluids proposed in Eq. 6.10 and the fitting parameters from **Table 6.1** were used. Additionally, the terminal velocity of the biogas bubbles obtained through the CFD simulations was compared with the terminal velocity obtained from the literature models. Thus, **Figure 6.10** depicts the terminal velocity of the literature models in greyscale marks and the terminal velocity of the CFD models in green (WAS) and red (AD).

From this figure, note that there was no drag model that fitted both types of anaerobic sludge for different bubble sizes. In the case of WAS, the Karamanev (1996) drag coefficient presented the best fit for bubbles higher than 1 cm^3 although, the drag coefficient of Mei et al., (1994) fitted better for smaller bubbles. For AD, the Karamanev, (1996) drag coefficient presented the best fit for most of the bubble sizes although at the smallest bubble size it gave the worst approximation. In the case of AD and bubbles smaller than 0.05 cm^3, the coefficients of Mei et al., (1994) or Margaritis et al., (1999) would be the best drag coefficient. Consequently, the drag coefficient should be carefully chosen attending to the bubble size that it is going to be modelled in the CFD simulation.

In addition, the drag coefficient could be calculated by means of the terminal velocity obtained from the CFD simulations. The drag coefficient (C_D) has been always presented as a function of the Reynolds Number in drag coefficient studies, so **Figure 6.11** represents this link. Note that most of the points were located in the same area, but an outlier point corresponding to the 0.065 cm^3 bubble size in WAS was clearly shown. Nevertheless, the other bubble sizes were in the same area showing a "jockey stick" shape which was in agreement with other works studying air bubbles and Non-Newtonian fluids (Margaritis et al., 1999; Sun et al., 2015). The points of the "jockey stick" could be fitted to a fifth-degree polynomial as the following equation, so this drag coefficient could be used in different mathematical models or set in two-phase CFD models.

$$C_D = 10^{0.008\times(\log(Re))^5+0.0566\times(\log(Re))^4+0.1198\times(\log(Re))^3+0.0925\times(\log(Re))^2-0.8129\times\log(Re)+1.5629} \quad 6.11$$

a)

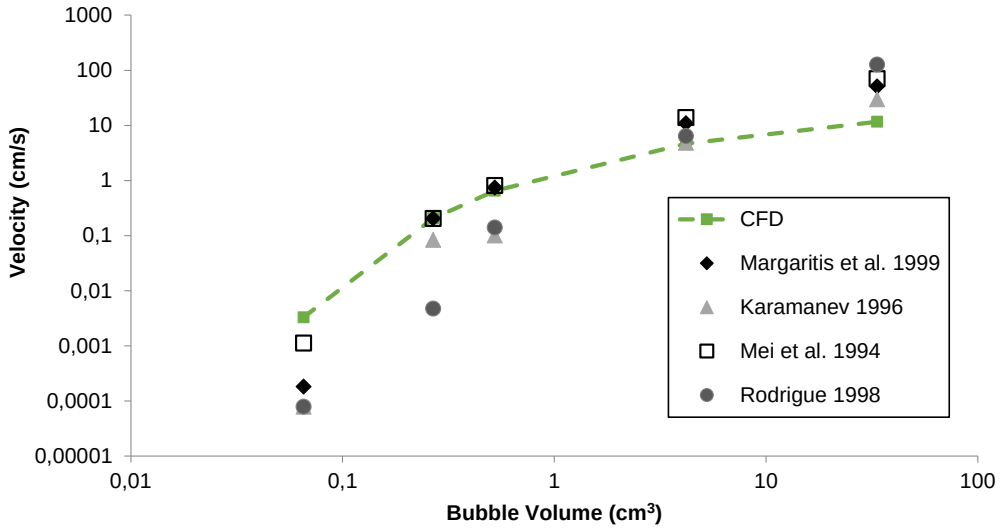

b)

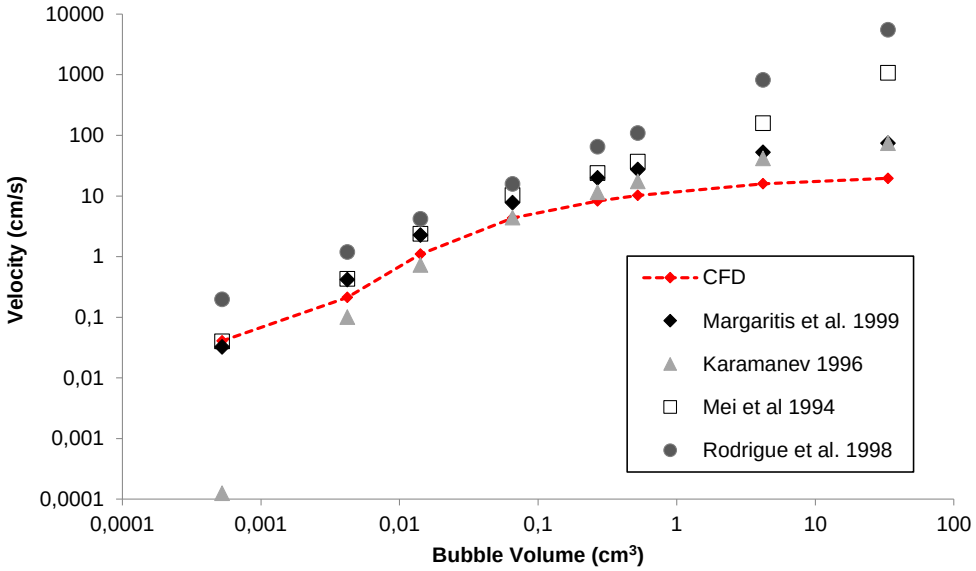

Figure 6.10: *Comparison of terminal velocities obtained with CFD simulations and drag coefficients from bibliography for a) WAS and b) AD.*

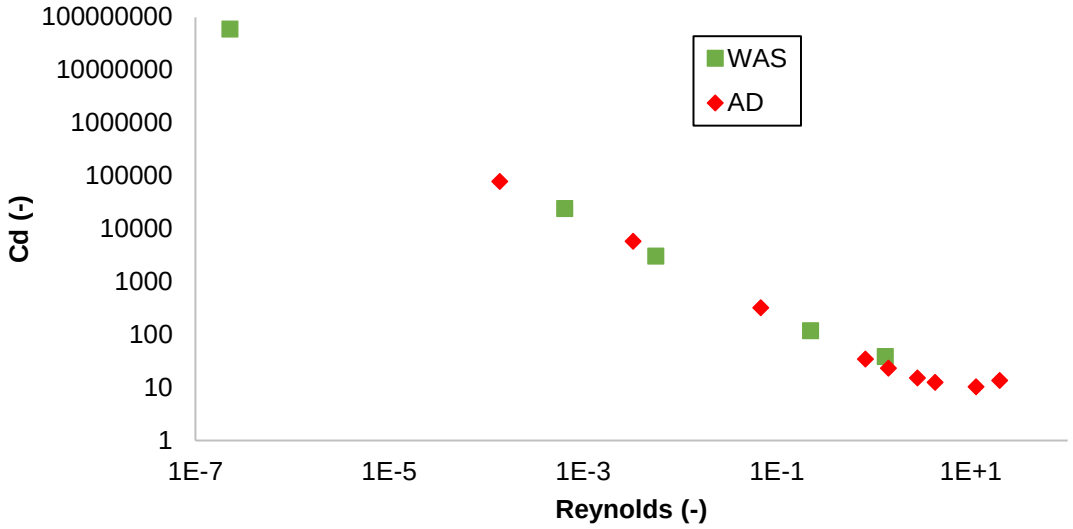

Figure 6.11: *Relationship between drag coefficient and Reynolds number for both sludge.*

6.4.6. Local mixing in an anaerobic sludge matrix

As mention before, mixing inside anaerobic digesters is a relevant issue to consider on their design. Different design parameters for anaerobic digesters has been suggested in literature such as Unit Power (UP) or Mixing Energy Level (MEL), Unit Gas Flow (UGF) or RMS Velocity Gradient (G) (Tchobanoglous et al., 2004; US EPA, 1979) (see Chapter 3). Thus, the Global Velocity Gradient (G) has been widely used on the design of different water and wastewater applications such as flocculators or biological reactors to measure the mixing degree within a tank. This parameter was defined theoretically by Camp and Stein (1943) and it has been agreed by different authors as:

$$G = \sqrt{2\left[\left(\frac{\partial u}{\partial x}\right)^2 + \left(\frac{\partial v}{\partial y}\right)^2 + \left(\frac{\partial w}{\partial z}\right)^2\right] + \left(\frac{\partial u}{\partial y} + \frac{\partial v}{\partial x}\right)^2 + \left(\frac{\partial u}{\partial z} + \frac{\partial w}{\partial x}\right)^2 + \left(\frac{\partial v}{\partial z} + \frac{\partial w}{\partial y}\right)^2} \qquad 6.12$$

where u, v and w are the velocity components in the x, y and z directions of a Cartesian coordinate system. In this case, it has been computed for each simulation in order to assess the local mixing that a single biogas bubble can produce in its surroundings as it moves towards the free surface. The area averaged value of the Velocity Gradient for each bubble size is compared in **Figure 6.12**.

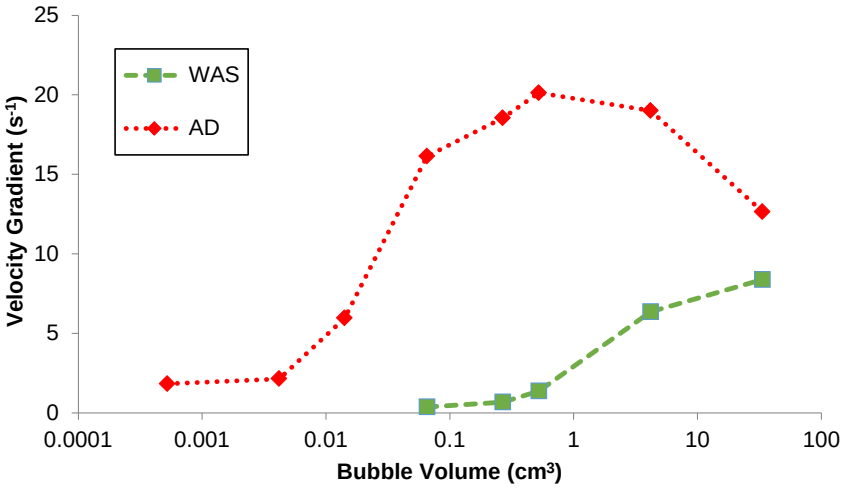

Figure 6.12: *Measurement of mean velocity Gradient in each biogas bubble volume*

Attending to this parameter, an increase in the Velocity Gradient was achieved with increasing bubble volume. The Velocity Gradients obtained in WAS were smaller than in AD for the same bubble size as result of its higher apparent viscosity. Referring to WAS, the bubble size with the highest local mixing was the bubble volume higher than 10 cm^3 (40 mm bubble diameter). In the AD, the Velocity Gradient increased until its maximum at 0.5 cm^3 (10 mm bubble diameter) and, afterwards, it decreased at larger bubble size. This behaviour could be related to different parameters such as bubble shape (see **Figure 6.6** and **Figure 6.7**). When the biogas bubble changed its shape from spherical to another shape, i.e. at 8 cm^3 in WAS and at 0.065 cm^3 in AD, the local mixing was significantly increased. Therefore, the shape that produced the maximum local mixing was the cap shape in both types of sludge.

The great utility of the Velocity Gradient in the design of different process units of a WWTP has been previously mentioned. The suggested design values for the RMS Velocity Gradient in anaerobic digesters ranges from 50 to 85 s^{-1} (US EPA, 1987). Comparing this threshold with the values obtained in the numerical simulations, bubbles larger than 8 cm^3 (20 mm bubble diameter) in WAS and larger than 0.01 cm^3 (3 mm bubble diameter) in AD could produce more than 10% of the design value by themselves. In fact, bubble volumes higher than 0.065 cm^3 (5 mm bubble diameter) in AD were producing between 30 and 40% of the suggested mixing. Accordingly, it was noticed that single biogas bubbles could produce a local mixing close to the design mixing values by themselves. Additionally, in Section 3.4.2.3, it was shown that RMS Velocity Gradients below 50 s^{-1} could ensure good mixing inside anaerobic digesters, so that biogas bubbles mixing could be enough in some setups. Furthermore, Sindall et al., (2013) proposed a threshold between 7.2 to 9.7 s^{-1} for the Velocity Gradient in lab-scale anaerobic digesters, as their research shown a better biogas production at these values (Sindall et al., 2013). Attending this threshold, the biogas bubbles would

produce enough mixing, and, at some point, exceed the Velocity Gradient of 9.7 s^{-1}.

Moreover, when biogas is produced inside anaerobic digesters, the biogas bubbles are not alone, so they suffer different phenomena such as break-up and coalescence with other biogas bubbles. Hence, these phenomena would modify the apparent viscosity and the shape of the bubbles and could lead to an increase in local mixing within the tank by means of biogas production. For instance, as there is more shear rate around big bubbles and on the wake of rising bubbles, the apparent viscosity would decrease, and more mixing would be produced. As a result, biogas production would be expected to produce higher Velocity Gradients than those presented in **Figure 6.12**. Accordingly, at a maximum biogas production rate, a Velocity Gradient close to 50 s^{-1} can be achieved without any additional mixing system. Nevertheless, different experiments on biogas production, biogas bubble size and velocity field measurement are needed to support this conclusion.

6.5. CONCLUSIONS

Through this study, the need for experimental studies of the biogas production inside the anaerobic sludge matrix comprising the size, shape and evolution of the biogas bubbles and the continuous phase velocity field inside the tank is stated. These measurements would help in the calculation of the real drag coefficient and the development of complex CFD models by means of the terminal velocity of biogas bubbles. Until these experiments are done, the CFD models developed in this work can help to establish some guidelines about the hydrodynamics of biogas production.

Different VOF numerical simulations with an anaerobic sludge matrix have been developed with rising biogas bubbles as a discontinuous phase. Biogas bubble size and the type of anaerobic sludge have been changed in these numerical simulations. The apparent viscosity of the WAS was higher than that of the AD, entailing different outcomes in terms of bubble shape and shear rate. For example, biogas bubbles in AD experience a wider range of shapes. Additionally, higher shear stress would be experienced in anaerobic digesters with higher SRT stemming from the lower apparent viscosity of the AD.

Regarding terminal velocity, the terminal velocity of the biogas bubbles in the AD matrix experienced greater velocity than WAS. Furthermore, the terminal velocity has indicated that big bubbles move upwards rapidly, so they would coalesce with smaller ones on their way to the biogas chamber. Nevertheless, small bubbles would remain static or with lower terminal velocity, and they would coalesce and grow by the mass transfer of methane, carbon dioxide and hydrogen from the liquid phase.

Referring to the drag model, this study confirms that drag coefficients from literature for power law fluids cannot be applied to Herschel-Bulkley Non-

Newtonian fluids, as these coefficients did not fit the CFD results. In this case, although it seems that some approximations might be possible, there is still no unique formulation that allows you to obtain the C_D based only on the coefficients of the Non-Newtonian model. Additionally, a new drag coefficient equation by means of CFD terminal velocity was proposed to set the proper drag coefficient in two-phase flow CFD models. Nonetheless, further research is needed to establish its general application to any pair of Non-Newtonian fluids, bubbles or droplets.

To conclude, this study provided some insights about the local mixing that biogas bubbles provide to the anaerobic digesters' content. The local RMS Velocity Gradient at different bubble sizes and the anaerobic sludge matrix was measured and it has been shown that biogas bubbles provide local mixing close to the threshold established in anaerobic digester design, i.e. between 30 to 40% of 50 s^{-1}.

7. GENERAL CONCLUSIONS AND FUTURE WORK

This chapter is devoted to describing the general conclusions of this thesis and outlining future work.

7.1. GENERAL CONCLUSIONS

This PhD thesis was focused on gaining more knowledge about different phenomena occurring in anaerobic digestion through computational fluid dynamics (CFD) techniques. The phenomena studied in this work were settling and mixing in chapter 3, transport of substances and reactions in chapters 4 and 5 and biogas production mixing in chapter 6. To achieve this general objective, a new CFD solver and different CFD models were developed and assessed considering experimental data from lab-scale and full-scale setups.

This thesis continues the research line of CFD modelling in anaerobic digesters started a decade ago, but it also opens new research lines, i.e. validation of full-scale CFD models, biochemical CFD modelling in anaerobic digesters, study of mixing regimes in full-scale anaerobic digesters and biogas mixing. Indeed, it continues the research line of the Multiphase Flow Research Group of the Universitat Jaume I on CFD modelling in environmental engineering.

In general, the specific objectives were fulfilled but it is necessary to group the conclusions in different topics: mixing in full-scale anaerobic digesters, dead volumes in anaerobic digesters, anaerobic digestion biochemical modelling and biogas bubbles rising inside the anaerobic sludge matrix.

7.1.1. Mixing in full-scale anaerobic digesters

The conclusions related to mixing in full-scale anaerobic digesters arising from Chapter 3 are:

- The recirculation system (DYNOMIX) and a 3-blades propeller were examined through Non-Newtonian single-phase CFD scenarios successfully.
- A compartmentalised structure was drawn with 3 regions: CORE, DYNOMIX and TF, studying the velocity field in the base scenario. Additionally, the hydrodynamics of these regions were defined according to circumferential velocity. The same methodology would be used to describe compartmental models in other anaerobic digesters' CFD models.
- The design parameters, i.e. DVTT, HRT, UP, and G, were evaluated taking into account the experimental tracer test and operational data, such as flows and energy demands. As other authors stated, their thresholds need to be revised to accurately and correctly calculate the energy required to achieve complete digester mixing.
- It has been proven that local mixing parameters establish the mixing degree and mixing type of each region. Thus, they were very helpful in describing the behaviour of the mixture in the different mixing scenarios

and marked compartments.

- The use of virtual tracers in CFD models has been shown to be of great help in the evaluation of global mixing parameters. The most commonly used global parameter is the UI, but the second-order moments was also proposed as a global parameter. Both global parameters were applied to the full-scale anaerobic digester scenarios where they proved to be useful in defining the homogenisation time.
- The homogenisation time shown by both parameters was very similar but, the second order unveiled details about the geometrical local mixing that were not possible to obtain through the UI. Thus, the second order moments were found to be more robust and simpler than the UI.
- The obtained homogenisation times should be used in planning the operation of anaerobic digesters for rapid dilution of cosubstrates and inhibiting compounds in this full-scale digester, but also in other CFD models.
- Intermittent mixing can reduce the energy consumption of mixing in anaerobic digesters and, here, its application in full-scale anaerobic digesters has been tested. Attending to this author's results, the use of this mixing regime in full-scale anaerobic digesters is encouraged.
- The momentum source of propellers was found to be valuable for increasing the velocity in poor mixed areas and more effective than increasing the recirculation flow. In this sense, if intermittent mixing is applied, the use of the propeller is highly recommended to avoid dead volumes.
- if it is decided to reduce the recirculation flow rate, the propeller mixing time should be increased, so that the following mixing scheme is applied: daily changes of the mixing regime with long periods of low recirculation flow (low mixing intensity) and short periods of propeller mixing (high mixing intensity).
- Accordingly, CFD modelling was a robust tool for examining hydraulic performance in full-scale anaerobic digesters.

7.1.2. Dead volumes in anaerobic digesters

The conclusions related to dead volumes in anaerobic digesters arising from Chapter 3 are as follows:

- Dead volume criteria from the literature have been evaluated in terms of usability and sensitivity in full-scale anaerobic digesters and compared with experimental measurements in full-scale anaerobic digesters. None of the criteria met the experimental dead volume and therefore lack generality. Additionally, most of them showed poor sensitivity, but Vesvikar and Al-Dahhan, (2005) criterion exposed a great sensitivity in displaying

dead volumes in the different scenarios.

- Two different dead volume criteria, i.e. Exponential Decay PDF and Gaussian PDF, were proposed and calibrated unveiling the experimental dead volume. These criteria considered the buoyancy force and low turbulence dispersion showing great sensitivity to different mixing scenarios. These new criteria would help in finding energy-efficient mixing regimes that avoid the formation of dead volumes.
- Dead volumes, from the hydrodynamic point of view, are isolated areas with low velocity in which the fluid cannot move and flows slowly and were extensively studied in chapter 3. From a biological activity point of view, dead volumes do not have biological activity. As observed in chapter 6, volumes with methanogenic activity were mixed by biogas bubbles, so the theoretical dead volumes would not be real dead volumes, if there was methanogenic activity from any point of view either.

7.1.3. Anaerobic digestion biochemical modelling

The conclusions related to anaerobic digestion biochemical modelling arising from Chapters 4 and 5 are:

- A new CFD solver coupling ADM1 to a single-phase CFD model, *ADM1Foam*, has been developed. The solver was tested and validated with experimental data and a 0D-CSTR model in a lab-scale setup. The 0D-CSTR model results and the *ADM1Foam* results agreed, so the new solver was successfully validated.
- After checking that the implementation of ADM1 in the solver was correct, the *ADM1Foam* has been implemented in an additional scenario with low mixing. This was done with the aim of estimating the impact of mixing on anaerobic digestion performance. The results revealed that less mixing would lead to lower acid production, so less biogas would be produced. Nonetheless, this statement would need to be tested against experimental data.
- The new solver was applied to the full-scale anaerobic digester from chapter 3 in three different mixing scenarios: the base scenario, the base scenario with 50% mixing and the base scenario without mixing. A 24-hour calculation was done to evaluate the impact of mixing on organic material degradation, methanogenesis and homogenisation. This proved that *ADM1Foam* can also be applied to full-scale anaerobic digester CFD models.
- The results in the full-scale mixing scenarios shown that the scenario without mixing was hampered and revealed less degradation and methanogenesis due to low content homogenisation. The base scenario and the 50% mixing scenario showed similar degradations and

methanogenesis, so both scenarios could be applied to produce a similar biogas flow. Hence, our knowledge about the relationship between mixing and organic material degradation in anaerobic digestion has been extended and the *ADM1Foam* solver is a powerful tool for studying the impact of mixing on the anaerobic digestion process.

- The methodology with 0D-CSTR models and *ADM1Foam* solver would be considered to simulate new anaerobic digesters designs where short periods of ADM modelling are enough to test their anaerobic digestion proficiency.
- The *ADM1Foam* results have affirmed that mixing is important to achieve good sludge homogenisation and thus sludge stabilisation. On the other hand, in the homogenisation and dilution process, the importance of hydrodynamic phenomena versus biological processes has been shown by calculating the TC, where hydrodynamic phenomena showed greater influence in the homogenisation process.

7.1.4. Biogas bubbles rising inside anaerobic sludge matrix

The conclusions related to biogas bubbles rising inside the anaerobic sludge matrix obtained in Chapter 6 are as follows:

- The terminal velocity, size and shape of biogas bubbles have been assessed by means of VOF modelling with different bubble size and two types of sludge, waste activated sludge (raw sludge that enters anaerobic digesters) and anaerobic digestate (stabilized sludge extracted from anaerobic digesters).
- Biogas bubbles inside the waste activated sludge had a lower terminal velocity and a smaller variety of shapes than those in the anaerobic digestate matrix. Furthermore, it was found that the larger the bubble size, the higher the upward velocity, so that smaller bubbles would be trapped in the sludge matrix and absorbed by large, rapidly ascending bubbles.
- The power-law drag coefficients found in literature were calculated and compared against the CFD results showing strong deviations from the simulation results. The results stated that these coefficients cannot be generally used in two-phase CFD models with the only information provided by the Herschel-Bulkley model. Instead, every non-Newtonian fluid must be accounted by its own drag correlation with the current formalism.
- Basing on the CFD results, a new drag coefficient equation has been obtained to be applied specifically in two-phase CFD models with biogas bubbles in anaerobic digesters.
- The mixing capacity of biogas production in anaerobic digestion has been calculated with two-phase VOF CFD models in terms of local RMS

Velocity Gradient. The results showed that new biogas bubbles generate significant local mixing that must be taken into account in the CFD models. In addition, new biogas bubbles generated in methanogenesis should be taken into account as an additional mixing input in the design of anaerobic digesters.

7.2. FUTURE WORK

The following list enumerates potential research lines that could be pursued in the short and long term to benefit anaerobic digestion performance and CFD modelling:

The biogas produced inside the anaerobic digester has never been evaluated experimentally inside anaerobic digesters, so deeper research and understanding of the formation of the gas phase in anaerobic digesters is needed. Additionally, it would also be essential for the development and validation of multiphase models in CFD.

Some of these aspects and other experimental tasks to gain knowledge of anaerobic digestion include:

- To conduct tracer tests by planning for more sampling at initial times. Furthermore, the concentration should be analysed not only at the anaerobic digester outlet, but also at different sampling points or recirculation streams (heating outlet or inlet, sludge recirculation streams, etc.) to help define an experimental homogenisation time.
- To conduct intermittent mixing in full-scale anaerobic digesters to test new efficient mixing regimes that ensure the same biogas production and avoid the formation of dead volumes.
- To study the variability and sensitivity of biokinetic parameters from ADM1 with different mixing degrees so as to link them to hydrodynamics.
- To measure different biogas formation properties:
    - The overall biogas production of anaerobic digesters
    - The study of the birth of biogas bubbles from the liquid phase and their growth. To track the size of the biogas bubbles from birth until they reach the free surface and the pressure impact on their size.
    - The shape of these biogas bubbles at the beginning and at their trajectory to the free surface.
    - The distribution of biogas formation within the anaerobic digester or the production of biogas locally within the digester.
    - The biogas composition locally at different locations and heights.

  Concerning the multiphase Euler-Euler models in anaerobic digestion:

- To introduce the generation, distribution and transport of biogas in these

models.

- To analyse the phase transfer through the bubble membrane from the liquid phase to the gas phase and from the gas phase to the liquid phase.
- To introduce the free-surface model to better control what happens at the surface when the gas phase rises.
- To introduce gas dissolution with depth.
- To introduce a third solid phase or granular phase for the study of granular anaerobic reactors, e.g. UASB or EGSB.
- To introduce models to consider the solid-liquid phases interactions so as to study the aggregation of the solid phase to produce dead volumes and the impact of agitation on dead volume growth or elimination processes.

Regarding the following CFD anaerobic digestion models, these tasks should be taken into account:

- To develop future models with different biological processes, algebraic algorithms or additional fluid phases which would be the next CFD generation models.
- To introduce gas phase formation from hydrogen, methane and carbon dioxide dissolved in the liquid phase.
- To develop new, simpler biological models that can reduce the computational time of the ADM1Foam solver.
- To define a methodology to create compartmental models that help with the biological modelling of anaerobic digestion.

REFERENCES

Acharya, A., Mashelkar, R.A., Ulbrecht, J., 1977. Mechanics of bubble motion and deformation in non-newtonian media. Chem. Eng. Sci. 32, 863–872.

Albadawi, A., Donoghue, D.B., Robinson, A.J., Murray, D.B., Delauré, Y.M.C., 2013. Influence of surface tension implementation in Volume of Fluid and coupled Volume of Fluid with Level Set methods for bubble growth and detachment. Int. J. Multiph. Flow 53, 11–28.

Alvarado, A., Vedantam, S., Goethals, P., Nopens, I., 2012. A compartmental model to describe hydraulics in a full-scale waste stabilization pond. Water Res. 46, 521–530.

ANSYS CFX, 2017. User Manual, Release 17.2.

ANSYS FLUENT, 2017. User Manual, Release 17.1.

Appels, L., Baeyens, J., Degrève, J., Dewil, R., 2008. Principles and potential of the anaerobic digestion of waste-activated sludge. Prog. Energy Combust. Sci. 34, 755–781.

Arias, A., Feijoo, G., Moreira, M.T., 2020. What is the best scale for implementing anaerobic digestion according to environmental and economic indicators? J. Water Process Eng. 35, 101235.

Arnell, M., Astals, S., Åmand, L., Batstone, D.J., Jensen, P.D., Jeppsson, U., 2016. Modelling anaerobic co-digestion in Benchmark Simulation Model No. 2: Parameter estimation, substrate characterisation and plant-wide integration. Water Res. 98, 138–146.

Astarita, G., Apuzzo, G., 1965. Motion of gas bubbles in non-Newtonian liquids. AIChE J. 11, 815–820.

Azargoshasb, H., Mousavi, S.M., Amani, T., Jafari, A., Nosrati, M., 2015. Three-phase CFD simulation coupled with population balance equations of anaerobic syntrophic acidogenesis and methanogenesis reactions in a continuous stirred bioreactor. J. Ind. Eng. Chem. 27, 207–217.

B. L. Loffell, 1959. Some Studies on the Movement of Sludge Within a Digestion Tank During the Digestion Process. Public Health.

Bache, D.H., Rasool, E., Moffat, D., McGilligan, F.J., 1999. On the strength and character of alumino-humic flocs. Water Sci. Technol. 40, 81–88.

Batstone, D.J., Keller, J., Angelidaki, I., Kalyuzhnyi, S. V., Pavlostathis, S.G., Rozzi, A., Sanders, W.T., Siegrist, H., Vavilin, V.A., 2002. The IWA Anaerobic Digestion Model No 1 (ADM1). Water Sci. Technol. 45, 65–73.

Batstone, D.J., Keller, J., Steyer, J.P., 2006. A review of ADM1 extensions, applications, and analysis: 2002-2005. Water Sci. Technol. 54, 1–10.

Batstone, D.J., Puyol, D., Flores-Alsina, X., Rodríguez, J., 2015. Mathematical modelling of anaerobic digestion processes: applications and future needs. Rev. Environ. Sci. Biotechnol. 14, 595–613.

Baudez, J.C., Gupta, R.K., Eshtiaghi, N., Slatter, P., 2013a. The viscoelastic behaviour of raw and anaerobic digested sludge: Strong similarities with soft-glassy materials. Water Res. 47, 173–180.

Baudez, J.C., Markis, F., Eshtiaghi, N., Slatter, P., 2011. The rheological behaviour of anaerobic digested sludge. Water Res. 45, 5675–5680.

Baudez, J.C., Slatter, P., Eshtiaghi, N., 2013b. The impact of temperature on the rheological behaviour of anaerobic digested sludge. Chem. Eng. J. 215–216.

Bel Fdhila, R., Rahmani, M.A., Thorin, E., 2013. Prediction and measurements of the gas bubbles induced mixing in a bio-reactor water model. In: The 5th International Conference on Applied Energy. Pretoria, South Africa.

Biggs, C.A., Lant, P.A., 2000. Activated sludge flocculation: On-line determination of floc size and the effect of shear. Water Res. 34, 2542–2550.

Bisgaard, J., Muldbak, M., Cornelissen, S., Tajsoleiman, T., Huusom, J.K., Rasmussen, T., Gernaey, K. V., 2020. Flow-following sensor devices: a tool for bridging data and model predictions in large-scale fermentations. Comput. Struct. Biotechnol. J. 18, 2908–2919.

Boe, K., Kougias, P.G., Pacheco, F., O-Thong, S., Angelidaki, I., 2012. Effect of substrates and intermediate compounds on foaming in manure digestion systems. Water Sci. Technol. 66, 2146–2154.

Brackbill, J.., Kothe, D.., Zemach, C., 1992. A continuum method for modeling surface tension. J. Comput. Phys. 100, 335–354.

Bridgeman, J., 2012. Computational fluid dynamics modelling of sewage sludge mixing in an anaerobic digester. Adv. Eng. Softw. 44, 54–62.

Bujalski, J.M., Jaworski, Z., Bujalski, W., Nienow, A.W., 2002. The Influence of the Addition Position of a Tracer on CFD Simulated Mixing Times in a Vessel Agitated by a Rushton Turbine. Chem. Eng. Res. Des. 80, 824–831.

Burgers, J., 1948. A mathematical model illustrating the theory of turbulence. Adv. Appl. Mech. 1, 171–199.

Camp, T.R.T.R., Stein, P.C.P.C., 1943. Velocity gradients and internal work in fluid motion. J. Bost. Soc. Civ. Eng.

Changgen Luo, 1997. Distribution of Velocities and Velocity Gradients in Mixing and Flocculation Vessels: Comparison Between LDV Data and CFD Predictions.

Chen, Y., Cheng, J.J., Creamer, K.S., 2008. Inhibition of anaerobic digestion process: A review. Bioresour. Technol. 99, 4044–4064.

Chhabra, R., 1986. Steady non-Newtonian flow about a rigid sphere. In: Encyclopedia of Fluid Mechanics. Houston, p. 983.

Chhabra, R., 1988. Hydrodynamics of bubbles and drops in rheologically complex liquids. In: Encyclopedia of Fluid Mechanics. Houston, p. 253.

Chhabra, R., 2006. Bubbles, drops, and particles in non-Newtonian fluids.

Chiti, F., Bakalis, S., Bujalski, W., Barigou, M., Eaglesham, A., Nienow, A.W., 2011. Using positron emission particle tracking (PEPT) to study the turbulent flow in a baffled vessel agitated by a Rushton turbine: Improving data treatment and validation. Chem. Eng. Res. Des. 89, 1947–1960.

Cholette, A., Cloutier, L., 1959. Mixing efficiency determinations for continuous flow systems. Can J Chem Eng 1959:35. Can. J. Chem. Eng. 37, 105–112.

Clair N. Sawyer, Jay S. Grumbling, 1961. Fundamental considerations in high-rate digestion. Trans. Am. Soc. Civ. Eng. 126, 514–526.

Clift, R., Grace, J., Weber, M., 1978. Bubbles, Drops and Particles. New York.

Climent Agustina, J., 2019. Development of a modelling tool to perform hydrodynamics coupled with biological processes in the secondary stage of wastewater treatment plants. Universitat Jaume I.

Climent, J., Basiero, L., Martínez-Cuenca, R., Berlanga, J.G., Julián-López, B., Chiva, S., 2018. Biological reactor retrofitting using CFD-ASM modelling. Chem. Eng. J. 348, 1–14.

Climent, J., Chiva, S., Julian-Lopez, B., Portes, N., Ferrer, C., Pastor, I., Berlanga Clavijo, J.G., Santos, J.M., Martinez, J.L., 2013. Computational fluid dynamics modeling of hydrodynamic flow behaviour inside anaerobic digester tank. In: 13th World Congress on Anaerobic Digestion (AD13): Recovering (Bio) Resources for the World.

Climent, J., Kiser, A., Arnau, R., Pita, C., Bonmatí-blasi, A., Chiva, S., 2019. Comparison between Potassium Bromide and Lithium Chloride as feasible tracer for assessing hydraulic performance in anaerobic digesters. In: 8th International Conference on Tracers and Tracing Methods.

Coughtrie, A.R., Borman, D.J., Sleigh, P.A., 2013. Effects of turbulence modelling on prediction of flow characteristics in a bench-scale anaerobic gas-lift digester. Bioresour. Technol. 138, 297–306.

Coyne, J., Wilson, C., Scarborough, M., Umble, A., 2017. Anaerobic Digestion Fundamentals. Water Environ. Fed. 1–6.

Craig, K.J., Nieuwoudt, M.N., Niemand, L.J., 2013. CFD simulation of anaerobic digester with variable sewage sludge rheology. Water Res. 47, 4485–4497.

Danckwerts, P., 1953. Continuous flow systems: Distribution of residence times. Chem. Eng. Sci. 2, 1–13.

Dapelo, D., Alberini, F., Bridgeman, J., 2015. Euler-Lagrange CFD modelling of unconfined gas mixing in anaerobic digestion. Water Res. 85, 497–511.

Dapelo, D., Bridgeman, J., 2018. Assessment of mixing quality in full-scale, biogas-mixed anaerobic digestion using CFD. Bioresour. Technol.

Dapelo, D., Bridgeman, J., 2020. A CFD strategy to retrofit an anaerobic digester to improve mixing performance in wastewater treatment. Water Sci. Technol.

Dapelo, D., Trunk, R., Krause, M.J., Bridgeman, J., 2019. Towards Lattice-Boltzmann modelling of unconfined gas mixing in anaerobic digestion. Comput. Fluids 180, 11–21.

Dewsbury, K., Karamanev, D., Margaritis, A., Dewsbury, K., Karamanev, D., M., 1999. Hydrodynamic characteristics of free rise of light solid particles and gas bubbles in non-Newtonian liquids. Chem. Eng. Sci. 54, 4825–4830.

Elmitwalli, T.A., Soellner, J., De Keizer, A., Bruning, H., Zeeman, G., Lettinga, G., 2001. Biodegradability and change of physical characteristics of particles during anaerobic digestion of domestic sewage. Water Res. 35, 1311–1317.

Eshtiaghi, N., Markis, F., Yap, S.D., Baudez, J.C., Slatter, P., 2013. Rheological characterisation of municipal sludge: A review. Water Res. 47, 5493–5510.

Eugene E. Petersen, 1965. Chemical Reaction Analysis. Prentice-Hall.

Fernandes del Pozo, D., 2020. Experimental and Computational Fluid Dynamics Study of an Axial Impeller in Anaerobic Digestion. Ghent University.

Fernandes del Pozo, D., Liné, A., Dedeyne, J., Van Geem, K., Nopens, I., 2019. Computational fluid dynamics validation study of an axial flow impeller often used in anaerobic digesters. In: Watermatex 2019 : The 10th IWA Symposium on Modelling and Integrated Assessment, Proceedings.

Froment, G.F., Bischoff, K.B., 1990. Chemical reactor analysis and design, 2nd ed.

Gaden, D.L.F., 2013. Modelling Anaerobic Digesters in Three Dimensions: Integration of Biochemistry with Computational Fluid Dynamics. University of Manitoba.

Grady, C.P.L., Daigger, G.T., Lim, H.C., 1999. Biological Wastewater Treatment, 2nd Editio. ed, Statewide Agricultural Land Use Baseline 2015.

Gualtieri, C., Angeloudis, A., Bombardelli, F., Jha, S., Stoesser, T., 2017. On the Values for the Turbulent Schmidt Number in Environmental Flows. Fluids 2, 17.

Gujer, W., 2007. Systems Analysis for Water Technology.

Hassan, N.M.S., Khan, M.M.K., Rasul, M.G., 2008. A Study of Bubble Trajectory and Drag Co-efficient in Water and Non- Newtonian Fluids. WSEAS Trans. FLUID Mech. 3, 261–270.

Henze, M., Gujer, W., Mino, T., van Loosdrecht, M.C.M., van Loosedrecht, M., 2000. Activated Sludge Models ASM1, ASM2, ASM2d and ASM3, IWA Publishing. IWA Publishing.

Herning, F., Zipperer, L., 1936. Calculation of the viscosity of technical gas mixtures from the viscosity of the individual gases. Gas u. Wasserfach. 79, 69.

Hirt, C.., Nichols, B.., 1981. Volume of fluid (VOF) method for the dynamics of free boundaries. J. Comput. Phys. 39, 201–225.

Hoffmann, R.A., Garcia, M.L., Veskivar, M., Karim, K., Al-Dahhan, M.H., Angenent, L.T., 2008. Effect of shear on performance and microbial ecology of continuously stirred anaerobic digesters treating animal manure. Biotechnol. Bioeng. 100, 38–48.

Holz, M., Heil, S.R., Sacco, A., 2000. Temperature-dependent self-diffusion coefficients of water and six selected molecular liquids for the calibration in acccurate HNMR PFG m. Phys. Chem. Chem. Phys. 2, 4740–4742.

Hurtado, F.J., Kaiser, A.S., Zamora, B., 2015. Fluid dynamic analysis of a continuous stirred tank reactor for technical optimization of wastewater digestion. Water Res. 71, 282–293.

Hysing, S., Turek, S., Kuzmin, D., Parolini, N., Burman, E., Ganesan, S., Tobiska, L., 2009. Quantitative benchmark computations of two-dimensional bubble dynamics. Int. J. Numer. Methods Fluids 60, 1259–1288.

Jacek Makinia, Ewa Zaborowska, 2020. Mathematical Modelling and Computer Sumulation of Activated Sludge Systems. IWA Publishing.

Jeppsson, U., 1996. Modeling aspects of wastewater treatment processes. Electr. Eng.

Jeppsson, U., Pons, M.N., Nopens, I., Alex, J., Copp, J.B., Gernaey, K.V., Rosen, C., Steyer, J.-P., Vanrolleghem, P.A., 2007. Benchmark simulation model no 2:

general protocol and exploratory case studies. Water Sci. Technol. 56, 67–78.

Kadlec, R.H., Wallace, S.D., 2009. Treatment Wetlands, 2nd ed, Treatment Wetlands, Second Edition.

Kaparaju, P., Buendia, I., Ellegaard, L., Angelidakia, I., 2008. Effects of mixing on methane production during thermophilic anaerobic digestion of manure: Lab-scale and pilot-scale studies. Bioresour. Technol. 99, 4919–4928.

Karamanev, D.G., 1996. Equations for calculation of the terminal velocity and drag coefficient of solid spheres and gas bubbles. Chem. Eng. Commun. 147, 75–84.

Karim, K., Thoma, G.J., Al-Dahhan, M.H., 2007. Gas-lift digester configuration effects on mixing effectiveness. Water Res. 41, 3051–3060.

Karim, K., Varma, R., Vesvikar, M., Al-Dahhan, M.H., 2004. Flow pattern visualization of a simulated digester. Water Res. 38, 3659–3670.

Kariyama, I.D., Zhai, X., Wu, B., 2018. Influence of mixing on anaerobic digestion efficiency in stirred tank digesters: A review. Water Res. 143, 503–517.

Karpinska, A.M., Bridgeman, J., 2016. CFD-aided modelling of activated sludge systems - A critical review. Water Res. 88, 861–879.

Khapre, A., Munshi, B., 2016. Data on the mixing of non-Newtonian fluids by a Rushton turbine in a cylindrical tank. Data Br. 8, 1416–1420.

Khopkar, A.R., Rammohan, A.R., Ranade, V. V., Dudukovic, M.P., 2005. Gas-liquid flow generated by a Rushton turbine in stirred vessel: CARPT/CT measurements and CFD simulations. In: Chemical Engineering Science. Pergamon, pp. 2215–2229.

Kim, B., Azevedo, V.C., Thuerey, N., Kim, T., Gross, M., Solenthaler, B., 2019. Deep Fluids: A Generative Network for Parameterized Fluid Simulations. Comput. Graph. Forum 38, 59–70.

Kim, M., Kim, B.C., Choi, Y., Nam, K., 2017. Minimizing mixing intensity to improve the performance of rice straw anaerobic digestion via enhanced development of microbe-substrate aggregates. Bioresour. Technol. 245, 590–597.

Kinyua, M.N., Zhang, J., Camacho-Céspedes, F., Tejada-Martinez, A., Ergas, S.J., 2015. Use of physical and biological process models to understand the performance of tubular anaerobic digesters. Biochem. Eng. J. 107, 35–44.

Kleerebezem, R., 2014. Biochemical Conversion: Anaerobic Digestion. In: Biomass as a Sustainable Energy Source for the Future: Fundamentals of Conversion Processes. John Wiley & Sons, Ltd, pp. 441–468.

Kleerebezem, R., van Loosdrecht, M.C.M., 2006. Critical analysis of some concepts proposed in ADM1. Water Sci. Technol. 54, 51–57.

Kulkarni, A.A., Joshi, J.B., 2005. Bubble formation and bubble rise velocity in gas-liquid systems: A review. Ind. Eng. Chem. Res.

Lali, A.M., Khare, A.S., Joshi, J.B., Nigam, K.D.P., 1989. Behaviour of solid particles in viscous non-newtonian solutions: Settling velocity, wall effects and bed expansion in solid-liquid fluidized beds. Powder Technol. 57, 39–50.

Lambert, M., 2020. EU Hydrogen Strategy: A case for urgent action towards

implementation.

Latha, S., Borman, D., Sleigh, P. a., 2009. CFD multiphase modelling for evaluation of gas mixing in an anaerobic digester. In: 4th European Biosolids and Organic Resources Conference and Exhibition. pp. 1–15.

Le Moullec, Y., Potier, O., Gentric, C., Leclerc, J.P., 2008. Flow field and residence time distribution simulation of a cross-flow gas-liquid wastewater treatment reactor using CFD. Chem. Eng. Sci. 63, 2436–2449.

Leite, W., Magnus, B.S., Guimarães, L.B., Gottardo, M., Belli Filho, P., 2017. Feasibility of thermophilic anaerobic processes for treating waste activated sludge under low HRT and intermittent mixing. J. Environ. Manage. 201, 335–344.

Levenspiel, O., 1999. Chemical reaction engineering, 3rd ed, Ind. Eng. Chem. Res.

Li, H., 2018. Global Trends & Challenges in Water Science, Research and Management, Water Intelligence Online. IWA Publishing.

Li, S., Xin, F., Li, L., 2017. Reaction Engineering. Jonathan Simpson.

Lindmark, J., Eriksson, P., Thorin, E., 2014a. The effects of different mixing intensities during anaerobic digestion of the organic fraction of municipal solid waste. Waste Manag. 34, 1391–1397.

Lindmark, J., Thorin, E., Bel Fdhila, R., Dahlquist, E., 2014b. Effects of mixing on the result of anaerobic digestion: Review. Renew. Sustain. Energy Rev. 40, 1030–1047.

López-Jiménez, P.A., Escudero-González, J., Montoya Martínez, T., Fajardo Montañana, V., Gualtieri, C., 2015. Application of CFD methods to an anaerobic digester: The case of Ontinyent WWTP, Valencia, Spain. J. Water Process Eng. 7, 131–140.

Lotito, V., Mininni, G., Antonacci, R., 1997. The rheology of sewage sludge at different steps of treatment. Water Sci. Technol. 36, 79–85.

M. Henze, C.P.L.G.C.P.L.G.J.W.G.G. v. R.M.T.M., 1987. Activated sludge model No.1. London.

MacMullin, R.B., Weber, M., 1935. The theory of short-circuiting in continuous-flow mixing vessels in series and kinetics of chemical reactions in such systems. Trans. Am. Inst. Chem. Eng. 31, 409–458.

Manas-Zloczower, I., 1994. Studies of mixing efficiency in batch and continuous mixers. Rubber Chem. Technol. 67, 504–528.

Margaritis, A., Te Bokkel, D.W., Karamanev, D.G., 1999. Bubble rise velocities and drag coefficients in non-Newtonian polysaccharide solutions. Biotechnol. Bioeng. 64, 257–266.

Markis, F., Baudez, J.C., Parthasarathy, R., Slatter, P., Eshtiaghi, N., 2014. Rheological characterisation of primary and secondary sludge: Impact of solids concentration. Chem. Eng. J. 253, 526–537.

Mata-Alvarez, J., 2003. Biomethanization of the organic fraction of municipal solid waste, IWA Publishing.

Mbaye, S., Dieudé-Fauvel, E., Baudez, J.C., 2014. Comparative analysis of anaerobically digested wastes flow properties. Waste Manag. 34, 2057–2062.

McLeod, J.D., Othman, M.Z., Parthasarathy, R., 2019. Process intensification of anaerobic digestion: Influence on mixing and process performance. Bioresour. Technol. 274, 533–540.

Mei, R., Klausner, J.F., Lawrence, C.J., 1994. A note on the history force on a spherical bubble at finite Reynolds number. Phys. Fluids.

Meister, M., Rezavand, M., Ebner, C., Pümpel, T., Rauch, W., 2018. Mixing non-Newtonian flows in anaerobic digesters by impellers and pumped recirculation. Adv. Eng. Softw. 115, 194–203.

Mendoza, A.M., Martínez, T.M., Montañana, V.F., López-Jiménez, P.A., 2011. Modeling flow inside an anaerobic digester by CFD techniques. Int. J. Energy Environ. 2, 963–974.

Menter, F.R., 1994. Two-Equation Eddy-Viscosity Turbulence Models for Engineering Applications. AIAA J. 32, 1598–1605.

Meroney, R.N., Colorado, P.E., 2009. CFD simulation of mechanical draft tube mixing in anaerobic digester tanks. Water Res. 43, 1040–1050.

Miyahara, T., Yamanaka, S., 1993. Mechanics of motion and deformation of a single bubble rising through quiescent highly viscous newtonian and non-newtonian media. J. Chem. Eng. Japan 26, 297–302.

Moeller, G., Torres, L.G., 1997. Rheological characterization of primary and secondary sludges treated by both aerobic and anaerobic digestion. Bioresour. Technol. 61, 207–211.

Monteiro, P.S., 1997. The influence of the anaerobic digestion process on the sewage sludge rheological behavior. Water Sci. Technol. 36, 61–67.

Monteith, H.D., Stephenson, J.., 1981. Mixing efficiencies in full-scale anaerobic digesters by tracer methods. J. Water Pollut. Control Fed. 53, 78–84.

Nichita, B.A., Zun, I., Thome, J.R., 2010. A Level Set Method Coupled With a Volume of Fluid Method for Modeling of Gas-Liquid Interface in Bubbly Flow. J. Fluids Eng. 132, 081302.

Oberkampf, W.L., Trucano, T.G., 2002. Verification and validation in computational fluid dynamics. Prog. Aerosp. Sci. 38, 209–272.

Papoulis, A., 1984. Probability, random variables and stochastic processes with errata sheet: solution, Technometrics. McGraw-Hill, New York.

Patón, M., Rodríguez, J., 2019. Integration of bioenergetics in the ADM1 and its impact on model predictions. Water Sci. Technol. 80, 339–346.

Paul, E.L., Atiemo-Obeng, V.A., Kresta, S.M., 2004. Handbook of industrial mixing. New Jersey.

Pellacani, F., 2012. Development and Validation of Bubble Breakup and Coalescence Constitutive Models for the One-Group Interfacial Area Transport Equation.

Peña-Monferrer, C., 2017. Computational fluid dynamics multiscale modelling of bubbly flow. A critical study and new developments on volume of fluid, discrete element and two-fluid methods.

Pollice, A., Giordano, C., Laera, G., Saturno, D., Mininni, G., 2007. Physical characteristics of the sludge in a complete retention membrane bioreactor.

Water Res. 41, 1832–1840.

Prades Martell, L., 2018. Computational fluid dynamics techniques for fixed-bed biofilm systems modeling : numerical simulations and experimental characterization [en línea]. TDX (Tesis Dr. en Xarxa). Universitat Politècnica de Catalunya.

Premlata, A.R., Tripathi, M.K., Karri, B., Sahu, K.C., 2017. Numerical and experimental investigations of an air bubble rising in a Carreau-Yasuda shear-thinning liquid. Phys. Fluids 29, 033103.

Ramin, E., Wágner, D.S., Yde, L., Binning, P.J., Rasmussen, M.R., Mikkelsen, P.S., Plósz, B.G., 2014. A new settling velocity model to describe secondary sedimentation. Water Res. 66, 447–458.

Ratkovich, N., Horn, W., Helmus, F.P., Rosenberger, S., Naessens, W., Nopens, I., Bentzen, T.R., 2013. Activated sludge rheology: A critical review on data collection and modelling. Water Res. 47, 463–482.

Rieger, L., Gillot, S., Langergraber, G., Ohtsuki, T., Shaw, A., Takács, I., Winkler, S., 2013. Guidelines for Using Activated Sludge Models. IWA Publishing, London.

Roache, P.J., 1998. Verification of codes and calculations. AIAA J. 36, 696–702.

Roberts, P.J.W., Webster, D.R., 2003. Turbulent diffusion. In: Environmental Fluid Mechanics: Theories and Applications. pp. 7–45.

Rodrigue, D., De Kee, D., Chan Man Fong, C.F., 1998. Bubble velocities: further developments on the jump discontinuity. J. Nonnewton. Fluid Mech. 79, 45–55.

Rodríguez, J., Patón, M., 2018. Modelado matemático en digestión anaerobia. In: Chiva, S., Berlanga Clavijo, J.G., Martínez-Cuenca, R., Climent, J. (Eds.), Depuración de Aguas Residuales: Digestión Anaerobia. Publicacions de la Universitat Jaume I, Castellón.

Rodríguez, J., Premier, G.C., Dinsdale, R., Guwy, A.J., 2009. An implementation framework for wastewater treatment models requiring a minimum programming expertise. Water Sci. Technol. 59, 367–380.

Rosen, C., Vrecko, D., Gernaey, K. V., Pons, M.N., Jeppsson, U., 2006. Implementing ADM1 for plant-wide benchmark simulations in Matlab/Simulink. Water Sci. Technol. 54, 11–19.

Sadino-Riquelme, C., Hayes, R.E., Jeison, D., Donoso-Bravo, A., 2018. Computational fluid dynamic (CFD) modelling in anaerobic digestion: General application and recent advances. Crit. Rev. Environ. Sci. Technol. 48, 39–76.

Sajjadi, B., Raman, A.A.A., Parthasarathy, R., 2016. Fluid dynamic analysis of non-Newtonian flow behavior of municipal sludge simulant in anaerobic digesters using submerged, recirculating jets. Chem. Eng. J. 298, 259–270.

Schramm, G., 1994. A Practical Approach to Rheology and Rheometry, 2nd Editio. ed.

Seghezzo, L., Zeeman, G., Van Lier, J.B., Hamelers, H.V.M., Lettinga, G., 1998. A review: The anaerobic treatment of sewage in UASB and EGSB reactors. Bioresour. Technol.

Seyssiecq, I., Marrot, B., Djerroud, D., Roche, N., 2008. In situ triphasic rheological characterisation of activated sludge, in an aerated bioreactor. Chem. Eng. J. 142, 40–47.

Sindall, R., Bridgeman, J., Carliell-Marquet, C., 2013. Velocity gradient as a tool to characterise the link between mixing and biogas production in anaerobic waste digesters. Water Sci. Technol. 67, 2800–2806.

Sindall, R.C., Dapelo, D., Leadbeater, T., Bridgeman, J., 2017. Positron emission particle tracking (PEPT): A novel approach to flow visualisation in lab-scale anaerobic digesters. Flow Meas. Instrum. 54, 250–264.

Singh, B., Szamosi, Z., Siménfalvi, Z., 2019. State of the art on mixing in an anaerobic digester: A review. Renew. Energy 141, 922–936.

Smart, J., 1978. An assessment of the mixing performance of several anaerobic digesters using tracer response techniques. Pollut. Control Branch, Ontario Minist. Environ. Can. 72.

Stroot, P.G., McMahon, K.D., Mackie, R.I., Raskin, L., 2001. Anaerobic codigestion of municipal solid waste and biosolids under various mixing conditions-I. digester performance. Water Res. 35, 1804–1816.

Sun, B., Guo, Y., Wang, Z., Yang, X., Gong, P., Wang, J., Wang, N., 2015. Experimental study on the drag coefficient of single bubbles rising in static non-Newtonian fluids in wellbore. J. Nat. Gas Sci. Eng. 26, 867–872.

Tanaka, M., 2014. Investigation of V&V process for thermal fatigue issue in a sodium cooled fast reactor – Application of uncertainty quantification scheme in verification and validation with fluid-structure thermal interaction problem in T-junction piping system. Nucl. Eng. Des. 279, 91–103.

Tanaka, M., Ohno, S., Ohshima, H., 2016. Development of V2UP (V&V plus uncertainty quantification and prediction) procedure for high cycle thermal fatigue in fast reactor—Framework for V&V and numerical prediction. Nucl. Eng. Des. 299, 174–183.

Tchobanoglous, G., Stensel, H.D., Burton, F.L., 2004. Wastewater Engineering: Treatment and Reuse, 4th Editio. ed. McGraw-Hill.

Terashima, M., Goel, R., Komatsu, K., Yasui, H., Takahashi, H., Li, Y.Y., Noike, T., 2009. CFD simulation of mixing in anaerobic digesters. Bioresour. Technol. 100, 2228–2233.

Tobo, Y.M., Rehman, U., Bartacek, J., Nopens, I., 2020. Partial integration of ADM1 into CFD: understanding the impact of diffusion on anaerobic digestion mixing. Water Sci. Technol.

Tomiyama, A., Kataoka, I., Zun, I., Sakaguchi, T., 1998. Drag Coefficients of Single Bubbles under Normal and Micro Gravity Conditions. JSME Int. J. Ser. B Fluids Therm. Eng. 41, 472–479.

Tu, J., Yeoh, G.-H., Liu, C., 2013. Computational Fluid Dynamics: A practical approach.

Turton, R., Levenspiel, O., 1986. A short note on the drag correlation for spheres. Powder Technol. 47, 83–86.

United Nations, 2015. Resolution Adopted by the General Assembly on 25 September 2015. In: Sustainable Development Goals. Wiley, pp. 333–374.

United Nations, 2020. The sustainable develoment goals report 2020. Technical report.

United Nations, 2021. Water and sanitation – SDGs [WWW Document]. URL https://www.un.org/sustainabledevelopment/es/water-and-sanitation/ (accessed 6.29.21).

US EPA, 1979. Process Design Manual for Sludge Treatment and Disposal, 625/1-79–0. ed. EPA, Cincinnati, Ohio.

US EPA, 1987. Anaerobic digester mixing systems, Water Pollution Control Federation.

van Haandel, A., van der Lubbe, J., 2012. Handbook of Biological Wastewater Treatment: Design and optimization of Activated Sludge Systems.

Vavilin, V.A., Angelidaki, I., 2005. Anaerobic degradation of solid material: Importance of initiation centers for methanogenesis, mixing intensity, and 2D distributed model. Biotechnol. Bioeng. 89, 113–122.

Verhoff, F.H., Tenney, M.W., Echelberger, W.F., 1974. Mixing in anaerobic digestion. Biotechnol. Bioeng. 16, 757–770.

Versteeg, H.K., Malalasekera, W., 2005. Introduction to Computational Fluid Dynamics, Second. ed.

Vesvikar, M., Al-Dahhan, M., 2005. Flow pattern visualization in a mimic anaerobic digester using CFD. Biotechnol. Bioeng. 89, 719–732.

Volcke, E., Hulle, S. Van, Deksissa, T., 2005. Calculation of pH and concentration of equilibrium components during dynamic simulation by means of a charge balance. Ghent, Belgium.

Wang, Y., Zhang, J., Sun, Y., Yu, J., Zheng, Z., Li, S., Cui, Z., Hao, J., Li, G., 2020. Effects of intermittent mixing mode on solid state anaerobic digestion of agricultural wastes. Chemosphere 248.

Wei, P., Mudde, R.F., Uijttewaal, W., Spanjers, H., Lier, J.B. van, Kreuk, M. de, 2018a. Characterising the two-phase flow and mixing performance in a gas-mixed anaerobic digester: importance for scaled-up applications. Water Res.

Wei, P., Tan, Q., Uijttewaal, W., van Lier, J.B., de Kreuk, M., 2018b. Experimental and mathematical characterisation of the rheological instability of concentrated waste activated sludge subject to anaerobic digestion. Chem. Eng. J. 349, 318–326.

White, F.M., 2011. Fluid mechanics. McGraw Hill.

White, K.E., 1974. The Use of Radioactive Tracers to Study Mixing and Residence-Time Distributions in Systems Exhibiting Three-Dimensional Dispersion. In: First European Conference on Mixing and Centrifugal Separation.

Wiewel, S., Becher, M., Thuerey, N., 2018. Latent-space Physics: Towards Learning the Temporal Evolution of Fluid Flow. Comput. Graph. Forum 38, 71–82.

Wilcox, D.C.., 1993. Turbulence Modeling for CFD.

Wu, B., 2010a. CFD simulation of mixing in egg-shaped anaerobic digesters. Water Res. 44, 1507–1519.

Wu, B., 2010b. Computational fluid dynamics investigation of turbulence models

for non-newtonian fluid flow in anaerobic digesters. Environ. Sci. Technol. 44, 8989–8995.

Wu, B., 2010c. CFD simulation of gas and non-Newtonian fluid two-phase flow in anaerobic digesters. Water Res. 44, 3861–3874.

Wu, B., 2011. CFD investigation of turbulence models for mechanical agitation of non-Newtonian fluids in anaerobic digesters. Water Res. 45, 2082–2094.

Wu, B., 2012a. Large eddy simulation of mechanical mixing in anaerobic digesters. Biotechnol. Bioeng. 109, 804–812.

Wu, B., 2012b. CFD simulation of mixing for high-solids anaerobic digestion. Biotechnol. Bioeng. 109, 2116–2126.

Wu, B., 2012c. Integration of mixing, heat transfer, and biochemical reaction kinetics in anaerobic methane fermentation. Biotechnol. Bioeng. 109, 2864–2874.

Wu, B., 2014. CFD simulation of gas mixing in anaerobic digesters. Comput. Electron. Agric. 109, 278–286.

Wu, B., Chen, S., 2008. CFD simulation of non-Newtonian fluid flow in anaerobic digesters. Biotechnol. Bioeng. 99, 700–711.

Yamoah, S., 2014. Numerical modelling of Isothermal Gas-Liquid Two-Phase Bubbly Flow in vertical pipes. University of Ghana.

Yu, L., Ma, J., Chen, S., 2011. Numerical simulation of mechanical mixing in high solid anaerobic digester. Bioresour. Technol. 102, 1012–1018.

Yu, L., Ma, J., Frear, C., Zhao, Q., Dillon, R., Li, X., Chen, S., 2013a. Multiphase modeling of settling and suspension in anaerobic digester. Appl. Energy 111, 28–39.

Yu, L., Wensel, P., Ma, J., Chen, S., 2013b. Mathematical Modeling in Anaerobic Digestion (AD). J. Bioremediatoin Biodegrad. S4, 12.

Zaher, U.E.-S., 2005. Modelling and monitoring the anaerobic digestion process in view of optimisation and smooth operation of WWTP's. Ghent University.

Zhai, X., Kariyama, I.D., Wu, B., 2018. Investigation of the effect of intermittent minimal mixing intensity on methane production during anaerobic digestion of dairy manure. Comput. Electron. Agric. 155, 121–129.

Zhang, L., Yang, C., Mao, Z.S., 2010. Numerical simulation of a bubble rising in shear-thinning fluids. J. Nonnewton. Fluid Mech. 165, 555–567.

Zhang, Y., Yu, G., Yu, L., Siddhu, M.A.H., Gao, M., Abdeltawab, A.A., Al-Deyab, S.S., Chen, X., 2016. Computational fluid dynamics study on mixing mode and power consumption in anaerobic mono- and co-digestion. Bioresour. Technol. 203, 166–172.

Zoltek, J., Gram, A.L., 1975. High rate digester mixing study using radioisotope tracer. J. Water Pollut. Control Fed. 47, 79–84.

APPENDIXES

APPENDIX A: DEAD VOLUME CRITERIA CONSTANTS

Table A.1: *Velocity constants.*

Velocity Constants
0
0.1
0.1
0.5
1
2
10
20
50
100

Table A.2: Turbulence Coefficients applied to the Exponential decay PDF and Gaussian PDF.

C turb Exponential Decay PDF	Cturb Gaussian PDF
0.01104854	0.015625
0.015625	0.02209709
0.02209709	0.03125
0.03125	0.04419417
0.04419417	0.0625
0.0625	0.08838835
0.08838835	0.125
0.125	0.1767767
0.1767767	0.25
0.25	0.35355339
0.35355339	0.5
0.5	0.70710678
0.70710678	1
1	1.41421356
1.41421356	2
2	2.82842712
2.82842713	4
4	5.65685425
5.65685425	8
8	11.3137085
11.3137085	16
16	22.627417
22.627417	32
32	45.254834
45.254834	64
64	90.509668

APPENDIX B: DETAILED DESCRIPTION OF THE FULL-SCALE ANAEROBIC DIGESTER

Figure B.1 show a detailed description of the ADer and its elements location. Different parameters of the different elements of the facility are defined in Table B.3, i.e. height and diameter, Cartesian Coordinates of the centroid of their face and unit normal vector.

Table B.3: *Description of the elements of the facility.*

Symbol	Element	Height (m)	Diameter (mm)	Centroid	Orientation
A	Dynomix Suction	6.85	400	[-4.55, 6.85, -9.30]	[-0.84, 0, 0.54]
B	Heat Exchanger Suction	4.2	145	[-3.54, 4.57, -10.29]	[0, -1, 0]
C	Inlet	1.5	200	[10.22, 1.51, -4.34]	[0.92, 0, -0.39]
D	Dynomix 2	0.9	200	[4.68, 0.9, 9.17]	[-0.07, 0, -1]
E	Outlet	-0.3	300	[0, -1.50, -0.70]	[0, -1, 0]
F	Dynomix 1	0.9	200	[-4.68, 0.9, 9.17]	[0.07, 0, 1]

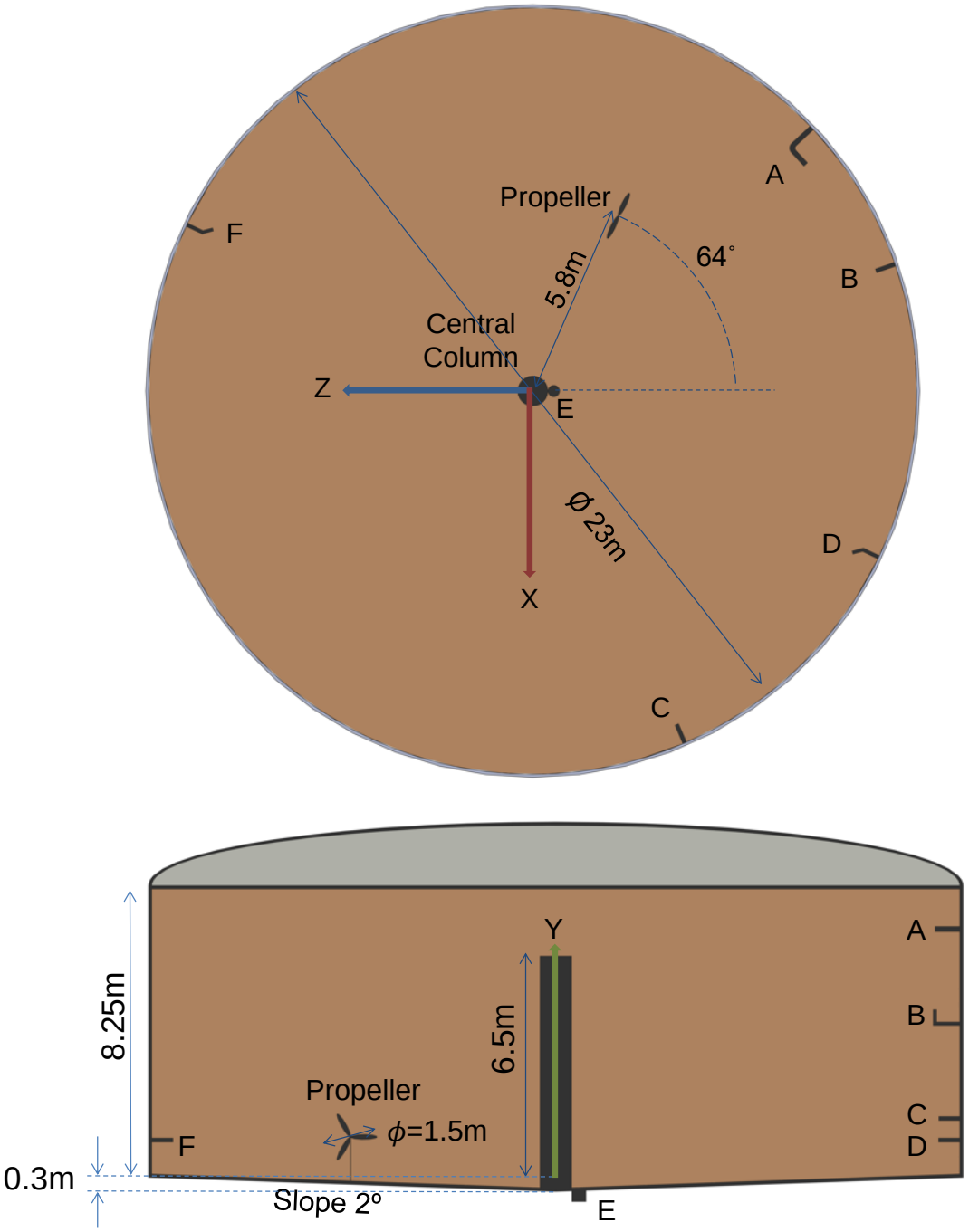

Figure B.1: *Scheme of Digester1.*

APPENDIX C: GCI CALCULATIONS

The values of area-weighted average velocity and flow (f_{1-3}) computed in mesh 1, 2 and 3 at different planes (near DYNOMIX and inlet nozzles and in Plane 1 (see **Figure 3.10**c)) are presented in **Table B.4**. The GCI was evaluated on these planes for the mesh convergence study (**Table B.5**).

Table B.4: *Area-weighted average velocity and flow.*

	N	**Dynomix 1 (m/s)**	**Dynomix 2 (m/s)**	**Inlet (m/s)**	**Plane 1 (m/s)**	**Half Plane 1 (m^3/s)**	**r**
M3	1490787	0.246633	0.246611	0.219681	0.171070	32.081	-
M2	2992010	0.249762	0.248801	0.222309	0.172275	32.296	r_{32}=1.26
M1	5195492	0.250478	0.250208	0.223923	0.172455	32.324	r_{21}=1.20

As the maximum GCI value between meshes 2 and 3 is slightly over 3% and falls up to 2.6% between meshes 1 and 2, mesh 2 was chosen for the simulations.

Table B.5*: Grid Convergence index*

GCI	**Dynomix 1**	**Dynomix 2**	**Inlet**	**Plane 1**	**Half Plane 1**
GCI_{32} (%)	0.817271	2.916148	3.177051	0.235803	0.183603
GCI_{21} (%)	0.29431	2.435231	2.550182	0.060837	0.042575

APPENDIX D: TIME EVOLUTION OF TRACER CONCENTRATION

The evolution of tracer concentration inside the digester in A100 transient simulation is shown in next figure.

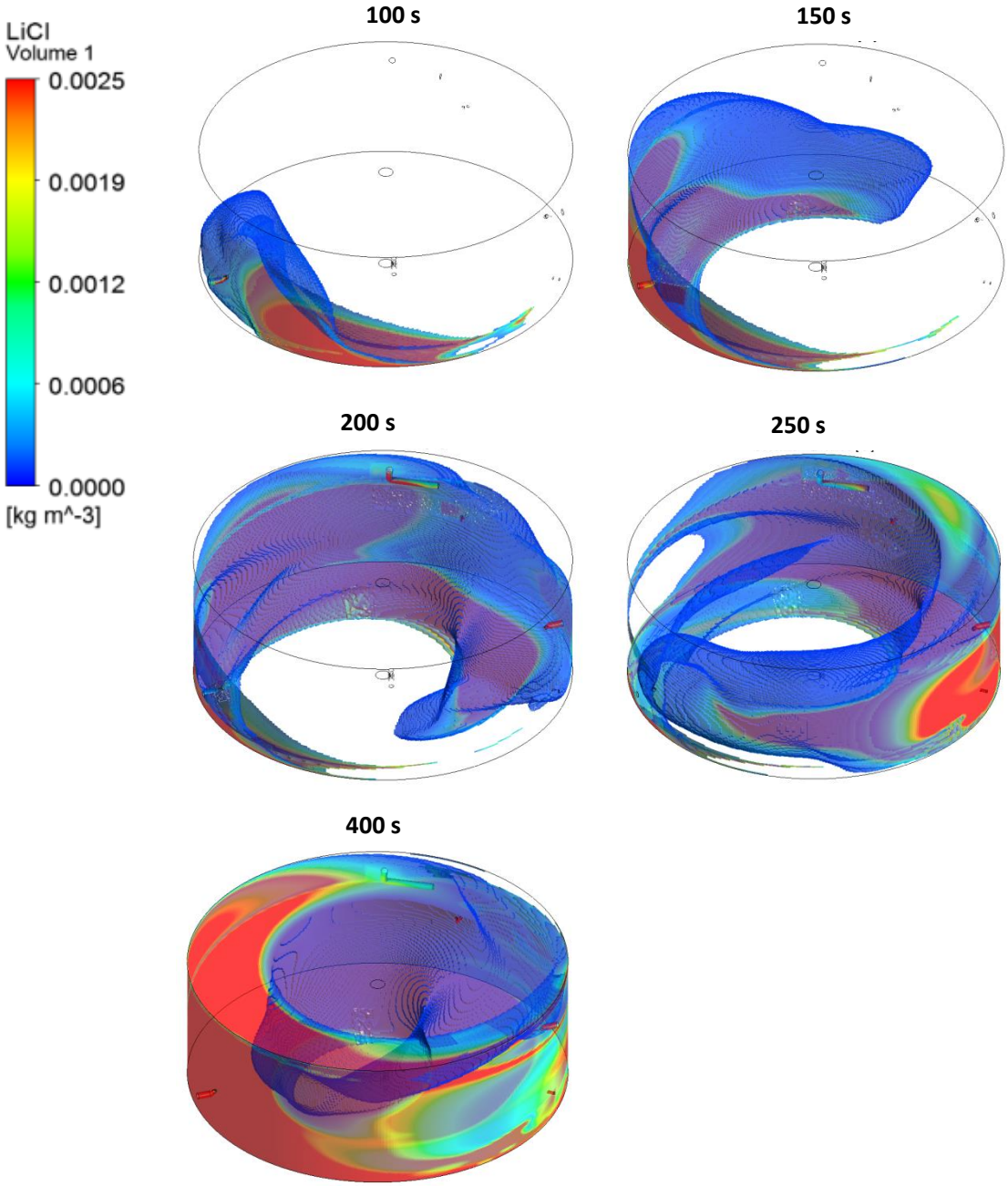

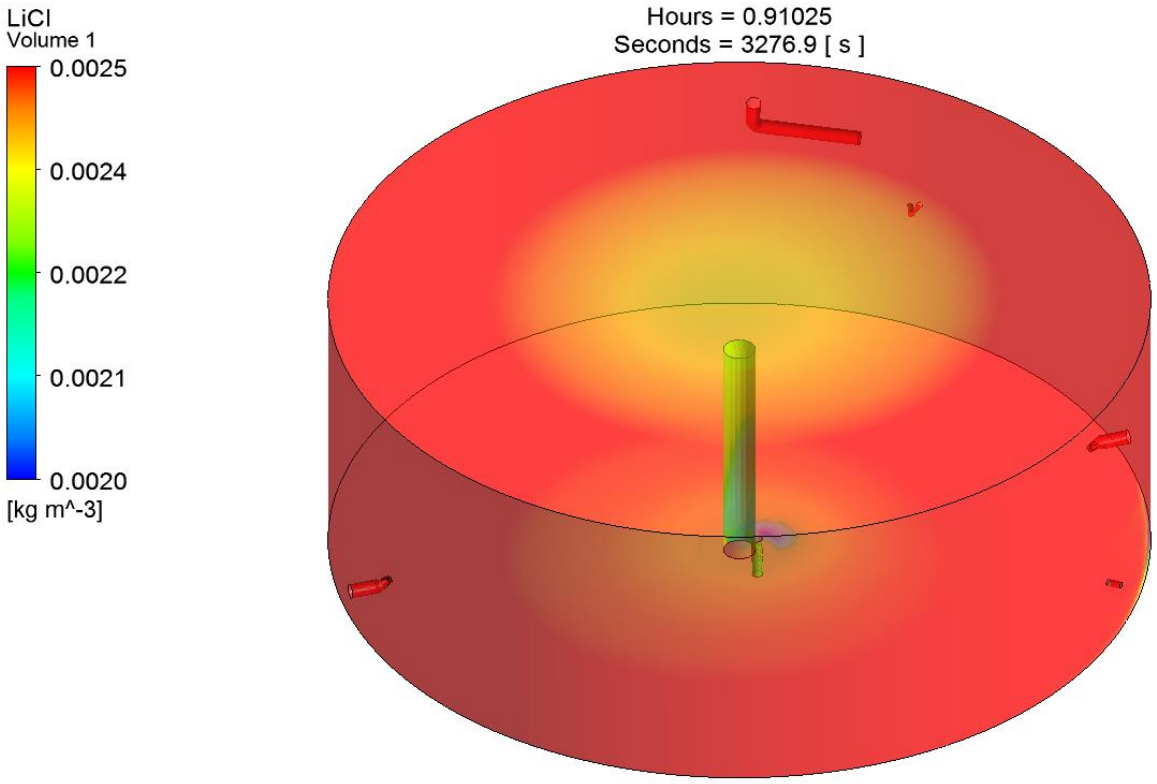

***Figure B.0.2**: Time evolution of tracer concentration inside the ADer in the A100 scenario.*

APPENDIX E: FITTING CURVE OF TURBULENT PROFILE

The circumferential velocity profile near wall at 5m height was fitted to a turbulent power law where fitting parameters a, b and R^2 were 0.34, 0.132 and 0.93, respectively

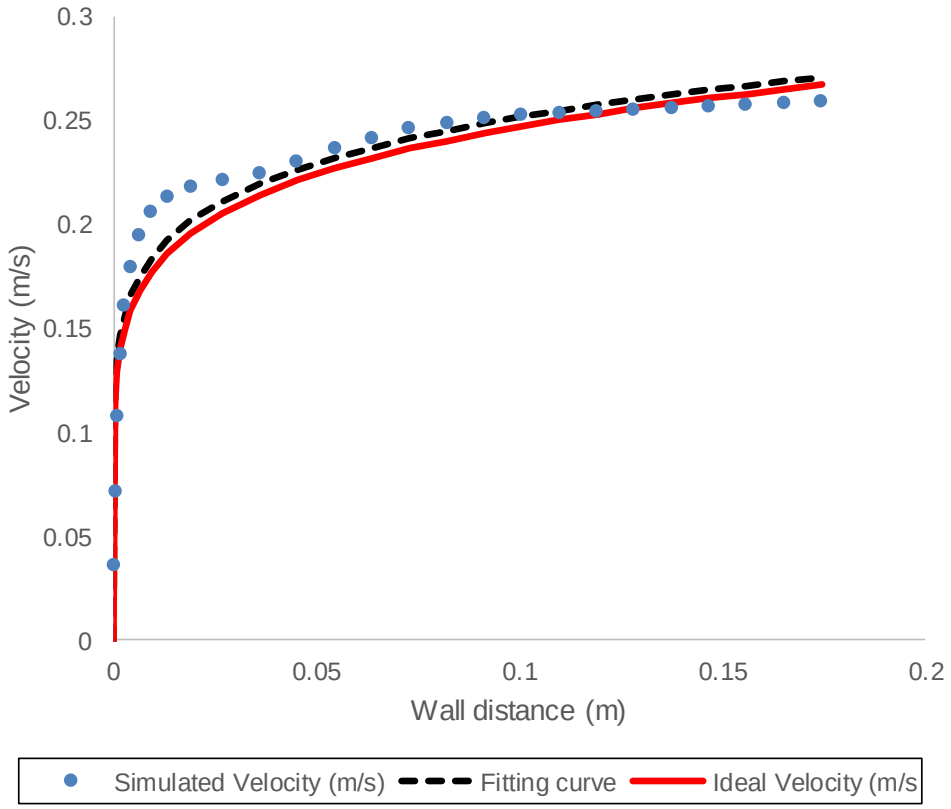

***Figure B.3**: Turbulent profile at the external part of A100 simulation.*

APPENDIX F: CIRCUMFERENTIAL, AXIAL AND RADIAL VELOCITY

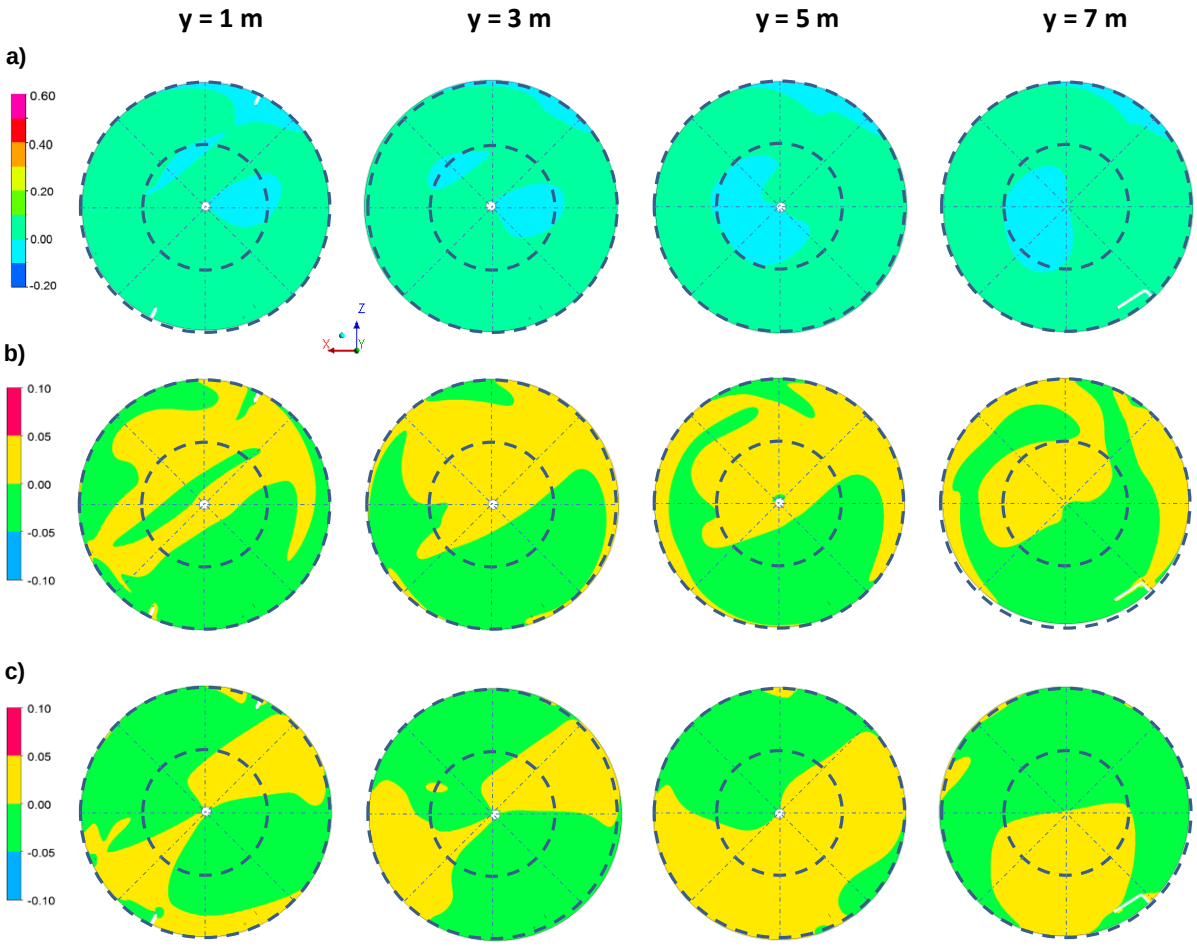

***Figure B. 4**: Velocity contours in different horizontal planes in scenario A0. The circumferential component is plot in a), the axial component in b) and the radial velocity in c).*

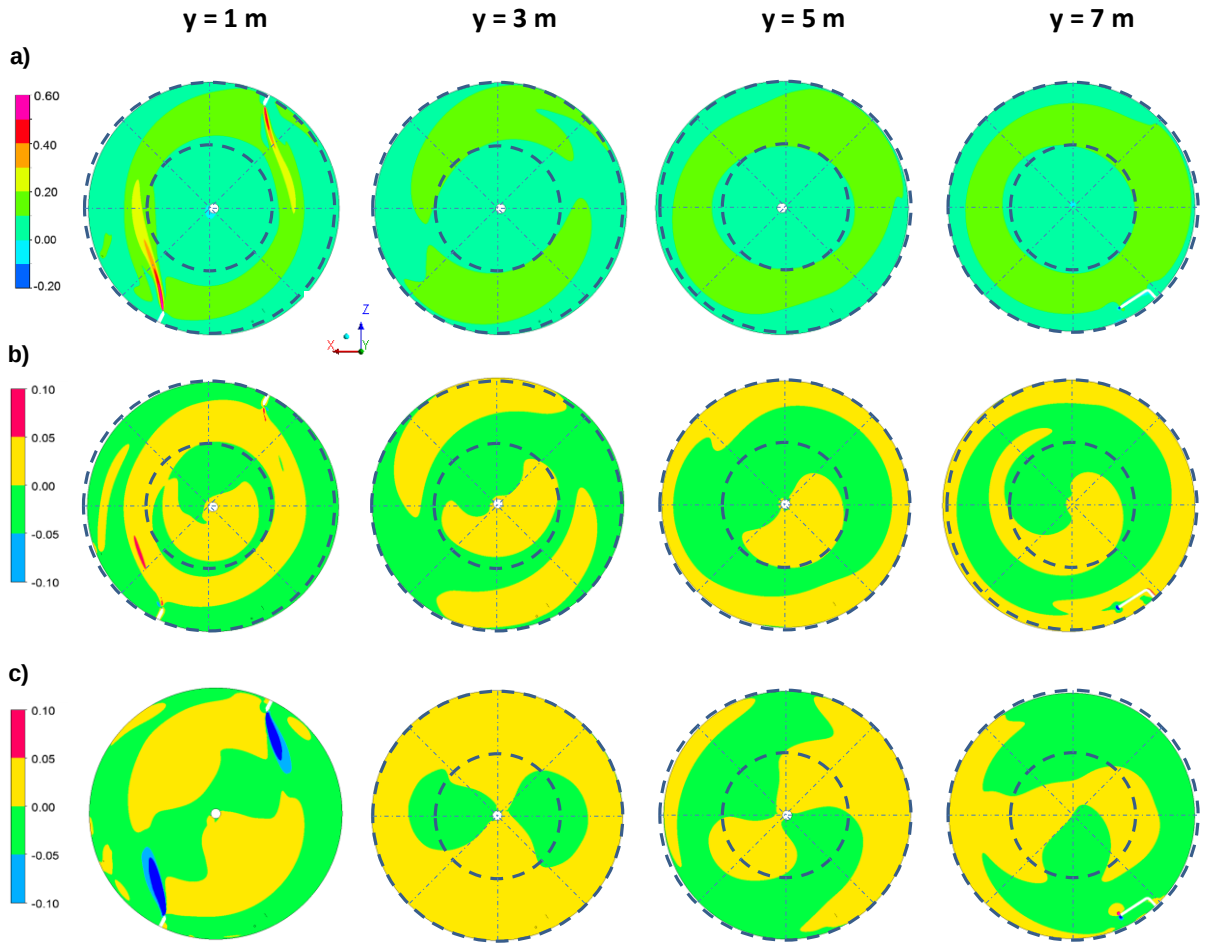

***Figure B. 5**: Velocity contours in different horizontal planes in scenario A50. The circumferential component is plot in a), the axial component in b) and the radial velocity in c).*

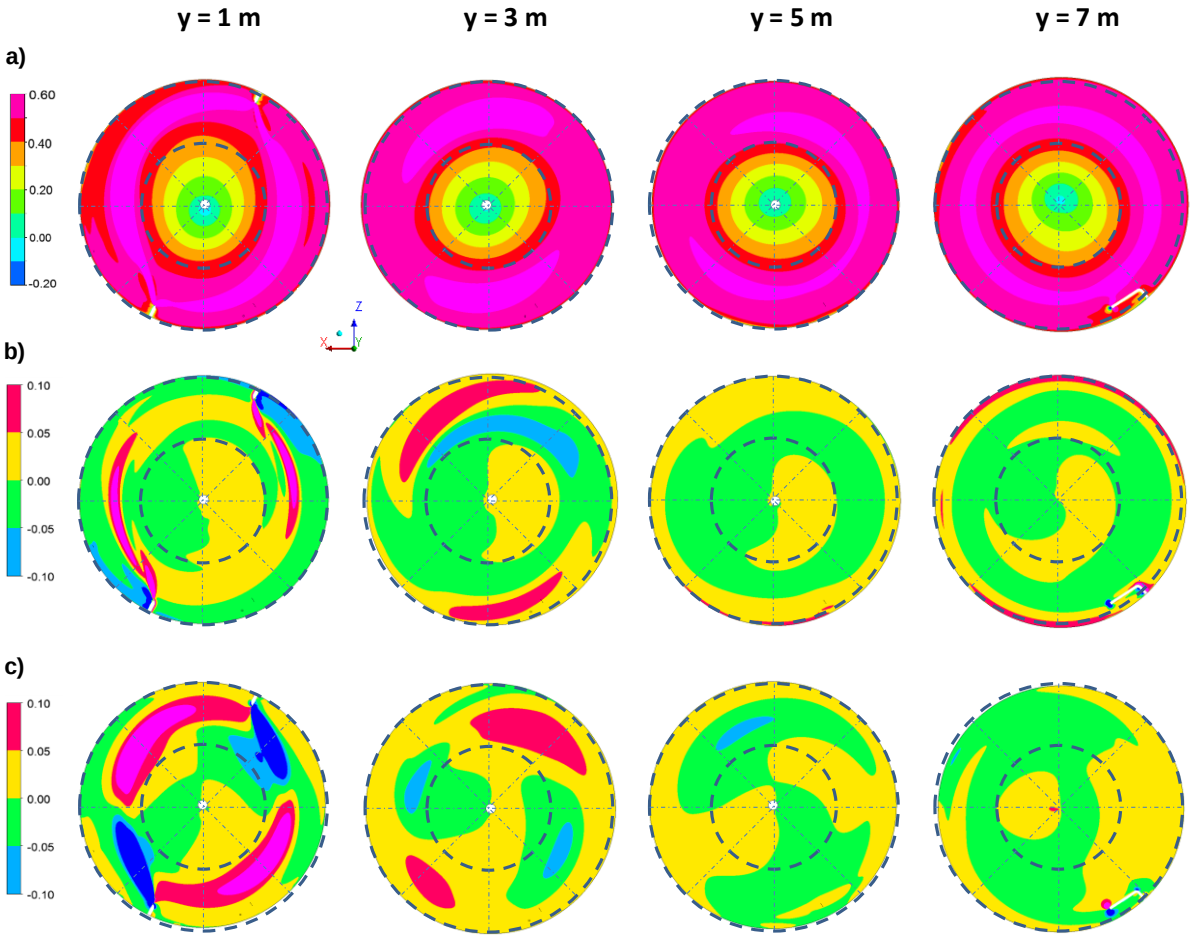

***Figure B.6**: Velocity contours in different horizontal planes in scenario A200. The circumferential component is plot in a), the axial component in b) and the radial velocity in c).*

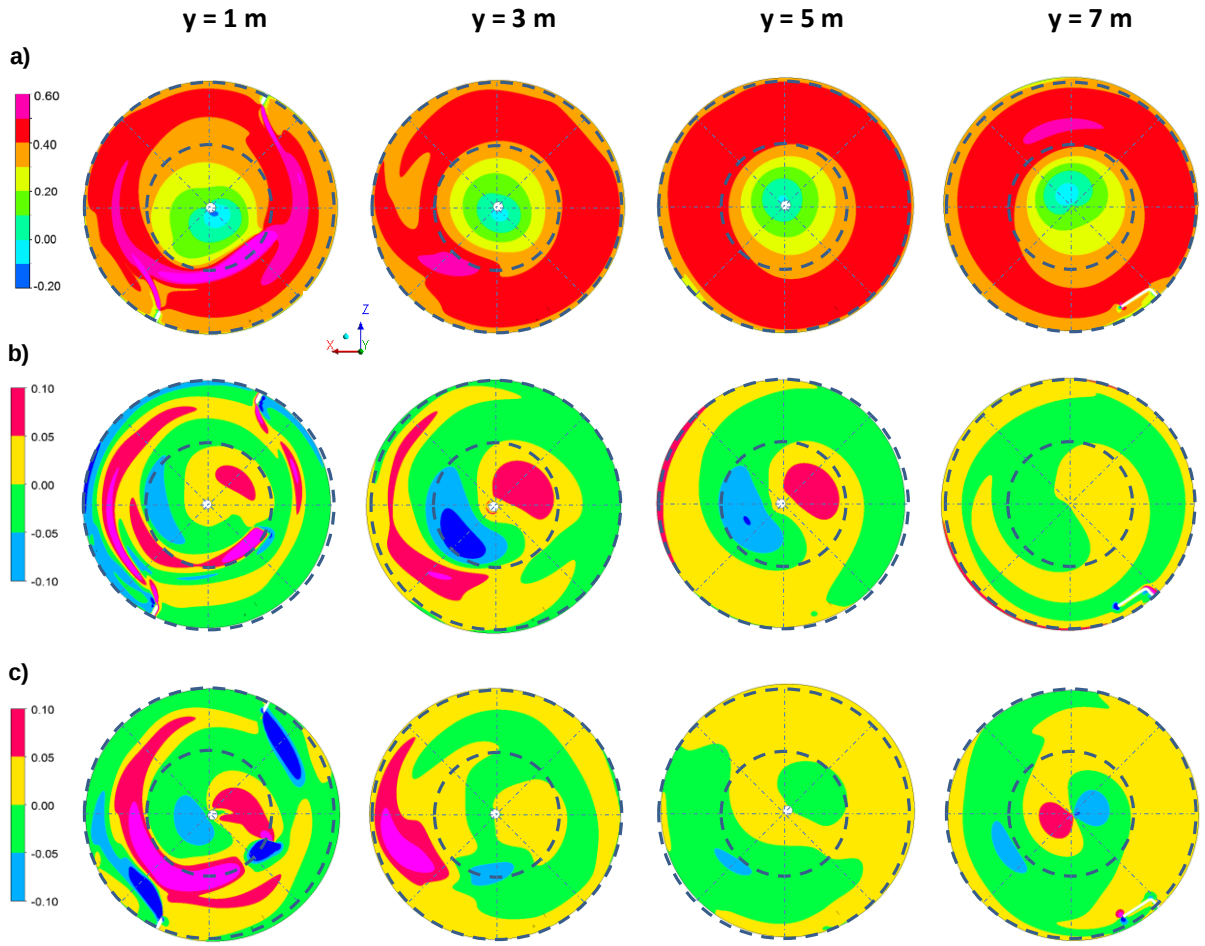

***Figure B. 7**: Velocity contours in different horizontal planes in scenario B100. The circumferential component is plot in a), the axial component in b) and the radial velocity in c).*

APPENDIX G: ADM1 INPUT DATA

G.i Lab-scale setup

Table G.6: *Influent and initial reactor values of each ADM1 variable at lab-scale setup.*

Variable	Units	Influent	Reactor
Ssu	kmol/m^3	Variable	0,00023634
Saa	kmol/ m^3	Variable	0,00061366
Sfa	kmol/ m^3	Variable	0,06308575
Sva	kmol/ m^3	0	0,0002664
Sbu	kmol/ m^3	Variable	0,00038754
Spro	kmol/ m^3	Variable	0,00308311
Sac	kmol/ m^3	Variable	0,03678039
Sch4	kmol/ m^3	0	0,00111061
Sh2	kmol/ m^3	0	6,2069X10^{-08}
Sic	kmolC/ m^3	Variable	0,03701157
Sin	kmolN/ m^3	Variable	0,01499522
Scat	kmol/ m^3	Variable	0,05628811
San	kmol/ m^3	Variable	0,00107046
Si	kmol/ m^3	0	0,00081307
Xc	kmolC/ m^3	Variable	0,00227641
Xch	kmolC/ m^3	0	2,4985X10^{-05}
Xpr	kmolC/ m^3	Variable	0,0003105
Xli	kmolC/ m^3	0	2,6381X10^{-05}
Xi	kmolC/ m^3	Variable	0,00136929
Xd	kmolC/ m^3	0	0,00029379
Xsu	kmolC/ m^3	0	0,0020861
Xaa	kmolC/ m^3	0	0,00485756
Xfa	kmolC/ m^3	0	0,00013367
Xc4	kmolC/ m^3	0	0,00178497
Xpro	kmolC/ m^3	0	0,00022105
Xac	kmolC/ m^3	0	0,00087048
Xh2	kmolC/ m^3	0	0,00093223
Shco3Neg	kmolC/ m^3	-	0,02956825

Table G.7: *Biological parameters at lab-scale setup.*

Parameter	Value	Units	*ADM1Foam*	Units *ADM1Foam*
kdis	0,020833	1/h	$5{,}7869 \times 10^{-6}$	1/s
k_hyd_ch	0,417	1/h	$1{,}1574 \times 10^{-4}$	1/s
k_hyd_pr	0,417	1/h	$1{,}1574 \times 10^{-4}$	1/s
k_hyd_li	0,417	1/h	$1{,}1574 \times 10^{-4}$	1/s
km_su	0,208	kmolSsu/kmolCxfer·h	$5{,}7869 \times 10^{-5}$	kmolSsu/kmolCxfer·s
Ks_su	0,003	kmolSsu/ m^3	$2{,}6042 \times 10^{-3}$	kmolSsu/ m^3
km_aa	2	kmolCsaa/kmolCxaa·h	$5{,}5556 \times 10^{-4}$	kmolCsaa/kmolCxaa·s
Ks_aa	0,009	kmolCsaa/ m^3	$9{,}0000 \times 10^{-3}$	kmolCsaa/ m^3
km_fa	0,174	kmolCsfa/kmolCxfa·h	$4{,}8308 \times 10^{-5}$	kmolCsfa/kmolCxfa·s
Ks_fa	0,009	kmolCsfa/ m^3	$8{,}6957 \times 10^{-3}$	kmolCsfa/ m^3
km_va	0,128	kmolSva/kmolCxc4·h	$3{,}5614 \times 10^{-5}$	kmolSva/kmolCxc4·s
Ks_va	0,001	kmolSva/ m^3	$9{,}6154 \times 10^{-4}$	kmolSva/ m^3
km_bu	0,167	kmolSbu/kmolCxc4·h	$4{,}6297 \times 10^{-5}$	kmolSbu/kmolCxc4·s
Ks_bu	0,001	kmolSbu/ m^3	$1{,}2500 \times 10^{-3}$	kmolSbu/ m^3
km_pro	0,155	kmolSpro/kmolCxpro·h	$4{,}2989 \times 10^{-5}$	kmolSpro/kmolCxpro·s
Ks_pro	0,001	kmolSpro/ m^3	$8{,}9286 \times 10^{-4}$	kmolSpro/ m^3
km_ac	0,167	kmolSac/kmolCxac·h	$4{,}6297 \times 10^{-5}$	kmolSac/kmolCxac·s
Ks_ac	0,002	kmolSac/ m^3	$2{,}3437 \times 10^{-3}$	kmolSac/ m^3
km_h2	2,917	kmolSh2/kmolCxh2·h	$8{,}1019 \times 10^{-4}$	kmolSs2/kmolCxs2·s
Ks_h2	$4{,}38 \times 10^{-7}$	kmolSh2/ m^3	$4{,}3750 \times 10^{-7}$	kmolSh2/ m^3
Ks_IN	0,0001	kmolSin/ m^3	$1{,}0000 \times 10^{-4}$	kmolSin/ m^3
Ki_h2_fa	$3{,}13 \times 10^{-7}$	kmolSh2/ m^3	$3{,}1250 \times 10^{-7}$	kmolSh2/ m^3
Ki_h2_c4	$6{,}25 \times 10^{-7}$	kmolSh2/ m^3	$6{,}2500 \times 10^{-7}$	kmolSh2/ m^3
Ki_h2_pro	$2{,}19 \times 10^{-7}$	kmolSh2/ m^3	$2{,}1875 \times 10^{-7}$	kmolSh2/ m^3
Ki_nh3	0,0018	kmolSnh3/ m^3	$1{,}8000 \times 10^{-3}$	kmolSnh3/ m^3
k_dec_Xsu	0,0008	1/h	$2{,}31481 \times 10^{-7}$	1/s
k_dec_Xaa	0,0008	1/h	$2{,}31481 \times 10^{-7}$	1/s
k_dec_Xfa	0,0008	1/h	$2{,}31481 \times 10^{-7}$	1/s
k_dec_Xc4	0,0008	1/h	$2{,}31481 \times 10^{-7}$	1/s
k_dec_Xpro	0,0008	1/h	$2{,}31481 \times 10^{-7}$	1/s
k_dec_Xac	0,0008	1/h	$2{,}31481 \times 10^{-7}$	1/s
k_dec_Xh2	0,0008	1/h	$2{,}31481 \times 10^{-7}$	1/s
k_hyd_Xd	0,0208	1/h	$5{,}78694 \times 10^{-6}$	1/s
pHll_acet_acid	4	[]	4	[]
pHul_acet_acid	5,5	[]	5,5	[]
pHll_ac	6	[]	6	[]
pHul_ac	7	[]	7	[]
pHll_H2	5	[]	5	[]
pHul_H2	6	[]	6	[]
Ks_co2	1×10^{-6}	kmol-Sco2/ m^3	1×10^{-6}	kmol-Sco2/ m^3

G.ii Full-scale setup

Table G.8: *Influent and initial reactor values of each ADM1 variable at the full-scale models.*

Variable	Units	Influent	Reactor
Ssu	kmol/m^3	Variable	6.667x10-5
Saa	kmol/ m^3	Variable	2.060x10-4
Sfa	kmol/ m^3	Variable	6.145x10-3
Sva	kmol/ m^3	Variable	1.188x10-4
Sbu	kmol/ m^3	Variable	1.494x10-4
Spro	kmol/ m^3	Variable	2.192x10-4
Sac	kmol/ m^3	1.695x10-5	3.390x10-3
Sch4	kmol/ m^3	6.250x10-7	3.438x10-3
Sh2	kmol/ m^3	5.000x10-9	1.150x10-7
Sic	kmolC/ m^3	0.04	0.150
Sin	kmolN/ m^3	0.01	0.130
Scat	kmol/ m^3	0.04	0.04
San	kmol/ m^3	0.02	0.02
Si	kmol/ m^3	7.476x10-4	1.234x10-2
Xc	kmolC/ m^3	Variable	1.233x10-2
Xch	kmolC/ m^3	Variable	9.333x10-4
Xpr	kmolC/ m^3	Variable	3.886x10-3
Xli	kmolC/ m^3	Variable	1.836x10-3
Xi	kmolC/ m^3	1.145	1.172
Xd	kmolC/ m^3	0	3.951x10-3
Xsu	kmolC/ m^3	0	1.858x10-2
Xaa	kmolC/ m^3	4.425x10-4	5.221x10-2
Xfa	kmolC/ m^3	4.425x10-4	1.062x10-2
Xc4	kmolC/ m^3	4.425x10-4	1.903x10-2
Xpro	kmolC/ m^3	4.425x10-4	6.195x10-3
Xac	kmolC/ m^3	4.425x10-4	3.363x10-2
Xh2	kmolC/ m^3	4.425x10-4	1.416x10-2

Table G.9: *Time-variable influent concentrations at the full-scale models*

Time from (h)	Ssu	Saa	Sfa	Sva	Sbu	Spro
0	0,000056	0,000039	0,000062	0,0000099	0,000011	0,000014
2	0,000078	0,000039	0,000062	0,0000099	0,000011	0,000014
4	0,000111	0,000078	0,000124	0,0000198	0,000023	0,000027
6	0,000222	0,000155	0,000248	0,0000396	0,000046	0,000055
8	0,000556	0,000389	0,000621	0,0000990	0,000115	0,000137

Time (h)	Xc	Xch	Xpr	Xli
0	0,08	0,17	0,78	0,32
2	0,08	0,17	0,78	0,32
4	0,16	0,67	3,11	1,27
6	0,32	0,67	3,11	1,27
8	0,80	1,67	7,77	3,17

Table G.10: *Biological parameters at the full-scale setup.*

Parameter	Value	Units	*ADM1Foam*	Units *ADM1Foam*
kdis	0.02083	1/h	5.787x10-6	1/s
k_hyd_ch	0.417	1/h	1.157x10-4	1/s
k_hyd_pr	0.417	1/h	1.157x10-4	1/s
k_hyd_li	0.417	1/h	1.157x10-4	1/s
km_su	0.157	kmolSsu/kmolCxfer·h	4.360x10-5	kmolSsu/kmolCxfer·s
Ks_su	2.78x10-3	kmolSsu/ m^3	2.778x10-3	kmolSsu/ m^3
km_aa	1.830	kmolCsaa/kmolCxaa·h	5.083x10-4	kmolCsaa/kmolCxaa·s
Ks_aa	1.17x10-2	kmolCsaa/ m^3	1.166x10-2	kmolCsaa/ m^3
km_fa	0.351	kmolCsfa/kmolCxfa·h	9.741x10-5	kmolCsfa/kmolCxfa·s
Ks_fa	2.48x10-2	kmolCsfa/ m^3	2.483x10-2	kmolCsfa/ m^3
km_va	0.186	kmolSva/kmolCxc4·h	5.180x10-5	kmolSva/kmolCxc4·s
Ks_va	1.98x10-3	kmolSva/ m^3	1.980x10-3	kmolSva/ m^3
km_bu	0.216	kmolSbu/kmolCxc4·h	6.013x10-5	kmolSbu/kmolCxc4·s
Ks_bu	2.30x10-3	kmolSbu/ m^3	2.299x10-3	kmolSbu/ m^3
km_pro	0.168	kmolSpro/kmolCxpro·h	4.658x10-5	kmolSpro/kmolCxpro·s
Ks_pro	1.37x10-3	kmolSpro/ m^3	1.370x10-3	kmolSpro/ m^3
km_ac	0.128	kmolSac/kmolCxac·h	3.547x10-5	kmolSac/kmolCxac·s
Ks_ac	2.54x10-3	kmolSac/ m^3	2.542x10-3	kmolSac/ m^3
km_h2	2.060	kmolSh2/kmolCxh2·h	5.722x10-4	kmolSs2/kmolCxs2·s
Ks_h2	4.38x10-7	kmolSh2/ m^3	4.375x10-7	kmolSh2/ m^3
Ks_IN	1x10-4	kmolSin/ m^3	1x10-4	kmolSin/ m^3
Ki_h2_fa	3.13x10-7	kmolSh2/ m^3	3.125x10-7	kmolSh2/ m^3
Ki_h2_c4	6.25x10-7	kmolSh2/ m^3	6.250x10-7	kmolSh2/ m^3
Ki_h2_pro	2.19x10-7	kmolSh2/ m^3	2.188x10-7	kmolSh2/ m^3
Ki_nh3	0.00180	kmolSnh3/ m^3	1.800x10-3	kmolSnh3/ m^3
k_dec_Xsu	8.33x10-4	1/h	2.315x10-7	1/s
k_dec_Xaa	8.33x10-4	1/h	2.315x10-7	1/s
k_dec_Xfa	8.33x10-4	1/h	2.315x10-7	1/s
k_dec_Xc4	8.33x10-4	1/h	2.315x10-7	1/s
k_dec_Xpro	8.33x10-4	1/h	2.315x10-7	1/s
k_dec_Xac	8.33x10-4	1/h	2.315x10-7	1/s
k_dec_Xh2	8.33x10-4	1/h	2.315x10-7	1/s
k_hyd_Xd	0.417	1/h	1.157x10-4	1/s
pHll_acet_acid	4	[]	4	[]
pHul_acet_acid	5.5	[]	5,5	[]
pHll_ac	6	[]	6	[]
pHul_ac	7	[]	7	[]
pHll_H2	5	[]	5	[]
pHul_H2	6	[]	6	[]
Ks_co2	1x10-6	kmol-Sco2/L	1x10-6	kmol-Sco2/ m^3

APPENDIX H: FIGURES FROM CHAPTER 4

H ADM1 state variables

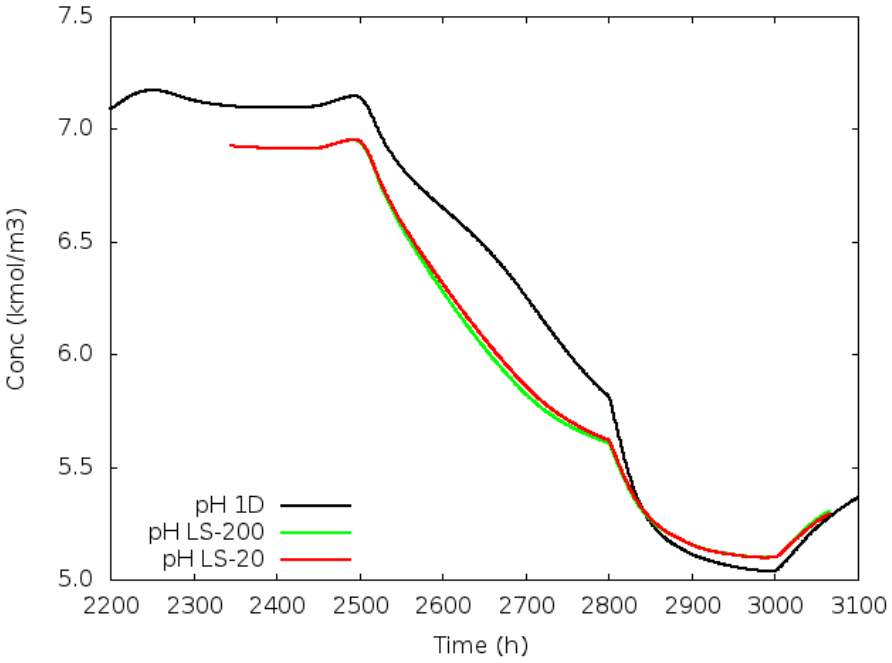

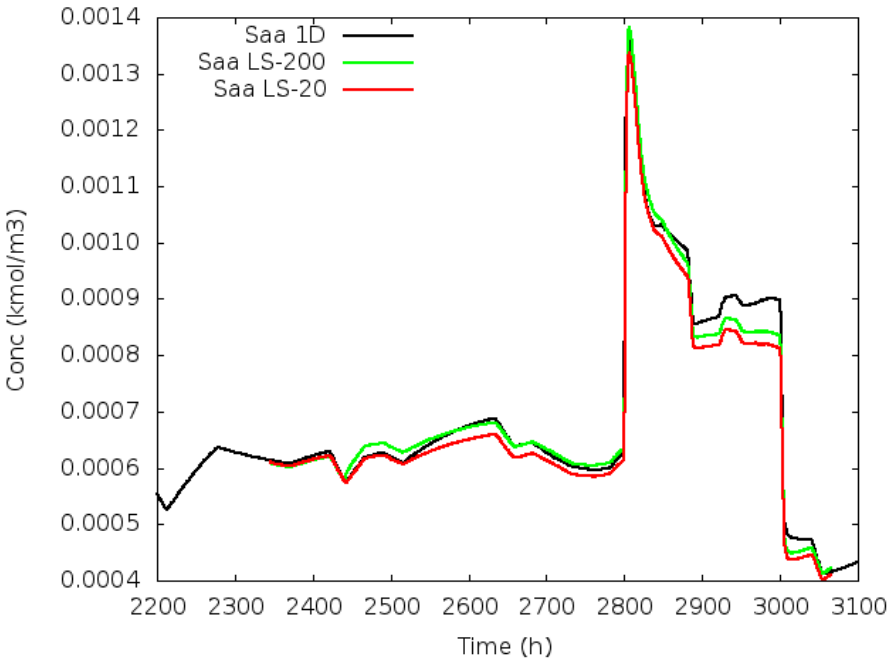

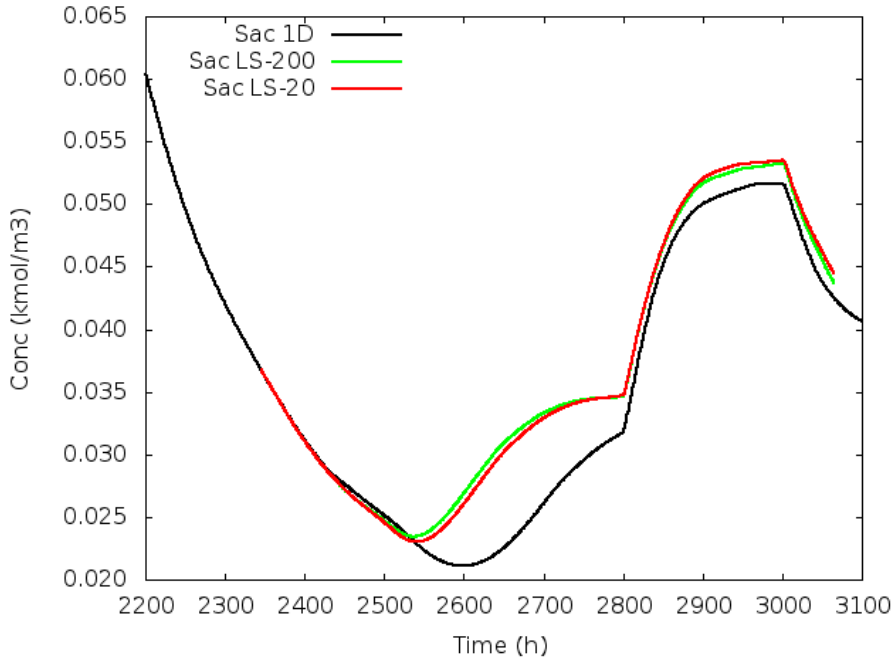
Sac 1D
Sac LS-200
Sac LS-20
Conc (kmol/m3)
Time (h)
0.065
0.060
0.055
0.050
0.045
0.040
0.035
0.030
0.025
0.020
2200
2300
2400
2500
2600
2700
2800
2900
3000
3100

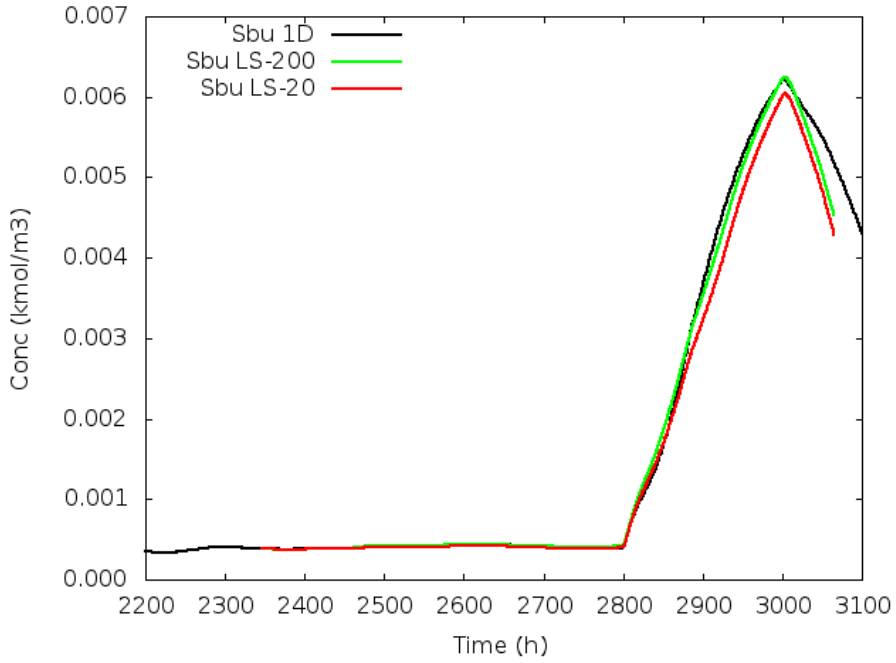
Sbu 1D
Sbu LS-200
Sbu LS-20
Conc (kmol/m3)
Time (h)
0.007
0.006
0.005
0.004
0.003
0.002
0.001
0.000
2200
2300
2400
2500
2600
2700
2800
2900
3000
3100

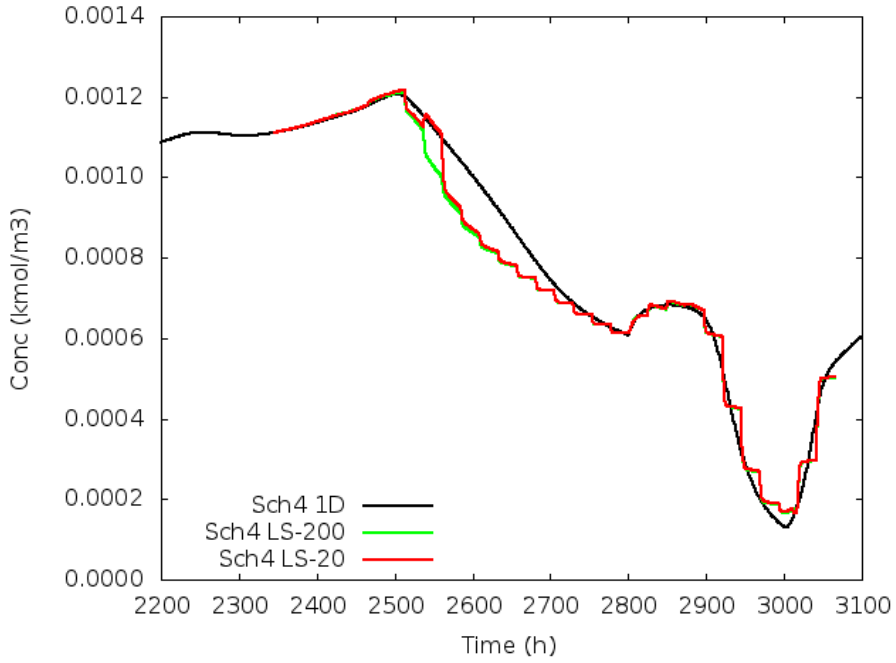
0.0014
0.0012
0.0010
0.0008
0.0006
0.0004
0.0002
0.0000
Conc (kmol/m3)
Sch4 1D
Sch4 LS-200
Sch4 LS-20
2200 2300 2400 2500 2600 2700 2800 2900 3000 3100
Time (h)

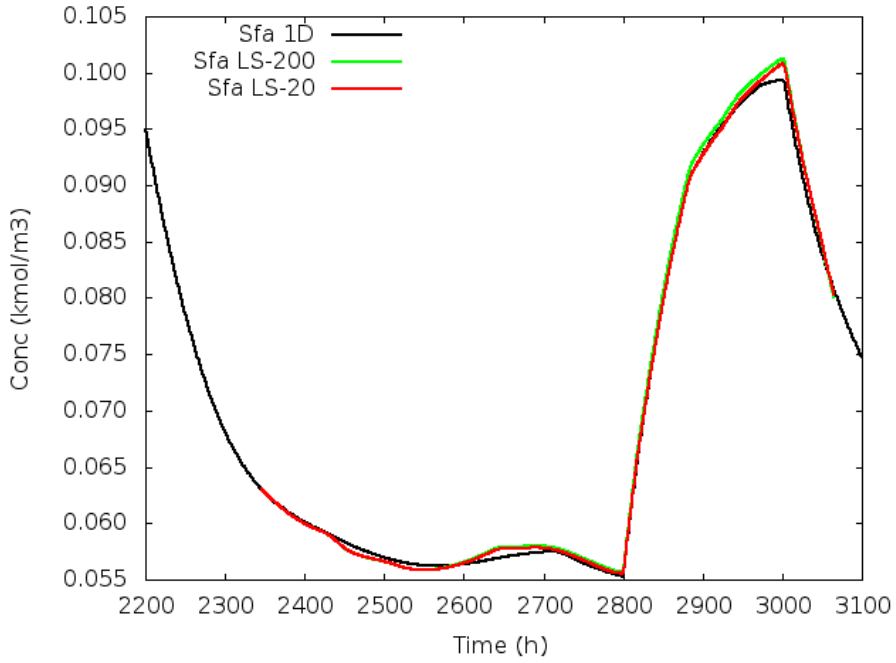
0.105
0.100
0.095
0.090
0.085
0.080
0.075
0.070
0.065
0.060
0.055
Conc (kmol/m3)
Sfa 1D
Sfa LS-200
Sfa LS-20
2200 2300 2400 2500 2600 2700 2800 2900 3000 3100
Time (h)

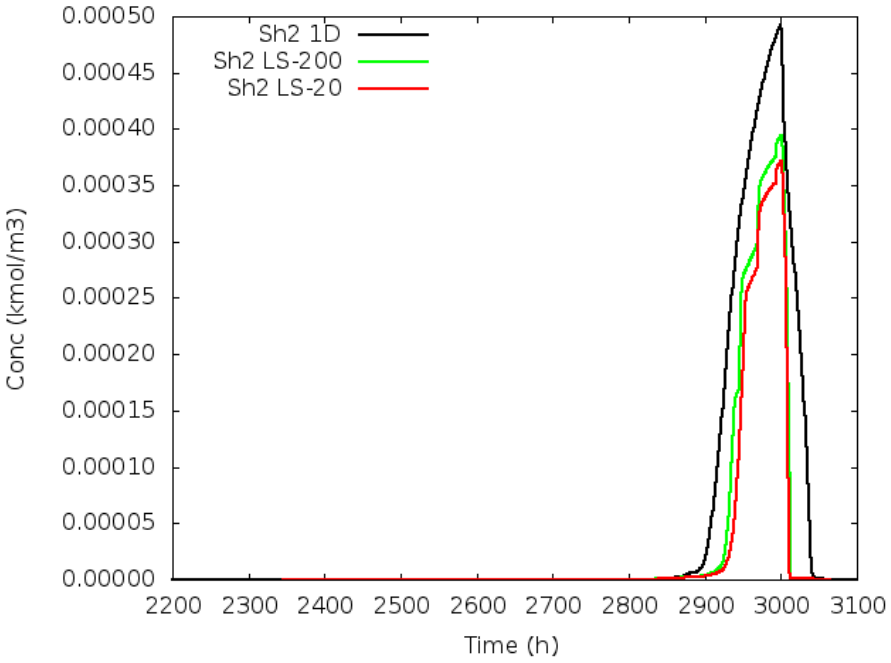
Sh2 1D
Sh2 LS-200
Sh2 LS-20
Conc (kmol/m3)
Time (h)
0.00050
0.00045
0.00040
0.00035
0.00030
0.00025
0.00020
0.00015
0.00010
0.00005
0.00000
2200 2300 2400 2500 2600 2700 2800 2900 3000 3100

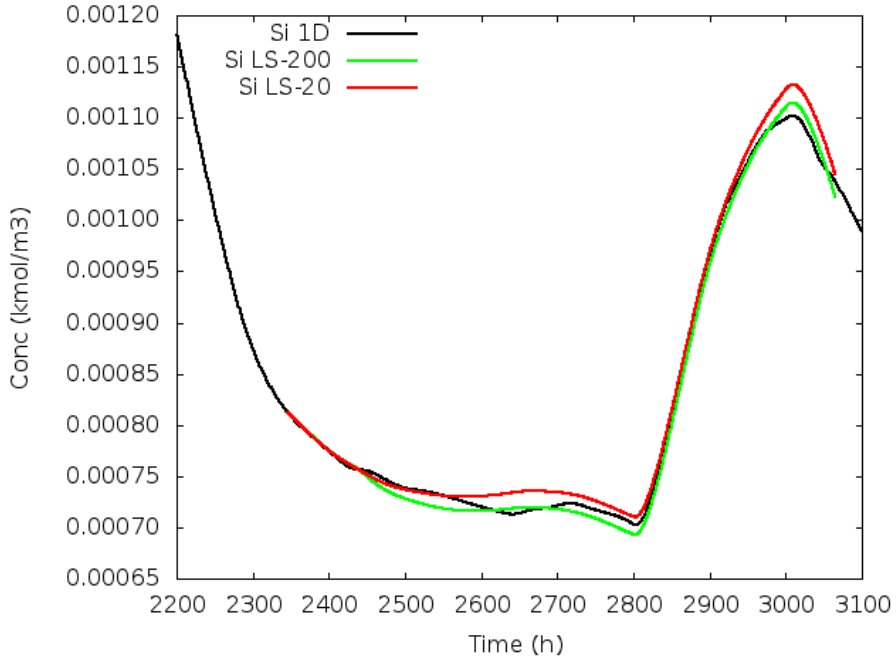
Si 1D
Si LS-200
Si LS-20
Conc (kmol/m3)
Time (h)
0.00120
0.00115
0.00110
0.00105
0.00100
0.00095
0.00090
0.00085
0.00080
0.00075
0.00070
0.00065
2200 2300 2400 2500 2600 2700 2800 2900 3000 3100

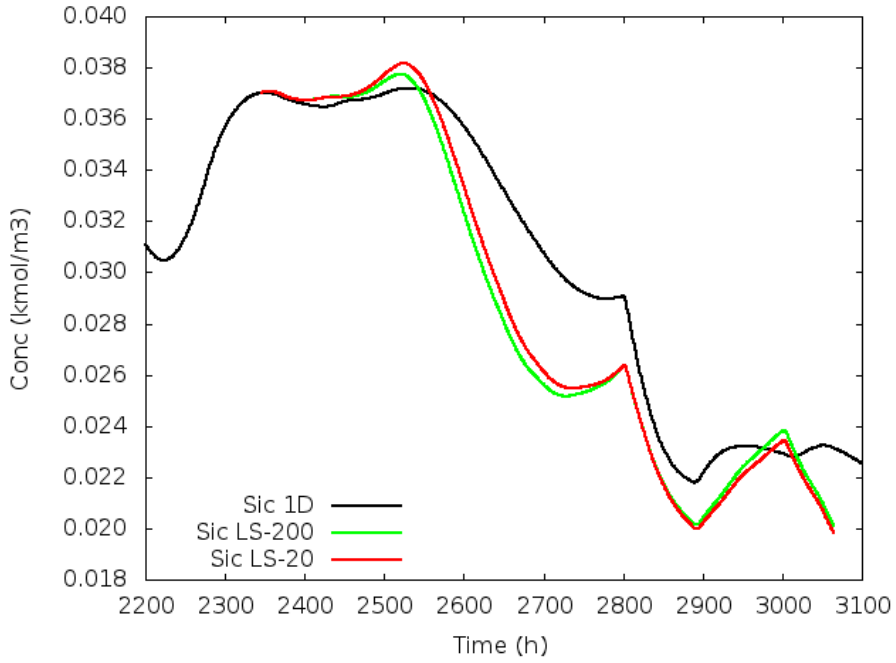
0.040
0.038
0.036
0.034
0.032
0.030
0.028
0.026
0.024
0.022
0.020
0.018
Conc (kmol/m3)
Sic 1D
Sic LS-200
Sic LS-20
2200
2300
2400
2500
2600
2700
2800
2900
3000
3100
Time (h)

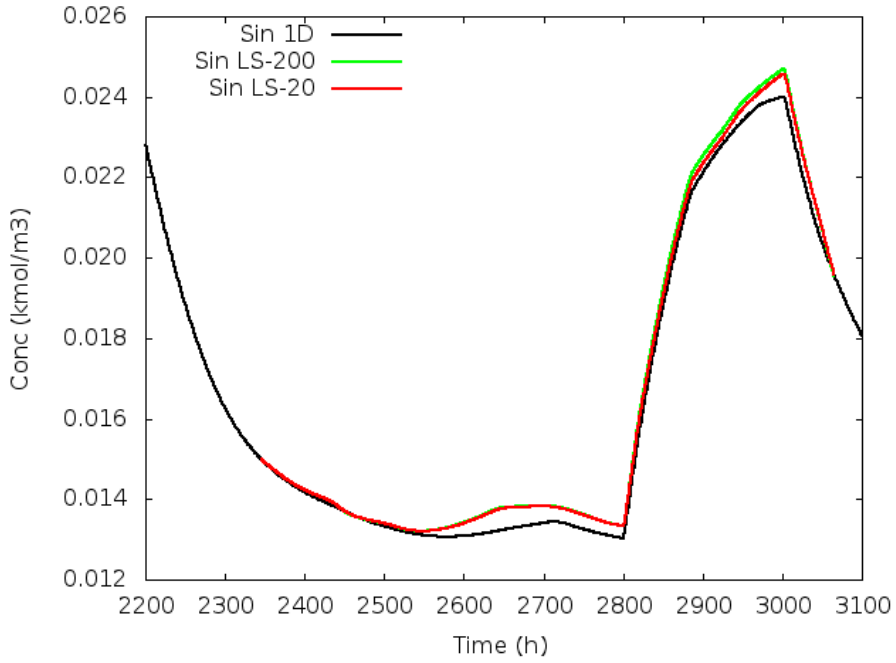
0.026
0.024
0.022
0.020
0.018
0.016
0.014
0.012
Conc (kmol/m3)
Sin 1D
Sin LS-200
Sin LS-20
2200
2300
2400
2500
2600
2700
2800
2900
3000
3100
Time (h)

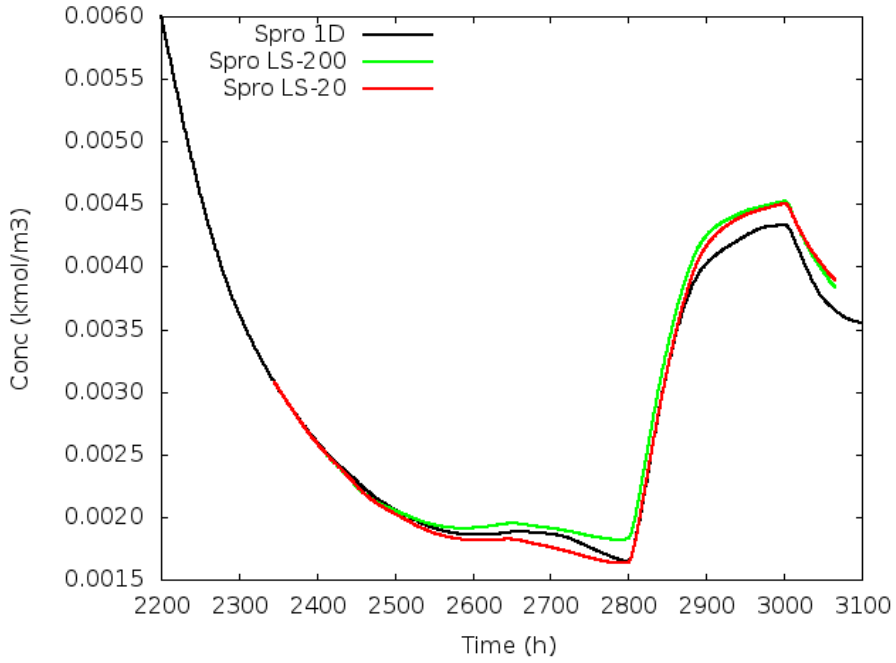
Spro 1D
Spro LS-200
Spro LS-20
Conc (kmol/m3)
Time (h)
0.0060
0.0055
0.0050
0.0045
0.0040
0.0035
0.0030
0.0025
0.0020
0.0015
2200
2300
2400
2500
2600
2700
2800
2900
3000
3100

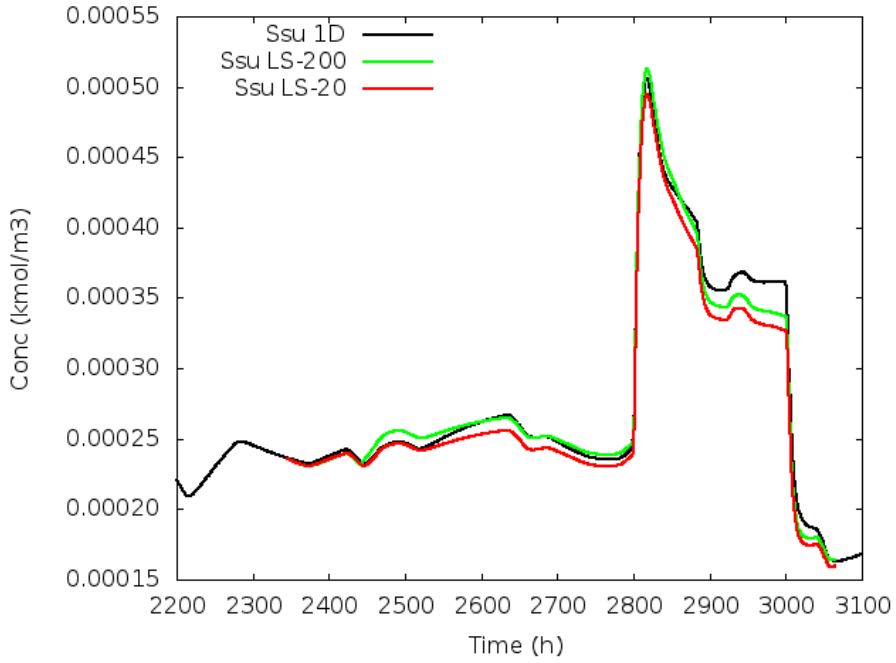
Ssu 1D
Ssu LS-200
Ssu LS-20
Conc (kmol/m3)
Time (h)
0.00055
0.00050
0.00045
0.00040
0.00035
0.00030
0.00025
0.00020
0.00015
2200
2300
2400
2500
2600
2700
2800
2900
3000
3100

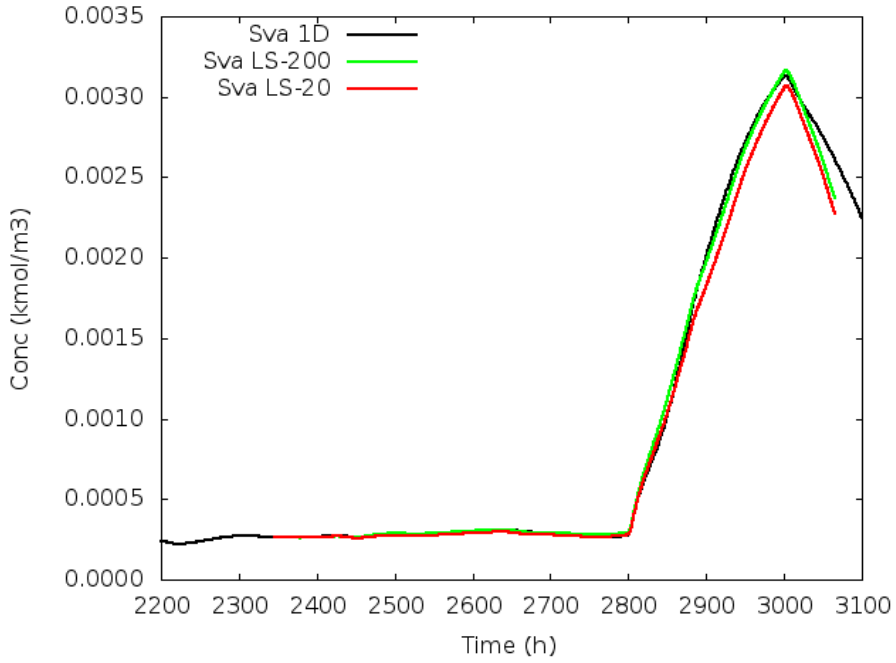
Sva 1D
Sva LS-200
Sva LS-20
Conc (kmol/m3)
Time (h)
0.0035
0.0030
0.0025
0.0020
0.0015
0.0010
0.0005
0.0000
2200
2300
2400
2500
2600
2700
2800
2900
3000
3100

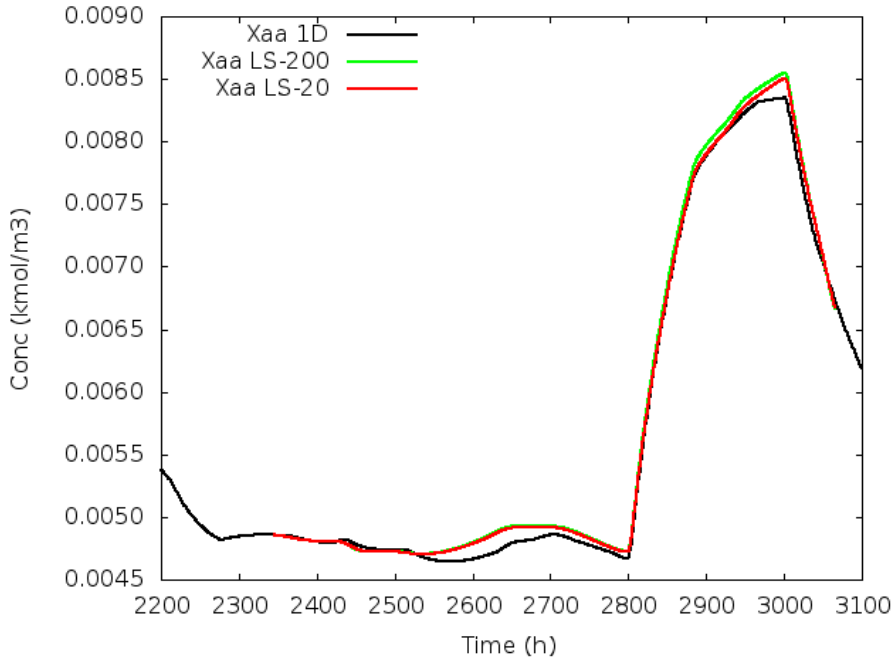
Xaa 1D
Xaa LS-200
Xaa LS-20
Conc (kmol/m3)
Time (h)
0.0090
0.0085
0.0080
0.0075
0.0070
0.0065
0.0060
0.0055
0.0050
0.0045
2200
2300
2400
2500
2600
2700
2800
2900
3000
3100

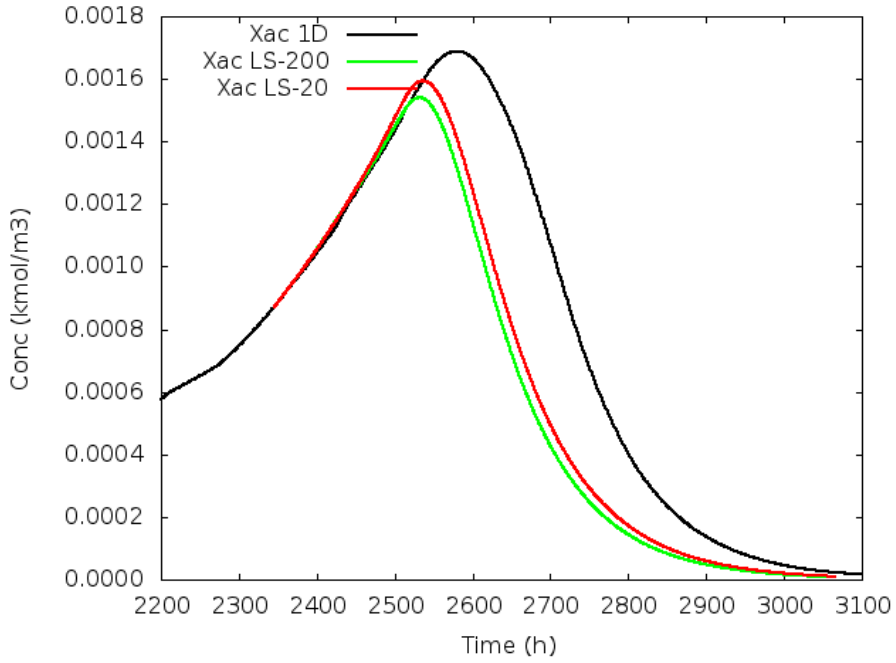
Xac 1D
Xac LS-200
Xac LS-20
Conc (kmol/m3)
Time (h)
0.0018
0.0016
0.0014
0.0012
0.0010
0.0008
0.0006
0.0004
0.0002
0.0000
2200
2300
2400
2500
2600
2700
2800
2900
3000
3100

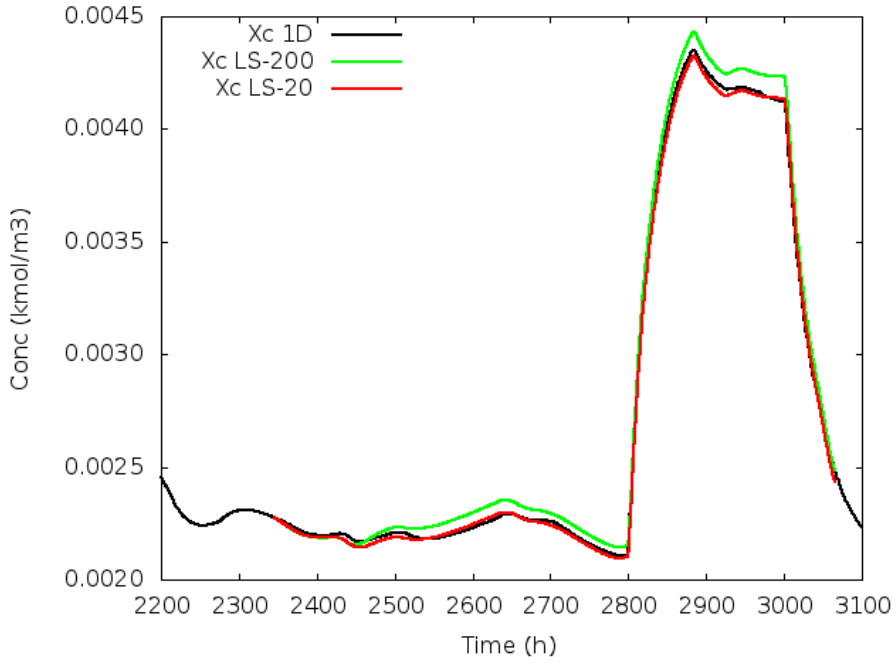
Xc 1D
Xc LS-200
Xc LS-20
Conc (kmol/m3)
Time (h)
0.0045
0.0040
0.0035
0.0030
0.0025
0.0020
2200
2300
2400
2500
2600
2700
2800
2900
3000
3100

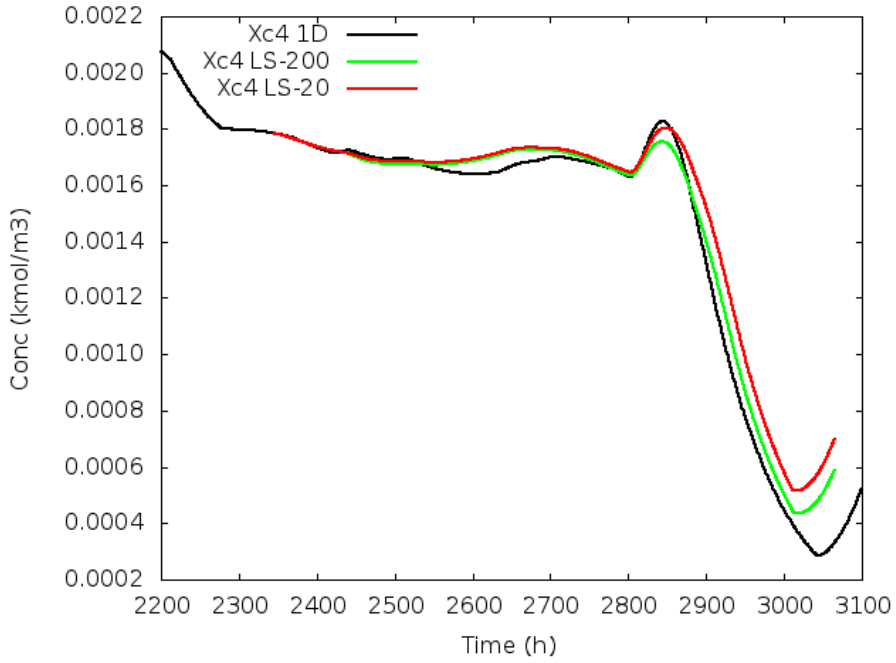
Xc4 1D
Xc4 LS-200
Xc4 LS-20
Conc (kmol/m3)
Time (h)
0.0022
0.0020
0.0018
0.0016
0.0014
0.0012
0.0010
0.0008
0.0006
0.0004
0.0002
2200 2300 2400 2500 2600 2700 2800 2900 3000 3100

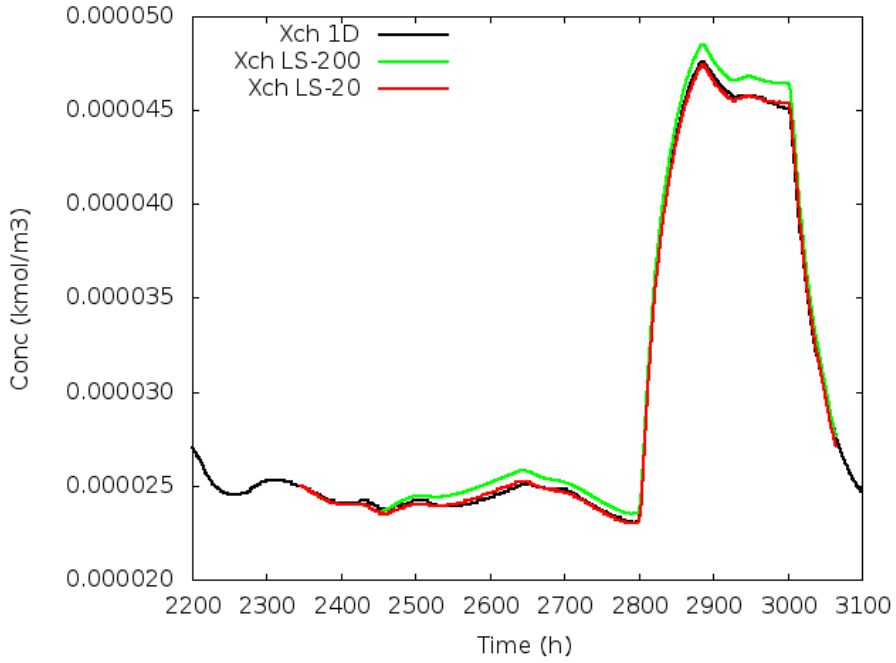
Xch 1D
Xch LS-200
Xch LS-20
Conc (kmol/m3)
Time (h)
0.000050
0.000045
0.000040
0.000035
0.000030
0.000025
0.000020
2200 2300 2400 2500 2600 2700 2800 2900 3000 3100

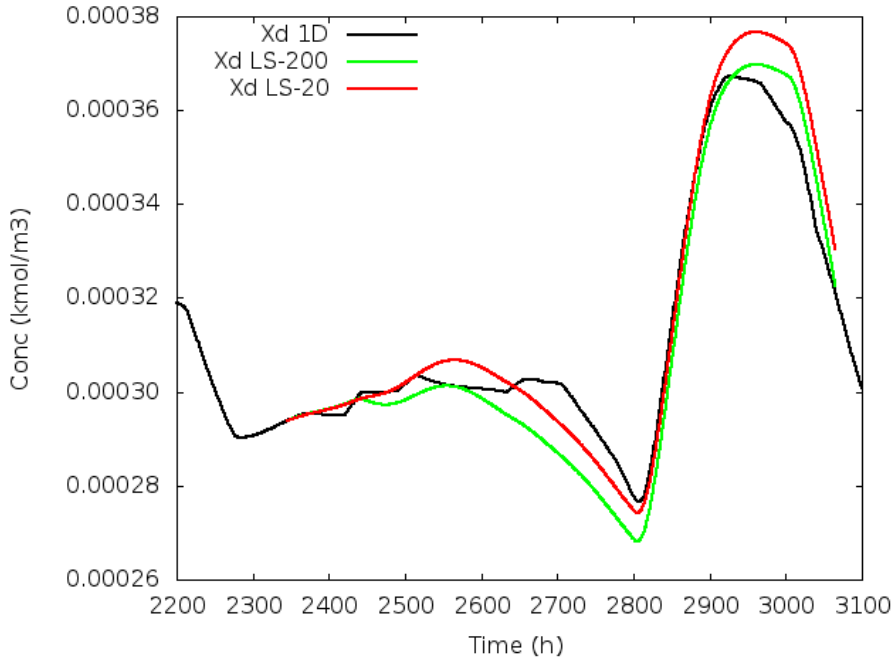
Xd 1D
Xd LS-200
Xd LS-20
Conc (kmol/m3)
Time (h)
0.00038
0.00036
0.00034
0.00032
0.00030
0.00028
0.00026
2200 2300 2400 2500 2600 2700 2800 2900 3000 3100

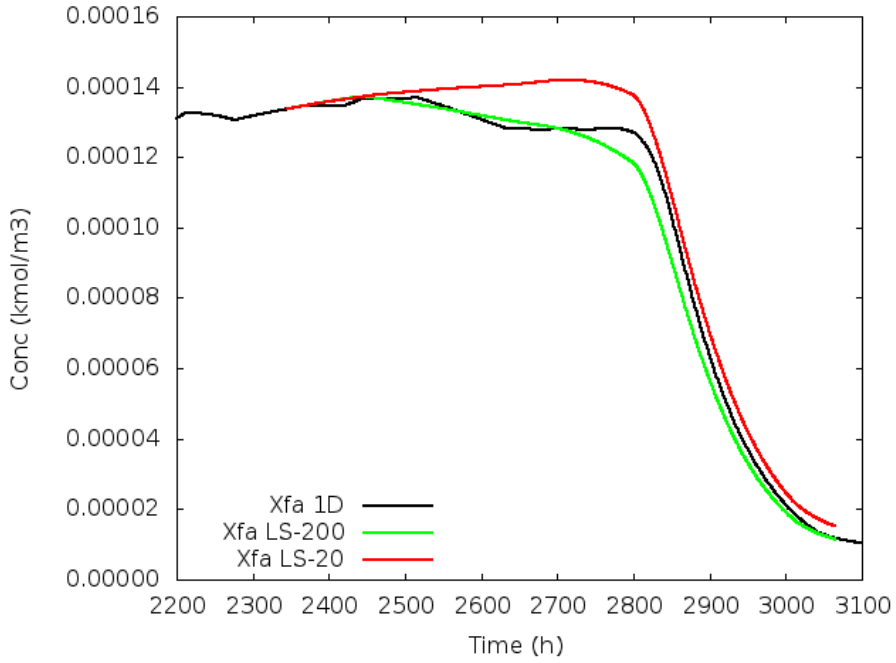
Xfa 1D
Xfa LS-200
Xfa LS-20
Conc (kmol/m3)
Time (h)
0.00016
0.00014
0.00012
0.00010
0.00008
0.00006
0.00004
0.00002
0.00000
2200 2300 2400 2500 2600 2700 2800 2900 3000 3100

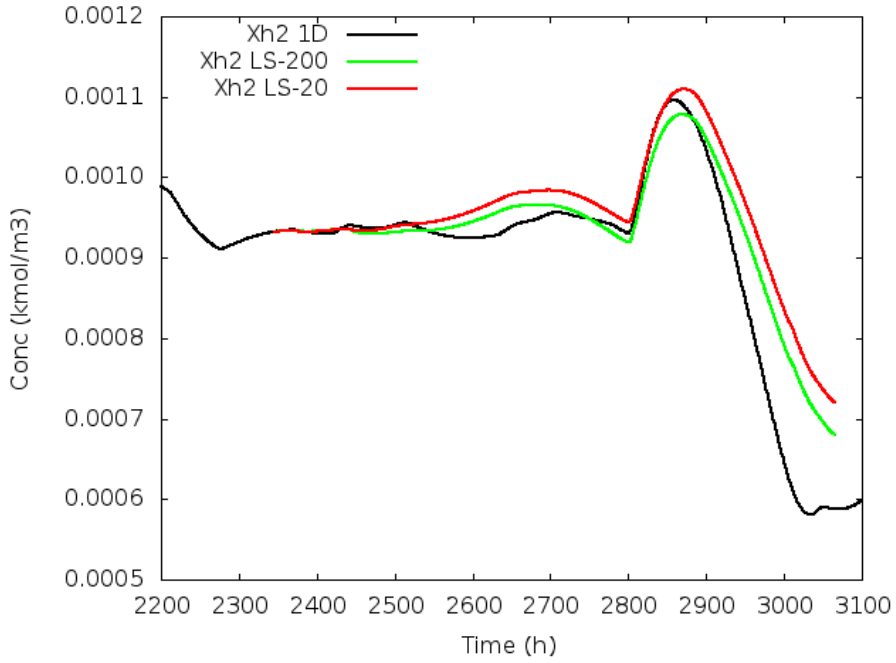
Xh2 1D
Xh2 LS-200
Xh2 LS-20
Conc (kmol/m3)
Time (h)
0.0012
0.0011
0.0010
0.0009
0.0008
0.0007
0.0006
0.0005
2200
2300
2400
2500
2600
2700
2800
2900
3000
3100

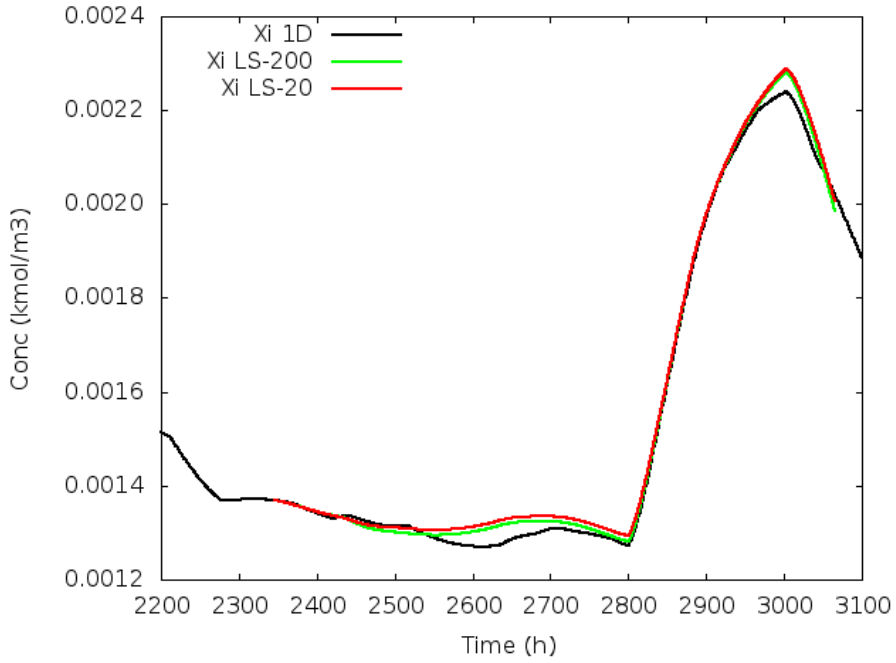
Xi 1D
Xi LS-200
Xi LS-20
Conc (kmol/m3)
Time (h)
0.0024
0.0022
0.0020
0.0018
0.0016
0.0014
0.0012
2200
2300
2400
2500
2600
2700
2800
2900
3000
3100

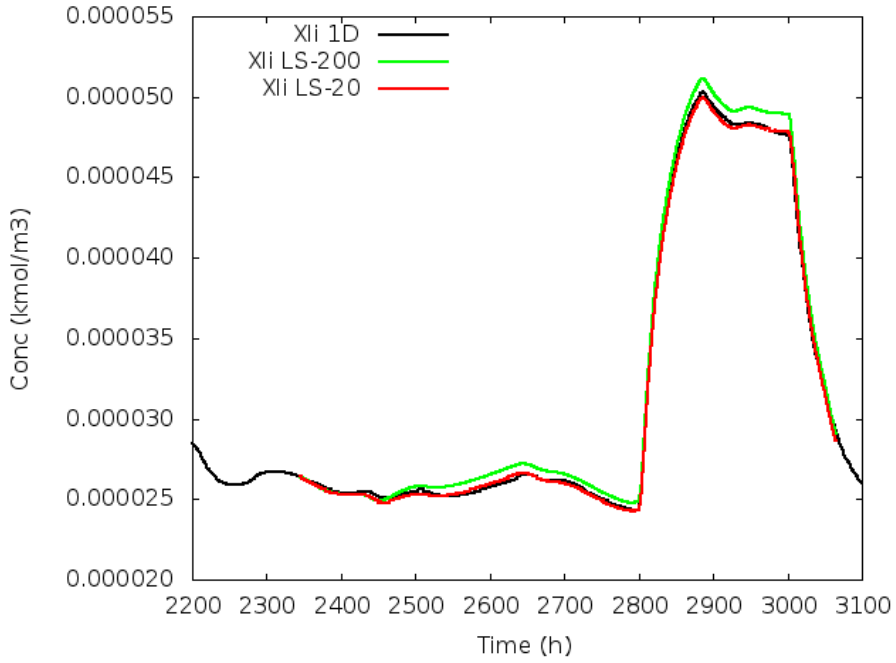
Xli 1D
Xli LS-200
Xli LS-20
Conc (kmol/m3)
Time (h)
0.000055
0.000050
0.000045
0.000040
0.000035
0.000030
0.000025
0.000020
2200 2300 2400 2500 2600 2700 2800 2900 3000 3100

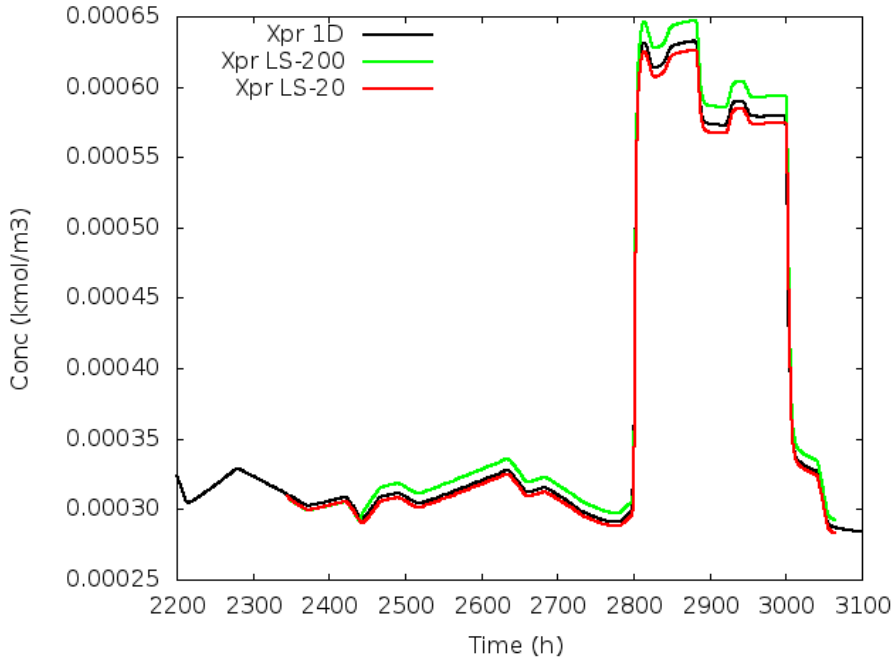
Xpr 1D
Xpr LS-200
Xpr LS-20
Conc (kmol/m3)
Time (h)
0.00065
0.00060
0.00055
0.00050
0.00045
0.00040
0.00035
0.00030
0.00025
2200 2300 2400 2500 2600 2700 2800 2900 3000 3100

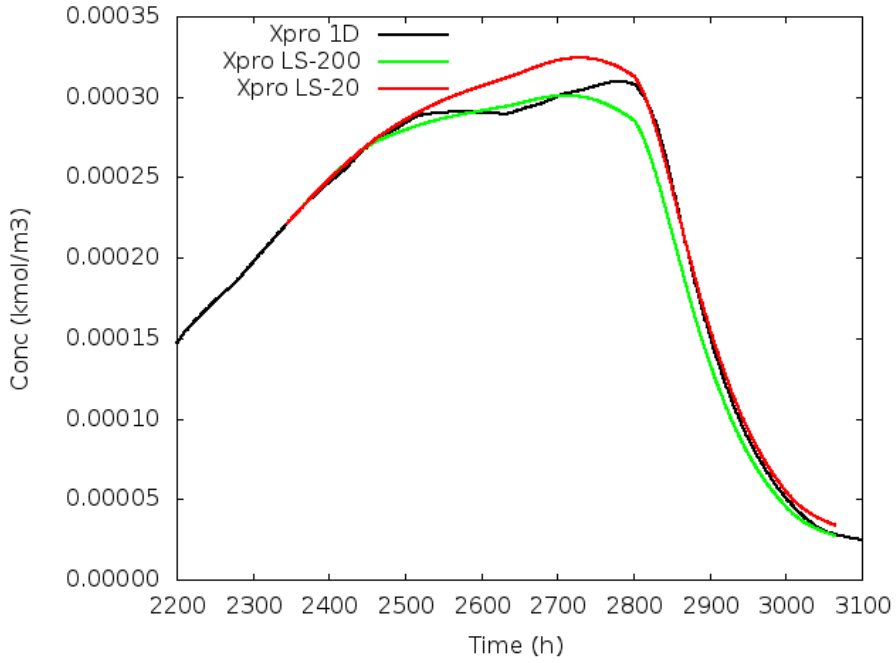
Xpro 1D
Xpro LS-200
Xpro LS-20
Conc (kmol/m3)
Time (h)
0.00035
0.00030
0.00025
0.00020
0.00015
0.00010
0.00005
0.00000
2200 2300 2400 2500 2600 2700 2800 2900 3000 3100

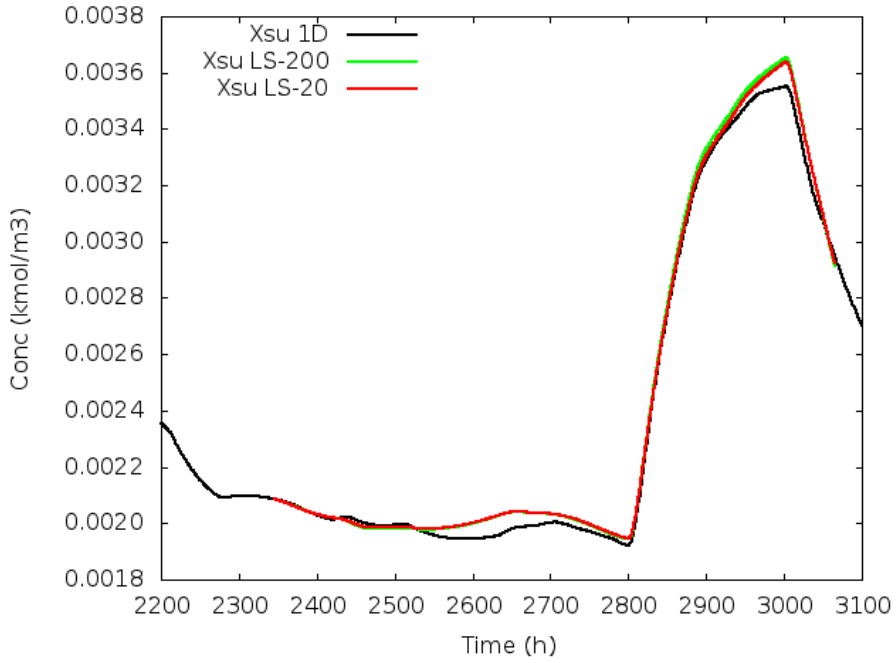
Xsu 1D
Xsu LS-200
Xsu LS-20
Conc (kmol/m3)
Time (h)
0.0038
0.0036
0.0034
0.0032
0.0030
0.0028
0.0026
0.0024
0.0022
0.0020
0.0018
2200 2300 2400 2500 2600 2700 2800 2900 3000 3100

APPENDIX I: FIGURES FROM CHAPTER 5

I.i ADM1 state variables

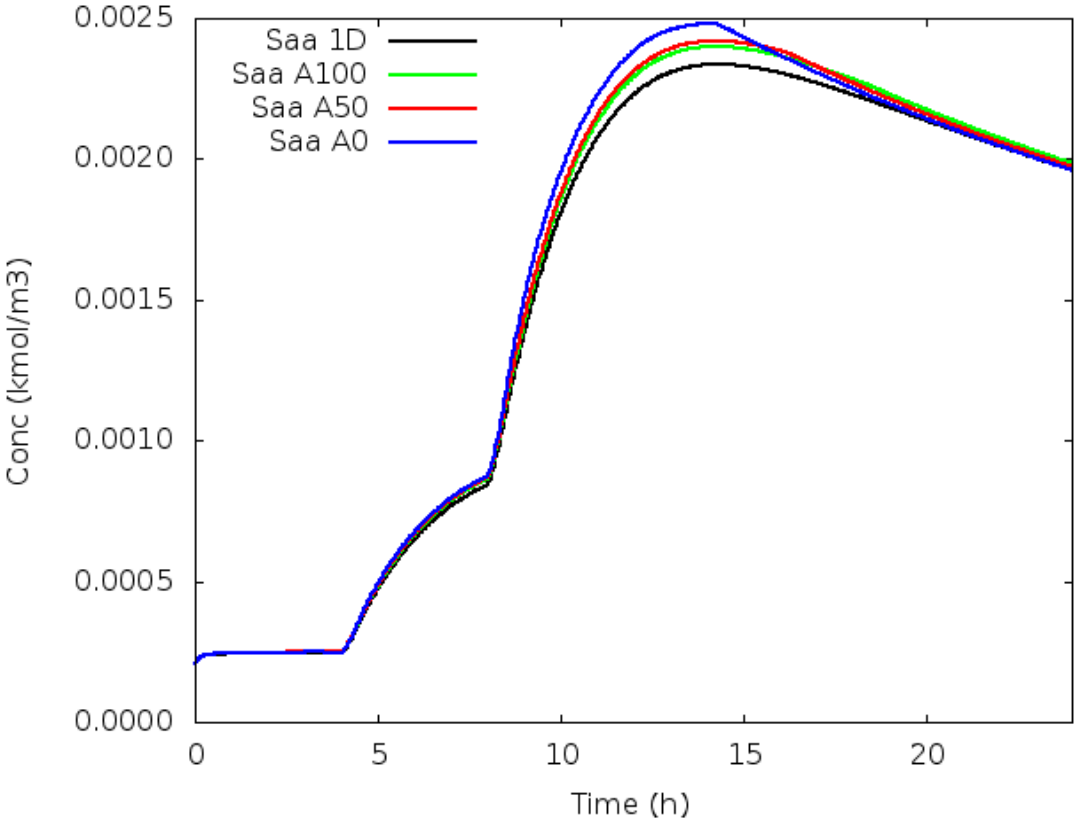

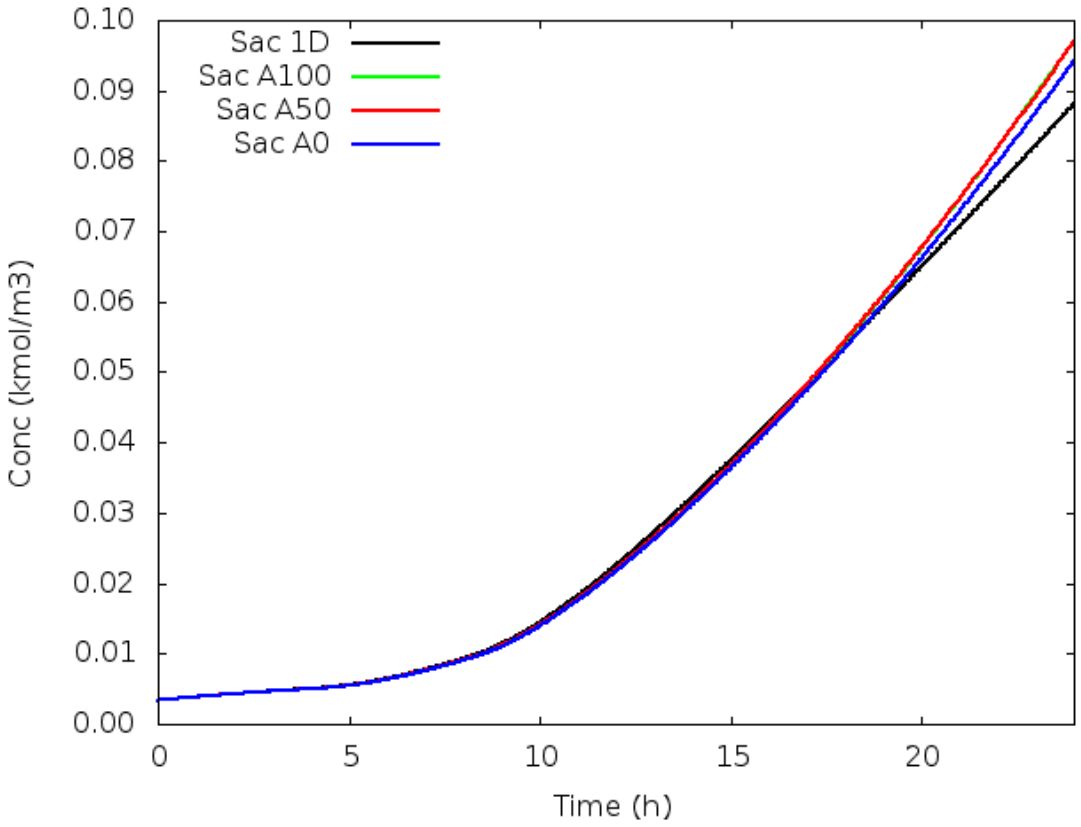
Sac 1D
Sac A100
Sac A50
Sac A0
Conc (kmol/m3)
Time (h)
0.00
0.01
0.02
0.03
0.04
0.05
0.06
0.07
0.08
0.09
0.10
0
5
10
15
20

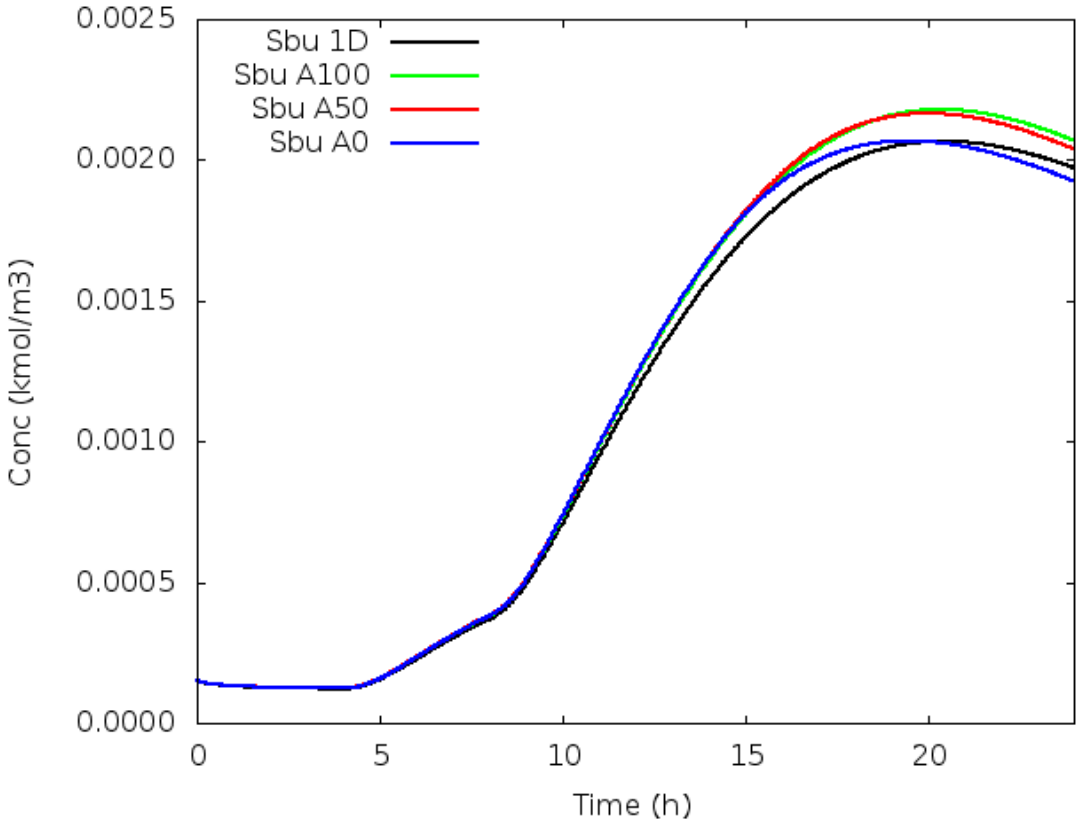
Sbu 1D
Sbu A100
Sbu A50
Sbu A0
Conc (kmol/m3)
Time (h)
0.0000
0.0005
0.0010
0.0015
0.0020
0.0025
0
5
10
15
20

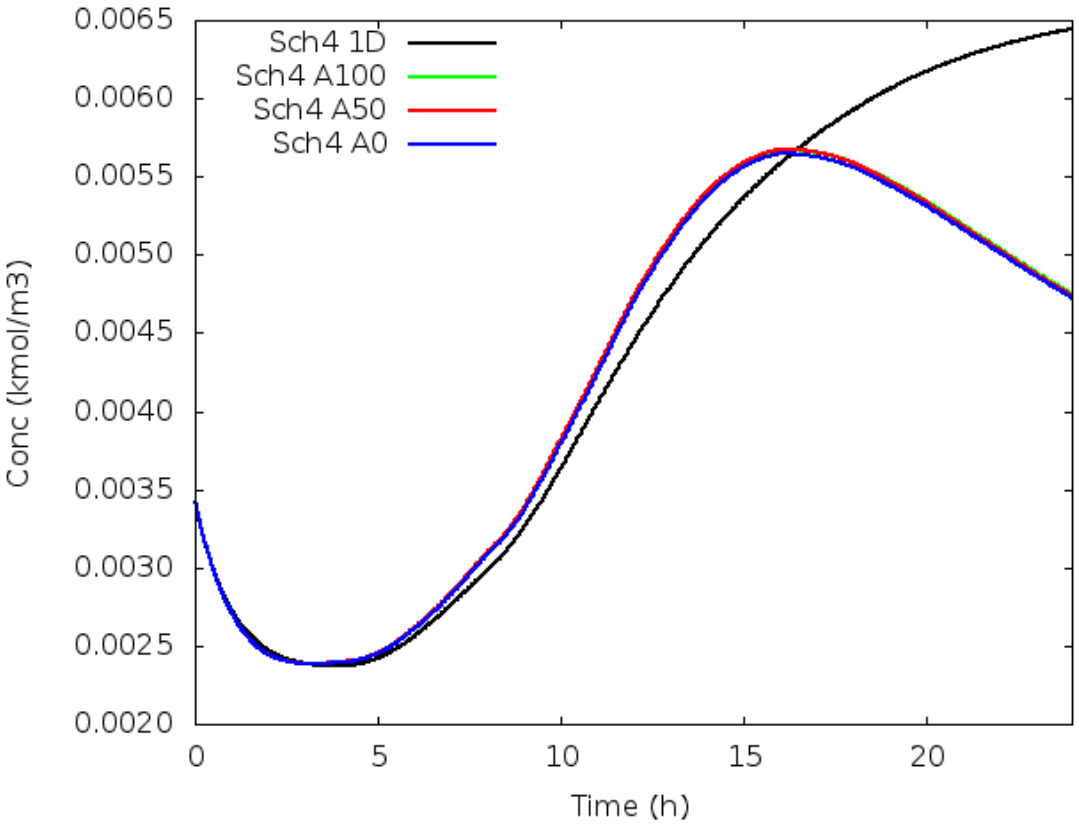
Sch4 1D
Sch4 A100
Sch4 A50
Sch4 A0
Conc (kmol/m3)
Time (h)
0.0065
0.0060
0.0055
0.0050
0.0045
0.0040
0.0035
0.0030
0.0025
0.0020
0
5
10
15
20

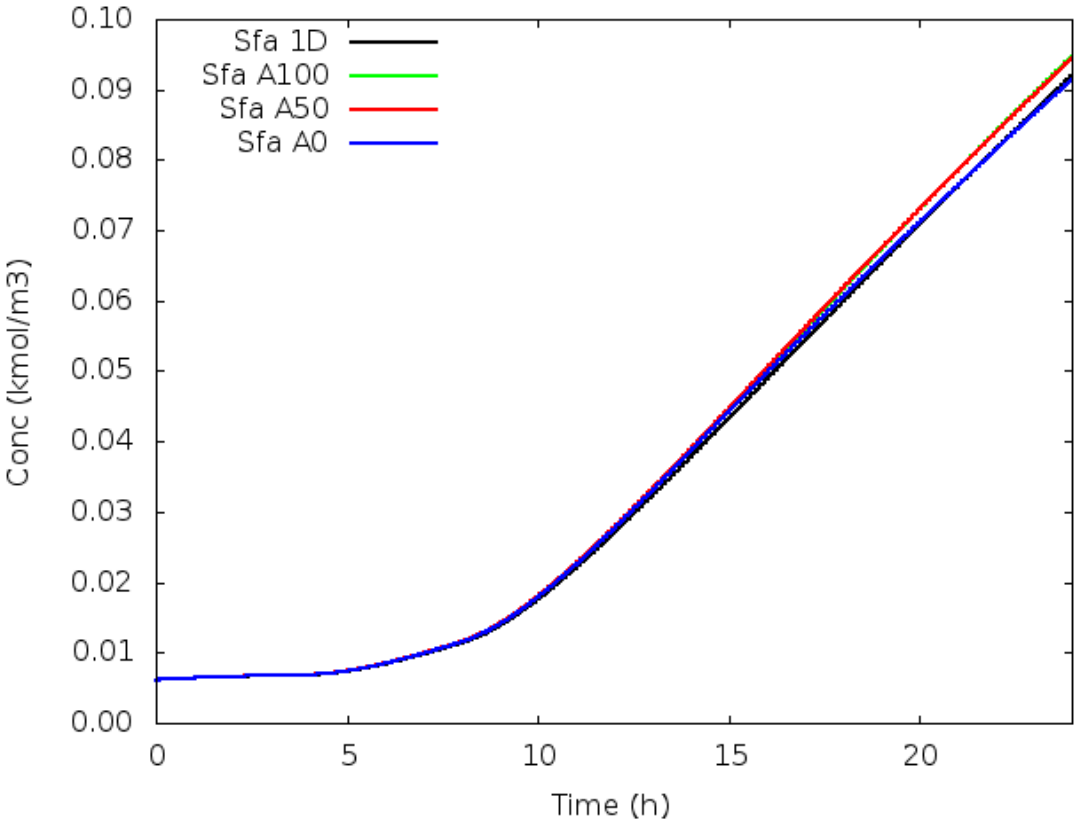
Sfa 1D
Sfa A100
Sfa A50
Sfa A0
Conc (kmol/m3)
Time (h)
0.10
0.09
0.08
0.07
0.06
0.05
0.04
0.03
0.02
0.01
0.00
0
5
10
15
20

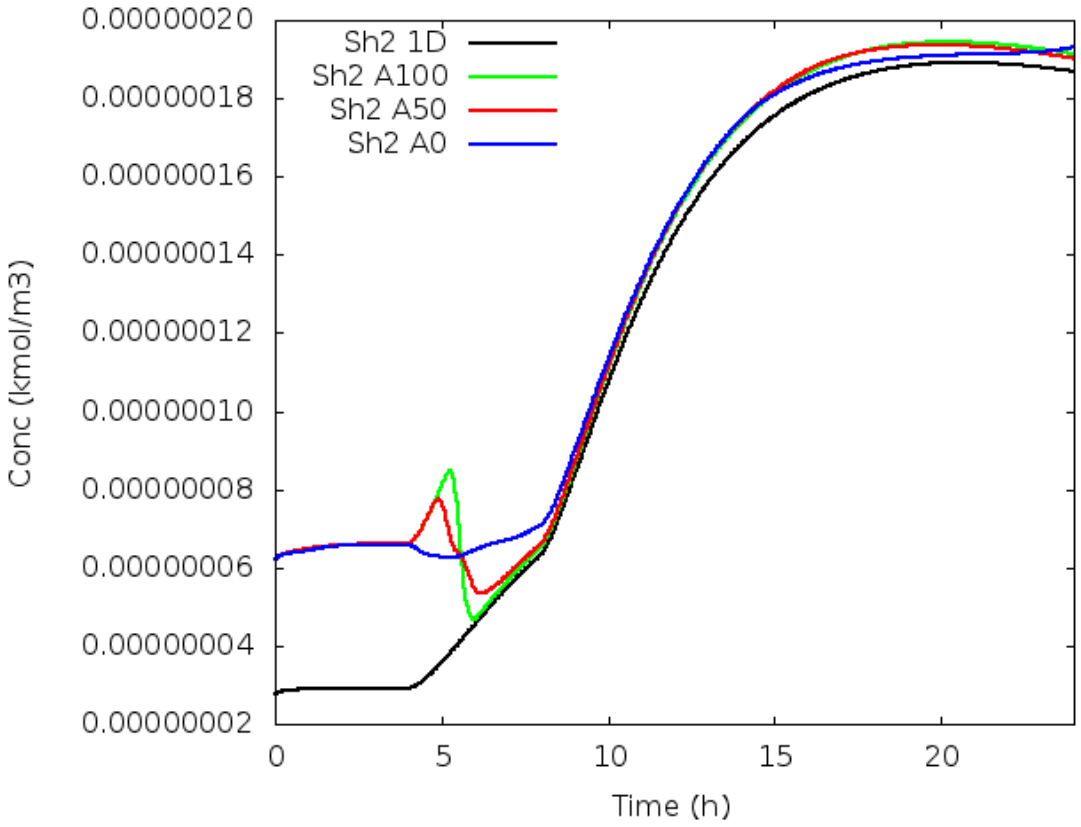
Sh2 1D
Sh2 A100
Sh2 A50
Sh2 A0
Conc (kmol/m3)
Time (h)
0.00000020
0.00000018
0.00000016
0.00000014
0.00000012
0.00000010
0.00000008
0.00000006
0.00000004
0.00000002
0
5
10
15
20

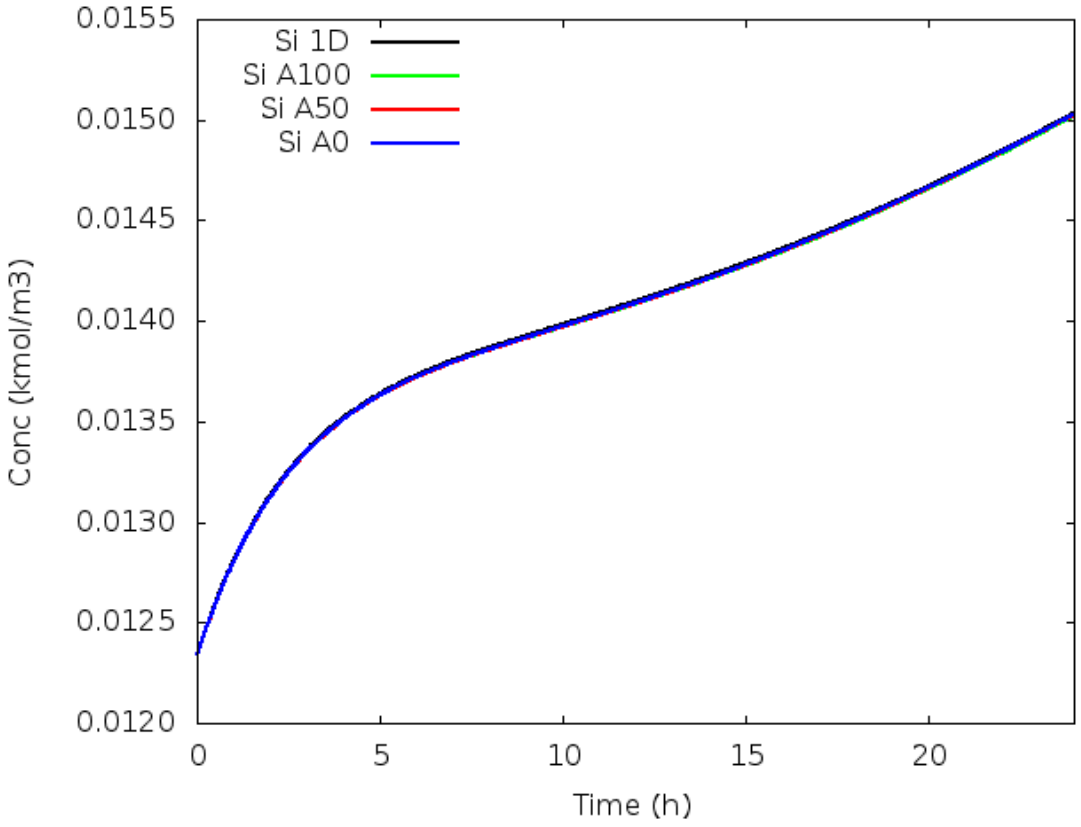
Si 1D
Si A100
Si A50
Si A0
Conc (kmol/m3)
Time (h)
0.0155
0.0150
0.0145
0.0140
0.0135
0.0130
0.0125
0.0120
0
5
10
15
20

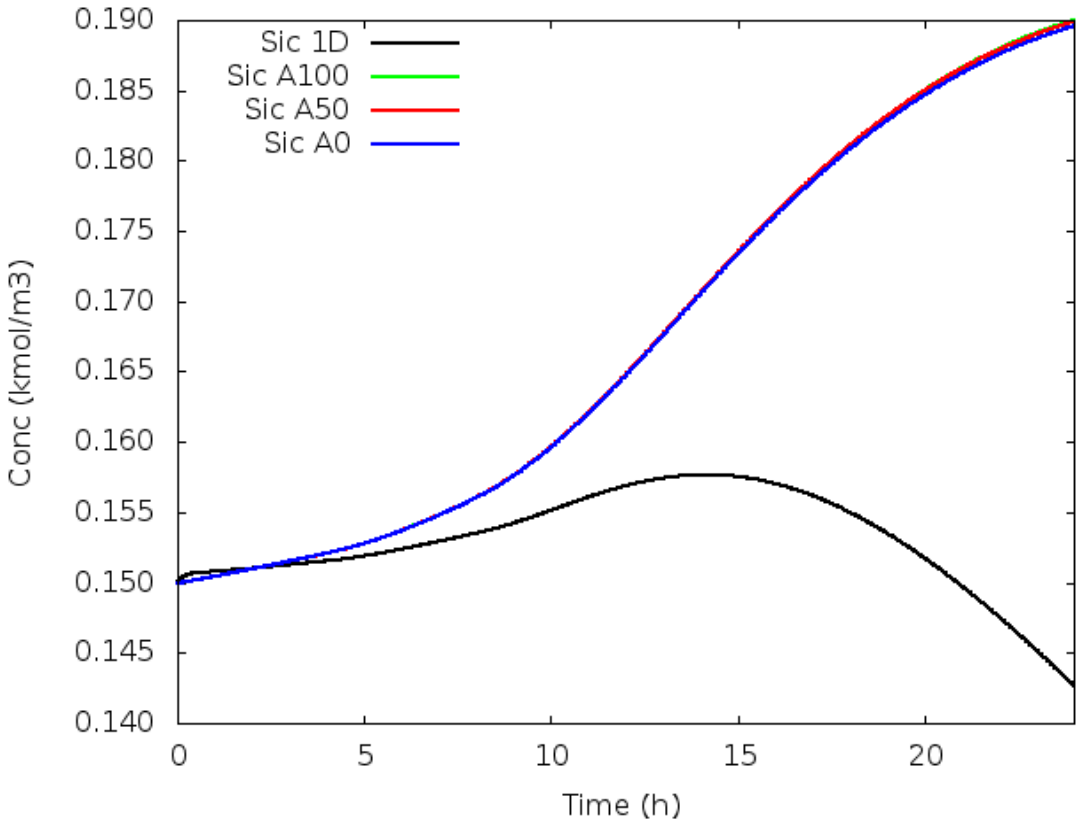
Sic 1D
Sic A100
Sic A50
Sic A0
Conc (kmol/m3)
Time (h)
0.190
0.185
0.180
0.175
0.170
0.165
0.160
0.155
0.150
0.145
0.140
0
5
10
15
20

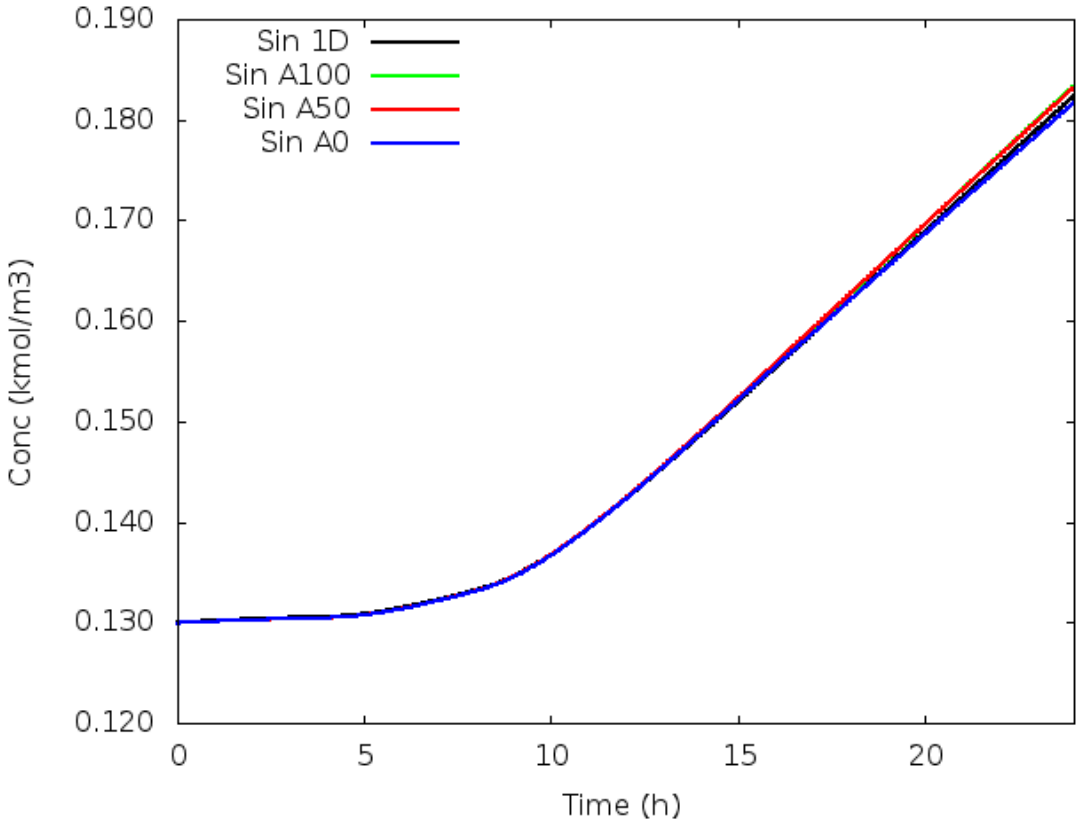
Sin 1D
Sin A100
Sin A50
Sin A0
Conc (kmol/m3)
Time (h)
0.190
0.180
0.170
0.160
0.150
0.140
0.130
0.120
0
5
10
15
20

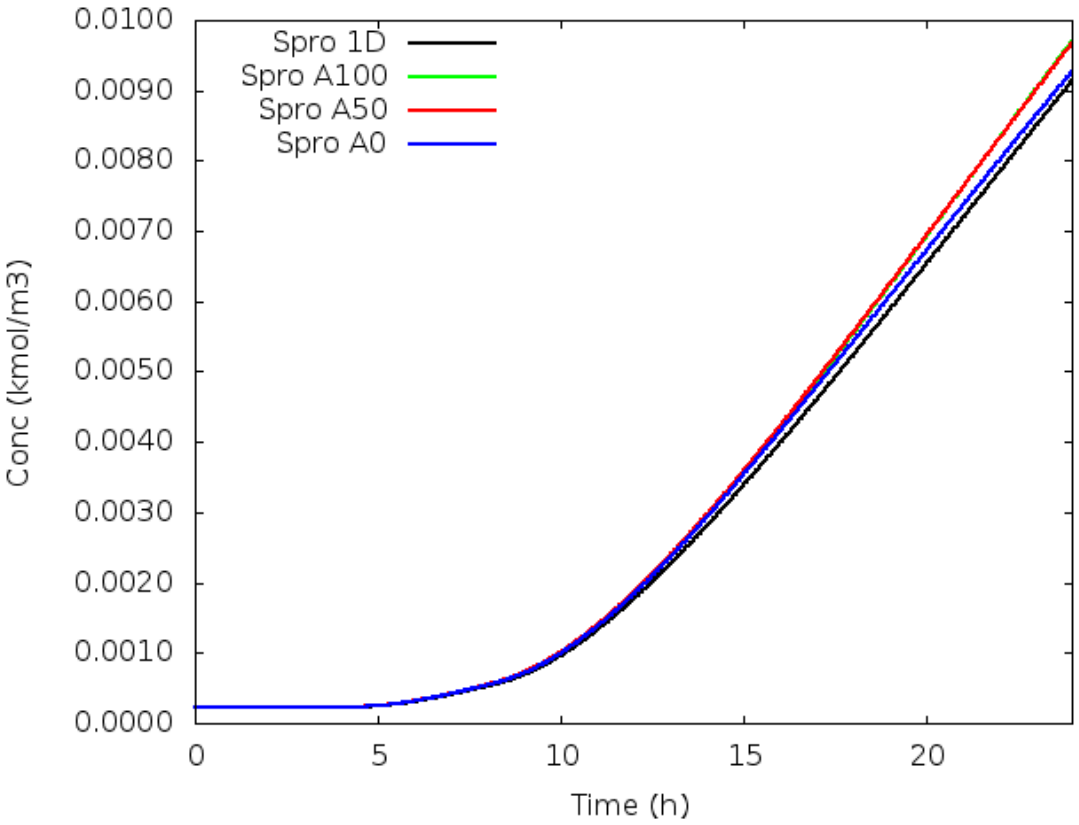
Spro 1D
Spro A100
Spro A50
Spro A0
Conc (kmol/m3)
Time (h)
0.0100
0.0090
0.0080
0.0070
0.0060
0.0050
0.0040
0.0030
0.0020
0.0010
0.0000
0
5
10
15
20

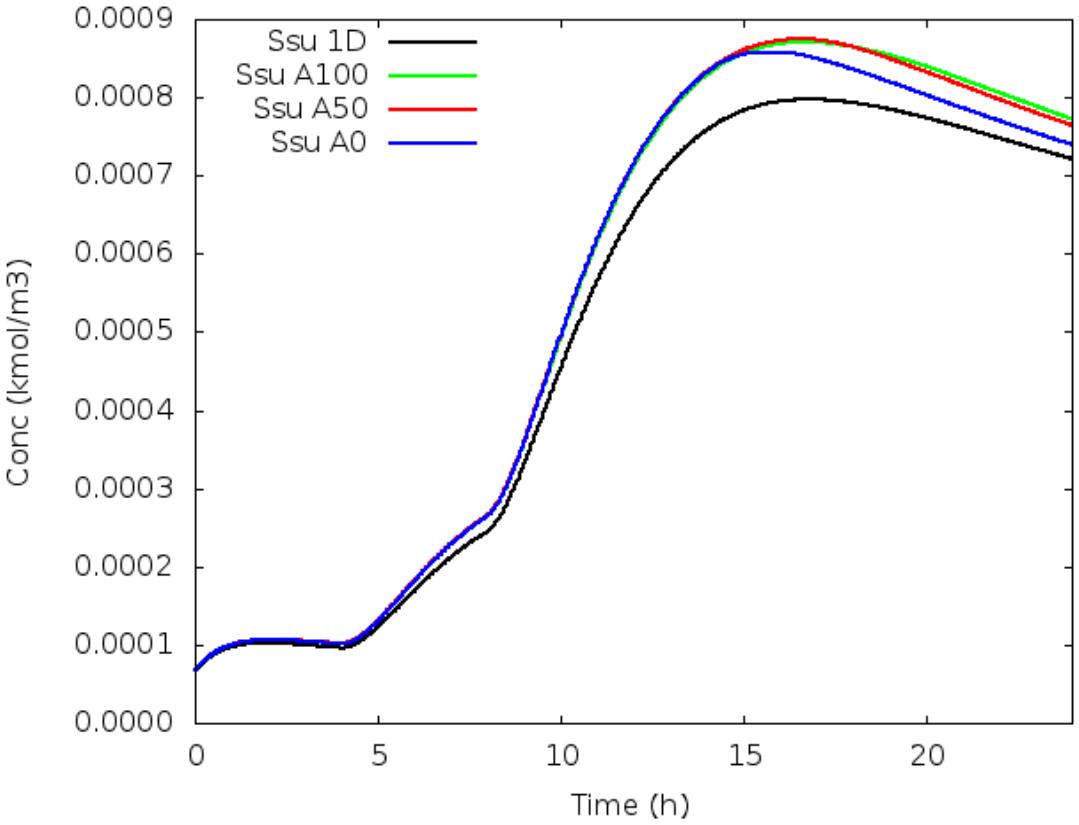
Ssu 1D
Ssu A100
Ssu A50
Ssu A0
Conc (kmol/m3)
Time (h)
0.0009
0.0008
0.0007
0.0006
0.0005
0.0004
0.0003
0.0002
0.0001
0.0000
0
5
10
15
20

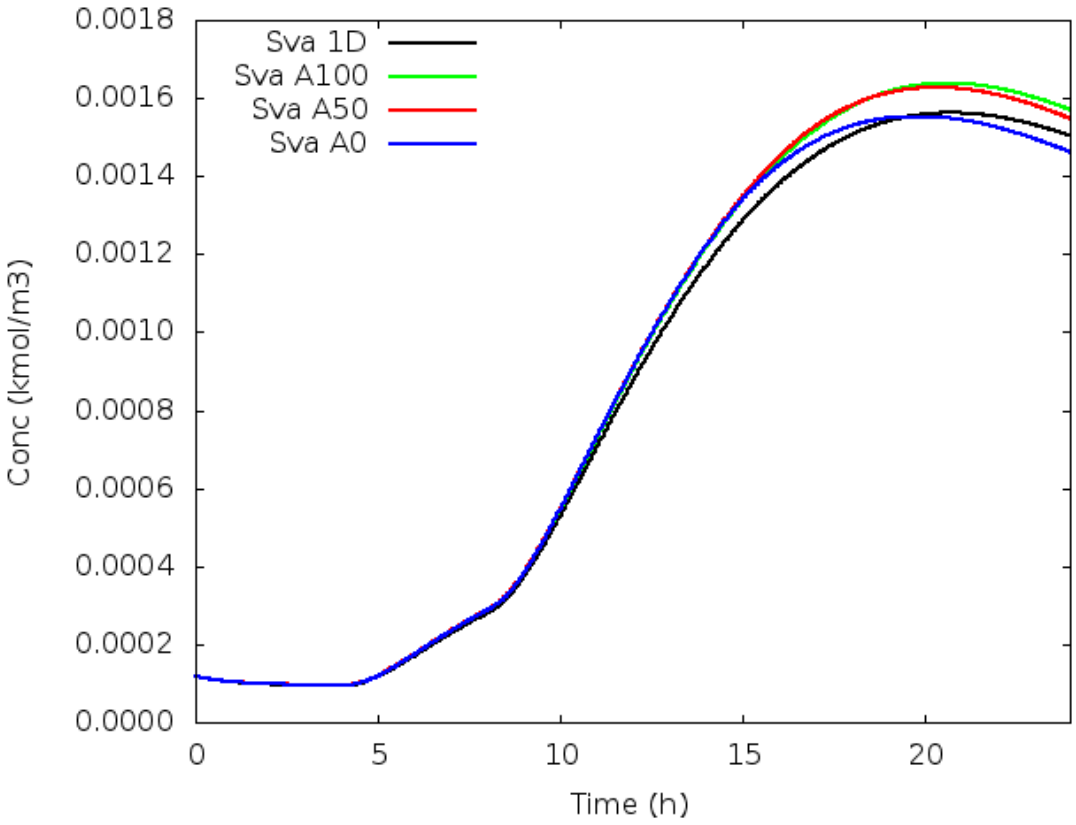
Sva 1D
Sva A100
Sva A50
Sva A0
Conc (kmol/m3)
Time (h)
0.0018
0.0016
0.0014
0.0012
0.0010
0.0008
0.0006
0.0004
0.0002
0.0000
0
5
10
15
20

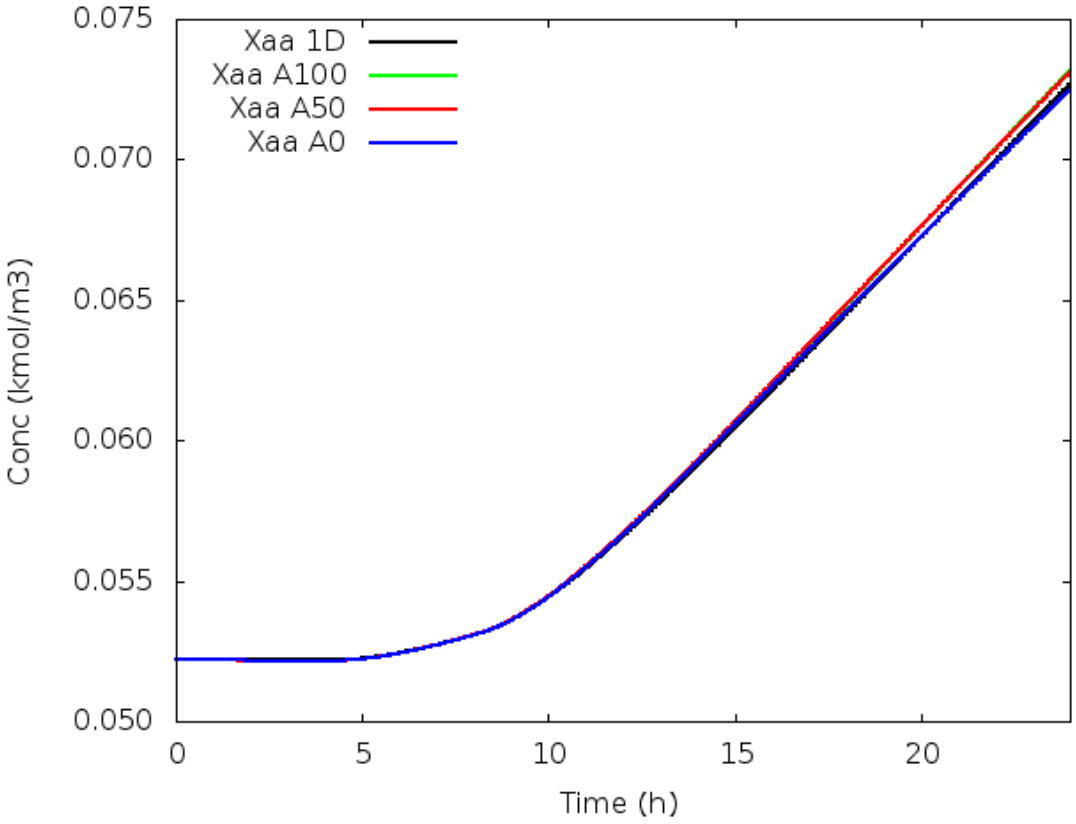
Xaa 1D
Xaa A100
Xaa A50
Xaa A0
Conc (kmol/m3)
Time (h)
0.075
0.070
0.065
0.060
0.055
0.050
0
5
10
15
20

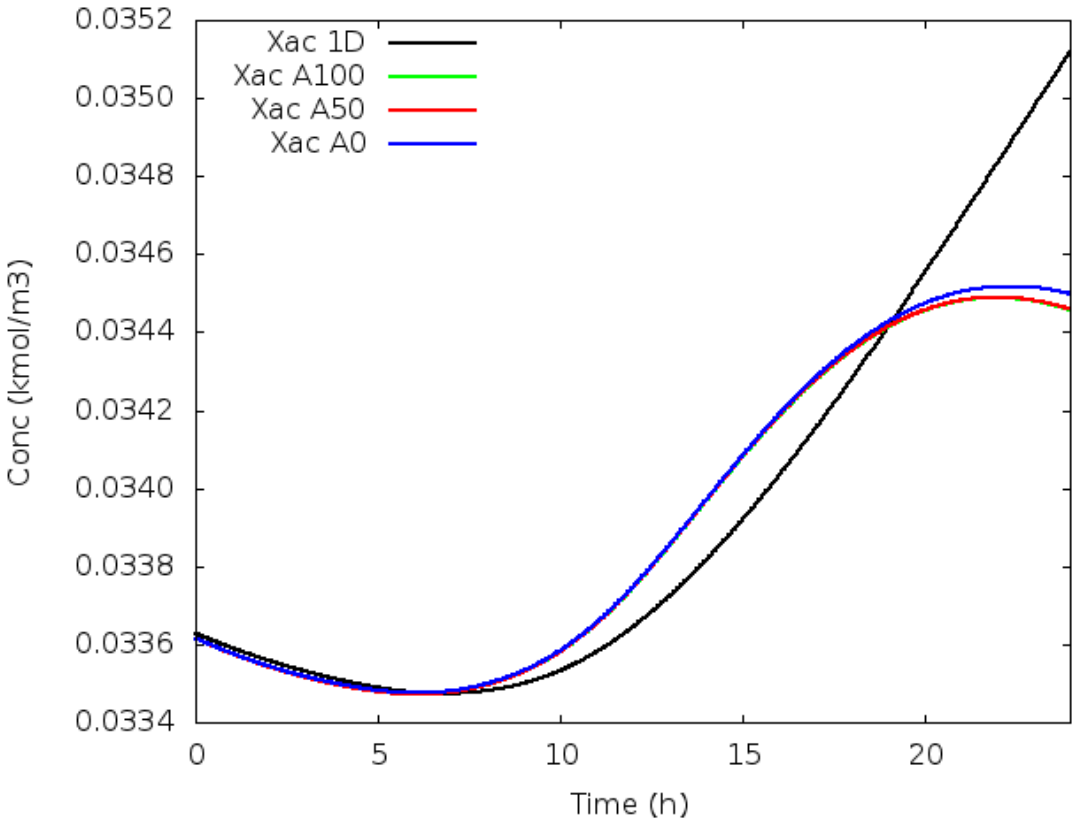
Xac 1D
Xac A100
Xac A50
Xac A0
Conc (kmol/m3)
Time (h)
0.0352
0.0350
0.0348
0.0346
0.0344
0.0342
0.0340
0.0338
0.0336
0.0334
0
5
10
15
20

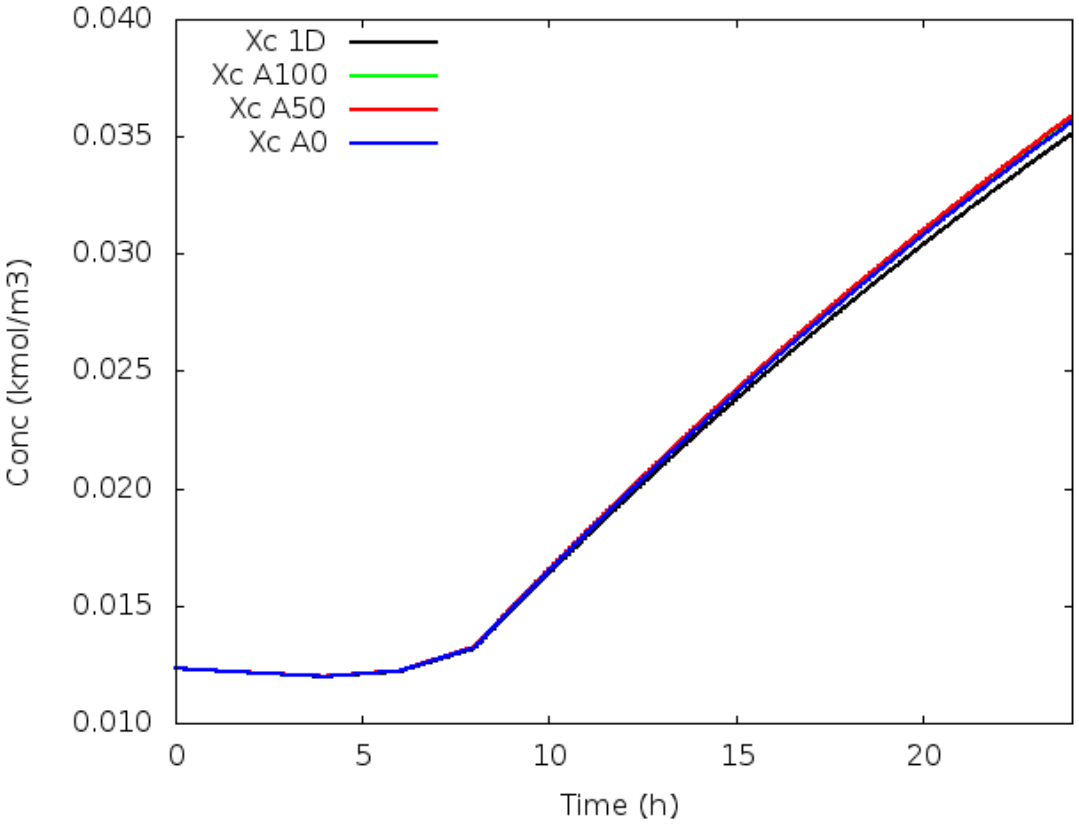
Xc 1D
Xc A100
Xc A50
Xc A0
Conc (kmol/m3)
Time (h)
0.040
0.035
0.030
0.025
0.020
0.015
0.010
0
5
10
15
20

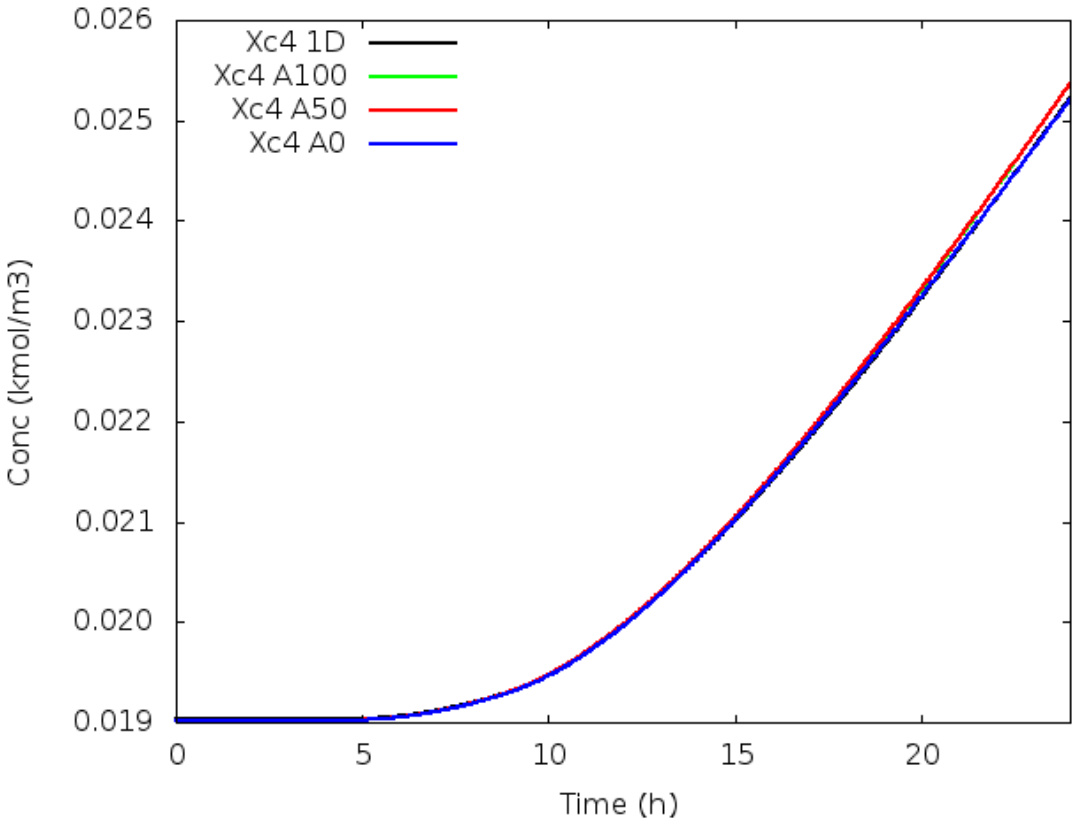
Xc4 1D
Xc4 A100
Xc4 A50
Xc4 A0
Conc (kmol/m3)
Time (h)
0.026
0.025
0.024
0.023
0.022
0.021
0.020
0.019
0
5
10
15
20

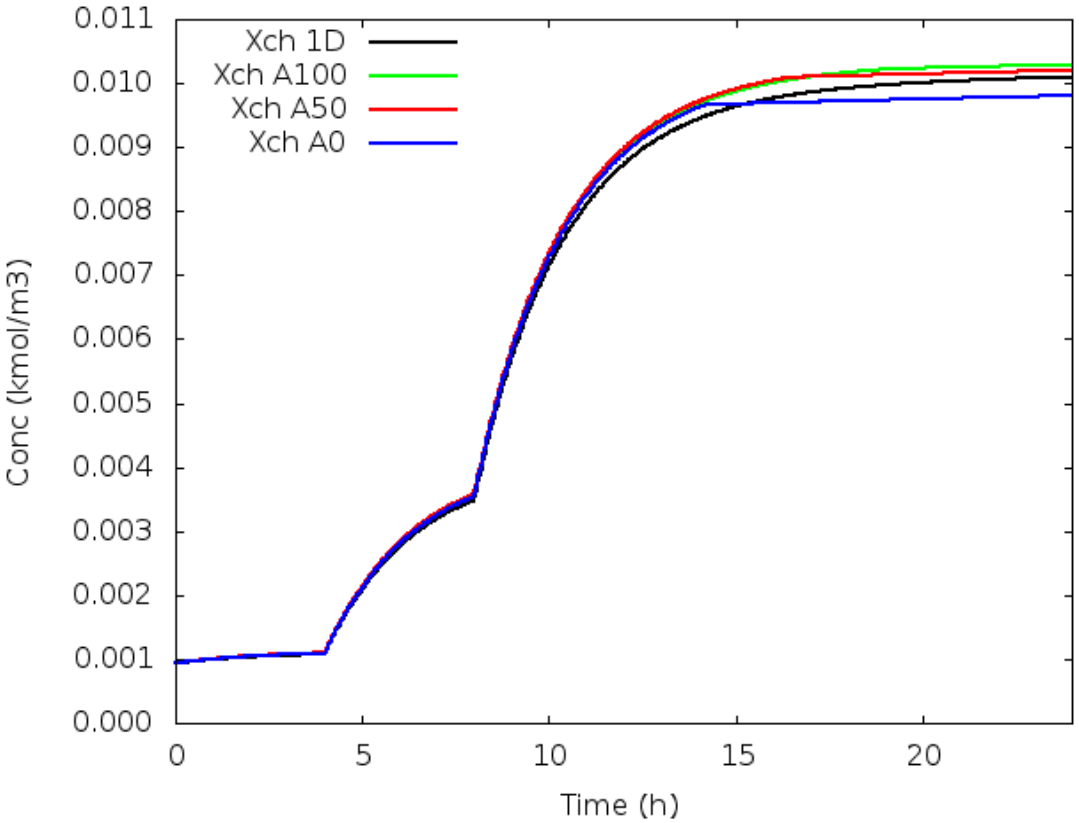
Xch 1D
Xch A100
Xch A50
Xch A0
Conc (kmol/m3)
Time (h)
0.011
0.010
0.009
0.008
0.007
0.006
0.005
0.004
0.003
0.002
0.001
0.000
0
5
10
15
20

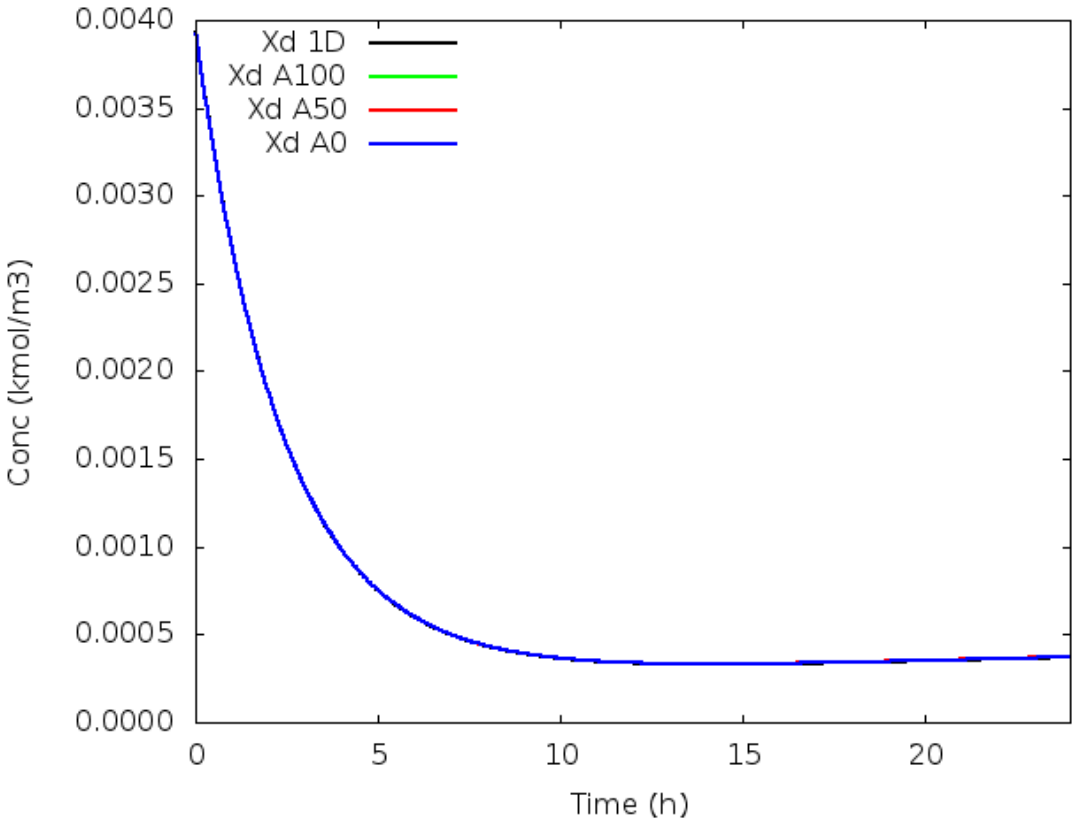
Xd 1D
Xd A100
Xd A50
Xd A0
Conc (kmol/m3)
Time (h)
0.0040
0.0035
0.0030
0.0025
0.0020
0.0015
0.0010
0.0005
0.0000
0
5
10
15
20

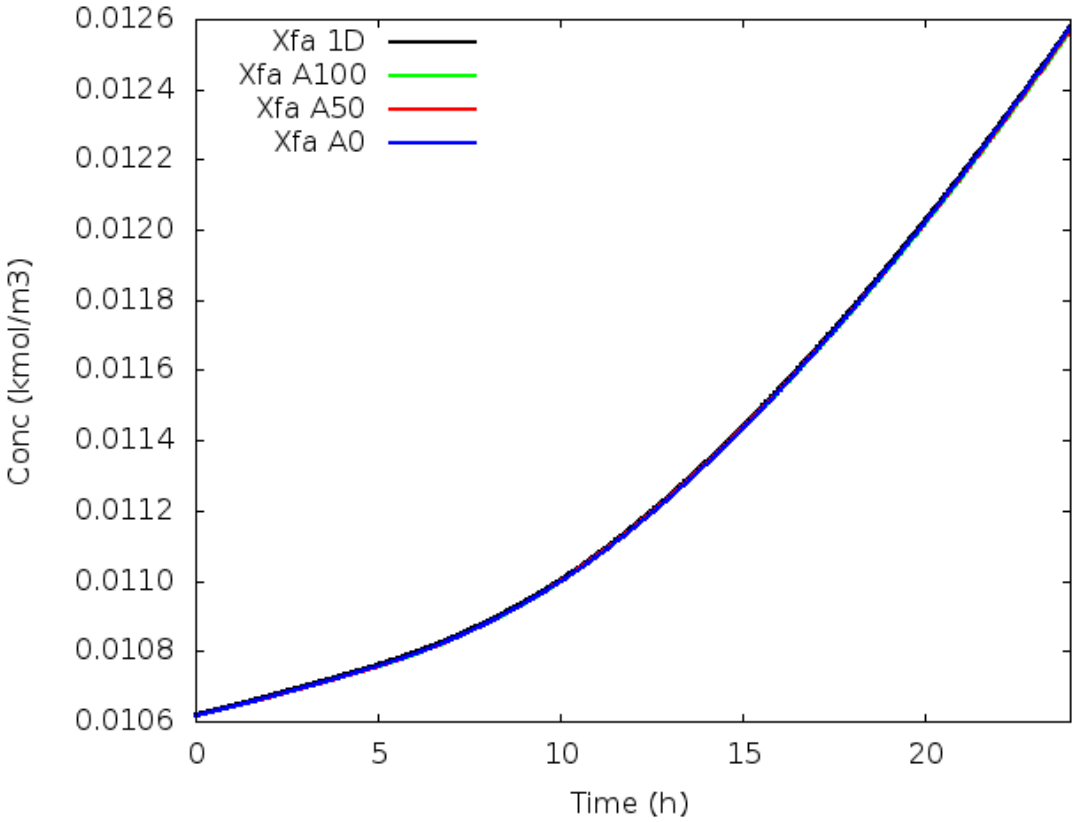
Xfa 1D
Xfa A100
Xfa A50
Xfa A0
Conc (kmol/m3)
Time (h)
0.0126
0.0124
0.0122
0.0120
0.0118
0.0116
0.0114
0.0112
0.0110
0.0108
0.0106
0
5
10
15
20

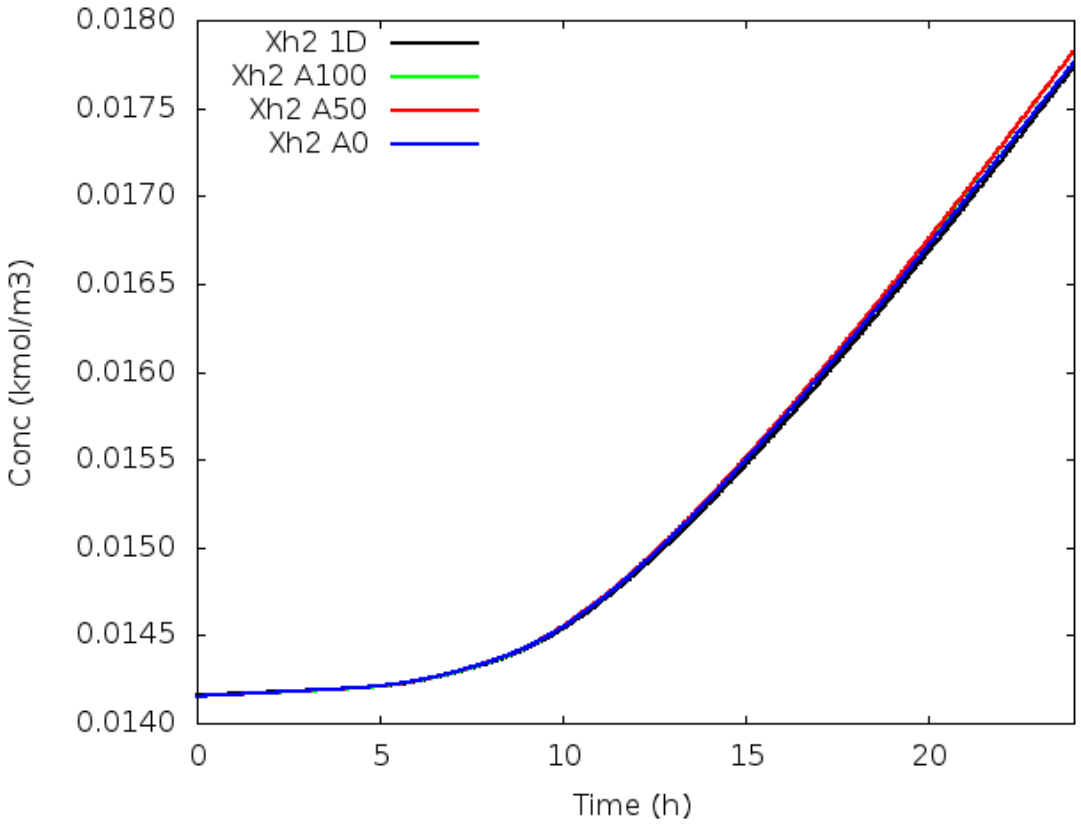
Xh2 1D
Xh2 A100
Xh2 A50
Xh2 A0
Conc (kmol/m3)
Time (h)
0.0180
0.0175
0.0170
0.0165
0.0160
0.0155
0.0150
0.0145
0.0140
0
5
10
15
20

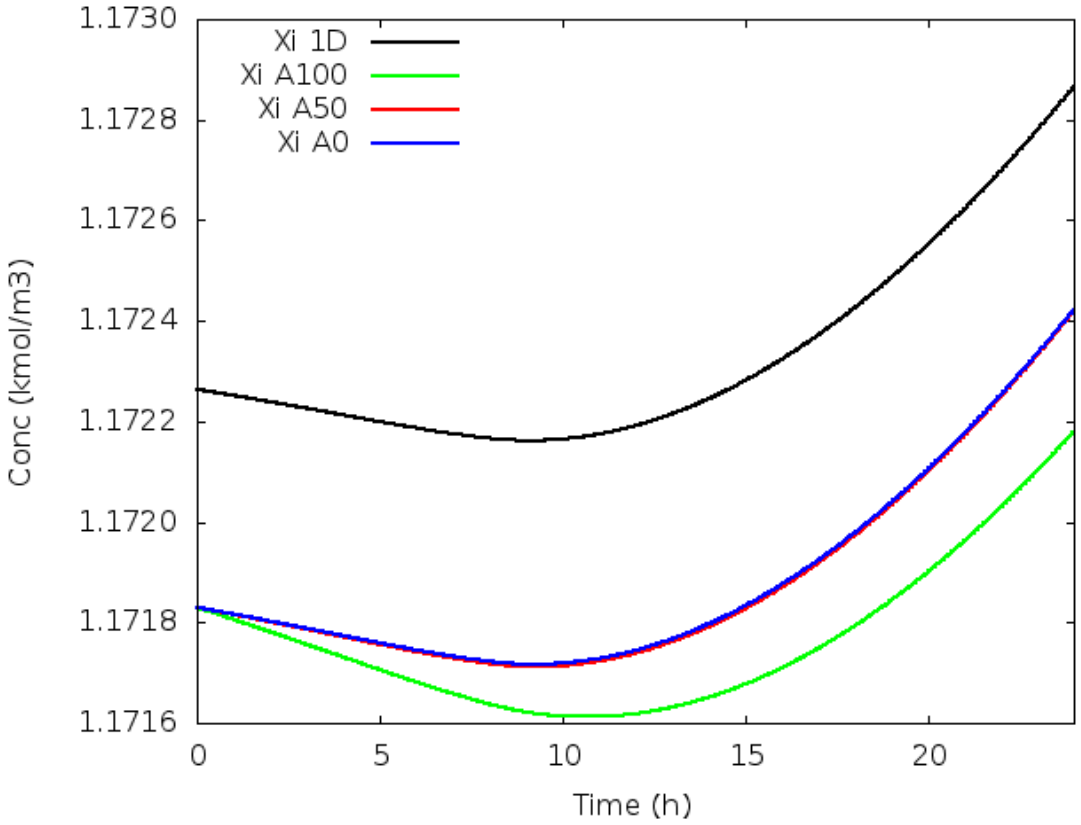
Xi 1D
Xi A100
Xi A50
Xi A0
Conc (kmol/m3)
Time (h)
1.1730
1.1728
1.1726
1.1724
1.1722
1.1720
1.1718
1.1716
0
5
10
15
20

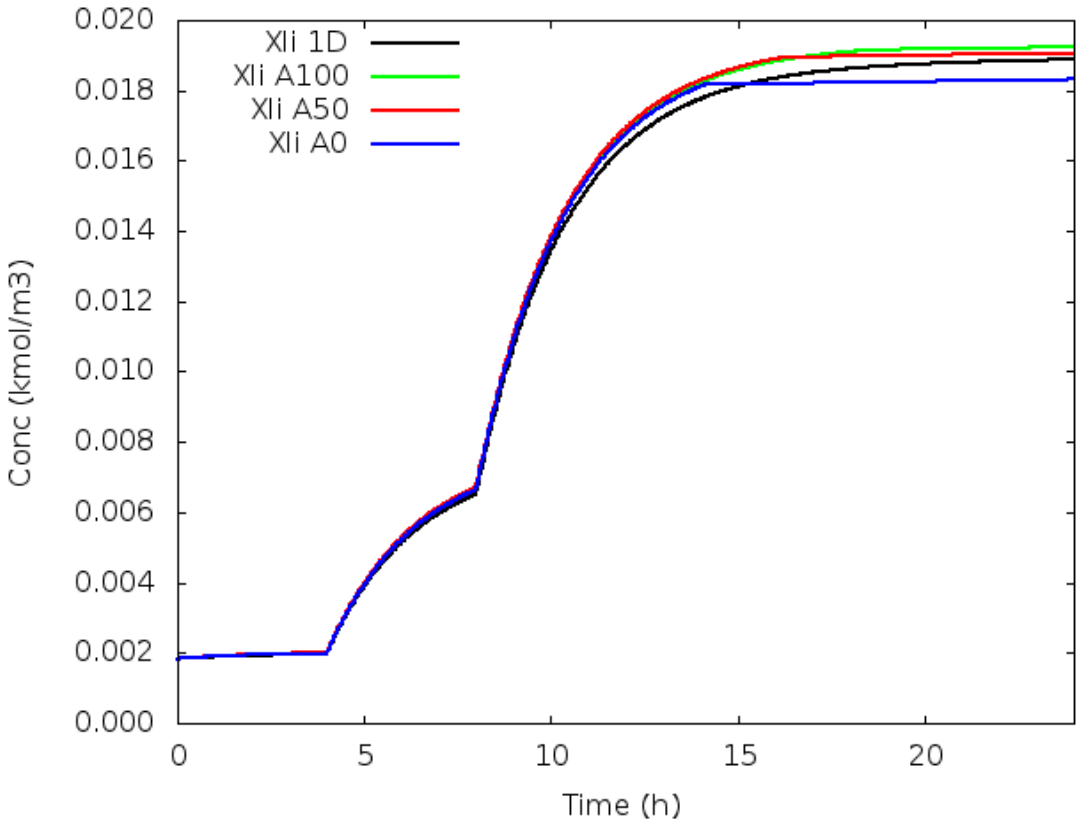
Xli 1D
Xli A100
Xli A50
Xli A0
Conc (kmol/m3)
Time (h)
0.020
0.018
0.016
0.014
0.012
0.010
0.008
0.006
0.004
0.002
0.000
0
5
10
15
20

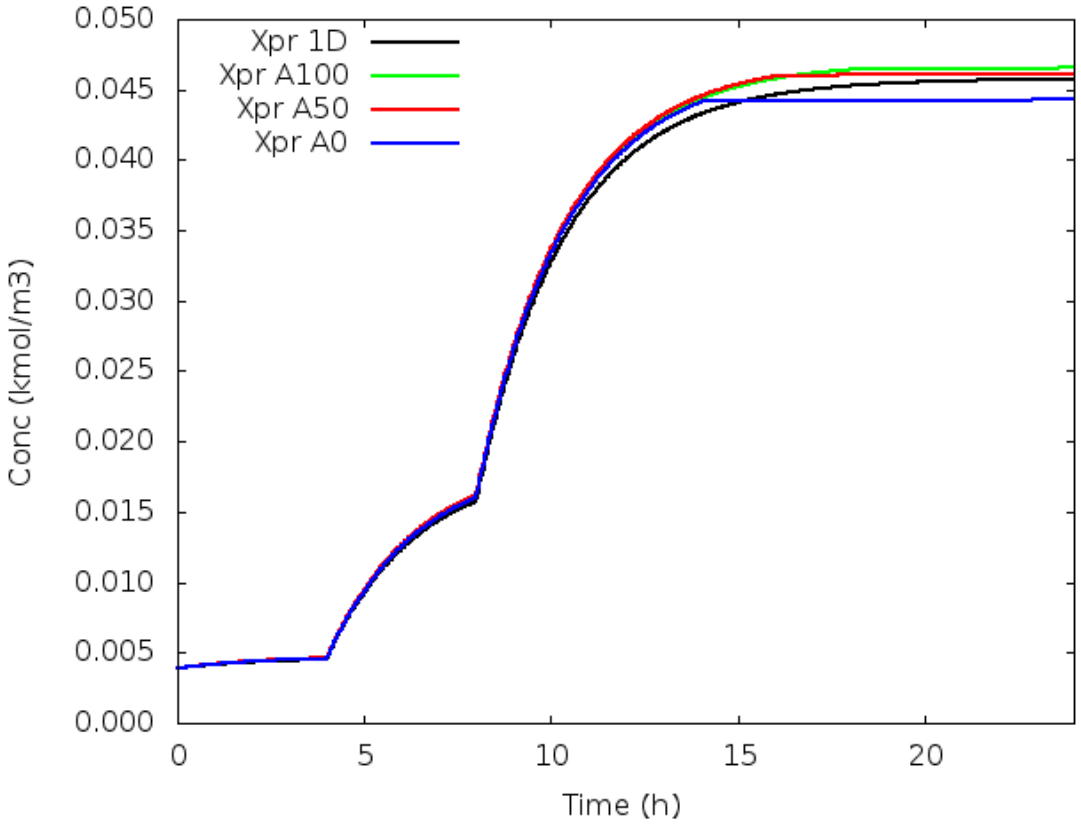
Xpr 1D
Xpr A100
Xpr A50
Xpr A0
Conc (kmol/m3)
Time (h)
0.050
0.045
0.040
0.035
0.030
0.025
0.020
0.015
0.010
0.005
0.000
0
5
10
15
20

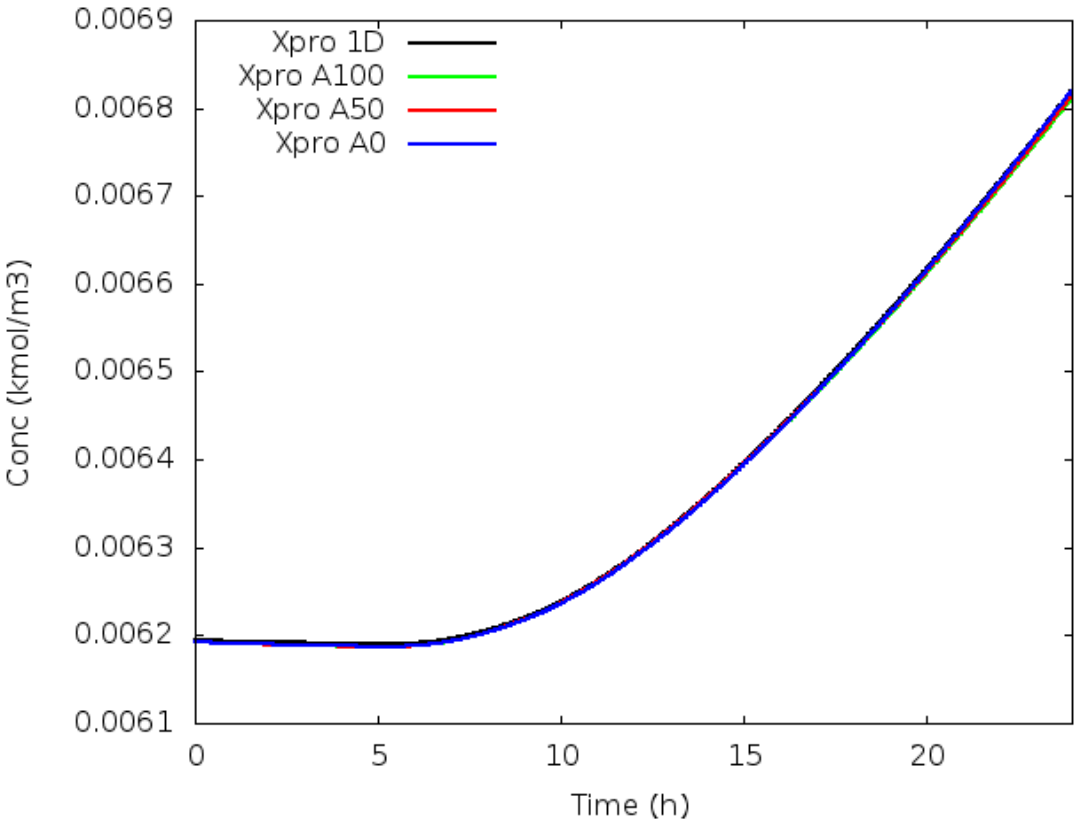
Xpro 1D
Xpro A100
Xpro A50
Xpro A0
Conc (kmol/m3)
Time (h)
0.0069
0.0068
0.0067
0.0066
0.0065
0.0064
0.0063
0.0062
0.0061
0
5
10
15
20

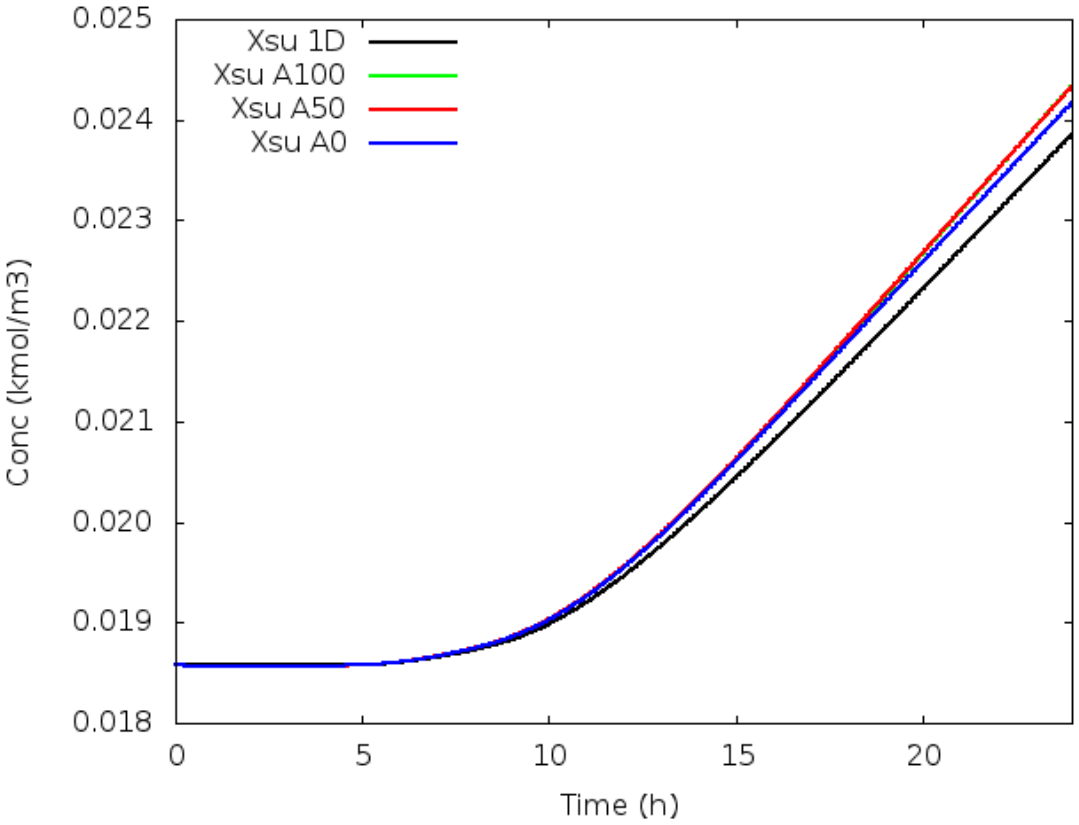
Xsu 1D
Xsu A100
Xsu A50
Xsu A0
Conc (kmol/m3)
Time (h)
0.025
0.024
0.023
0.022
0.021
0.020
0.019
0.018
0
5
10
15
20

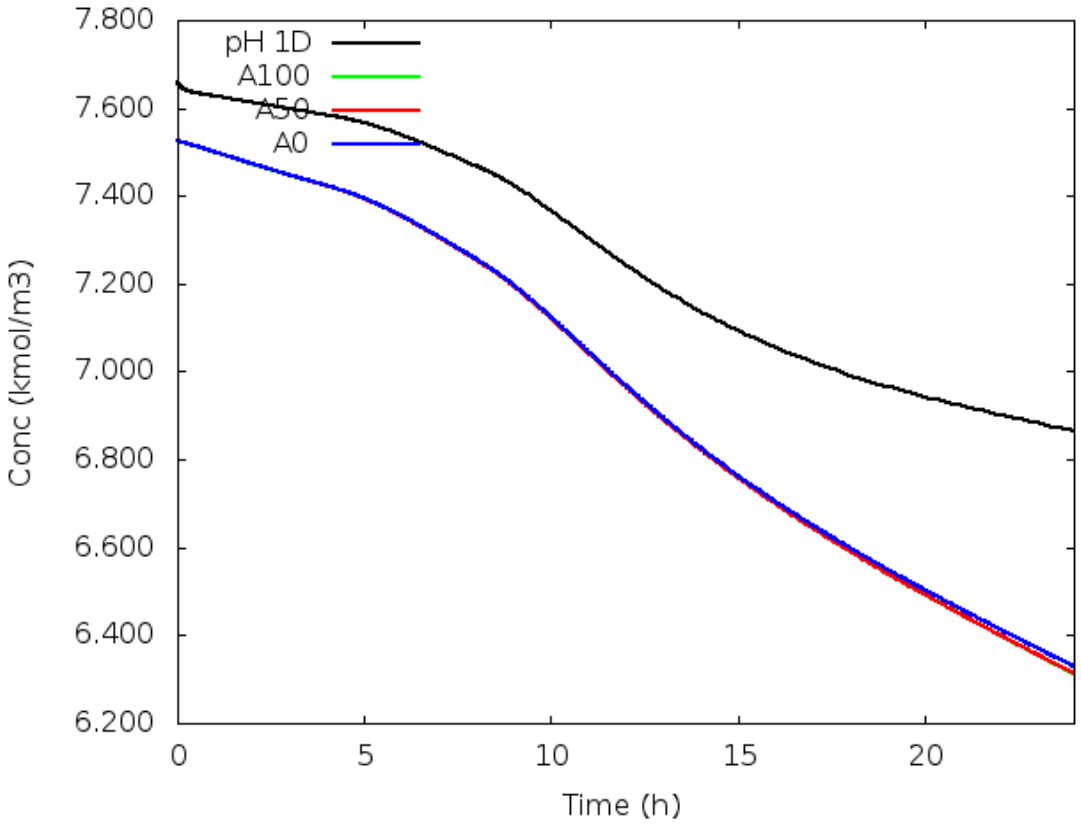
pH 1D
A100
A50
A0
Conc (kmol/m3)
Time (h)
7.800
7.600
7.400
7.200
7.000
6.800
6.600
6.400
6.200
0
5
10
15
20

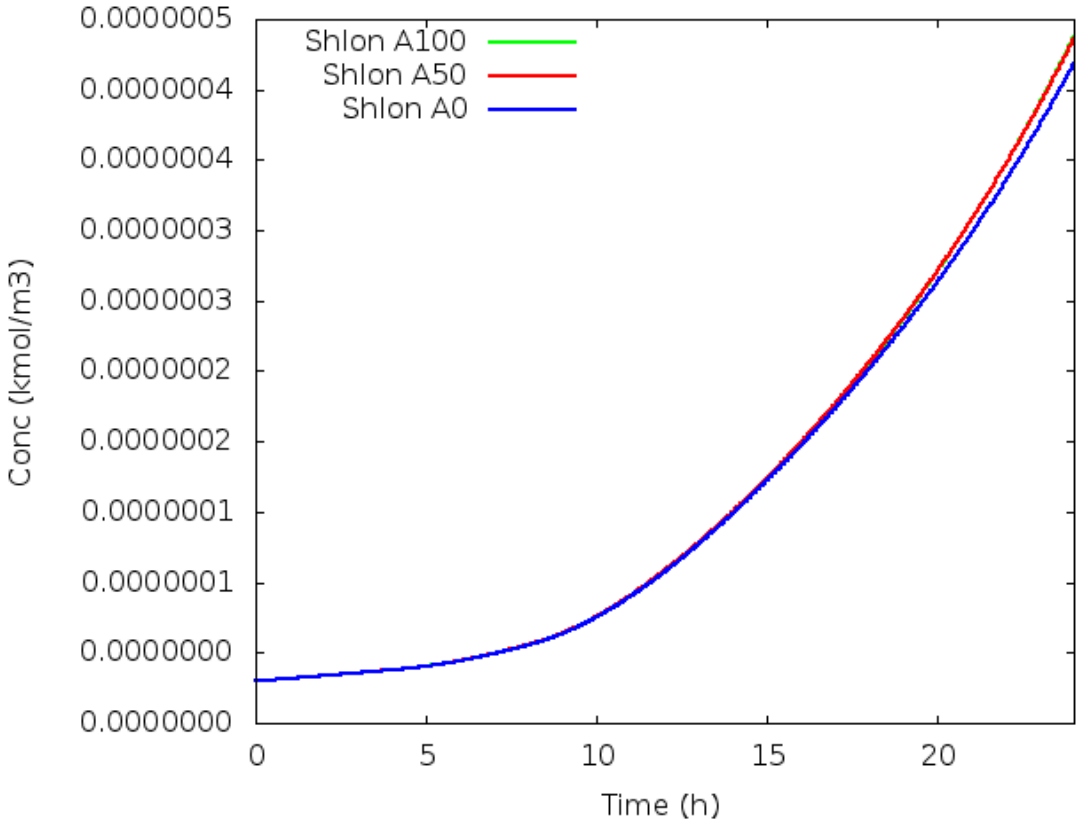
Shlon A100
Shlon A50
Shlon A0
Conc (kmol/m3)
Time (h)
0.0000005
0.0000004
0.0000004
0.0000003
0.0000003
0.0000002
0.0000002
0.0000001
0.0000001
0.0000000
0.0000000
0
5
10
15
20

I.ii ADM1 state variables-relative difference

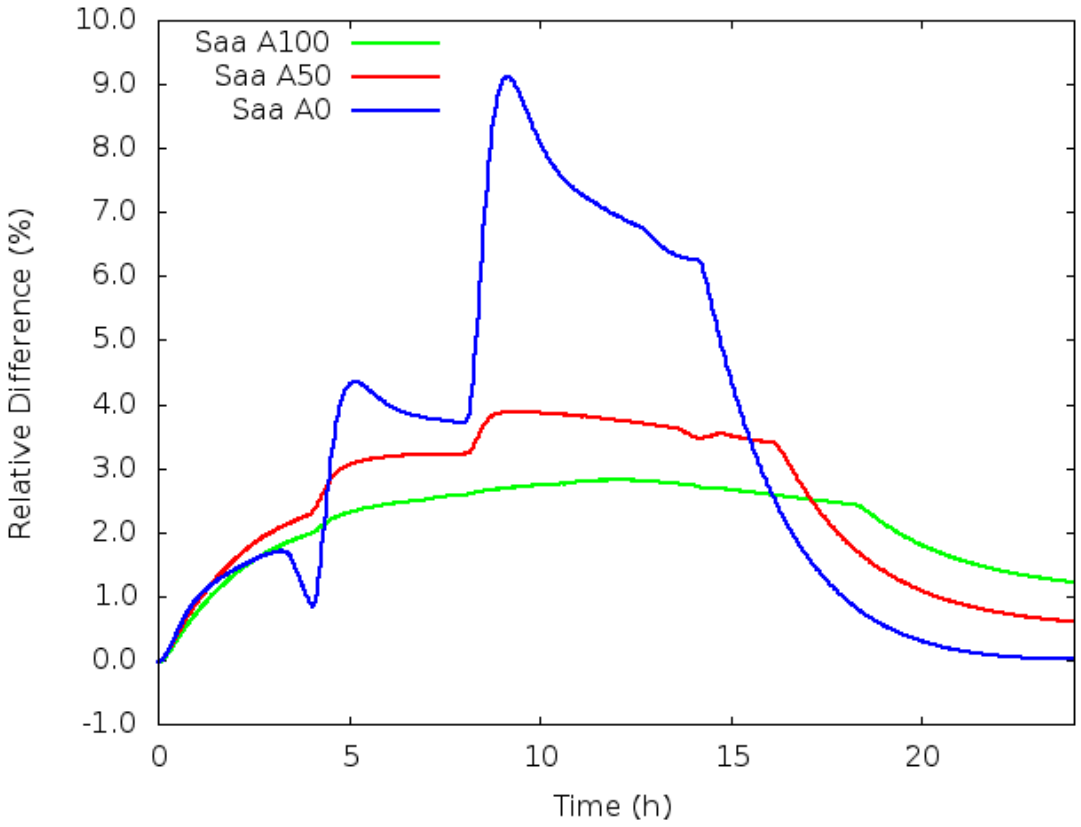

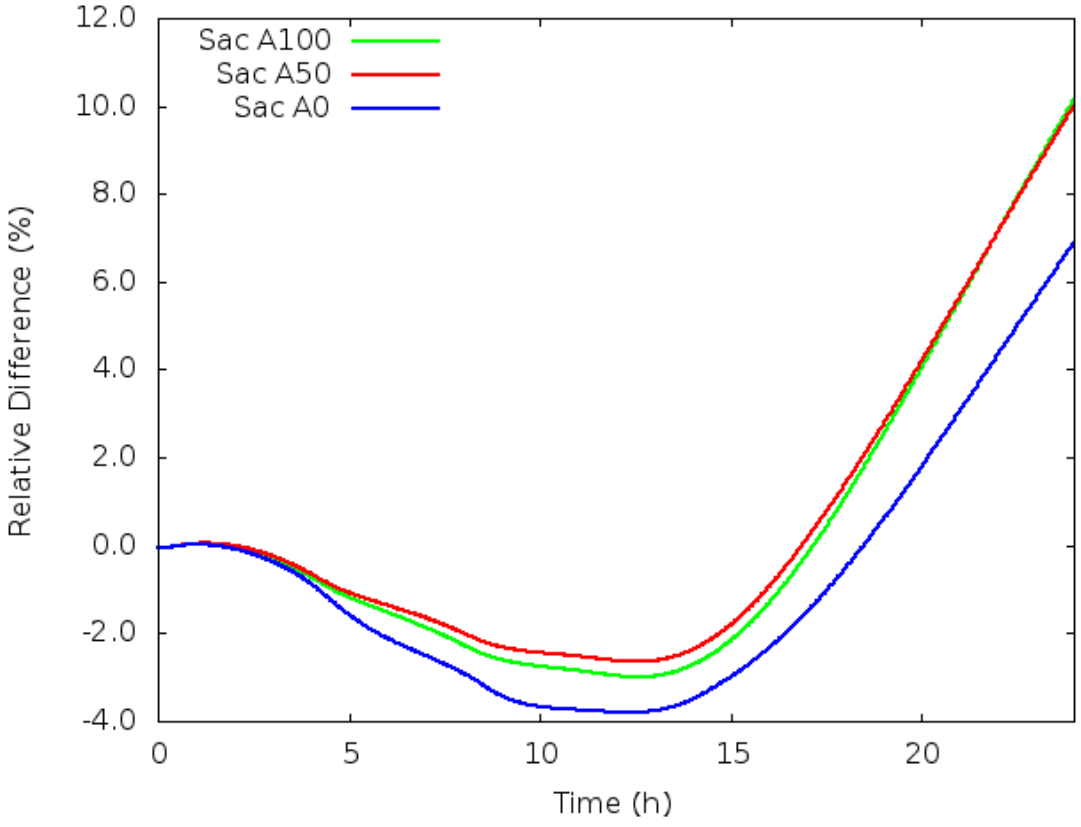

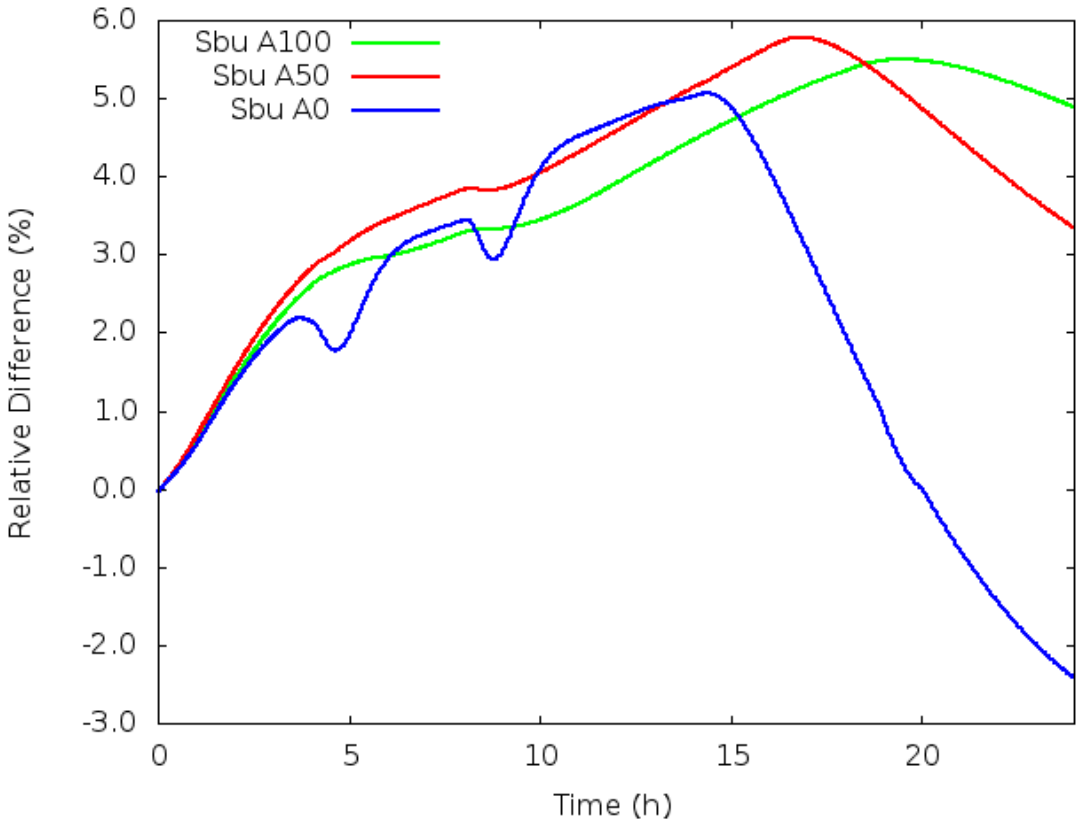
Sbu A100
Sbu A50
Sbu A0
Relative Difference (%)
Time (h)
6.0
5.0
4.0
3.0
2.0
1.0
0.0
-1.0
-2.0
-3.0
0
5
10
15
20

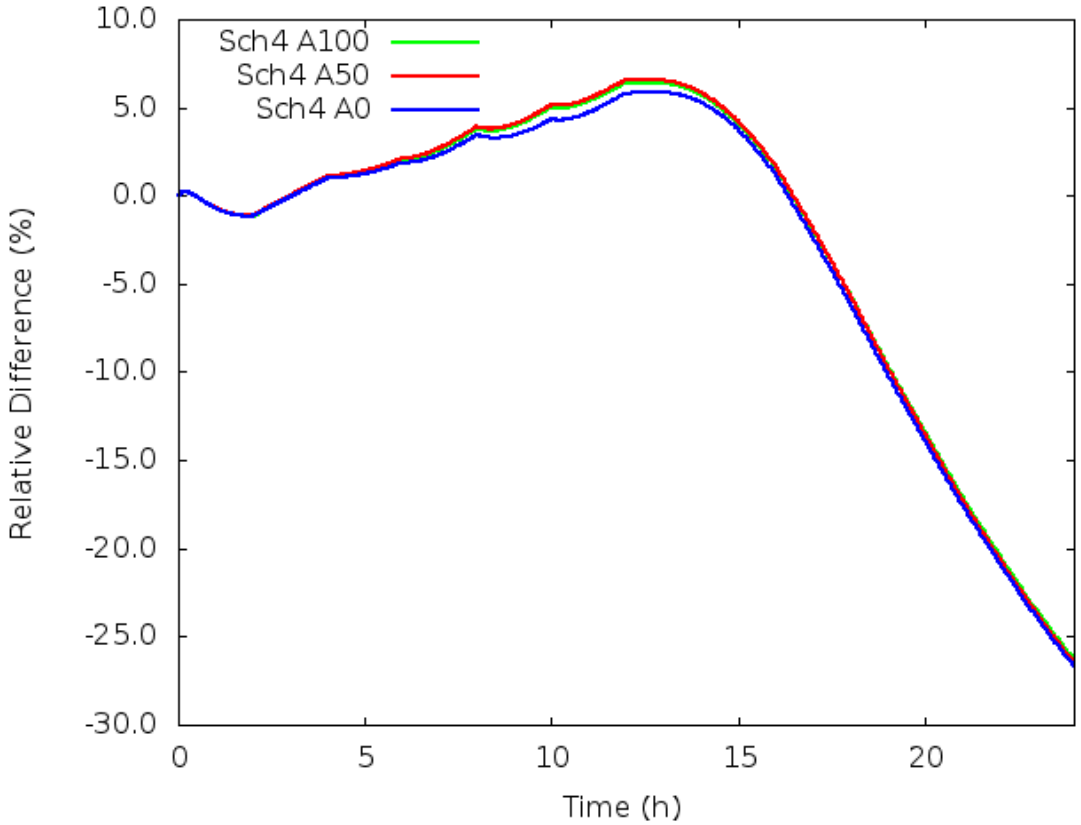
Sch4 A100
Sch4 A50
Sch4 A0
Relative Difference (%)
Time (h)
10.0
5.0
0.0
-5.0
-10.0
-15.0
-20.0
-25.0
-30.0
0
5
10
15
20

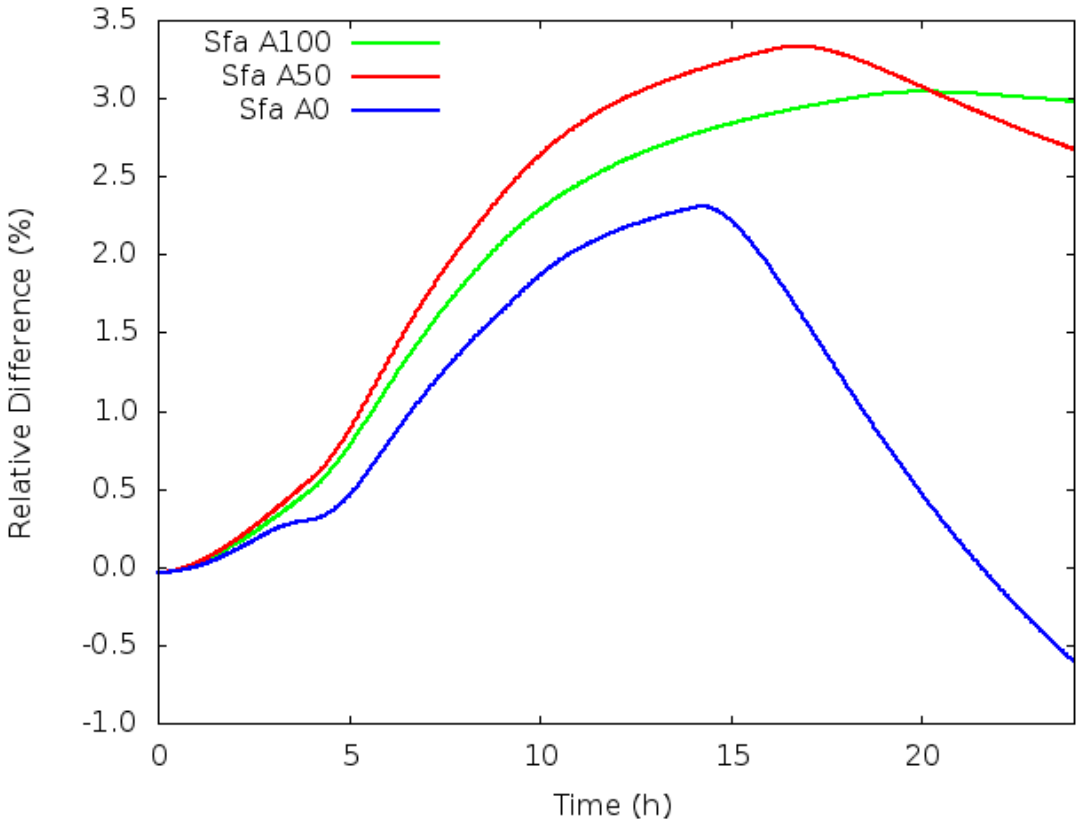
Sfa A100
Sfa A50
Sfa A0
Relative Difference (%)
Time (h)
3.5
3.0
2.5
2.0
1.5
1.0
0.5
0.0
-0.5
-1.0
0
5
10
15
20

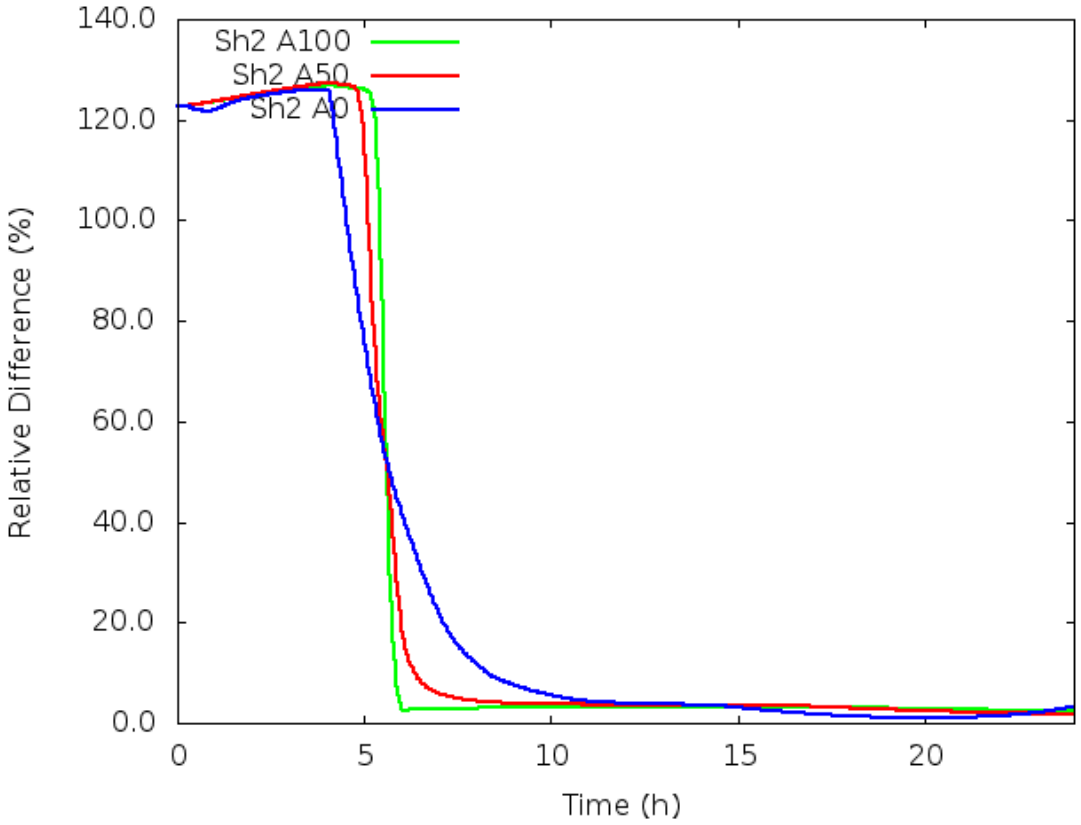
Sh2 A100
Sh2 A50
Sh2 A0
Relative Difference (%)
Time (h)
140.0
120.0
100.0
80.0
60.0
40.0
20.0
0.0
0
5
10
15
20

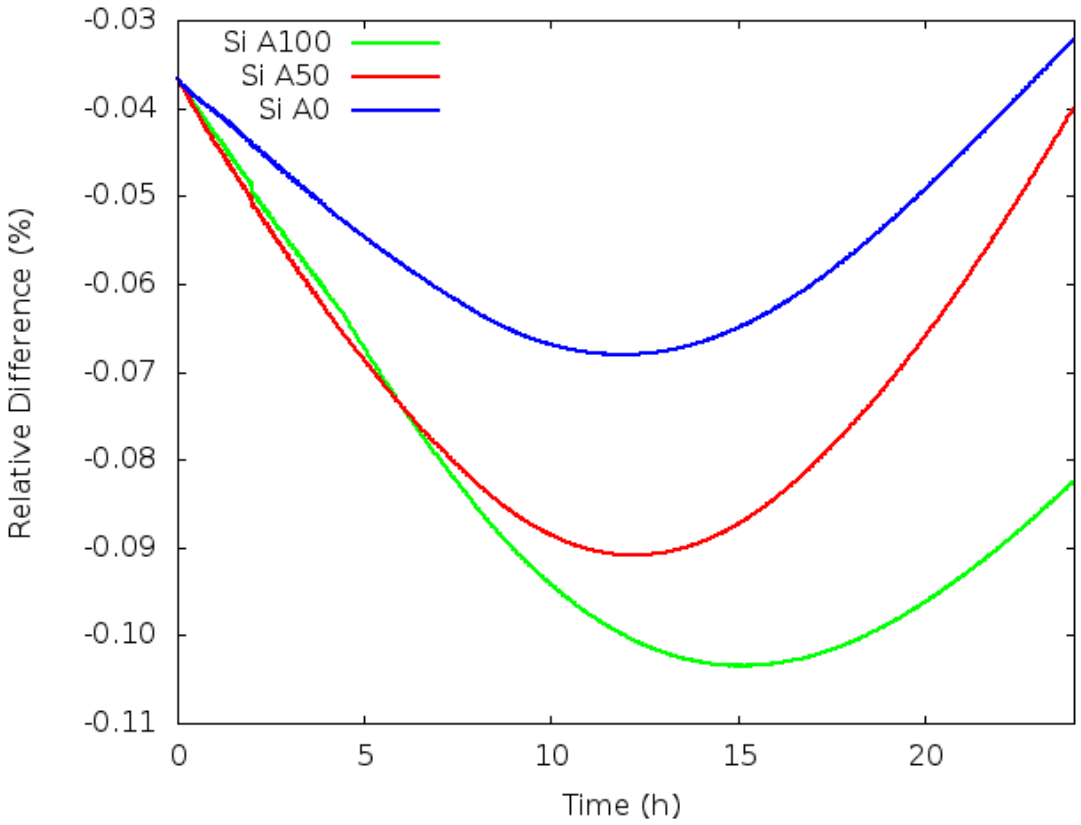
Si A100
Si A50
Si A0
Relative Difference (%)
-0.03
-0.04
-0.05
-0.06
-0.07
-0.08
-0.09
-0.10
-0.11
0
5
10
15
20
Time (h)

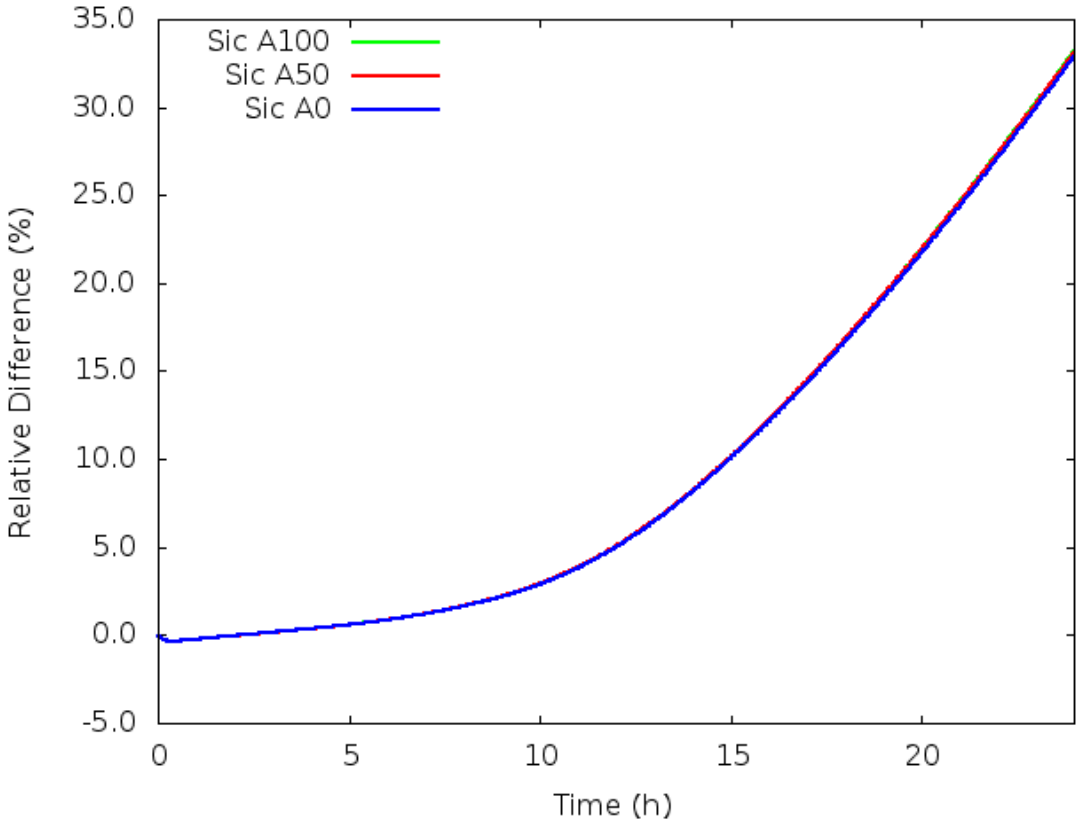
Sic A100
Sic A50
Sic A0
Relative Difference (%)
35.0
30.0
25.0
20.0
15.0
10.0
5.0
0.0
-5.0
0
5
10
15
20
Time (h)

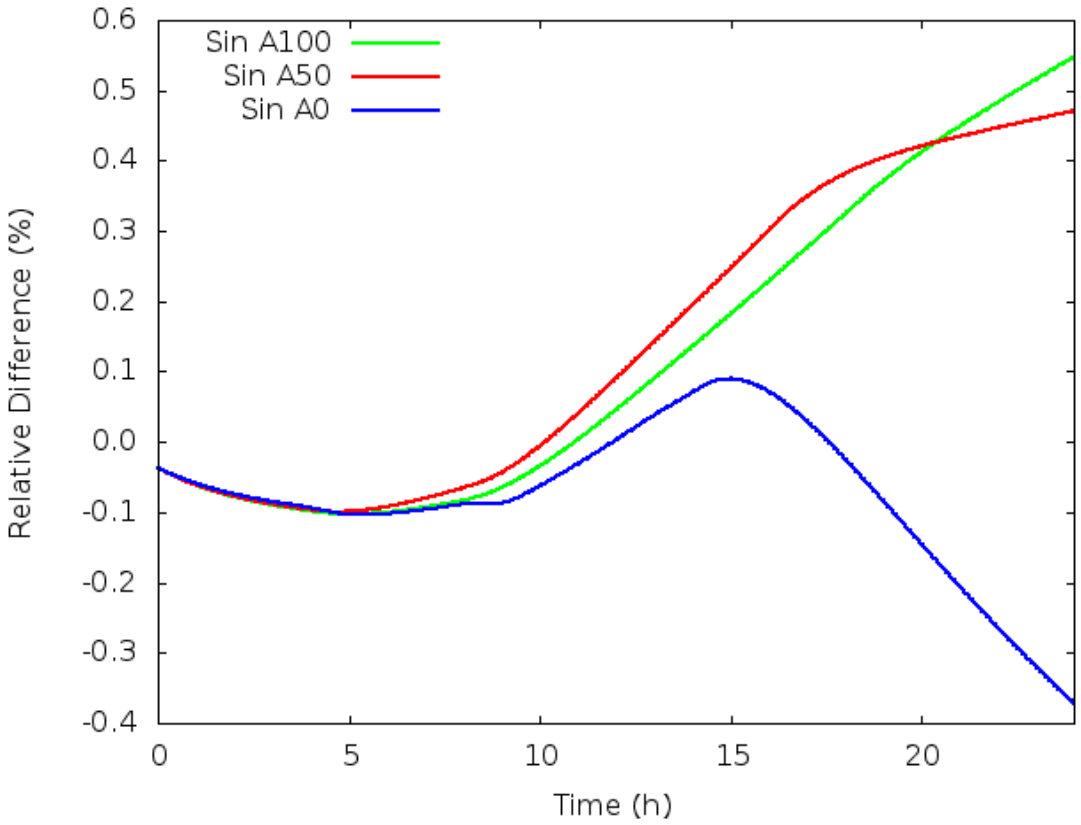
Sin A100
Sin A50
Sin A0
Relative Difference (%)
Time (h)
0.6
0.5
0.4
0.3
0.2
0.1
0.0
-0.1
-0.2
-0.3
-0.4
0
5
10
15
20

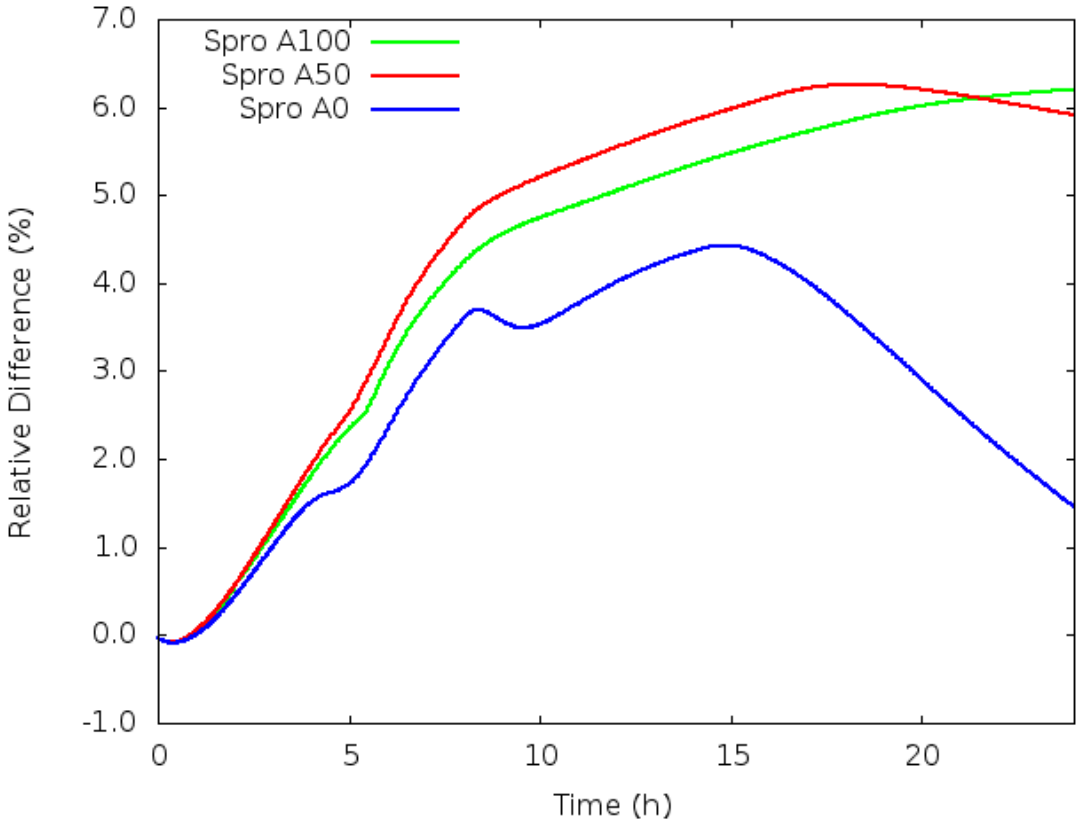
Spro A100
Spro A50
Spro A0
Relative Difference (%)
Time (h)
7.0
6.0
5.0
4.0
3.0
2.0
1.0
0.0
-1.0
0
5
10
15
20

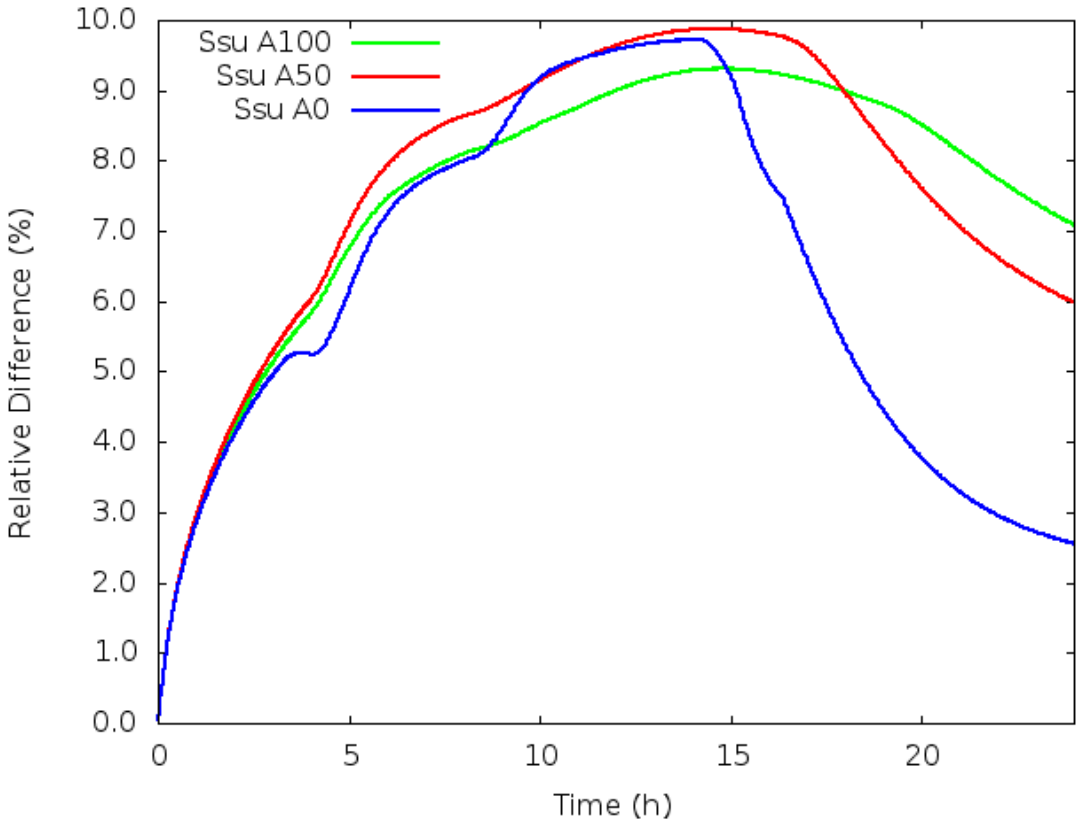
Ssu A100
Ssu A50
Ssu A0
Relative Difference (%)
Time (h)
10.0
9.0
8.0
7.0
6.0
5.0
4.0
3.0
2.0
1.0
0.0
0
5
10
15
20

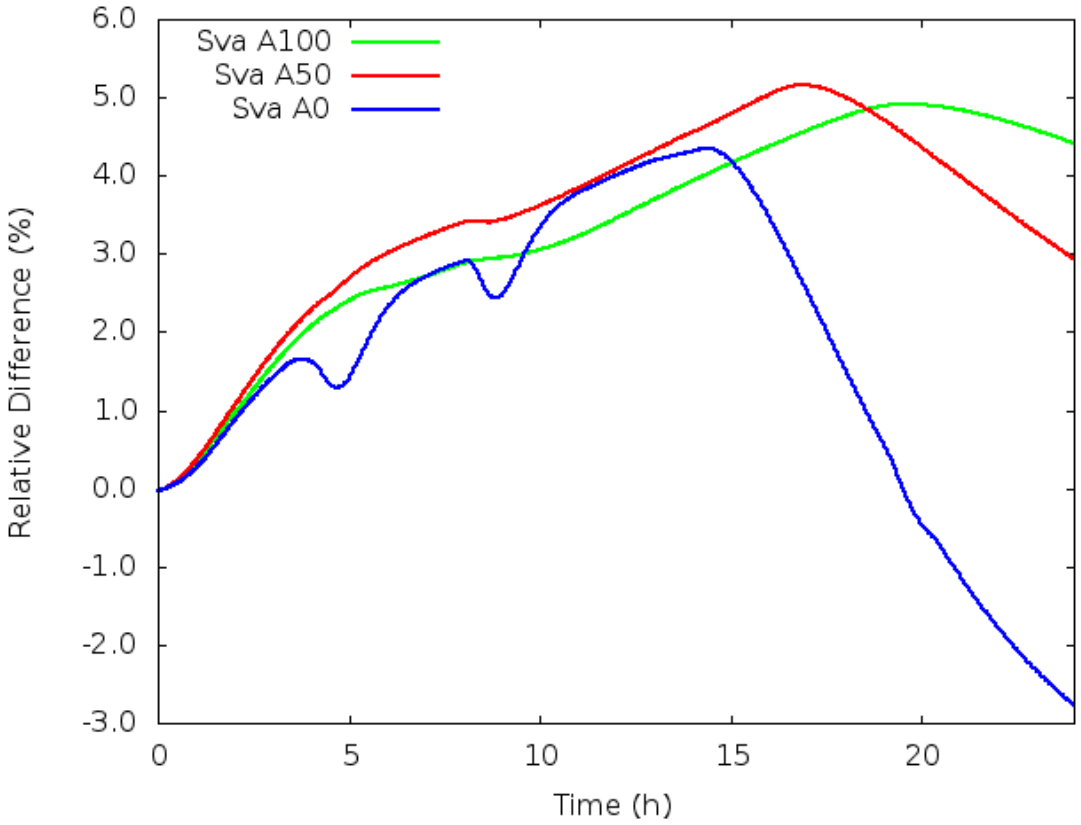
Sva A100
Sva A50
Sva A0
Relative Difference (%)
Time (h)
6.0
5.0
4.0
3.0
2.0
1.0
0.0
-1.0
-2.0
-3.0
0
5
10
15
20

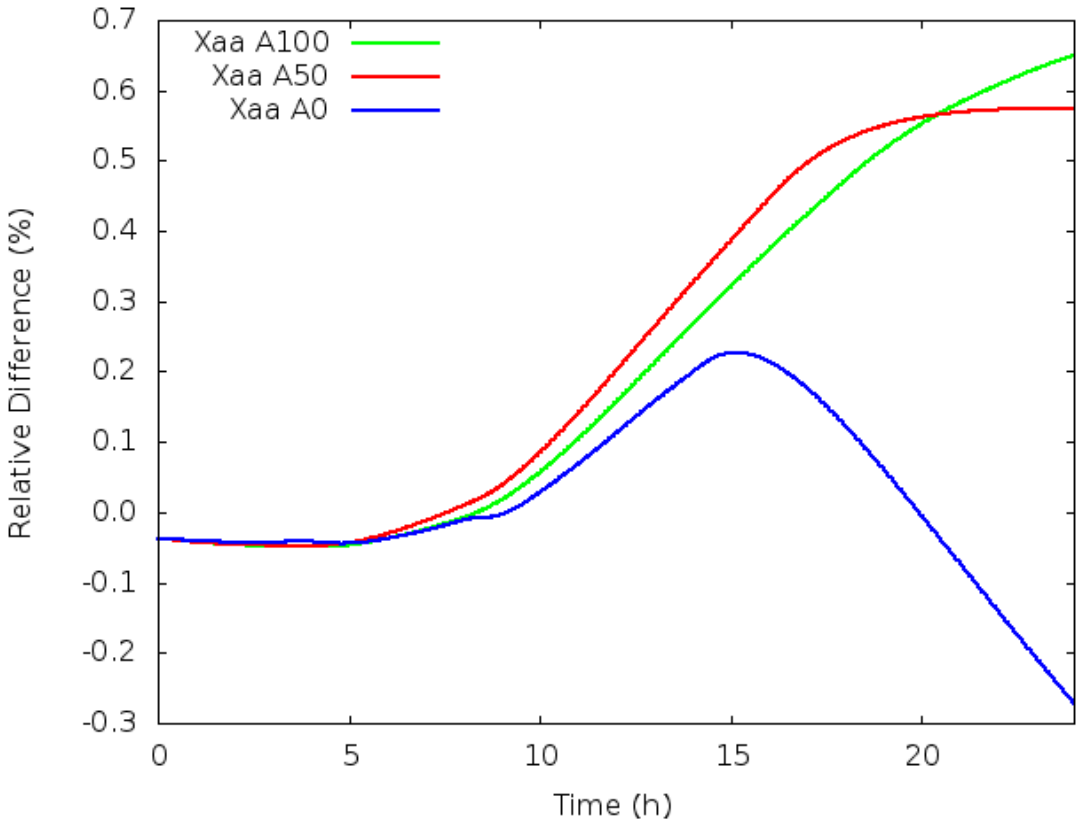
Xaa A100
Xaa A50
Xaa A0
Relative Difference (%)
Time (h)
0.7
0.6
0.5
0.4
0.3
0.2
0.1
0.0
-0.1
-0.2
-0.3
0
5
10
15
20

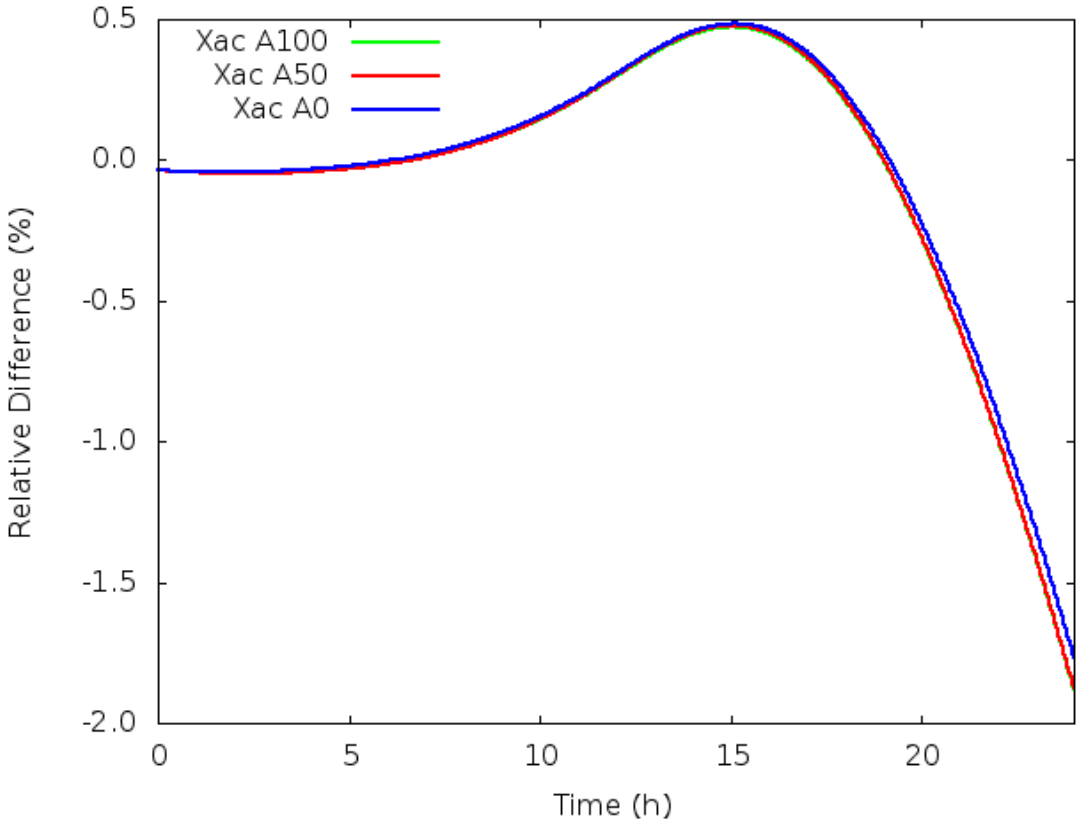
Xac A100
Xac A50
Xac A0
Relative Difference (%)
Time (h)
0.5
0.0
-0.5
-1.0
-1.5
-2.0
0
5
10
15
20

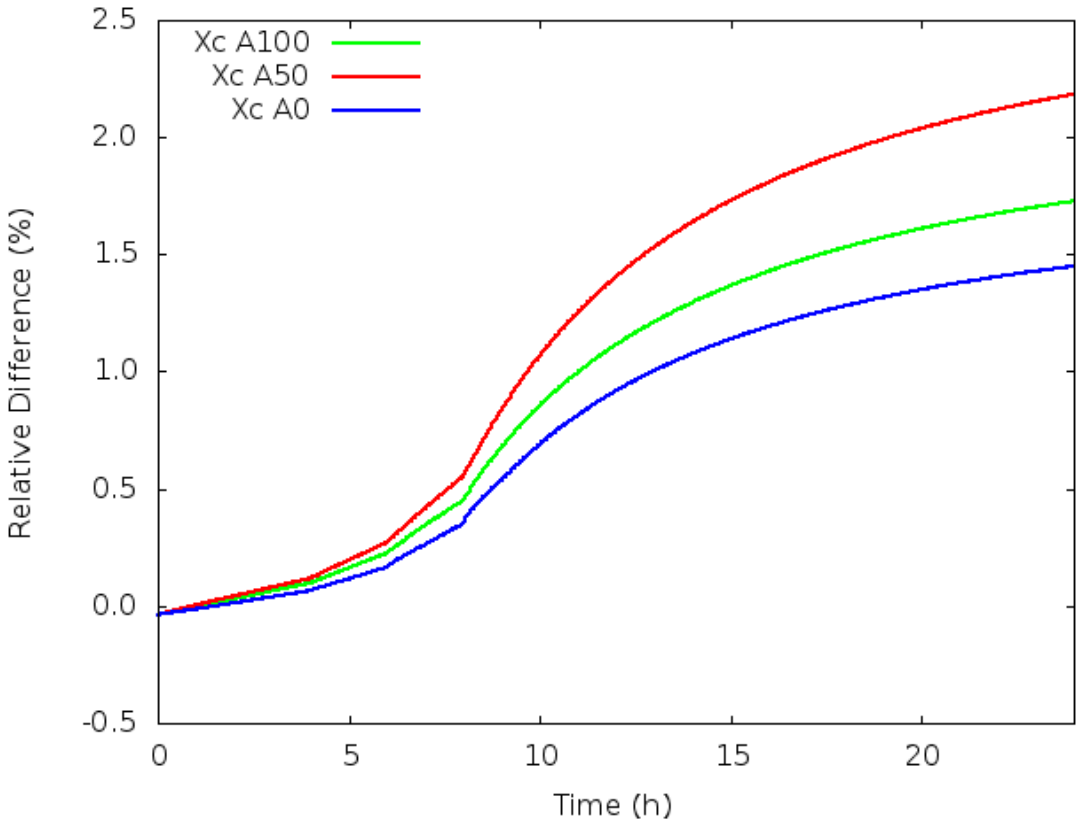
Xc A100
Xc A50
Xc A0
Relative Difference (%)
Time (h)
2.5
2.0
1.5
1.0
0.5
0.0
-0.5
0
5
10
15
20

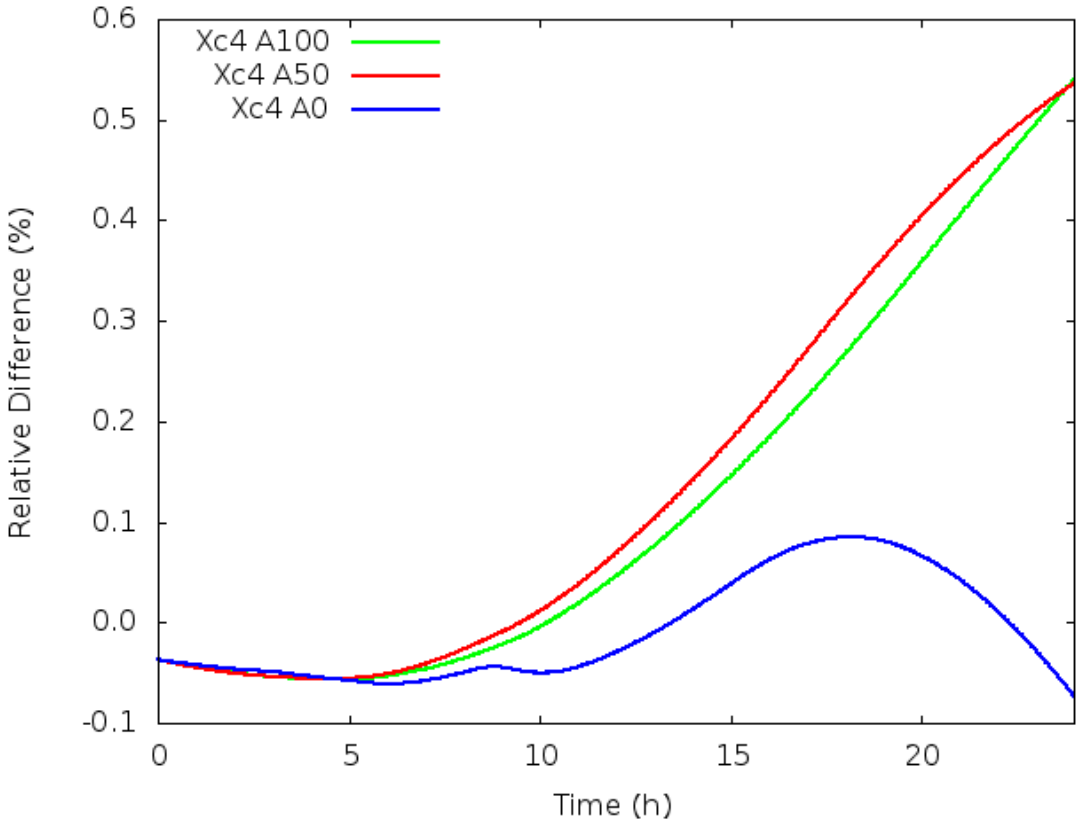
Xc4 A100
Xc4 A50
Xc4 A0
Relative Difference (%)
Time (h)
0.6
0.5
0.4
0.3
0.2
0.1
0.0
-0.1
0
5
10
15
20

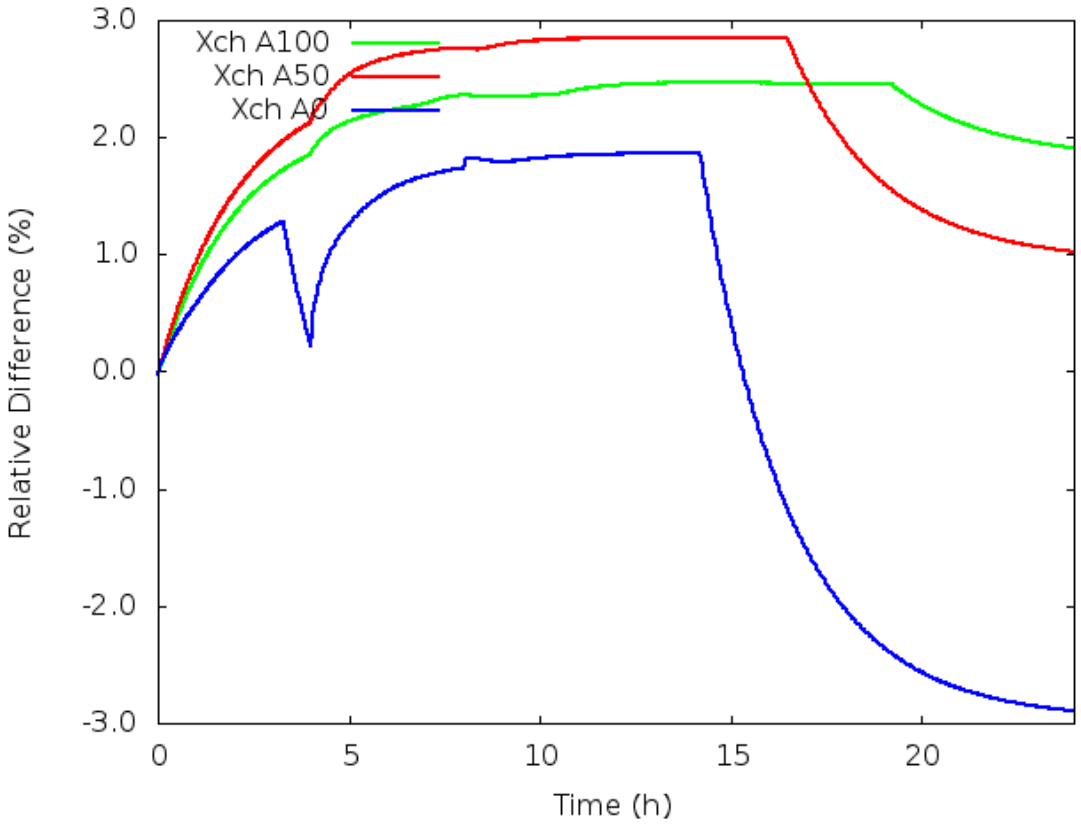
Xch A100
Xch A50
Xch A0
Relative Difference (%)
Time (h)
3.0
2.0
1.0
0.0
-1.0
-2.0
-3.0
0
5
10
15
20

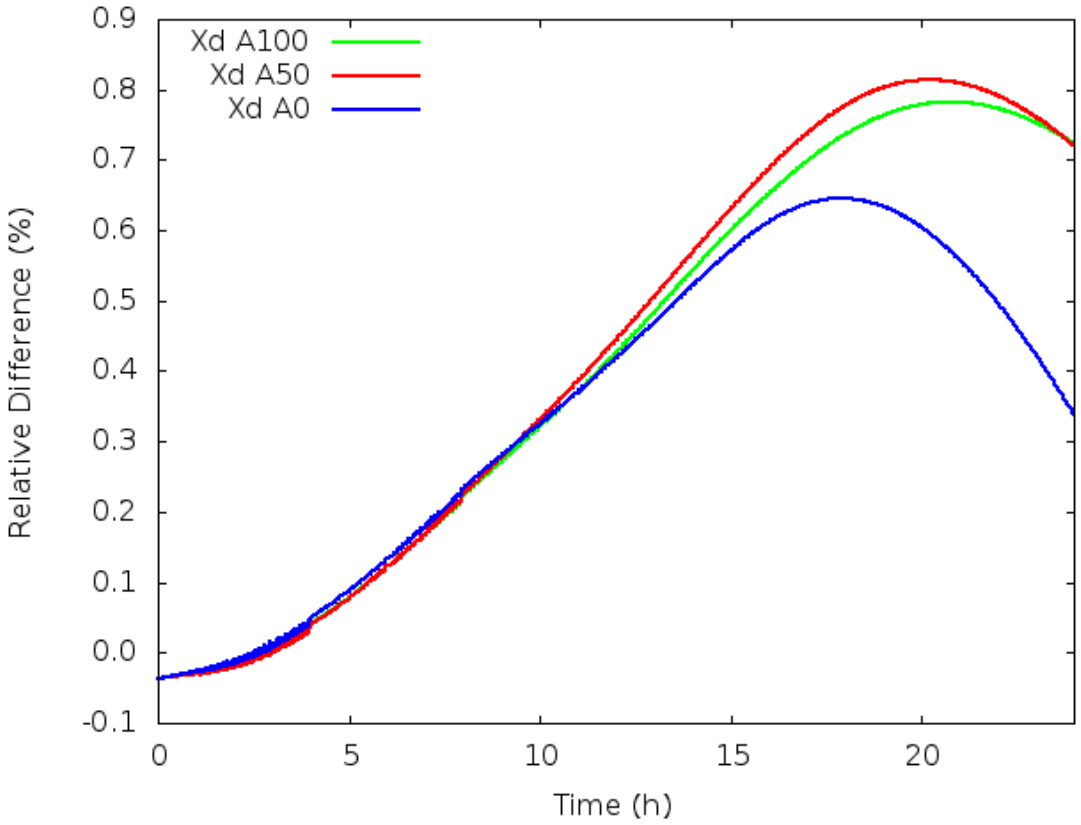
Xd A100
Xd A50
Xd A0
Relative Difference (%)
Time (h)
0.9
0.8
0.7
0.6
0.5
0.4
0.3
0.2
0.1
0.0
-0.1
0
5
10
15
20

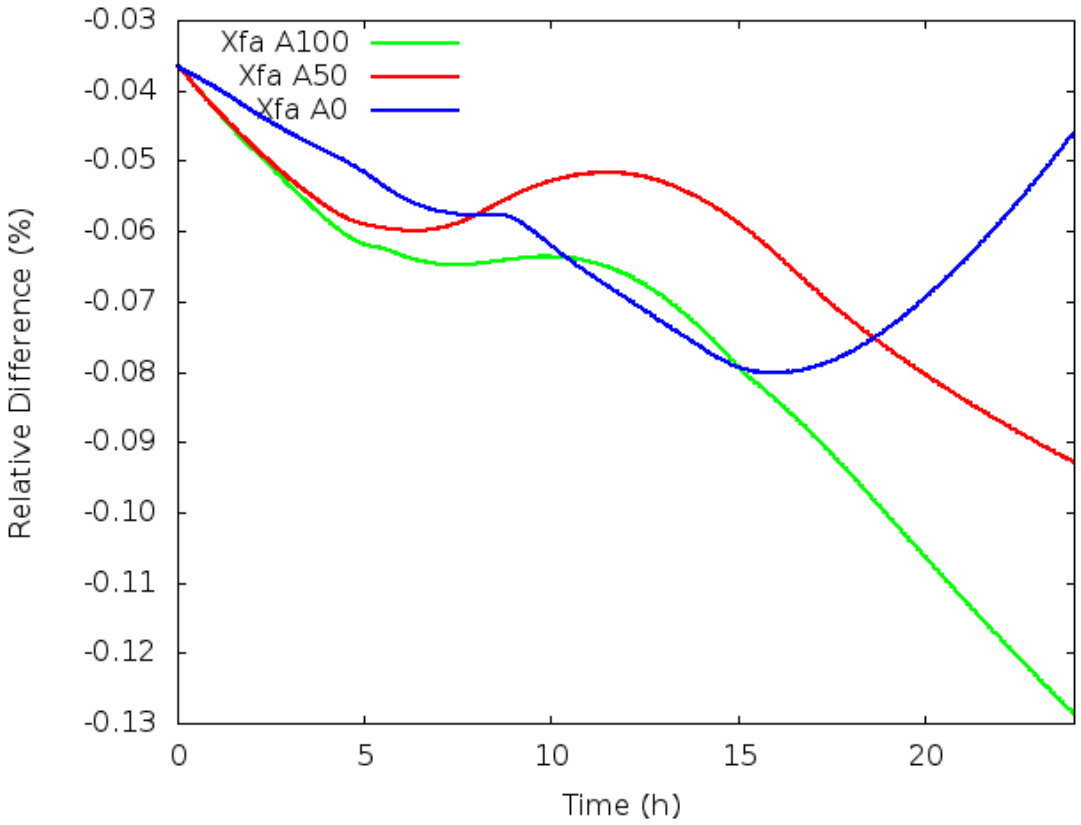
Xfa A100
Xfa A50
Xfa A0
Relative Difference (%)
-0.03
-0.04
-0.05
-0.06
-0.07
-0.08
-0.09
-0.10
-0.11
-0.12
-0.13
0
5
10
15
20
Time (h)

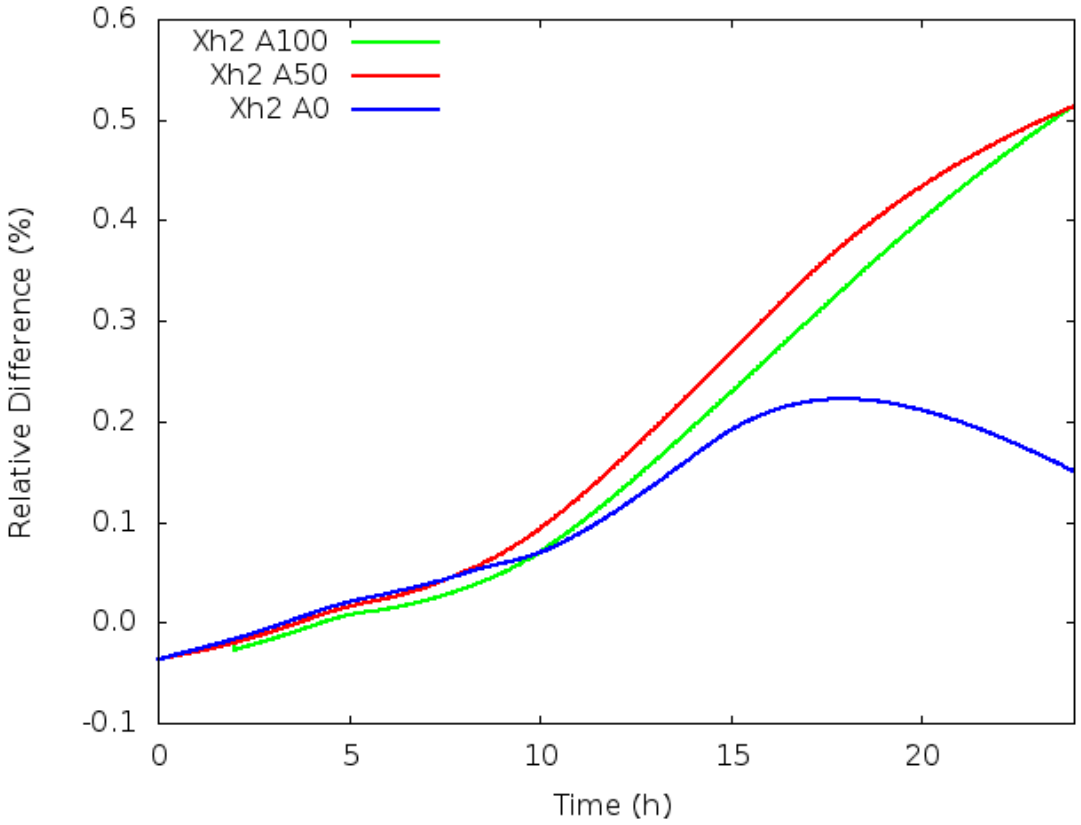
Xh2 A100
Xh2 A50
Xh2 A0
Relative Difference (%)
0.6
0.5
0.4
0.3
0.2
0.1
0.0
-0.1
0
5
10
15
20
Time (h)

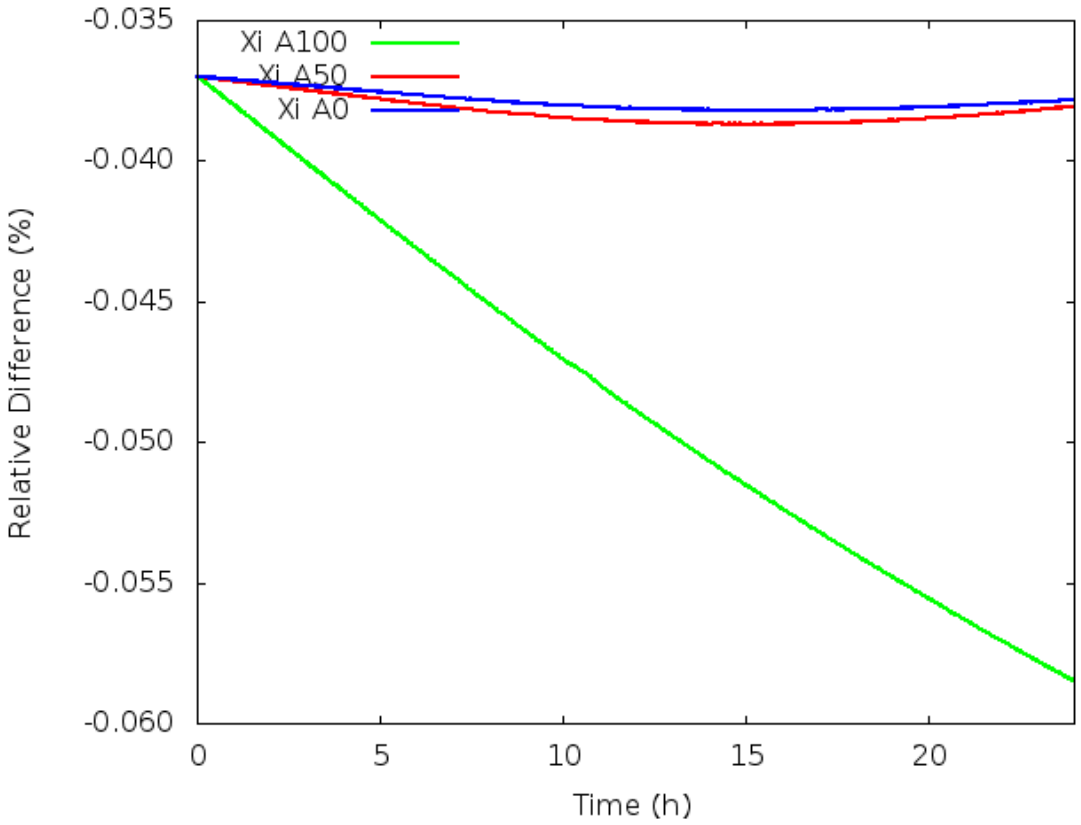
Xi A100
Xi A50
Xi A0
-0.035
-0.040
-0.045
-0.050
-0.055
-0.060
0
5
10
15
20
Time (h)
Relative Difference (%)

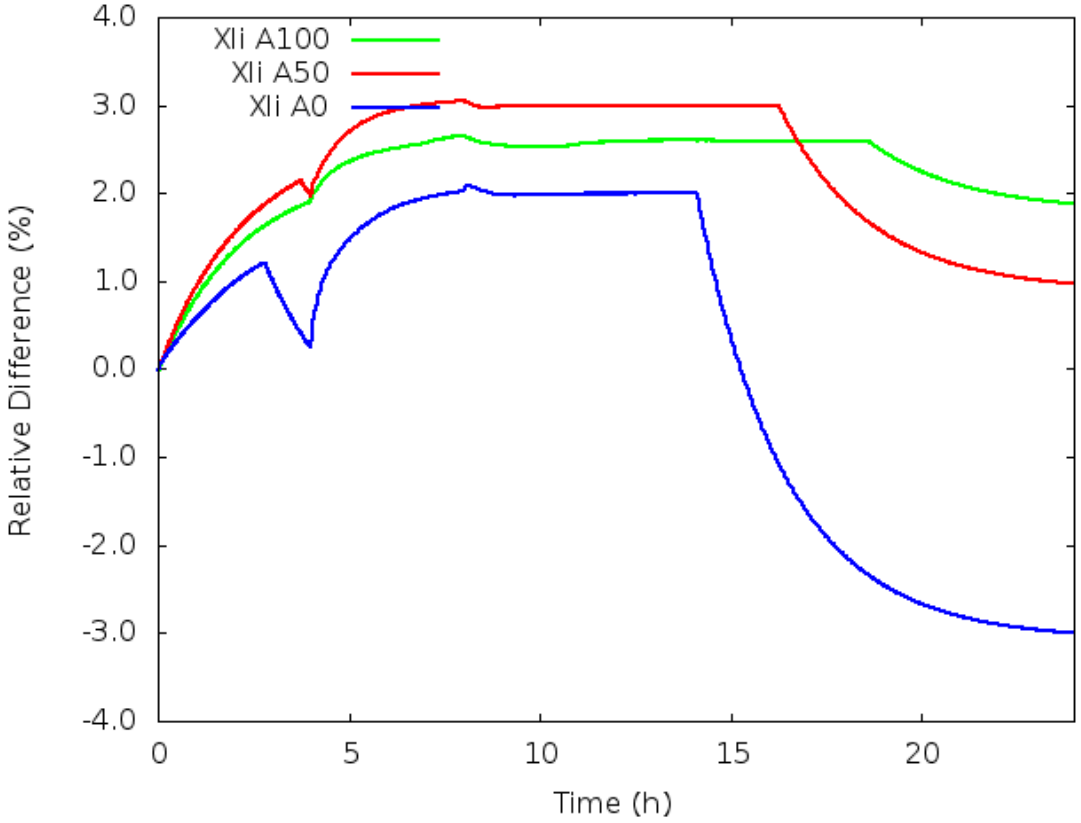
Xli A100
Xli A50
Xli A0
4.0
3.0
2.0
1.0
0.0
-1.0
-2.0
-3.0
-4.0
0
5
10
15
20
Time (h)
Relative Difference (%)

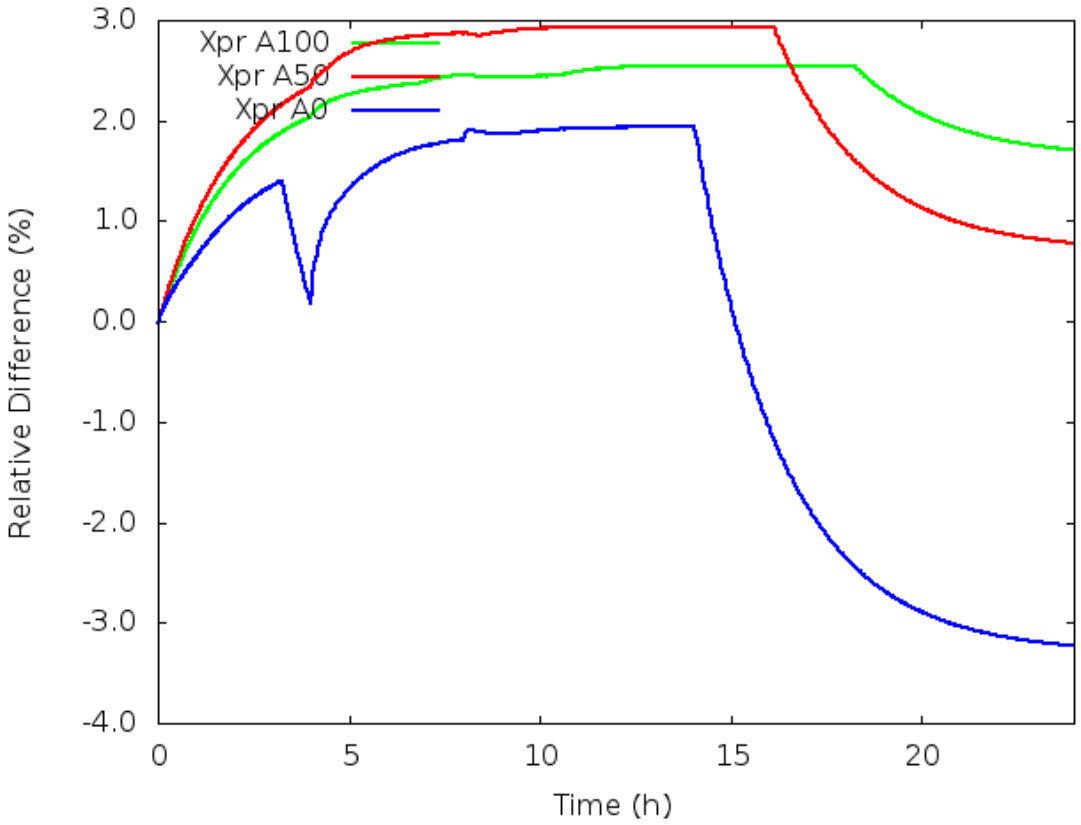
Xpr A100
Xpr A50
Xpr A0
Relative Difference (%)
Time (h)
3.0
2.0
1.0
0.0
-1.0
-2.0
-3.0
-4.0
0
5
10
15
20

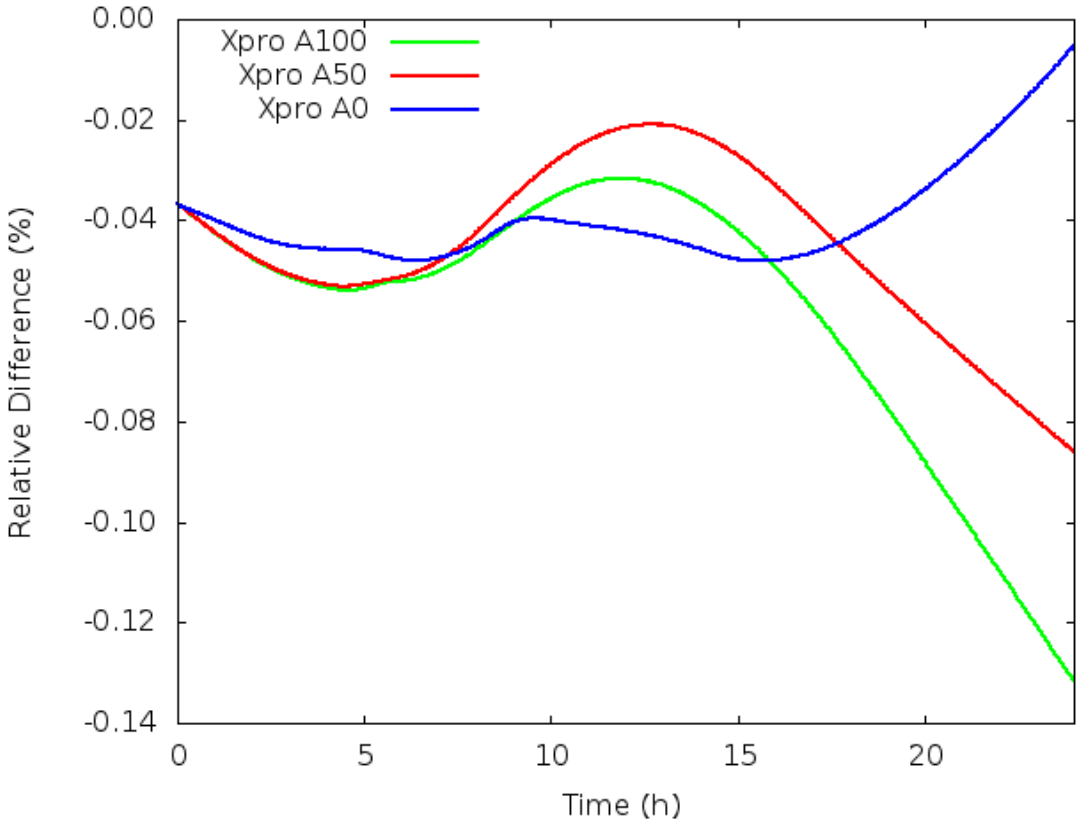
Xpro A100
Xpro A50
Xpro A0
Relative Difference (%)
Time (h)
0.00
-0.02
-0.04
-0.06
-0.08
-0.10
-0.12
-0.14
0
5
10
15
20

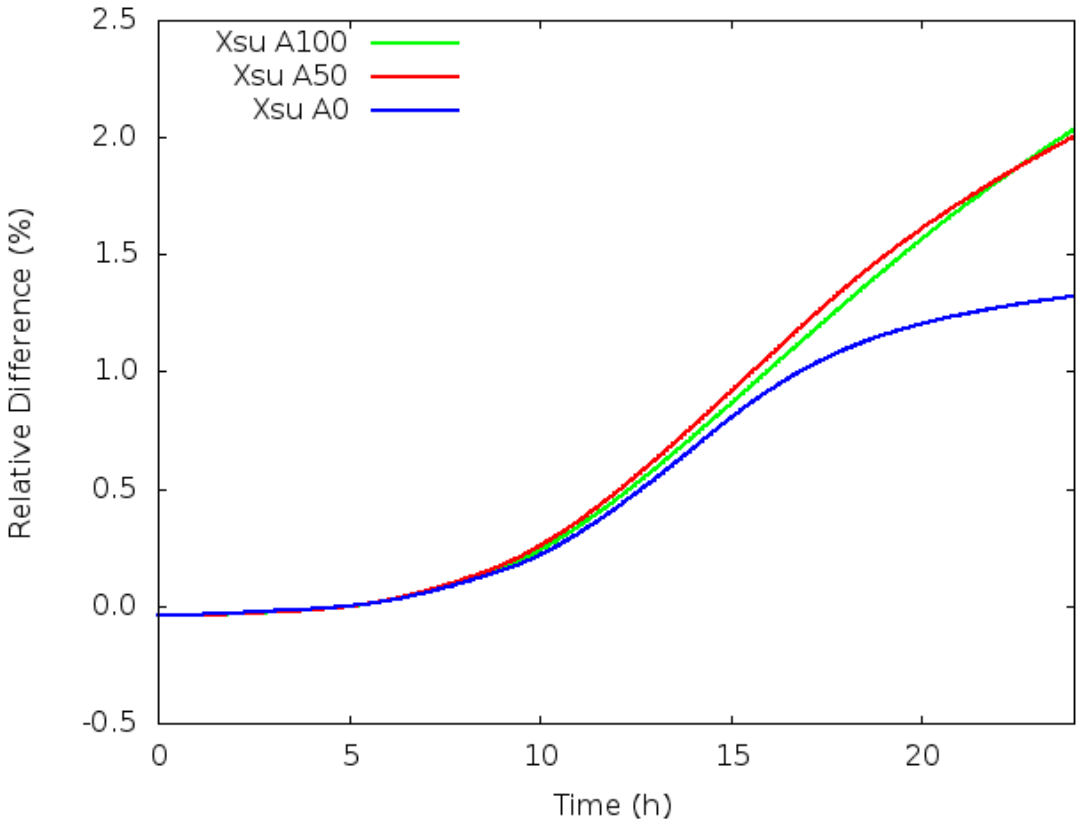
Xsu A100
Xsu A50
Xsu A0
Relative Difference (%)
Time (h)
2.5
2.0
1.5
1.0
0.5
0.0
-0.5
0
5
10
15
20

I.iii ADM1 processes rates

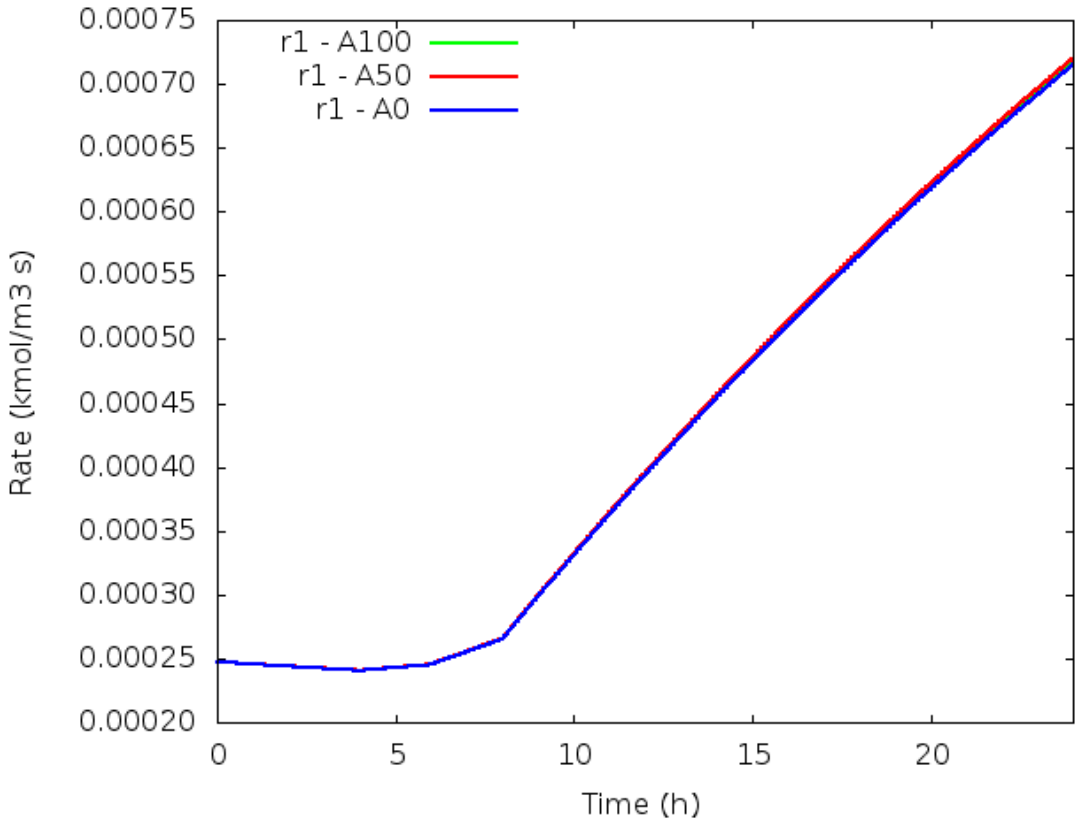

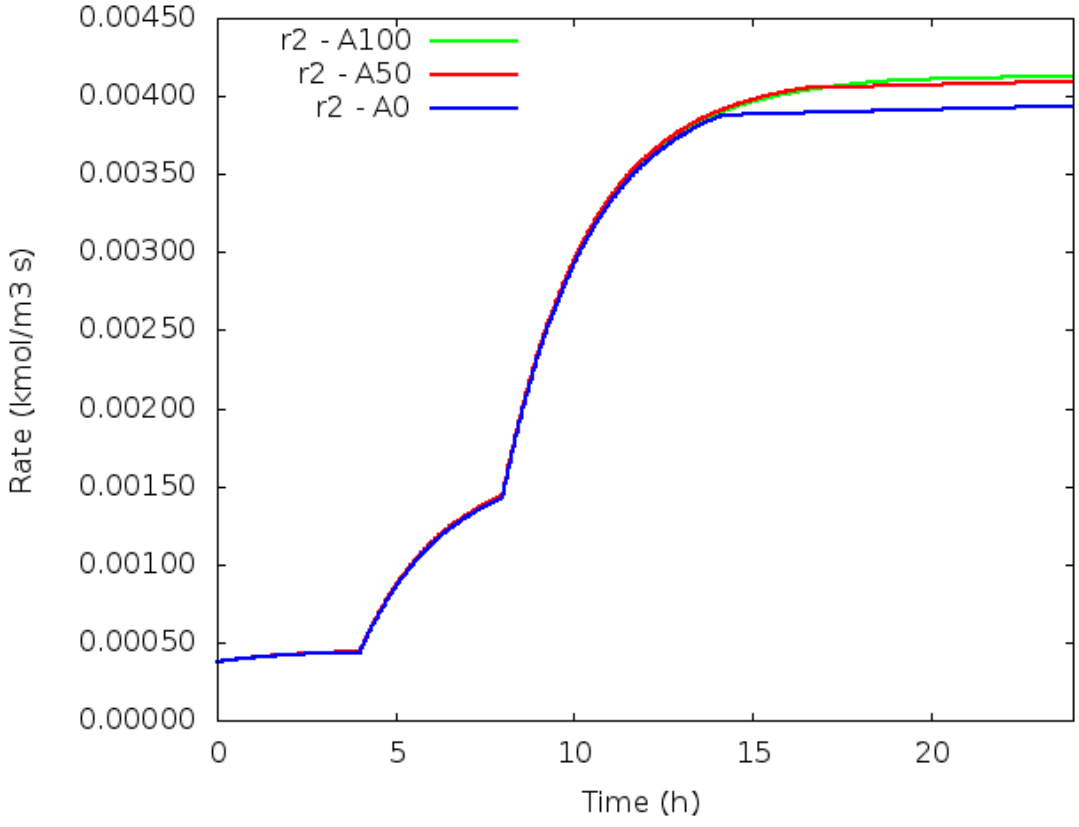

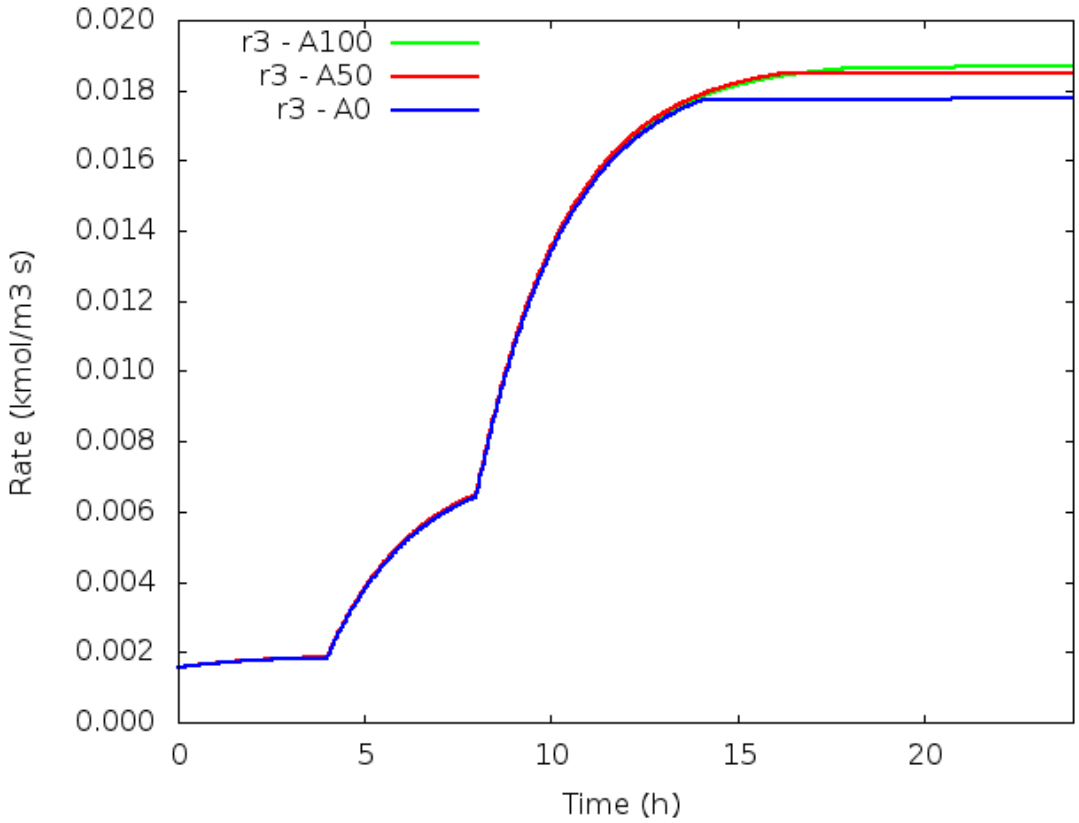
r3 - A100
r3 - A50
r3 - A0
Rate (kmol/m3 s)
Time (h)
0.020
0.018
0.016
0.014
0.012
0.010
0.008
0.006
0.004
0.002
0.000
0
5
10
15
20

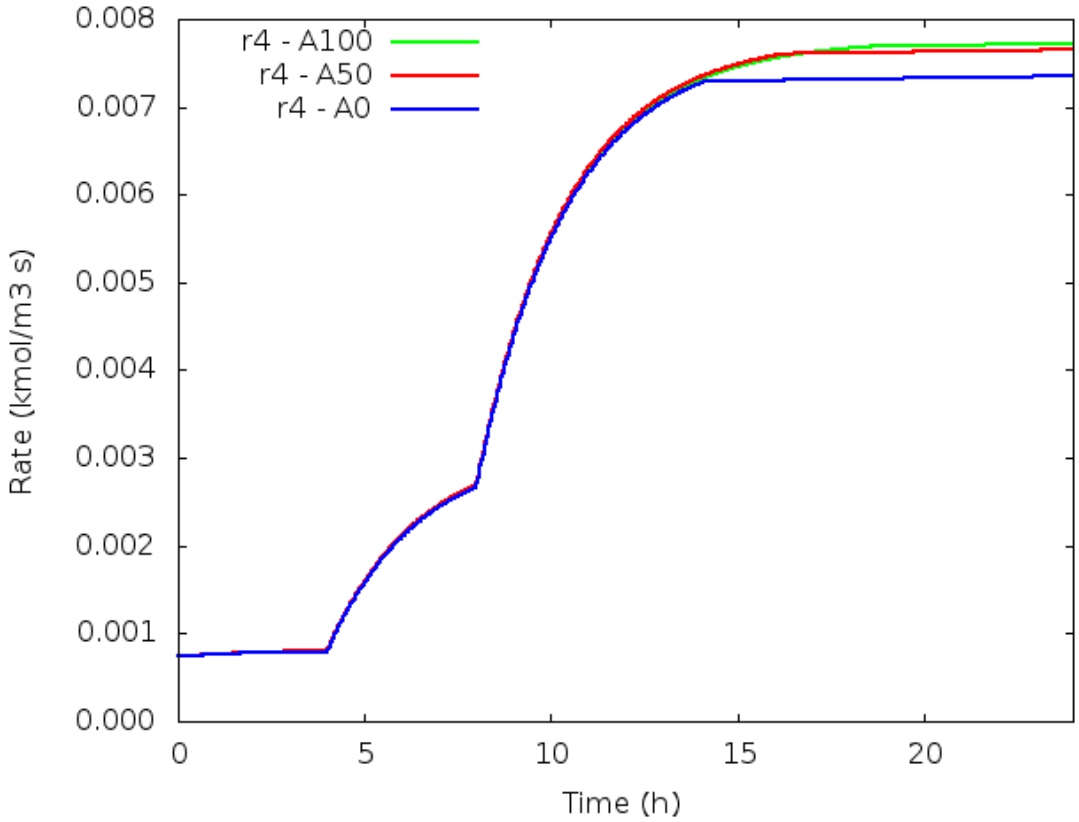
r4 - A100
r4 - A50
r4 - A0
Rate (kmol/m3 s)
Time (h)
0.008
0.007
0.006
0.005
0.004
0.003
0.002
0.001
0.000
0
5
10
15
20

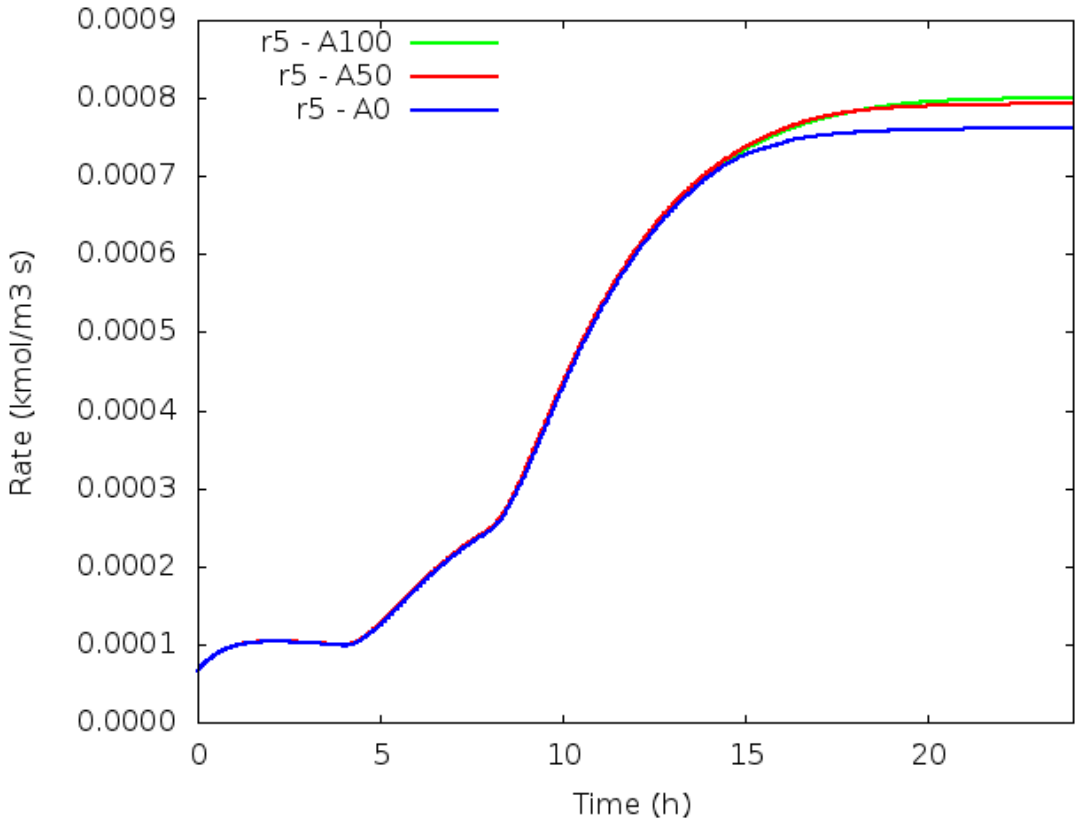
r5 - A100
r5 - A50
r5 - A0
Rate (kmol/m3 s)
Time (h)
0.0009
0.0008
0.0007
0.0006
0.0005
0.0004
0.0003
0.0002
0.0001
0.0000
0
5
10
15
20

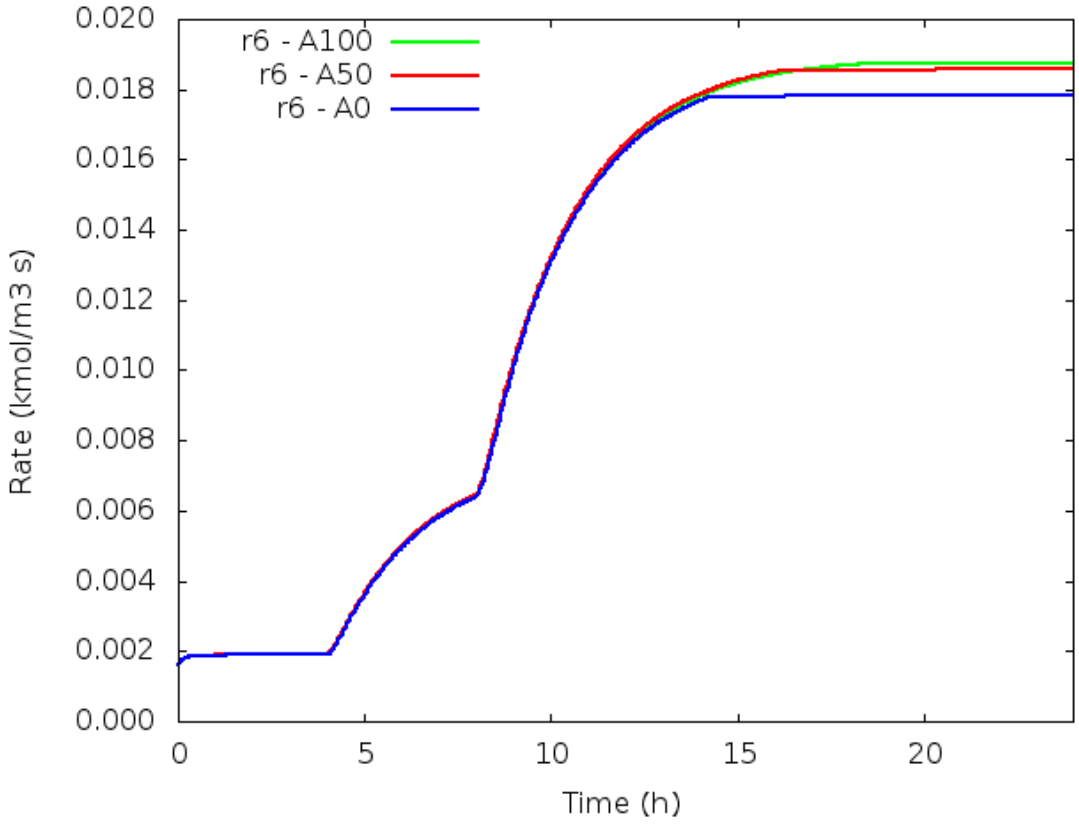
r6 - A100
r6 - A50
r6 - A0
Rate (kmol/m3 s)
Time (h)
0.020
0.018
0.016
0.014
0.012
0.010
0.008
0.006
0.004
0.002
0.000
0
5
10
15
20

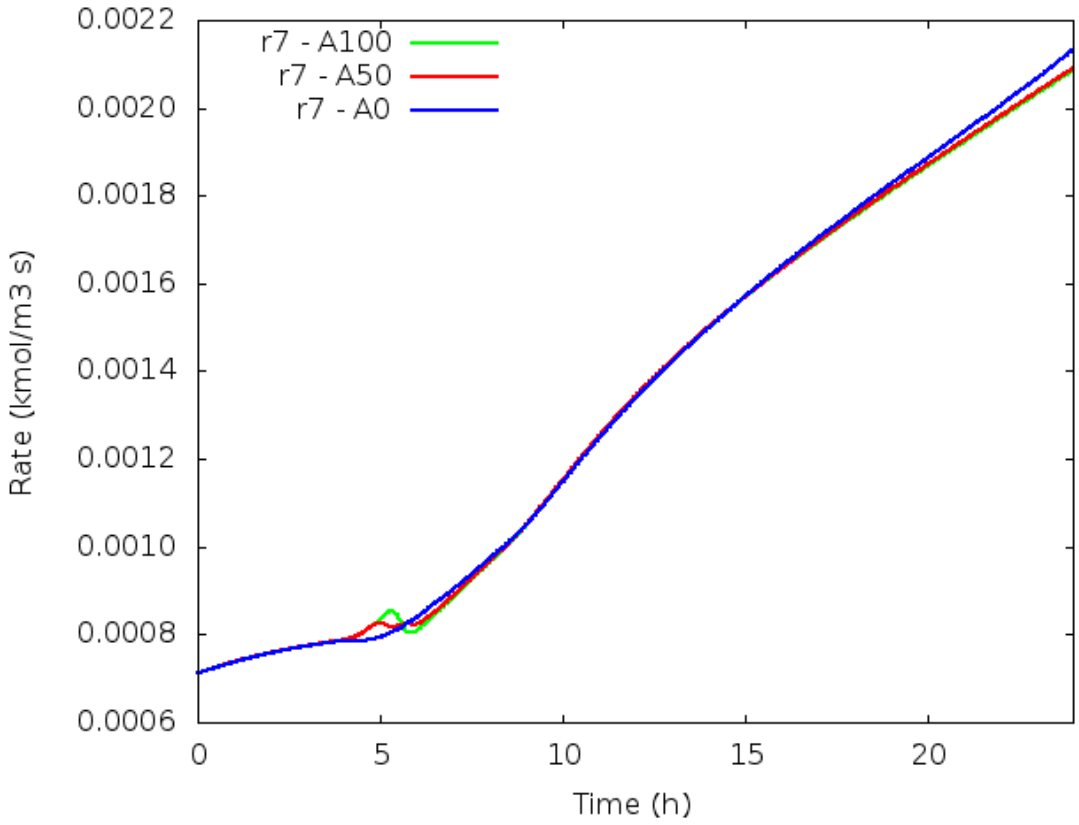
r7 - A100
r7 - A50
r7 - A0
Rate (kmol/m3 s)
Time (h)
0.0022
0.0020
0.0018
0.0016
0.0014
0.0012
0.0010
0.0008
0.0006
0
5
10
15
20

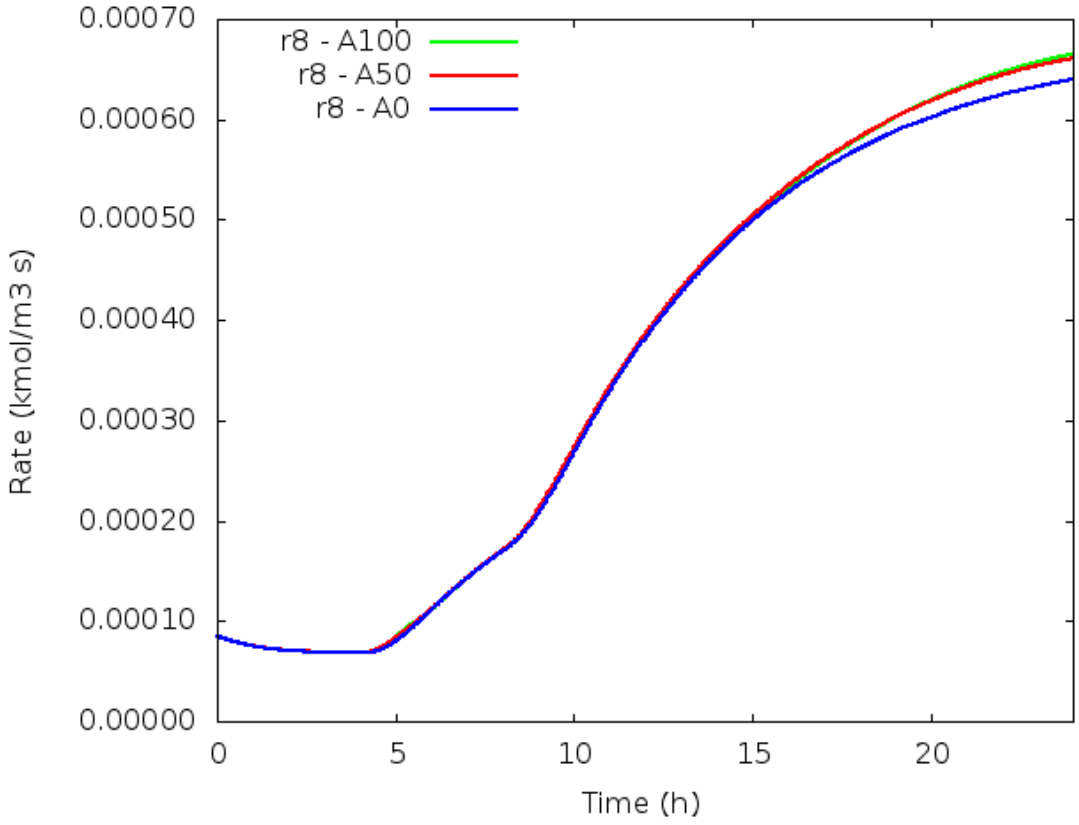
r8 - A100
r8 - A50
r8 - A0
Rate (kmol/m3 s)
Time (h)
0.00070
0.00060
0.00050
0.00040
0.00030
0.00020
0.00010
0.00000
0
5
10
15
20

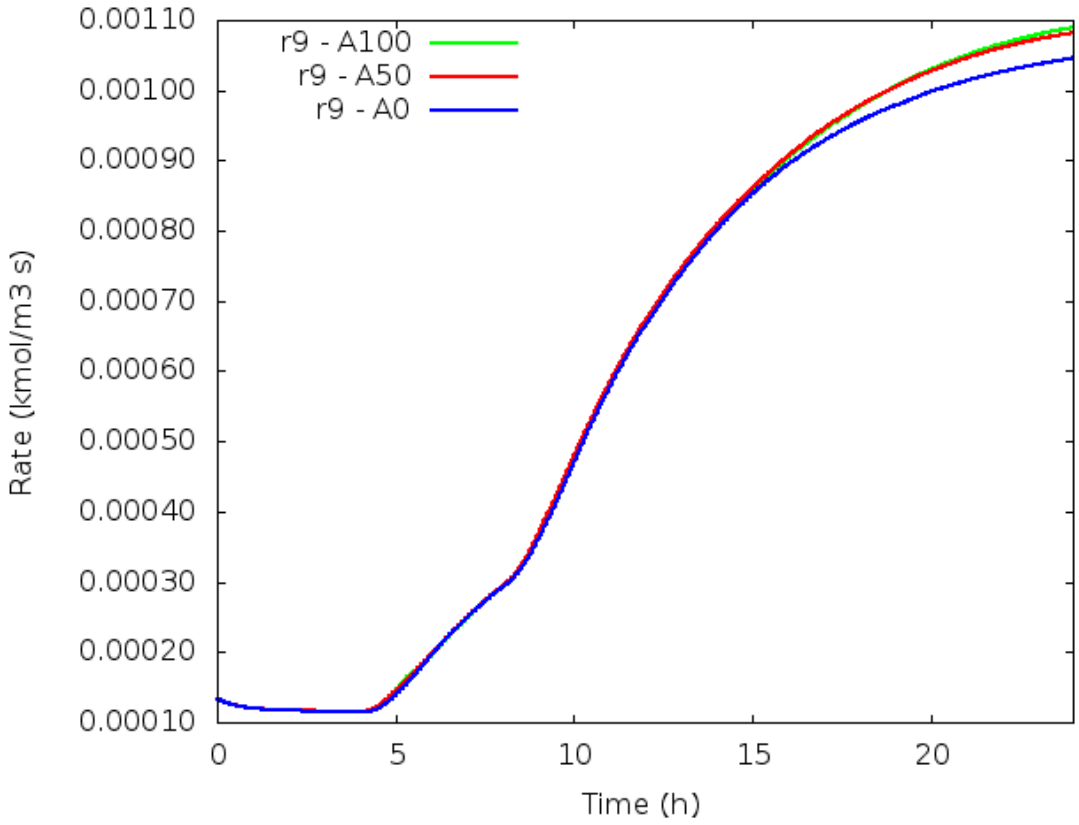
r9 - A100
r9 - A50
r9 - A0
Rate (kmol/m3 s)
Time (h)
0.00110
0.00100
0.00090
0.00080
0.00070
0.00060
0.00050
0.00040
0.00030
0.00020
0.00010
0
5
10
15
20

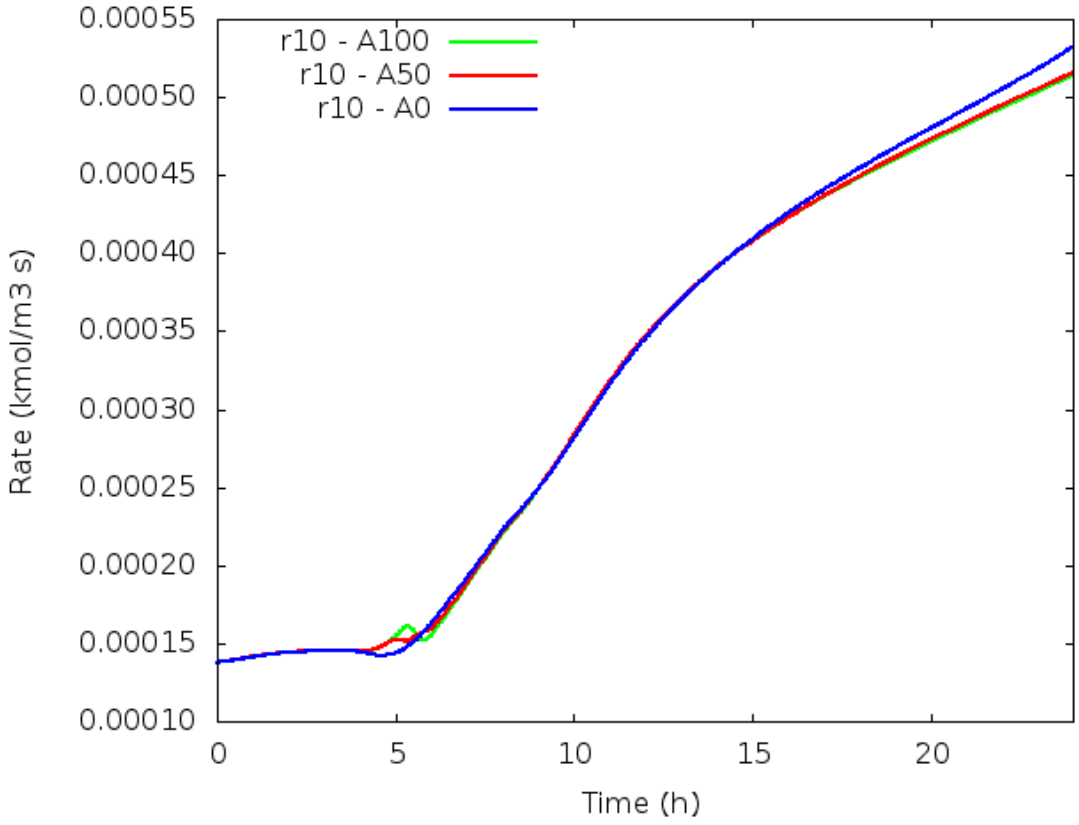
r10 - A100
r10 - A50
r10 - A0
Rate (kmol/m3 s)
Time (h)
0.00055
0.00050
0.00045
0.00040
0.00035
0.00030
0.00025
0.00020
0.00015
0.00010
0
5
10
15
20

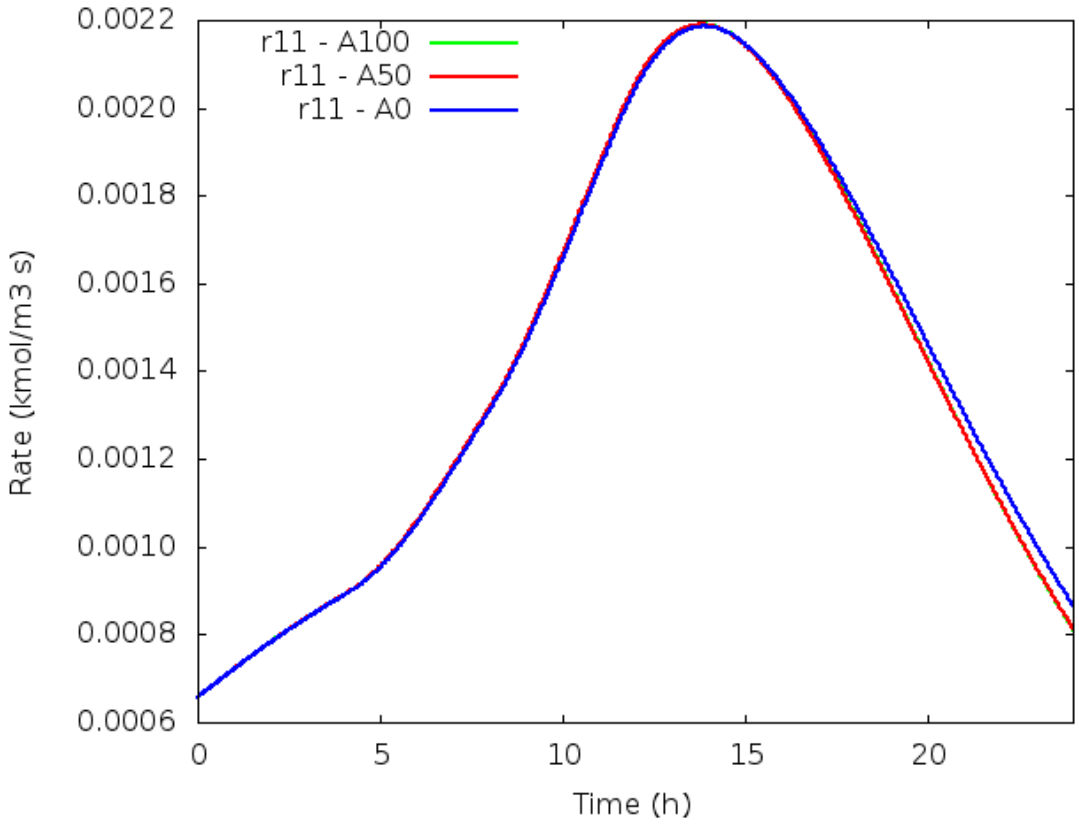
r11 - A100
r11 - A50
r11 - A0
Rate (kmol/m3 s)
Time (h)
0.0022
0.0020
0.0018
0.0016
0.0014
0.0012
0.0010
0.0008
0.0006
0
5
10
15
20

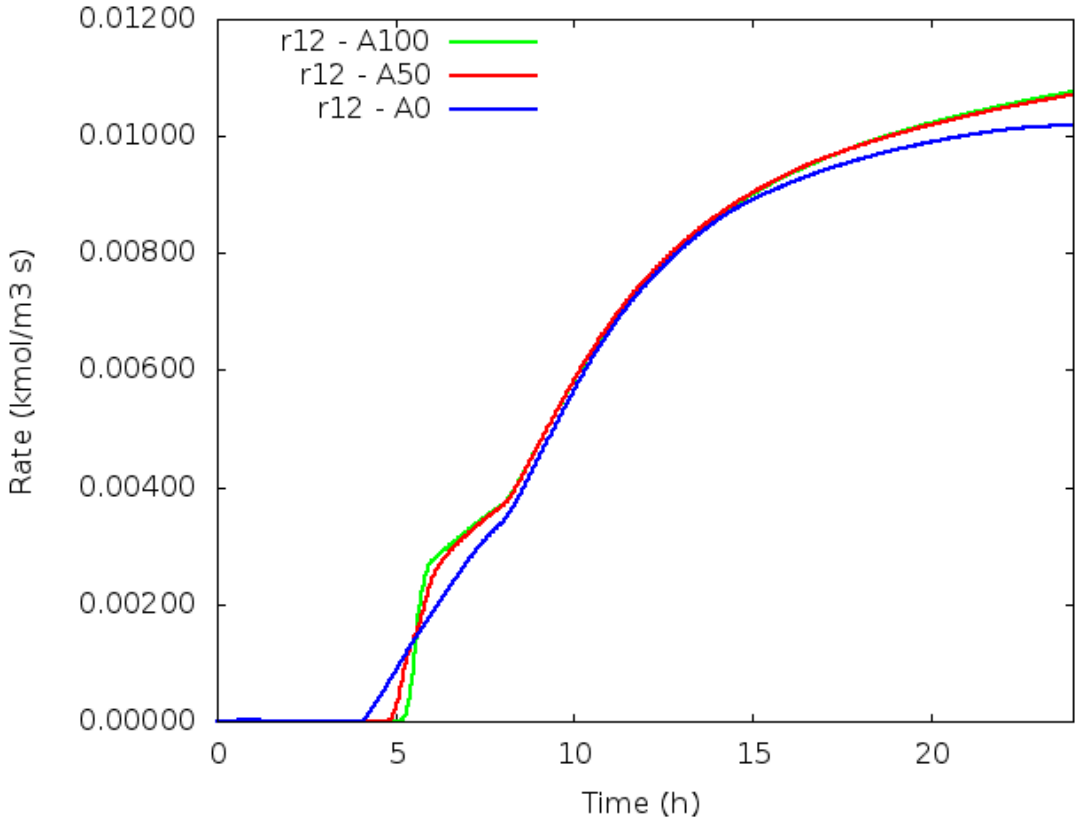
r12 - A100
r12 - A50
r12 - A0
Rate (kmol/m3 s)
Time (h)
0.01200
0.01000
0.00800
0.00600
0.00400
0.00200
0.00000
0
5
10
15
20

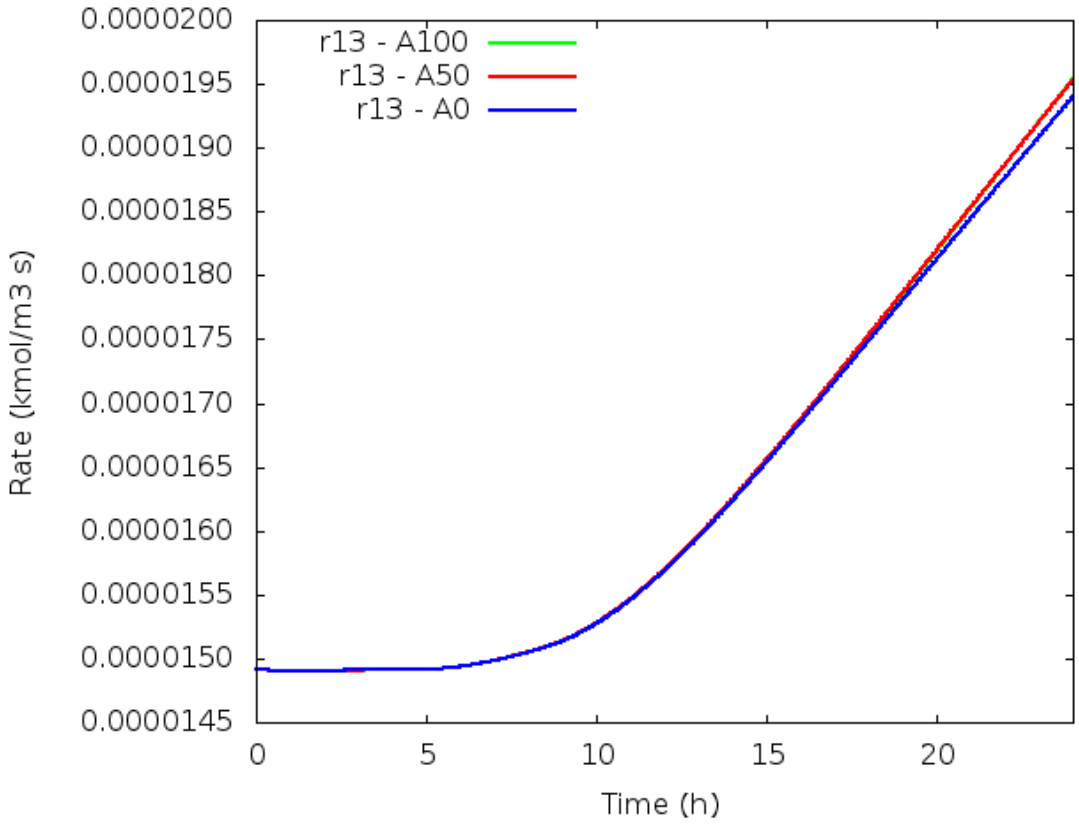
r13 - A100
r13 - A50
r13 - A0
Rate (kmol/m3 s)
Time (h)
0.0000200
0.0000195
0.0000190
0.0000185
0.0000180
0.0000175
0.0000170
0.0000165
0.0000160
0.0000155
0.0000150
0.0000145
0
5
10
15
20

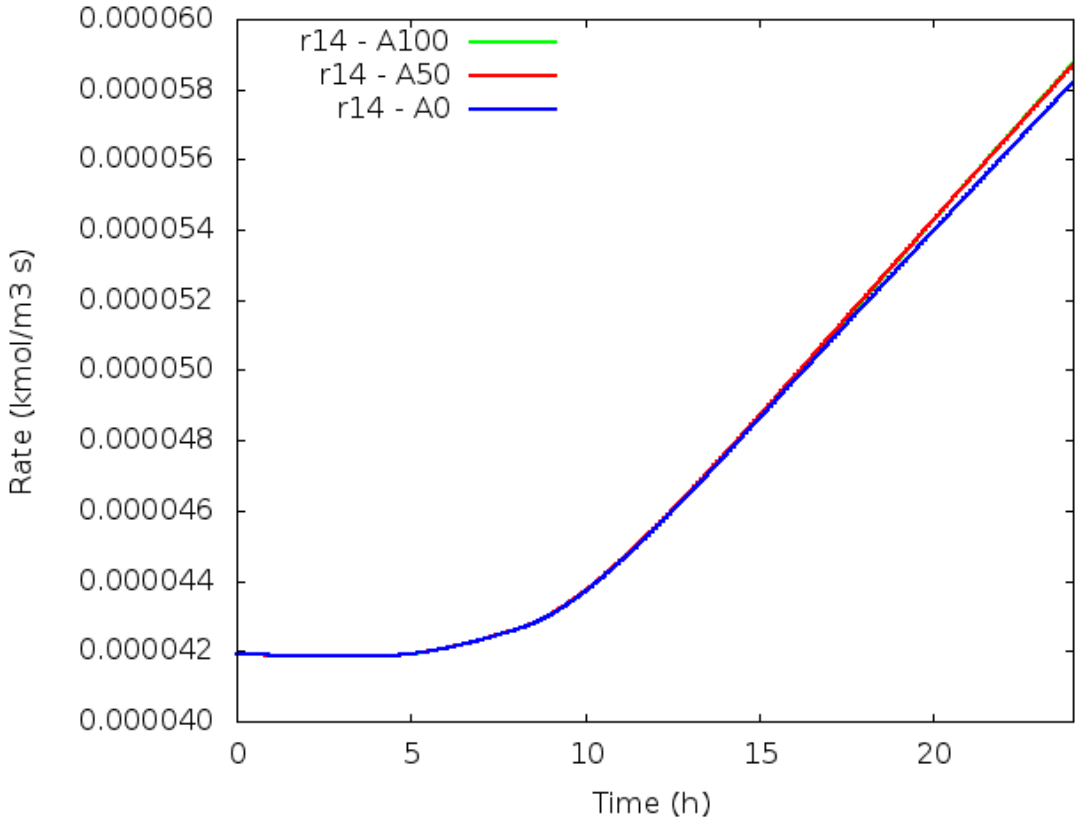
r14 - A100
r14 - A50
r14 - A0
Rate (kmol/m3 s)
Time (h)
0.000060
0.000058
0.000056
0.000054
0.000052
0.000050
0.000048
0.000046
0.000044
0.000042
0.000040
0
5
10
15
20

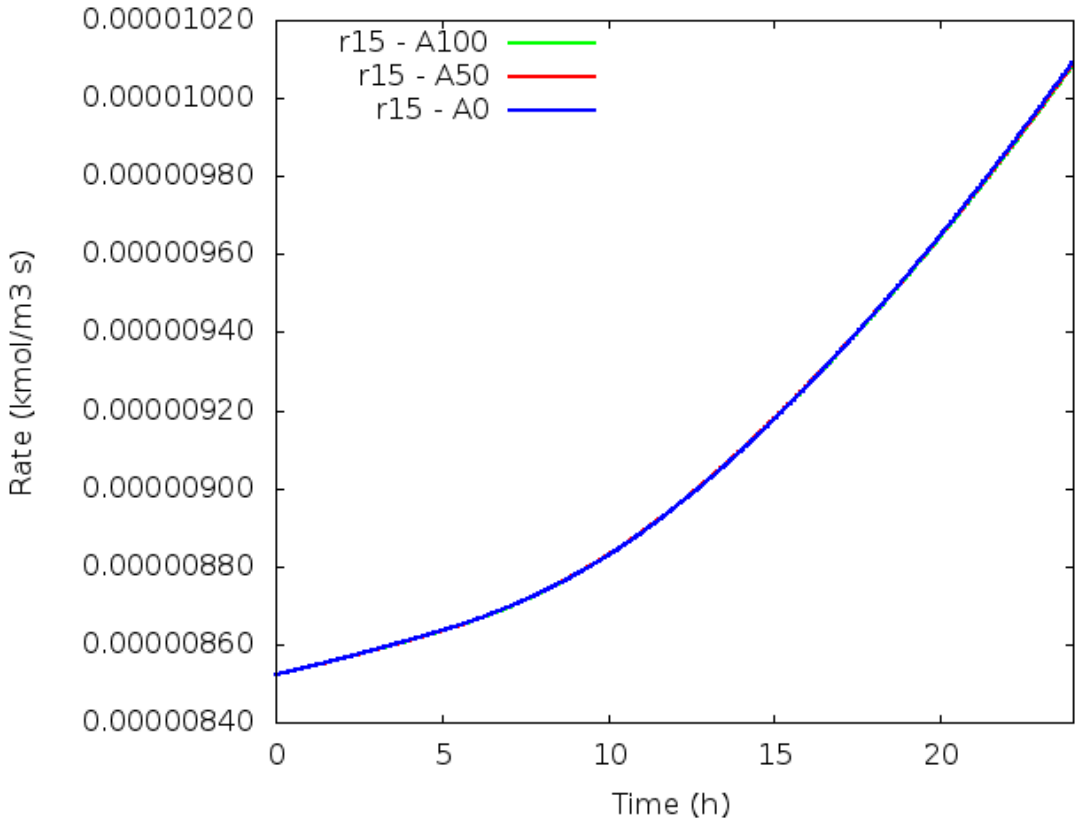
r15 - A100
r15 - A50
r15 - A0
Rate (kmol/m3 s)
Time (h)
0.00001020
0.00001000
0.00000980
0.00000960
0.00000940
0.00000920
0.00000900
0.00000880
0.00000860
0.00000840
0
5
10
15
20

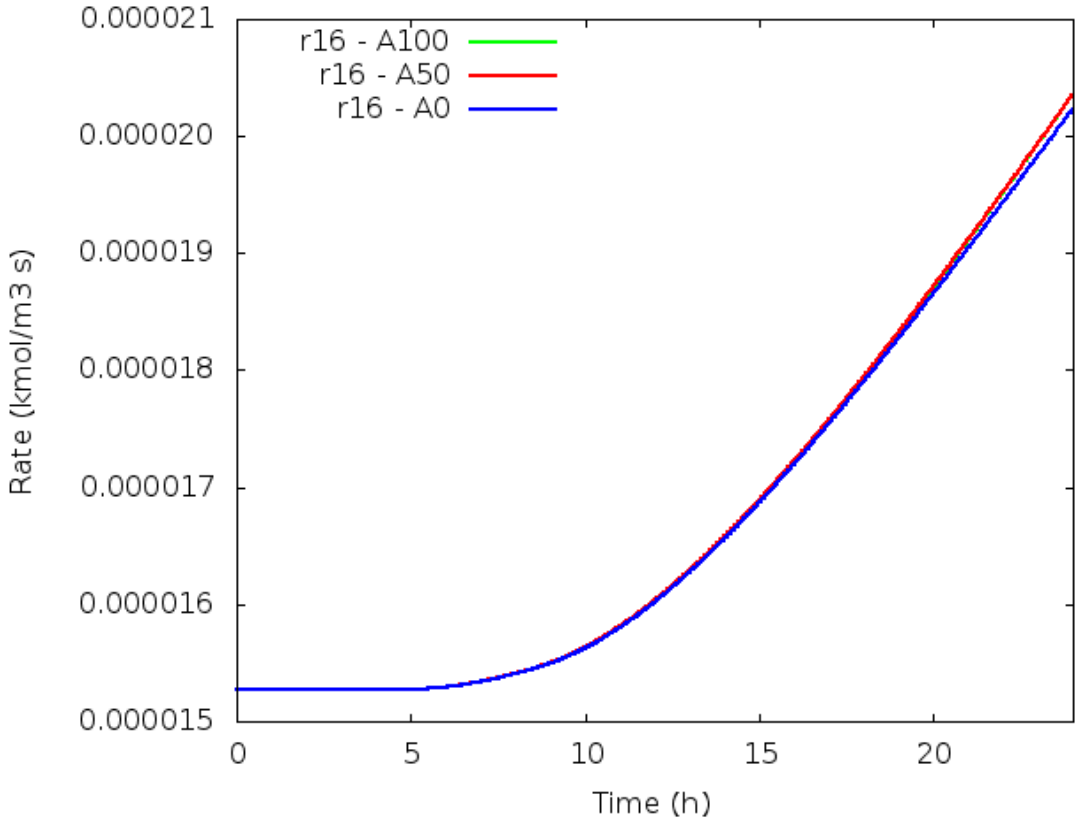
r16 - A100
r16 - A50
r16 - A0
Rate (kmol/m3 s)
Time (h)
0.000021
0.000020
0.000019
0.000018
0.000017
0.000016
0.000015
0
5
10
15
20

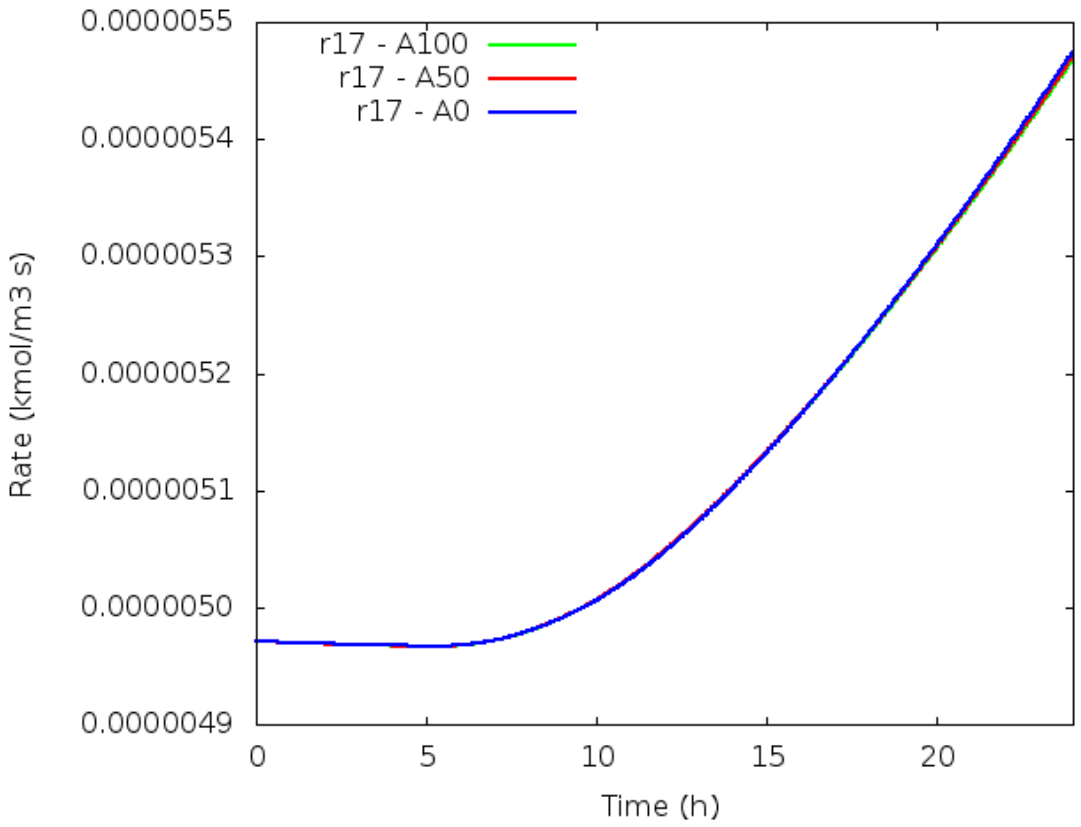
r17 - A100
r17 - A50
r17 - A0
Rate (kmol/m3 s)
0.0000055
0.0000054
0.0000053
0.0000052
0.0000051
0.0000050
0.0000049
0
5
10
15
20
Time (h)

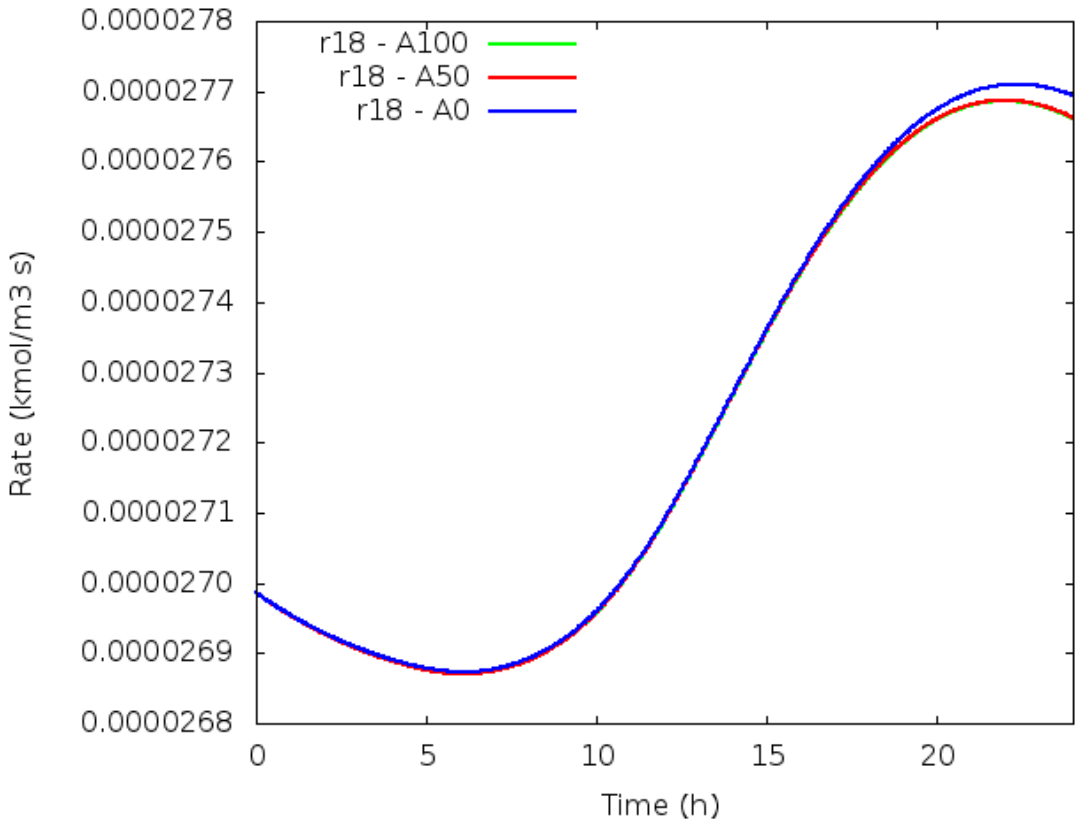
r18 - A100
r18 - A50
r18 - A0
Rate (kmol/m3 s)
0.0000278
0.0000277
0.0000276
0.0000275
0.0000274
0.0000273
0.0000272
0.0000271
0.0000270
0.0000269
0.0000268
0
5
10
15
20
Time (h)

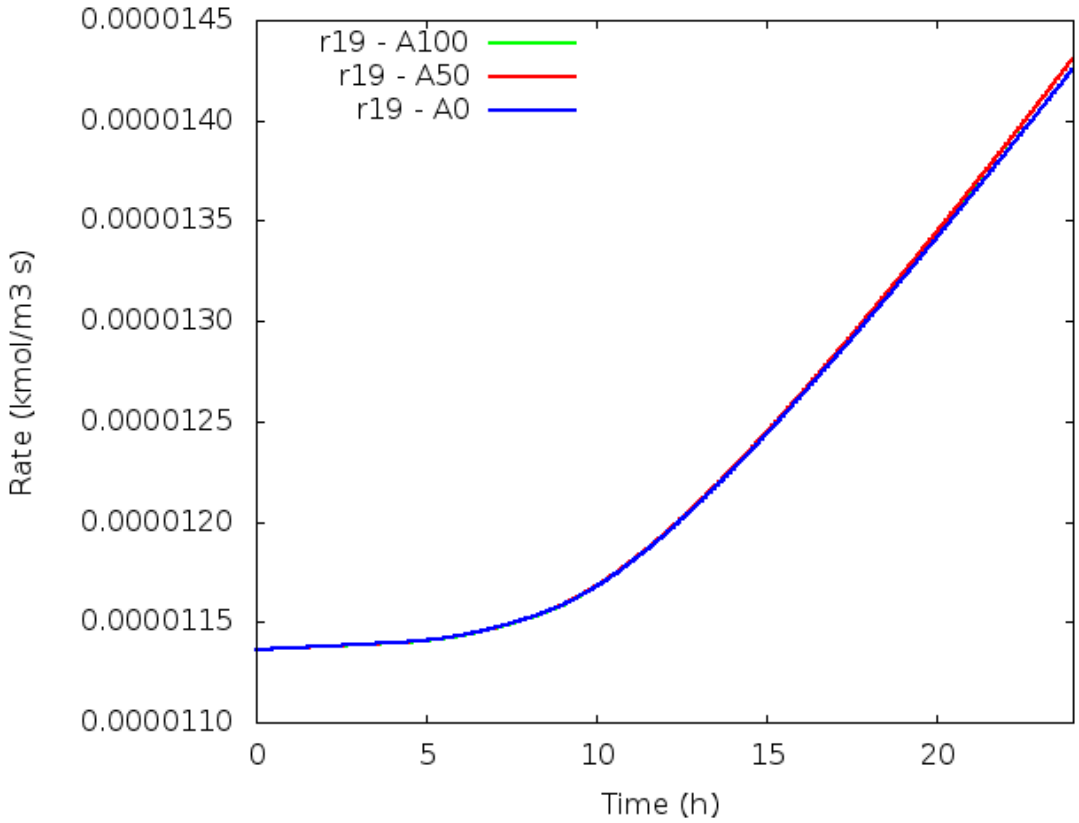
r19 - A100
r19 - A50
r19 - A0
Rate (kmol/m3 s)
Time (h)
0.0000145
0.0000140
0.0000135
0.0000130
0.0000125
0.0000120
0.0000115
0.0000110
0
5
10
15
20

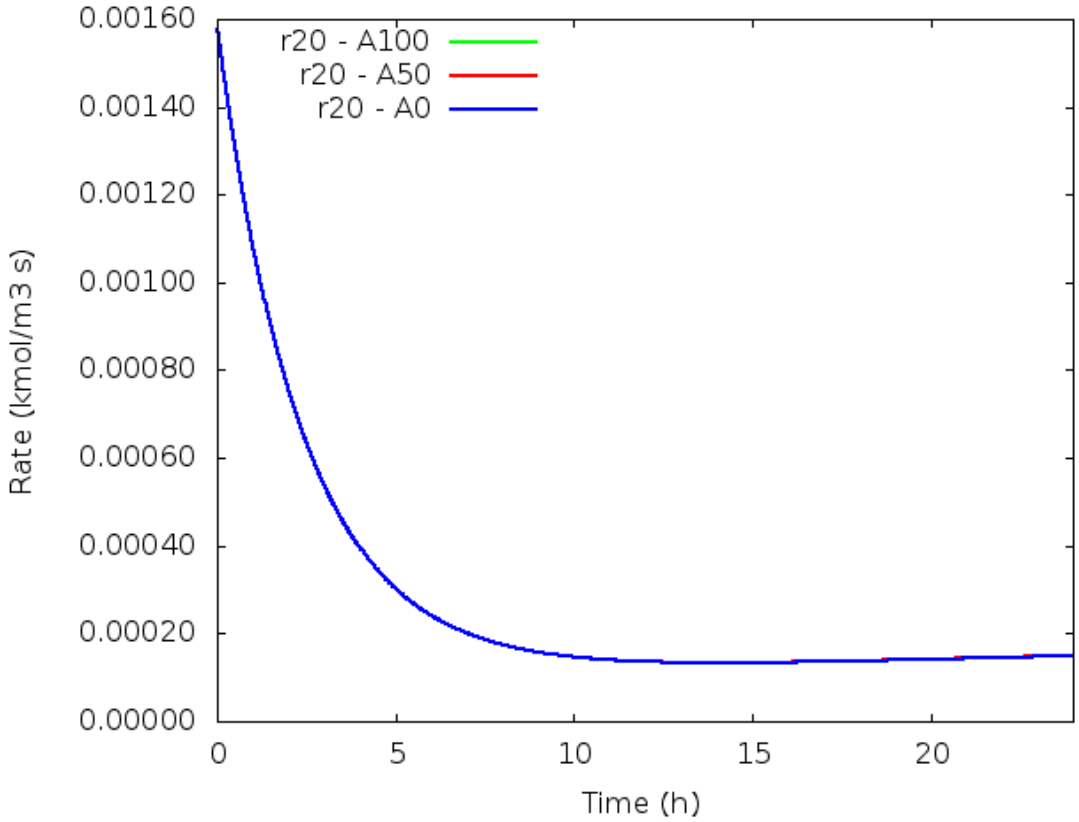
r20 - A100
r20 - A50
r20 - A0
Rate (kmol/m3 s)
Time (h)
0.00160
0.00140
0.00120
0.00100
0.00080
0.00060
0.00040
0.00020
0.00000
0
5
10
15
20

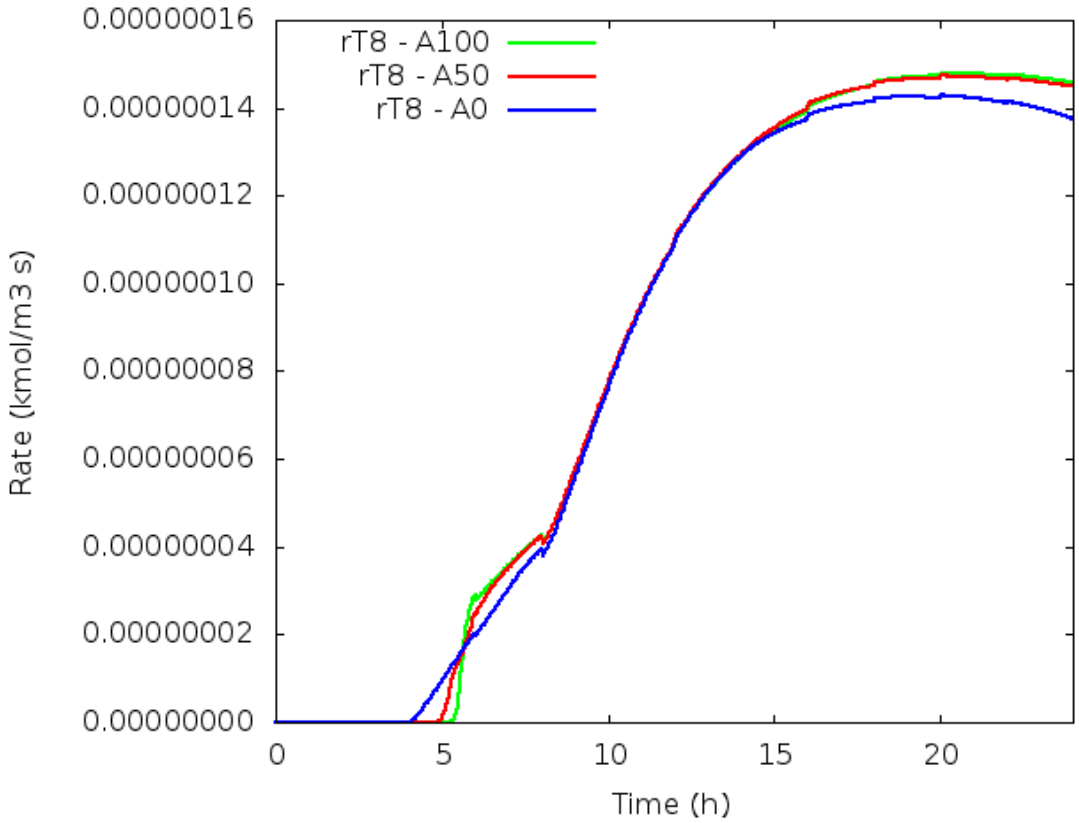
rT8 - A100
rT8 - A50
rT8 - A0
Rate (kmol/m3 s)
Time (h)
0.00000016
0.00000014
0.00000012
0.00000010
0.00000008
0.00000006
0.00000004
0.00000002
0.00000000
0
5
10
15
20

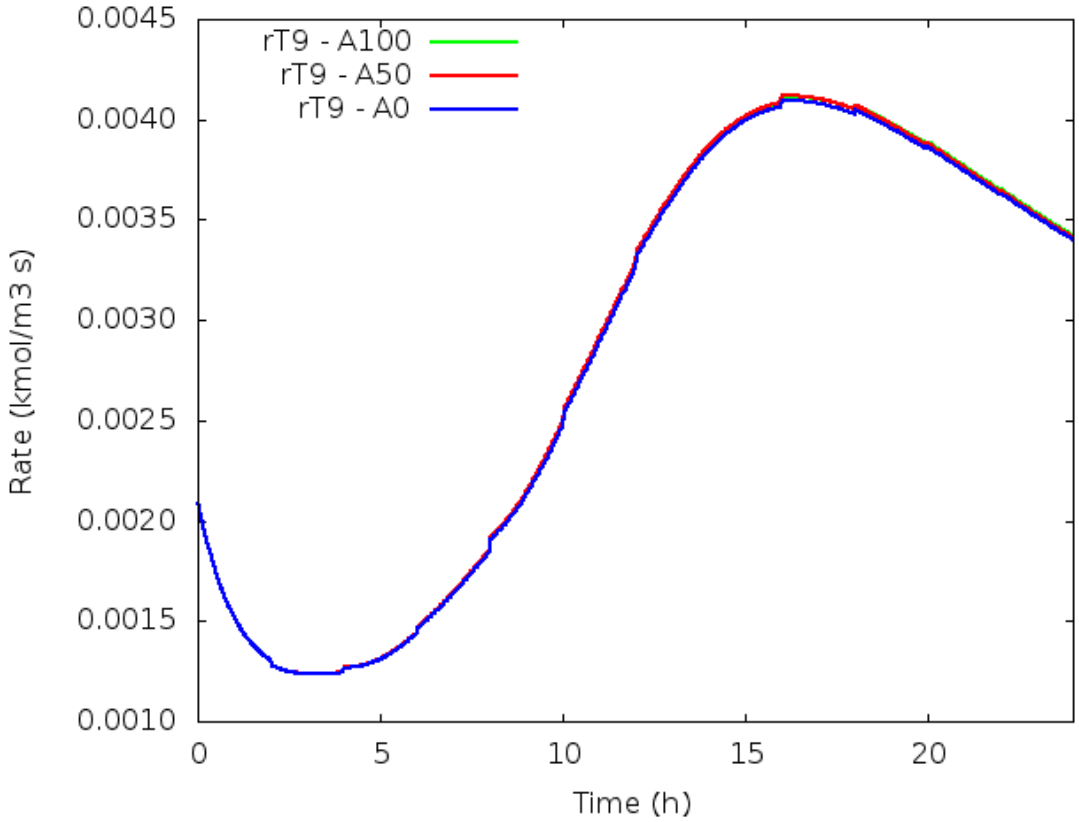
rT9 - A100
rT9 - A50
rT9 - A0
Rate (kmol/m3 s)
Time (h)
0.0045
0.0040
0.0035
0.0030
0.0025
0.0020
0.0015
0.0010
0
5
10
15
20

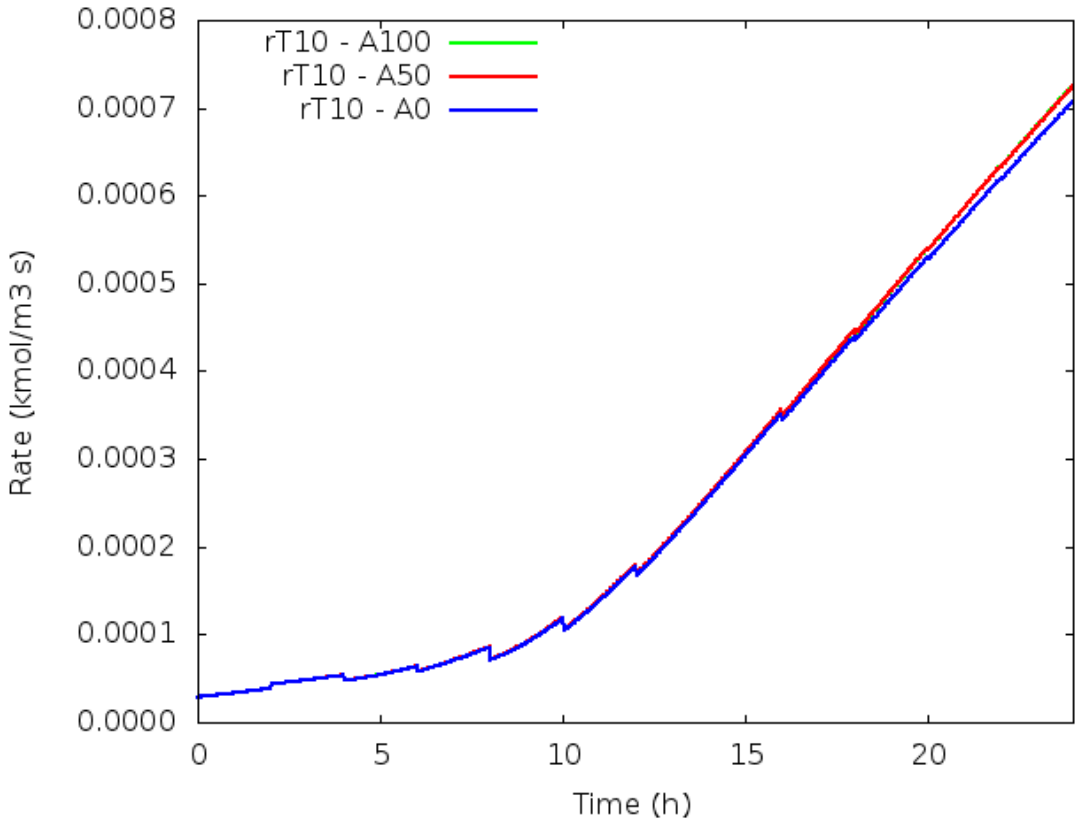
rT10 - A100
rT10 - A50
rT10 - A0
Rate (kmol/m3 s)
Time (h)
0.0000
0.0001
0.0002
0.0003
0.0004
0.0005
0.0006
0.0007
0.0008
0
5
10
15
20